

Résumés

22^{ème} Colloque Louis Néel

Vogüé



17-20 juin 2025

Programme des Journées

	Mardi	Mercredi	Jeudi	Vendredi
Matin		Oraux session 1 8h20-10h30	Oraux session 4 8h30-10h50	Oraux session 5 8h30-10h30
		Pause café	Pause café	Pause café
		Oraux session 2 11h00-13h00	Posters session 2 10h50-13h00	Oraux session 6 11h00-13h00
		Déjeuner	Déjeuner	Panier repas
Après-midi	Accueil et PEPR Spin 15h30-19h00 <i>Remise des clés à partir de 17h</i>	Oraux session 3 14h30-16h50	Rallye pédestre, temps libre 14h30-18h00	
		Pause café Posters session 1 16h50-19h00	Conférence invitée 18h00-19h00	
Soirée	Apéritif 19h45	Apéritif 19h00	Apéritif 19h00	
	Dîner 20h30	Dîner 20h00	Dîner de Gala 20h00	

Informations :

- Numéro de téléphone du village vacances Lou Capitelle : 04 75 37 71 32.
- Le petit-déjeuner est servi de 7h30 à 9h30.
- Les oraux se déroulent dans la salle « Ardèche ».
- Les présentations doivent être copiées sur l'ordinateur des oraux avant chaque session.
- Le français et l'anglais peuvent être utilisés, au choix, pour les présentations et les questions.
- Les sessions poster se déroulent sous la salle « Ardèche ».
- Les posters de la session 1 doivent être décrochés jeudi matin avant 10h50.
- Le dîner de Gala sera suivi d'une soirée dansante dans la salle « Ardèche ».
- Les chambres doivent être libérées pour vendredi 10h00.
- Les navettes pour la gare de Valence TGV partiront vendredi 20 Juin à 13h30.
- Piscine extérieure : 9h-12h et 15h-19h. les shorts de bain sont interdits.
- Piscine balnéo : 10h-12h, 15h-19h et nocturne le mercredi (21h-23h).

Le comité d'organisation est heureux de vous accueillir à cette nouvelle édition du colloque Louis Néel. Nous remercions chaleureusement les participants, les intervenants, ainsi que nos [partenaires et sponsors](#) pour leur contribution au succès de cet événement.

Comité d'organisation :

F. Tournus, A. Tamion, D. Le Roy, V. Dupuis, D. Farjot, J. Moreau.

Résumés

Oraux session 1 : Optique et dynamique ultra-rapide — Mercredi 8h30-10h30	10
Single-shot all-optical magnetization switching in ferrimagnetic Co-RE alloys single layers	11
All-optical helicity-dependent switching in magneto-plasmonic nanostructures	13
Ultrafast dynamics of magnetic structure in ferrimagnetic CoTb thin films	15
Magneto-optical distinction of magnetization dynamics from spin currents and its role in switching mechanism in ferromagnetic spin valve	17
Magnetization switching for circular polarized LEDs	19
Exciting and probing high-frequency spin waves in BiYIG/Co heterostructure using laser pulses	21
Oraux session 2 : Nanomagnétisme et dynamique — Mercredi 11h00-13h00	23
Complex dynamics of nano-oscillators with dual vortex free layers coupled via spin-torques	24
Excitation of vortex gyration through non-linear interaction with Floquet magnon modes	26
Complexity Analysis of Chaotic Magnetization Dynamics	28
Development of an ultrasensitive skyrmion-based magnetic field sensor	30
Antiferromagnetic order control in 2D CrSBr	32
Imaging magnetic vortices in a van der Waals magnet at room temperature with scanning NV magnetometry	33
Oraux session 3 : Spintronique et matériaux — Mercredi 14h30-16h50	34
Composition-dependent charge-to-spin current conversion in topological insulators $\text{Bi}_{1-x}\text{Sb}_x$ thin films	35
Spin-dependent transport properties of epitaxial DyVO_3 and GdVO_3 thin films on (110)-oriented NdGaO_3 substrate	37
Large Orbital Rashba Edelstein Effect induced Torques in Atomically Thin Co/Al Systems	39
Alternative harmonic detection approach for quantitative determination of spin and orbital torques	41
Proximity Effects In Superconductor/Magnetic Epitaxial Heterostructures With Magnetic Noncollinearity	43
Orbital-to-spin conversion material exploration for improving SOT-MTJ performances	45
Low Temperature Out-of-Plane Nonlinear Hall Effect in Epitaxial GeTe	47
Oraux session 4 : Systèmes neuro-inspirés — Jeudi 8h30-10h50	48
Synaptic metaplasticity in a magnetoionic synapse	49
Neuromorphic weighted sums with magnetic skyrmions	51
Dynamic control of weight-update linearity in magneto-ionic synapses	53
Exploiting spin textures in a magnetic tunnel junction for logic and neuromorphic computing applications	55
Towards a spintronic Ising Machine simulator	57
Experimental implementation of a programmable Ising Machine using vortex-based Spin-Torque Nano-Oscillators	59
Non-volatile binary radio-frequency synapses using vortex polarities	61
Conférence invitée — Jeudi 18h00-19h00	63
From Ampère's Molecular Currents to the Magnetism of Materials : Einstein's Role	64
Oraux session 5 : Ondes de spin & imagerie — Vendredi 8h30-10h30	65
Spatially Resolved Investigation of Spin Wave Frequency Multiplication	66
Imaging of domain-wall motion and spin-wave propagation in cylindrical nanowires with a 3D core-shell magnetization distribution	68
Magneto-resistive detection of spin-waves	70
Unravelling spin-wave propagation regimes using NV magnetometry	72
Imaging spin waves by Electron Holography	74
Spectroscopy of the spin wave acoustic mode in synthetic antiferromagnets	76
Oraux session 6 : Magnéto-phononique & ondes — Vendredi 11h00-13h00	78
Giant magneto-elasticity & strong phonon-magnon coupling in FeRh.	79
Phononic manipulation of magnetic domains in Co-doped YIG : from a labyrinth to stripes and bubbles	81
Coupling the orbital angular momentum of elastic waves with the gyromotion of a magnetic vortex	83
Structural and Magnetic Insights into Ti/Mn-Substituted Hexaferrite Thick Films for Applications beyond 20 GHz.	85
A study of non-reciprocal behaviors in multi-sphere loaded chiral cavity	87
Experimental observations of Suhl instabilities in a 500nm Bismuth Yttrium Iron Garnet disk	89
Posters session 1— Mercredi 16h50-19h00	91
Magnetoresistance-based current limiter — S1P1	92
Imprinting of skyrmions and bimerons in a thin film of an antiferromagnet — S1P2	93
Giant stability of nanoscale skyrmions and bimerons in oxidized van der Waals Fe_3GeTe_2 — S1P3	95
Altermagnetic variants in thin films of Mn_5Si_3 — S1P4	96
Asymptotically exact formulas for the stripe domains period in ultrathin ferromagnetic films with out-of-plane anisotropy — S1P5	97

Spin-Orbit-Torque in Co/Al interfaces — S1P6	99
Metallicity regeneration of chemically ordered FeRh nanoparticles studied by in situ UHV spectroscopy — S1P7	100
<i>Ab initio</i> study of nanoscale skyrmions and bimerons in atomically thin van der Waals layers — S1P8	102
Stability of high-Q topological spin textures beyond skyrmions in a van der Waals heterostructure — S1P9	104
Ultrafast dynamics of a spin-polarized electron gas — S1P10	105
Interlayer dipolar fields stabilize bimerons without Dzyaloshinskii-Moriya interaction in magnetic bilayers — S1P11	107
Addressing bottlenecks in fabrication and reading/writing procedures for PSA-STT-MRAMs — S1P12	108
Altermagnetism from Orbital Ordering the Ruddelsden-Popper Chromates — S1P13	110
Engineering magnetic domain wall energies in multiferroic BiFeO ₃ via epitaxial strain — S1P14	111
Towards switchable magnetic tunnel junctions based on polyoxometalates monolayer — S1P15	112
Design of an arithmetic logic unit (ALU) using ferroelectric spin orbit (FESO) devices — S1P16	114
Vortex gyrotropic mode excited by surface acoustic waves — S1P17	116
Towards ultrafast deterministic switching in magnetic memory by laser excitation — S1P18	117
Study of skyrmions in ferromagnetic metallic superlattices using in situ Lorentz magnetic methods — S1P19	119
Optimization of synthesis and growth of layered ferromagnetic oxide — S1P20	121
Polarization analysis of multi-magnon excitations in LaFeO ₃ thin films using RIXS — S1P21	122
Imaging Antiferromagnetic Texture in Epitaxial Mn ₃ Sn Thin Films with Scanning NV center Magnetometry — S1P22	124
Probing the antiferromagnetic to ferromagnetic transition in FeRh using surface acoustic waves — S1P23	126
THz emission from topological spintronics elements probed by electro-optic sampling (EOS) — S1P24	128
Level attraction in a quasiclosed cavity: Antiresonance in magnonic devices — S1P25	130
Unraveling temperature-dependent spin-polarized electron transport in Fe via spin-wave Doppler shift — S1P26	132
Nonreciprocal spin waves in adaptive Bi-YIG nanomagnonic devices utilizing domain walls — S1P27	134
Engineering Spin Wave dispersion and Surface Acoustic Wave-driven FMR in Fe thin films by N-implantation — S1P28	135
Revealing the three-dimensional nature of the field-driven movement of magnetic topological defects — S1P29	137
Unconventional flat lifetimes of solitons in 2D easy-plane magnets — S1P30	138
Carbon Doping Effects on MgO Tunneling Barriers and Their Influence on Magnetic Tunnel Junction Noise — S1P31	140
Étude de textures magnétiques générées par impulsion laser sur couches minces — S1P32	142
Étude de la désaimantation ultrarapide des alliages et multicouches CoPt par dichroïsme circulaire magnétique des rayons X — S1P33	144
A step forward with 3D spintronics: electrical control of cocoons — S1P34	146
Entropy-Assisted Nanosecond Stochastic Operation in Perpendicular Superparamagnetic Tunnel Junctions — S1P35	148
Eigenmode following for magnetic lifetime calculations beyond harmonic approximation — S1P36	150
Growth, characterization and THz time-domain spectroscopy of Bi _{1-x} Sb _x /Co — S1P37	152
Inverse Rashba Edelstein THz emission modulation induced by ferroelectricity in van der Waals heterostructures — S1P38	154
Detection of magnetic textures via 3-Terminal MRAM devices — S1P39	156
Strategies to measure picoTesla magnetic fields in space — S1P40	157
Passive microwave rectification in perpendicular magnetic tunnel junctions for wireless sensor networks — S1P41	159
Reconfiguring Tunnel Magnetoresistance sensors with Spin-Orbit Torque — S1P42	161
Spin-wave and mechanical modes of suspended YIG microdisks — S1P43	163
Coercivity-driven surface acoustic wave ferromagnetic resonance — S1P44	165
Non-reciprocal caustic spin-wave beams in extended ferromagnetic film — S1P45	167
Spin Hall magnetoresistance at the altermagnetic insulator/Pt interface — S1P46	169
Direct CVD graphene integration for Spintronics — S1P47	171
Depth-resolved magnetization dynamics in Fe thin films after ultrafast laser excitation — S1P48	173
Proximity effect between 2D ferromagnetic and 2D ferroelectric materials — S1P49	175
Epitaxial growth of (LaVO ₃) _n /(PrVO ₃) _m superlattices for emerging multiferroicity — S1P50	177
Contribution of non-uniform magnetization states to the initial susceptibility of soft magnetic materials — S1P51	179
Dissipation properties of altermagnetic versus ferromagnetic Hall devices — S1P52	181
Spin-wave circulation in unbounded ferromagnetic film — S1P53	183
Spin charge conversion with Homo and Hetero bilayers of TMDs : 1H/1T and 1T/1T case study — S1P54	185
Spin and orbital Rashba effects at the Ni/HfO ₂ interface — S1P55	187
Magnetic imaging under high pressure with a spin-based quantum sensor integrated in a van der Waals heterostructure — S1P56	189
Exploring Interconversion of Charge Current to Spin Current in Sputter-Deposited Topological Insulating Materials — S1P57	191
Static macromagnetic modelling of multilayers applied to spin-orbit torque characterization — S1P58	193
Exploring NbN-based stacks for superconducting spintronics — S1P59	195
Three terminal devices for improved efficiency — S1P60	197

Multistate MTJs crossbar arrays as hardware AI co-processors: coping with non-idealities — S1P61	198
Magnetic properties of $\text{YCo}_{12}\text{B}_6$ compound studied with neutrons, X-rays and macroscopic characterization techniques — S1P62	200
Micromagnetic analysis of skyrmion trajectories in weak Dzyaloshinskii-Moriya interaction system — S1P63	202
Efficiency of Spin Transfer Torque and Characteristic Switching Times in Unconventional Double-MgO Magnetic Memories — S1P64	204
Low-temperature epitaxial magnetic garnet thin films for quantum magnonics II — S1P65	206
Posters session 2— Jeudi 10h50-13h00	207
(Mis)estimation of spin-orbit torques in the presence of current-induced magnon creation and annihilation — S2P1	208
Method of analysis of the spectra obtained by microfocused Brillouin light scattering — S2P2	210
High-resolution X-ray spectroscopy of highly charged ions for magnetic surface investigation — S2P3	212
Magneto-Ionic Control of Magnetic Anisotropy in Pt/Co/Al Multilayers — S2P4	213
Gate controlled magnetoresistances on antiferromagnetic semiconductor 2D material — S2P5	215
Epitaxial growth of $\text{Mn}_5(\text{Si}_x\text{Ge}_{1-x})_3$ thin films on Ge(111) substrate by MBE: from ferro- to alter-magnetism? — S2P6	216
Spin-torque nano-oscillators for unconventional computing and wireless communication applications — S2P7	217
Self-learning physical neural networks utilising superparamagnetic tunnel junctions — S2P8	219
TMD Engineering of 2D-Magnetic Tunnel Junctions – From Barriers to Electrodes — S2P9	221
Deterministic modelling of ultrafast demagnetization in 3d ferromagnetic elements — S2P10	222
Magnetic properties of epitaxial Mn_4N films doped with non-magnetic elements — S2P11	224
Effets d'épaisseur et de température sur les propriétés magnétiques des systèmes à base de Ir/FeV — S2P12	225
Growth and Characterisation of the Non-Collinear Antiferromagnet Mn_3Sn — S2P13	227
All-inductive observation of linear dynamics and nonlinear processes of spin waves in synthetic antiferromagnets — S2P14	229
Electric field effects on the spin/orbital conversion into charge — S2P15	231
Neuro-Inspired Computing in k-Space: Harnessing Spin Wave Dynamics in YIG Microdisks — S2P16	233
Oersted field driven dynamics in spin-torque vortex oscillators — S2P17	235
Structural and magnetic characterization of $\text{Mn}_{100-x}\text{Sn}_x$ chiral antiferromagnets epitaxial films — S2P18	237
Periodic nanostructures subjected to mechanical stress: Experimental and numerical study of spin waves mode — S2P19	238
Terahertz emission using the spin and orbital Hall effect — S2P20	240
Inductive magnon noise spectroscopy of thermally excited magnons — S2P21	242
Metallised 3D printed plastic resonator demonstrates superconductivity below 4 K — S2P22	243
Using Artificial Intelligence to Explore Magnetic Topological Structures — S2P23	245
Convergence: A Flexible Tool for Developing Materials at SPINTEC — S2P24	247
Graphene/CoFeB-Based Heterostructures : Influence of Direct and Oxide-Separated Interfaces on Dynamic Magnetic Properties — S2P25	249
Stochastic phase dynamics of an array of coupled, injection-locked spin-torque nano-oscillators — S2P26	251
Singulus advanced thin-film deposition sputtering system: Capabilities and Applications — S2P27	253
Integration of new materials with strong spin-orbit coupling (van der Waals tellurides) for SOT-MRAM memories — S2P28	254
Interference effects in the parametric excitation of spin waves in confined geometry — S2P29	255
Embedded nano-magnets for thermoelectric applications — S2P30	257
Propagation of spin waves in magnetic non-uniform textures — S2P31	259
Optimisation de la sensibilité de capteurs AMR $\text{La}_{1-x}\text{Sr}_x\text{MnO}_3$ sur substrat vicinal SrTiO_3 par intégration de concentrateurs de flux magnétique — S2P32	261
Room temperature detectivity of anisotropic magnetoresistive sensors patterned in $\text{La}_{2/3}\text{Sr}_{1/3}\text{MnO}_3$ and in Cr_4Te_5 thin films — S2P33	263
Magnetoelectric coupling reprogrammed magnonic waveguides in multiferroic/ferromagnetic heterostructure — S2P34	265
Bi:YIG garnet thin films for spintronics — S2P35	267
Anomalous thermal drift of skyrmions in frustrated magnets under spin-orbit torques — S2P36	269
Magnetization dynamics in Bismuth-doped Yttrium Iron Garnet Films — S2P37	270
Enhancement of the current-induced torque by orbital torque — S2P38	271
SOT- and Magnetic Field-Driven Domain Wall Dynamics — S2P39	273
Influence of applied deformation on magnetic properties: ferromagnetic $\text{Ni}_{60}\text{Fe}_{40}$ thin films deposited on polymeric substrate — S2P40	275
Dzyaloshinskii-Moriya interaction in Fe_5GeTe_2 epitaxial thin films — S2P41	277
Spin-Orbit Torque Magnetic Tunnel Junctions at Cryogenic Temperatures — S2P42	279
Symmetry of the dissipation of surface acoustic waves by ferromagnetic resonance — S2P43	281
Experimental and numerical study of dipolar interactions in complex magnetic fluids — S2P44	283

Magnetic textures and dynamics in ultra-thin bidimensionnal ferromagnets Fe_xGeTe_2 — S2P45	285
Ferroelectric control of spin-charge interconversion in oxide-based two-dimensional electron gases — S2P46	287
Brillouin Light Scattering and BiYIG epitaxial films — S2P47	289
Spin-polarized transport across a fluctuating molecular spin 1/2 two-level system — S2P48	290
Tuning the magnetic anisotropy of Pt/Co-based thin films using electric fields — S2P49	292
Towards Fiber-Integrated Cryogenic NV Microscopy for High-Resolution Magnetic Mapping — S2P50	294
Nonlinear interactions between parametrically excited spin-wave modes in a YIG microdisk — S2P51	295
Skyrmions for neuromorphic computing applications — S2P52	297
Multiscale atomistic code for material design Matjes — S2P53	299
Caustiques d'ondes de spin dans un matériau non-réciproque confiné latéralement — S2P54	300
RF magnonic devices: modelling, experiment and integration — S2P55	302
Monolithic integration of magneto-optic garnet deposited by RF sputtering on LNOI — S2P56	304
A scanning tunneling microscope combined with radio frequency to detect magnetic resonance at the atomic scale — S2P57	306
Higher order topological defects in the moiré lattice of a van der Waals magnetic material — S2P58	307
Controlling encirclement of an exceptional point using coupled spintronic nano-oscillators — S2P59	309
Magnetic vortex dynamics probed by time-resolved magnetic helicoidal dichroism — S2P60	311
Imaging of Gate-Controlled Suppression of Superconductivity by Scanning Nitrogen-Vacancy Magnetometry — S2P61	313
Study of (Gd,Bi) iron garnet films with high orthorhombic magnetic anisotropy grown by liquid-phase epitaxy for Dzyaloshinskii-Moriya interaction investigation — S2P62	314
Spectroscopy of Azimuthal Magnon Modes by NV-Center Magnetometry — S2P63	316
Phase analysis of 1f injection locked spin transfer nano-oscillator — S2P64	317
Manipulation of topological spin textures for reservoir computing — S2P65	319



CAYLAR
INSTRUMENTATION SCIENTIFIQUE

**MAGNETIC SYSTEMS
MANUFACTURER**



ELECTROMAGNETS

We specialize in magnetic systems, from simulation to precise measurement. We design custom magnetic solutions to meet your specific needs, based on our standards or by creating entirely new designs.



POWER SUPPLIES

Ultra-stable power current sources with precision up to 1ppm.



NMR TESLAMETERS

Absolute magnetic field sensors using Nuclear Magnetic Resonance, offering a precision of 0.5 μ T and a resolution of 10 nT.

MAGNETIC SYSTEMS

CAYLAR is the ideal partner for designing complex magnetic systems. We are one of the few manufacturers of magnetic field devices offering electromagnets, current sources, and magnetic field measurement instruments.

In addition to our expertise in magnetic simulation and electronics, CAYLAR possesses diverse mechanical skills. We develop ultra-high vacuum chambers, positioning tables, rotary tables, and much more.

Here are two examples of systems we have developed in collaboration with research teams :



MOKE UHV

Here is a compact magnetic system designed for magneto-optical experiments under ultra-high vacuum. Optimized to generate a field of 2.2 T in a 13 mm gap, it allows for rapid field variations (<1s).



CALIBRATION BENCH

Magnetic system regulated by NMR in a temperature-controlled chamber, providing an absolute field reference for calibrating relative magnetic field sensors at various temperature points.

22^e édition du Colloque Louis Néel, 17 au 20 juin 2025 Vogüé,
Lou Capitelle, Ardèche



Advanced Research Systems

Complete cryogenic solutions for your
experimental applications from 4 K to
800 K



RHK Technology

Beetle and Pan Scan Freedom UHV STM/AFM
with the R10 Controller

AFM Cantilevers :



Andeen Hagerling Capacitance Bridges



AH 2700A Capacitance Bridge



AH 1100 Capacitance Standard System



Contact : Tel : 04  26 46 01 60

denis.radosavkic@france-scientifique.fr

Magnetic Measurements Solutions

PPMS[®] DynaCool[™] Physical Properties Measurement System



- Truly cryogen-free - no need for liquid cryogen
- Temperature range of 1.9 K to 400 K
- 9 T and 14 T magnets available
- Continuous low-temperature control maintains temperatures below 4.2 K for indefinite period of time and offers smooth temperature changes when warming and cooling through 4.2 K
- Fully automated operation of PPMS DynaCool measurement options

MPMS[®] 3 SQUID Magnetometer

- Fully automated, with SQUID Sensitivity
- DC, VSM and AC Susceptibility Measurements
- 7 Tesla Magnet with sweep rate up to 700 Oe/sec
- 1.8 - 400 K with Rapid Temp[™], He3 insert
- Cryogen Free with EverCool[®]
- Large option choice: Ultra Low Field, VSM oven, FOSH, Rotator, High Pressure, Electrical Transport



OptiCool[®] and OptiCool[®] Vector[®] 7 Tesla and Vector Magnet Optical Cryostat

- Temperature range: 1.7 K to 350 K
- 7 T split-coil conical magnet or 4-1-1 vector magnet
- Automated control of temperature and magnetic field
- Low Vibration: <10 nm peak-to-peak
- 89 mm x 84 mm Sample Volume
- Cryogen Free



Magnetic Measurements Solutions

PhaseFMR

Ferromagnetic resonance spectroscopy

NanOsc
Instruments



- Frequency range: 2-8 GHz, 2-18 GHz, 2-40 GHz and 2-60 GHz (prel.)
- Measures ultra-thin films down to 2 nm
- No external microwave or detection instruments needed
- Labview interface
- Low-Temperature Version, the CryoFMR

CryoAdvanceTM 4 K optical cryostat

MONTANA INSTRUMENTS

- 3.2 K -350 K temperature range, extendible to 1.2 K
- Low vibrations at nanometer level
- High temperature stability
- Freespace optical access
- Numerous options incl. high NA objective and magnet



M81-SSM

Synchronous source and measure system

Lake Shore
CRYOTRONICS



- All source and measurement channels capable of DC and AC up to 100 kHz
- Modular concept perfectly suited to a specific electrical measurement application
- Common DAC/ADC sampling clock for consistent source and measurement timing
- Optimized for fundamental, harmonic, and phase AC plus DC bias measurements
- Coming soon: SMU module with AC and DC capabilities



Optique et dynamique ultra-rapide

Single-shot all-optical magnetization switching in ferrimagnetic Co-RE alloys single layers

B. Kunyanguyen^{1,*}, G. Malinowski¹, D. Lacour¹, J.-X. Lin¹, Y. Le Guen¹, J. Gorchon¹, S. Mangin¹, J. Hohlfeld¹, and M. Hehn¹

¹Université de Lorraine, CNRS, IJL, F-54000 Nancy, France
*boonthum.kunyanguyen@univ-lorraine.fr

Ultrafast All Optical- Helicity Independent switching (AO-HIS) represents the ability to reverse the magnetization of a nanostructure without any applied field with a characteristic time scale to cross zero magnetization of 1 ps. This reversal process, the fastest ever reported for magnetic materials, appears to be of crucial importance for generating smaller, faster and less energy costly storage technologies. First observed in the $(\text{FeCo})_x\text{Gd}_{1-x}$ ferrimagnetic alloy [1, 2], AO-HIS has been attributed to an ultrafast heating process, characterized by distinct dynamics between the rare earth (RE) and transition metal (TM) elements, and driven by a high transient electron temperature that is out of equilibrium with the lattice. The exchange-driven angular momentum transfer from the rare earth, Gd, and transition metals, Fe and Co, elements results in total magnetization reversal of $(\text{FeCo})_x\text{Gd}_{1-x}$ alloy [3, 4].

The extension to other TM-RE alloys single layers failed up to now. Only a partial single-pulse all-optical switching has been observed only for the first few pulses in case of $\text{Co}_{0.75}\text{Dy}_{0.25}$ or $\text{Co}_{0.75}\text{Tb}_{0.25}$ films [5]. On the other hand, AO-HIS could be observed in thin Co/Ho multilayer [6] or adding Gd in $\text{Co}_x\text{Dy}_{1-x}$, $\text{Co}_x\text{Tb}_{1-x}$ and $\text{Co}_x\text{Ho}_{1-x}$ led to AO-HIS while it fails when Gd concentration is reduced to zero [7].

This presentation will address single-pulse AO-HIS observed in cobalt-rare earth (Co-RE) alloy single layers, specifically where the rare earth elements are Tb, Dy, Ho, or Er. Notably, AO-HIS is observed in Dy- and Ho-based alloys when their composition is near the magnetic compensation point. Conversely, alloys with Tb or Er show only demagnetization. This behavior is counterintuitive, as the reversal mechanism varies significantly with the rare earth element. By studying Hall crosses, we reveal that the reversal process involves the nucleation and propagation of magnetic domain walls, occurring on a microsecond timescale—much slower than in Gd-based materials. I will summarize the current understanding of this intriguing process and its implications for magnetic switching.

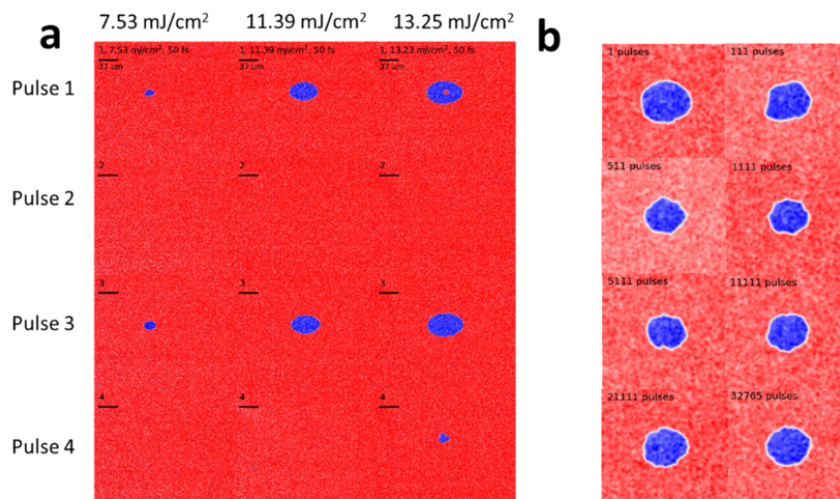


Figure 1: (a) Single shot experiment on $\text{Co}_{75.7}\text{Ho}_{24.3}$ 3nm thick film for 4 shots increasing the fluence from the left to the right column; (b) Single shot experiment on $\text{Co}_{75.7}\text{Ho}_{24.3}$ 3nm thick film for 1, 111, 511, 1111, 21111 and 32765 shots. Each shot induces a toggle switching. Measurements done for a fluence of 11.02 mJ/cm^2 and a pulse duration of 50 fs.

Acknowledgments

We acknowledge financial support from the Region Grand Est through its FRCR call (NanoTeraHertz and RaNGE projects), by the impact project LUE-N4S part of the French PIA project “Lorraine Université d’Excellence”, reference ANR-15IDEX-04-LUE and by the “FEDER-FSE Lorraine et Massif Vosges 2014-2020”, a European Union Program. We acknowledge financial support from the ANR (ANR-17-CE24-0007 UFO project) and (ANR-23-CE30-0047 Slam Project) and through the France 2030 government grants PEPR Electronic EMCOM (ANR-22- PEEL-0009) and PEPR SPIN (ANR-22-EXSP 0007). We also thank the NSRF (Thailand) via the Program Management Unit for Human Resources & Institutional Development, Research and Innovation [grant number B05F650024] and the French Government Scholarship through the Franco-Thai Program.

References

- [1] I Radu, K Vahaplar, C Stamm, et al. Transient ferromagnetic-like state mediating ultrafast reversal of antiferromagnetically coupled spins. *Nature* 472, 205–208 (2011).
- [2] TA Ostler, J Barker, RFL Evans, et al. Ultrafast heating as a sufficient stimulus for magnetization reversal in a ferrimagnet. *Nature communications* 3, 666 (2012).
- [3] Unai Atxitia, Joseph Barker, Roy W Chantrell, and Oksana Chubykalo-Fesenko. Controlling the polarity of the transient ferromagneticlike state in ferrimagnets. *Physical Review B* 89, 224421 (2014).
- [4] CS Davies, T Janssen, JH Mentink, et al. Pathways for single-shot all-optical switching of magnetization in ferrimagnets. *Physical Review Applied* 13, 024064 (2020).
- [5] Zexiang Hu, Jean Besbas, Ross Smith, et al. Single-pulse all-optical partial switching in amorphous Dy_xCo_{1-x} and Tb_xCo_{1-x} with random anisotropy. *Applied Physics Letters* 120 (2022).
- [6] Y Peng, Grégory Malinowski, J Gorchon, et al. Single-shot helicity-independent all-optical switching in Co/Ho multilayers. *Physical Review Applied* 20, 014068 (2023).
- [7] Wei Zhang, Julius Hohlfeld, Tian Xun Huang, et al. Criteria to observe single-shot all-optical switching in Gd-based ferrimagnetic alloys. *Physical Review B* 109, 094412 (2024).

All-optical helicity-dependent switching in magneto-plasmonic nanostructures

Y. Le Guen^{1,2,*}, J. Hohlfeld¹, M. Hehn¹, S. Mangin¹, and S. van Dijken²

¹Université de Lorraine, CNRS, Institut Jean Lamour, F-54000 Nancy, France

²NanoSpin, Department of Applied Physics, Aalto University School of Science, Aalto FI-00076, Finland

*yann.le-guen@univ-lorraine.fr

As the demand for information storage continues to grow, the challenges of increasing data storage density and improving energy efficiency have become increasingly significant. In this context, magneto-optic data storage devices, which use laser light to read and write magnetic media at ultra-high speeds, hold great promise. When combined with magneto-plasmonic nanostructures, the optical writing and reading processes can be performed with minimal energy consumption[1].

The writing process relies on the all-optical switching (AOS) of magnetisation, which can be one of two identified types: All-optical helicity-independent switching (AO-HIS) and all-optical helicity-dependent switching (AO-HDS)[2][3]. The latter, AO-HDS is the process of switching the magnetisation of a system using ultrafast circularly polarised optical pulses (from a 100 fs to a few ps). It has been observed in various magnetic materials, including ferromagnetic multi-layers such as Co/Pt[4]. The final magnetisation state is dictated by the helicity of the laser light. The origin of AO-HDS remains debated, with two main mechanisms under consideration: the inverse Faraday effect (IFE) and magnetic circular dichroism (MCD), which are challenging to disentangle.

Magneto-plasmonic systems, with their enhanced near-field effects due to plasmon resonances[5][6][7], provide a promising platform for studying and optimising AO-HDS. The IFE is proportional to the intensity of the optical near field[8][9]. In magneto-plasmonic structures, IFE is enhanced when the incident laser light matches the wavelength of a plasmon resonance. MCD, on the other hand, is characterised by opposite shifts of the resonance wavelength for opposite magnetisation states. In magneto-plasmonic structures, the MCD will change sign at the wavelength of a plasmon resonance[10]. Since plasmon excitations influence IFE and MCD differently, they offer a unique opportunity to clarify the contributions of these effects to AO-HDS.

Co/Pt multi-layers have been selected for this study because they exhibit AO-HDS with a small number of laser pulses[11]. The magnetic thin films have been grown using magnetron sputtering, then patterned into square lattice nano-disk arrays using electron beam lithography and ion beam etching (see Fig. 1). The array's periodicity and disk size were optimised to obtain a surface lattice resonance (SLR) in the visible to near-infrared range. The magneto-optical properties (MCD and Kerr/Faraday effect) of the Co/Pt multilayer films and arrays have been characterised using optical and magneto-optical spectroscopy. Finally, AO-HDS experiments were performed on the full films and on the arrays at different wavelengths around the plasmonic resonance using a wavelength tunable femtosecond laser source.

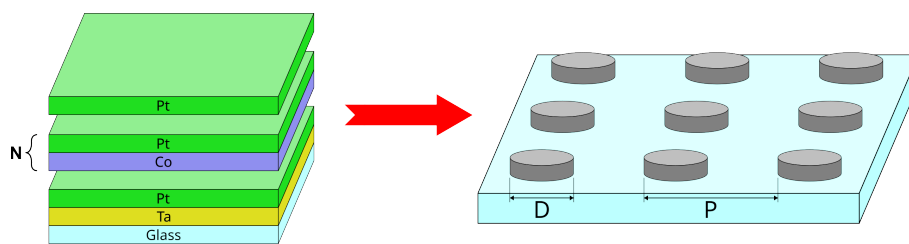


Figure 1: Typical magnetic stack and nano-structure used in this study.

The magneto-optical characterisation of the array shows that near the SLR wavelength (Fig. 1a) the Faraday rotation reached its maximum (Fig. 1b in black), while the ellipticity (Fig. 1b in red) and the MCD (Fig. 1c) cross zero. The MCD showed maximum amplitude with opposite signs on opposite sides of the resonance.

The AOS measurement revealed wavelength dependent switching behaviour. Above a certain fluence where linearly polarised light induces demagnetisation (50% of the full Kerr signal), Kerr signal plateaus were observed for circular polarisations (up to 65% of the full Kerr signal) as shown in (Fig. 1d). The resulting Kerr signal for circular polarisation varies noticeably around the SLR wavelength (Fig. 1e), indicating that the plasmonic resonance affects the AO-HDS process and its efficiency. The observed partial switching variation cannot be explained by IFE or MCD alone.

More measurements on different magnetic stacks and geometries are being undertaken to further expand the understanding of the mechanism behind AO-HDS in magneto-plasmonic structures. These results are a step towards ultrafast magnetic data storage technology.

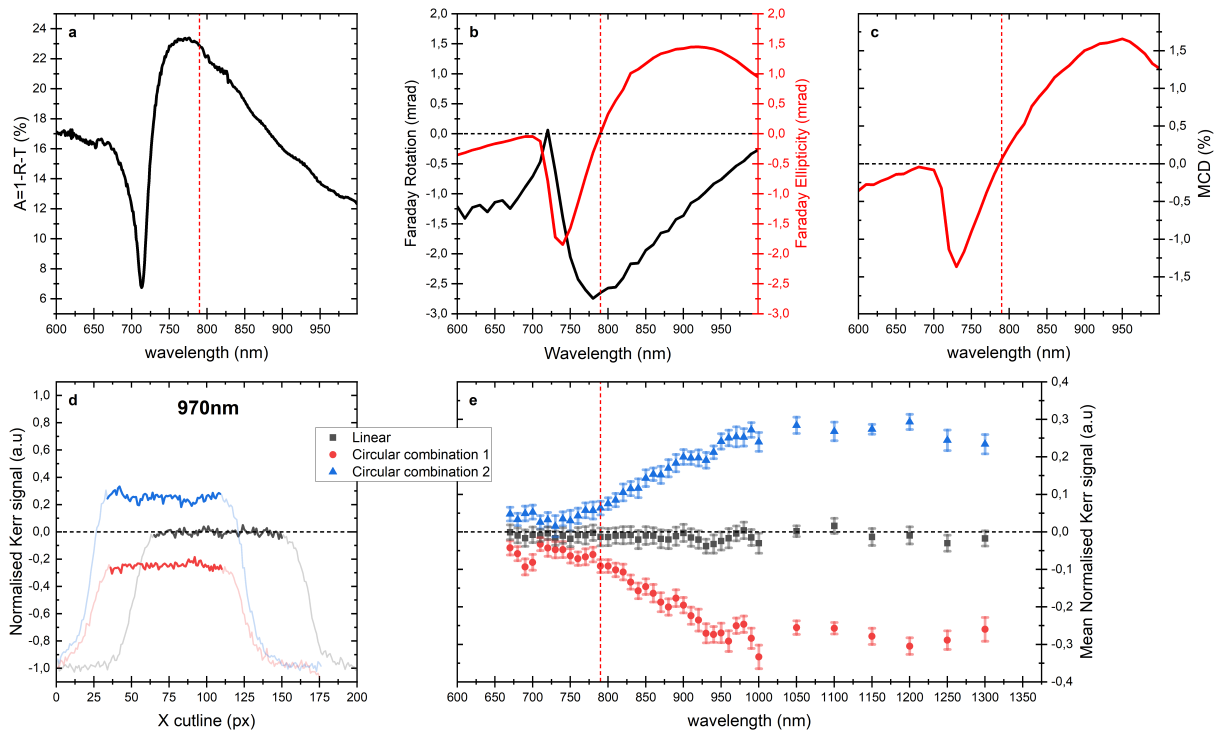


Figure 2: Results for a 10 repetition Co/Pt film patterned into a plasmonic nanodisk array of periodicity $P = 470$ nm and of diameter $D = 200$ nm. (a) Measured absorption spectrum. (b) Measured Faraday rotation and ellipticity spectra. (c) Measured MCD spectrum. (d) Cut-line of the normalised Kerr signal at wavelength of 970 nm after AO-HDS sweeping experiments. (e) Spectrum of the normalised Kerr signal after AO-HDS sweeping experiments. The red dashed line in (a) – (c) & (e) indicates the wavelength where magneto-optical effects are maximized or cross zero.

Acknowledgments

This project is funded by the Magnus Ehrnrooth Foundation.

References

- [1] Maxime Vergès, Sreekanth Perumbilavil, Julius Hohlfeld, et al. [Energy Efficient Single Pulse Switching of \[Co/Gd/Pt\]_N Nanodisks Using Surface Lattice Resonances](#). *Advanced Science* 10, 2204683 (2023).
- [2] Alexey V. Kimel and Mo Li. [Writing magnetic memory with ultrashort light pulses](#). *Nature Reviews Materials* 4, 189–200 (2019).
- [3] M. S. El Hadri, P. Pirro, C.-H. Lambert, et al. [Two types of all-optical magnetization switching mechanisms using femtosecond laser pulses](#). *Physical Review B* 94, 064412 (2016).
- [4] S. Mangin, M. Gottwald, C-H. Lambert, et al. [Engineered materials for all-optical helicity-dependent magnetic switching](#). *Nature Materials* 13, 286–292 (2014).
- [5] Péter Dombi, Zsuzsanna Pápa, Jan Vogelsang, et al. [Strong-field nano-optics](#). *Reviews of Modern Physics* 92, 025003 (2020).
- [6] V. I. Belotelov, I. A. Akimov, M. Pohl, et al. [Enhanced magneto-optical effects in magnetoplasmonic crystals](#). *Nature Nanotechnology* 6, 370–376 (2011).
- [7] M. Kataja, T. K. Hakala, A. Julku, et al. [Surface lattice resonances and magneto-optical response in magnetic nanoparticle arrays](#). *Nature Communications* 6, 7072 (2015).
- [8] J. P. Van Der Ziel, P. S. Pershan, and L. D. Malmstrom. [Optically-Induced Magnetization Resulting from the Inverse Faraday Effect](#). *Physical Review Letters* 15, 190–193 (1965).
- [9] Riccardo Hertel and Manfred Fähnle. [Macroscopic drift current in the inverse Faraday effect](#). *Physical Review B* 91, 020411 (2015).
- [10] Mikko Kataja, Sara Pourjamal, and Sebastiaan van Dijken. [Magnetic circular dichroism of non-local surface lattice resonances in magnetic nanoparticle arrays](#). *Optics Express* 24, 3562 (2016).
- [11] G. Kichin, M. Hehn, J. Gorchon, et al. [From Multiple- to Single-Pulse All-Optical Helicity-Dependent Switching in Ferromagnetic Co / Pt Multilayers](#). *Physical Review Applied* 12, 024019 (2019).

Ultrafast dynamics of magnetic structure in ferrimagnetic CoTb thin films

Mohamed El Moundji Hemili^{1,2,*}, Anju Ahlawat¹, Renaud Delaunay¹, Valentin Chardonnet¹, Jan Lüning⁴, Clemens Von Korff Schmising³, Bastian Pfau³, Michel Hehn⁶, Flavio Capotondi⁵, Gheorghe Sorin Chiuzbăian¹, Emmanuelle Jal¹, Marcel Hennes², and Boris Vodungbo¹

¹*Sorbonne Université, CNRS, Laboratoire Chimie Physique - Matière et Rayonnement, LCPMR, 75005, Paris, France*

²*Sorbonne Université, CNRS, Institut des NanoSciences de Paris, INSP, UMR7588, F-75005 Paris, France*

³*Max-Born-Institut für Nichtlineare Optik und Kurzzeitspektroskopie, Berlin, Germany.*

⁴*Helmholtz-Zentrum Berlin für Materialien und Energie, Berlin, Germany.*

⁵*FERMI, Elettra-Sincrotrone Trieste, Basovizza, Trieste, Italy.*

⁶*Université de Lorraine, CNRS, Institut Jean Lamour, 54000 Nancy, France.*

*mohamed.hemili@sorbonne-universite.fr

30 years ago, Beaurepaire's groundbreaking pump-probe experiment on pure nickel revealed ultrafast demagnetization occurring on sub-picosecond timescales, marking the start of the femtomagnetism field [1]. While several theories have been proposed to explain this phenomenon, no consensus has been reached [1–3]. Nonetheless, this observation has enabled magnetization reversal at record-breaking times, all without the use of a magnetic field. The first deterministic observation of all-optical switching (AOS) was made by Stanciu in a GdFeCo alloy [4] and has been observed since in a variety of ferrimagnetic rare-earth (RE)-transition metal (TM) alloys [5, 6]. In these materials, the two sub-systems exhibit distinct ultrafast magnetization dynamics when subjected to a femtosecond infrared pulse. This has also been observed in CoTb thin films [7, 8], but Co and Tb were probed separately so far, preventing the study of a possible difference in the onset of the Co and Tb demagnetization as seen in other alloys [9]. Furthermore, the optically-induced change of the magnetic structure which has been observed in [7] highlights the need for systematic measurements of the transient magnetic pattern as a function of the pump fluences and x-ray probe wavelengths.

In the present work, we focus on amorphous, ferrimagnetic CoTb alloys grown by magnetron sputtering [10]. Due to local chemical ordering [11], CoTb thin films exhibit perpendicular magnetic anisotropy which results in the creation of nanometer-scaled magnetic domains with out-of-plane magnetization. The size of the latter can be tuned by changing the thickness and composition of the magnetic layers. This turns them into an interesting testbed for magnetic scattering experiments [3, 7]. Using VSM, MOKE and MFM in combination with analytical modeling [12, 13] and micromagnetic simulations, we determined how key magnetic parameters depend on thin film thickness and composition. This allowed us, on the one hand, to obtain a detailed picture of the impact of magnetic anisotropy, saturation magnetization, and exchange stiffness on the spin texture of the magnetic layers (Figure (1)), on the other hand, this helped us to select appropriate samples for time-resolved pump-probe experiments.

To gain insights into the dynamic properties of such alloys following femtosecond laser-excitation, we conducted time-resolved Small-Angle X-ray Scattering (Tr-SAXS) experiments [7] at the DIPROI beamline at FERMI. We utilized FERMI's capability to deliver two X-ray pulses of different wavelengths simultaneously to probe the 3d Co and 4f Tb valence electrons, using the absorption edges $M_{2,3}$ (58.9 eV) for Co and $N_{4,5}$ (150.5 eV) for Tb, respectively. The experimental setup, consisting of two CCD cameras, allowed us to record simultaneously the light scattered by Co and Tb atoms. The magnetic domains act as an optical grating due to the XMCD effect. This approach allowed us to retrieve the temporal evolution of the magnetization with elemental selectivity and nanometer spatial resolution. By analyzing the azimuthal integration of the scattering intensities as a function of the time delay, we also extracted the domain size, and domain size distribution for both TM and RE elements. As shown in Figure 2, we observe two types of demagnetization : a rapid sub-ps quenching of the magnetization and a slower reduction on picosecond timescales. In addition, we find a 2% reduction of the domain size within 500 ps and characteristic oscillations with frequencies of 25 GHz. We discuss these results by linking them to laser-induced modifications of the magnetic anisotropy [6] and provide a qualitative discussion of magneto-elastic coupling effects.

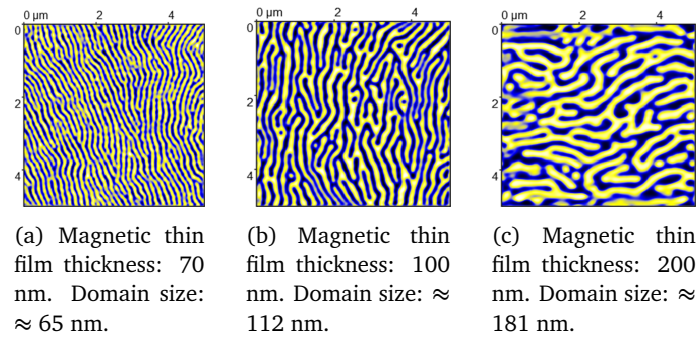


Figure 1: Magnetic force microscopy (MFM) images of $\text{Co}_{92}\text{Tb}_8$ thin films. The images show the variation of magnetic domain size as a function of film thickness. The blue and yellow regions correspond to magnetic domains pointing in opposite directions.

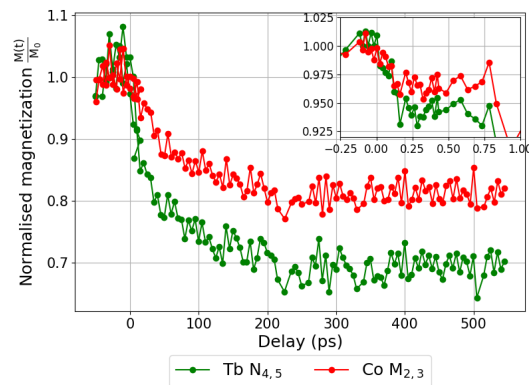


Figure 2: Magnetization dynamics of a 50 nm thick $\text{Co}_{90}\text{Tb}_{10}$ sample extracted from measurements close to $\text{Co } M_{2,3}$ edge (55 eV, red) and $\text{Tb } N_{4,5}$ edge (165 eV, green) for an infrared pump of 2.2 mJ/cm^2 .

References

- [1] E. Beaurepaire et al. Ultrafast Spin Dynamics in Ferromagnetic Nickel. *Physical Review Letters* 76 (1996).
- [2] B. Koopmans et al. [Explaining the paradoxical diversity of ultrafast laser-induced demagnetization](#). *Nature Materials* 9, 259–265 (2010).
- [3] B. Vodungbo et al. [Laser-induced ultrafast demagnetization in the presence of a nanoscale magnetic domain network](#). *Nature Communications* 3, 999 (2012).
- [4] C. D. Stanciu et al. [All-Optical Magnetic Recording with Circularly Polarized Light](#). *Physical Review Letters* 99, 047601 (2007).
- [5] P. Scheid et al. [Light induced ultrafast magnetization dynamics in metallic compounds](#). *Journal of Magnetism and Magnetic Materials* 560, 169596 (2022).
- [6] Y. Peng et al. [In-plane reorientation induced single laser pulse magnetization reversal](#). *Nature Communications* 14, 5000 (2023).
- [7] M. Hennes et al. [Laser-induced ultrafast demagnetization and perpendicular magnetic anisotropy reduction in a \$\text{Co}_{88}\text{Tb}_{12}\$ thin film with stripe domains](#). *Physical Review B* 102, 174437 (2020).
- [8] S. Alebrand et al. [Subpicosecond magnetization dynamics in TbCo alloys](#). *Physical Review B* 89, 144404 (2014).
- [9] S. Jana et al. [Experimental confirmation of the delayed Ni demagnetization in FeNi alloy](#). *Applied Physics Letters* 120, 102404 (2022).
- [10] P. Hansen et al. [Magnetic and magneto-optical properties of rare-earth transition-metal alloys containing Gd, Tb, Fe, Co](#). *Journal of Applied Physics* 66, 756–767 (1989).
- [11] V. G. Harris et al. [Structural origins of magnetic anisotropy in sputtered amorphous Tb-Fe films](#). *Physical Review Letters* 69, 1939–1942 (1992).
- [12] Z. Q. Zou et al. [A computational method of temperature characteristics of magneto-optical Kerr effect in amorphous TbFeCo films with a multilayered structure](#). *Journal of Applied Physics* 93, 5268–5273 (2003).
- [13] F. Viot et al. [Theory of magnetic domains in uniaxial thin films](#). *Journal of Physics D: Applied Physics* 45, 405003 (2012).

Magneto-optical distinction of magnetization dynamics from spin currents and its role in switching mechanism in ferromagnetic spin valve

Harjinder Singh^{1,*}, Alberto Anadón¹, Quentin Remy², Michel Hehn¹, Gregory Malinowski¹, and Jon Gorchon¹

¹Université de Lorraine, CNRS, IJL, Nancy, F-54000, France

²Department of Physics, Freie Universität Berlin, 14195 Berlin, Germany

*harjinder.singh@univ-lorraine.fr

Magneto-optical techniques are powerful and widely used tools that enable the investigation of ultrafast spin dynamics in various magnetic materials[1–5]. Currently, these techniques are becoming one of the emerging tools for studying the accumulation of spin and/or orbital angular momentum in magnetic/non-magnetic materials[6–9]. However, it has long been believed that the signal due to these accumulations was orders of magnitude smaller than the magnetization itself. Here we show that under certain conditions the accumulation signals can be comparable to or even exceed the signal coming from the magnetization itself during the ultrafast demagnetization. Furthermore, we show that accumulations are not only limited to simple structures but can also be observed in more complex systems such as [Pt/Co]/Cu/[Co/Pt] spin valves. In this case, we experimentally demonstrate how to isolate the accumulation signal, allowing us to better understand the mechanisms at play in the ultrafast optical switching recently discovered in ferromagnetic spin-valves[10].

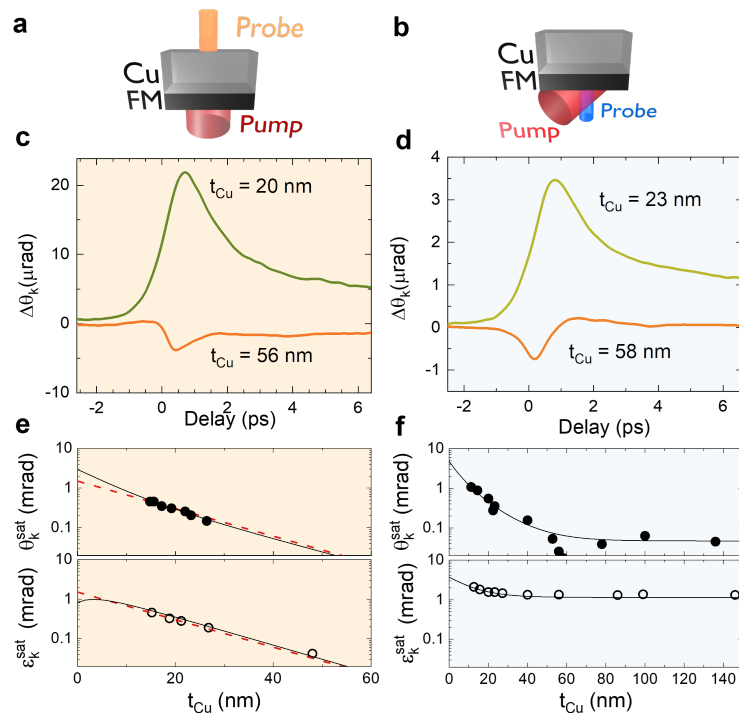


Figure 1: Sample stack with experimental configuration along with static and dynamic magneto-optical measurements. (a,b) sample structure consists of [Co/Ni] as a FM and Cu as NM material. In both the cases pump is always incident on FM side whereas probe is incident on (a) Cu side and (b) FM side. (c,d) Dynamic time-resolved magneto-optical measurements for two different Cu thicknesses when probe is on (a) Cu side and (b) FM side. (e,f) Static magneto-optical response as a function of Cu thickness for both rotation and ellipticity at saturation (without pump) with probe on (a) Cu side and (b) FM side. The red(black) dashed(solid) lines are an exponential decay fit to the data using the transmission matrix method[11].

The simple bilayer structure of ferromagnet (FM) and non-magnetic (NM) material used in this study consists of [Co/Ni] multilayers and Cu, respectively, and the experimental configurations are shown in Fig.1(a,b). Fig.1 (c) shows the time-resolved magneto-optical measurements obtained when the pump is incident on the FM side and the probe is on the Cu side for $t_{Cu} = 20$ nm and 56 nm. For $t_{Cu} = 20$ nm, a typical demagnetization curve is measured, while for the larger thickness $t_{Cu} = 56$ nm most of the probe light is blocked by the thick Cu and hence this time-dependent change in magneto-optical signal is safely attributed to spin accumulation in Cu [6]. When both the pump and probe interact with the sample from the FM side, the $\Delta\theta_k$ shown in Fig.1 (d) performed for $t_{Cu} = 23$ nm unveils a similar demagnetization trace. For higher

Cu thickness of $t_{\text{Cu}} = 58$ nm, the trace is inverted and is bipolar with different timings similar to what we obtained as shown in Fig.1 (c) and $t_{\text{Cu}} = 56$ nm. However, in this measurement, the probe always interacts with the sample on the FM side, making these changes unexpected. To further understand this phenomenon, we performed static magneto-optical measurements as a function of t_{Cu} as shown in Fig.1 (e,f). We therefore investigated Kerr rotation (θ_k^{sat}) and Kerr ellipticity (ϵ_k^{sat}) in saturation for both cases where the probe is on the Cu side and the FM side. When the probe is on the Cu side (Fig.1 (e)) both θ_k^{sat} and ϵ_k^{sat} decrease exponentially following a Beer Lambert decay which is not the case when the probe is on the FM side shown in Fig.1 (f) where for θ_k^{sat} the value drops by an order of magnitude within the t_{Cu} from 10 to 50 nm, while in the case of ϵ_k^{sat} the decay is small and the maximum value remains around 1 mrad.

The Cu thickness dependence of the time-resolved signals measured in the different configurations indicates that the spin currents can be observed and even dominate in the case of the Kerr rotation while its contribution is almost negligible for the Kerr ellipticity. Our results highlight the complexity of time-resolved magneto-optical measurements in magnetic multilayers and provide a new framework for accessing and isolating the spin accumulations, allowing for direct probing of transported spin and/or orbital angular momentum.

Acknowledgments

This work is supported by the ANR through the SLAM project (ANR-23-CE30-0047) and the France 2030 government grants PEPR Electronic EMCOM (ANR-22-PEEL-0009) and PEPR SPIN (ANR-22-EXSP-0002), as well as the MAT-PULSE-Lorraine Université d'Excellence project (ANR-15-IDEX-04-LUE).

References

- [1] E. Beaurepaire et al. Ultrafast Spin Dynamics in Ferromagnetic Nickel. *Physical Review Letters* 76 (1996).
- [2] B. Koopmans, M. Van Kampen, J. T. Kohlhepp, and W. J. M. De Jonge. [Ultrafast Magneto-Optics in Nickel: Magnetism or Optics?](#) *Physical Review Letters* 85, 844–847 (2000).
- [3] Luca Guidoni, Eric Beaurepaire, and Jean-Yves Bigot. [Magneto-optics in the Ultrafast Regime: Thermalization of Spin Populations in Ferromagnetic Films.](#) *Physical Review Letters* 89, 017401 (2002).
- [4] B Koopmans, M Van Kampen, and W J M De Jonge. [Experimental access to femtosecond spin dynamics.](#) *Journal of Physics: Condensed Matter* 15, S723–S736 (2003).
- [5] G. Malinowski, F. Dalla Longa, J. H. H. Rietjens, et al. Control of speed and efficiency of ultrafast demagnetization by direct transfer of spin angular momentum. *Nature Physics* 4, 855–858 (2008).
- [6] Gyung-Min Choi and David G. Cahill. [Kerr rotation in Cu, Ag, and Au driven by spin accumulation and spin-orbit coupling.](#) *Phys. Rev. B* 90, 214432 (2014).
- [7] Gyung-Min Choi, Byoung-Chul Min, Kyung-Jin Lee, and David G. Cahill. [Spin current generated by thermally driven ultrafast demagnetization.](#) *Nature Communications* 5, 4334 (2014).
- [8] Gyung-Min Choi, Chul-Hyun Moon, Byoung-Chul Min, Kyung-Jin Lee, and David G. Cahill. [Thermal spin-transfer torque driven by the spin-dependent Seebeck effect in metallic spin-valves.](#) *Nature Physics* 11, 576–581 (2015).
- [9] Young-Gwan Choi, Daegeun Jo, Kyung-Hun Ko, et al. [Observation of the orbital Hall effect in a light metal Ti.](#) *Nature* 619, 52–56 (2023).
- [10] Junta Igarashi, Wei Zhang, Quentin Remy, et al. [Optically induced ultrafast magnetization switching in ferromagnetic spin valves.](#) *Nature Materials* 22, 725–730 (2023).
- [11] J. Zak, E. R. Moog, C. Liu, and S. D. Bader. [Magneto-optics of multilayers with arbitrary magnetization directions.](#) *Phys. Rev. B* 43, 6423–6429 (1991).

Magnetization switching for circular polarized LEDs

Rodrigo Torráo Victor^{1,*}, Pambiang Abel Dainone², Sophie Collin¹, Florian Godel¹, Nicolas Reyren¹, Yuan Lu², Henri Jaffres¹, and Jean-Marie George¹

¹Laboratoire Albert Fert, CNRS, Thales, Université Paris-Saclay, Palaiseau, France

²Institut Jean Lamour, Université de Lorraine, CNRS, UMR 7198, Nancy, France

*rodrigo.torrao-victor@cnrs.fr

Information processing, transmission, and storage form the core of modern computing and communications technologies. Information processing typically involves the manipulation of the electron charge in semiconductor materials, while data transmission relies on the ability to emit light. On the other hand, information storage has traditionally been tied to magnetic materials, where the manipulation of electron spins plays a key role and enables the stable data storage by forming the basis of current magnetic data storage technologies. However, integrating these three pillars -processing, storage, and transmission- into a single device remained a major challenge.

A promising solution for this integration on a single chip at room temperature has recently been proposed using photonics, electronics and spintronics [1]. This device integrates these three pillars using semiconductor light-emitting diodes (LEDs) with circularly polarized light. The polarization of the light is controlled by the magnetic orientation of an adjacent ferromagnetic (FM) layer. In turn, this magnetic orientation can be controlled by an electric current in an adjacent layer through the spin-orbit torque (SOT) effect. This setup allows for simultaneous information transfer by light emission, processing by spin currents, and storage by magnetization of the ferromagnetic material. The lower part of Figure 2 Panel A shows a schematic of the LED structure (highlighted in blue), including the layers of materials involved in light emission. On top of the LED emitter, highlighted in green, is the spin injector composed of the FM material (CoFeB) and a tungsten/chromium (W/Cr) layer to control the FM orientation using spin-orbit torques.

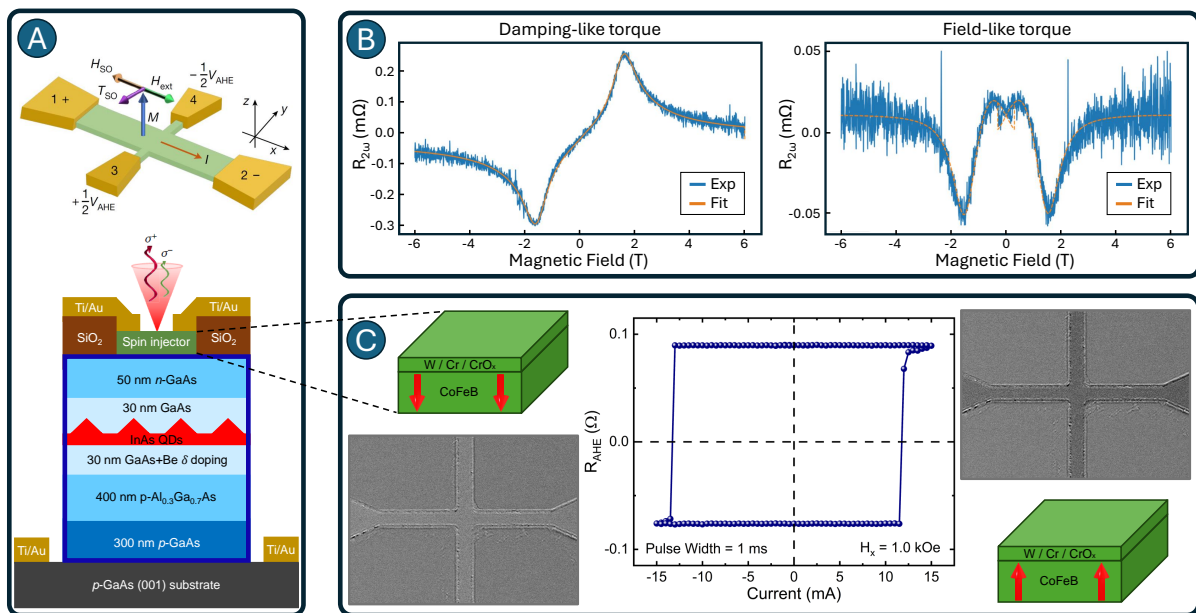


Figure 1: The Panel A is adapted from [1]. In the bottom part is presented the schematic of the semiconductor light-emitting diodes (LEDs) with circularly polarized light. The LED structure is highlighted in blue, while the spin injector controlling the light polarization is highlighted in green. In the upper part of this panel, the spin injector Hall bar configuration is shown in detail. Panel B shows a representative second-harmonic Hall measurement of the damping-like (DL) and field-like (FL) spin-orbit torque contributions for a CFB (1.1 nm)/W (3 nm)/Cr (5 nm) sample. Panel C shows the current-induced magnetization switching measured by anomalous Hall effect (AHE) and magneto-optical Kerr effect (MOKE) microscopy.

In the upper part of Figure 2 Panel A, the Hall bar geometry of the spin injector is presented, which is used to control the FM orientation through the spin-orbit torque effect. Traditionally, the SOT effect occurs when an electric current is passed through a heavy metal layer adjacent to the ferromagnetic material. Due to the strong spin-orbit coupling in the heavy metal, the current creates a spin current that exerts a torque on the magnetization of the FM. This torque can align the magnetization depending on the charge current direction, allowing manipulation of the magnetization state. The key to magnetization inversion is the interplay between the spin current and the exchange interaction in the FM which, if the first is sufficiently strong, causes the magnetization to flip.

The helicity of the emitted light is directly related to the magnetization of the ferromagnetic material, creating a direct link between the optical output of the device and its magnetic state. This magnetic orientation determines the polarization of the emitted light. When charge carriers with spin-polarized states pass through the ferromagnetic material, their spins

are aligned along the direction of magnetization, and when injected into the LED, the spin imbalance of the carriers is transferred to the circular polarization of the emitted light due to the conservation of total angular momentum. Therefore, if the magnetization is oriented in a specific direction, the emitted light will have a corresponding circular polarization, either left-handed or right-handed.

However, the realization of such devices is not an easy task as they must meet a number of requirements. First, the materials must be compatible with existing growth technologies used in semiconductor manufacturing to ensure scalability and manufacturability. In addition, low power consumption is a critical requirement for practical applications, as high energy costs or heat generation would undermine the efficiency of the device. Low-cost materials and manufacturing processes are essential for commercialization and devices must operate reliably at room temperature to be viable for use in the real world.

Furthermore, since magnetization is controlled by a charge current in a layer on top of a semiconductor multilayer structure, it is extremely important that this current does not exceed the metal-insulator-semiconductor (MIS) Schottky barrier to avoid shunt problems. If the current exceeds the threshold that the Schottky barrier can handle, it could result in significant efficiency losses, as the current would flow in unintended paths instead of inducing the desired spin-polarized current in the ferromagnetic layer. This would result in inadequate control of the magnetization and, consequently, reduced light polarization; thus, careful design of the spin injector is critical to ensure the operation of the roll device. In addition, it is also desirable to control the magnetization in an ultrafast regime, which requires magnetization reversibility with current pulses on the order of nanoseconds. The ability to control magnetization in the ultrafast regime requires precise control of the current pulse characteristics and the geometry of the device.

To meet these requirements, we investigate a promising system composed of heavy metal materials such as platinum (Pt) and tungsten (W), known for their high spin-orbit coupling (SOC) and spin Hall effect (SHE), coupled with light metals such as chromium (Cr), recently explored for their high orbital Hall effect (OHE). The SHE in Pt and W generates spin currents that allow efficient angular momentum transfer and contribute to the magnetization switching, while the OHE in Cr enhances the overall device performance by coupling the spin and orbital degrees of freedom, providing a complementary mechanism to control the magnetization. In this work, we explore the potential of Cr as a light metal material, to suggest several desirable properties, such as the reduction in the critical current needed for magnetization switching [2, 3]. In addition, when chromium is partially oxidized, the interface between Cr and its oxide (CrO_x) can give rise to the Rashba Edelstein Effect (REE), a phenomenon in which the spin polarization of electrons at the interface could further enhance control over magnetization switching by providing additional spin- or orbital-polarized currents. In order to induce or prevent the formation of the oxide layer, different stack combinations were investigated.

To investigate the influence of the OHE and REE, we used second-harmonic Hall techniques to measure both damping-like (DL) and field-like (FL) spin-orbit torque contributions. Figure 2 Panel B shows a representative second-harmonic Hall measurement of the DL and FL contributions for a CFB (1.1 nm)/W (3 nm)/Cr (5 nm) sample. These measurements allow us to distinguish the different contributions to the spin-orbit torque and study how they affect the magnetization dynamics.

We further correlated these torques with the current-induced magnetization switching measured using the anomalous Hall effect (AHE), as shown in Figure 2 Panel C. These measurements were performed for several current pulse widths to analyze the critical current dependence on the pulse width. To further confirm that the magnetization is indeed switching and to get a better insight into the device geometry dependence of the switch, we combined the AHE measurements with magneto-optical Kerr effect (MOKE) microscopy, which provides spatial information on the magnetization distribution. With a simple Hall bar geometry, it was possible to switch the magnetization with pulses of 9 ns.

Further improvements are expected by exploring device geometries, sizes, and thicknesses. The relationship between switching current and DL and FL torque is not yet fully understood and requires further investigation. In addition, MOKE microscopy can be used to investigate how these factors affect the switching, nucleation, and propagation of magnetization reversal. Potentially, density functional theory (DFT) calculations can also be used to support our experimental findings, with a particular focus on the orbital texture in Cr and CrO_x , which plays a crucial role in the magnetization dynamics.

Acknowledgments

This work is supported by the French National Research Agency (ANR) SOTspinLED project (No. ANR-22-CE24-0006-01).

References

- [1] Pambiang Abel Dainone, Nicholas Figueiredo Prestes, Pierre Renucci, et al. Controlling the helicity of light by electrical magnetization switching. *Nature* 627, 783–788 (2024).
- [2] Soogil Lee, Min-Gu Kang, Dongwook Go, et al. Efficient conversion of orbital Hall current to spin current for spin-orbit torque switching. *Communications Physics* 4, 234 (2021).
- [3] Hongfei Xie, Yuhan Chang, Xi Guo, et al. Orbital torque of Cr-induced magnetization switching in perpendicularly magnetized Pt/Co/Pt/Cr heterostructures. *Chinese Physics B* 32, 037502 (2023).

Exciting and probing high-frequency spin waves in BiYIG/Co heterostructure using laser pulses

Dimple Sneha Pamarthi^{1,*}, Elena Popova², Nirina Randrianantoandro¹, Gwenaëlle Vaudel¹, Pascal Ruello¹, Michel Hehn³, Niels Keller², and Marwan Deb¹

¹Institut des Molécules et Matériaux du Mans, CNRS UMR 6283, Le Mans Université, 72085 Le Mans, France

²Institut de Physique de Rennes (IPR), CNRS UMR6251, Université Rennes, 35000 Rennes, France

³Institut Jean Lamour (IJL), CNRS UMR 7198, Université de Lorraine, 54506 Vandoeuvre-s-Nancy, France

*Dimple_Sneha.Pamarthi@univ-lemans.fr

Nowadays, transitioning from electric currents to spin waves (SWs), or magnons, is considered highly promising for advancing data transport and processing technologies [1]. However, generating high-frequency SWs with low damping and minimal energy consumption remains a critical challenge for ultrafast and energy-efficient applications. Among all magnetic materials, yttrium iron garnet (YIG) has attracted significant attention because of its low magnetic damping coefficient, which allows SWs to propagate over long distances [2]. In addition, doping YIG with bismuth (BiYIG) induces a substantial increase in the magneto-optical (MO) response while only slightly affecting the magnetic damping, making it particularly suitable for the development of new photomagnonic devices [3]. Recently, we have demonstrated that femtosecond laser pulses can effectively trigger and probe high-frequency exchange standing SWs (SSWs) in nanoscale dielectric Bi-YIG thin films. Despite this progress, a high laser energy density ($\sim 120 \text{ mJ/cm}^2$) [4] is still necessary to trigger SWs, posing a significant challenge for achieving low-power operation. Thus, developing methods to excite high-frequency SWs with minimal energy input remains a critical objective for both fundamental research and practical applications.

To address this challenge, we have explored novel and promising heterostructures based on BiYIG. The specific heterostructure investigated is Al (3 nm)/Co (10 nm)/BiYIG (110 nm) grown on a GGG(100) substrate [see Fig. 1(a)]. The BiYIG layer was deposited on GGG by pulsed laser deposition (PLD), while the Co/Al magnetic bilayer was deposited using a dc magnetron sputtering system. The deposition of Co/Al bilayer is limited to one half of the sample, which offers an important opportunity to study magnetic phenomena in both the bare and functionalized BiYIG layers by selecting different regions on the sample. The sample was excited with femtosecond laser pulse of wavelength 800 nm from the Al/Co side and probed (400 nm) from the GGG substrate side. Due to the large bandgap of GGG, the probe traverses it and reaches the BiYIG and Co/Al layer. The reflected probe beam then measures both the differential changes of the MO Kerr rotation $\Delta\Theta_K(t)$ and reflectivity $\Delta R(t)$ as a function of pump-probe delay time. This configuration allows us to measure the magnetization dynamics in both magnetic layers of the heterostructure and to detect acoustic strain pulses through time-domain Brillouin scattering modulations of the reflectivity signal as they propagate through the GGG.

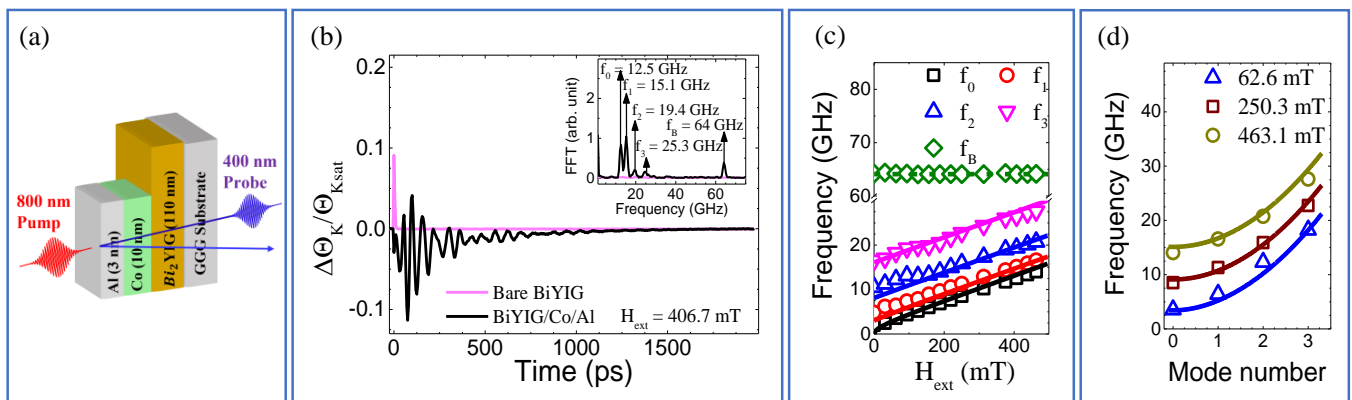


Figure 1: **Laser-induced ultrafast spin dynamics in BiYIG/Co based- Heterostructure and bare BiYIG thin films:** (a) A sketch of the experimental configuration. Depending on the sample position, the magnetization dynamics in either the $\text{Bi}_2\text{Y}_1\text{Fe}_5\text{O}_{12}/\text{Co}$ -based heterostructure or the bare $\text{Bi}_2\text{Y}_1\text{Fe}_5\text{O}_{12}$ layer is measured. (b) Comparison of $\Delta\Theta_K/\Theta_{K\text{sat}}$ measured in BiYIG/Co based-heterostructure and bare BiYIG thin films with the pump laser fluence of 1.9 mJ/cm^2 . The H_{ext} is applied at an angle of 22° from the film plane. The insets show the FFT spectra. (c) Field dependence of the precession frequency. (d) Spin precession frequency as a function of the mode number at different values of H_{ext} . The solid line in (c) and (d) are the fits with Kittel formula for SSWs.

In this talk, I will present our work on laser induced ultrafast magnetization dynamics in BiYIG/Co based heterostructures using laser pulses and compare the results with bare BiYIG. We demonstrate that femtosecond laser pulses can trigger

high-frequency SSWs in the BiYIG-based heterostructure with very low laser energy density, which cannot excite spin precession in bare BiYIG [Fig. 1(b)]. This is reflected at zero external magnetic field by spin dynamics with a frequency up to 16 GHz [Fig. 1(c)], which is 8 times higher than that associated with the ferromagnetic resonance mode. This result highlights the importance of heterostructure for energy-efficient generation of high-frequency SSWs.

By varying the pump fluence, external magnetic field, and pump polarization, we systematically studied the behavior of the magnetization dynamics. The field dependence of the precession frequency [Fig. 1(c)] indicates that the physical origin of the high-frequency mode f_B is clearly different from the modes f_0, f_1, f_2 , and f_3 . Specifically, the frequency of the mode f_B shows field-independent behavior, consistent with a Brillouin interference origin, whereas the modes f_0 to f_3 exhibit a linear dependence on H_{ext} . These linear dependences can be well described by the Kittel formula for SSWs: $\omega = \gamma \sqrt{(H_{ext} + D_{ex}k^2)(H_{ext} + H_{eff} + D_{ex}k^2)}$, where ω is the angular precession frequency, γ is the gyromagnetic ratio, D_{ex} is the exchange stiffness, $k = n\pi/d$ is the wave-vector of the SSWs with n being the mode number and d the film thickness, and the effective field H_{eff} is defined as $(4\pi M_s - H_K)$, where H_K is the uniaxial anisotropy field. Additionally, spin precession frequency exhibits a quadratic dependence on the mode number [Fig. 1(d)], further supporting the SSW nature of the modes. Indeed, a fit of the experimental data with the Kittel formula for SSWs using $(\gamma/2\pi) = 28 \text{ GHz/T}$ yields an excellent agreement with the experimental results [Figs. 1(c) and 1(d)]. We obtain an exchange stiffness $D_{ex} = (6.9 \pm 0.6) \times 10^{-17} \text{ Tm}^2$ in good agreement with those reported in the literature for YIG and BiYIG [5]. This clearly demonstrates the SSW nature of the observed magnetic resonance modes.

To gain a deeper understanding of the excitation mechanism, additional investigations were performed, including measurements of laser-induced changes in reflectivity and experiments with an altered configuration, where both pumping and probing were conducted from the Co/Al side. Based on the results of these measurements, we attribute the excitation mechanisms to changes in magnetic anisotropy induced by coherent and incoherent phonons, as well as possible dynamical exchange and spin transfer torque at the BiYIG/Co interface [6]. Additionally, in this talk, I will emphasize on the critical role of advanced magneto-optical techniques in detecting higher-order SW modes. These results can open exciting perspectives for ultrafast and energy-efficient data transport and processing applications.

Acknowledgments

This work was supported by the ANR-CPJ Project (Grant No. ANR-22-CPJ2-0001-01) and the ANR ULTRAMAG Project (Grant No. ANR-23-CE30-0004). This work was also partly supported by the France 2030 PEPR SPIN program, through the ANR TOAST Project (Grant No. ANR-22-EXSP-0003) and the ANR SPINMAT Project (Grant No. ANR-22-EXSP-0007).

References

- [1] Dirk Grundler. [Nanomagnonics](#). *Journal of Physics D: Applied Physics* 49, 391002 (2016).
- [2] A A Serga, A V Chumak, and B Hillebrands. [YIG magnonics](#). *Journal of Physics D: Applied Physics* 43, 264002 (2010).
- [3] M Deb, E Popova, A Fouchet, and N Keller. [Magneto-optical Faraday spectroscopy of completely bismuth-substituted Bi3Fe5O12 garnet thin films](#). *Journal of Physics D: Applied Physics* 45, 455001 (2012).
- [4] Marwan Deb, Elena Popova, Henri-Yves Jaffrès, Niels Keller, and Matias Bargheer. [Controlling High-Frequency Spin-Wave Dynamics Using Double-Pulse Laser Excitation](#). *Phys. Rev. Appl.* 18, 044001 (4 2022).
- [5] S. Klingler, A. V. Chumak, T. Mewes, et al. [Measurements of the exchange stiffness of YIG films using broadband ferromagnetic resonance techniques](#). *Journal of Physics D Applied Physics* 48, 015001, 015001 (2015).
- [6] Dimple Sneha Pamarthi, Elena Popova, Nirina Randrianantoandro, Gwenaëlle Vaudel, Pascal Ruello, Michel Hehn, Niels Keller, Marwan Deb. Energy-efficient generation of high-frequency spin-waves in BiYIG/Co-based heterostructures using laser pulses. *Physical Review Applied* (Under review).

Nanomagnétisme et dynamique

Complex dynamics of nano-oscillators with dual vortex free layers coupled via spin-torques

Loukas Kokkinos^{1,*} and Joo-Von Kim¹

¹Centre de Nanosciences et de Nanotechnologies, CNRS, Université Paris-Saclay, 91120 Palaiseau, France
*loukas.kokkinos@universite-paris-saclay.fr

Spin torque nano-oscillators (STNOs) exhibit properties, such as wide frequency tunability, that could be useful for technological applications in telecommunications and RF detection. These systems are also promising for unconventional computing and artificial neural networks, owing to the complex dynamical regimes they can access [1, 2]. One of the most commonly studied types of STNOs are Spin-Torque Vortex Oscillators (STVOs). These structures typically consist of a stacking of a ferromagnetic free layer in a vortex state, a non-magnetic spacer layer, and a pinned ferromagnetic layer, called polarizer. When a sufficiently large current traverses these devices, the vortex core can exhibit self-sustained gyrotropic motion through spin-transfer torque (STT). The gyrotropic dynamics can depend strongly on the magnetic configuration of the polarizer layer [1, 3].

In this work, we explore the dynamics in a STNO comprising two vortex free layers, where each layer serves as a dynamic polarizer for the other. This raises the number of degrees of freedom and therefore, the complexity of the system. We refer to such systems as *Slonczewski windmills* [4, 5] whereby coupling between the two layers results from spin torques, rather than magnetic interactions such as dipolar coupling or RKKY interlayer exchange. The study consists of a numerical investigation using a modified version of the open source micromagnetic simulator MuMax3 [6], which accounts for the mutual spin-transfer torque coupling between the two layers. We also take into account Zeeman coupling to the current-induced Ampere-Oersted field. The simulated layers are disks with thicknesses $d_0 = d_1 = 7$ nm and of radius $r_{disk} = 125$ nm. The magnetic vortices are defined by their respective chiralities, c_0 and c_1 , (in-plane curl) and core polarities, p_0 and p_1 . A schematic of the studied geometry is given in Fig. 1a for $p_0 = p_1 = 1$ and $c_0 = c_1 = -1$.

Two main studies were conducted to highlight the role of asymmetry between the two vortex states in determining the overall dynamics. In the first, we introduce asymmetry in the magnetic vortex states, by considering either opposite polarities (OP) or chiralities (OC). A notable dynamical regime found is the transition from regular gyration of the vortex core, termed the G-state (Fig. 1b), to the rotation of a C-state magnetization (Fig. 1c) which corresponds to the gyration of a virtual core outside the disk. In contrast to single free layer STVOs [1], this OP windmill system does not rely on strong perpendicular applied fields or high currents to enter the C-state. The current-dependence of the gyration frequency is also qualitatively different, where the frequency *decreases* with current at high currents (Fig. 1d).

In the second study, asymmetry is imposed on the geometry and material parameters, namely in the $M_{sat}d$ product which models free layers with different thicknesses. Figure 2 summarizes the dynamics obtained for $M_{sat,1}d_1 = 1.2M_{sat,0}d_0$. Figure 2a shows the power spectral density map as a function of the applied current. Up to $I \approx 13$ mA, both cores enter self-sustained gyration inside their respective layer (G-state). The predicted in-plane magnetization signal exhibits clear sinusoidal variations (Fig. 2b), which result from well-defined circular orbits of the vortex cores (Fig. 2e). In the current range $I = [13, 16]$ mA, the m_x time traces and orbits show fluctuations (Figs. 2c and 2f), which results in significant broadening of the power spectra. Finally, in the regime $I > 16$ mA, a second frequency band appears around $f_0 = 40$ MHz. This dual frequency regime represents chaotic transitions between G- and C-state in layer 0, a clear example of which is given in the time trace in Figure 2d, and the trajectories in Figure 2g (C-state) and 2h (G-state). These also result in distinct resistance states (Fig. 2i), rendering the transitions electrically measurable. Applied external fields can be used to modify this transition. For instance a field perpendicular to the plane can favor one state over the other, as seen in the resistance distributions ρ for different fields in Fig. 2j.

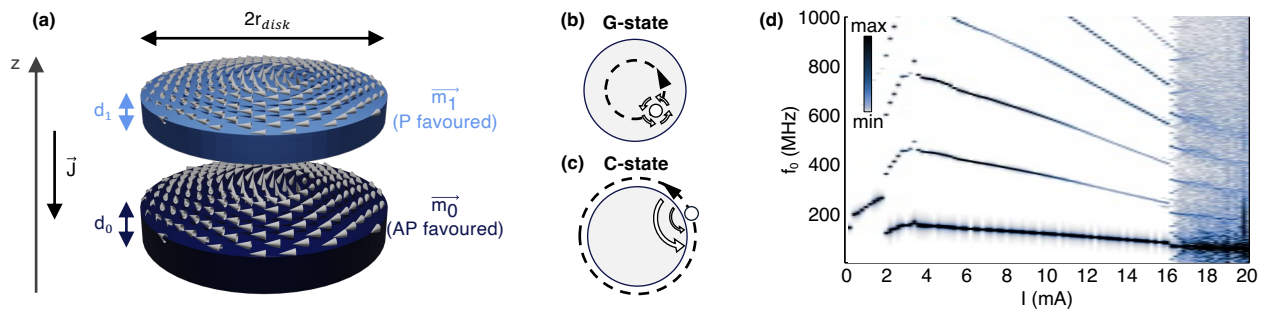


Figure 1: (a) Schematic of the two free layers for $p_0 = p_1 = 1$ and $c_0 = c_1 = -1$. d_0 , d_1 and r_{disk} are the layers dimensions. \vec{J} is the current density flow. Layer 0 (1) favors an antiparallel (parallel) configuration in respect to layer 1 (0) due to STT. (b) G-state schematic, where the vortex core gyrates inside the disk. (c) C-state schematic, where the virtual vortex core gyrates outside the disk. (d) PSD map of the gyration frequency in layer 0 as a function of the current in OP configuration. G- to C-state transition at 2 mA characterized by sudden frequency drop.

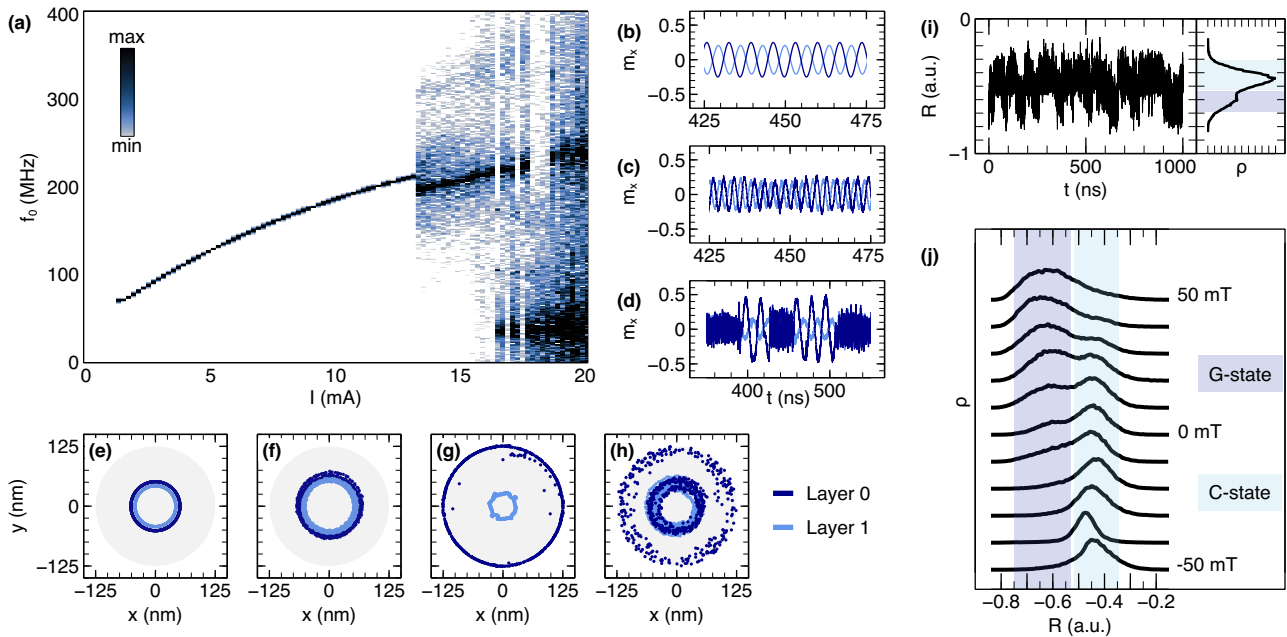


Figure 2: Overview of dynamics for $p_0 = p_1 = 1$, $c_0 = c_1 = -1$ and $M_{\text{sat},1}d_1 = 1.2M_{\text{sat},0}d_0$. (a) PSD map of the gyration frequency in layer 0 as a function of the current. (b), (c) and (d) are respectively the time traces of m_x in each layer at currents $I = 3, 15$ and 19 mA respectively. Light blue plots correspond to layer 1 and dark blue to layer 0. (e) and (f) are the trajectories of the vortex cores at currents $I = 3$ and 15 mA. (g) and (h) are the trajectories of the vortex cores at current $I = 19$ mA, for C- and G- states respectively. In (g), core centers appearing at the disk edges correspond to the C-state. (i) Time trace of the magnetoresistance, $R = -\int m_0(\vec{r}) \cdot m_1(\vec{r}) d\vec{r}^2 / \pi r_{\text{disk}}^2$, at current $I = 20$ mA (left panel) and resistance distribution ρ (right panel). Two peaks observed at $R \approx -0.44$ (light blue area, C-state) and $R \approx -0.61$ (dark blue area, G-state). (j) Resistance distribution at current $I = 20$ mA and perpendicular field B_z going from -50 to 50 mT. Negative (positive) fields favor the C-state (G-state).

Our simulations suggest that the complex dynamics arising from mutual spin torque coupling could be useful for unconventional computing. For example, stochastic transitions between the G- and C- states could be harnessed for generating random numbers for encryption and probabilistic computing, while complex transients could be useful for pattern recognition tasks.

Acknowledgments

This work is supported by France 2030 government investment plan managed by the French National Research Agency under grant reference PEPR SPIN – SPINCOM ANR-22-EXSP-0005.

References

- [1] S. Wittrock, P. Talatchian, M. Romera, et al. [Beyond the gyrotropic motion: Dynamic C-state in vortex spin torque oscillators](#). *Applied Physics Letters* 118, 012404 (2021).
- [2] M.-W. Yoo, D. Rontani, J. Létang, et al. [Pattern generation and symbolic dynamics in a nanocontact vortex oscillator](#). *Nature Communications* 11, 601 (2020).
- [3] A. V. Khvalkovskiy, J. Grollier, A. Dussaux, K. A. Zvezdin, and V. Cros. [Vortex oscillations induced by spin-polarized current in a magnetic nanopillar: Analytical versus micromagnetic calculations](#). *Physical Review B* 80, 140401 (2009).
- [4] R. Matsumoto, S. Lequeux, H. Imamura, and J. Grollier. [Chaos and Relaxation Oscillations in Spin-Torque Windmill Spiking Oscillators](#). *Phys. Rev. Applied* 11, 044093 (2019).
- [5] N. Locatelli, V. V. Naletov, J. Grollier, et al. [Dynamics of two coupled vortices in a spin valve nanopillar excited by spin transfer torque](#). *Applied Physics Letters* 98, 062501 (2011).
- [6] A. Vansteenkiste, J. Leliaert, M. Dvornik, et al. [The design and verification of MuMax3](#). *AIP Advances* 4, 107133 (2014).

Excitation of vortex gyration through non-linear interaction with Floquet magnon modes

Gauthier Philippe^{1,*} and Joo-Von Kim¹

¹Centre de Nanosciences et de Nanotechnologies, CNRS, Université Paris-Saclay, 91120 Palaiseau, France
*gauthier.philippe@universite-paris-saclay.fr

Magnetic vortices are topological spin configurations consisting of circulating in-plane magnetic moments, with the magnetization extending out of the plane within a compact central region known as the core. The dynamics of these vortices are characterized by sub-GHz gyration of the core, which describes a circular motion around the disk's center, and GHz-range spin wave excitations about the vortex state. These excitations are geometrically quantized and indexed by radial and azimuthal numbers [1, 2]. Nonlinear interactions involving these spin waves have potential applications in pattern recognition tasks [3].

Recent studies have demonstrated that the coupling between gyration and spin wave modes can be effectively described using Floquet theory [4]. In this framework, the gyration acts as a periodic modulation of the background spin wave potential, giving rise to magnon Floquet states. These states manifest as a frequency comb around the original spin wave spectrum, with the comb spacing determined by the gyration frequency. Experimental and simulation evidence confirms that exciting the core gyration via RF fields directly generates these Floquet states, whose existence is intrinsically linked to the presence of the vortex core [5]. In this presentation, we will discuss a theoretical investigation utilizing micromagnetic simulations [6] to elucidate the emergence of magnon Floquet states through the excitation of higher-order spin wave modes. Our study focuses on a CoFeBSi disk with a 300-nm diameter and 20-nm thickness, where the ground-state configuration forms a vortex. By employing a supercell approach [7], we resolve the spin wave spectra under radiofrequency magnetic field excitation.

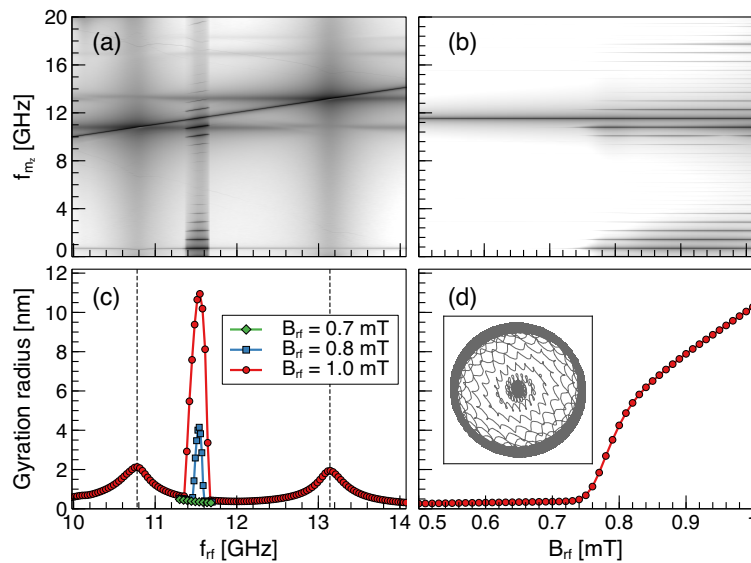


Figure 1: Fig. 1(a) shows a colormap of the power spectrum of the magnetization dynamics in the disk as a function of the RF field frequency. Horizontal lines represent frequencies of the linear eigenmodes, with the low frequency mode at 727 MHz corresponding to the gyration, while higher-frequency branches around 10.8 and 13.1 GHz indicate the first order azimuthal $m \pm 1$ modes. As the RF field frequency is swept through this range, we observe the appearance of a frequency comb around the azimuthal modes and the gyration mode. The appearance of this comb depends on the strength of the RF field amplitude, as shown in Fig. 1(b). Here, we see that the comb emerges above 0.7 mT, with the number of sidebands increasing with the RF field amplitude. The presence of the comb is linked to the gyration, where the average radius of gyration is shown as a function of RF field frequency for three values of the RF field amplitude Fig. 1(c). While direct excitation of the modes $m \pm 1$ (highlighted here by the dashed lines) leads to a small gyration amplitude, we see that it is the off-resonant excitation of both modes simultaneously (at a frequency of 11.5 GHz) that results in a large gyration orbit. The insert in Fig. 1(d) shows the typical core trajectory from the center to a large gyration orbit. This phenomenon exhibits a clear threshold behaviour, as shown in Fig. 1(d), where the gyration orbital radius is shown as a function of RF field strength at a frequency of 11.5 GHz.

Our study highlights a straightforward method for generating Floquet states in magnetic systems without the need for direct modulation of magnetic parameters such as exchange or anisotropy. We foresee that magnon Floquet physics in topological spin textures could serve as a promising platform for advancing the understanding of nonlinear magnonics, with potential applications in signal processing and unconventional computing.

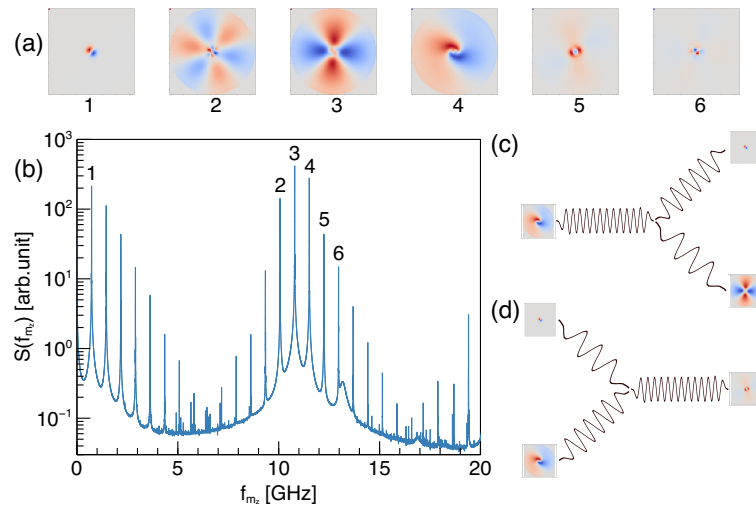


Figure 2: Fig. 2(a) shows the spatial profiles of six selected modes. Mode 1 corresponds to the gyration, while Mode 4 is the primary mode excited by the RF field and resembles a $m = \pm 1$ mode deformed by the core gyration. The modes that constitute the comb around mode 4, i.e., modes 2, 3, 5, and 6, resemble deformed versions of azimuthal modes $m = \pm 3, \pm 2, 0,$ and ± 1 . These are in fact Floquet states that appear due to the nonlinear interaction between the gyration and the original azimuthal mode, which remained sustained as long as the core gyration is present. Fig. 2(b) illustrates the power spectrum under an RF field excitation of 1.0 mT at a frequency of 11.5 GHz. It shows a prominent frequency comb that spans the gyration frequency up to and beyond the azimuthal mode frequencies. Fig. 2(c) and (d) are respectively representation of the non-linear splitting and non-linear confluence of magnon, sum of frequencies and azimuthal indices remain conserved during these processes. These results show how a new class of eigenmodes can arise through the nonlinear interaction between a linear mode and the core gyration.

Acknowledgments

This work was supported by the Horizon Europe Research and Innovation Programme of the European Commission under contract number 101070290 (NIMFEIA).

References

- [1] Gino Hrkac, Paul S Keatley, Matthew T Bryan, and Keith Butler. [Magnetic vortex oscillators](#). *Journal of Physics D: Applied Physics* 48, 453001 (2015).
- [2] Boris Taurel, Thierry Valet, Vladimir V. Naletov, et al. [Complete mapping of the spin-wave spectrum in a vortex-state nanodisk](#). *Phys. Rev. B* 93, 184427 (18 2016).
- [3] Lukas Körber, Christopher Heins, Tobias Hula, et al. [Pattern recognition in reciprocal space with a magnon-scattering reservoir](#). *Nature Communications* 14, 3954 (2023).
- [4] Christopher Heins, Lukas Körber, Joo-Von Kim, et al. [Self-induced Floquet magnons in magnetic vortices](#) (2024).
- [5] Christopher Heins, Attila Kákay, Joo-Von Kim, et al. [Control of magnon frequency combs in magnetic rings](#). 2025. arXiv: 2501.05080 [cond-mat.mes-hall].
- [6] Arne Vansteenkiste, Jonathan Leliaert, Mykola Dvornik, et al. [The design and verification of MuMax3](#). *AIP Advances* 4, 107133 (2014).
- [7] Maryam Massouras, Salvatore Perna, Massimiliano D'Aquino, Claudio Serpico, and Joo-Von Kim. [Mode-resolved micromagnetics study of parametric spin wave excitation in thin-film disks](#). *Phys. Rev. B* 110, 064435 (6 2024).

Complexity Analysis of Chaotic Magnetization Dynamics

Amel Kolli^{1,*}, Hugo Merbouche¹, Grégoire de Loubens¹, Sébastien Petit-Watlot², Slavisa Jovanovic², Joo-Von Kim³, and Damien Rontani⁴

¹SPEC, CEA, CNRS, Université Paris-Saclay, 91190 Gif-sur-Yvette, France

²Institut Jean Lamour, CNRS, Université de Lorraine, 54011 Nancy, France

³Centre de Nanosciences et de Nanotechnologies, CNRS, Université Paris-Saclay, 91120 Palaiseau, France

⁴LMOPS EA 4423 Laboratory, CentraleSupélec, Université de Lorraine, 57070 Metz, France

*amel.kolli@cea.fr

Magnetization dynamics is highly nonlinear, yielding a set of interesting phenomena, among which spin-wave turbulence and chaos [1]. One of the goals is to take advantage of complex magnetization dynamics in nano-oscillators for the generation of true random numbers used for data encryption and secure wireless communication, as well as efficient pre-processing of fast time-varying signals [2]. Dynamical systems and chaos exhibit diverse mathematical structures, offering a compelling explanation for irregular temporal patterns and anomalies in systems that do not appear inherently random.

In this presentation, we will discuss results from the analysis of chaotic time traces obtained through micromagnetic simulations of magnetization dynamics in FeCoB nanodisks. The studied system is an out-of-plane magnetized nanodisk in which the uniaxial anisotropy nearly compensates the shape anisotropy, leading to a highly tunable magnetic response. By driving the system's ferromagnetic resonance (FMR) into the nonlinear regime through an RF magnetic field, we observe a threshold above which a self-modulation instability occurs, yielding chaotic time traces of the average magnetization dynamics (see Fig.1). These chaotic oscillations manifest as irregular, aperiodic variations in the magnetization components, indicating the presence of deterministic chaos. The observed oscillations result from the coupling of multiple spin-wave modes within the nanodisk [3], each contributing to the complex temporal behavior of the magnetization. By adjusting the disk geometry, magnetic parameters, and operating conditions, the frequency and amplitude of these modes can be modified, providing additional control over the onset and characteristics of chaos. This tunability highlights the potential of such nanostructures for applications where chaotic dynamics can be exploited.

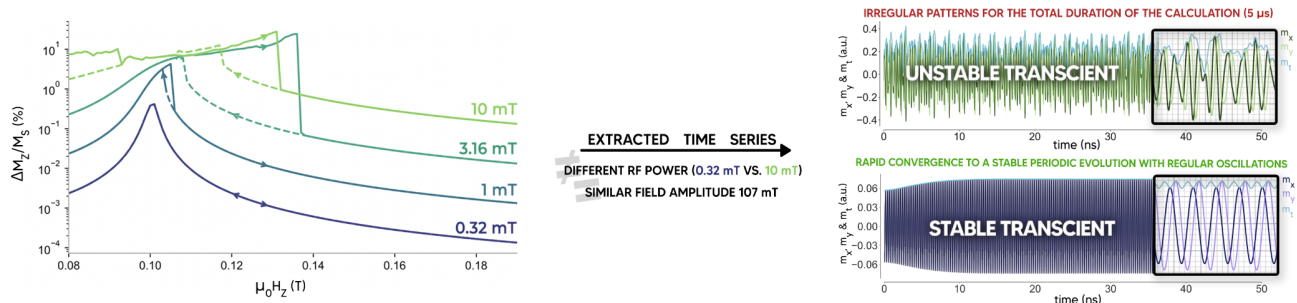


Figure 1: The ferromagnetic resonance curves (**left**) reveal the transition from linear to nonlinear dynamics as the RF field amplitude increases. Time-resolved magnetization evolution (**right**) demonstrate the emergence of chaotic oscillations at high RF field amplitude (unstable transient) versus periodic motion at low amplitude (stable transient).

By reconstructing the attractor in phase space (see Fig.2) using Takens' embedding theorem [4], we map the time series onto a higher-dimensional manifold to study the system's dynamics. This method allows us to visualize the phase space and extract key quantities like the largest Lyapunov exponent and fractal dimension. The Lyapunov exponent measures sensitivity to initial conditions, a hallmark of chaos, while the fractal dimension reveals the attractor's geometric complexity. These tools are essential for distinguishing deterministic chaos from random noise, confirming the chaotic behavior in the magnetization dynamics [5].

Our analysis focuses on identifying the instability threshold and mapping the transition from periodic to chaotic regimes in the control plane (H_z, h_{rf}) where H_z is the applied static magnetic field and h_{rf} denotes the amplitude of the RF magnetic field. It also reveals how the degree of chaos depends on these control parameters. In particular, we identify distinct dynamical behaviors, including quasi-periodic oscillations, chaotic regimes, and intermittent transitions between order and chaos [6]. This provides valuable control levers for tuning the system's response.

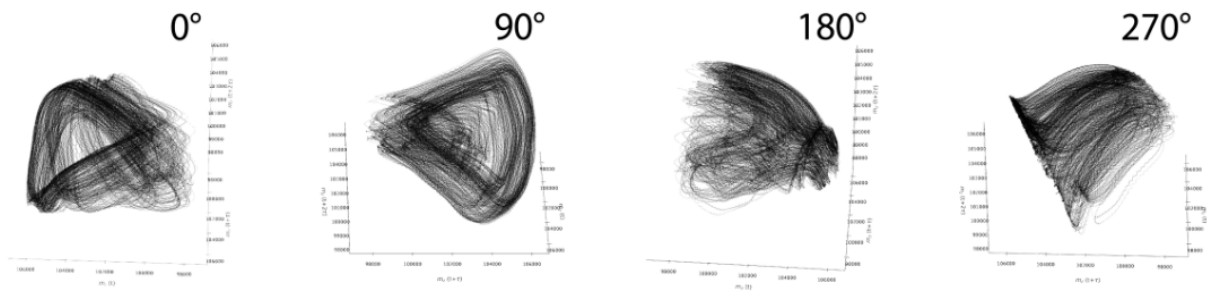


Figure 2: Rotational view of the system's reconstructed attractor in the phase space considering delayed coordinates (t , $t+\tau$, $t+2\tau$) used in the embedding of Takens' theorem.

To ensure that chaotic signals generated by nanostructures can serve as a reliable source of true random numbers, we exploit the sensitivity to initial conditions and the exponential divergence of nearby phase space trajectories to produce random numbers from the inherent unpredictability of chaos. The resulting bit streams are then validated through rigorous statistical tests such as the NIST Randomness Test Suite [7]. These tests evaluate the randomness across multiple statistical criteria to confirm that the generated numbers exhibit the unpredictability and entropy required for cryptographic and sensing applications.

This overall methodology aims to develop a comprehensive framework for understanding the mechanisms that govern chaotic dynamics in coupled spin-torque nano-oscillators (STNOs) or those with delayed feedback, and how these can be controlled and exploited for advanced technological purposes [8], such as secure communication systems and high-speed signal processing. This approach will lay the groundwork for future investigations where nanodisks are integrated into magnetic tunnel junctions, offering a path toward more complex, integrated systems with enhanced capabilities.

Acknowledgments

This work is supported by France 2030 government investment plan managed by the French National Research Agency under grant reference PEPR SPIN – SPINCOM ANR-22-EXSP-0005.

References

- [1] Philip E. Wigen. "Nonlinear Phenomena and Chaos in Magnetic Materials". World Scientific, (1994).
- [2] Myoung-Woo Yoo, Damien Rontani, Jérémy Létang, et al. [Pattern generation and symbolic dynamics in a nanocontact vortex oscillator](#). *Nature Communications* 11 (2020).
- [3] Igor Ngouagnia Yemeli. "Magnetization dynamics of nanostructures in strongly out-of-equilibrium regimes". PhD thesis. Université Paris-Saclay, (2022).
- [4] Floris Takens. "Detecting strange attractors in turbulence". *Dynamical Systems and Turbulence, Warwick 1980*. Springer Berlin Heidelberg, (1981).
- [5] Holger Kantz and Thomas Schreiber. *Nonlinear Time Series Analysis*. Cambridge University Press, (2003).
- [6] Henry D. I. Abarbanel. *Analysis of Observed Chaotic Data*. Springer New York, (1996).
- [7] Meltem Sönmez Turan, Elaine Barker, John Kelsey, et al. *Recommendation for the entropy sources used for random bit generation*. (2018).
- [8] Nhat-Tan Phan, Nitin Prasad, Abderrazak Hakam, et al. [Unbiased random bitstream generation using injection-locked spin-torque nano-oscillators](#). *Phys. Rev. Appl.* 21, 034063 (2024).

Development of an ultrasensitive skyrmion-based magnetic field sensor

Lucia Malucelli^{1,*}, Mariana Caseiro², Isabelle Joumard¹, Eyub Yildiz¹, Nicolas Mollard¹, Stéphane Auffret¹, Jérôme Faure-Vincent¹, Claire Baraduc¹, Claude Fermon², Aurélie Solignac², Myriam Pannetier-Lecoer², Johanna Fischer¹, and H el ene B ea^{1,3}

¹Univ. Grenoble Alpes, CNRS, CEA, SPINTEC, Grenoble, France

²Universit e Paris-Saclay, CEA, CNRS, SPEC, 91191, Gif-sur-Yvette, France

³Institut Universitaire de France (IUF), France

*lucia.malucelli@cea.fr

Magnetic field sensors represent one of the key application in spintronics [1]. Sensors based on magnetoresistive effects have attracted great attention as they combine small dimensions, reduced cost and high magnetic field sensitivity. However, a big challenge nowadays is to improve the level of detectivity beyond the pico-Tesla range, while maintaining a small size and low noise. The development of such a sensor is essential in multiple areas, ranging from the detection of biomedical fields [2] to space exploration [3]. A sensor's performance depends on the estimation of two main quantities: the *sensitivity*, defined as the output signal (S_{out}) slope normalized by the input bias (S_{in}) ($S = \frac{1}{S_{in}} \frac{dS_{out}}{dH}$, expressed in V/V/T or in %/T) and the *noise* arising from multiple sources, expressed in V^2/Hz . The ratio $D = \frac{\sqrt{Noise}}{\frac{dS_{out}}{dH}}$ (expressed in T/\sqrt{Hz}) is the *detectivity* that refers to the lowest signal the sensor can measure at a given frequency. Hence, a combined high sensitivity and low noise is needed in order to obtain low detectivity values and, in this way, achieve a good sensing performance.

In the last few years, multilayer hetero-structures with spin textures, like skyrmions, have been widely studied for low-energy-consumption memory applications or probabilistic and neuromorphic computing [4]. However, there exist only few studies where skyrmions are used for sensing applications: they have been used, for example, for counting the number of rotations of a permanent magnet [5] or for fabricating a 3D magnetic field sensor without pushing for a low limit of detection [6].

Recently, we discovered that skyrmion multilayers with perpendicular magnetic anisotropy can exhibit an extremely high sensitivity to very small out-of-plane magnetic fields (see Figure 1a). Moreover, due to the anomalous Hall effect [7], it is possible to convert this response into an electrical signal in a micrometer-sized sensor. In addition to the high sensitivity, reaching low intrinsic noise is crucial for the characterization of such a sensor.

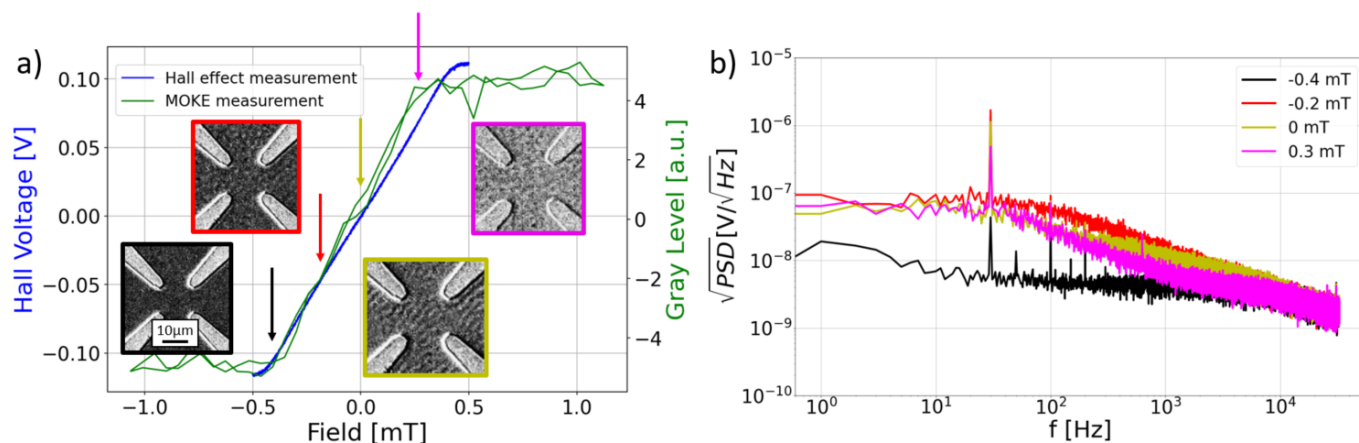


Figure 1: (a) Sensitivity measurements of a Ta/FeCoB/TaO_x trilayer: comparison between the electrical Hall effect (blue line) measurement and the magneto optical Kerr effect (MOKE) measurement (green line). MOKE image insets depict the magnetic domains at four distinct field values. Each image corresponds to the field value indicated by the arrow matching the color of its outline. (b) Noise measurement of the same magnetic trilayer at the same constant static external field values (same colour-code than in (a)). The square root of the power spectral density (\sqrt{PSD}) is plotted in the frequency domain as a function of the applied magnetic field. The peak at 30Hz corresponds to a known excitation signal and serves for calibrating.

We study a heavy-metal/ferromagnet/metal oxide magnetic trilayer made of Ta/FeCoB/TaO_x with perpendicular magnetic anisotropy (PMA). A thickness gradient of the FeCoB and the top Ta layer allows, among other properties, a very fine tuning of the magnetic anisotropy. In the transition zone where magnetization shifts from PMA to a paramagnetic regime, low domain wall energy facilitates thermal demagnetization and the nucleation of skyrmions under the influence of exceptionally small external magnetic fields (in the μ T range). This leads to remarkably low saturation fields, around 200 μ T, accompanied

by a quasi-linear response (Figure 1a). With a magneto-optical Kerr effect (MOKE) microscope, it is possible to optically image the evolution of the magnetic domains while simultaneously recording a hysteresis loop. An electrical anomalous Hall effect measurement of the loop is performed in the same multilayer stack, patterned into Hall bar crosses, with a sensing area of $10 \times 10 \mu\text{m}^2$. Figure 1a shows the comparison between the loop measured electrically (in blue, $I_{\text{bias}} = 100 \mu\text{A}$) and the one measured magnetically with the MOKE (in green). The four images visible inside are taken by the MOKE microscope and represent the magnetic domains of the central part of a hall bar cross at four representative field values: in the saturation regime ($-400 \mu\text{T}$, image with black outline), in the region where skyrmions are nucleated with negative field ($-200 \mu\text{T}$, red outline), at zero field where magnetic domains are characterized by stripes ($0 \mu\text{T}$, yellow outline) and in the region where skyrmions are nucleated with positive field ($300 \mu\text{T}$, violet outline).

We performed a series of noise measurements with the sensor operating at the same four representative static field values described before: the saturation regime ($-400 \mu\text{T}$), the region where skyrmions are nucleated with negative field ($-200 \mu\text{T}$), at zero field where magnetic domains are characterized by stripes ($0 \mu\text{T}$) and the region where skyrmions are nucleated with positive field ($300 \mu\text{T}$). Additionally, an AC magnetic field of 0.1 mT at 30 Hz was applied, to serve as a calibration signal for the sensitivity. Figure 1b shows the square root of the power spectral densities ($\sqrt{\text{PSD}}$) in the frequency domain measured while injecting a current of $I_{\text{bias}} = 100 \mu\text{A}$ in the Hall bar cross, considering the four representative field values mentioned before. It is possible to clearly identify two different levels of noise: a lower one ($\sim 10^{-8} \text{ V}/\sqrt{\text{Hz}}$) corresponding to the region where the sensor is operating outside the sensitive field range, that is the saturation zone, and a higher one ($\sim 10^{-7} \text{ V}/\sqrt{\text{Hz}}$) corresponding to the linear region where the sensor is operating along the sensitive field range ($\pm 300 \mu\text{T}$). In the first case, the thermal noise is predominant at high frequencies, while in the second case the $1/f$ noise become the main contribution. Moreover, we were able to correlate the domain wall structure at different static magnetic fields, as seen on the MOKE images, with the observed noise behavior. It appears that the thermally activated domain wall motion/distortion results in an additional source of noise for the sensor. Despite that, in this work we present an ultrasensitive skyrmion-based magnetic field sensor with an unexpectedly low noise level and an overall detectivity in the $300\text{--}400 \text{ nT}/\sqrt{\text{Hz}}$ range. These values are comparable to the ones found in the literature for similar anomalous Hall-effect sensors [7], so we remain highly optimistic to push this limit with further optimizations.

Acknowledgments

This work has benefited from a government grant operated by the French National Research Agency as part of the France 2030 program, via grant reference «ANR-22-EXSP-0006 » ADAGE, and it has been supported also by the CAPSKY project (IRGA, UGA).

References

- [1] Paulo P. Freitas, Ricardo Ferreira, and Susana Cardoso. [Spintronic Sensors](#). *Proceedings of the IEEE* 104, 1894–1918 (2016).
- [2] Chloé Chopin, Jacob Torrejon, Aurélie Solignac, et al. [Magnetoresistive Sensor in Two-Dimension on a \$25 \mu\text{m}\$ Thick Silicon Substrate for In Vivo Neuronal Measurements](#). *ACS Sensors* 5, 3493–3500 (2020).
- [3] Samuel Manceau, Thomas Brun, Johanna Fischer, et al. [Large amplification of the sensitivity of symmetric-response magnetic tunnel junctions with a high gain flux concentrator](#). *Applied Physics Letters* 123 (2023).
- [4] Albert Fert, Nicolas Reyren, and Vincent Cros. [Magnetic skyrmions: advances in physics and potential applications](#). *Nature Reviews Materials* 2 (2017).
- [5] Kilian Leutner, Thomas Brian Winkler, Raphael Gruber, et al. [Skyrmion automotion and readout in confined counter-sensor device geometries](#). *Physical Review Applied* 20 (2023).
- [6] Sabri Koraltan, Rahul Gupta, Reshma Peremadathil Pradeep, et al. [Skyrmionic device for three dimensional magnetic field sensing enabled by spin-orbit torques](#). 2024.
- [7] Yiyou Zhang, Kang Wang, and Gang Xiao. [Noise characterization of ultrasensitive anomalous Hall effect sensors based on \$\text{Co}_{40}\text{Fe}_{40}\text{B}_{20}\$ thin films with compensated in-plane and perpendicular magnetic anisotropies](#). *Applied Physics Letters* 116 (2020).

Antiferromagnetic order control in 2D CrSBr

Clément Pellet-Mary^{1,*}

¹Physics department, Basel University, Basel, Switzerland

*clement.pellet-mary@unibas.ch

CrSBr is an emerging van der Waals (vdW) magnet that has been gaining significant attention, as it exfoliates easily down to the monolayer, which remains stable under ambient conditions. It also supports a relatively high Curie temperature of 140 K and exhibits magneto-optical coupling through its excitons [1].

The magnetic structure of CrSBr, an A-type antiferromagnet (AF), presents a lot of opportunities in spintronics, combining two recent trends in the field: 2D materials and AF spintronics. Similar to synthetic AFs, CrSBr can exhibit giant tunneling magnetoresistance, a property recently utilized to create non-volatile memory devices [2].

However, a key challenge in working with AF materials is the control and measurement of their order parameter. In our work, we propose a novel method to manipulate the AF order in a CrSBr bilayer by leveraging lateral exchange interactions within a single crystalline flake. As a demonstration, we present the first observation of an AF domain wall in an atomically thin vdW magnet.

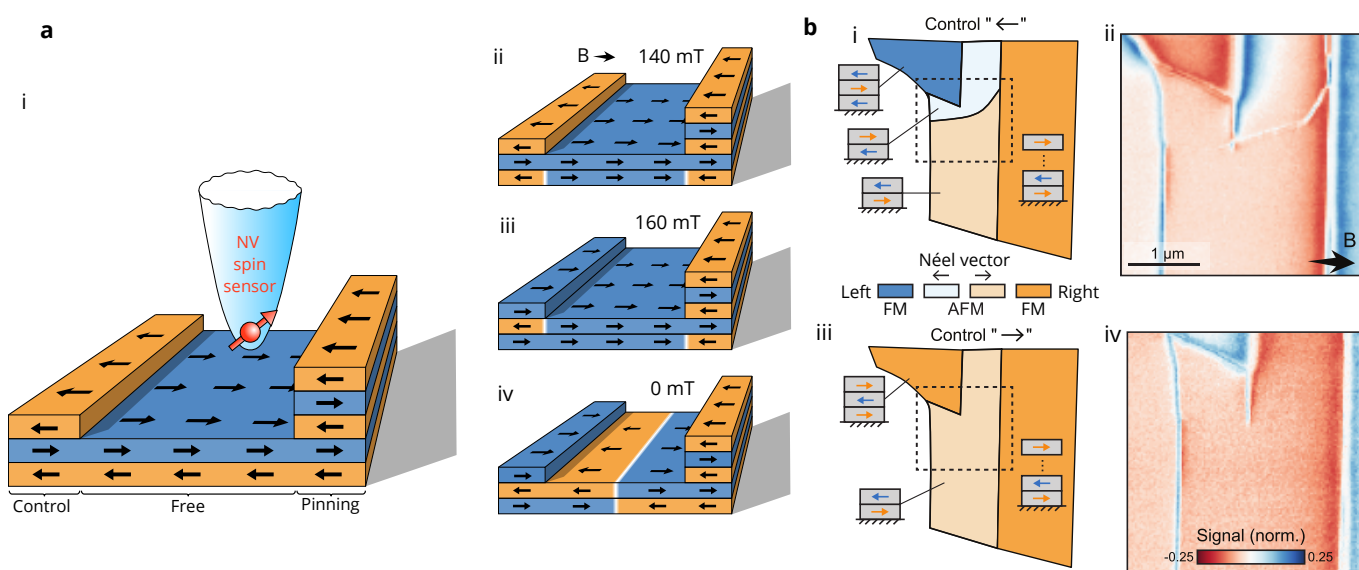


Figure 1: **a** Illustration of the protocol used to create AF domains in a bilayer sandwiched by two odd-layered stacks. The independent manipulation of the stacks relies on the spin-flip dependence on the number of layers [3]. **b** Depiction of the magnetization of a flake (left) and corresponding magnetic imaging by NV magnetometry (right) for two sets of boundary conditions. An AF domain wall is visible when the bilayer boundary conditions are non-uniform.

The process for creating AF domains in a CrSBr bilayer is illustrated in Fig. 1 a. This technique exploits a fundamental property of 2D A-type AFs: only regions with an even number of layers are truly AF, while regions with an odd number of layers exhibit intrinsic magnetization (due to one uncompensated layer), making them responsive to external fields. By independently manipulating neighboring odd-layer stacks, it is possible to establish boundary conditions that favor the formation of distinct AF orders, thereby generating AF domains.

An experimental demonstration is shown in Fig. 1 b. The trilayer control gate is flipped between the top and bottom panels. As a result, an AF domain wall appears and disappears, as observed using scanning NV magnetometry.

This protocol shares similarities with the process of imprinting a ferromagnetic (FM) pattern into an AF through exchange bias. However, in this case, the exchange occurs laterally through the 1D channel separating the stacks, rather than vertically. This opens new possibilities for 2D architectures in spintronic devices.

References

- [1] Michael E. Ziebel, Margalit L. Feuer, Jordan Cox, et al. [CrSBr: An Air-Stable, Two-Dimensional Magnetic Semiconductor](#). *Nano Lett.* 24, 4319–4329 (2024).
- [2] Yuliang Chen, Kartik Samanta, Naafis A. Shahed, et al. [Twist-assisted all-antiferromagnetic tunnel junction in the atomic limit](#). *Nature* 632, 1045–1051 (2024).
- [3] Chen Ye, Cong Wang, Qiong Wu, et al. [Layer-Dependent Interlayer Antiferromagnetic Spin Reorientation in Air-Stable Semiconductor CrSBr](#). *ACS Nano* 16, 11876–11883 (2022).

Imaging magnetic vortices in a van der Waals magnet at room temperature with scanning NV magnetometry

Carolin Schrader^{1,*}, Elias Sfeir¹, Mário Ribeiro², Giulio Gentile², Alain Marty², Céline Vergnaud², Frédéric Bonell², Isabelle Robert-Philip¹, Matthieu Jamet², Vincent Jacques¹, and Aurore Finco¹

¹Laboratoire Charles Coulomb, Université de Montpellier, CNRS, Montpellier, France

²Université Grenoble Alpes, CEA, CNRS, IRIG-SPINTEC, Grenoble, France

*carolin.schrader@umontpellier.fr

Since their discovery in 2017 [1], two-dimensional (2D) van der Waals (vdW) magnets have gained significant attention for their potential application in spintronics. However, this would require room temperature magnetism and large-scale fabrication, and despite extensive research, only few 2D materials exhibiting ferromagnetism at room temperature have been found so far. Recently, ferromagnetic order at room temperature has been demonstrated in thin Fe_5GeTe_2 grown by Molecular Beam Epitaxy (MBE) [2]. The development of further technological applications requires understanding of the magnetism in these materials, and magnetic imaging techniques are crucial for studying a material's magnetic phases and magnetisation patterns. In this work, we use a single-spin scanning probe technique to study the magnetism in few-layer Fe_5GeTe_2 .

Scanning NV magnetometry employs the single spin of a nitrogen-vacancy (NV) defect in diamond to measure a sample's stray magnetic field, making use of its spin-dependent fluorescence. In order to achieve close proximity between the sample and the sensor, a single NV centre is embedded into the tip of an all-diamond cantilever and brought into close contact with the sample via tuning fork-based atomic force microscopy (Fig. 1). By scanning the NV centre across a sample and recording its fluorescence, the sample's magnetic stray field can be imaged. This technique offers a high sensitivity of several $\mu\text{T}/\sqrt{\text{Hz}}$ and spatial resolution of a few tens of nanometres, and is thus well suited to map out the magnetism in two-dimensional materials [3].

Here, we employ scanning NV magnetometry to quantitatively image the magnetic texture in 12 nm-thin MBE-grown Fe_5GeTe_2 at the nanoscale. We investigate the effect of patterning on the magnetic order and demonstrate the stabilisation of magnetic vortices in various micron-sized structures at room temperature (Fig. 2). Upon application of an external magnetic field of a few mT we obtain a single ferromagnetic domain in these structures, which allows us to extract a saturation magnetisation of about 160 kA/m. Our results show the role of confinement for the stabilisation of complex magnetic structures in 2D magnets and highlight the potential of the room temperature vdW magnet Fe_5GeTe_2 for applications in spintronics.

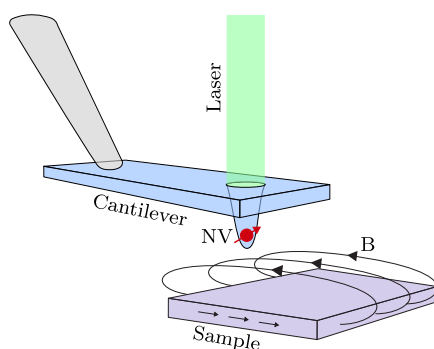


Figure 1: Illustration of a scanning NV magnetometry experiment.

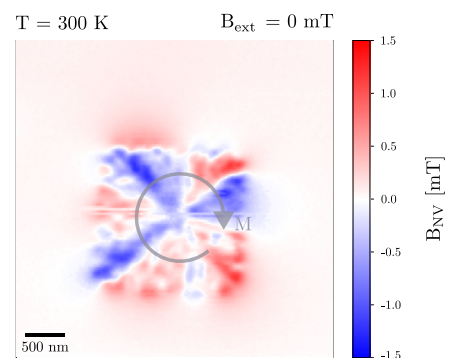


Figure 2: NV magnetometry scan showing the stray field of a magnetic vortex in a 12 nm-thin square Fe_5GeTe_2 .

References

- [1] C. Gong, L. Li, Z. Li, et al. [Discovery of intrinsic ferromagnetism in two-dimensional van der Waals crystals](#). *Nature* 546, 265–269 (2017).
- [2] M. Ribeiro, G. Gentile, A. Marty, et al. [Large-scale epitaxy of two-dimensional van der Waals room-temperature ferromagnet \$\text{Fe}_5\text{GeTe}_2\$](#) . *npj 2D Materials and Applications* 6 (2022).
- [3] E. Marchiori, L. Ceccarelli, N. Rossi, et al. [Nanoscale magnetic field imaging for 2D materials](#). *Nature Reviews Physics* 4, 49–60 (2022).

Spintronique et matériaux

Composition-dependent charge-to-spin current conversion in topological insulators $\text{Bi}_{1-x}\text{Sb}_x$ thin films

D.P.G. Nyoma¹, M.S. Dehaghani^{1,2,*}, M.A. Khaled², S. Fekraoui², R. Daubriac², C. Bigi³, F. Bertran³, Q. Gravelier², A. Arnoult², R. Monflier², L. Petit¹, B. Lassagne¹, C. Durand², S.R. Plissard², and T. Blon¹

¹LPCNO, INSA - Université de Toulouse, France

²LAAS-CNRS, Université de Toulouse, France

³Synchrotron SOLEIL, L'Orme des Merisiers, Saint-Aubin, France

*sadeghian-d@insa-toulouse.fr

Current-induced magnetization manipulation is a promising approach for high-performance MRAM, especially Spin Orbit Torque (SOT) which allows sub-ns speed with high endurance. SOT relies on the spin-orbit interaction, prominent in materials such as topological insulators (TI) which exhibit spin-momentum locking on their surface. By minimizing bulk conduction in TI, charge transport is preferentially routed through the surface states, enhancing the charge-to-spin conversion efficiency [1]. $\text{Bi}_{1-x}\text{Sb}_x$ TI alloys stand out with a band structure that can be tuned by the composition and with large spin Hall angles [2]. While early studies have demonstrated topologically protected surface states in BiSb alloys, challenges persist in understanding the impact of surface roughness, oxidation and crystallinity on device performances.

Here we investigate the topological surface states in BiSb films using ARPES (17K), Hall measurements and current-induced magnetic switching of interfaced magnetic layers. Fig. 1 presents ARPES measurements on 2 μm and 100 nm thick $\text{Bi}_{1-x}\text{Sb}_x$ layers grown by MBE on GaAs(111)A for varying Sb compositions in the TI window, ranging from $x = 0.07$ to 0.19.

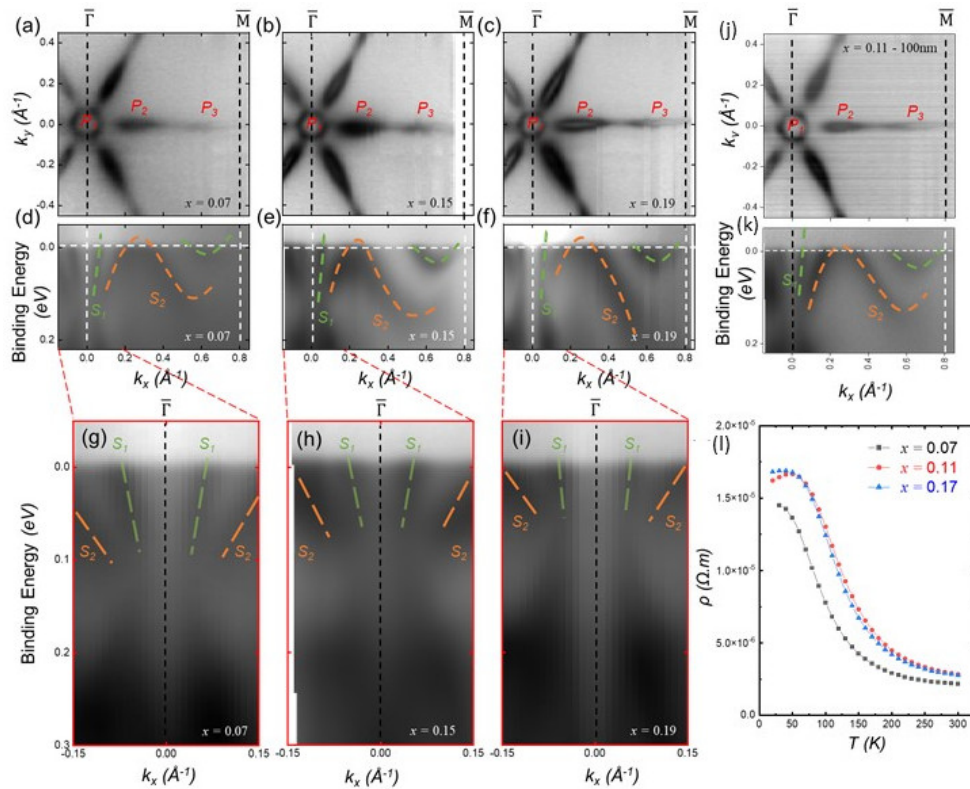


Figure 1: (a),(b),(c) Fermi surface maps measured by ARPES at 17K on $\text{Bi}_{1-x}\text{Sb}_x$ 2 μm films for $x = 0.07$, 0.15, 0.19, resp.. (d),(e),(f) are cross sections of the band dispersion along the $\bar{\Gamma}\bar{M}$ direction with zoomed-in region in (g),(h),(i). (j) ARPES Fermi surface maps and (k) cross sections of the band dispersion of a 100 nm-thick $\text{Bi}_{0.89}\text{Sb}_{0.11}$ film. (l) Temperature dependence of the resistivity of 100 nm thick $\text{Bi}_{1-x}\text{Sb}_x$ films with $x = 0.07$, 0.11, 0.17.

As reported previously [3], the surface state intensity exhibits an hexagonal core (P_1) at the $\bar{\Gamma}$ point, corresponding to the S_1 surface state band crossing the Fermi level. P_1 is surrounded by six petals, oriented along the $\bar{\Gamma}\bar{M}$ direction, corresponding to the P_2 hole pockets of the S_2 band and the P_3 electron pockets at the local minima of the S_1 band. Although the surface states display a six-fold symmetry, all samples exhibit a strong three-fold symmetry, which corresponds to the projection of the bulk states to the surface, consistent with single crystalline BiSb. The size of the carrier pockets is composition-dependent, with smaller petals and reduced intensity for Bi-rich samples. The band dispersions shown in Fig. 1(d-f) display five distinct crossings, confirming the non-trivial topological insulating nature of the samples. Interestingly, the S_1 and S_2 surface bands cross the Fermi level at distinct k_x , which is correlated to the evolution of the bulk bands: as Sb increases, the

valence bands at the $\bar{\Gamma}$ point approaches the Fermi level, pulling up S_1 and S_2 . Interestingly, reducing the BiSb thickness to 100 nm give similar results (Fig. 1(j)-(k)).

Resistivity measurements are presented Fig. 1(l) for 100 nm thick films. From values as low as $2.3 \times 10^{-6} \Omega \cdot \text{m}$ at 300K, it increases from 300K to 70K, indicating a semiconductor behavior, to reach a maximum around 50-60K. At lower temperatures, it decreases, a sign of the metallic behavior typical of TIs : as the temperature drops, the concentration of thermally excited bulk carriers decreases, enhancing the contribution of the metallic surface states. Activation energies are estimated to be approximately 18.7, 23.7, 23.2 meV for $x=0.07, 0.11, 0.17$. These values are in the same order of magnitude as half the bandgap energies expected for $\text{Bi}_{1-x}\text{Sb}_x$ [4]. Our findings are in good agreement with the expected band gap evolution, where highest values are expected at the center of the TI composition-window.

Finally, a Pt 4nm/Co 0.6nm/Pt 1nm trilayer was deposited on the 100 nm thick $\text{Bi}_{1-x}\text{Sb}_x$ films for $x=0.07, 0.11, 0.17$ (Fig.2(a)). After patterning into Hall bar (Fig. 2(b)), anomalous Hall measurements display the perpendicular anisotropy of the magnetic stacking whatever x (Fig. 2(c)). For $x=0.07$, no current-induced magnetization switching is obtained. For $x=0.11$, the current toggles the Co magnetization between up and down states (Fig. 2(e)), but the associated R_H variation is lower than the one driven by an in-plane magnetic field sweeping (Fig. 2(d)), indicating that the current-induced reversal is limited to some magnetic domains. For $x=0.17$, a complete current-induced switching is obtained (Fig. 2(g)), as attested by the comparable R_H change with the R_H - B_z (Fig. 2(c)) and R_H - B_x curves (Fig. 2(f)). The switching critical current density is $J_{SW}=1\text{MA}/\text{cm}^2$, significantly lower than the typical 10-100 MA/cm^2 obtained in heavy metal (HM)/ferromagnet structures. This suggests high SOT efficiency despite the additional SbOx 1nm/Pt 1nm layers at TI/FM interface. Interestingly, the SOT switching power dissipation (ρJ_{SW}^2) is here as low as $3 \times 10^{14} \text{W}\cdot\text{m}^{-3}$, which significantly distinguishes MBE-grown BiSb as efficient SOT materials in comparison to HM and sputtering grown BiSb, which require switching powers larger than 5×10^{15} and $10^{15} \text{W}\cdot\text{cm}^{-3}$, resp. [5].

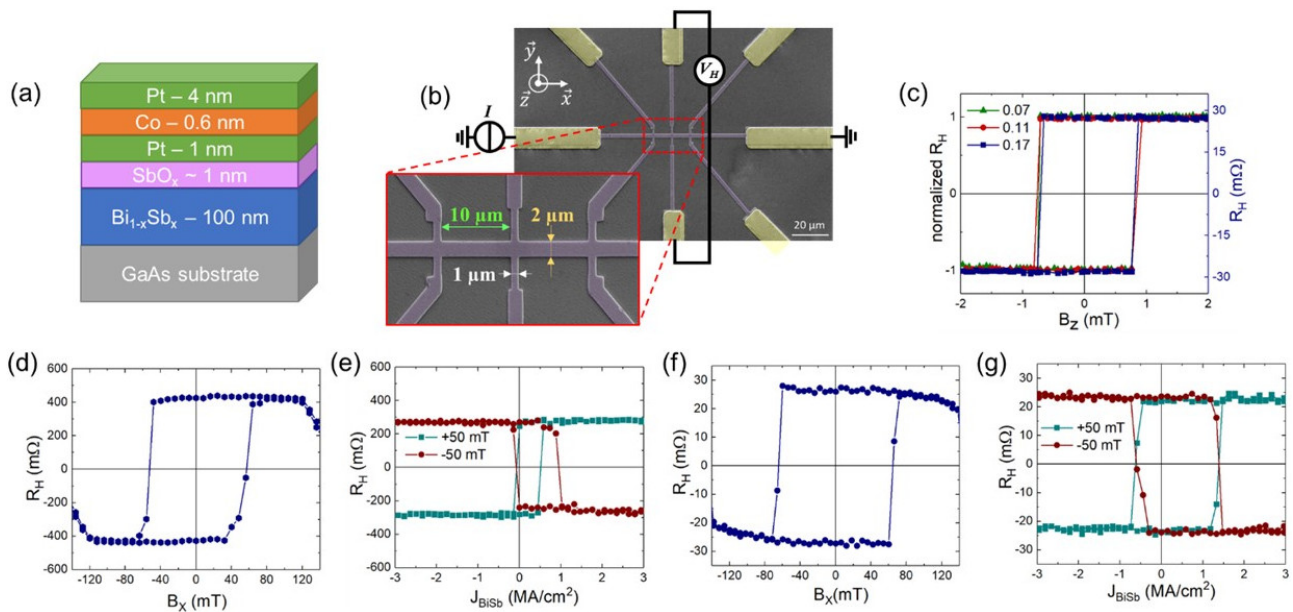


Figure 2: (a) Pt/Co/Pt/BiSb/GaAs heterostructure. (b) SEM image of a patterned device. (c) Normalized Hall resistance R_H as a function of B_z at 300K. (d) R_H as a function of B_x applied along the current direction x for $x=0.11$. (e) R_H as a function of current density in $\text{Bi}_{0.89}\text{Sb}_{0.11}$ with $B_x=\pm 50\text{mT}$. (f) R_H as a function of B_x for $x=0.17$. (g) R_H as a function of current density in $\text{Bi}_{0.83}\text{Sb}_{0.17}$ with $B_x=\pm 50\text{mT}$.

References

- [1] Mellnik A.R. et al. [Spin-transfer torque generated by a topological insulator](#). *Nature* 511, 449 (2014).
- [2] Binda F et al. [Spin-Orbit Torques and Spin Hall Magnetoresistance Generated by Twin-Free and Amorphous \$\text{Bi}_{0.9}\text{Sb}_{0.1}\$ Topological Insulator Films](#). *Adv. Mat.* 35, 2304905 (2023).
- [3] Baringthon L. et al. [Topological surface states in ultrathin \$\text{Bi}_{1-x}\text{Sb}_x\$ layers](#). *Phys. Rev. Mater.* 6, 074204 (2022).
- [4] Lenoir B. et al. [Effect of antimony content on the thermoelectric figure of merit of \$\text{Bi}_{1-x}\text{Sb}_x\$ alloys](#). *J. Phys. Chem. Sol.* 59, 129 (1998).
- [5] Ruixian Z. et al. [High spin Hall angle in BiSb topological insulator and perpendicularly magnetized CoFeB/MgO multilayers with metallic interfacial layers](#). *App. Phys. Lett.* 124, 072402 (2024).

Spin-dependent transport properties of epitaxial DyVO₃ and GdVO₃ thin films on (110)-oriented NdGaO₃ substrate

Mariam Martirosyan^{1,*}, Sébastien Petit-Watelot¹, Jaafar Ghanbaja¹, Ludovic Pasquier¹, Sylvie Migot¹, Karine Dusmenil¹, Pierre-Eymeric Janolin², Alexandre Bataille², Alessandro Coati³, Andrea Resta³, Alina Vlad³, and Olivier Copie¹

¹*Institut Jean Lamour, CNRS, Université de Lorraine, F-54000 Nancy, France*

²*Université Paris-Saclay, CentraleSupélec, CNRS, Laboratoire SPMS, F-91190 Gif-sur-Yvette, France*

³*Synchrotron SOLEIL, L'Orme des Merisiers, F-91190 Saint-Aubin, France*

**mariam.martirosyan@univ-lorraine.fr*

The increasing interest in low-energy cost control of magnetic states has led to the consideration of pure spin currents generation, enabling, for example, the manipulation of spins in magnetic insulators. A pure spin current can be generated by injecting a charge current into a non-magnetic heavy metal with a strong spin-orbit coupling. This charge current induces a transverse spin current via the spin Hall effect (SHE). Considering an adjacent layer as a magnetic material, the accumulation of spin at the interface generates a perpendicular charge current, which influences the resistance of the heavy metal via the inverse spin Hall effect (ISHE).

The spin current propagating in the adjacent material can influence its magnetization, potentially reversing it, through spin-orbit torque (SOT) [1]. The resistance of the heavy metal depends on the relative orientation of the spin polarization and the magnetization of the material, a phenomenon known as Spin Hall Magnetoresistance (SMR), which provides information on the magnetization direction of the magnetic material.

Although spin effects on the transport properties of ferromagnetic materials have been widely studied [2, 3] antiferromagnetic materials have received less attention. However, these materials are of considerable interest. Unlike ferromagnetic materials, antiferromagnetic materials show little or no net magnetization, which makes them less sensitive to magnetic fields and gives them greater robustness. Furthermore, their ultra-fast dynamics in the terahertz (THz) range make them particularly interesting, compared to the resonance of ferromagnetic materials in the gigahertz (GHz) range.

In this context, we are interested in transition metal oxides with ABO₃ perovskite structure. These materials have demonstrated a wide range of intriguing phenomena, from magneto-electric effects to high critical temperature superconductivity [4, 5]. These characteristics are the result of the structure's ability to adapt to different atoms of the periodic table and are closely related to the strong correlations between spin, orbital, and charge degrees of freedom of the B electrons [6, 7]. RVO₃ compounds share the typical characteristics of transition metal oxides, they are Mott insulators with a complex phase diagram presented in the Fig.1(a), with various magnetic, orbital and structural transitions [8]. Below the Néel temperature, these compounds adopt a C-type antiferromagnetic order. In addition, for lighter rare earths, a transition to a G-type order is observed, and this order can be controlled by the application of a magnetic field [9].

While PrVO₃ and LaVO₃ have mainly been studied as thin films [10, 11], less focus has been placed on other rare earths. To address this gap, we investigate the synthesis of DyVO₃ (DVO) and GdVO₃ (GVO) on NdGaO₃ (NGO). The positions of these rare earths in the phase diagram make them particularly interesting for the study of magnetotransport properties. Indeed, DVO and GVO are located at the boundary of different structural, magnetic, and orbital transitions [8].

In this study, we focus on the behavior of epitaxial Pt/GVO//NGO(110) and Pt/DVO//NGO(110) heterostructures grown using the pulsed laser deposition (PLD) technique, specifically examining the transport properties of platinum influenced by the spin characteristics of the vanadates. The orthorhombic NGO substrate is used to stabilize a single orientation of the orthorhombic film, which typically exhibits multiple domains when deposited on a cubic substrate [10–12]. Additionally, due to the strong spin-orbit coupling in Pt, a pure spin current can be generated, which then interacts with the magnetization of GVO and DVO through the SOT.

We will first present the result of the in-depth structural characterization of GVO//NGO(110) and DVO//NGO(110) heterostructures by X-Ray Diffraction (XRD) using laboratory and synchrotron sources, High-Resolution Transmission Electron Microscopy (HRTEM) and Scanning Transmission Electron Microscopy (STEM), see Fig.1(b-c). Next, we investigate the magnetotransport properties of the Hall-cross patterned heterostructures (with 10nm Pt), displayed in Fig.1(d), through angle-dependent magnetotransport measurements. For this purpose, we use harmonic voltage analysis with different field geometries, which allows the separation of the different effects related to magnetotransport. First harmonic measurements group together the magnetoresistive effects, which vary linearly with the current, while those at the second harmonic mainly reflect the thermoelectric effects and the oscillation of the magnetization around its equilibrium position. Combining this approach while varying the temperature and the field, see Fig.1(e-g), enables to disentangle the effects due to platinum polarization and direct interfacial contribution between platinum and GVO or DVO.

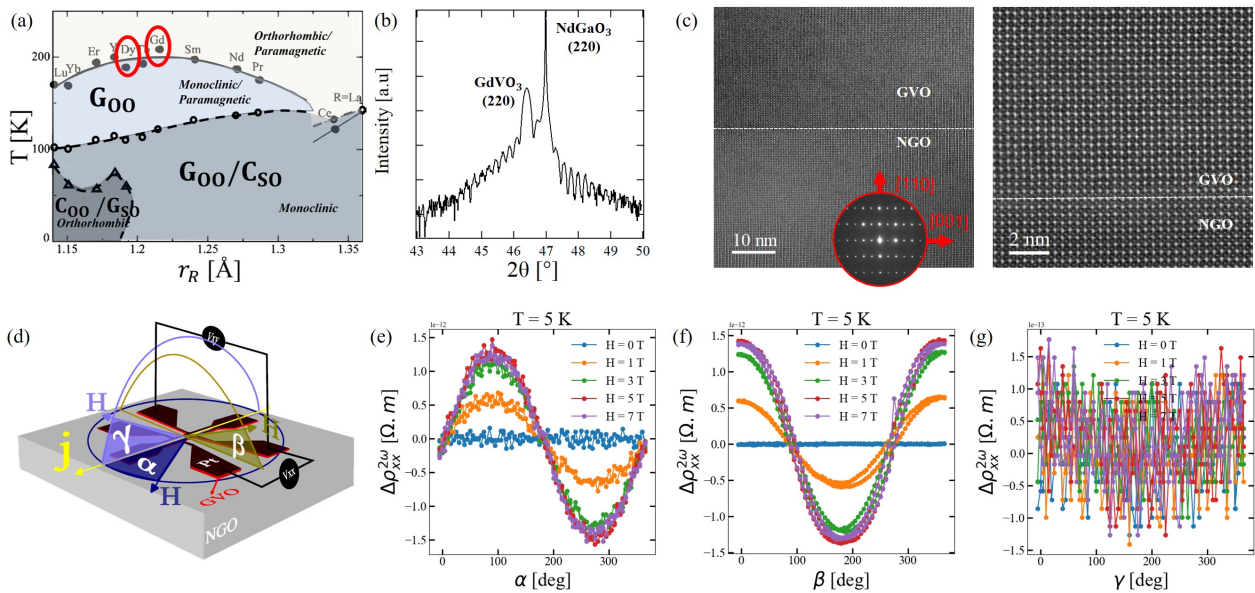


Figure 1: (a) Phase diagram of RVO_3 compounds adapted from [8]. (b) XRD $\theta/2\theta$ measurement around the (220) direction of the $GdVO_3$ (GVO) film deposited on a (220)-oriented $NdGaO_3$ (NGO) substrate. (c) HRTEM (left) and HAADF-STEM (right) micrographs of the GVO/NGO interface. (d) Hall bar device of a Pt/GVO/NGO heterostructure, with measurements of the longitudinal and transverse voltages by rotating the bar around three different angles, α , β , and γ . (e)-(g) Angle (α , β , γ)-dependent magnetotransport measurements at 5 K and magnetic fields ranging from 0 to 7 T.

Acknowledgments

This work was supported by the French National Research Agency (ANR) under project CITRON (ANR-21-CE09-0032), the Région Grand Est under project RHUM (AAP-013-075), and the France 2030 government investment plan under grant PEPR SPIN - SPINMAT (ANR-22-EXSP-0007). The work has benefited of the resources of experimental platforms at IJL: Tube Davm (funded by FEDER EU, ANR, Région Grand Est, and Métropole Grand Nancy), 3M, Magnetism & Cryogenics and XGamma, supported by the LUE-N4S project, part of the French PIA project Lorraine Université d'Excellence (ANR-15IDEX-04-LUE), and by FEDER-FSE Lorraine et Massif Vosges 2014-2020, an EU program.

References

- [1] S. Li, S. Goolaup, J. Kwon, et al. [Deterministic Spin-Orbit Torque Induced Magnetization Reversal In Pt/\[Co/Ni\]_n/Co/Ta Multilayer Hall Bars](#). *Scientific Reports* 7, 972 (2017).
- [2] Ł. Karwacki, K. Grochot, S. Łazarski, et al. [Optimization of spin Hall magnetoresistance in heavy-metal/ferromagnetic-metal bilayers](#). *Scientific Reports* 10, 10767 (2020).
- [3] J. M. Gomez-Perez, X. P. Zhang, F. Calavalle, et al. [Strong Interfacial Exchange Field in a Heavy Metal/Ferromagnetic Insulator System Determined by Spin Hall Magnetoresistance](#). *Nano Letters* 20, 6815–6823 (2020).
- [4] T. Kimura, T. Goto, H. Shintani, et al. [Magnetic Control of Ferroelectric Polarization](#). *Nature* 426, 55–8 (2003).
- [5] J. B. Goodenough. [Electronic and ionic transport properties and other physical aspects of perovskites](#). *Reports on Progress in Physics* 67, 1915–1993 (2004).
- [6] M. Imada, A. Fujimori, and Y. Tokura. [Metal-insulator transitions](#). *Rev. Mod. Phys.* 70, 1039–1263 (1998).
- [7] Y. Tokura and N. Nagaosa. [Orbital Physics in Transition-Metal Oxides](#). *Science* 288, 462–468 (2000).
- [8] S. Miyasaka, Y. Okimoto, M. Iwama, and Y. Tokura. [Spin-orbital phase diagram of perovskite-type \$RVO_3\$ \(\$R = \text{rare-earth ion or Y}\$ \)](#). *Phys. Rev. B* 68, 100406 (2003).
- [9] S. Miyasaka, T. Yasue, J. Fujioka, et al. [Magnetic Field Switching between the Two Orbital-Ordered States in \$DyVO_3\$](#) . *Physical Review Letters* 99, 217201 (2007).
- [10] G. Masset, O. Copie, J. Ghanbaja, et al. [Epitaxial growth and structure of \$LaVO_3\$ and \$PrVO_3\$ thin films](#). *Physical Review Materials* 4, 064417 (2020).
- [11] H. Meley, Karandeep, L. Oberson, et al. [Structural analysis of \$LaVO_3\$ thin films under epitaxial strain](#). *APL Materials* 6, 046102 (2018).
- [12] H. Rotella, U. Lüders, P. E. Janolin, et al. [Octahedral tilting in strained \$LaVO_3\$ thin films](#). *Physical Review B* 85, 184101 (2012).

Large Orbital Rashba Edelstein Effect induced Torques in Atomically Thin Co/Al Systems

Nicolas Sebe^{1,*}, Sachin Krishnia¹, Sougata Mallick¹, Armando Pezo¹, Sergey Nikolaev², Yanis Sassi¹, Sophie Collin¹, Thibaud Denneulin³, András Kovács³, Rafal E. Dunin-Borkowski³, Albert Fert¹, Jean-Marie George¹, Kévin Garello⁴, Vincent Cros¹, and Henri Jaffrès¹

¹Laboratoire Albert Fert, CNRS, Thales, Université Paris-Saclay, Palaiseau, France

²The University of Osaka, Toyonaka, Osaka, Japan

³Ernst Ruska-Centrum für Mikroskopie und Spektroskopie mit Elektronen (ER-C), Forschungszentrum Jülich GmbH, Germany

⁴Univ. Grenoble Alpes, CEA, CNRS, Grenoble INP, SPINTEC, Grenoble, France

*nicolas.sebe@cnrs-thales.fr

Spin-orbit interaction (SOI) at metallic interfaces [1] has been recently the centre of spintronic research because it enables fast and efficient magnetisation dynamics for spin-based memory (e.g. SOT-MRAM), or skyrmion based devices. Indeed, the dynamics of magnetisation in spintronics devices is mainly controlled by the efficient spin-orbit torques (SOT) exerted by the generated out-of-equilibrium transverse angular momentum like for instance spin currents. Two main mechanisms have been investigated for SOT generation: the spin Hall effect (SHE) in heavy metals such as Pt or Ta and the Rashba Edelstein effect (REE) at interfaces. The two effects contribute to a damping-like (DL) and a field-like (FL) torque applied to the magnetization [2]. Recently, the occurrence of orbital Rashba Edelstein effect (OREE) and orbital Hall effect (OHE) in systems integrating light metallic elements were also shown to generate torques or to enhance the already existing SOT in well engineered heterostructures. Though, there remain open questions on the actual mechanism leading to the generation of orbital angular momentum in light metals in particular.[3, 4].

In order to tackle these fundamental issues and provide some routes for improvement of SOT-based devices, we demonstrate here how the insertion of a light metallic element interface profoundly affects with a strong benefit both the nature of spin-orbit torque and its efficiency in terms of damping-like and field-like effective fields acting on an adjacent ultrathin Co layer. We focus on the case of Pt/Co/Al/Pt system with variable thicknesses (Figure 1(i)) and compare it to Pt/Co/Cu/Pt to exhibit the role of the top Co/Al interface [5]. We show how the insertion of a Co/Al interface leads to a huge enhancement of the FL torque, upon increasing the Al thickness to 3 nm. By varying the Al and the Co thicknesses, we undoubtedly demonstrate the occurrence of a Rashba interaction in Co/Al interface (Figure 1(ii)). Moreover, from the variation of the torque with the different layers thicknesses at the very low thickness limit (t_{Co} varying from 0.55 to 1.4 nm) (see Fig. 1), we extract the main parameters governing the transverse spin dissipation related to spin precession and spin decoherence and discuss the ensemble of those phenomena that we correlate to the anomalous Hall effect (AHE) response.

Besides this experimental characterization of SOT in Co/Al, we also performed density functional theory (DFT) calculations [6]. Those calculations outcome is to show an orbital momentum locking (OML) texture at the interface of Co/Al. This effect is lost when Al is replaced by Cu. Therefore, DFT calculations confirm our experimental conclusions and allow us to understand the strong SOT as a consequence of an OREE. Combining DFT calculations and linear response theory, we are also able to predict the effective field applied by the SOT on the magnetization and find it to be consistent with the experiments.

To further probe experimentally the physical properties of Co/Al interface, we modify it by adding a dusting of another material between Co and Al. We have chosen to add material with strong SOI to see whether or not it would enhance SOT. Hence, we have grown samples of Pt/Co/dusting Pt/Al/Pt and characterized them using the same techniques as with the previous samples. We measure a decrease in the SOI related properties (PMA and SOT, Figure 1(iii)) when this Pt dusting is added. We are able to reproduce these experimental results in the DFT calculations. According to these calculations, OML vanishes when Pt is inserted between Co and Al. This explains the clear drop in the FL torque. Besides, we measure an increase in the AHE in samples with dusting Pt, suggesting that spin flipping is stronger with Pt dusting. According to our transport model, this explains the decline in DL torque.

After having characterized SOT in Co/Al interface, we investigate how relevant it is to current induced magnetization switching. In that purpose we fabricate Co/Al/Pt pillars of 300 nm diameter laid on Pt tracks using e-beam lithography. This design imitates the geometry of a free layer in SOT-MRAM device. Electrical current pulses of width down to 50 ns are then applied to measure the critical switching current required to achieve magnetization switching (Figure 1(iv)). The magnetization state is probed through the measurement of the transverse resistance. From this study, we demonstrate a reduction in the critical current with Al insertion. This reduction is opposite to the increase in magnetic anisotropy and shows how stronger SOT are beneficial to magnetization switching. However, the quantitative role of the FL component of the torques remain unclear, in spite of it being larger than the DL component in Co/Al interface.

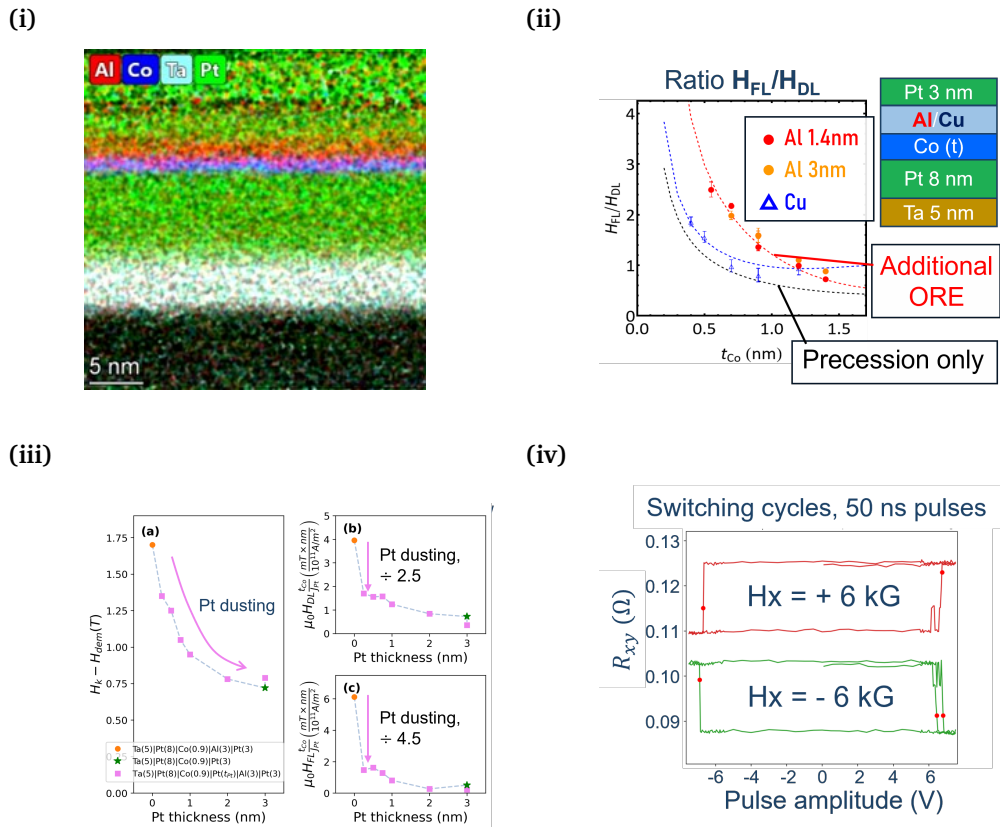


Figure 1: (i) EDX elemental map of a multilayer (from [5]). (ii) Ratio of the SOT FL component over the DL component for series of sample with varying Co thickness and Co/Al interface or Co/Cu. Dotted lines are fit to our model. (iii) Measured SOI related properties when dusting of Pt (thickness in absix) is added between Co and Al. (iv) Magnetization switching cycles obtained in Pt/Co/Al/Pt.

Acknowledgements

This work has been supported by the ANR-20-CE30-0022 “ORION” as well as France 2030 government grant managed by the ANR: (ANR-22-PEPR-Electronique-EMCOM), (grant no. ANR-22-EXSP-0007 PEPR SPIN SPINMAT and (grant no. ANR-22-EXSP-0009 PEPR SPIN SPINTHEORY

References

- [1] Anjan Soumyanarayanan, Nicolas Reyren, Albert Fert, and Christos Panagopoulos. Emergent phenomena induced by spin-orbit coupling at surfaces and interfaces. *Nature* 539, 509–517 (2016).
- [2] Aurelien Manchon, Jakub Železný, Ioan M Miron, et al. Current-induced spin-orbit torques in ferromagnetic and antiferromagnetic systems. *Reviews of Modern Physics* 91, 035004 (2019).
- [3] Kyung-Jin Lee, Vincent Cros, and Hyun-Woo Lee. Electric-field-induced orbital angular momentum in metals. *nature materials* 23, 1302–1304 (2024).
- [4] Shilei Ding, Andrew Ross, Dongwook Go, et al. Harnessing orbital-to-spin conversion of interfacial orbital currents for efficient spin-orbit torques. *Physical review letters* 125, 177201 (2020).
- [5] Sachin Krishnia, Yanis Sassi, Fernando Ajejas, et al. Large interfacial Rashba interaction generating strong spin-orbit torques in atomically thin metallic heterostructures. *Nano Letters* 23, 6785–6791 (2023).
- [6] Sergey A Nikolaev, Mairbek Chshiev, Fatima Ibrahim, et al. Large chiral orbital texture and orbital Edelstein effect in Co/Al heterostructure. *Nano Letters* 24, 13465–13472 (2024).

Alternative harmonic detection approach for quantitative determination of spin and orbital torques

Y. Xu^{1,*}, B. Bony¹, S. Krishnia¹, R. Torrão Victor¹, S. Collin¹, A. Fert¹, J.-M. George¹, V. Cros³³, and H. Jaffrès³³

¹Laboratoire Albert Fert, CNRS, Thales, Université Paris-Saclay, 91767 Palaiseau, France

*yaohan.xu@cnrs-thales.fr

Recently, orbital angular momentum (OAM), the previously underestimated degree of freedom, has been found to respond to charge current stimuli in a weak spin-orbit coupling (SOC) system[1–4]. Two counterpart phenomena, the so-called orbital Hall effect (OHE)[2, 5, 6] and the orbital Rashba-Edelstein effect (OREE)[1, 7, 8] have been proposed to efficiently realize orbital torque *via* OAM currents. In particular, in our previous work on Co(2)/Pt(t_{Pt})/CuO_x(3) multilayers with in-plane magnetic anisotropy (IMA)[9], it exhibits a significant DLT up to 2.38 mT/(10¹¹ A/m²). The most pronounced effect is observed with a $t_{Pt} \simeq 4$ nm thick Pt insertion layer. Our work emphasized the critical role of OAM for the benefit of a more efficient charge-spin conversion.

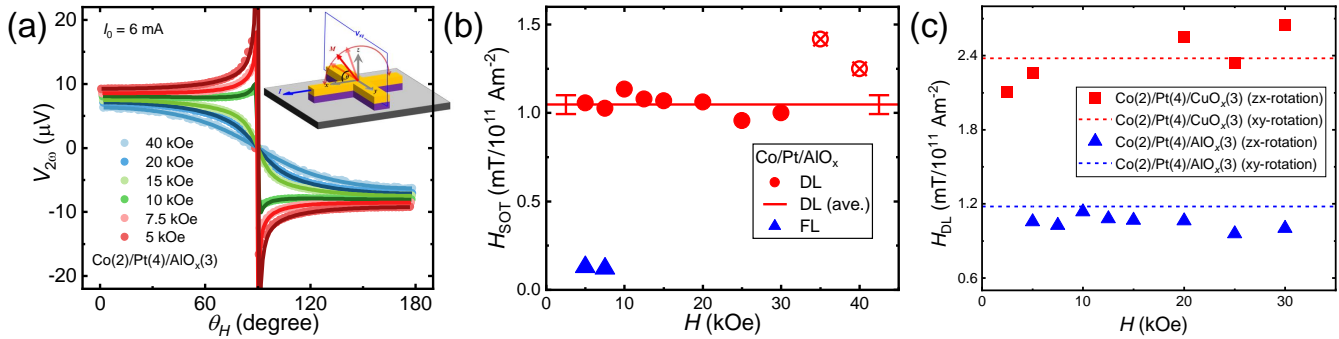


Figure 1: (a) Angular-dependent 2nd harmonic Hall voltages (color dots) measured with an AC of 6 mA under different H_{ext} and corresponding fitting curves (colored lines). Experiments are performed at 300 K. The inset shows the schematics of the device designed for the electrical and torque measurements and the geometry conventions. (b) The values of torque efficiency extracted from the fitting for various H_{ext} . (c) Comparison of HDL of the reference and orbital samples obtained by different harmonic measurements in the OOP and IP geometry.

In this study, we have developed and experimentally validated angular harmonic Hall measurements in the out-of-plane (OOP) geometry for two in-plane magnetized samples consisting of two different oxidized light metals, either CuO_x or AlO_x, different in that the former provides additional orbital torque. The interest in the angular OOP measurement approach prevails because it offers distinct advantages over the commonly used in-plane (IP) geometry[10]. First, we demonstrate that, unlike the IP geometry, a quantitative determination of the torques does not require a complete set of measurements at different magnetic fields. This is due to the distinct angular signature from the thermal effects. Second, the proposed OOP method provides greater accuracy in properly separating and quantifying the field-like and damping-like torque components if the planar Hall (PHE) and anomalous Hall (AHE) effects are of the same order of magnitude due to their distinct responses. The counterpart of angular OOP is the possible occurrence of additional in-plane thermoelectric effects with respect to an in-plane temperature gradient, which can also be accurately examined and disentangled.

We give the expressions for the 1st and 2nd harmonic Hall signals in the OOP measurement geometry, which read:

$$V_{\omega} = I_0 R_{AHE} \sin(\theta_M), \quad (1)$$

and

$$V_{2\omega} = -\frac{1}{2} \frac{dV_{\omega}}{d\theta_M} \frac{H_{DL}}{[H_{ext} \cos(\theta_H - \theta_M) + H_K \cos(2\theta_M)]} - I_0 R_{PHE} \cos^2(\theta_M) \frac{H_{FL} + H_{OE}}{H_{ext} \cos(\theta_H)} + I_0 \alpha (T_{OOP} \cos(\theta_M) + T_{IP} \sin(\theta_M)) \quad (2)$$

To verify its applicability, we first measure identical samples providing both spin and orbital torque response as the one studied in Krishnia *et al* [9], which is SiO₂(sub.)|Co(2)|Pt(4)|CuO_x(3) (number in parentheses is the thickness in units of nanometers). Moreover, a reference sample of Co(2)|Pt(4)|AlO_x(3) free of any orbital contribution, only integrating Co|Pt SHE source, is used for direct comparison [9].

In Fig. 1(a) 2nd harmonic signals vs. θ_H are measured using an AC of 19 Hz and peak amplitude I_0 of 6 mA. We have checked that the $V_{2\omega}$ signals correctly scale as J_0^2 , as expected. The curves are the fitting results using Eq. 2. In Figs. 1(b), we display the different values of the torques for all H_{ext} and compare them. The magnitudes of H_{DL} remain almost constant throughout the field window, except for those obtained in the largest fields. Note that the torque signals are quite small at large fields, reducing the signal-to-noise ratio, and consequently, the measurement accuracy. Having confirmed the ability of the OOP angular 2nd harmonic measurement method, we have measured and analyzed the characteristic effective SOT generated from the Co(2)|Pt(4)|CuO_x(3) orbital sample involving an orbital contribution. In Fig. 1(c), we compare the values of H_{DL} taken from the reference (blue) and those resulting from the orbital samples (red) obtained via the two different geometries. Dashed lines are the result of Krishnia *et al.* (Ref. [9]) of the angular variation geometry of the IP and the scatter points are the results obtained from OOP showing a very excellent consistency between these two methods. In addition, the twofold increase in H_{DL} for the orbital sample with an oxidized Cu capping layer, from $H_{\text{DL}} \simeq 1.2 \text{ mT}/(10^{11} \text{ A/m}^2)$ to $H_{\text{DL}} \simeq 2.4 \text{ mT}/(10^{11} \text{ A/m}^2)$ quantitatively confirms the unique role of the Cu | CuO_x interface in terms of the production of an orbital current.

In conclusion, we have provided the experimental proof of an alternative harmonic technique consistent with the IP geometry in terms of the parameter extraction of SOT effective fields. Notably, using this geometrical method, we emphasized the critical role of the naturally oxidized copper layer in generating orbital current and orbital torque with a twofold larger DL field than the reference sample. More generally, this method paves the way for further investigations of theoretical aspects, accurate measurements and applications of the magnetic torques resulting from non-equilibrium orbital angular momentum, in particular for materials characterized by large thermoelectric effects as Bi-based compounds and related topological insulators.

Acknowledgments

This work has been supported by the French National Research Agency under the Project “ORION” ANR-20-CE30-0022-02, ANR grant STORM (ANR-22-CE42-0013-02), by France 2030 government investment plan managed by the French National Research Agency under grant reference PEPR SPIN –ADAGE ANR-22-EXSP-0006, and the European Horizon Europe Framework Programme for Research and Innovation (2021-2027) EC Grant Agreement No. 101129641 (OBELIX).

References

- [1] Junyeon Kim, Dongwook Go, Hanshen Tsai, et al. [Nontrivial torque generation by orbital angular momentum injection in ferromagnetic-metal/Cu/Al₂O₃ trilayers](#). *Phys. Rev. B* 103, L020407 (2 2021).
- [2] Young-Gwan Choi, Daeyeun Jo, Kyung-Hun Ko, et al. Observation of the orbital Hall effect in a light metal Ti. *Nature* 619, 52–56 (2023).
- [3] Dongwook Go, Daeyeun Jo, Changyoung Kim, and Hyun-Woo Lee. Intrinsic spin and orbital Hall effects from orbital texture. *Phys. Rev. Lett.* 121, 086602 (2018).
- [4] Kyung-Jin Lee, Vincent Cros, and Hyun-Woo Lee. [Electric-field-induced orbital angular momentum in metals](#). *Nature Materials* 23, 1302–1304 (10 2024).
- [5] Igor Lyalin, Sanaz Alikhah, Marco Berritta, Peter M. Oppeneer, and Roland K. Kawakami. [Magneto-Optical Detection of the Orbital Hall Effect in Chromium](#). *Phys. Rev. Lett.* 131, 156702 (15 2023).
- [6] Hiroki Hayashi and Kazuya Ando. [Orbital Hall magnetoresistance in Ni/Ti bilayers](#). *Applied Physics Letters* 123, 172401 (2023).
- [7] Shilei Ding, Zhongyu Liang, Dongwook Go, et al. [Observation of the Orbital Rashba-Edelstein Magnetoresistance](#). *Phys. Rev. Lett.* 128, 067201 (6 2022).
- [8] Shilei Ding, Andrew Ross, Dongwook Go, et al. [Harnessing Orbital-to-Spin Conversion of Interfacial Orbital Currents for Efficient Spin-Orbit Torques](#). *Phys. Rev. Lett.* 125, 177201 (17 2020).
- [9] S. Krishnia, B. Bony, E. Rongione, et al. [Quantifying the large contribution from orbital Rashba-Edelstein effect to the effective damping-like torque on magnetization](#). *APL Materials* 12, 051105 (2024).
- [10] Can Onur Avci, Kevin Garello, Mihai Gabureac, et al. [Interplay of spin-orbit torque and thermoelectric effects in ferromagnet/normal-metal bilayers](#). *Phys. Rev. B* 90, 224427 (22 2014).

Proximity Effects In Superconductor/Magnetic Epitaxial Heterostructures With Magnetic Noncollinearity

H.C. Tadaha^{1,*}, L. Pasquier¹, S. Wang², J.W.A. Robinson², T. Hauet¹, and K. Dumesnil¹

¹*Institut Jean Lamour, Université de Lorraine, 2 allée André Guinier, 54011 Nancy, France*

²*Department of Materials Science, University of Cambridge, 27 Charles Babbage Road, Cambridge, CB3 0FS, UK*

*hyacinthe-cabrel.tadaha@univ-lorraine.fr

The interplay between magnetism and superconductivity has been heavily studied during the past 30 years and recently led to the concept of superconducting spintronics [1]. This field of research aims at combining magnetic and superconducting properties in hybrid systems, in order to develop new devices that would enable data processing in a highly energy-efficient way. The underlying mechanisms that play a key role in such heterostructures are the so-called proximity effects. The proximity effect at an interface between a thin film superconductor (S) and a ferromagnet (F) is sensitively-dependent on fundamental processes such as Andreev reflection as well as the magnetic-configuration (orientation, domains, domain walls) and structural properties. In a S/F heterostructure, the magnetic exchange field from the collinear F is known to suppress the superconductivity (short range inverse proximity effect). Conversely, the presence of magnetic noncollinearity (MNC), in reducing the exchange field, can restore the superconductivity, thus enhancing the critical temperature (T_C) as in $F/S/F$ spin valves with an antiparallel-magnetization-alignment [2] and in S/F bilayers with misoriented magnetic domains [3]. However, it has also been theoretically predicted [4] and experimentally shown that the MNC at a S/F interface may lead to the opposite effect: the reduction in T_C . This phenomenon relies on the generation of spin-aligned triplet Cooper pairs that, much less sensitive to the exchange field, can deeply leak into the F layer(s) [5], giving rise to a long-range proximity effect. The controlled creation and manipulation of long-range equal-spin triplet supercurrents let envision fascinating physics and developments, which currently drives an active field of research.

To further investigate the role of MNC in these proximity effects, we have undertaken a study based on epitaxial hybrid structures involving rare earth elements. These later gather several interesting aspects that can benefit to the field of superconducting spintronics: (i) They exhibit magnetic modulated phases that are a natural source of MNC to promote triplet components [6] (ii) They possess a strong orbital moment that could lead to enhanced spin switch effects [7] (iii) They can be epitaxially grown as high-quality systems in which dimension, strains, alloying, etc are powerful levels to control their magnetic phases and properties [8].

We focus here on epitaxially grown $Nb(30nm)/F(50nm)$ structures, where F is a pure Ho film, a Ho -based alloy (with Lu or Tb), or a Ho -based superlattice (SL). Epitaxial heterostructures are synthesized in a UHV (base pressure $4.10^{-11} Torr$) Molecular Beam Epitaxy chamber on (11 – 20) orientated sapphire substrates. Nb is evaporated from an e-gun while Rare Earth elements are (co)evaporated from effusion cells. Evaporation rates are carefully monitored by highly sensitive quartz microbalances and stabilized by the temperature control of effusion cells. The Nb layers grows along the [110] direction while the RE elements grow along the [0001] direction, with an in-plane $a - axis$ ($< 11 - 20 >$) parallel to $Nb[001]$.

The temperature and field stability of the magnetic phases, more specifically in the vicinity of the Nb superconducting transition, are investigated by SQUID. Transport measurements are carried out to explore the superconductivity dependence on the magnetic order, under zero field for different remanent states and/or under in-plane applied field in comparing increasing and decreasing field branches.

Figure 1 presents the results obtained in the cases of four different F components (pure Ho , $Ho_{1-x}Lu_x$ and $Ho_{1-x}Tb_x$, [Ho/Lu] SL). Note that the direct influence of the external field on Nb superconductivity has been removed here by either subtracting the field dependence obtained in the saturated state Nb/Ho and $Nb/Ho_{1-x}Lu_x$ or by measuring under zero field after stabilization of different remanent states ($Nb/Ho_{1-x}Tb_x$ and $Nb/[Ho/Lu]$). The magnetization measurements (bottom) confirm a modulated phase in Ho that is favored (increasing of critical field) when alloying with Lu . At the opposite, an aligned state is favored when alloying with Tb and in the SL structure.

It appears that the Nb superconducting critical temperature (top curves) is significantly affected by changes in the magnetic state. In both Nb/Ho and $Nb/Ho_{1-x}Lu_x$, the lowest T_C is observed in the saturated state and the non-collinear phase stabilized for intermediate fields gives rise to an increase of T_C that reaches $200mK$ in Nb/Ho . This is expected from the reduced exchange field probed over the Nb coherence length. A similar but larger enhancement ($380mK$) is also observed during the magnetization reversal in $Ho/Nb/Ho$ spin valves.

At the opposite, in the case of $Nb/Ho_{1-x}Tb_x$, T_C is maximum in the saturated state and the magnetization reversal leads to a reduction in T_C , especially for magnetic states related to steps in the magnetization curve. A similar but larger decrease ($-120mK$) is observed for a $Nb/[Ho/Lu]$ heterostructure in which the magnetization reversal also exhibits similar steps.

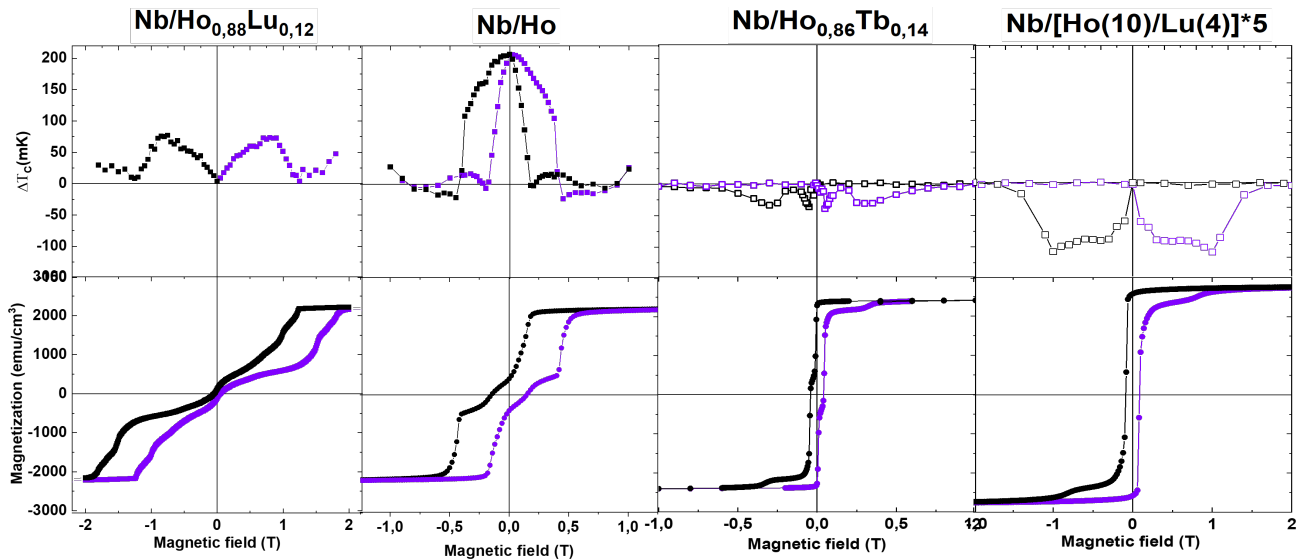


Figure 1: Correlation between magnetic (bottom) and electronic (top) properties for Nb/Ho , $Nb/Ho_{0.88}Lu_{0.12}$, $Nb/Ho_{0.86}Tb_{0.14}$ and $Nb/[Ho/Lu]$ heterostructures. Bottom curves are magnetization measurements, the black (purple) curve corresponding to the decreasing (increasing) branch. Top curves are the relative variations of the superconducting critical temperature related to changes in the magnetic state.

Such a decrease in T_c could be a hint of long-range triplet components. These would possibly arise from the stack of 60° rotated magnetic blocks, aligned along the strong easy b – axis in the hexagonal basal plane. Complementary Polarized Neutron Reflectometry experiments are planned to get depth-dependent information on the magnetic arrangement.

In these RE-based hybrid heterostructures, the development of MNC observed by SQUID out of the saturated state thus generates either an increase of T_c related to the short-range inverse proximity effect, or a decrease of T_c , that could reveal the presence of spin-aligned triplet component. We will discuss how the nature and characteristics of the MNC could explain its influence on both short- and long-range proximity effects. Exploring these effects in systems with MNC is vital to aid theory towards improved modelling and to develop superconducting spintronic devices.

References

- [1] Jacob Linder and Jason WA Robinson. Superconducting spintronics. *Nature Physics* 11, 307–315 (2015).
- [2] Sangjun Oh, D Youm, and MR Beasley. A superconductive magnetoresistive memory element using controlled exchange interaction. *Applied physics letters* 71, 2376–2378 (1997).
- [3] A Yu Rusanov, M Hesselberth, J Aarts, and Alexandre I Buzdin. Enhancement of the Superconducting Transition Temperature in Nb/Permalloy Bilayers by Controlling the Domain State of the Ferromagnet. *Physical review letters* 93, 057002 (2004).
- [4] FS Bergeret, AF Volkov, and KB Efetov. Long-range proximity effects in superconductor-ferromagnet structures. *Physical review letters* 86, 4096 (2001).
- [5] Ya. V. Fominov, A. A. Golubov, T. Yu. Karminskaya, et al. Superconducting triplet spin valve. *JETP Letters* 91, 308–313 (2010).
- [6] Daniel Fritsch and James F Annett. Proximity effect in superconductor/conical magnet heterostructures. *Journal of Physics: Condensed Matter* 26, 274212 (2014).
- [7] Yuanzhou Gu, Gábor B Halász, JWA Robinson, and MG Blamire. Large superconducting spin valve effect and ultra-small exchange splitting in epitaxial rare-earth-niobium trilayers. *Physical review letters* 115, 067201 (2015).
- [8] PP Swaddling, RA Cowley, RCC Ward, MR Wells, and DF McMorro. Magnetic structures of holmium-lutetium alloys and superlattices. *Physical Review B* 53, 6488 (1996).

Orbital-to-spin conversion material exploration for improving SOT-MTJ performances

M. Biagi^{1,*}, C. C. M. Capriata¹, C. Bouchard¹, L. Hutin², B. Viala², R. Sousa¹, and K. Garello¹

¹Univ. Grenoble Alpes, Grenoble-INP, CEA, CNRS, SPINTEC, Grenoble, France

²LETI, CEA, Grenoble, France

*marco.biagi@cea.fr

The development of electrically controlled nanomagnets for spintronics applications is attracting significant attention, particularly for the realization of nonvolatile magnetic memories (MRAMs) [1]. This interest is driven by the pressing challenges faced by the microelectronics industry due to the volatility of CMOS-based cache memory elements, such as SRAM and eDRAM. MRAMs represent promising low-power, high-speed alternatives capable of competing with SRAM for cache-level integration. Spin-orbit torque (SOT) based magnetic tunnel junctions (MTJs) are credible next-generation MRAM technology, targeting replacement of SRAM owing to their fast switching processes and large endurance [1]. In such structure, the spin current controlling the switching is generated by a non magnetic material, typically a heavy metal (HM). When an electric current is injected in such material, a pure spin current is generated due to the Spin Hall Effect (SHE) and the Rashba-Edelstein effect (REE), and it is then transferred to the free layer (FL) (Fig.2a).

Recently, the SHE and REE have been predicted to arise from more fundamental effects [2], namely Orbital Hall effect (OHE) and Orbital Rashba-Edelstein effect (OREE). These effects feature greater magnitudes and diffusion lengths compared to the spin counterpart [2, 3], and they are present in a much wider class of materials, including light metals with low resistivity. In an analogous way to the SHE and REE, these orbital effects give rise to an orbital current that can propagate into adjacent materials. However, the orbital moment does not directly interact with the spin moment. To exploit these effects in MRAM devices, spin-orbit coupling (SOC) is required to convert the orbital current into spin current. This can be achieved by selecting a ferromagnet (FM) with sizable SOC (such as Ni). Another solution, which has the benefit of a less restrictive material system choices, is to introduce a spacer layer with strong SOC between the orbital source and the FL (Fig.1b) [4-6]. In this configuration, the orbital current is converted into the spacer layer and transferred to the FL (Fig. 1c). Moreover, if the spacer is a HM, two independent channels of spin current are expected to add up linearly (SHE + OHE), further increasing the efficiency of the MTJ [5]. It remains a key challenge to identify and optimize materials systems that are compatible with MRAM fabrication processes, including perpendicular magnetic anisotropy (PMA) ferromagnets, that can sustain thermal annealing processes at 400°C.

This work aims to clarify whether orbital-to-spin conversion mechanisms can be regarded as a promising solution for improving current SOT-MRAM technology. In this talk, I will report the results of our study on the characterization of various orbital/HM/FM material systems with an orbital-to-spin conversion scheme as illustrated in Fig.1c. In this scheme, an orbital source material is topped by a heavy metals, which acts as an "active" conversion layer capable of both converting orbital currents and generating spin currents, and a PMA ferromagnet (FeCoB). We systematically quantify the damping-like efficiency (ξ_{DL}) by harmonic Hall voltage methods [7] in both as-deposited and annealed systems, varying the thickness of the heavy metal and/or the orbital source (e.g., Ru-based systems in Fig.2a as deposited, and Fig.2b annealed). The results are compared to reference HM/FM bilayer (Fig.2 for Ru-based systems), and I will discuss the impact of the orbital layer insertion and annealing on ξ_{DL} . In addition, we tentatively attempt to separate the contributions from the SHE and OHE in the orbital stacks by means of a simple current distribution model. The distinct behaviors of the HMs employed as conversion layer are also discussed. Finally, I will present the application of the best material solutions to fabricate 3-terminal SOT-MTJ devices, demonstrating proof-of-concept switching using orbital torques in sub-ns regime (Fig.2c), and benchmarking their performances against standard SOT material systems.

Acknowledgments

This work was partly supported by the French RENATECH network, implemented at the Upstream Technological Platform in Grenoble PTA (ANR-22-PEEL-0015), and by France 2030 government investment plan managed by the French National Research Agency under grant reference PEPR Electronique (ANR-22-PEEL-0009).

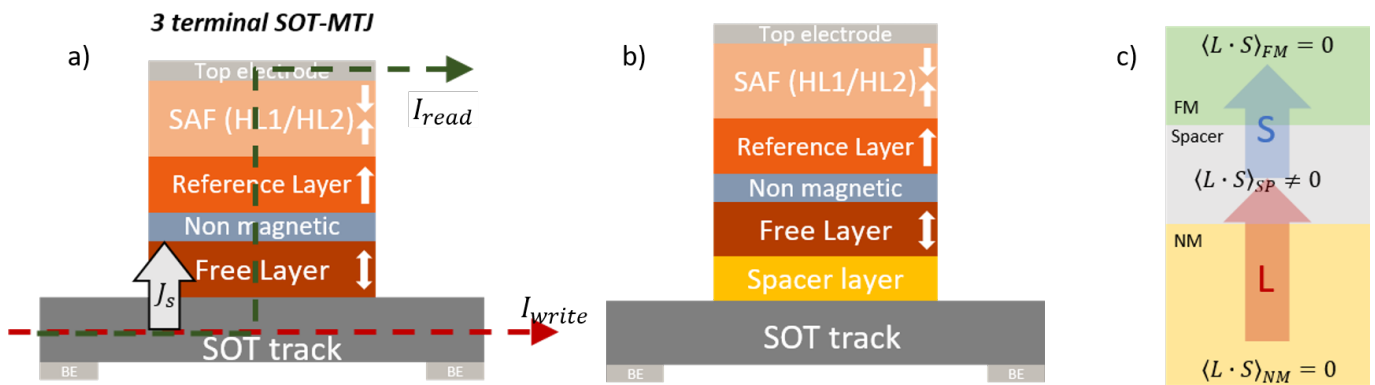


Figure 1: a) Top-pinned 3-terminal SOT-MRAM MTJ, b) proposed layout with addition of spacer layer X, c) simple picture of the orbital-to-spin conversion scheme: the orbital current is generated in the orbital material (red arrow) and is then converted into spin current (blue arrow) in the spacer layer with strong spin-orbit coupling. FM = ferromagnet, NM = nonmagnetic material.

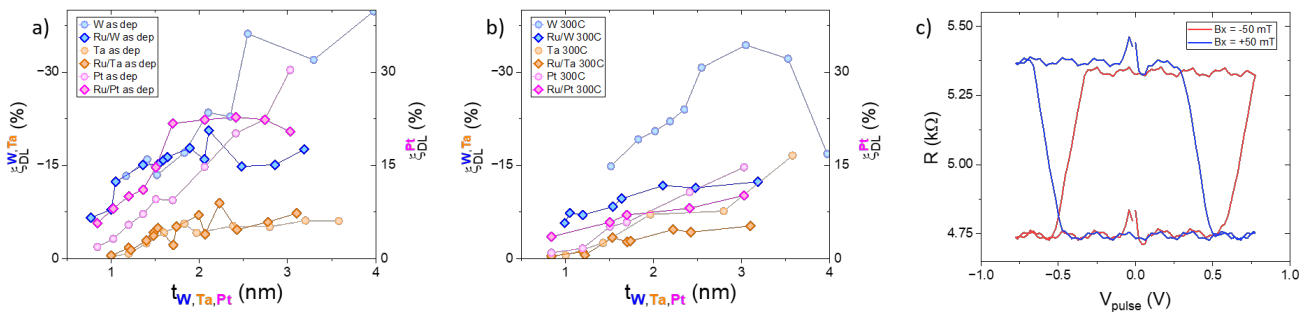


Figure 2: a) damping-like efficiency as function of the heavy metal thickness in as deposited orbital (dark lines) and reference stacks (light lines) for Ru-based systems. b) damping-like efficiency as function of the heavy metal thickness in annealed orbital (dark lines) and reference stacks (light lines) for Ru-based systems. c) sub-ns switching for Ru(3)/W(1.5) MTJ sample for $\tau_p = 0.5$ ns, the switching polarity is opposite with opposite in-plane field as expected for SOT switching.

References

- [1] Viola Krizakova, Manu Perumkunnil, Sébastien Couet, Pietro Gambardella, and Kevin Garello. [Spin-orbit torque switching of magnetic tunnel junctions for memory applications](#). *Journal of Magnetism and Magnetic Materials* 562, 169692 (2022).
- [2] Dongwook Go, Daegun Jo, Changyoung Kim, and Hyun-Woo Lee. Intrinsic spin and orbital Hall effects from orbital texture. *Phys. Rev. Lett.* 121, 086602 (2018).
- [3] Leandro Salemi and Peter M Oppeneer. First-principles theory of intrinsic spin and orbital Hall and Nernst effects in metallic monoatomic crystals. *Phys. Rev. Mater.* 6 (2022).
- [4] Giacomo Sala and Pietro Gambardella. Giant orbital Hall effect and orbital-to-spin conversion in 3d, 5d, and 4f metallic heterostructures. *Phys. Rev. Res.* 4 (2022).
- [5] Soogil Lee, Min-Gu Kang, Dongwook Go, et al. Efficient conversion of orbital Hall current to spin current for spin-orbit torque switching. *Commun. Phys.* 4 (2021).
- [6] Rahul Gupta, Chloé Bouard, Fabian Kammerbauer, et al. [Harnessing orbital Hall effect in spin-orbit torque MRAM](#). *Nature Communications* 16 (2025).
- [7] Kevin Garello, Ioan Mihai Miron, Can Onur Avci, et al. [Symmetry and magnitude of spin-orbit torques in ferromagnetic heterostructures](#). *Nature Nanotechnology* 8, 587–593 (2013).

Low Temperature Out-of-Plane Nonlinear Hall Effect in Epitaxial GeTe

Théo Frottier^{1,*}, Diego García Ovalle², Michael Wissmann¹, Panagiotis Pappas¹, Williams Savero Torres¹, Maxime Culot¹, Paolo Sgarro¹, Boris Croes², Jean-Philippe Attané¹, Pierre Noé³, Aurélien Manchon², Frédéric Leroy², Fabien Cheynis², and Laurent Vila¹

¹SPINTEC, Université Grenoble Alpes / CEA / IRIG, Grenoble, France

²CINAM, Aix Marseille Université / CNRS, Marseille, France

³LETI, Université Grenoble Alpes / CEA, Grenoble, France

*theo.frottier@cea.fr

Hall effects have always been a source of profound insight into condensed matter physics. For instance, the anomalous Hall effect in alternating magnetic materials can allow the electrical measurement of the anisotropic Berry curvature which is a direct information on the geometry of the electronic bands. A nonzero second-order term of the anomalous Hall was recently described [1], measured [2], and coined the nonlinear anomalous Hall effect (NLAHE). It is quadratic with the applied current and appears both at twice the frequency of the said current and in the continuous regime as an offset:

$$j_H^0 = \alpha(E_{\parallel}^{\omega})^2 \quad ; \quad j_H^{2\omega} = \alpha(E_{\parallel}^{\omega})^2 \quad (3)$$

Where j_H is the Hall current in the transverse direction of the applied electrical field E and α a constant of the material.

The NLAHE, unlike its first-order parent, does not require time-reversal symmetry breaking. It is a Hall effect without any magnetization or magnetic field. Instead, space-inversion symmetry breaking (ISB) is needed. Most of the work done so far on the NLAHE was performed on two-dimensional systems where ISB can be — rather easily — fulfilled. However, the most natural direction for finding ISB-exhibiting systems is toward ferroelectric materials.

With their reversible nonvolatile electric polarizations, ferroelectric materials exhibit ISB and can even change the direction of the ISB through a polarization change. Most commonly found ferroelectric materials are insulating oxides, with no direct access to their conduction bands, making bulk transport difficult and the geometry of the bands inaccessible.

Ferroelectric Rashba semiconductors (FERSC) are a new class of ferroelectric materials with great potential for spintronics applications [3]. Their natural ISB and their semiconducting properties might exhibit the NLAHE, but also enable the control of the sign of it through their ferroelectric polarization (FE-NLHE).

Germanium telluride (GeTe) is a bulk FERSC [4] usually found degenerated with a Fermi level in the valence band. Our GeTe has been epitaxially grown using molecular beam epitaxy (MBE) on silicon(111) [5] thus inducing a ferroelectric polarization out-of-plane. The ISB being along the ferroelectric polarization, the Hall voltage of the NLAHE need to be measured out-of-plane.

In this work, using symmetry analysis of the signals and lock-in techniques, we provide evidence for the presence of a nonlinear Hall effect at low temperatures in GeTe along the direction of the ISB (Fig. ??). We propose a new Hall bar geometry that allows the measurement of an out-of-plane voltage in any MBE film grown on an insulating substrate (Fig. ??). The second harmonics arising from the substrate and the imperfect current source are analyzed. We also measure a nontrivial temperature dependency of the effect. The ferroelectric control of the polarization of GeTe is hinted by the modulation of the conductance of the Schottky barrier between GeTe and silicon. This work opens the road to the FE-NLHE and, therefore, a potential reconfigurable frequency doubling or rectifying device. This work can also be used as a methodology to measure and exhibit NLAHE in other systems and decouple it from other parasitic effects.

References

- [1] Inti Sodemann and Liang Fu. Quantum nonlinear Hall effect induced by Berry curvature dipole in time-reversal invariant materials. *Physical review letters* 115, 216806 (2015).
- [2] Kaifei Kang, Tingxin Li, Egon Sohn, Jie Shan, and Kin Fai Mak. Nonlinear anomalous Hall effect in few-layer WTe₂. *Nature materials* 18, 324–328 (2019).
- [3] Sara Varotto, Luca Nesi, Stefano Cecchi, et al. Room-temperature ferroelectric switching of spin-to-charge conversion in germanium telluride. *Nature Electronics* 4, 740–747 (2021).
- [4] Boris Croes, Alexandre Llopez, Calvin Tagne-Kaegom, et al. Pushing the thickness limit of the giant Rashba effect in ferroelectric semiconductor GeTe. *Nano Letters* 24, 13224–13231 (2024).
- [5] Boris Croes, Fabien Cheynis, Yannick Fagot-Revurat, et al. Early-stage growth of GeTe on Si (111)-Sb. *Physical Review Materials* 7, 014409 (2023).

Systemes neuro-inspirés

Synaptic metaplasticity in a magnetoionic synapse

Himadri Nandan Mohanty^{1,*}, Guillaume Bernard¹, Kellian Cottart¹, Maria-Andromachi Syskaki², Alan Durnez¹, Juergen Langer², Damien Querlioz¹, and Liza Herrera Diez¹

¹Centre de Nanosciences et de Nanotechnologies, CNRS, Université Paris-Saclay, 91120 Palaiseau, France

²Singulus Technology AG, Hanauer Landstrasse 103, 63796 Kahl am Main, Germany

*himadri.mohanty@universite-paris-saclay.fr

In the era of artificial intelligence, neuromorphic hardware is paving the way for computational systems that mimic the human brain's functionality. To achieve this, artificial synapses and neurons are crucial for building complex neural networks. One promising approach is magnetoionics, a novel technology that combines the digital properties of magnetic materials with the analog characteristics of ion migration to replicate synaptic plasticity. Magnetic materials, for instance, possess a binary memory state with spin-up and spin-down states. However, magnetoionic gating can switch the magnetic anisotropy of the system between in-plane (IP) and out-of-plane (OOP) anisotropy. This transition can be gradually tuned into multiple analog memory states by controlling the oxidation or reduction of the magnetic material through ion migration[1]. Recently, our group utilized magnetoionic synapses to efficiently perform machine learning tasks, such as image recognition, achieving 96 % accuracy in identifying MNIST handwritten digits[2]. However, catastrophic forgetting is one of the major challenges in neuromorphic computing, where the system forgets previously learned tasks when trained on new ones. This limitation poses problems for real-time data processing, where retaining past information is critical. Interestingly, the human brain overcomes this issue by adjusting synaptic weights based on past experiences. As highlighted by Fusi et al., each synapse should have hidden states with varying degrees of plasticity, a concept known as "metaplasticity", to ensure effective task retention[3]. In machine learning, Laborieux et al. tackled the issue of catastrophic forgetting by utilizing hidden weights in binarized neural networks as metaplastic variables, enabling effective multitask learning[4]. Similarly, magnetoionic devices hold significant potential for addressing this challenge at the hardware level due to their unique binary memory states, coupled with concealed internal ionic states that function as metaplastic variables.

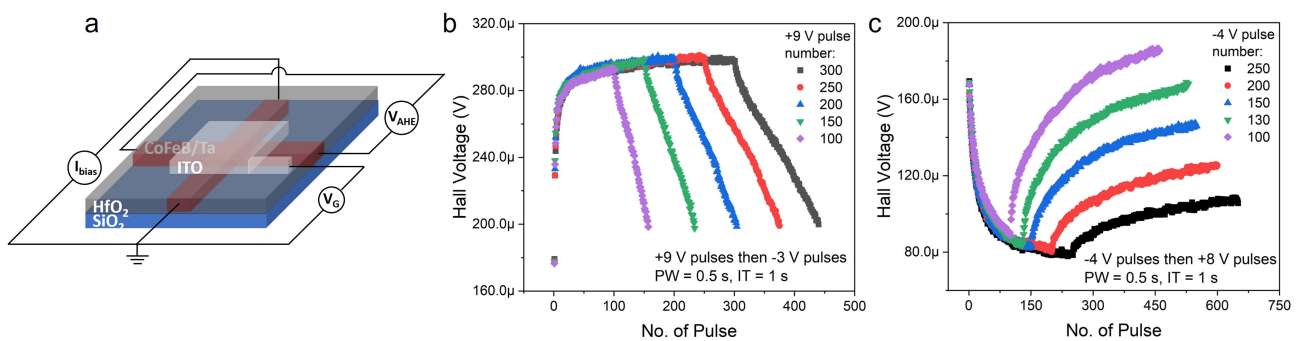


Figure 1: (a) Schematic illustration of magnetoionic device. Hall voltage as a function of number of gate-voltage pulses in (b) Out-of-plane magnetization and (c) In-plane magnetization regimes. Here, PW: Pulse width and IT: Interval time.

In this work, we present a magnetoionic device designed to demonstrate metaplasticity through the use of gate voltage-modulated anomalous Hall effect (AHE). The device features a CoFeB Hall cross fully encapsulated by an HfO₂ layer, as illustrated in Fig. 2(a). An Indium Tin Oxide (ITO) electrode placed above the HfO₂ to apply gate voltage pulses and manipulate the system's magnetization state. During measurements, a small OOP magnetic field was applied to prevent the formation of magnetic domains. Under a positive gate bias, oxygen ions migrate towards the gate electrode, reducing the CoFeB layer and inducing an out-of-plane (OOP) magnetic state. Conversely, a negative gate bias oxidizes the CoFeB layer, resulting in an in-plane (IP) magnetic state. Bernard et al. demonstrated synaptic potentiation and depression leveraging the redox process at the CoFeB layer [2]. In this study, when gate voltage pulses were applied in one direction, the Hall voltage of the system eventually saturated after a certain number of pulses, providing no information about the internal ionic state of the system. As shown in Fig. 2(b), applying a series of positive gate voltage pulses results in a constant final Hall voltage. However, variations in the pulse scheme lead to differences in the system's magnetic anisotropy. Interestingly, when negative voltage pulses were applied to restore the Hall voltage to its initial value, the required number of pulses and the rate of voltage change varied. This variability stems from differences in the internal ionic states of the system. The dependence upon negative pulse count can be considered as hidden states, which introduce metaplasticity into the magnetoionic system. A similar behavior was observed in the IP magnetic state, as depicted in Fig. 2(c). However, excessive negative pulses can over-oxidize the CoFeB layer, rendering the IP-to-OOP transition irreversible. This unique metaplasticity behavior makes magnetoionic systems a promising candidate for addressing catastrophic forgetting, paving the way for significant advancements in neuromorphic computing.

Acknowledgments

We gratefully acknowledge financial support from the Horizon Europe program (EIC Pathfinder METASPIN (101098651)).

References

- [1] T Bhatnagar-Schöffmann, A Kovács, R Pachat, et al. Controlling interface anisotropy in CoFeB/MgO/HfO₂ using dusting layers and magneto-ionic gating. *Applied Physics Letters* 122 (2023).
- [2] G Bernard, K Cottart, M.-A Syskaki, et al. Dynamic control of weight-update linearity in magneto-ionic synapses. *Nano Letters* (2025).
- [3] Marcus K Benna and Stefano Fusi. Computational principles of synaptic memory consolidation. *Nature neuroscience* 19, 1697–1706 (2016).
- [4] Axel Laborieux, Maxence Ernout, Tifenn Hirtzlin, and Damien Querlioz. Synaptic metaplasticity in binarized neural networks. *Nature communications* 12, 2549 (2021).

Neuromorphic weighted sums with magnetic skyrmions

Tristan da Câmara Santa Clara Gomes^{1,2,*}, Yanis Sassi¹, Dedalo Sanz-Hernandez¹, Sachin Krishna¹, Marie-Blandine Martin¹, Pierre Seneor¹, Tanvi Bhatnagar-Schöffmann³, Dafiné Ravelosona³, Damien Querlioz³, Liza Herrera-Diez³, Vincent Cros¹, Julie Grollier¹, and Nicolas Reyren¹

¹Laboratoire Albert Fert, CNRS, Thales, Université Paris-Saclay, Palaiseau, France

²INESC Microsistemas e Nanotecnologias, 1000-029 Lisbon, Portugal

³Centre de Nanosciences et de Nanotechnologies, CNRS, Université Paris-Saclay, Palaiseau, France

*tristan.gomes@inesc-mn.pt

Magnetic skyrmions, which are topological magnetic solitons, display a range of features that make them promising candidates for energy-efficient computing operations [1–3], such as stability at room temperature, sub-micron dimensions, non-volatility, particle-like behavior, and motion at low power. These characteristics seamlessly align with the requisites of neuromorphic computing, rendering them attractive candidates for integration into neuromorphic circuits [1–3]. Recent experimental studies have shown that magnetic skyrmions can be nucleated [4–6], moved [5], annihilated [6] and electrically detected using the anomalous Hall effect (AHE) [7] or tunneling magnetoresistance [8]. However, an experimental demonstration of the weighted sum operation is still missing in the context of skyrmions [3]. In our recent works [9, 10], we exploit the non-volatile and particle-like characteristics of magnetic skyrmions, akin to synaptic vesicles and neurotransmitters, and making them easily countable and summable to perform this weighted sum operation in a compact, biologically-inspired manner. The concept is schematized in Fig. 1a: a number $N_{\text{Sk},i}$ of magnetic skyrmions, proportional to the input values J_i^{In} and the synaptic weight w_i so that $N_{\text{Sk},i} = w_i J_i^{\text{In}}$, is generated in at nucleation sites in parallel tracks. Then, they are displaced to accumulate at the read line location, enabling a spatial summation expressed as $N_{\text{Sk,tot}} = \sum_i N_{\text{Sk},i}$ [9].

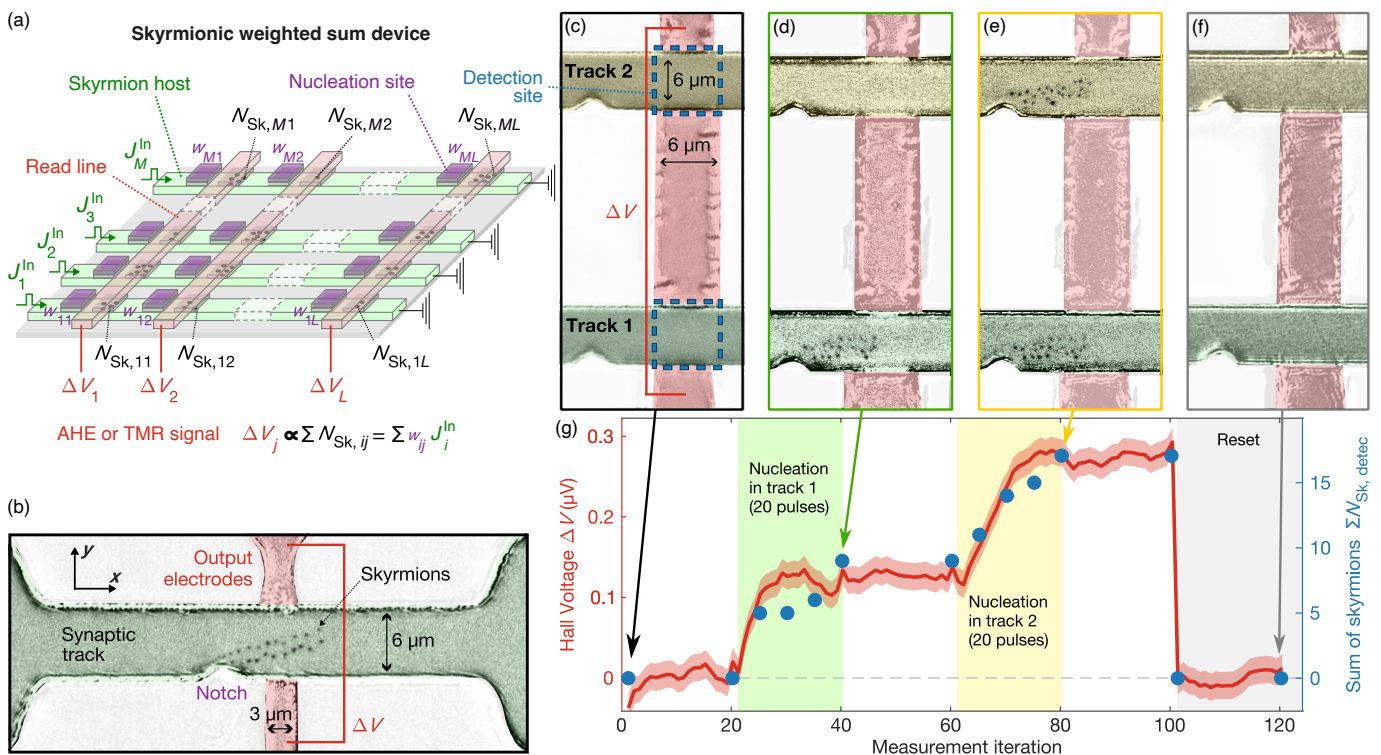


Figure 1: (a) Illustration of our skyrmionic weighted sum device, inspired from their biological counterpart using vesicles containing neurotransmitters, as depicted in the inset. Electrical inputs J_i^{In} are applied to skyrmion host tracks (in green) to nucleate controlled number of skyrmions $N_{\text{Sk},i}$ at nucleation sites, each with an assigned synaptic weight w_i so that $N_{\text{Sk},i} = w_i J_i^{\text{In}}$. These skyrmions are moved into a transverse electrical detection zone, established by the intersection of the track and the read line for the electrical output (in red), where the cumulative number of skyrmions $N_{\text{tot}} = \sum_i N_{\text{Sk},i}$ can be electrically detected through an output voltage ΔV arising from the anomalous Hall effect (AHE) or the tunnel magnetoresistance (TMR). (b) Kerr microscopy difference image of the device with magnetic skyrmions (dark spots), which were nucleated from a notch in a synaptic track and moved between the detection electrodes. (c-f) Kerr microscopy images of the device composed of two parallel magnetic multilayer tracks connected by a transverse Hall electrode. After the saturation of the track (c), skyrmions can be selectively nucleated in track 1 (d) and track 2 (e), before being magnetically erased (f). (g) Hall voltage ΔV (in red) and the corresponding sum of the number of detected skyrmions in both tracks $\sum N_{\text{Sk,detec}}$ (in blue) for successive injection of skyrmion in the tracks. 20 nucleation pulses are successively applied to each track (indicated by the green and yellow areas for track 1 and 2). Figures from [9].

We implement this concept in hardware by using the building block shown in the Kerr microscopy image of Fig. 1b. The skyrmions hosting track, colored in green, is 6- μm wide and consist of a magnetic multilayered stack: Ta(5 nm)/Pt(8 nm)/[Co(1.2 nm)/Al(3 nm)/Pt(3 nm)]₁₀. The track contains a skyrmion nucleation site implemented by a triangular-shape notch. The skyrmions are detected electrically using AHE and concomitantly counted through Kerr microscopy for validation. For the AHE detection, we use highly-resistive 10-nm thick tantalum (Ta)-based Hall electrodes (colored red in Fig. 1b), which are connected solely to the track edge. This minimizes spatial variations of the current density and eliminates potential current leaks that might disrupt skyrmion movement. As seen in Fig. 1b, we observe that the train of skyrmions can completely cross the area of the Ta-based electrodes without any detectable reduction of their velocity and perturbation of their trajectory.

Using this building block, we demonstrate the precise electrical control of skyrmion nucleation and motion, the number of generated skyrmions $N_{(\text{sk},i)}$ being determined by the electrical pulse input J_i^{In} multiplied by the track synaptic weight w_i as $N_{(\text{sk},i)} = w_i J_i^{\text{In}}$. We observe a proportional relationship between the recorded Hall voltage variation ΔV and the count of skyrmions derived from the magneto-optic Kerr images, demonstrating the capability of electrically counting skyrmions with high precision using AHE. Additionally, we show that adjusting the magnetic properties at the nucleation site can effectively modulate the synaptic weight w_i .

We experimentally validate the weighted sum operation using two electrical inputs in a crossbar array configuration with two tracks (see Fig. 1c-g) [9]. Skyrmions are successively injected in both tracks (Figs. 1d-e), before reset (Fig. 1f). The Hall voltage variation ΔV and total counted skyrmion number in the detection zone (dashed blue boxes in Fig. 1c) are shown in Fig. 1g. It demonstrates that the measured Hall voltage ΔV is directly proportional to the sum of the skyrmion numbers in the two tracks $\sum_i N_{(\text{sk},i)}$. This ensures efficient execution of the fundamental weighted sum operation, a cornerstone for neuromorphic computing. Our experimental demonstration is scalable to accommodate multiple inputs and outputs using a crossbar array design, potentially approaching the energy efficiency observed in biological systems.

Additionally, we explore the integration of magneto-ionic effects for non-volatile and reversible control over local magnetic properties on [Pt(3 nm)/Co(1.2 nm)/Al(3 nm)]-multirepeat stacks, capped by a Co(1.2 nm)/Al(0.8 nm) bilayer oxidized in air [10]. We demonstrate non-volatile and reversible voltage gating control of the magnetic anisotropy through the application of an electric field from the top AlO_x layer, allowing for the in-plane to out-of-plane anisotropy switch in the top Co layer [10]. These results pave the way towards non-volatile gate voltage control of skyrmion nucleation and motion, and therefore to achieve non-volatile control of the synaptic weights within our device.

Acknowledgments

This work is supported by the Horizon 2020 Framework Program of the European Commission under FET-Proactive Grant SKYTOP (no. 824123), by the European Research Council advanced grant GrenaDyn (reference no. 101020684), by the EU project SkyANN (reference no. 101135729) and from a France 2030 government grant managed by the French National Research Agency (grant no. ANR-22-EXSP-0002 PEPR SPIN CHIREX).

References

- [1] Albert Fert, Nicolas Reyren, and Vincent Cros. [Magnetic skyrmions: advances in physics and potential applications](#). *Nature Reviews Materials* 2 (2017).
- [2] Kyung Mee Song, Jae-Seung Jeong, Biao Pan, et al. [Skyrmion-based artificial synapses for neuromorphic computing](#). *Nature Electronics* 3, 148–155 (2020).
- [3] J. Grollier, D. Querlioz, K. Y. Camsari, et al. [Neuromorphic spintronics](#). *Nature Electronics* 3, 360–370 (2020).
- [4] William Legrand, Davide Maccariello, Nicolas Reyren, et al. Room-Temperature Current-Induced Generation and Motion of sub-100 nm Skyrmions. *Nano Letters* 17, 2703–2712 (2017).
- [5] A. Hrabec, J. Sampaio, M. Belmeguenai, et al. [Current-induced skyrmion generation and dynamics in symmetric bilayers](#). *Nature Communications* 8, 15765 (2017).
- [6] Seonghoon Woo, Kyung Mee Song, Xichao Zhang, et al. Deterministic creation and deletion of a single magnetic skyrmion observed by direct time-resolved X-ray microscopy. *Nature Electronics* 1, 288–296 (2018).
- [7] Davide Maccariello, William Legrand, Nicolas Reyren, et al. Electrical detection of single magnetic skyrmions in metallic multilayers at room temperature. *Nature Nanotechnology* 13, 233–237 (2018).
- [8] Christian Hanneken, Fabian Otte, André Kubetzka, et al. [Electrical detection of magnetic skyrmions by tunnelling non-collinear magnetoresistance](#). *Nature Nanotechnology* 10, 1039–1042 (2015).
- [9] Tristan da Câmara Santa Clara Gomes, Yanis Sassi, Dédalo Sanz-Hernández, et al. [Neuromorphic weighted sums with magnetic skyrmions](#). *Nature Electronics* (2025).
- [10] Tristan da Câmara Santa Clara Gomes, Tanvi Bhatnagar-Schöffmann, Sachin Krishnia, et al. Control of the magnetic anisotropy in multirepeat Pt/Co/Al heterostructures using magnetoionic gating. *Phys. Rev. Appl.* 21, 024010 (2024).

Dynamic control of weight-update linearity in magneto-ionic synapses

Guillaume Bernard^{1,*}, Kellian Cottart¹, Maria-Andromachi Syskaki², Victor Porée³, Andrea Resta³, Alessandro Nicolaou³, Alan Durnez¹, Shimpei Ono⁴, Ariam Mora Hernandez², Juergen Langer², Damien Querlioz¹, and Liza Herrera Diez¹

¹Centre de Nanosciences et de Nanotechnologies, CNRS, Université Paris-Saclay, 91120 Palaiseau, France

²Singulus Technology AG, Hanauer Landstrasse 103, 63796 Kahl am Main, Germany

³Synchrotron SOLEIL, L'Orme des Merisiers, 91190 Saint-Aubin, France

⁴International Center for Synchrotron Radiation Innovation Smart, Tohoku University, Aoba-Ku, Sendai 980-8572, Japan

*guillaume.bernard@universite-paris-saclay.fr

Multifunctional hardware technologies for neuromorphic computing architectures are essential for emulating the complexity of biological neural systems and enhancing the performance of artificial synapses and neurons. The integration of ionic and spintronic technologies introduces new degrees of freedom to the depression and potentiation behavior of artificial synapses, combining advanced magnetic functionalities with established ionic analog behavior. Magneto-ionics, a rapidly expanding field in spintronics, leverages ionic motion to manipulate magnetic properties in a non-volatile manner, offering a promising path toward low-energy, non-volatile memory devices and high-performance information storage and processing solutions.

In Ta/CoFeB/HfO₂ systems, ionic gating induces oxygen-ion migration within the stack, leading to spin-reorientation transitions. Our previous work [1] demonstrated a highly reversible and cyclable regime during transitions from perpendicular magnetic anisotropy (PMA) to in-plane (IP) magnetization, attributed to the non-equivalent distribution and binding of mobile oxygen species at the magnetic layer's surface across different magneto-ionic regimes.

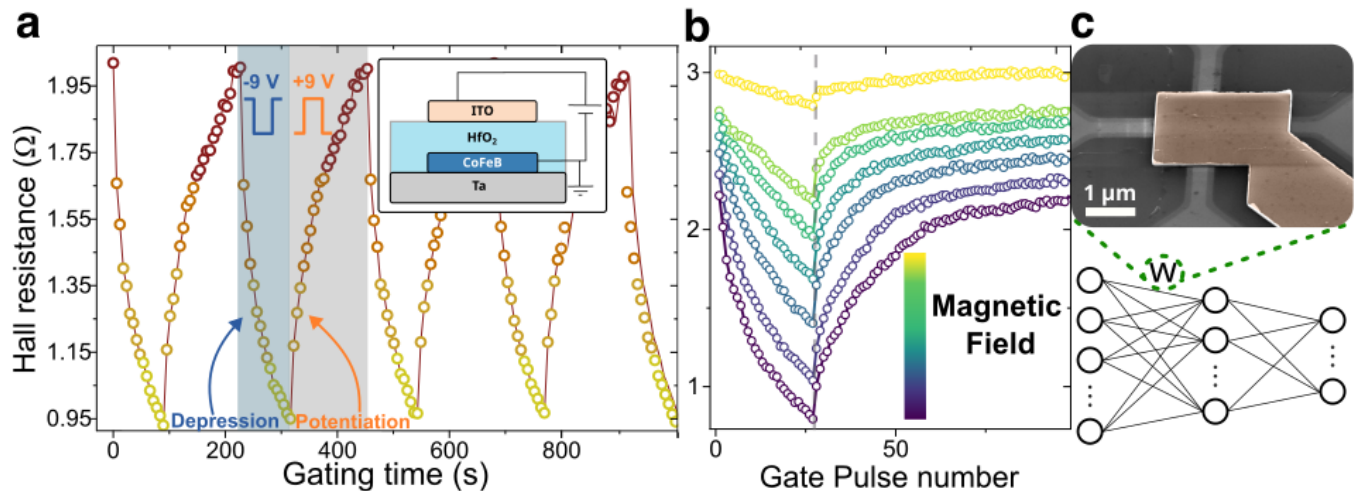


Figure 1: (a) Hall resistance as a function of the gating time at a constant field of 5 mT, each point is recorded after the application of a gate voltage pulse of -9 V or +9 V for depression and potentiation, respectively. (b) Hall resistance potentiation and depression behaviour conducted under different magnetic fields. (c) SEM image of a magneto-ionic device. A cartoon of the three-layer neural network used in the simulations is also depicted.

In this study [2], 300 nm wide Hall-bar devices incorporating a solid-state gate were fabricated using the same Ta/CoFeB/HfO₂ wafer as in [1], with an HfO₂ layer deposited via atomic layer deposition (ALD) replacing the ionic liquid gate. The devices exhibited PMA in their as-fabricated state and demonstrated a reversible PMA-to-IP transition under magneto-ionic gating. We showed that multiple stable intermediate magneto-ionics states are accessible through gate voltage pulses.

We employed these magneto-ionic devices as tunable synaptic elements, wherein the linearity of the potentiation and depression profiles was dynamically modulated by applying a magnetic field. Magnetic fields ranging from 5 mT to 78 mT significantly reduced the non-linearity of synaptic depression, transitioning from an exponential dependence to linearity at higher fields. Neural network simulations revealed that this magnetically-induced linearity enhancement in weight updates improved learning accuracy over a wide learning rate range (500–5000). This feature mimics the neuromodulation observed in biological systems, demonstrating that the integration of ionics into magnetic systems introduces a crucial new degree of freedom that is essential for advancing multifunctional hardware technologies in neuromorphic applications.

Acknowledgments

We gratefully acknowledge financial support from the Horizon Europe program (EIC Pathfinder METASPIN (101098651)) and the French National Research Agency (Splasy ANR-21-CE24-0008-01). This work was also partly supported by the French RENATECH network.

References

- [1] R. Pachat, D. Ourdani, J.W. van der Jagt, et al. [Multiple Magnetoionic Regimes in Ta/Co₂₀Fe₆₀B₂₀/HfO₂](#). *Phys. Rev. Appl.* 15, 064055 (6 2021).
- [2] G. Bernard, K. Cottart, M. Syskaki, et al. Dynamic control of weight-update linearity in magneto-ionic synapses. *Nano Letters* (accepted 2025).

Exploiting spin textures in a magnetic tunnel junction for logic and neuromorphic computing applications

Ilaria Di Manici^{1,*}, Rodrigo Guedas Garcia¹, Florian Disdier¹, Sebastien Wintz², Rachid Belkhou³, Bruno Fernandez⁴, Stephane Auffret¹, Philippe Talatchian¹, Gilles Gaudin¹, and Olivier Boulle¹

¹Univ. Grenoble Alpes, CEA, CNRS, Grenoble INP, SPINTEC, 38054 Grenoble

²Helmholtz-Zentrum Berlin für Materialien und Energie GmbH, D-14109 Berlin, Germany

³Synchrotron SOLEIL, L'Orme des Merisiers, 91190 Saint-Aubin, France

⁴Univ. Grenoble Alpes, CNRS, Institut Néel, 38042 Grenoble, France

*ilaria.dimanici@cea.fr

Magnetic skyrmions are spin textures that have been attracting large interest due to their nanometric sizes combined with topological stability, which confers them a particle-like behavior [1]. Their stabilization at room temperature, along with their current-induced motion in ferromagnetic structures, has been demonstrated in the last years, making them interesting candidates as bits of information for memories and logic devices [2, 3]. More recently, the use of skyrmions to perform neuromorphic computing applications has been proposed [4]. All these works rely mainly on imaging techniques to characterize the skyrmion manipulation and achieve their fundamental understanding. But, integrated applications would require an electrical detection of skyrmions. One possibility to achieve skyrmion detection with large electrical signal is to exploit the TMR in a Magnetic Tunnel Junction (MTJ).

In this presentation, I will demonstrate the electrical detection and manipulation of skyrmions in an MTJ dot and show how this can be exploited to perform neuromorphic operations, including task recognition.

To achieve an unambiguous demonstration of the electrical detection and manipulation of the skyrmions, *operando* microscopy was performed using Scanning Transmission X-Ray Microscopy (STXM). To this end, submicronic MTJ dots are patterned on membranes made of SiN, a material transparent to X-Rays.

Both high and low RA MTJs were considered for the experiments, in order to better explore the effects of respectively either Voltage Controlled Magnetic Anisotropy (VCMA) or Spin Transfer Torque (STT) for the manipulation of the magnetization. In both cases, we observed an electrical nucleation of skyrmions, but, while with high RA only a nucleation was achieved [5], we demonstrated the full electrical nucleation and annihilation with a low RA MTJ.

In Figure 1a, I show an example of a skyrmion in a 1.2 μm dot nucleated by injecting a current of -6 mA. By decreasing the current applied, the device recovers the AP state. By bringing back the current to -6 mA, the intermediate state is re-nucleated, with a corresponding ΔR of 0.5 Ω . This is a demonstration of the full read and write operations loop exploiting the STT mechanism to nucleate and annihilate spin textures.

In the second part of the presentation, I will show that the complex response of skyrmions to the applied voltage can be leveraged to achieve pattern recognition within the reservoir computing scheme. Reservoir computing is a type of recurrent neural network that maps the input data into a high-dimensional space in order to solve complex cognitive tasks ranging from image or speech recognition to time series prediction. Physical systems that are able to provide a non-linear response to the input data along with a fading memory of past inputs can be suitable as "reservoir". The response of the physical system to the input is then used to train the output layer of the network with a simple linear regression [6], making reservoir computing a type of neural network with low computational costs. In Figure 1b, a schematic of a reservoir computing is shown. Spintronic devices have shown to be quite suitable for performing Reservoir Computing due to their complex dynamics as well as their inherent nonlinearity [7, 8].

Here, we show the results obtained on the classifications of sines and square by exploiting a MTJ with intermediate states as the reservoir part of a RC. The MTJ shows intermediate states when excited by DC voltage for a range of magnetic fields. The resistance vs. voltage curve presents a non-linear increase as it can be observed in Figure 1c on top, for a magnetic field of -16 mT. The input sines and squares are provided to the system as a voltage signal with an amplitude that covers the non-linear range of system response. The frequency of the signal is tuned in order to see where the magnetic behavior of the device better provides a memory of past inputs. In Figure 1c, bottom plot, is shown the resistance in response to a voltage pulse from -0.15 to -0.65 V of 200 μs . The resistance grows and eventually reaches its final value after a typical time scale of about 70 μs . First results prove a recognition accuracy up to 92% in the sine and squares recognition task. To increase the dimensionality of the system a technique called temporal multiplexing is adopted, which consists of the preprocessing of the signal to generate virtual neurons [9].

The classification of sines and squares is a simple task that still enables to understand if the system can work as a RC, before moving to more complex tasks like voice recognitions.

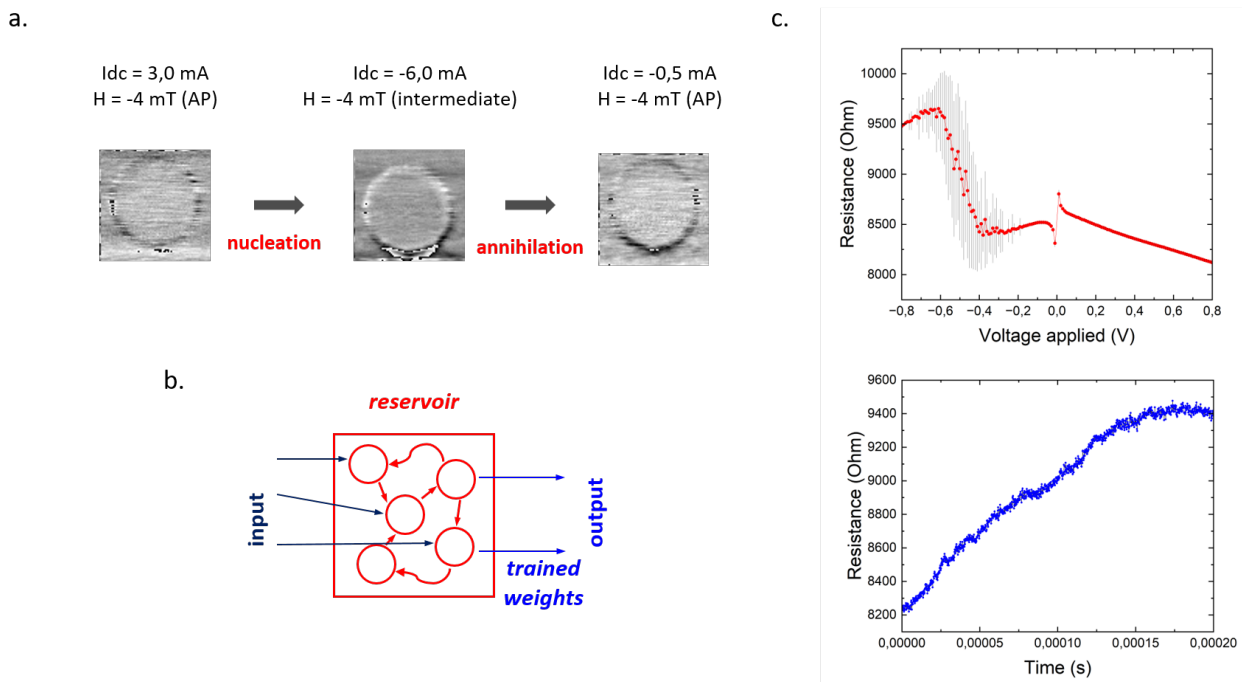


Figure 1: a. XMCD-STXM sequence of the nucleation with DC current and subsequent annihilation with DC current of an intermediate state inside a $1.2 \mu\text{m}$ MTJ pillar. The measured resistance variation is 0.5 Ohm from the AP state, both measured at -6 mA of DC current. b. Schematic of a reservoir computing. The reservoir part can be implemented using a physical system presenting nonlinearity and fading memory. c. Non-linear response to the applied DC voltage of an MTJ pillar at -160 Oe magnetic field. The non-linear curve is obtained averaging 50 times as the MTJ presents stochastic jumps in between several intermediate states.

Acknowledgments

References

- [1] Albert Fert, Vincent Cros, and João Sampaio. [Skyrmions on the track](#). *Nature Nanotechnology* 8, 152–156 (2013).
- [2] Olivier Boulle, Jan Vogel, Hongxin Yang, et al. [Room temperature chiral magnetic skyrmion in ultrathin magnetic nanostructures](#). *Nature Nanotechnology* 11, 449–454 (2016).
- [3] Roméo Juge, Soong-Geun Je, Dayane de Souza Chaves, et al. [Current-Driven Skyrmion Dynamics and Drive-Dependent Skyrmion Hall Effect in an Ultrathin Film](#). *Physical Review Applied* 12, 044007 (2019).
- [4] Tomoyuki Yokouchi, Satoshi Sugimoto, Bivas Rana, et al. [Pattern recognition with neuromorphic computing using magnetic field-induced dynamics of skyrmions](#). *Science Advances* 8, eabq5652 (2022).
- [5] Joseba Urrestarazu Larrañaga, Naveen Sisodia, Rodrigo Guedas, et al. [Electrical Detection and Nucleation of a Magnetic Skyrmion in a Magnetic Tunnel Junction Observed via Operando Magnetic Microscopy](#). *Nano Letters*, acs.nanolett.4c00316 (2024).
- [6] Matteo Cucchi, Steven Abreu, Giuseppe Ciccone, Daniel Brunner, and Hans Kleemann. [Hands-on reservoir computing: a tutorial for practical implementation](#). *Neuromorphic Computing and Engineering* 2, 032002 (2022).
- [7] J. Grollier, D. Querlioz, K. Y. Camsari, et al. [Neuromorphic spintronics](#). *Nature Electronics* 3, 360–370 (2020).
- [8] Mathieu Riou. Brain-inspired computing leveraging the transient non-linear dynamics of magnetic nano-oscillators, 254 O.
- [9] L. Appeltant, M.C. Soriano, G. Van der Sande, et al. [Information processing using a single dynamical node as complex system](#). *Nature Communications* 2, 468 (2011).

Towards a spintronic Ising Machine simulator

Chloé Chopin^{1, *}, Abderrazak Hakam¹, Mateo Ibarra Gomez¹, Liliana D. Buda-Prejbeanu¹, Simon de Wergifosse², Flavio Abreu Araujo², Erwan Aubouin¹, Louis Hutin², Franck Badets², Philippe Talatchian¹, and Ursula Ebels¹

¹Univ. Grenoble Alpes, CEA, CNRS, Grenoble-INP, SPINTEC, 38000 Grenoble, France.

²Institute of Condensed Matter and Nanosciences, Université catholique de Louvain, Place Croix du Sud 1, 1348 Louvain-la-Neuve, Belgium.

³Univ. Grenoble Alpes, CEA, LETI, 38000 Grenoble, France.

*chloe.chopin@cea.fr

Ising machines (IMs) are gaining interest as specialized systems designed to efficiently solve widespread combinatorial optimization problems (COPs) like the travelling salesman problem or graph coloring. Indeed, when using conventional computer architecture to solve COP, the time needed to solve them can scale exponentially with the size of the problem. IMs leverage the Ising model (see Fig. 1) and are a promising hardware implementation to solve COP efficiently. IMs are a network of binary-valued spins with specific spin coupling interactions. The configuration of collective spin states seeks its lowest energy state or ground state, representing the COP solution. While several hardware implementations [1] are under study, our proposal leverages the stochastic IM's cost-free thermal noise, exploring the complex energy landscape while escaping local minima (Fig. 1).

Spin-torque nano-oscillators (STNOs) are good candidates for such stochastic IMs [2, 3]: (i) when injection-locked to a microwave signal at twice its frequency, the phase difference between the STNO and source phases Φ_{osc} becomes binarized (cf Fig. 1); (ii) thermal noise stochastically triggers transitions between those two phase states, see Fig. 2; (iii) several controllable coupling mechanisms exist to control Ising spin interactions.

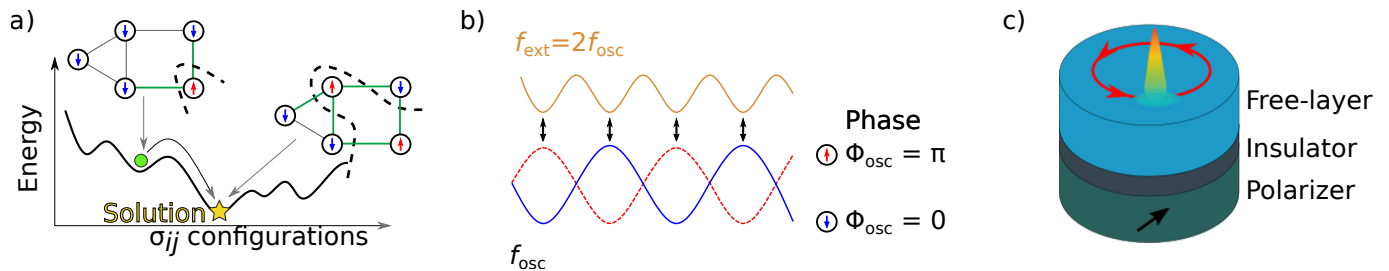


Figure 1: a) Illustration of the Ising machine based on the Ising Hamiltonian $\mathcal{H} = -\sum_{i,j} J_{ij} \sigma_i \sigma_j - \sum_j h_j \sigma_j$ and the corresponding energy landscape. Here σ_i, σ_j are binarized spins of values ± 1 , J_{ij} are the coupling constants and h_j is a bias. Relaxation toward the global energy minimum corresponds to the algorithm for finding the solution. b) Illustration of the phase binarization of an oscillator due to second harmonic injection locking. c) Illustration of an STNO composed of a polarizer, an insulating non-magnetic spacer layer, and a free layer that has a magnetic vortex configuration.

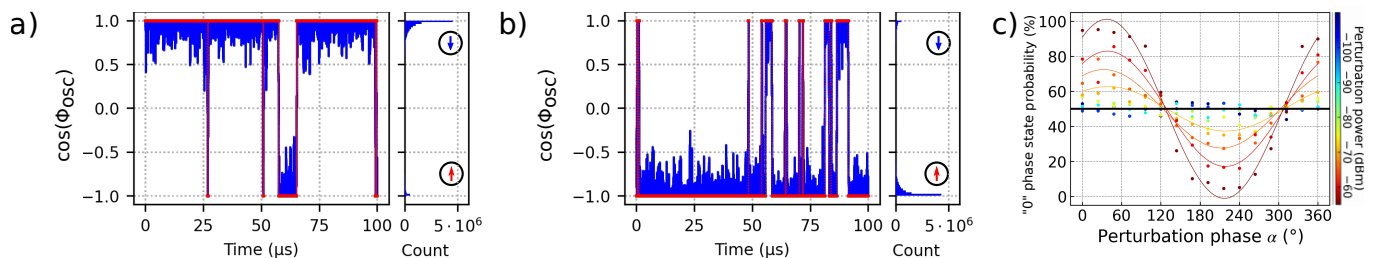


Figure 2: Simulated time traces showing phase jumps when a) the 0 phase state (or spin down state) is favored and b) when the π state (or spin up state) is favored. The data are in blue and the corresponding digitalisation is in red. The histogram shows the count for simulation time traces of 1.5 ms. c) Evolution of the probability of 0 phase state occurrence with the perturbation angle α and power.

While these requirements have been verified experimentally [2], setting coupling weights that encode a COP in IMs remains challenging. Indeed, they depend significantly on the STNO's output power, which varies from device to device, possibly impacting the COP solution. Therefore, it is crucial to fully understand the impact of those couplings on the dynamics of an STNO array, in particular for arrays of non-identical STNOs.

This calls for a digital twin to precisely model experimental STNO output signals within large arrays. Ongoing experiments make use of vortex-based STNOs, which can be well modeled using the stochastic Thiele equation approach (sTEA)[4, 5]. We successfully reproduced experimental results where the phase α of an additional RF magnetic field emulating an STNO array controls the probability of being preferentially in one of the two phase states, see Fig. 2. Combining these sTEA results with our experimental data-driven approach [5] is key to build an IM simulator close to experimental challenges. It is a major asset in determining experimental couplings and finally solving a given COP.

Acknowledgments

This work was supported in part by the French National Research Agency project SpinIM ANR-22-CE24-0004 and by the France 2030 government investment plan managed by the French National Research Agency under grant reference « PEPR SPIN – SPIN THEORY ANR-22-EXSP-0009 and SPINCOM ANR-22-EXSP-0005 ». Mateo Ibarra Gomez acknowledges financial support from the French Space Agency (CNES) and the European Union’s Horizon 2020 research and innovation programme under grant agreement No 800945 — NUMERICS — H2020-MSCA-COFUND-2017.

References

- [1] Yi Zhang, Yi Deng, Yinan Lin, et al. [Oscillator-Network-Based Ising Machine](#). *Micromachines* 13, 1016 (2022).
- [2] Nhat-Tan Phan, Nitin Prasad, Abderrazak Hakam, et al. [Unbiased random bitstream generation using injection-locked spin-torque nano-oscillators](#). *Physical Review Applied* 21 (2024).
- [3] Dagur Ingi Albertsson, Mohammad Zahedinejad, Afshin Houshang, et al. [Ultrafast Ising Machines using spin torque nano-oscillators](#). *Applied Physics Letters* 118 (2021).
- [4] Alfred Almsted Thiele. [Steady-State Motion of Magnetic Domains](#). *Physical Review Letters* 30, 230–233 (1973).
- [5] Flavio Abreu Araujo, Chloé Chopin, and Simon de Wergifosse. [Ampere–Oersted field splitting of the nonlinear spin-torque vortex oscillator dynamics](#). *Scientific Reports* 12 (2022).

Experimental implementation of a programmable Ising Machine using vortex-based Spin-Torque Nano-Oscillators

Abderrazak Hakam^{1,*}, Leandro Martins¹, Louis Hutin², Franck Badets², Luana Benetti³, Alex Jenkins³, Ricardo Ferreira³, Philippe Talatchian¹, and Ursula Ebels¹

¹Univ. Grenoble Alpes, CEA, CNRS, Grenoble INP, SPINTEC, 38000 Grenoble, France

²Université Grenoble Alpes, CEA, LETI, 38000, Grenoble, France

³International Iberian Nanotechnology Laboratory (INL), 4715-31 Braga, Portugal

*abderrazak.hakam@cea.fr

Solving computational problems of ever-increasing complexity and size goes hand in hand with an increase in the energy consumption related to the computing architecture that imposes a constant data transfer between memory and processing units. Therefore, novel hardware approaches are needed to remedy the issue of energy consumption while improving crucial parameters such as computation speed, compactness, and integrability at the same time. One of these novel approaches are Ising machines (IMs), physics-inspired computing systems that can efficiently solve combinatorial optimization problems (COPs). IMs are hardware implementations of the Ising model $H_{\text{Ising}} = -\sum_{\langle ij \rangle} J_{ij} \sigma_i \sigma_j - \mu \cdot \sum_i h_i \sigma_i$ that describes a 2D lattice of binary-valued spins σ_i, σ_j . An IM inherently seeks to minimize its total energy, where spin-coupling interactions J_{ij} are used to encode an arbitrary COP and map it into the IM, making the lowest energy states the solutions of the mapped COP. Instead of fine-tuning annealing schemes [1] to gradually stabilize the system onto the ground state, we aim to use the IM's thermal noise to stochastically explore the spin state configurations and infer the lowest energy states from the maxima of the resolved probability distribution.

Spin-torque nano-oscillators (STNOs) are excellent spintronic candidates for building IMs [1], as they do not suffer from the limitations of other proposed technologies, which are often restricted to time-multiplexing proof of concepts [2], cryogenic temperatures [3], or macroscopic-sized spins [4]. Leveraging CMOS compatibility, nanoscale size and rich nonlinear dynamics at MHz-GHz frequencies, STNOs have been used for neuromorphic computing with frequency encoding schemes [5]. However, the theoretically predicted potential of phase encoding [6][7] remains largely unexplored in experiments.

We aim to implement a spatial and programmable IM that operates through the stochastic phase dynamics of coupled vortex-based STNOs (frequency $f \sim 200\text{-}300\text{MHz}$). To emulate a binary spin, we use the fact that when the STNO is synchronized to a microwave signal at twice its natural frequency $2f$, its phase adopts two perfectly equiprobable states ψ_1 and ψ_2 that are π shifted, $\psi_2 = \psi_1 + \pi$ [8]. In a first experiment, we demonstrated experimentally that an external microwave signal at f disrupts this equiprobability, the key for controlling spin's probability state.

As a first proof of concept consisting of a two-spin IM ($N=2$), we demonstrate programmable coupling through an adjustable resistance representing the spin-coupling strength; see Figure 1 (a) and (b). To evaluate the influence of this coupling resistance, we computed the Pearson correlation between the phases of the coupled STNOs. We show that we can either increase or decrease the correlation between the STNO phases and alter its sign depending on the resistance value, see Figure 1 (c). This result indicates that the coupling between the phases of STNOs is very sensitive to the mediating component (here a passive resistance) and that a passive element is sufficient to implement an efficient and tunable coupling, highlighted by a correlation that varies between 35% and -6.2%. Further results will be discussed to scale to larger arrays ($N>2$), using the coupling matrix described in Figure 1 (d), to build a full spatial and programmable stochastic IM using vortex-based STNOs.

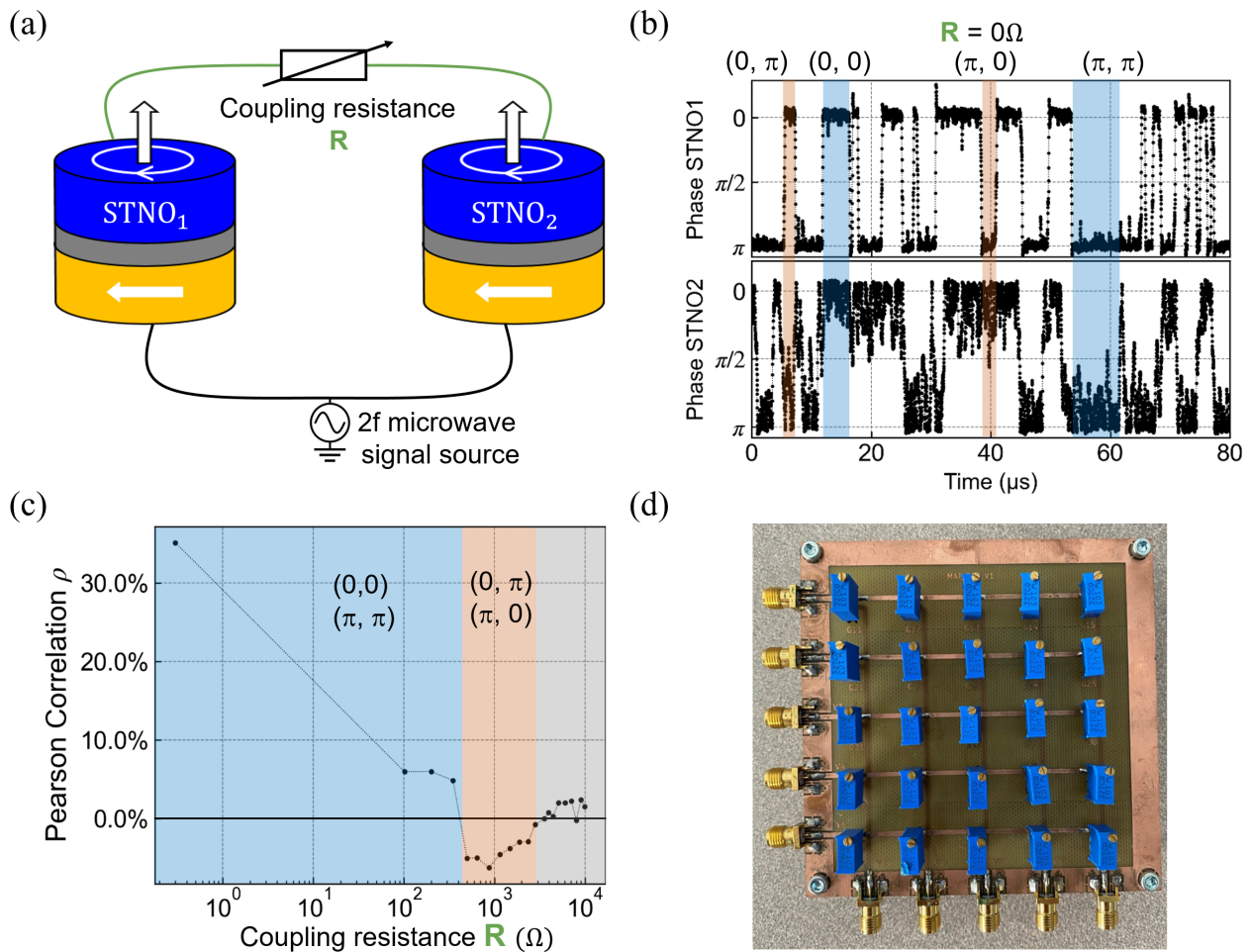


Figure 1: (a) Schematic of a two-spin IM using vortex-based STNOs. (b) Time traces showing the simultaneous electric phase readout of STNO1 and STNO2 for a coupling resistance of $R=0\Omega$. (c) Pearson correlation of the two STNO phases as a function of the coupling resistance. (d) 5x5 crossbar coupling matrix based on analog potentiometers to enable the coupling of up to five STNOs.

Acknowledgments

This research was funded partially by l'Agence Nationale de la Recherche (ANR), projects SpinIM ANR-22-CE24-0004, StochNet NSF-ANR-21-CE94-0002 and by the CEA under the project PTC-MINOS. A.H acknowledges funding from the program CEA FOCUS "Numérique Frugal".

References

- [1] Dagur Ingi Albertsson, Mohammad Zahedinejad, Afshin Houshang, et al. [Ultrafast Ising Machines using spin torque nano-oscillators](#). *Applied Physics Letters* 118 (2021).
- [2] Artem Litvinenko, Roman Khymyn, Victor H. González, et al. [A spinwave Ising machine](#). *Communications Physics* 6 (2023).
- [3] M. W. Johnson, M. H. S. Amin, S. Gildert, et al. [Quantum annealing with manufactured spins](#). *Nature* 473, 194–198 (2011).
- [4] Peter L. McMahon, Alireza Marandi, Yoshitaka Haribara, et al. [A fully programmable 100-spin coherent Ising machine with all-to-all connections](#). *Science* 354, 614–617 (2016).
- [5] Miguel Romera, Philippe Talatchian, Sumito Tsunegi, et al. [Vowel recognition with four coupled spin-torque nano-oscillators](#). *Nature* 563, 230–234 (2018).
- [6] Dmitri E. Nikonov, Gyorgy Csaba, Wolfgang Porod, et al. [Coupled-Oscillator Associative Memory Array Operation for Pattern Recognition](#). *IEEE Journal on Exploratory Solid-State Computational Devices and Circuits* 1, 85–93 (2015).
- [7] Nitin Prasad, Prashansa Mukim, Advait Madhavan, and Mark D Stiles. [Associative memories using complex-valued Hopfield networks based on spin-torque oscillator arrays](#). *Neuromorphic Computing and Engineering* 2, 034003 (2022).
- [8] Nhat-Tan Phan, Nitin Prasad, Abderrazak Hakam, et al. [Unbiased random bitstream generation using injection-locked spin-torque nano-oscillators](#). *Physical Review Applied* 21 (2024).

Non-volatile binary radio-frequency synapses using vortex polarities

M. Menshawy^{1,*}, L. Mazza², V. Puliafito², M. Carpentieri², A. Jenkins³, R. Ferreira³, L. Benetti³, A. Schulman³, D. Sanz-Hernández¹, J. Grollier¹, and F.A. Mizrahi¹

¹Laboratoire Albert Fert, CNRS, Thales, Université Paris-Saclay, Palaiseau, France

²Politecnico di Bari, Bari, Italy

³International Iberian Nanotechnology Laboratory (INL), Braga, Portugal

*mohamed.menshawy@cnrs-thales.fr

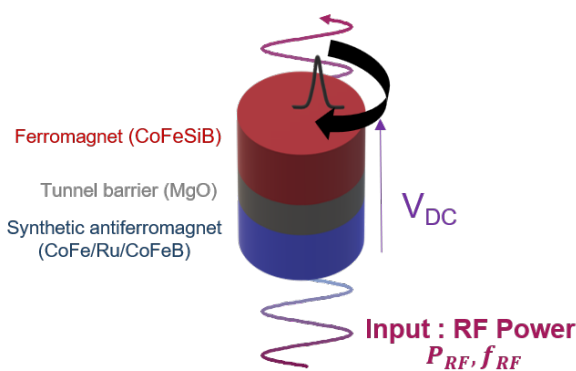


Figure 1: Vortex based magnetic tunnel junction. Receives RF power as input and output DC voltage.

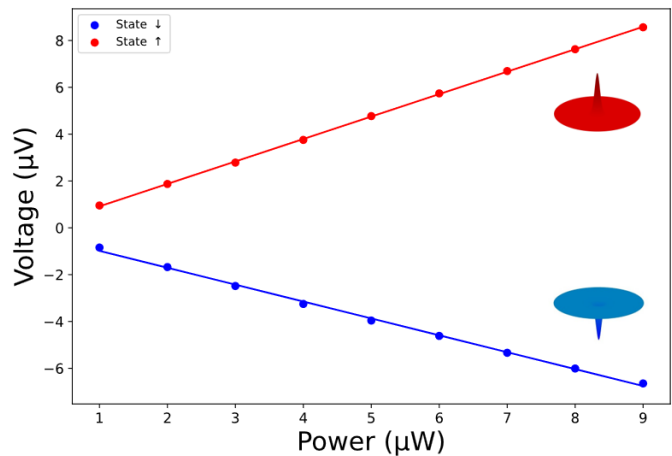


Figure 2: Binary weights for the polarity up (red) and down (blue) in a vortex-based magnetic tunnel junction.

Spintronic devices have been identified as promising candidates for neuromorphic computing. Ross et al. [1] have demonstrated a fully spintronic neural network where magnetic tunnel junctions implement both neurons and synapses. In particular, magnetic junctions perform weighted sums – an operation at the core of neural networks – on radio-frequency (RF) signals, through the spin-diode effect. The synaptic weights are controlled by the resonance frequency of the devices. However, in [1], the control of the resonance frequency is volatile, which is an obstacle to building large artificial neural networks with low energy consumption. Here, we propose to implement non-volatile RF synapses using vortex-based magnetic tunnel junctions. In such a device, the free layer is in a vortex state which magnetic core is out-of-plane and can thus take two opposite directions, called polarities. We observe that each polarity has a different resonance frequency, leading to two synaptic weights of opposite signs. The polarity state is stable and thus the binary synapse is non-volatile. We control the polarity state (i.e. the weight) by sending an RF signal of large amplitude (about 1 mW). This leads the vortex to gyrate at a critical velocity where it reverses. We demonstrate that we can selectively program the synaptic weight by choosing the frequency of the RF signal. We connect magnetic tunnel junctions of different frequencies in series. The chain performs a weighted sum of RF inputs of different frequencies sent in parallel. Furthermore, leveraging the frequency-selectivity of the vortex polarity reversal, we can program each synapse by sending RF signals in the chain. This removes the need for individual accesses to the devices to program them. Our system uses frequency-multiplexing both to perform the weighted sum and to program the synaptic weights, which greatly simplifies the architecture and opens the path to scaling up the size of the network and the density of its connections.

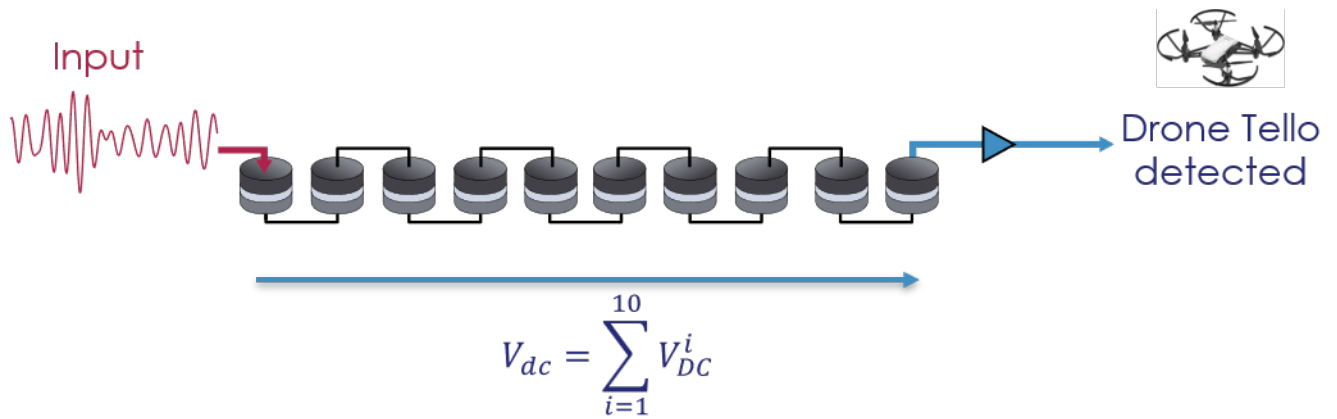


Figure 3: Classification of a drone signal with a synaptic chain of 10 magnetic tunnel junctions. Each device output DC voltage response, the total voltage output is a sum of voltages.

We demonstrate the programming of chains of 10 magnetic tunnel junctions each (i.e. 1024 weight configurations per chain). We demonstrate by experiments that vortex-based binary neural networks can be trained to classify drones from their recorded RF emissions. These results are a key step towards large-scale spintronic RF networks capable of real-life artificial intelligence tasks.

References

- [1] Andrew Ross, Nathan Leroux, Arnaud De Riz, et al. [Multilayer spintronic neural networks with radiofrequency connections](#). *Nature Nanotechnology* 18, 1273–1280 (2023).

Conférence invitée :
From Ampère's Molecular Currents to the Magnetism of Materials :
Einstein's Role

From Ampère's Molecular Currents to the Magnetism of Materials : Einstein's Role

Alfonso San Miguel^{1,2,*}

¹*Université Claude Bernard Lyon 1, CNRS, Institut Lumière Matière UMR 5306, F-69622, Villeurbanne, France*

²*Musée Ampère, 300 route d'Ampère, 69250 Poleymieux au-Mont-d'Or*

**alfonso.san-miguel@univ-lyon1.fr*

An exceptional experimental device was recently rediscovered in the storage rooms of the Ampère Museum: an original and little-known version of the Einstein–de Haas (EdH) experiment. Carried out in 1914–1915 by Albert Einstein and Wander de Haas, this experiment aimed to demonstrate the existence of molecular currents, as postulated by André-Marie Ampère to explain the magnetism of materials. It showed that magnetizing a material could induce a measurable rotation, thus confirming—at least as it was understood at the time—the presence of orientable electron orbitals responsible for magnetism.

The EdH apparatus preserved at the Ampère Museum, donated in 1959 by Geertruida de Haas-Lorentz, is a rare testimony to Einstein's direct involvement in experimental work. It sheds light on a pivotal moment in the history of our understanding of magnetism, just before the discovery of electron spin.

Ondes de spin & imagerie

Spatially Resolved Investigation of Spin Wave Frequency Multiplication

Roméo Beignon^{1,*}, Chris Körner², Rouven Dreyer², Georg Woltersdorf², Vincent Jacques¹, and Aurore Finco¹

¹Laboratoire Charles Coulomb, Université de Montpellier, CNRS, Montpellier, France

²Martin Luther University Halle-Wittenberg, Halle, Germany

*romeo.beignon@umontpellier.fr

Interactions between spin waves and magnetic textures offer a nice playground to study non-linear phenomena, as well as promising tools for designing magnonic devices. Among new developments, a frequency multiplication phenomenon has been observed in permalloy (Py) microstructures [1]. Magnetic resonance measurements on NV center ensembles reveal spin wave generation with frequencies at more than 60 times the excitation frequency. Micromagnetic simulations point towards the involvement of spatial variations of the magnetization in this phenomenon. These films of Py are indeed known to produce "ripples" of magnetization due to inhomogeneities [2]. Additional time-resolved magneto-optical Kerr effect measurements also show coherent standing spin-wave patterns for the amplitude of the spin waves generated by frequency multiplication. These observations motivate further measurements to resolve the spatial features involved in the phenomenon. Our goal is to understand the interplay between spatial features of the magnetization, and the harmonic generation.

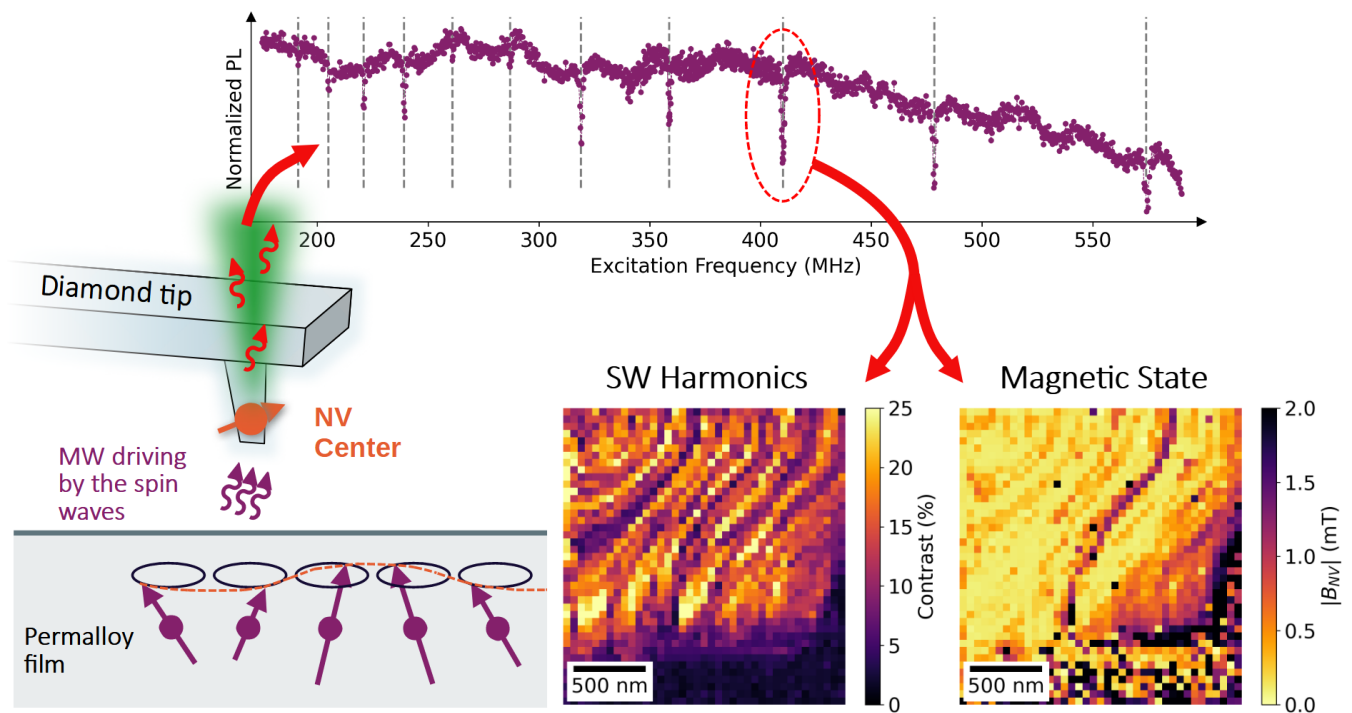


Figure 1: **Bottom left:** schematic of the experiment. Placed at the apex of an AFM tip, an NV center is sensitive to the microwave stray field generated by spin waves. **Top:** ESR spectrum featuring replicas of the NV center resonance. Each resonance results from the multiplication of the excitation frequency to reach the NV resonance at around 2870 MHz. **Bottom right:** NV resonance contrast map giving insight into the spin waves amplitude and simultaneously measured magnetic field map.

Here, we rely on NV-center scanning microscopy to perform spatially resolved measurements of the frequency comb. This method enables us to image both the magnetic state of the material and the generation of spin waves with a spatial resolution of about 50 nm [3]. The principle of the experiment is presented in Figure 1. Spin waves are generated by applying a microwave field to the Py microstructures. Non-linear processes create spin waves with higher frequencies. These spin waves then produce a microwave stray field, which can drive the NV center magnetic resonance. At zero field, the resonance is driven for an excitation frequency of 2870 MHz. It results in a drop of photoluminescence (PL). Measuring the PL while sweeping the excitation frequency results in an electron spin resonance (ESR) spectrum, as presented in Figure 1. Each dip in the PL indicates the generation of spin waves at the resonance frequency. The replica of the resonance ESR spectrum is characteristic of a frequency multiplication phenomenon.

The presence of a static magnetic field lifts the degeneracy of the energy states involved in NV center's resonance. This results in the splitting of the resonances on the ESR spectrum proportionally to the magnitude of the field along a particular axis. We use this phenomenon to quantitatively measure the stray field emitted by the magnetic state of the Py film. The PL contrast between resonant and non-resonant states gives a qualitative insight into the spin wave's amplitude. For the different harmonics, we aim to simultaneously image their amplitudes and the magnetic state of the Py microstructures (edges, domain walls, ...). Studying the correlation between the two measurements will help to understand the phenomenon leading to the frequency multiplication.

Our results show that we can detect the spin wave frequency comb with the single NV center placed in an AFM tip. We could sense spin waves with a frequency up to 15 times the excitation frequency. Furthermore, we are able to spatially map the effect of each harmonic on the NV center. Our spatial resolution enables us to see strong spatial variations in the ESR contrast. These spatial patterns are non-trivial and vary between the different harmonics. Finally, we could simultaneously measure the corresponding magnetic state. These measurements are a first step towards the understanding of the interplay between the nonlinear process that generates the spin wave harmonics and the magnetic texture.

References

- [1] Chris Koerner, Rouven Dreyer, Martin Wagener, et al. [Frequency multiplication by collective nanoscale spin-wave dynamics](#). *Science* 375, 1165–1169 (2022).
- [2] Jutta Steiner, Rudolf Schäfer, Holm Wiczoreck, Jeffrey McCord, and Felix Otto. [Formation and coarsening of the concertina magnetization pattern in elongated thin-film elements](#). *Physical Review B* 85, 104407 (2012).
- [3] Francesco Casola, Toeno van der Sar, and Amir Yacoby. [Probing condensed matter physics with magnetometry based on nitrogen-vacancy centres in diamond](#). *Nature Reviews Materials* 3, 17088 (2018).

Imaging of domain-wall motion and spin-wave propagation in cylindrical nanowires with a 3D core-shell magnetization distribution

L. Gómez-Cruz^{1,2,*}, L. Álvaro-Gómez¹, C. Fernández-González³, N. Martín², S. Ruiz-Gómez³, L. Aballe³, E. Pereiro³, R. Belkhou⁴, A. Masseboeuf², O. Fruchart², and L. Pérez^{1,5}

¹*Dpto. Física de Materiales, Universidad Complutense de Madrid, Madrid, 28040, Spain*

²*Univ. Grenoble Alpes, CNRS, CEA, SPINTEC, Grenoble, 38000, France*

³*ALBA Synchrotron, CELLS, Cerdanyola del Vallès, 08290, Barcelona, Spain*

⁴*SOLEIL Synchrotron, Saint Aubin, BP 48, 91192 Gif-sur-Yvette, France*

⁵*IMDEA Nanociencia, Campus de Cantoblanco, Madrid, 28049, Spain*

**lugome11@ucm.es*

One-dimensional magnetic conduits with lateral size in the range of nanometers are textbook cases for the understanding of magnetization dynamics, especially motion of domain walls (DWs) under magnetic field or spin transfer torques, or the emission and propagation of spin waves (SWs). Cylindrical magnetic nanostructures are currently receiving significant attention, namely nanowires and nanotubes [1], as a counterpart to flat strips. More generally, these structures fall under the topic of 3D nanomagnetism, which is rapidly rising [2]. New physical effects have been predicted for DWs in these systems, due to a specific topology in a 3D shape: new types of DWs and a larger DW speed as a consequence of the delay of the Walker breakdown, an instability common to all other DWs in the 2D geometry [3]. Moreover, it has been predicted that the dispersion curve of spin waves can be nonreciprocal, e.g. in nanotubes with azimuthal magnetization, resulting from curvature [4]. In short, this is a Daemon-Eshbach propagation geometry with spin waves confined at opposite surfaces for $\pm k$ with degeneracy lifted as the inner and outer surfaces of a tube are not equivalent, both in terms of magnetic exchange and magnetostatics. Besides interest in these new physical effects, 3D nanostructures may possibly benefit to the concept of race-track for 3D memories, in the context that Magnetic Random Access Technologies are already booming in the semiconducting industry. Other technologies like RF generation, artificial intelligence or neuromorphic computing may be well based on DWs manipulated by spin-polarized currents and benefit to an extension to 3D.

There have been already numerous theoretical predictions and experimental reports concerning magnetic nanowires and nanotubes, which are simple elements. However, 3D nanomagnetism allows to imagine more complex situations, possibly coming with further fundamental effects. In particular, the counterpart to spintronic stacks in the planar geometry could take the form of core-shell structures in 3D. Here, we consider a prototypical system to explore this situation: permalloy-like magnetic nanowires with a significant diameter, around 200 nm, which have been shown to sometimes develop a three-dimensional distribution of magnetization, characterized by longitudinal magnetization close to the axis and a tendency for azimuthal magnetization at the periphery [5]. Note that dipolar energy is not responsible for this magnetization arrangement, as azimuthal magnetization is found in micrometer-long wires, bringing no gain in dipolar energy while costing exchange energy. While the underlying microscopic mechanism responsible for this 3D arrangement of magnetization is unclear at present, it provides the opportunity to investigate magnetization dynamics in a 3D object.

We propose a system based on Permalloy cylindrical nanowires of diameter 200 nm with periodic Fe₇₀Ni₃₀ chemical modulations of 40 nm in length. They were synthesized using template-assisted electrochemical deposition and electrically contacted using laser lithography on high-resistivity Si substrates with Si₃N₄ windows. This design allows the injection of electric current from dc to sub-ns pulses. In such large-diameter NWs the main stimulus is not spintronic effects, but the Oersted field associated to the charge current [6]. In the presented system, we consider the situation with a homogeneous longitudinal magnetization on the axis and several domains with opposite circulation at the periphery, from clock-wise to counter-clock-wise (Figure 1). The resulting DWs stabilized have the proper geometry to be directly addressed by the Oersted field. We used transmission X-Ray Microscopy (TXM) at ALBA Synchrotron to access the 3-dimensional magnetization textures, obtaining X-Ray Magnetic Circular Dichroism (XMCD) images using both right- and left-handed circular polarizations. To investigate the effect of the Oersted field, nanosecond current pulses were injected into the nanowire. The sense of the Oersted field generated by these pulses depends on the polarity of the current, and it shares the same geometry as the azimuthal component of magnetization. The protocol followed during TXM experiments consists in taking a first XMCD image of the sample to observe the initial magnetic state. Next, a current pulse is applied to induce DW motion. Finally, a subsequent XMCD image is taken to examine the resulting changes in the magnetic state. We observe that the change of DW location is consistent with the increase of azimuthal domains expected to be favored by the Oersted field, as shown in Figure 1 (A, B). We evidenced changes of DW positions under current with density from 10⁹ to 10¹⁰ A/m². For the higher values, DWs move from one modulation to another (Figure 1 (A)), while for the lower values DWs move for a shorter distance, not reaching the next modulation (Figure 1 (B)). Assuming that the underlying phenomenon is DW motion, velocities were estimated by dividing the distance DW moved by the duration of the applied pulse. With this definition, we get values for velocities from 300 m/s to over 4 km/s. The highest values of velocity raise questions of their origin, whether they result from DW motion or another phenomenon. To be able to address this, we have performed time-resolved ptychography experiments in SOLEIL Synchrotron, which we believe are the first to be performed.

This allows us to obtain information of magnetization dynamics with a time resolution of a few tens of picoseconds and a spatial resolution in the range of ten nanometers. This is achieved through the synchronization of the electron packets in the synchrotron ring with the generation of the CErsted field. Measuring with different time delays allowed us to access the different magnetic states during the excitation. We evidence that for the lowest current values the underlying mechanism is DW motion (Figure 1C(a)), while it tends to be more the global and coherent switching of entire domains for the largest currents ((Figure 1C(b)). The latter may explain that extremely large DW speed may result if analyzed in the case of DW motion. The velocity of 600 m/s measured in this experiment is consistent with those obtained in TXM experiments, but the higher values require further investigations by simulations to address their origin. For this reason, great care must be taken while extracting DW velocities during the analysis of image-pulse-image (e.g. TXM) data.

Below, we outline two aspects for further fundamental studies:

- From the topology of the 3D distribution of magnetization, we expect that the exchange coupling between magnetization on the axis and at the periphery acts as an effective Dzyaloshinskii-Moriya interaction, lifting the degeneracy between Néel-like configurations. This should contribute to delay Walker-breakdown effects, possibly further than for DMI in films with perpendicular magnetization, because of the exchange-spring effect. We are currently investigating via simulations the type of DW in such magnetic core-shell nanowires, and its impact on DW dynamics.
- We propose to use these domain walls as sources of spin waves. In preliminary experiments, we have excited them with an AC charge current at a frequency that is a harmonic of the ring's RF frequency, up to several GHz. The sharpness of the walls, combined with their rotational symmetry, provides a textbook situation to study spin waves in a curvilinear system, avoiding the complexity of work already reported on tubes with a hexagonal cross-section [7]. We will show such spin wave emission resolved in frequency and wavelength to outline their dispersion curve.

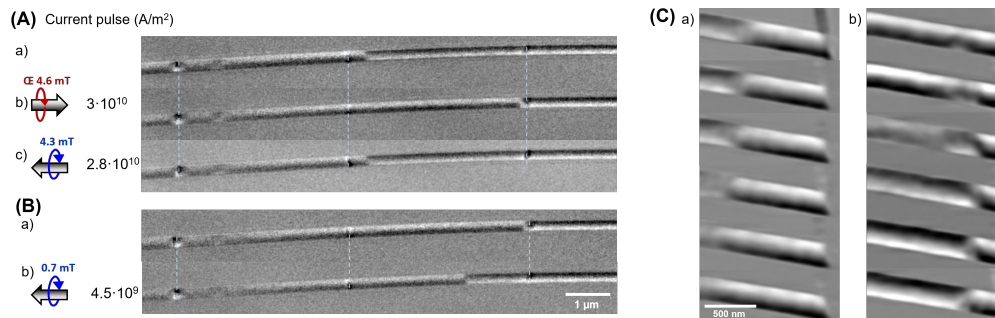


Figure 1: (A),(B) Sequence of consecutive XMCD-TXM images of an 245nm-diameter azimuthally magnetized nanowire of permalloy with $\text{Fe}_{70}\text{Ni}_{30}$ modulations. Images A(b,c) and B(b) were taken after applying a current pulse with polarity indicated in the figure and a duration of 2 ns to their previous state. (C) Time-resolved ptychography measurements of a 200nm-diameter nanowire. The nanowire was excited with an AC current with frequency of the RF frequency of the ring (352.202 MHz) and values of current density of (a) $J = 3.8 \cdot 10^{10} \text{ A/m}^2$ and (b) $J = 4.9 \cdot 10^{10} \text{ A/m}^2$. Each frame of the sequence was taken with a delay of 240 ps relative to the previous one.

References

- [1] M. Staňo and O. Fruchart. Handbook of Magnetic Materials. 27 (2018). Ed. by E. Brück.
- [2] A. Fernandez-Pacheco, R. Streubel, O. Fruchart, et al. [Three-dimensional magnetism](#). *NatComm* 8, 15756 (2017).
- [3] A. Thiaville and Y. Nakatani. [Spin dynamics in confined magnetic structures III](#). Topics Appl. Physics 101, 161–205 (2006). Ed. by B. Hillebrands and A. Thiaville.
- [4] J. A. Otálora, M. Yan, H. Schultheiss, R. Hertel, and A. Kákay. [Curvature-Induced Asymmetric Spin-Wave Dispersion](#). *Physical Review Letters* 117, 227203 (2016).
- [5] S. Ruiz-Gómez, C. Fernández-González, E. Martínez, et al. [Helical surface magnetization in nanowires: the role of chirality](#). *Nanoscale* 12, 17880–17885 (2020).
- [6] M. Schöbitz, A. De Riz, S. Martin, et al. [Fast domain walls governed by topology and CErsted fields in cylindrical magnetic nanowires](#). *Physical Review Letters* 123, 217201 (2019).
- [7] L. Körber, M. Zimmermann, S. Wintz, et al. [Symmetry and curvature effects on spin waves in vortex-state hexagonal nanotubes](#). *Physical Review B* 104 (2021).

Magneto-resistive detection of spin-waves

Quentin ROSSI^{1,*}, Hicham MAJJAD¹, Grégoire DE LOUBENS², Hugo MERBOUCHE², Igor NGOUAGNIA¹, Aurélie SOLIGNAC², and Matthieu BAILLEUL¹

¹IPCMS, CNRS, Université de Strasbourg, 67034 Strasbourg, France

²SPEC, CEA, CNRS, Paris-Saclay, 91190 Gif-sur-Yvette, France

*quentin.rossi@ipcms.unistra.fr

Until now, spin-waves have been detected either by magneto-optical imaging (magneto-optical Kerr effect, micro Brillouin light scattering) or by inductive microwave measurements. These methods are now reaching their limits in terms of signal sensitivity and spatial resolution, which constitutes a technological bottleneck for the miniaturization of magnonic devices and for the exploration of the fundamental physics of spin-waves. Recently, several high-resolution techniques have

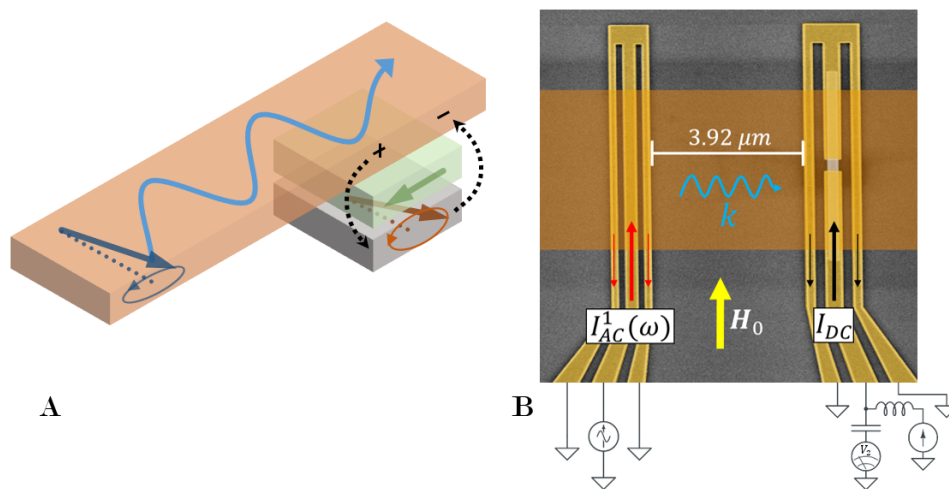


Figure 1: Magneto-resistive detection of spin-waves. A Working principle. In orange, the waveguide in which a spin-wave propagates. In gray, the soft (free) layer with its magnetisation oscillating around its equilibrium state (dashed line) due to the dipolar stray fields generated by the spin wave (dashed arrows). In green the hard (reference) layer supposed unperturbed by the spin-wave. B Annotated picture of a typical measured sample. On the left, the exciting microwave antenna (yellow), connected to the port 1 of the vector network analyzer. On the right, the sensor in which the gray center part is the magneto-resistive detection area. The sensor is connected to the port 2 of the vector network analyzer. In orange, the Ni₈₀Fe₂₀ waveguide covering the excitation antenna and the sensor.

been developed, such as nitrogen vacancy magnetometry and time-resolved X-ray imaging. However, such methods, which require advanced instrumentation, are still limited in terms of versatility, and are certainly not directly compatible with a micro-electronic environment. As an alternative strategy, we resort to a standard element of spintronics, which is a giant magneto-resistive (GMR) sensor. The so-called spin-valve with orthogonal magnetisations arrangement is a device that constitutes a high-performance magnetic field sensor, already exploited in various applications, including magnetic read heads, automotive sensors or bio-medical imaging. The total resistance of a GMR sensor vary according to the relative orientation of the magnetisation of the layers that compose it.

In this work, we directly integrate such a magneto-resistive sensor [1] below a ferromagnetic track serving as a waveguide for spin-waves (Fig. 1A). The sensor is electrically insulated from the track, but is located close enough to be coupled to it via stray dipole fields. When the spin-wave passes over the sensor, it generates an oscillating dipole field which induces a precession of the magnetisation of one of the ferromagnetic layers of the stack (the free layer), the other being magnetically pinned. This translates in an oscillation of the mutual impedance Z_{21} of the sensor, which, for a given current bias, results in a voltage that can be accessed via suitable microwave measurements.

The fabricated device is made of three main parts shown in Fig. 1B. First, spin-waves are excited by an antenna [2], which consists of a set of three conducting tracks in the coplanar waveguide geometry as shown in Fig. 1B (left gold structure). An oscillating microwave Ørsted stray field is generated, which is able to pump spin-waves with wavelength in the range of 1 – 2 μm in the nearby ferromagnetic waveguide.

This waveguide consists of a Permalloy (Ni₈₀Fe₂₀) slab that is 60 μm long, 7 μm wide and 22 nm thick and is located about 350 nm above the antenna. Its magnetisation is saturated along the width using an external static field H_0 which corresponds to the so-called Damon-Eshbach configuration of spin-wave propagation. The measurement of the sample is performed under the two polarities of the direct current flowing in the GMR sensor. Thus, by calculating the sum and the difference of the two measured signals, we extract the inductive (Fig. 2.A) and magneto-resistive (Fig. 2.B) contributions of the overall signal, respectively. Those measurements show that magneto-resistive detection exhibits a signal level about

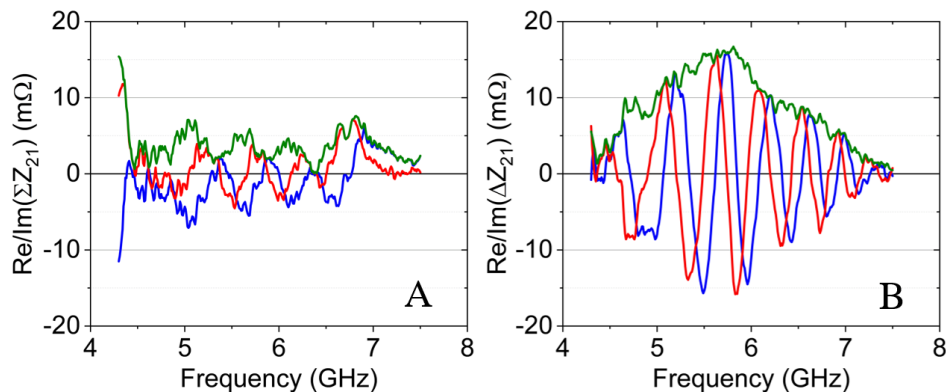


Figure 2: Analysis of measured mutual impedance under an external field $\mu_0 H_0 = 20$ mT, for a direct current bias $I_{DC} = 1.5$ mA and using a spin-wave pumping power $P = -15$ dBm. A Inductive contribution of the mutual impedance. Real part (blue), imaginary part (red) and modulus (green) are plotted. B Magneto-resistive contribution of the mutual impedance. Real part (blue), imaginary part (red) and complex modulus (green) are plotted.

five times higher than the usual inductive detection. Noting that the inductive signal is proportional to the antenna's length covered by the waveguide ($\approx 7 \mu\text{m}$) when the magneto-resistive signal only arises from the 600 nm long detection area, we estimate that the magneto-resistive signal is indeed 50 times more intense than the inductive one for a given detection volume. These experimental results are also corroborated by micromagnetic simulations of a numerical twin of this device.

The key advantage of the proposed detection stands in the signal's scaling law. The signal of a conventional inductive detection scales as the area of the sensing antenna, when the magneto-resistive signal depends mostly on the available voltage, which can remain very high down to the nanometer scale.

Acknowledgments

This work has benefited from a government grant operated by the French National Research Agency as part of the France 2030 program, reference ANR-22-EXSP-0004 (SWING).

References

- [1] J Moulin, A Doll, E Paul, et al. Optimizing magnetoresistive sensor signal-to-noise via pinning field tuning. *Applied Physics Letters* 115, 122406 (2019).
- [2] V Vlaminc and M Bailleul. Spin-wave transduction at the submicrometer scale: Experiment and modelling. *Physical Review B* 81, 014425 (2010).

Unravelling spin-wave propagation regimes using NV magnetometry

Julien Berthomier^{1,*}, Romain Lebrun¹, Karim Bouzehouane¹, Vincent Cros¹, Marie-Pierre Adam², Jean-François Roch², Jamal Ben Youssef³, and Abdelmadjid Anane¹

¹Laboratoire Albert Fert, Unité mixte CNRS-Thales, , Université Paris-Saclay, 91767 Palaiseau, France

²Laboratoire Lumière, Matière et Interfaces, 91190 Gif-sur-Yvette, France

³Labsticc UMR 6285, Technopole Brest-Iroise - CS 83818 29238 Brest Cedex 3, France

*julien.berthomier@cnrs-thales.fr

Spin waves are the fundamental propagating excitations of the magnetic order, with an associated bosonic quasiparticle called a magnon. Research in magnonics classically aims at harvesting the unique properties of spin-waves for digital or analog signal processing, neuromorphic computing, but also more recently to use magnons as potential quantum buses for quantum computing [1].

Studying and controlling spin wave propagation and (non-)linear magnon-magnon interactions require the development of fast and efficient 2D imaging techniques of nanostructured magnonic devices. Until recently, the laboratory techniques have solely relied on magneto-optical effects (such as Kerr microscopy and micro-Brillouin light scattering (μ -BLS)). With the emergence of NV centers as ultrasensitive quantum sensors of magnetic fields, new approaches are being developed to image magnonic transport through their oscillating stray field [2, 3].

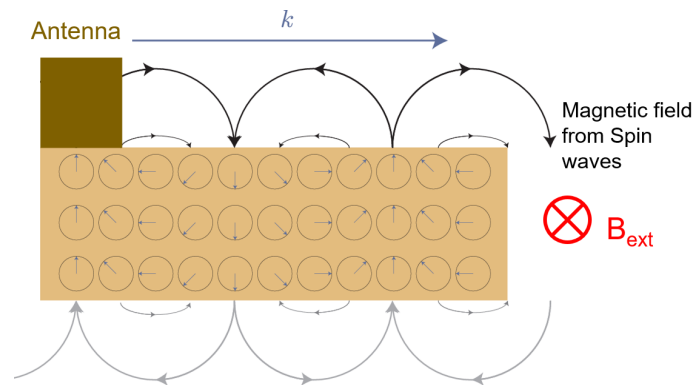


Figure 1: Sketch of spin waves propagating in Damon-Eschbach configuration.

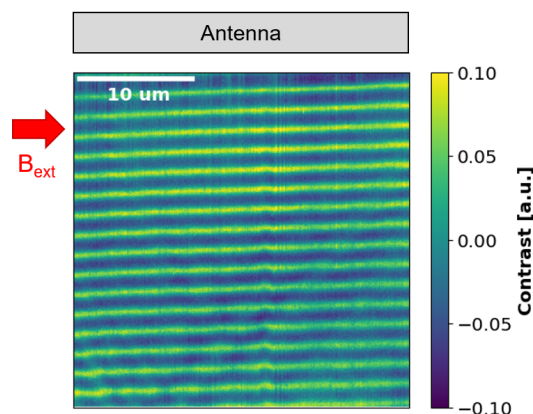


Figure 2: NV imaging of propagating spin-waves in Damon-Eschbach configuration: The image are obtained through the spatial electron spin-resonance contrast of a single NV center mounted on an atomic force microscope (AFM).

Following this approach, we develop NV microscopy techniques to image spin-waves in various garnet films (YIG, BiYIG) with thicknesses ranging from 20 to 500 nm (Fig. 1-2). In these systems, we could first image the expected highly anisotropic dispersion relation of spin waves in both real and k spaces (Fig. 3-4). We then report the presence of standing wave patterns arising from nonlinear scattering processes from short-wave length magnons and evidence the key role of lithography irregularities in these processes. These results illustrate the potential of NV magnetometry to unravel nonlinear phenomena at the nanoscale and to optimize nanofabrication processes of magnonic devices. We finally discuss the interactions between spin-waves and spin-textures, and use NV magnetometry to transition between different regimes of spin-waves excitations. Our approach paves the way for the study of nonlinear spin-waves dynamics in complex geometries in presence of topology and potential quantum phenomena.

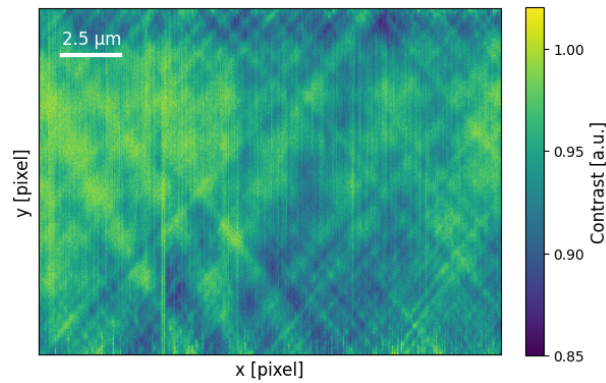


Figure 3: Figure a).

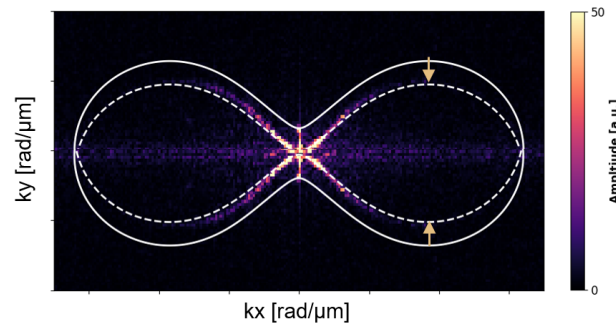


Figure 4: Figure b). Imaging of spin-wave scattering processes in (a) real and (b) k spaces. These processes are revealed by imaging closer to the sample surface, which enables to image spin-wave with short k vectors. The k space image is obtained by simple Fourier transform from the real space image and reveals a shifted dispersion relation [4].

Acknowledgments

This work has benefited from a government grant operated by the French National Research Agency as part of the France 2030 program, reference ANR-22-EXSP-0004 (SWING).

Ce travail a bénéficié d'une aide de l'État portant la référence ANR TACTIQ project, Grant No.23-CE47-0009

Ce travail a bénéficié d'une aide de l'État au titre de France 2030 (QuanTEdu-France) portant la référence ANR-22-CMAS-0001.

References

- [1] A Chumak and al. [Advances in Magnetism Roadmap on Spin-Wave Computing](#). *IEEE Transactions on Magnetics* 58 (2022).
- [2] Iacopo Bertelli, Joris J. Carmiggelt, Tao Yu, et al. [Magnetic resonance imaging of spin-wave transport and interference in a magnetic insulator](#). *Science Advances* 6, eabd3556 (11, 2020).
- [3] Baptiste Vindolet. "Utilisation des défauts du diamant comme capteurs en conditions extrêmes". These de doctorat. université Paris-Saclay, 30, 2021.
- [4] B. A. Kalinikos and A. N. Slavin. [Theory of dipole-exchange spin wave spectrum for ferromagnetic films with mixed exchange boundary conditions](#). *Journal of Physics C: Solid State Physics* 19, 7013 (1986).

Imaging spin waves by Electron Holography

M. Resano^{1,*}, C. Gatel^{1,2}, and N. Biziere¹

¹*CEMES-CNRS, 29 rue Jeanne Marvig, Toulouse, 31055, France*

²*Université Paul Sabatier, 31062 Toulouse, France*

*marine.resano@cemes.fr

The field of magnonics, which focuses on manipulating spin waves to create energy-efficient devices, has rapidly advanced, presenting new challenges in understanding spin dynamics at the nanoscale. One effective approach to address these challenges is imaging spin waves in nanoscale objects. However, only a limited number of techniques offer the sufficient spatial resolution of a few nanometers. In this context, we present the concept of an innovative experimental approach using Electron Holography to image spin waves in nano-objects with nanometer-scale spatial resolution. This method leverages electron microscopy to correlate the mapping of local magnetization precession with structural and chemical information, thus improving the modeling of spin dynamics at the nanoscale—an essential step for the development of gigahertz magnonic devices.

Off-axis Electron Holography is an imaging technique that relies on the formation of an interference pattern. From the resulting hologram, it is possible to measure the phase shift of the electron beam induced by the object's electrical and magnetic potentials, thereby mapping the associated fields with sub-nanometer spatial resolution. To map the precessing magnetization, one can take advantage of the small variations in the magnetization component along the equilibrium direction. The fundamental principle is illustrated in Fig. 1a. When exposed to a microwave field at the spin wave frequency, the local magnetization precesses around its equilibrium position, denoted as M_{stat} . As a consequence, the spatial variations of magnetization ΔM induced by the precession can be measured as small variations (i.e small gradients) in the time-averaged electron phase shift image relative to the equilibrium state.

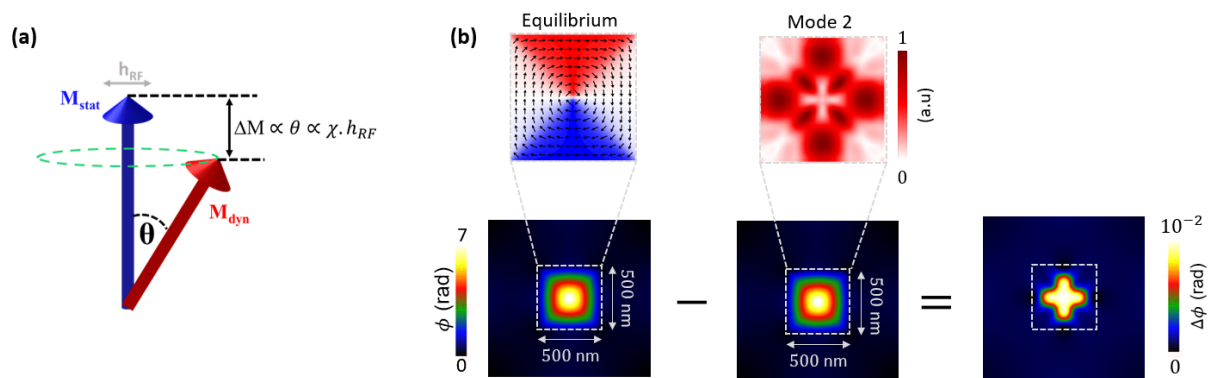


Figure 1: (a) Principle of measure. (b) Reconstruction of the phase image: by subtracting the phase shift image under precession from the equilibrium phase shift image, the local variations ΔM can be recovered. The color scale corresponds to the renormalized amplitude of the FFT.

We demonstrate the feasibility of this approach by conducting micromagnetic simulations of spin wave modes in model systems and reconstructing the corresponding experimental electron hologram. Such simulations allow to define possible experimental conditions such as the orientation and amplitude of the pumping field with respect to the magnetic object to obtain experimentally achievable signal-to-noise ratio. Indeed, the intrinsic background noise present in electron holography experiments is around 1 mrad with the new direct electron cameras [1]. As an example, the uniform mode at 10 GHz in the domains of a permalloy dot in the equilibrium vortex state excited with an out of plane pumping field along Z (direction parallel to electron beam) is shown in the Fig. 1b. The simulation show that the local magnetization precession amplitude can be recovered from the magnetic phase image extracted from the hologram with a S/N ratio of about 3 and 10 with a microwave amplitude of 3 Oe and 5 Oe respectively.

We also demonstrate how to take into account other constraint related to electron microscopy. For example, samples must be transparent to electrons. As an example of achievable device replicating the micromagnetic simulations, the Fig. 2 shows a NiFe stripe of squared dots surrounded by a micro-antenna fabricated using laser lithography and e-beam lithography at CEMES, followed by Physical Vapor Deposit. These dots are deposited on a 30 nm silicon nitride membrane. Finally, the last constraint consists in injecting a microwave signal inside the microscope. For this, we present two new sample holders that have been developed by the CEMES allowing to inject 2 or 4 microwave signals up to 18 GHz via microstrip lines, with insertion loss below 10 dB in the frequency range, and with less than 5 dB of loss below 10 GHz (Fig. 2).

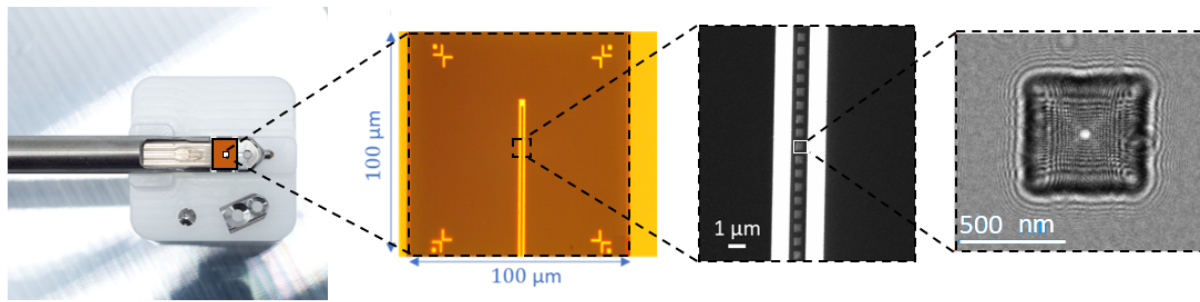


Figure 2: From left to right: Dedicated sample holder for RF excitation and example of sample location (orange rectangle), optical image of the electron transparent silicon nitride membrane, SEM image of the micro-antenna, Lorentz TEM image of the NiFe stripe of squared dots.

References

- [1] C. Gatel, J. Dupuy, F. Houdellier, and M.J. Hÿtch. [Unlimited acquisition time in electron holography by automated feedback control of transmission electron microscope](#). *Appl. Phys. Rev.* 113, 133102 (2018).

Spectroscopy of the spin wave acoustic mode in synthetic antiferromagnets

G. Y. Thiancourt^{1,*}, S. M. Ngom¹, N. Bardou¹, and T. Devolder¹

⁷⁴Université Paris-Saclay, CNRS, Centre de Nanosciences et de Nanotechnologies, 91120, Palaiseau, France
*gael-yann.thiancourt@universite-paris-saclay.fr

Magnonics has been attracting increasing interest from the research community in recent years. Spin waves (SWs) offer unique properties such as non-linearity and non-reciprocity, but a deep understanding of their dynamics is crucial for their implementation in future devices. This becomes possible using a Vector Network Analyzer and the fabrication of micro-antennas which allow propagation spin wave spectroscopy (PSWS) for a high-resolution in wavevector k [1].

In this study, we perform PSWS on a synthetic antiferromagnet (SAF) of CoFeB(17 nm)/Ru(0.7 nm)/CoFeB(17 nm) under an in-plane applied field \vec{H} below saturation, with the field direction either along the x or y direction [see Fig. 1(a)]. In this case, the magnetizations of the two CoFeB layers are in a scissors configuration, exhibiting two eigenmodes, the optical mode and the acoustic mode, respectively characterised by out-of-phase and in-phase precession of the magnetizations. In particular, we characterise the SWs acoustic mode whose dispersion relation $\omega(k)$ has been proven to be extremely non-reciprocal for $\vec{k} \parallel \vec{H}$, with a group velocity remaining positive regardless of the sign of the wavevector, or reciprocal around $k = 0$ for $\vec{k} \perp \vec{H}$ [2–4].

We pattern the magnetic material into 20 μm -wide SW conduits. Single-wire antennas are fabricated on top to excite and detect SWs propagating in the y -direction [Fig. 1(b)]. The different devices exhibit antenna widths denoted $w_{\text{ant}} = 1, 2$ and $2 \mu\text{m}$ and respective center-to-center distances of $r = 3.4, 4$, and $6 \mu\text{m}$. In this abstract, we focus on the device for $r = 4 \mu\text{m}$ and $w_{\text{ant}} = 2 \mu\text{m}$.

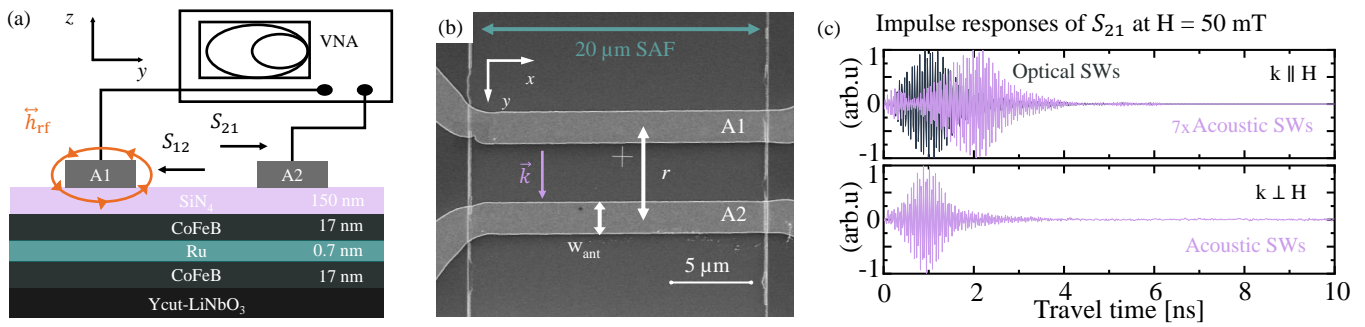


Figure 1: (a) Sketch of the setup used for propagating spin wave spectroscopy (PSWS). (b) Scanning electron microscopy image of a PSWS device. Light gray: single-wire antennas. Medium gray: Synthetic antiferromagnet conduit. An in plane external field is applied either along x or y giving two main configurations $\vec{k} \perp \vec{H}_x$ or $\vec{k} \parallel \vec{H}_y$. (c) Spinwave wavepacket in time domain for an applied field of 50 mT.

PSWS has been performed for the different field configurations, i.e., $\vec{k} \perp \vec{H}_x$ and $\vec{k} \parallel \vec{H}_y$. We calculate the derivative of raw data $\tilde{S}_{21}(f)$ with respect to the applied field, and use time-of-flight spectroscopy [5] to isolate the SW contribution in the signal. The latter involves calculating the impulse response $s_{21}(t)$ from $\tilde{S}_{21}(f)$. Fig. 1(c) shows the calculated impulse responses for $r = 4 \mu\text{m}$ and $\mu_0 H = 50$ mT, the acoustic SW wavepackets have a travel time $t_{\text{travel}} = 2$ ns for $\vec{k} \parallel \vec{H}_y$ and $t_{\text{travel}} = 1$ ns for $\vec{k} \perp \vec{H}_x$, allowing a first estimation of the SW group velocity $v_g \approx r/t_{\text{travel}}$, i.e. $\approx 2 \text{ km}\cdot\text{s}^{-1}$ and $\approx 4 \text{ km}\cdot\text{s}^{-1}$, respectively. We isolate the wavepackets of interest by applying a time window. Then we apply a back Fourier transformation to the truncated responses and recover a spectrum free of the noise.

Additionally, using Eq. 22 and Eq. 35 from Ref. [6] and considering only the χ_{yy} part of the magnetic susceptibility, we show that the argument of \tilde{S}_{21} , which describes the phase accumulation of SWs during their propagation, can be written as,

$$(i) \quad \arg\left(\frac{\partial \tilde{S}_{21}^{yy}}{\partial H_x}(\omega, \vec{k} \perp \vec{H}_x)\right) = kr - \frac{\pi}{2} + 2n\pi \quad \text{and} \quad (ii) \quad \arg\left(\frac{\partial \tilde{S}_{21}^{yy}}{\partial H_y}(\omega, \vec{k} \parallel \vec{H}_y)\right) = kr_{\text{eff}} + \frac{\pi}{2} + 2n\pi,$$

where $n \in \mathbb{Z}$ and $r_{\text{eff}} = \left(r + \frac{w_{\text{ant}}^2}{6L_{\text{att}}} + \frac{w_{\text{ant}}^2}{6r}\right)$ is an effective length dependent on the attenuation length L_{att} of SWs and setup dimensions r and w_{ant} . Indeed, depending on the nature of the SWs, the phase accumulation during propagation depends only on r in the reciprocal case, while for non-reciprocal SWs, it is also influenced by other parameters of the system. Using (i) and (ii) we extract SWs dispersion relations for non-reciprocal SWs [Fig. 2.(a)] and reciprocal SWs acoustic mode [Fig. 2.(b)]. Therefore, the group velocity can be obtained using linear fits around specific values of k [3, 4]. These results remain consistent for the different devices that support the reliability of our approach. Overall, this work provides an all-inductive characterisation of the SAF acoustic SWs including precise data on the group velocity of these waves within a magnetic device using only PSWS measurements.

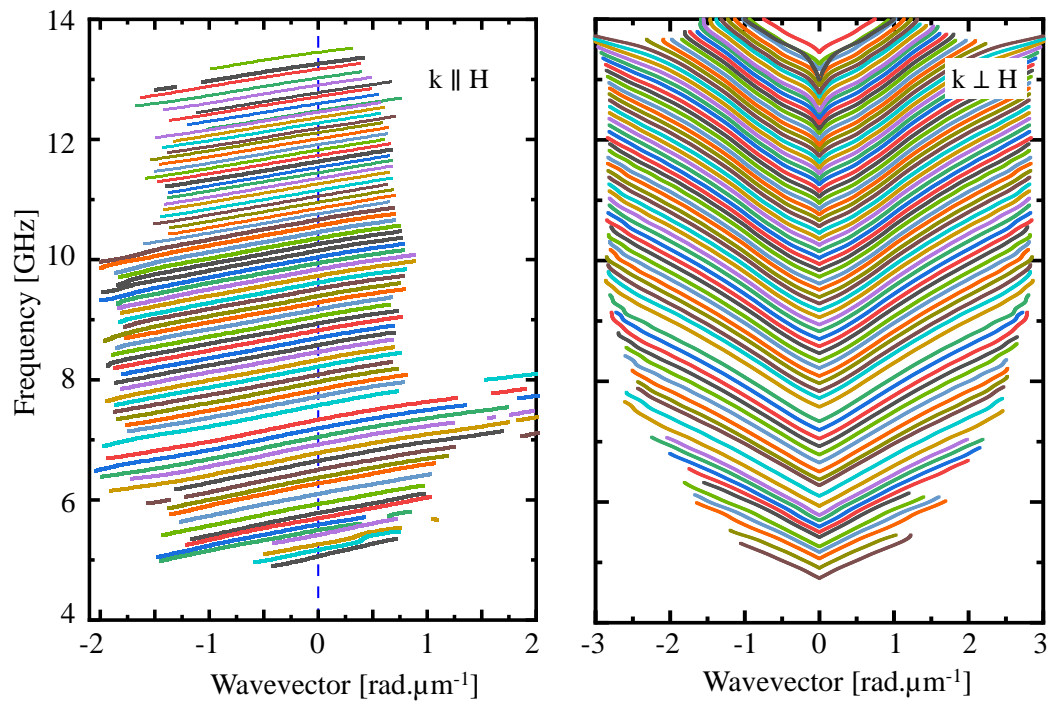


Figure 2: Experimental dispersion relations for reciprocal (a) and non-reciprocal (b) SAF acoustic spinwaves obtained from PSWS on a device with an antenna width $w_{\text{ant}} = 2 \mu\text{m}$ and antenna center-to-center distance $r = 4 \mu\text{m}$. The different curves correspond to the different applied fields starting from 30 to 139 mT (a) and to 136 mT for (b). The field is incremented by steps of ≈ 1.4 mT.

Acknowledgments

This work was supported by the French RENATECH network, by the French National Research Agency (ANR) as part of the “Investissements d’Avenir” and France 2030 programs. This includes the SPICY project of the Labex NanoSaclay: ANR-10-LABX-0035, the MAXSAW project ANR-20-CE24-0025 and the PEPR SPIN projects ANR 22 EXSP 0008 and ANR 22 EXSP 0004. We acknowledge Aurélie Solignac for material growth and Joo-Von Kim, Loukas Kokkinos, Nessrine Benaziz and Maryam Massouras for helpful comments. Special thanks to Claude Chappert for the comments on the abstract.

References

- [1] Matthieu Bailleul, Dominik Olligs, and Claude Fermon. Propagating spin wave spectroscopy in a permalloy film: A quantitative analysis. *Applied Physics Letters* 83, 972–974 (2003).
- [2] R. L. Stamps. [Spin configurations and spin-wave excitations in exchange-coupled bilayers](#). *Physical Review B* 49, 339–347 (1994).
- [3] G.Y. Thiancourt, S.M. Ngom, N. Bardou, and T. Devolder. [Unidirectional spin waves measured using propagating-spin-wave spectroscopy](#). *Phys. Rev. Appl.* 22, 034040 (3 2024).
- [4] G. Y. Thiancourt, S. M. Ngom, N. Bardou, and T. Devolder. *Spectroscopy of the spin waves of a synthetic antiferromagnet grown on a piezoelectric substrate*. 2024. arXiv: [2411.18202 \[cond-mat.mtrl-sci\]](#).
- [5] T. Devolder, G. Talmelli, S. M. Ngom, et al. [Measuring the dispersion relations of spin wave bands using time-of-flight spectroscopy](#). *Physical Review B* 103, 214431 (2021).
- [6] Thibaut Devolder. [Propagating-spin-wave spectroscopy using inductive antennas: Conditions for unidirectional energy flow](#). *Physical Review Applied* 20, 054057 (2023).

Magnéto-phononique & ondes

Giant magneto-elasticity & strong phonon-magnon coupling in FeRh.

D. Ourdani^{1,2,*}, C. Gourdon¹, B. Perrin¹, V. Uhlíř³, J. A. Arregi³, Y. Roussigné², and L. Thevenard¹

¹*Institut des Nanosciences de Paris (INSP), Sorbonne Université, Paris, France.*

²*Laboratoire des Sciences des Procédés et des Matériaux (LSPM), Université Sorbonne Paris Nord, Villetaneuse, France.*

³*CEITEC BUT, Brno University of Technology, Purkyňova 123, 612 00 Brno, Czech Republic.*

*djoudi.ourdani@insp.jussieu.fr

Phonons and magnons, two types of collective excitations in solids, represent promising alternatives to conventional information carriers, making it possible to avoid losses associated with the Joule effect. Acoustic phonons stand out for their ability to propagate over long distances, benefiting from particularly long coherence times. Magnons, on the other hand, offer remarkable frequency tunability, covering a wide range from GHz to THz. This flexibility, combined with their potential for high-speed, low-power applications, makes them promising candidates for the development of next-generation technologies. In this context, the study of materials, metamaterials and devices devoted to the observation, enhancement and control of phonon-magnon interactions is a fast-growing field of research [1–4]. This approach makes it possible to exploit the unique advantages of these two types of excitation while combining them, paving the way for innovative phenomena. These advances promise to transform key modern technologies, such as analog, digital and quantum information processing, particularly in the microwave frequency range.

FeRh is an intriguing material that exhibits a first-order phase transition, changing from an antiferromagnetic (AF) to a ferromagnetic (FM) state when heated. The temperature at which this transition occurs is highly sensitive to the Fe and Rh stoichiometry, the material's deformation state [5], and the applied magnetic field [6]. This unique property makes FeRh a promising candidate for thermally assisted magnetic recording applications [7]. Additionally, it has been demonstrated that the AF-FM transition can be initiated by ultrafast laser pulses, which induce a heating effect [8], highlighting its potential for use in optical information storage.

In this work, Brillouin Light Scattering (BLS) was used to study phonon-magnon coupling in a 36 nm thick epitaxial FeRh alloy on a single-crystal MgO substrate. Figure 1-a displays BLS magnon spectra obtained in the pure FM phase (at 400 K) for various wavevectors in the backward geometry ($M||k$). Two magnetic modes are identified: the first perpendicular standing mode around 21 GHz and the backward volume spin wave (BW spin wave) at lower frequencies. Notably, an additional mode emerges alongside the BW mode over a specific wavevector range, creating an anti-crossing gap of approximately 1.1 GHz around $15 \mu\text{m}^{-1}$ in the dispersion relation (figure 1-b). This gap strongly indicates coupling between two waves, consistent with prior studies [3, 9].

To identify the acoustic mode interacting with the BW mode, phonon dispersion was also measured (blue circles, figure 1-b). Surprisingly, the modes identified as Rayleigh and Sezawa waves do not match with the anti-crossing region. However, calculations of the dispersion relation for uncoupled Love waves align perfectly with this anti-crossing (dashed lines figure 1-b). Notably, Love waves are generally not expected to be observed using BLS in opaque materials like FeRh [10]. Their observation here suggests the presence of a hybrid magneto-elastic mode (magnon-polaron quasi particle), which combines magnetic and elastic characteristics, underscoring the strength of this coupling.

For a complete description of the coupled system, the Landau-Lifshitz-Gilbert (LLG) equation (for magnon dynamics) and the Christoffel equation (for phonon dynamics), including the magnetoelastic contribution, are solved. This was made possible by a detailed experimental study of the magnetic exchange constant A_{ex} and the elastic constants C_{ij} of FeRh, as described in [11]. Finally, we accurately reproduced our observations (black lines in figure 1-b) and extracted the magnetoelastic coupling constant B , which is the only fitting parameter in the model. Its value was determined to be 17 MJ m^{-3} . This value is significantly larger than those typically reported in the literature for other magnetostrictive materials [3, 12, 13], further highlighting the exceptional strength of the magnetoelastic coupling in FeRh.

Such findings underscore the relevance of FeRh as a promising material for hybrid magnonic devices, where efficient coupling between magnetic and elastic excitations is essential. The observed anti-crossing behavior not only advances the understanding of magnetostrictive phenomena in FeRh but also opens new perspectives for its integration into spintronic, straintronic and magnonic applications.

Acknowledgments

This work has been partly supported by the French Agence Nationale de la Recherche (ANR ACAF 20-CE30-0027).

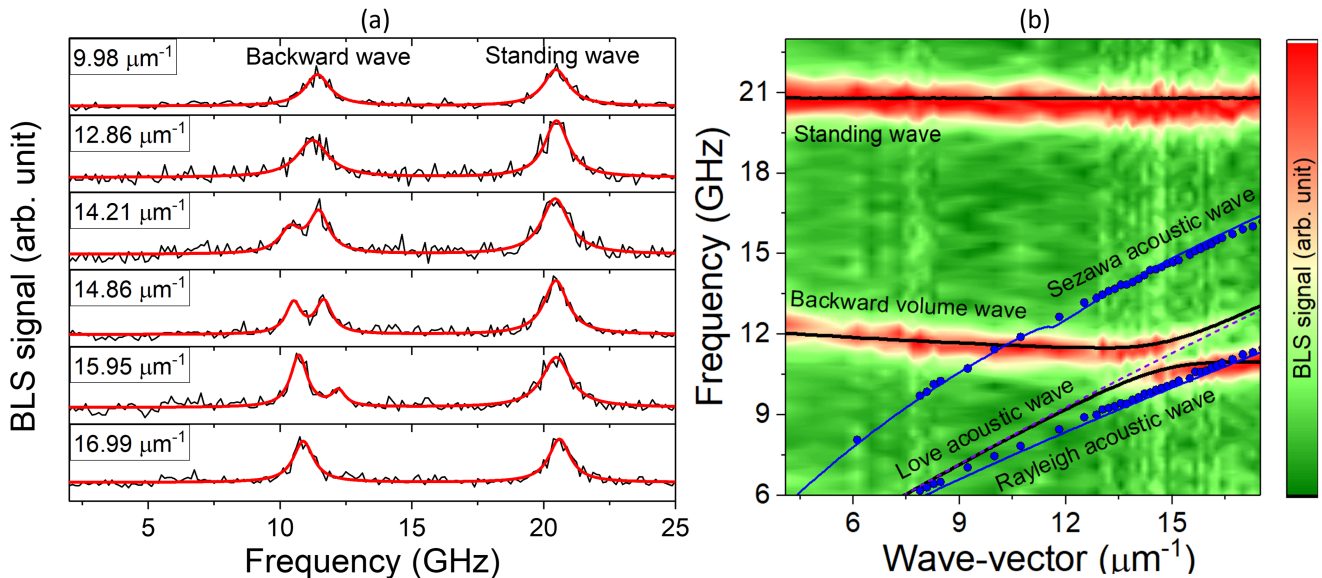


Figure 1: (a) Representative spectra obtained from Brillouin light scattering measurements for various wave vectors in the backward geometry ($M \parallel k$) at a fixed temperature of 400 K and applied magnetic field of 100 mT. (b) Mapping of dispersion relations illustrating the coupling between the Love-type acoustic wave and the backward volume spin wave. The black lines represent the calculated dispersion relations of the Love and backward modes for the magnetoelastic coupled system. Dashed lines show the calculated dispersion relation of the uncoupled Love mode. The blue lines and circles correspond to the calculated and measured dispersion relations of the Rayleigh and Sezawa acoustic waves, respectively.

References

- [1] L. Thevenard, C. Gourdon, J. Y. Prieur, et al. [Surface-acoustic-wave-driven ferromagnetic resonance in \(Ga,Mn\)\(As,P\) epilayers](#). *Phys. Rev. B* 90, 094401 (9 2014).
- [2] J.-Y. Duquesne, P. Rovillain, C. Hepburn, et al. [Surface-Acoustic-Wave Induced Ferromagnetic Resonance in Fe Thin Films and Magnetic Field Sensing](#). *Phys. Rev. Appl.* 12, 024042 (2 2019).
- [3] Nandan K. P. Babu, Aleksandra Trzaskowska, Piotr Graczyk, et al. [The Interaction between Surface Acoustic Waves and Spin Waves: The Role of Anisotropy and Spatial Profiles of the Modes](#). *Nano Letters* 21, 946–951 (27, 2021).
- [4] Yunyoung Hwang, Jorge Puebla, Kouta Kondou, et al. [Strongly Coupled Spin Waves and Surface Acoustic Waves at Room Temperature](#). *Phys. Rev. Lett.* 132, 056704 (5 2024).
- [5] R. O. Cherifi, V. Ivanovskaya, L. C. Phillips, et al. [Electric-field control of magnetic order above room temperature](#). *Nature Materials* 13, 345–351 (1, 2014).
- [6] S. Maat, J.-U. Thiele, and Eric E. Fullerton. [Temperature and field hysteresis of the antiferromagnetic-to-ferromagnetic phase transition in epitaxial FeRh films](#). *Phys. Rev. B* 72, 214432 (21 2005).
- [7] Jan-Ulrich Thiele, Stefan Maat, and Eric E. Fullerton. [FeRh/FePt exchange spring films for thermally assisted magnetic recording media](#). *Applied Physics Letters* 82, 2859–2861 (2003).
- [8] Jan-Ulrich Thiele, Matthias Buess, and Christian H. Back. [Spin dynamics of the antiferromagnetic-to-ferromagnetic phase transition in FeRh on a sub-picosecond time scale](#). *Applied Physics Letters* 85, 2857–2859 (2004).
- [9] P. Carrara, M. Brioschi, R. Silvani, et al. [Coherent and Dissipative Coupling in a Magnetomechanical System](#). *Phys. Rev. Lett.* 132, 216701 (21 2024).
- [10] R Loudon and J R Sandercock. [Analysis of the light-scattering cross section for surface ripples on solids](#). *Journal of Physics C: Solid State Physics* 13, 2609 (1980).
- [11] D. Ourdani, A. Castellano, A. K. Vythelingum, et al. [Experimental determination of the temperature- and phase-dependent elastic constants of FeRh](#). *Phys. Rev. B* 110, 014427 (1 2024).
- [12] A. B. Smith and R. V. Jones. [Magnetostriction Constants from Ferromagnetic Resonance](#). *Journal of Applied Physics* 34, 1283–1284 (1963).
- [13] D. E. Parkes, L. R. Shelford, P. Wadley, et al. [Magnetostrictive thin films for microwave spintronics](#). *Scientific Reports* 3, 2220 (17, 2013).

Phononic manipulation of magnetic domains in Co-doped YIG : from a labyrinth to stripes and bubbles

Héloïse Damas^{1,*}, C. S. Davies¹, V. I. Belotelov², A. Stupakiewicz³, and A. Kirilyuk¹

¹*FELIX Laboratory, Radboud University, Nijmegen, The Netherlands*

²*Russian Quantum Center, Moscow, Russia*

³*Faculty of Physics, University of Bialystok, Bialystok, Poland*

*heloise.damas@ru.nl

The exploration of energy-efficient ways to manipulate the magnetisation has long been a challenge of critical interest for the development of advanced technologies such as sensors and data recording technologies. Among the explored pathways, ultrafast laser techniques have attracted considerable attention and have achieved important milestones such as the single-shot helicity-independent all optical switching of multi-sublattice systems [1, 2]. However, this phenomenon is restricted to metallic systems, and the underlying mechanisms are attributed to laser-induced thermal effects [3]. To overcome this limitation, alternative approaches based on resonance phenomena have emerged as a promising avenue for energy efficient control of magnetisation. One such alternative involves the resonant excitation of infrared-active phonons to modify the crystal environment through nonlinear phononic effects [4, 5], ultimately influencing magnetic order.

Ultrafast *phononic switching* was first successfully demonstrated in Co:YIG in 2021 [6]. Since then, phononic manipulation of the magnetisation has been extended to various YIG crystals [7, 8], antiferromagnetic nickel oxide [9] and antiferromagnetic iron borate [10]. The distinctive macroscopic patterns of the switched domains in these systems have been qualitatively attributed to light-induced elastic strain, which generates a magnetoelastic field acting on the magnetisation [6, 8]. In that regard, these domain shapes effectively serve as fingerprints of the underlying magnetoelastic field. By further investigating phononic switching in multidomain structures, we aim to develop a more quantitative understanding of the distribution of magnetoelastic interactions.

We present a study of phononic switching in a Co:YIG film exhibiting a labyrinth-like magnetic domain structure (see Fig. 1(a)). To resonantly excite the phonon modes, we used narrow-band pulses from the free electron laser facility *Free Electron Lasers for Infrared eXperiments* (FELIX) in Nijmegen, the Netherlands [11]. Upon illuminating the film with a single 8- μ s-long macropulse targeting optical phonon modes at resonance, we observe new permanent domains consisting of stripes (see Fig. 1(b)).

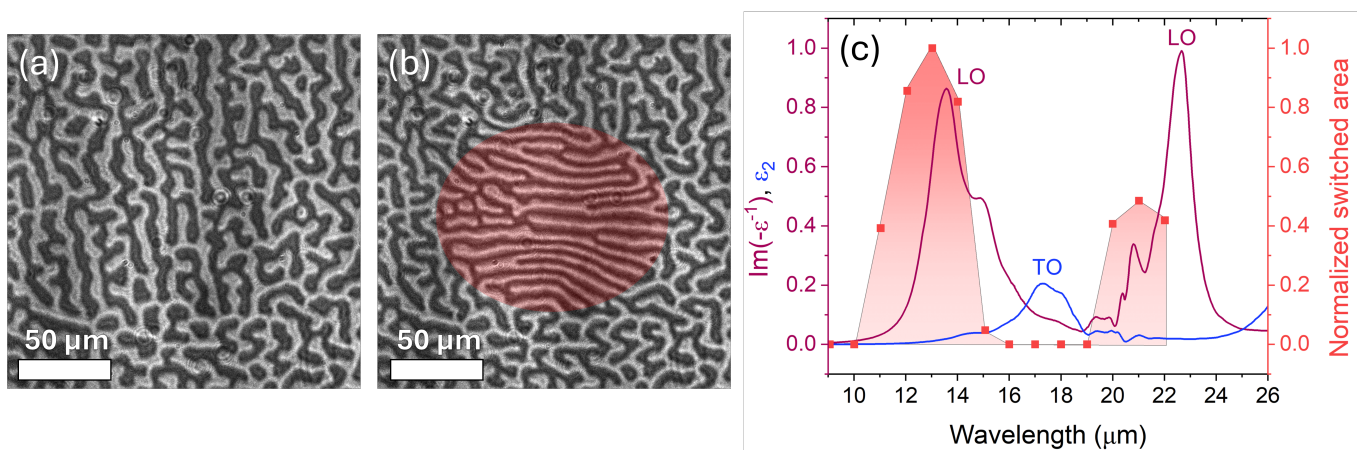


Figure 1: (a) Faraday image of the magnetic domain structure before illumination. (b) Faraday image of the magnetic domain structure after illumination with an 8- μ s-long macropulse delivered from FELIX (wavelength $\lambda = 13.5 \mu\text{m}$). (c) Spectral dependencies: the normalised switched area (red), the loss function $\text{Im}(-\epsilon^{-1})$ highlighting the spectral positions of the longitudinal optical (LO) phonons (pink), and the imaginary part of the dielectric function ϵ_2 indicating the spectral position of the transverse optical (TO) phonons (blue). The graph shows that switching occurs specifically at the spectral positions of the LO phonons.

The evolution of the normalised switched area as a function of the pump wavelength, spanning the range 9–22 μm , is shown in Fig. 1(c). It shows two peaks at spectral positions 12.5 μm and 21 μm which correlate with the spectral dependence of the longitudinal optical (LO) phonon modes as derived by the loss function $\text{Im}(-\epsilon^{-1})$ (pink line, Fig. 1(c)). Notably, no switching was observed at the resonance frequencies of the transverse optical (TO) phonon modes, highlighted by the imaginary part of the dielectric function ϵ_2 (blue line, Fig. 1(c)). This behaviour confirms findings from previous studies [6, 7, 9] and raises questions about the role of the epsilon-near-zero regime in the switching process [12, 13]. The spatial distribution of strain and the associated magneto-elastic field will be discussed in detail. Mumax3 micromagnetic simulations [14] provide support for the formation of both stripes and magnetic bubbles under an applied magnetic field. In addition, illumination of the film with a single macropulse under a 6 mT in-plane magnetic field induces the formation of magnetic bubbles. Remarkably, these bubbles remain stable even after the field is removed, revealing a novel approach to generate stable magnetic bubbles by lattice excitation.

This study highlights the potential of phononic switching as a non-thermal method for manipulating magnetisation and generating stable magnetic bubbles in Co:YIG. The analysis of the permanent magnetic domain shape offers valuable insights into the magnetoelastic field distribution, advancing toward a better understanding of the phononic switching process.

References

- [1] I Radu, K Vahaplar, C Stamm, et al. Transient ferromagnetic-like state mediating ultrafast reversal of antiferromagnetically coupled spins. *Nature* 472, 205–208 (2011).
- [2] C. S. Davies, J. H. Mentink, A. V. Kimel, T. Rasing, and A. Kirilyuk. Helicity-independent all-optical switching of magnetization in ferrimagnetic alloys. *Journal of Magnetism and Magnetic Materials* 563, 169851 (2022).
- [3] T. D. Cornelissen, R. Córdoba, and B. Koopmans. Microscopic model for all optical switching in ferromagnets. *Applied Physics Letters* 108 (2016).
- [4] A. Subedi, A. Cavalleri, and A. Georges. Theory of nonlinear phononics for coherent light control of solids. *Physical Review B* 89, 220301 (2014).
- [5] R. Mankowsky, M. Först, and A. Cavalleri. Non-equilibrium control of complex solids by nonlinear phononics. *Reports on Progress in Physics* 79, 064503 (2016).
- [6] A. Stupakiewicz, C. S. Davies, K. Szerenos, et al. Ultrafast phononic switching of magnetization. *Nature Physics* 17, 489–492 (2021).
- [7] M. Gidding, T. Janssen, C. S. Davies, and A. Kirilyuk. Dynamic self-organisation and pattern formation by magnon-polarons. *Nature Communications* 14, 2208 (2023).
- [8] M. Gidding, C. S. Davies, and A. Kirilyuk. Reorientation of magnetic stripe domains by mid-infrared pulses. *Physical Review B* 109, L060408 (2024).
- [9] P. Stremoukhov, A. Safin, S. Nikitov, A. Kirilyuk, et al. Phononic manipulation of antiferromagnetic domains in NiO. *New Journal of Physics* 24, 023009 (2022).
- [10] T. Janssen, M. Gidding, C. S. Davies, A. V. Kimel, and A. Kirilyuk. Strain-induced magnetic pattern formation in antiferromagnetic iron borate. *Physical Review B* 108, L140405 (2023).
- [11] D. Oepf, A. F. G. Van der Meer, and P. W. Van Amersfoort. The free-electron-laser user facility FELIX. *Infrared physics & technology* 36, 297–308 (1995).
- [12] M. Kwaaitaal, D. G. Lourens, C. S. Davies, and A. Kirilyuk. Epsilon-near-zero regime enables permanent ultrafast all-optical reversal of ferroelectric polarization. *Nature Photonics*, 1–5 (2024).
- [13] C. S. Davies and A. Kirilyuk. Epsilon-near-zero regime for ultrafast opto-spintronics. *npj Spintronics* 2, 20 (2024).
- [14] A. Vansteenkiste, J. Leliaert, M. Dvornik, et al. The design and verification of MuMax3. *AIP advances* 4 (2014).

Coupling the orbital angular momentum of elastic waves with the gyromotion of a magnetic vortex

Olivetti G.^{1,2,*}, Pigeau B.², Yamamoto K.³, Valet T.¹, Otani Y.⁴, and Klein O.¹

¹Université Grenoble Alpes, CEA, CNRS, Grenoble INP, Spintec, 38054 Grenoble, France

²Université Grenoble Alpes, CNRS, Grenoble INP, Institut Néel, Grenoble, France

³Advanced Science Research Center, Japan Atomic Energy Agency, Tokai, Ibaraki 319-1195, Japan

⁴Institute for Solid State Physics, The University of Tokyo, Kashiwa, Chiba 277-8581, Japan

*giovanni.olivetti@neel.cnrs.fr

In the context of a growing interdisciplinary interest in the angular momentum transfer between different objects, with the extensively studied notion of spin transport being only part of the story, that between phonons and magnons is currently attracting a lot of attention. This interest is based on recent experiments on magneto-elasticity[1] showing that the transduction of the spin angular momentum (SAM) component of the magnetization dynamics to chiral phonon can provide long-range coherent coupling between two distant macrospins at millimeter distances. This work, however, focuses on SAM of spin-waves, leaving their orbital angular momentum (OAM) [2] counterpart experimentally unexplored, which may also be placed in the context of the general difficulty in directly observing wave OAM.

In this work, we report on the design of an experiment to spectroscopically excite and detect non-vanishing OAM in an axisymmetric magnetic nanostructure. Our interest focuses on the coupling between the fundamental mode of a magnetic vortex texture (the so-called gyromotion of the vortex core) and an elastic wave-carrying OAM. The dependence of the magnetic vortex polarity on the external magnetic field allows to change the gyration sense of the magnetic vortex dynamics with respect to the acoustic one, therefore studying the effect of the polarity of OAM transfer in the coupling efficiency [3].

The proposed system consists of a magnetic disk in the magnetic vortex state surrounded by a circular interdigital transducer (IDT) capable of exciting a surface acoustic wave vortex by the inverse piezoelectric effect (see Fig. 1a). We have used a Python simulation code to optimize the IDT design on x-cut LiNbO₃. The design takes into account not only the anisotropy in acoustic propagation and piezoelectric interconversion, but also the geometric constraints necessary to obtain a circular phase at the center of the pattern. Fig. 1 shows the local amplitude (b) and phase (c) measured by scanning local interferometry of the acoustic vertical displacement, which experimentally confirms the presence of an acoustic vortex at the center of the IDT pattern oscillating in the hundreds of MHz regime.

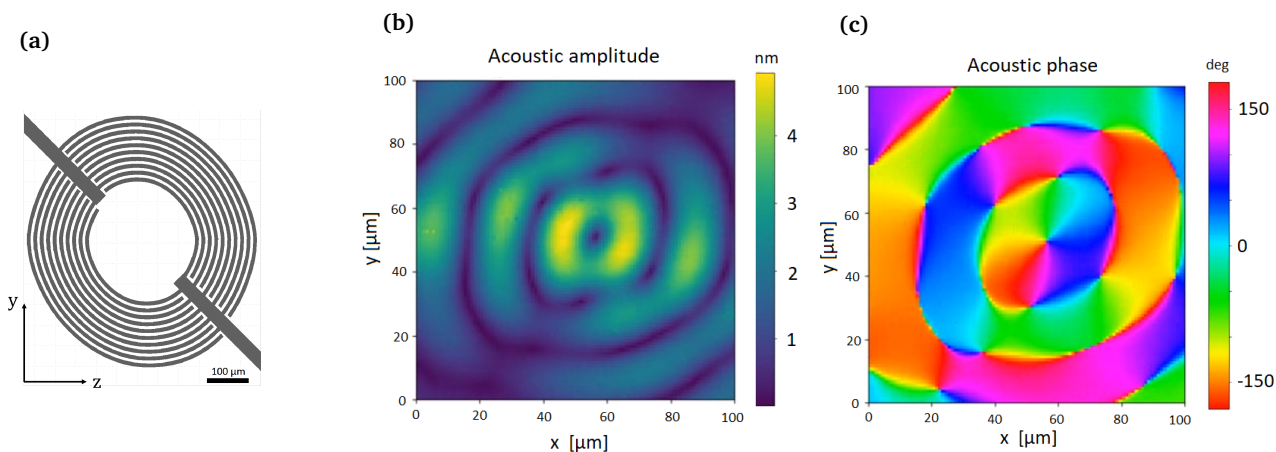


Figure 1: Generation of phonons with OAM by piezo-electric effect. a) Design of the IDTs electrodes for x-cut LiNbO₃. Measurement near the central region of the vertical oscillation of the surface using time-resolved local interferometry sensitive to both the amplitude b) and phase c) of the elastic wave. The experiment is performed at 110 MHz on x-cut LiNbO₃.

In parallel, we have performed micromagnetic simulations of the modal response of the magnetic system. For this purpose, we use a home-developed eigensolver for axi-symmetric geometries, which reduces a 3D problem to a 2D one and efficiently computes the volumetric standing spin-wave solution. The solver inherently sorts the eigensolutions by their total angular momentum (n_θ) as shown in Fig. 2. This information, together with the strain field associated with an acoustic vortex, is fundamental for estimating the overlap integral and determining the selection rules involved in the coupling.

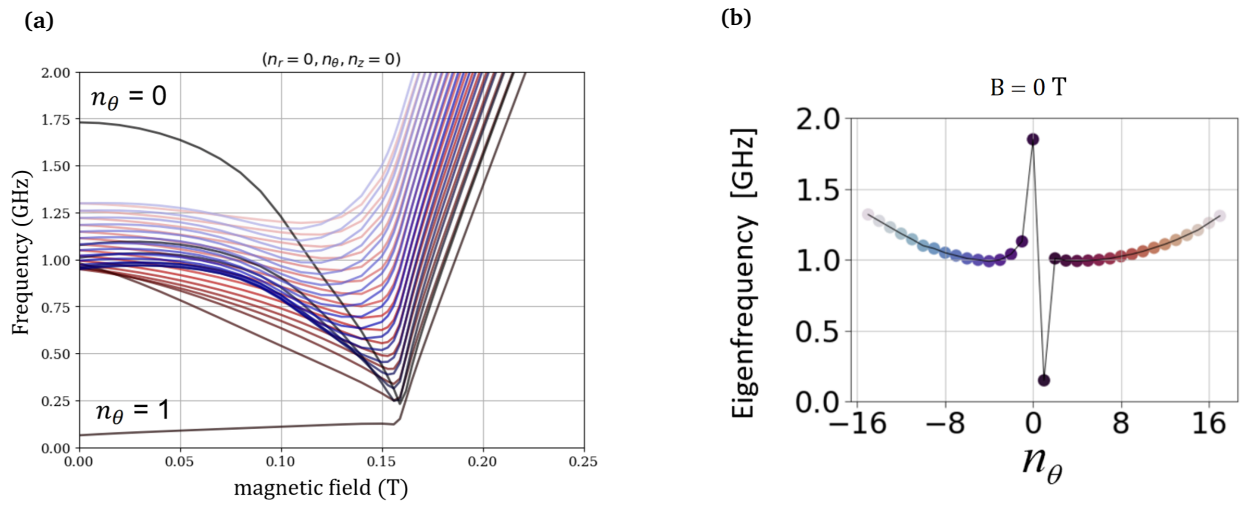


Figure 2: Micromagnetic simulation of the azimuthal magnon eigenmodes of index (n_R, n_θ, n_Z) inside a micron-sized disk whose magnetization is $\mu_0 M_s = 0.17$ T. The figure shows the morphing of the eigenmodes as a function of an external magnetic field applied along the normal. The plot is restricted to the modes with $n_R = 0, n_Z = 0$, ordered by their azimuthal index n_θ (represented with a color scale), which represents their total angular momentum. In figure a) the field $\mu_0 H \approx 0.16$ T marks the saturation field. Figure b) shows the spectrum at zero field in the magnetic vortex texture. Our focus concerns the gyrotropic mode, which corresponds to the mode having $n_\theta = +1$ and lays in the hundreds of MHz range.

The same solver can also be used to calculate the field-dependent spectral shift of the individual spin wave modes (see Fig. 2a), which can be used to tune the gyrofrequency of the magnetic vortex core to be equal to the one of the elastic wave vortex shown in Fig 1.

This effort also represents a test platform to investigate the possibility of accessing non-trivial mechanical modes by magnetic texture dynamics and vice versa.

Acknowledgments

This work was supported by the LANEF Chaire of Excellence Q-SPIN for Prof. Otani. Additionnaly it was partially supported by the EU-project HORIZON-EIC-2021-PATHFINDER OPEN PALANTIRI-101046630; the French Grants ANR-21-CE24-0031 Harmony; the PEPR SPIN - MAGISTRAL ANR-24-EXSP-0004; the French Renatech network; and the REIMEI Research Program of Japan Atomic Energy Agency. K.Y. acknowledges support from JST PRESTO Grant No. JPMHPR20LB, Japan, JSPS KAKENHI (No. 21K13886), and JSPS Bilateral Program Number JPJSBP120245708.

References

- [1] K. An, A. N. Litvinenko, R. Kohno, et al. [Coherent long-range transfer of angular momentum between magnon Kittel modes by phonons](#). *Physical Review B* 101 (6 2020).
- [2] D. A. Garanin and E. M. Chudnovsky. [Angular momentum in spin-phonon processes](#). *Physical Review B - Condensed Matter and Materials Physics* 92 (2 2015).
- [3] B. Pigeau, G. De Loubens, O. Klein, et al. [A Frequency-controlled Magnetic Vortex Memory](#). *Applied Physics Letters* 96 (2010).

Structural and Magnetic Insights into Ti/Mn-Substituted Hexaferrite Thick Films for Applications beyond 20 GHz

Maria Jose Vazquez Bernardez^{1,*}, Daniel Stoeffler¹, Christophe Lefevre¹, Laurent Schlur¹, Matthieu Bailleul¹, and Nicolas Vukadinovic²

¹*Institut de Physique et Chimie des Matériaux, CNRS-Université de Strasbourg, Strasbourg, France*

²*Dassault Aviation, 92552 St-Cloud, France*

*mariajose.vazquez@ipcms.unistra.fr

The research for magnetic materials resonating at frequencies above 20 GHz has become a subject of rising interest for the fabrication of integrated circuit components (antennas, microwave filters, detectors) [1]. Within the family of materials suitable for low-GHz S, C and X band applications, iron alloys and iron-based oxides such as YIG are notable for their natural ferromagnetic resonances (FMR) at frequencies below 20 GHz [2, 3]. However, the amount of materials capable of resonating at higher frequencies within the K, Ka and Q bands is limited. M-type hexagonal ferrites of chemical formula $BaFe_{12}O_{19}$ are excellent candidates for this purpose and numerous applications already exploit the excellent properties of this family of compounds. Two main reasons explain their success : (1) despite having FMR frequency comprised between 46 and 48 GHz [4], it is possible to decrease or increase it by substituting ferric Fe^{3+} or Ba^{2+} ions respectively and (2) one can change the anisotropy from uniaxial to planar by replacing Fe^{3+} cations [5]. This results in a family of oxides where one can control both the operating frequency and the direction of the easy axis. Some studies have shown that a partial substitution of Fe^{3+} by diamagnetic cations can induce a longitudinal conical magnetic structure inducing a magnetoelectric contribution [6, 7] that is highly attractive for applications involving multiferroicity.

While $BaFe_{12}O_{19}$ hexaferrites may have higher magnetic losses (damping) compared to YIG films, they are widely used in thin-film applications such as magnetic recording, microwave devices (phase shifters, circulators), and electromagnetic interference suppression [1, 8]. Several decades ago, a race to achieve the minimum FMR linewidth in pure $BaFe_{12}O_{19}$ films deposited on sapphire (001) culminated in a value of 16 Oe at 60.3 GHz, obtained in the best-crystallized films grown by pulsed laser deposition (PLD) [9]. Since then, various attempts have been made to fabricate hexaferrites on substrates with better lattice matching, but a further reduction in FMR linewidth has not been achieved. These losses are ten times greater than those of YIG. While reducing damping is important, it is not the only factor to consider and these materials exhibit unique properties that make them valuable for various device applications. The effects of substituting ferric ions on the static and dynamic properties of M-type hexaferrites remain largely unexplored. Given the limited number of known magnetoelectric hexaferrites, studying these materials is essential and offers a promising avenue for both experimental and theoretical research.

The objective of this work is to investigate the relationship between the structural and magnetic properties of Ti/Mn-substituted hexaferrite films of chemical structure $BaTi_xMn_xFe_{12-2x}O_{19}$ with x comprised between 0.4 and 2.0. This study has a dual focus: first, to identify the key structural factors that help reduce magnetic losses in Ti/Mn-substituted thin films, and second, to investigate how Ti/Mn substitution affects the magnetic properties, particularly its influence on magnetic exchange. Determining the magnetic exchange constant for this material is challenging, as it requires achieving narrow enough FMR linewidths and excellent film crystallization, to enable the indexing of perpendicular standing spin wave (PSSW) modes. We have synthesized for the first time Ti/Mn substituted hexaferrite thin films by Pulsed Laser Deposition on sapphire Al_2O_3 (001) substrate. The influence of the deposition conditions: temperature, oxygen pressure, laser energy and the number of laser shots has been carefully optimized to produce highly crystalline epitaxial thick films (evidenced by Kikuchi lines on RHEED Patterns). The influence of film thickness on the structural and magnetic properties has been followed by Reflection High-Energy Electron Diffraction (RHEED), X-Ray Diffraction with theta-2theta curves and reciprocal space mapping (RSM) to extract lattice parameters, electron scanning microscopy (SEM) and SQUID-Vibrating sample magnetometry (VSM) to propose a model on how the strain induced by the substrate evolves with the thickness of the film deposited. The dynamic magnetic properties of the best fabricated films were measured in both in-plane and out-of-plane configurations by using a coplanar wave guide in FMR set-up with ac field modulation and lock-in detection which lead to the identification of the FMR resonance, a surface mode only visible for some films (depending on the broadening of the FMR mode) and up to 5 satellite peaks appearing at fields lower than the FMR mode corresponding to perpendicular standing spin waves.

With this work we present the first experimental determination of the exchange constant in Ti/Mn substituted hexaferrites as well as a comprehensive understanding on how the fabrication conditions impact the structural and magnetic properties of the resulting films. Complementary micromagnetic simulations illustrating the FMR spectra with the presence of domain walls will also be introduced.

With these results, we aim to propose an alternative to YIG for higher operating frequencies and pave the way for the investigation of substituted hexaferrite thin films, both for device fabrication and multiferroic applications. Several questions remain to be addressed like the role played by the concentration of substituents, the occurrence of a magnetoelectric coupling and the further reduction of the damping in this family of hexaferrites.

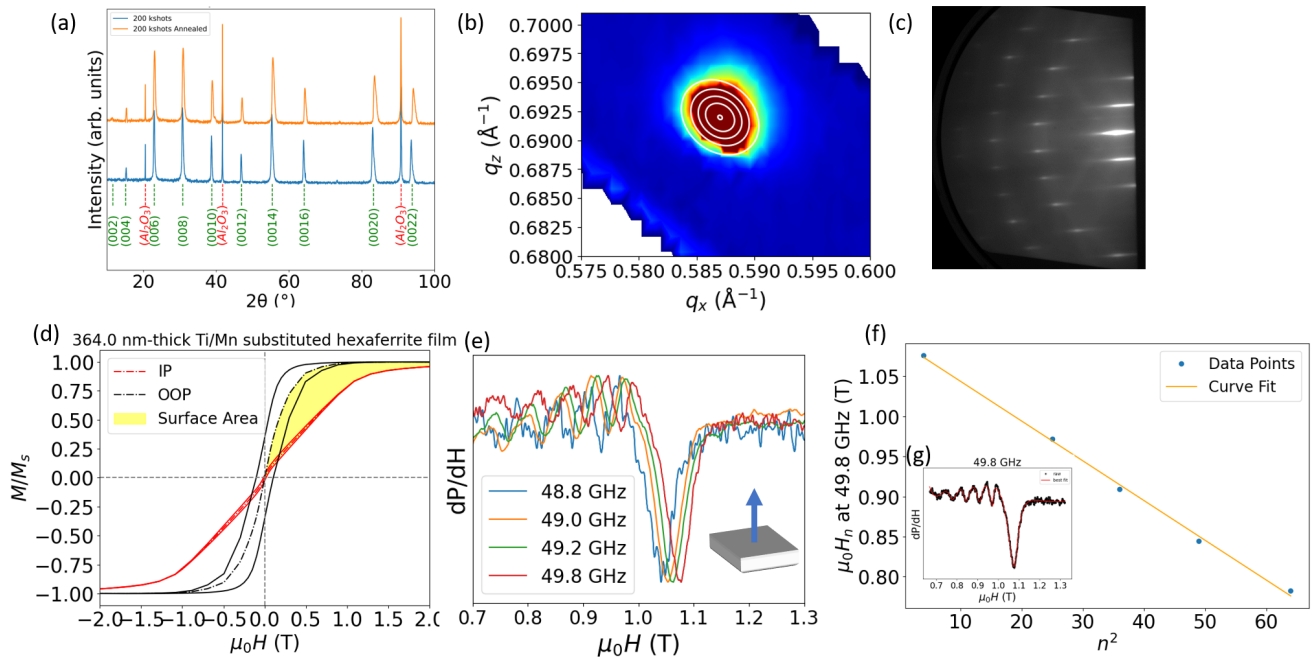


Figure 1: (a) Theta-2-theta diffraction patterns of a Ti/Mn substituted hexaferrite 364 nm-thick film before and after annealing. (b) RSM of the annealed film giving lattice parameters: $a=5.9010 \pm 0.001 \text{ \AA}$ and $c=23.122 \pm 0.001 \text{ \AA}$. (c) RHEED patterns of the film before annealing. (d) Magnetization versus applied magnetic field curves of the annealed film for in-plane (IP) and out-of-plane (OOP) configurations, the surface between the curves is colored in yellow. (e) Out-of-plane lock-in response of the annealed film at different frequencies displaying PSSW modes. (f) Mode field $\mu_0 H_n$ versus the square of the mode index n for the annealed film in the out-of-plane configuration at 49.8 GHz (see fit in inset (g)).

References

- [1] Vincent G. Harris, Anton Geiler, Yajie Chen, et al. [Recent advances in processing and applications of microwave ferrites](#). *Journal of Magnetism and Magnetic Materials*. Current Perspectives: Modern Microwave Materials 321, 2035–2047 (2009).
- [2] J BenYoussef, H Le Gall, N Vukadinovic, et al. [Ferromagnetic resonance in epitaxial FePd thin films with perpendicular anisotropy](#). *Journal of Magnetism and Magnetic Materials* 202, 277–284 (1999).
- [3] S. Klingler, A. V. Chumak, T. Mewes, et al. [Measurements of the exchange stiffness of YIG films using broadband ferromagnetic resonance techniques](#). *Journal of Physics D: Applied Physics* 48, 015001 (2014).
- [4] Robert C. Pullar. [Hexagonal ferrites: A review of the synthesis, properties and applications of hexaferrite ceramics](#). *Progress in Materials Science* 57, 1191–1334 (2012).
- [5] Han-Shin Cho and Sung-Soo Kim. [M-hexaferrites with planar magnetic anisotropy and their application to high-frequency microwave absorbers](#). *IEEE Transactions on Magnetics* 35, 3151–3153 (1999).
- [6] P. Borisov, J. Alaria, T. Yang, S. R. C. McMitchell, and M. J. Rosseinsky. [Growth of M-type hexaferrite thin films with conical magnetic structure](#). *Applied Physics Letters* 102, 032902 (2013).
- [7] Marjan Mohebbi, Khabat Ebnabbasi, and Carmine Vittoria. [First observation of magnetoelectric effect in M-type hexaferrite thin films](#). *Journal of Applied Physics* 113, 17C710 (2013).
- [8] Zihui Wang, Young-Yeal Song, Yiyan Sun, et al. [Millimeter wave phase shifter based on ferromagnetic resonance in a hexagonal barium ferrite thin film](#). *Applied Physics Letters* 97, 072509 (2010).
- [9] Young-Yeal Song, Sangita Kalarickal, and Carl E. Patton. [Optimized pulsed laser deposited barium ferrite thin films with narrow ferromagnetic resonance linewidths](#). *Journal of Applied Physics* 94, 5103–5110 (2003).

A study of non-reciprocal behaviors in multi-sphere loaded chiral cavity

Maxime Ardisson^{1,2,*}, Julien Haumant³, Romain Lebrun⁴, Isabella Boventer⁴, and Vincent Castel^{1,2}

¹IMT Atlantique, Technopole Brest-Iroise, CS 83818, 29238 Brest Cedex 3, France

²Lab-STICC (UMR 6285), CNRS, Technopole Brest-Iroise, CS 83818, 29238 Brest Cedex 3, France

³Elliptika, 29804 Brest Cedex 9, France

⁴Laboratoire Albert Fert, Thales, Université Paris-Saclay, Palaiseau 91767, France

*maxime.ardisson@imt-atlantique.fr

Cavity magnonics has received significant attention over the past decade. Central to this area is the study of cavity magnon polaritons —hybrid quasiparticles originated from the strong coupling of magnons and photons. These systems, typically composed of a magnetic sample inside an electromagnetic cavity, hold promising opportunities for advancements in quantum information processing and high-precision sensing [1, 2], while also serving as a novel platform for disruptive radio-frequency (RF) technologies. In particular, several cavity magnonics systems demonstrate non-reciprocity [3–5], which is a critical feature for classical communication applications. Non-reciprocal microwave components like isolators are able to protect circuits from unwanted reflections by selectively blocking propagation in one direction. While previous studies have thoroughly explored both theoretically [6, 7] and experimentally [8] chiral microwave-magnon coupling, a complete understanding of non-reciprocal effects for multiple ferrimagnetic insulators in an integrable and functional system is still lacking. In this work, we propose a new built-in platform for the investigation of chiral interactions and non-reciprocity in cavity magnonics.

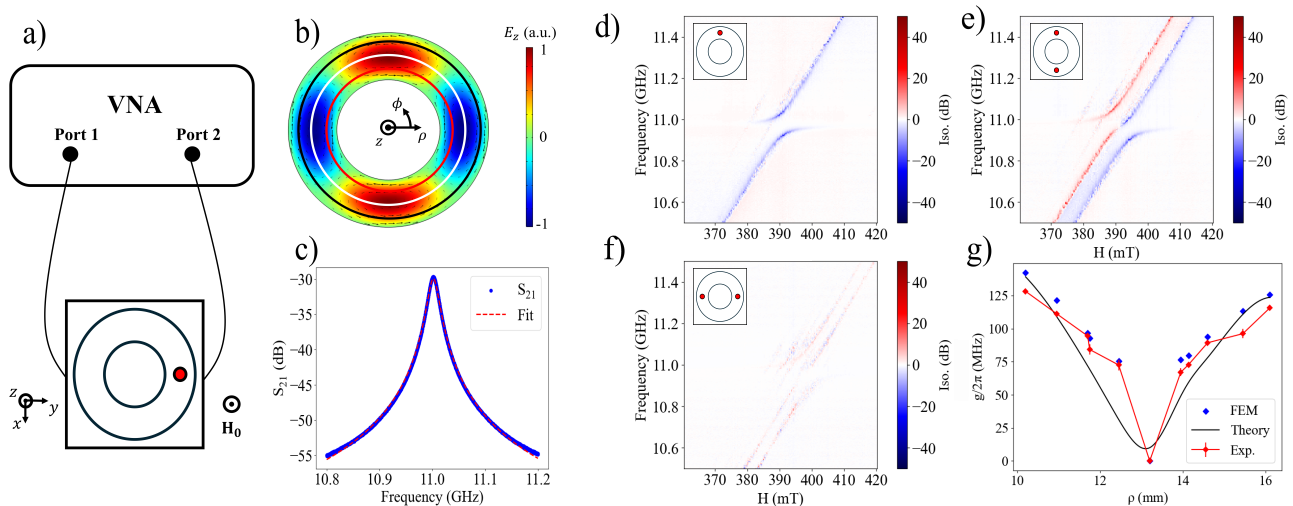


Figure 1: **a)** Sketch of the experimental setup where the chiral cavity loaded with a YIG sphere (red dot) is connected to a vector network analyzer (VNA) for reflection (S_{11}) and transmission (S_{21}) measurements. **b)** Distribution of the resonator's electric field z -component and the orientation of its magnetic field in black arrows. The three circles denote the special positions of the resonator: in red ρ_- , white ρ_0 , and black ρ_+ . **c)** Measured resonant mode of the cavity (blue) and its fit (red). **d-e-f)** Measured isolation ratio: $\text{Iso.} = 20 \cdot \log(S_{21}/S_{12})$ in dB as a function of frequency and bias magnetic field for $N = 1$ at $\phi = 0$, $N = 2$ at $\phi_1 = 0$, $\phi_2 = \pi$ and $N = 2$ at $\phi_1 = \pi/2$, $\phi_2 = -\pi/2$ (insets) on the chiral line ρ_- respectively. **g)** The analytical (black), simulated (blue) and measured (red) radial dependency of the coupling strength for $N = 1$.

We address the non-reciprocal behavior of a system constituted of N yttrium iron garnet (YIG) spheres, strongly coupled to chiral cavity modes. Our chiral resonator is comprised of a substrate integrated waveguide (SIW) cavity which consists in a dielectric wedged between two metallic layers. This design leads to a significant reduction of the cavity's geometrical volume, allowing larger magnon-photon coupling strength compared to previous studies using circular cavities [8]. An array of $60 \mu\text{m}$ radius vias acts as the cavity's walls to enclose the electromagnetic field [4] and forms the toroidal shape of our chiral resonator (see Figure 1 a)). In this context, chirality accounts for the orientation of the photon's spin angular momentum within the resonator. According to Maxwell's equations, at certain special positions inside the cavity (chiral lines), the polarization of the photon modes is linked to the propagation direction.

Chiral interaction is achievable when the YIG are placed on the chiral lines ρ_- and ρ_+ and brought into resonance with the cavity modes (see Figure 1. b)). Under these conditions, the magnon mode will couple to photons with the same polarization, inducing a spatial dependency of the coupling strength for each YIG sphere (c.f. Figure 1. g)).

As illustrated in Figure 1. d-f), we measure a direct dependency of the non-reciprocity —quantified by using the isolation ratio : $\text{Iso.} = 20 \cdot \log(S_{21}/S_{12})$ — according to the configuration of the YIG spheres, achieving isolation ratio values twice

as high as the values reported by Bourhill *et al.*. While prior studies [8, 9] have highlighted the fundamental working principle of single-YIG-based chiral cavities, our work extends this framework to the N -spheres configuration. This contribution sheds a new light on the mechanisms and tunability of non-reciprocity, laying the groundwork for further investigation of multi-sphere cavity magnonics. Our setup offers promising prospects for an emerging class of non-reciprocal devices that could also be used for cavity-mediated magnon-magnon interaction [10], paving the way for the development of multimode quantum memories.

Acknowledgments

We acknowledge the financial support of ANR project ICARUS under grant agreement: ANR-22-CE24-0008-03. ICARUS is a collaborative project between IMT Atlantique, Thales Research & Technology and Elliptika.

References

- [1] Dany Lachance-Quirion, Yutaka Tabuchi, Arnaud Gloppe, Koji Usami, and Yasunobu Nakamura. [Hybrid quantum systems based on magnonics](#). *Applied Physics Express* 12, 070101 (2019).
- [2] Babak Zare Rameshti, Silvia Viola Kusminskiy, James A. Haigh, et al. [Cavity magnonics](#). *Physics Reports* 979, 1–61 (2022).
- [3] Shasha Wang, Jin Tang, Weiwei Wang, et al. [Electrical Detection of Magnetic Skyrmions](#). *Journal of Low Temperature Physics* 197, 321–336 (2019).
- [4] Yiyou Zhang, Kang Wang, and Gang Xiao. [Noise characterization of ultrasensitive anomalous Hall effect sensors based on Co40Fe40B20 thin films with compensated in-plane and perpendicular magnetic anisotropies](#). *Applied Physics Letters* 116 (2020).
- [5] Lihua Zhong, Chao Zhang, and B. M. Yao. [Controlling the dynamics of cavity magnon polariton via microwave polarization](#). *AIP Advances* 12 (2022).
- [6] Ziyang Yu, Maokang Shen, Zhongming Zeng, et al. Voltage-controlled skyrmion-based nanodevices for neuromorphic computing using a synthetic antiferromagnet. *Nanoscale Advances* 2, 1309–1317 (2020).
- [7] Tao Yu, Xiang Zhang, Sanchar Sharma, Yaroslav M. Blanter, and Gerrit E. W. Bauer. [Chiral coupling of magnons in waveguides](#). *Physical Review B* 101 (2020).
- [8] Jeremy Bourhill, Weichao Yu, Vincent Vlaminck, et al. [Generation of Circulating Cavity Magnon Polaritons](#). *Physical Review Applied* 19 (2023).
- [9] Zhi-Yuan Fan, Xuan Zuo, Hao-Tian Li, and Jie Li. [Nonreciprocal entanglement in cavity magnomechanics exploiting chiral cavity-magnon coupling](#). 2024.
- [10] Xufeng Zhang, Chang-Ling Zou, Na Zhu, et al. [Magnon dark modes and gradient memory](#). *Nature Communications* 6 (2015).

Experimental observations of Suhl instabilities in a 500nm Bismuth Yttrium Iron Garnet disk

Sali Salama^{1,2,*}, Joo-Von Kim¹, Jamal Ben Youssef³, Maryam Massouras¹, Ping Che², Abdelmadjid Anane², and Jean-Paul Adam¹

¹Centre de Nanosciences et de Nanotechnologies, CNRS, Université Paris-Saclay, Palaiseau, 91120, France

²Laboratoire Albert Fert, CNRS, Thales, Université Paris Saclay, Palaiseau, 91767, France

³UMR CNRS 6285, Université de Bretagne Occidentale, 29238 Brest Cedex 3, France

*sali.salama@universite-paris-saclay.fr

One of the attractive properties of spin waves, the elementary excitations of magnetic material, is their nonlinearity, which can be reached with moderate radio frequency RF excitation fields. The nonlinear interactions between spin waves attract increasing attention in neuromorphic computing [1] and magnonic logic devices [2]. This study presents micro-focused Brillouin light spectroscopy (μ BLS) of nonlinear processes in a 500 nm Bismuth Yttrium Iron Garnet (BiYIG) disk [3]. Such material is a soft ferrimagnet with moderate cubic anisotropy and has one of the lowest dampings among all the magnetic materials. The spin waves are excited with RF excitation generated by an Ω -shaped antenna. The disk is positioned slightly off center within the antenna, approximately 100 nm from the exact center which introduces a small in-plane RF component along with the predominant out-of-plane excitation. An in-plane static magnetic field is applied, resulting in an in-plane magnetized disk with some nonuniformity at low static field strengths. We vary three parameters to investigate the nonlinear dynamics: the in-plane static field, the rf power (ranging from -15 dBm to 10 dBm), and the rf frequency.

The thermal spin wave spectrum of the 500nm BiYIG disk is obtained using μ BLS at different in-plane static fields. The probing light is focused at the center of the disk. We can identify a large number of thermal spin wave modes as shown in Fig.1(a), for a frequency range from 0.4 to 5 GHz. The large number of spin wave modes can lead to rich nonlinear dynamics. Spin-wave modes can interact with each other through different processes.

Starting from an in-plane field of -30 mT, the mode frequencies decrease as the field strength is reduced, reaching a minimum at -7 mT where the applied field equals the effective anisotropy field. BiYIG has cubic anisotropy and the value of the effective anisotropy field depends on the orientation of the applied static field with respect to the crystallographic axis. When the applied field is lower than the effective anisotropy field (in the range between -7 mT and 4 mT), we observe mode softening [4]. This suggests that the field applied along the x -axis corresponds to a hard axis of the cubic anisotropy. From the thermal spectra obtained at various in-plane fields, we identified the mode with the highest intensity, which probably corresponds to the uniform mode. This identification is validated by comparing the experimental spectra with micromagnetic simulations.

Exciting the uniform mode f_0 can result in the first, second, and third Suhl instabilities [5]. The first Suhl instability involves three-magnon splitting, where a magnon at f_0 decays into two magnons at $f_0/2$ [6]. The second Suhl instability involves four-magnon scattering, in which two magnons at f_0 annihilate to generate two new magnons. The third Suhl instability occurs through the annihilation of three magnons at f_0 , resulting in the creation of two magnons around $3f_0/2$.

To investigate these processes, we sweep the inplane static field while exciting the uniform mode at each field, as shown in Fig.2. From -12 mT to -17 mT, we observe rich nonlinear dynamics. For instance, the spectrum at -16 mT is plotted in Fig.2(b). When we excite the resonance mode at frequency $f=1.3$ GHz, we observe modes around f labeled f_1 and f_2 with frequency spacing $\delta f=0.2$ GHz from the pumped mode. We also observe modes around $3f/2$.

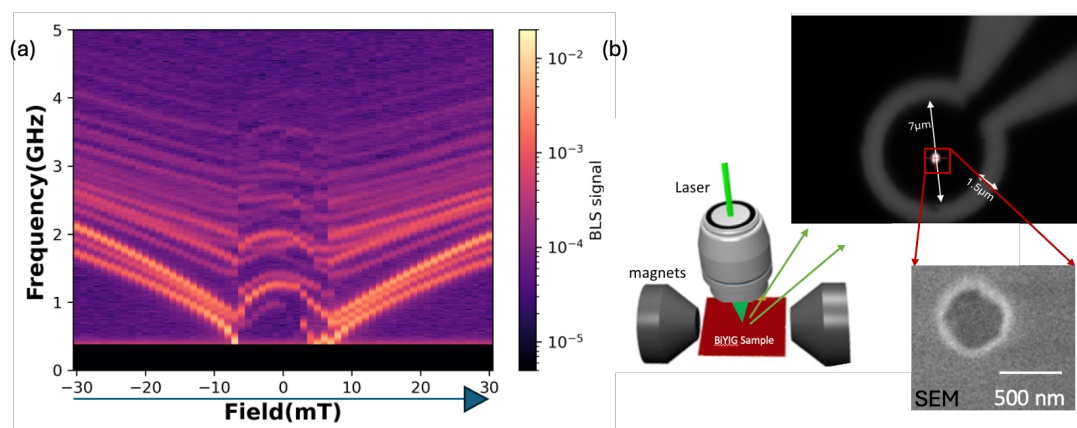


Figure 1: (a) Thermal BLS spectrum for 500 nm BiYIG disk when the in plane static field is varied from -30 mT to 30 mT in steps of 1 mT. (b) Experimental set up scheme with a picture of the Ω -shaped antenna taken by μ BLS and SEM image of the studied disk.

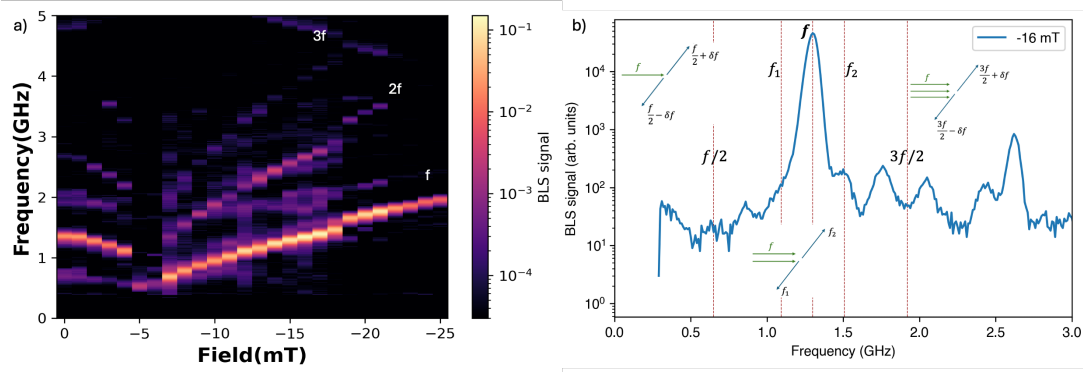


Figure 2: (a) BLS spectra for in-plane static field is swept between 0 and -25mT while the resonance frequency is excited for each field at 5 dBm. The excited mode is indicated by f . (b) BLS spectra for -16 mT in plane static field when the uniform mode is excited at 5 dBm.

We identified the power thresholds for each nonlinear process, finding that four-magnon scattering has the lowest threshold. As the excitation power increases, modes at $f/2$ and around $3f/2$ appear, with energy being transferred from the pumped mode to these secondary modes. This results in a decrease in the intensity of the pumped mode, as the energy is progressively redistributed throughout the generated modes.

Time-resolved BLS measurements provide the temporal evolution of the spin wave populations. The first modes to populate are the two modes around frequency f which results from four magnon scattering. Following the modes around f , the modes around $f/2$ are populated. These modes correspond to the magnons generated via three magnon splitting. Finally, the modes around $3f/2$ appear and complete the cascade of nonlinear interactions.

All these nonlinear interactions were also reproduced using micromagnetic simulations, demonstrating a strong alignment between measurements and computational predictions.

In summary, we studied nonlinear spin wave dynamics in an inplane magnetized BiYIG disk, focusing on the uniform mode f_0 and its resulting Suhl instabilities. Using μ BLS and micromagnetic simulations, we observed sequential nonlinear interactions including first, second and third-order instabilities. We determined the power thresholds to reach the nonlinear regime and tracked the temporal evolution of the generated modes.

Acknowledgments

This work was supported by the French National Research Agency (ANR) [under a public grant overseen as part of the Investissements d'Avenir program (Labex NanoSaclay, reference: ANR-10-LABX-0035), SPICY, and a research contract No. ANR-20-CE24-0012 (MARIN)].

References

- [1] Lukas Körber, Christopher Heins, Tobias Hula, et al. Pattern recognition in reciprocal space with a magnon-scattering reservoir. *Nature Communications* 14, 3954 (2023).
- [2] Alexey B Ustinov, Erkki Lähderanta, Mitsuteru Inoue, and Boris A Kalinikos. Nonlinear spin-wave logic gates. *IEEE Magnetics Letters* 10, 1–4 (2019).
- [3] AA Serga, AV Chumak, and Burkard Hillebrands. YIG magnonics. *Journal of Physics D: Applied Physics* 43, 264002 (2010).
- [4] Nikodem Lesniewski and Pawel Gruszecki. "Spin waves softening in thin films with perpendicular anisotropy". *2023 IEEE International Magnetic Conference-Short Papers (INTERMAG Short Papers)*. IEEE. 2023, 1–2.
- [5] Harry Suhl. The Nonlinear Behavior of Ferrites at High Microwave Signal Levels. *Proceedings of the IRE* 44, 1270–1284 (1956).
- [6] H Merbouche, P Che, T Srivastava, et al. Degenerate and nondegenerate parametric excitation in yttrium iron garnet nanostructures. *Physical Review Applied* 21, 064041 (2024).

Posters session 1

Magnetoresistance-based current limiter

Jérémy Létang^{1,*}, Luiz Enger¹, Perla Malagò¹, Peter Leitner², and Michael Ortner¹

¹*Silicon Austria Labs, Villach, Austria*

²*Silicon Austria Labs, Graz, Austria*

*jeremy.letang@silicon-austria.com

Extraordinary magnetoresistance (EMR) sensors are geometry-dependent 4-terminal devices based on high-conductivity semiconductors and metal inclusions, that can achieve over 10^6 % magnetoresistance ratios [1–3]. The origin of such effect can be explained by the Lorentz force, rewriting the conductivity tensor of the semiconductor with a magnetic field dependence. Deviations of the current path result in charge accumulation in the semiconductor, leading to large voltage differences.

In this work, this effect is employed for passive current-limiting applications with a 2-terminal device. With the possibility to integrate a magnetic circuit in the current path, the rise in current will create a field on the EMR device, in turn increasing its resistance and thus limiting the current overshoot [4, 5]. Investigations of the analytical model of this device show that the maximum achievable MR ratio is $\mu^2 B^2$, where μ is the charge-carrier mobility of the semiconductor and B is the magnitude of the applied magnetic field. Therefore, we seek to use the highest mobility materials and reach the highest magnetic field possible. In contrast to the 4-terminal sensor, metal inclusions do not improve the current limiter performance, and charge accumulation at the edges degrades the obtained MR. The model indicates that this can be mitigated by engineering the geometry of the device, increasing the dimension parallel to the deviated current path. To approach the theoretical limit, the length of the device must be at least μB times its thickness. We also present a second solution to avoid charge accumulation by short-circuiting the semiconductor edges, improving the MR without changing the device geometry. In addition, we propose a way to mitigate this by tweaking the device geometry to minimize contact resistivity between the semiconductor and the metal electrodes, which is known to negatively influence the MR ratio [6].

In current limiter applications, it is the current of the main circuit itself that passes through the device, and not a small bias current as is the case in sensor applications. Electric current levels can reach units of amperes, and as high current passes through the EMR element, resistive power dissipation becomes relevant. Electric and thermal simulations with the finite element method (COMSOL) in 3D for different device sizes corroborate the analytical model and are used to investigate resistance variations and Joule heating.

Finally, we show first implementation of such a magnetoresistance-based current limiter. This includes the microfabrication of the EMR component, the simulation and fabrication of the magnetic field generator, and the integration of both the EMR component and field generator in one system. Electrical, magnetic, and thermal measurements are performed to characterize the current limiter.

Acknowledgments

This work has been jointly supported by the NOVETROL Grant under Grant Number 101192615 and by Silicon Austria Labs (SAL), owned by the Republic of Austria, the Styrian Business Promotion Agency (SFG), the federal state of Carinthia, the Upper Austrian Research (UAR), and the Austrian Association for the Electric and Electronics Industry (FEEL).

References

- [1] S. A. Solin, Tineke Thio, D. R. Hines, and J. J. Heremans. [Enhanced Room-Temperature Geometric Magnetoresistance in Inhomogeneous Narrow-Gap Semiconductors](#). *Science* (2000).
- [2] Jian Sun and Jürgen Kosel. [Extraordinary Magnetoresistance in Semiconductor/Metal Hybrids: A Review](#). *Materials* 6, 500–516 (2013).
- [3] Thierry Désiré Pomar, Ricci Erlandsen, Bowen Zhou, et al. [Extraordinary magnetometry: A review on extraordinary magnetoresistance](#). *Applied Materials Today* 38, 102219 (2024).
- [4] Petr Kopejtko. *Current controlling element based on saturation of a magnetic circuit*. 2022.
- [5] Jérémy Létang, Stefano Lumetti, Perla Malagò, et al. “Extraordinary magnetoresistance in a 2-terminal structure”. *2023 IEEE International Magnetic Conference - Short Papers (INTERMAG Short Papers)*. 2023.
- [6] Jian Sun and Jürgen Kosel. [Finite Element Analysis on the Influence of Contact Resistivity in an Extraordinary Magnetoresistance Magnetic Field Micro Sensor](#). *Journal of Superconductivity and Novel Magnetism* 25, 2749–2752 (2012).

Imprinting of skyrmions and bimerons in a thin film of an antiferromagnet

Coline Thevenard^{1,*}, Miina Leiviskä¹, Richard F. L. Evans², Daria Gusakova¹, and Vincent Baltz¹

¹Univ. Grenoble Alpes, CNRS, CEA, Grenoble INP, IRIG-SPINTEC, F-38000 Grenoble, France

²School of Physics, Engineering and Technology, University of York, York YO10 5DD, United Kingdom

*coline.thevenard@cea.fr

Controlling the magnetic order of antiferromagnets is challenging due to the vanishing net magnetization. For this reason, the study of topologically protected real-space states of antiferromagnets is restricted by the difficulty in nucleating these states [1]. Here, using atomistic simulations we demonstrate how to overcome the challenge of nucleating skyrmions and bimerons in thin films of prototypical bipartite antiferromagnets (Fig. 1) [2], like NiO and Mn₂Au. Utilizing the exchange bias coupling between a ferromagnet, Pt/Co and the antiferromagnet, we imprint the spin structure of the former through the latter by means of a thermal and field cycling procedures. The use of a prototypical antiferromagnet and stack, free from the layers intermixing and polycrystallinity earlier considered [3], allowed us to calculate the three key parameters to attest to the intricate topology of skyrmions and bimerons: polarity, vorticity and helicity, and the related topological charge. We demonstrate unequivocally that the textures imprinted in the antiferromagnets are actual skyrmions and bimerons. How various parameters: temperature, Dzyaloshinskii-Moriya interaction, anisotropy, affect the efficiency of this imprinting, and the nature and morphology of the imprinted textures will be discussed. In particular we will show that the skyrmion and the bimeron penetrate into the core of the antiferromagnet, resulting in tubular topological objects. This work paves way for further studies on topologically protected real-space phases in antiferromagnets and promotes the development of denser and faster spintronic devices.

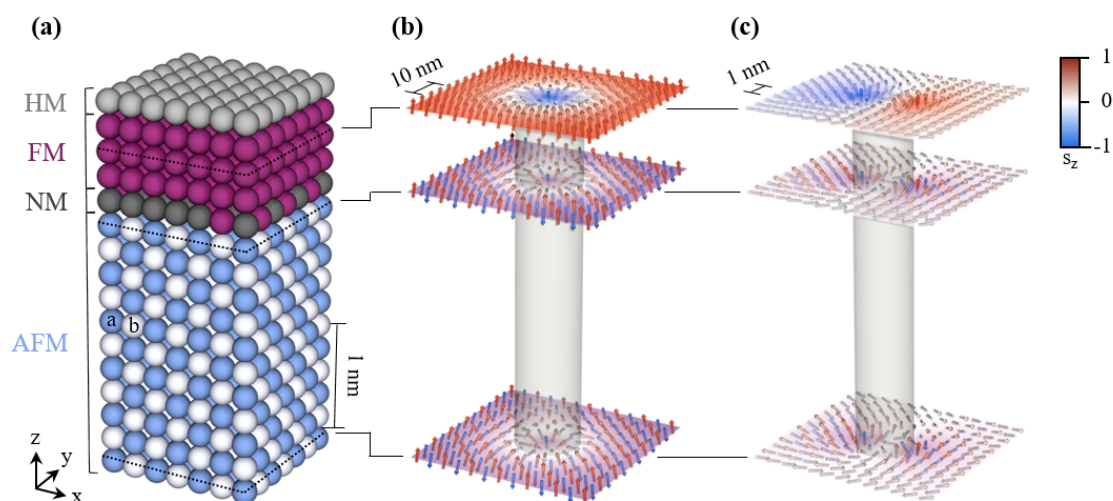


Figure 1: **(a)** Zoom on the atomic structure of the rocksalt monocrystalline simulation system consisting of: (i) a heavy-metal(HM)/ferromagnet (FM) bilayer for skyrmion nucleation, (ii) a 75%-rich non-magnetic (NM) interface for coupling, and (iii) a prototypical bipartite antiferromagnetic layer (AFM) made of two sublattices: AFMa and AFMb. In their ground state, the spins of AFMa and AFMb are collinear and opposite. The full size of the simulation system is $100 \times 100 \times 3.35 \text{ nm}^3$ corresponding to 1 monolayer (ML) of HM, 3 MLs of FM, 1 ML of NM and 11 MLs of AFM. **(b)** 3D view of the skyrmion tube obtained in the FM and imprinted in the 11 MLs-thick AFM, following thermal and magnetic field cycling procedures to (i) nucleate the skyrmion in the FM while the AFM is disordered, above its Néel temperature T_N , (ii) replicate the skyrmion in the AFM upon crossing T_N , and (iii) stabilize the skyrmion at remanence. The simulated spins oriented in the xy -plane define the contour of the tube. **(c)** Same when an in-plane anisotropy is considered, resulting in the imprint of a bimeron in the AFM. The simulated spins oriented in the yz -plane define the contour of the tube.

Acknowledgments

This study was partially supported by the CNRS international research project (IRP) "CITRON" and the U.K. EPSRC program (Grant No. EP/V007211/1). This work used the ARCHER2 UK National Supercomputing Service.

References

- [1] M. Leiviskä, C. Thevenard, C. Cronshaw, et al. [Antiferromagnetic skyrmions in spintronics](#). *Book chapter, Elsevier (Eds A. Hirohata et al.)*, under review (2024).
- [2] C. Thevenard, M. Leiviskä, D. Gusakova, R. F. L. Evans, and V. Baltz. Imprinting of skyrmions and bimerons in a thin film of an antiferromagnet, in preparation, soon to appear in HAL and arXiv (2025).
- [3] M. Leiviskä, S. Jenkins, R. F. L. Evans, D. Gusakova, and V. Baltz. [Local setting of spin textures in a granular antiferromagnet](#). *Physical Review B* 108, 184424 (2023).

Giant stability of nanoscale skyrmions and bimerons in oxidized van der Waals Fe_3GeTe_2

Megha Arya^{1,*}, Bhanu Jai Singh¹, Lionel Calmels¹, Stefan Heinze², and Dongzhe Li¹

¹CEMES, Université de Toulouse, CNRS, France

²Institute of Theoretical Physics and Astrophysics, University of Kiel, Germany

*megha.megha@cemes.fr

Chiral magnetic solitons, which hold great promise in spintronic applications [1], are often attributed to Dzyaloshinskii–Moriya interaction (DMI). However, in most 2D van der Waals magnets, the DMI is suppressed due to inversion symmetry. Here, we propose a strategy to induce strong DMI via oxygen adsorption on the surface of 2D magnets – an experimentally feasible approach [2]. By combining *ab initio* theory and atomistic spin simulations, we predict highly stable skyrmions with radii below 10 nm in an oxidized Fe_3GeTe_2 (FGT) monolayer. Notably, we find very large skyrmion energy barriers of more than 150 meV, comparable to the ones at ferromagnetic/heavy metal interfaces. Interestingly, oxygen adsorption breaks the in-plane symmetry of FGT, inducing an anisotropic DMI. This gives rise to multiple topological spin textures beyond skyrmions. Moreover, the oxygen adsorption site strongly influences the magnetocrystalline anisotropy energy of FGT, inducing an inverse spin reorientation transition from out-of-plane to in-plane. As a result, isolated bimerons can be stabilized at zero-field and transformed into skyrmions under an applied field. Finally, we demonstrate that skyrmions are stable for hours in oxidized FGT, at temperatures up to 27 K.

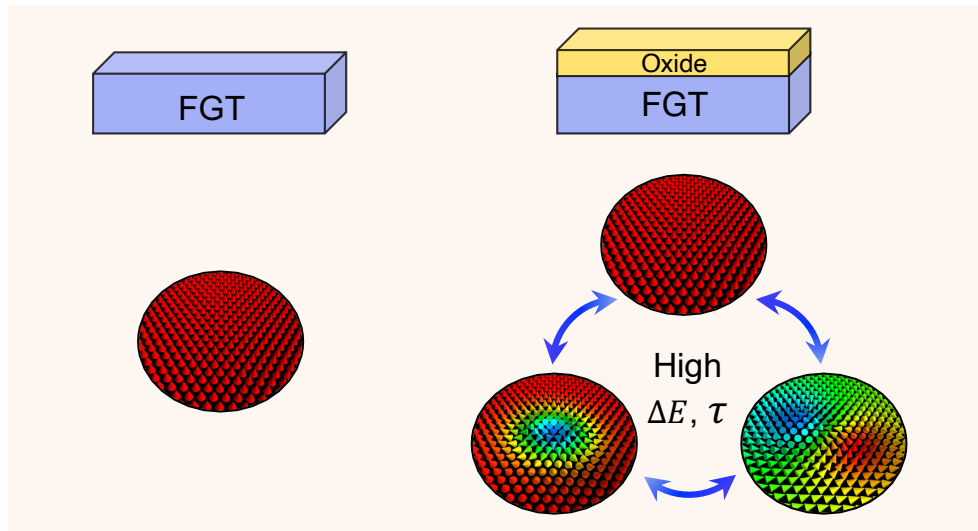


Figure 1: Oxygen-induced highly stable topological spin textures in monolayer Fe_3GeTe_2 and their transformation via external stimuli.

Acknowledgments

This study has been supported through the ANR Grant No. ANR-22-CE24-0019. This work is supported by France 2030 government investment plan managed by the French National Research Agency under grant reference PEPR SPIN – [SPIN THEORY] ANR-22-EXSP-0009. This work was performed using the HPC resources provided by CALMIP (Grant 2022/2024-[P21008]).

References

- [1] Albert Fert et al. [Magnetic skyrmions: advances in physics and potential applications](#). *Nat. Rev. Mater.* 2, 1–15 (2017).
- [2] Tae-Eon Park et al. [Néel-type skyrmions and their current-induced motion in van der Waals ferromagnet-based heterostructures](#). *Phys. Rev. B* 103, 104410 (2021).

Altermagnetic variants in thin films of Mn_5Si_3

Javier Rial¹, Miina Leiviskä^{1,2}, Gregor Skobjin³, Antonín Bad'ura^{2,4}, Gilles Gaudin¹, Florian Disdier¹, Richard Schlitz³, Ismaïla Kounta⁵, Sebastian Beckert⁶, Dominik Kriegner², Andy Thomas^{6,7}, Eva Schmoranzzerová⁴, Libor Šmejkal^{2,8}, Jairo Sinova^{8,9}, Tomáš Jungwirth^{2,10}, Lisa Michez⁵, Helena Reichlová², Sebastian T. B. Goennenwein³, Olena Gomonyay¹, and Vincent Baltz^{1,*}

¹Univ. Grenoble Alpes, CNRS, CEA, Grenoble INP, IRIG-SPINTEC, F-38000 Grenoble, France

²Institute of Physics, Czech Academy of Sciences, Prague, Czechia

³Department of Physics, University of Konstanz, Konstanz, Germany

⁴Faculty of Mathematics and Physics, Charles University, Prague, Czechia

⁵Aix-Marseille University, CNRS, CINaM, Marseille, France

⁶Institute of Solid State and Materials Physics, TU Dresden, Dresden, Germany

⁷Leibniz Institute of Solid State and Materials Science (IFW Dresden), 01069 Dresden, Germany

⁸Institute for Physics, Johannes Gutenberg University Mainz, Mainz, Germany

⁹Department of Physics, Texas A&M University, College Station, Texas, USA

¹⁰School of Physics and Astronomy, University of Nottingham, Nottingham, United Kingdom

*vincent.baltz@cea.fr

The altermagnet candidate Mn_5Si_3 has attracted wide attention in the context of non-relativistic spin physics, due to its composition of light elements [1–3]. However, the presumed structure of the altermagnetic phase had yet to be demonstrated. In this study [4], we demonstrate a hallmark of altermagnetism in Mn_5Si_3 thin films, namely the three options, or variants, for the checkerboard distribution of the magnetic Mn atoms. The magnetic symmetries were altered by field-rotation of the Néel vector along relevant crystal directions, resulting in anomalous Hall effect anisotropy. The experimental results in nanoscale devices were corroborated by a theoretical model involving atomic site dependent anisotropy due to electric multipoles and bulk Dzyaloshinskii-Moriya interaction for a single variant. These findings elevate Mn_5Si_3 from a candidate to a proven altermagnet.

Acknowledgments

This work was supported by the French national research agency (ANR) and the Deutsche Forschungsgemeinschaft (DFG) (Project MATHEEIAS - Grant No. ANR-20-CE92-0049-01 / DFG-445976410, and Project PEPR SPIN - Grant No. ANR-22-EXSP-0007).

References

- [1] Helena Reichlova, Rafael Lopes Seeger, Rafael González-Hernández, et al. [Observation of a spontaneous anomalous Hall response in the \$\text{Mn}_5\text{Si}_3\$ d-wave altermagnet candidate](#). *Nature Communications* 15, 4961 (2024).
- [2] Ismaïla Kounta, Helena Reichlova, Dominik Kriegner, et al. [Competitive actions of MnSi in the epitaxial growth of \$\text{Mn}_5\text{Si}_3\$ thin films on Si\(111\)](#). *Physical Review Materials* 7, 024416 (2023).
- [3] Miina Leiviskä, Javier Rial, Antonín Bad'ura, et al. [Anisotropy of the anomalous Hall effect in thin films of the altermagnet candidate \$\text{Mn}_5\text{Si}_3\$](#) . *Physical Review B* 109, 224030 (2024).
- [4] Javier Rial, Miina Leiviskä, Gregor Skobjin, et al. [Altermagnetic variants in thin films of \$\text{Mn}_5\text{Si}_3\$](#) . *Physical Review B* 110, L220411 (2024).

Asymptotically exact formulas for the stripe domains period in ultrathin ferromagnetic films with out-of-plane anisotropy

Anne Bernard-Mantel^{1,*}, Valeriy V. Slastikov², and Cyrill B. Muratov³

¹Centre d'Elaboration de Matériaux et d'Etudes Structurales, CEMES-CNRS, 29 rue Jeanne Marvig, 31055 Toulouse, France

²School of Mathematics, University of Bristol, Bristol 1UG 1TW, United Kingdom

³Dipartimento di Matematica, Università di Pisa, Largo B. Pontecorvo, 5, 56127 Pisa, Italy

*anne.bernand-mantel@cemes.fr

Modeling of magnetization patterns in thin films requires to evaluate precisely the demagnetizing energy, a notoriously difficult task owing to the slow convergence and often singular behavior of the demagnetizing energy integrals in space due to the long-range nature of the magnetostatic interaction. Despite the extensive efforts in modeling the stripe patterns in magnetic thin films, at present there exists no clarity about the regime of validity of various existing analytical formulas for the equilibrium stripe periods. Formulas with a prefactor proportional to the film thickness or the Bloch wall width are used indiscriminately for ultrathin films, despite presenting up to more than one order of magnitude difference. Additionally, even among the models which take into account the domain wall long-range dipolar contributions in the stripe energy, resulting in an analytical formula with a prefactor proportional to the Bloch wall width, there exist discrepancies in the estimated constants in front of the prefactor up to a factor of 3.

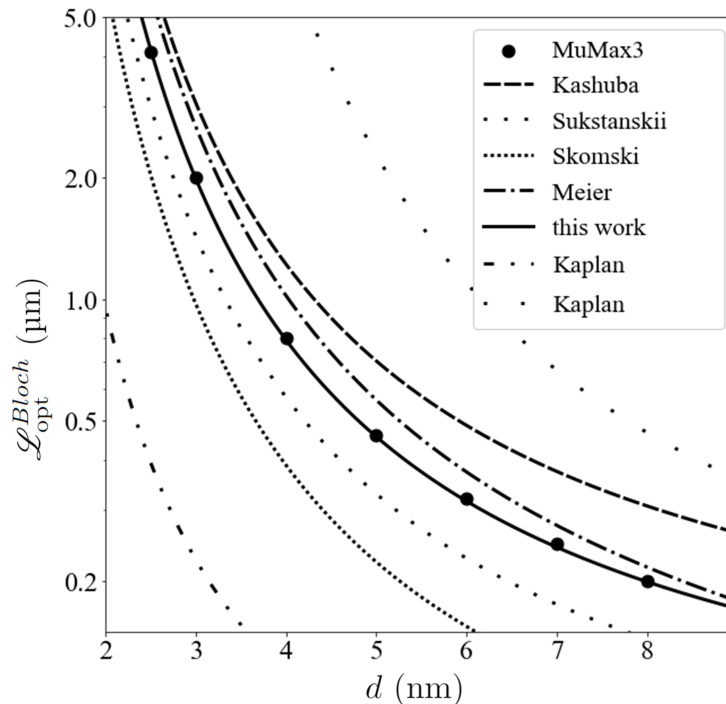


Figure 1: Equilibrium stripe period $\mathcal{L}_{\text{opt}}^{\text{Bloch}}$ as a function of the film thickness d in the regime of Bloch walls (zero DMI). The material parameters are $A_{\text{ex}} = 10$ pA/m, $M_s = 1$ MA/m and $K_{u1} = 0.75$ MJ/m³.

In the present work [1] we settle this issue by calculating an asymptotically exact analytical formula for the equilibrium magnetic stripe period valid in the ultrathin film regime, where the prefactor is calculated explicitly for the case of both Bloch and Néel domain walls. The formulas are applied to classical sets of system parameters, including the Bloch and the Néel regimes and a film thickness varying from one monolayer to about 10 nm. The comparison with micromagnetic simulations in the considered regimes shows excellent agreement, confirming the applicability of our formula in the ultrathin film regime. This agreement represents a quantitative improvement as compared to the state of the art formulas in the literature, as previous studies did not succeed to obtain the correct asymptotics for vanishing thicknesses. The accuracy of our formulas is remarkably robust up to thicknesses of at least twice the exchange length. The variation of the wall width with the film thickness does not affect this accuracy and the formulas remain accurate as long as the thickness is smaller than the Bloch wall width. We also highlight the inapplicability, in the ultrathin film regime, of an alternative formula obtained by neglecting the wall width (thin wall approximation) which leads to a prefactor proportional to the film thickness. This settles a controversy with regards to which formula should be used for predicting the equilibrium stripe period in ultrathin films. We explicitly clarify the conditions of validity of the respective formulas as well as the proper choice of domain wall surface tension in the different regimes.

References

- [1] Anne Bernand-Mantel, Valeriy V. Slastikov, and Cyrill B. Muratov. *Asymptotically exact formulas for the stripe domains period in ultrathin ferromagnetic films with out-of-plane anisotropy*. 2024. arXiv: [2410.20373](https://arxiv.org/abs/2410.20373) [[cond-mat](#) [mes-hall](#)].

Spin-Orbit-Torque in Co/Al interfaces

Armando Pezo^{1,*}

¹Laboratoire Albert Fert, CNRS, Thales, Université Paris-Saclay, 91767 Palaiseau, France

*armando-arquimedes.pezo-lopez@cnrs-thales.fr

Recent efforts to manipulate electronic quantum properties in materials have highlighted the significance of the orbital degree of freedom [1, 2]. In this context, the emergence of the orbital Hall effect, driven by orbital textures, and the generation of Orbital-Rashba effects at light metal interfaces [3] represents remarkable alternatives to the heavy-metal-based materials traditionally used in Spintronics over the past few decades. In this study, we conduct a theoretical investigation into the emergence of Spin-Orbit Torque in Co/Al bilayers. Starting with state-of-the-art density functional theory (DFT) simulations, we further apply linear response theory to calculate the actual values of the torque exerted on the magnetic layer, we also addressed the influence of proximity effects with Pt and the role of strain.

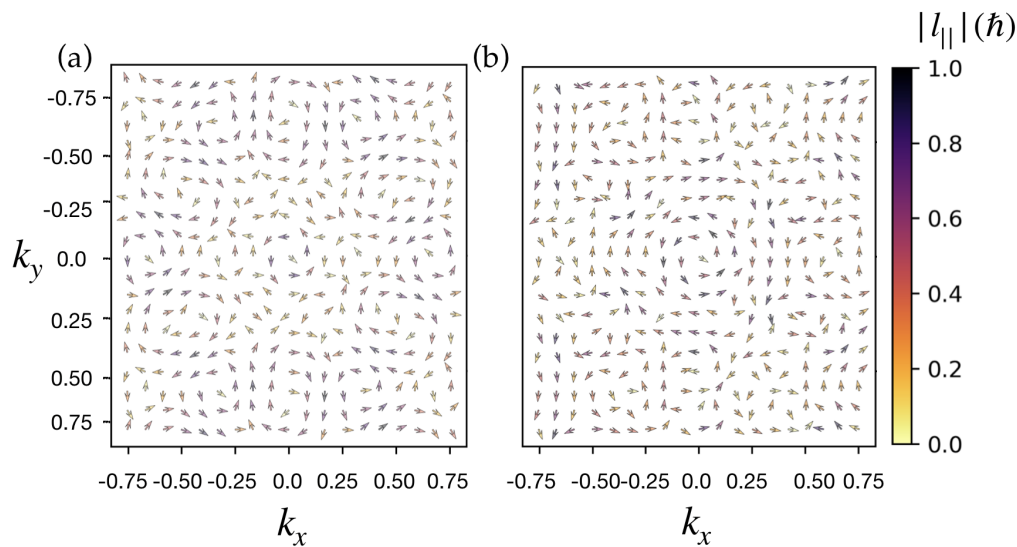


Figure 1: Orbital texture for Co/Al interfaces with (a) and without (b) a Pt layer at the interface.

Acknowledgments

This study has been supported by the French National Research Agency under project “ORION” ANR-20-CE30-0022-02, project “DYNTOP” ANR-22-CE30-0026, and by a France 2030 government grant managed by the French National Research Agency PEPR SPIN under project “SPINTHEORY” ANR-22-EXSP0009.

References

- [1] Dongwook Go, Daegun Jo, Changyoung Kim, and Hyun-Woo Lee. [Intrinsic Spin and Orbital Hall Effects from Orbital Texture](#). *Phys. Rev. Lett.* 121, 086602 (8 2018).
- [2] Armando Pezo, Diego García Ovalle, and Aurélien Manchon. [Orbital Hall effect in crystals: Interatomic versus intra-atomic contributions](#). *Phys. Rev. B* 106, 104414 (10 2022).
- [3] S. Krishnia, B. Bony, E. Rongione, et al. [Quantifying the large contribution from orbital Rashba-Edelstein effect to the effective damping-like torque on magnetization](#). *APL Materials* 12, 051105 (2024). eprint: https://pubs.aip.org/aip/apm/article-pdf/doi/10.1063/5.0198970/19918228/051105_1_5.0198970.pdf.

Metallicity regeneration of chemically ordered FeRh nanoparticles studied by *in situ* UHV spectroscopy.

Olivier Boisson^{1,*}, Guillermo Herrera¹, Damien Le Roy¹, Florent Tournus¹, Sara Gonzalez², Ingrid C. Infante², Matthieu Bugnet³, Edwige Otero⁴, Philippe Ohresser⁴, and Véronique Dupuis¹

¹Institut Lumière Matière, UMR 5306, Université Lyon 1-CNRS, Université de Lyon, F-69622 Villeurbanne

²Institut des Nanotechnologies de Lyon, UMR 5270, CNRS ECL INSA UCBL CPE, F-69621 Villeurbanne

³MATEIS, UMR5510, CNRS, INSA Lyon, Université Claude Bernard Lyon 1, F-69621 Villeurbanne

⁴Synchrotron SOLEIL, L'Orme de Merisiers, F-91190 Saint-Aubin

*olivier.boisson@univ-lyon1.fr

Chemically ordered equiatomic FeRh thin films in B2-CsCl structure exhibit Antiferromagnetic /Ferromagnetic (AFM/FM) transition near room temperature accompanied by a 1 per cent volume expansion. By using a Ferroelectric substrate, such metamagnetic transition can be electrically driven by only few volts [1]. From our part, we have prepared mass-selected FeRh equiatomic nanocrystallites pre-formed in gas phase from LECBD (Low Energy Cluster Beam Deposition) in order to study chemical and magnetic order phase transition at nanoscale. We clearly evidenced a crystallographic phase transition from FCC chemically disordered A1 phase to B2 chemical ordered for FeRh nanoparticles (NPs) in a carbon matrix upon UHV annealing at 700°C but with a FM order persistence at low temperature even for equivalent NPs diameter as large as 10 nm [2], [3]. In order to try to control the magnetic order using external parameters in ultimate nanostructures, we have deposited FeRh clusters on a surface consisting of a film full-strained BaTiO₃(BTO) grown on SrTiO₃(001) (STO) monocrystalline substrate. Once more, we have shown that annealing at high temperature under vacuum allows to reach B2 chemical order for FeRh NPs over oxide perovskite substrates. But for the first time, we have obtained epitaxial relationships between randomly oriented B2 FeRh nanocrystals in intimate contact with perovskite monocrystalline substrate and atomic coherence with unusual orientations at the Metal/Oxide interface from grazing Incidence X-ray scattering technics [4] but also by using advanced scanning electron transmission microscopy (STEM) (see Fig. 1a) .

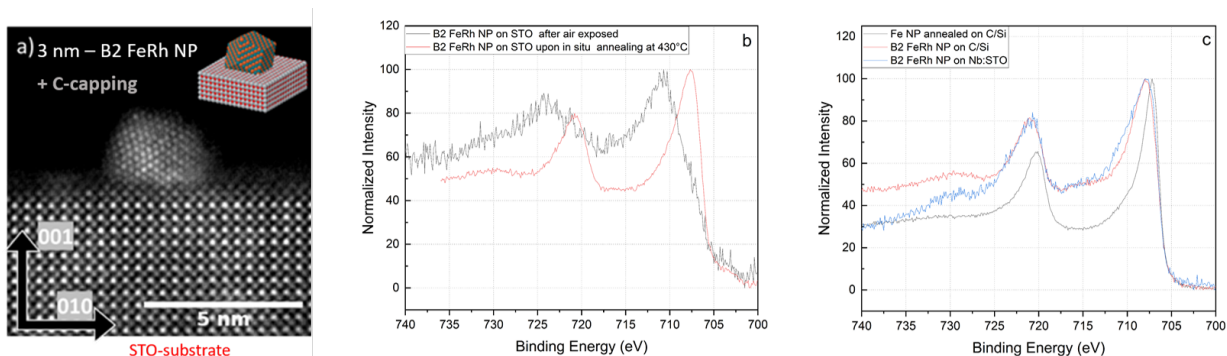


Figure 1: B2 FeRh NP on STO substrate: STEM-HAADF in cross section (a) and XPS after transfer in air and upon *in situ* annealing at 430 °C (b). XPS comparison between *in situ* UHV prepared B2 FeRh NPs on C/Si, on STO and full metallic BCC Fe NPs on C/Si substrate

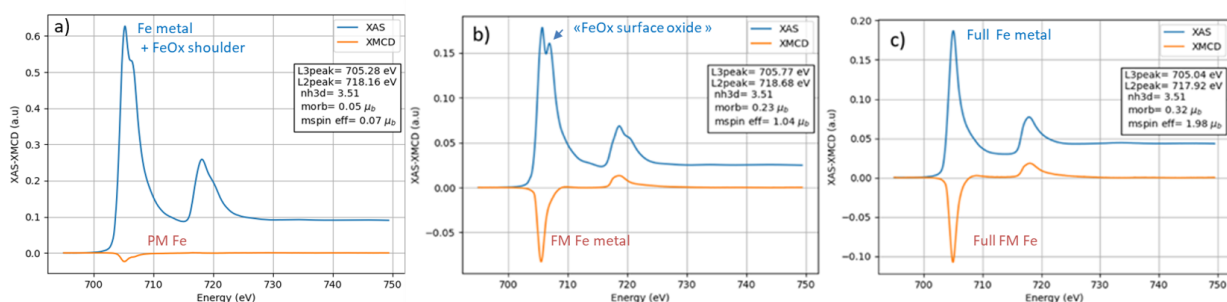


Figure 2: XAS/XMCD of FeRh NPs on STO at L-Fe edge: (a) Paramagnetic PM (A1)→ FM (B2) transition from post-annealing at $T > 600^{\circ}\text{C}$ and (b-c) Surface de-oxidization to full metallic FeRh NPs from *in situ* UHV annealing at $T > 430^{\circ}\text{C}$

Because the high sensitivity of the nanomagnets to their surface atoms offers a great opportunity to gradually control the interfacial electronic properties of hybrid multiferroic systems, we check if strain and/or charge transfer at the faces of

B2 FeRh nanoparticles deposited on SrTiO₃ (001) crystals (STO) could tune the metamagnetic phase transition by using the chemical selectivity of X-ray photoelectron spectroscopy (XPS) connected to our UHV chamber and of X-ray absorption spectroscopy (XAS) simultaneously to X-ray magnetic circular dichroism (XMCD) on DEIMOS beamline at SOLEIL synchrotron. The as-prepared sample initially in the chemically disorder FCC A1 phase structure present a very weak magnetic signal and become FM after post-annealing in UHV at 700°C by achieving the chemically ordered CsCl B2 phase (see Fig. 2 a and b). But after transfer in air, we systematically observed the formation of a oxide shell passivating a metallic FeRh cluster core as 35 percent of atoms are at surface for 3nm-NPs diameter. In one hand, we obtained a 2 eV shift of the metallic Fe 2p XPS peak characteristic to a FeOx oxidation in surface (see Fig. 1b) while a clear doublet peak has been observed on XAS at the Fe L_{2,3} edges with an half decomposition into a metallic and an oxide part for B2 FeRh NPs on perovskite substrate (see Fig. 2b). In the other hand, the corresponding XMCD signals measured at very low temperature 2 K reveal FM signature with a spin magnetic moment of 1.5 μ_B per iron atom corresponding to half of the XMCD signal measured for B2 metallic FeRh NPs embedded in Carbon.[2]

To examine electronic structure modifications occurring during de-oxidization and phase transition process, both surface-sensitive quantitative spectroscopic experiments have been performed during progressive *in situ* UHV sample annealing. We show that the metallicity of FeRh NPs on perovskite oxide substrate has been regenerated from *in situ* 430°C annealing though reversible redox processes. By comparing the Fe 2p XPS peak of pure Fe metallic clusters and of FeRh NPs *in situ* 700°C annealed, 0.8 eV induced binding energy shifts has been observed due to charge transfer and hybridization effects in bimetallic nanoalloys (see Fig. 1c). In agreement with theoretical calculations based on the Anderson impurity model, two XPS satellite peaks at 730 eV (resp. 717 eV) for Fe 2P_{1/2} (resp. Fe 2p_{3/2}) have been clearly observed with an increase of the magnetic Fe moment in B2 FeRh NPs after iron oxide reduction (see Fig. 2c) [5]. As a conclusion, the fine electronic structure examination at core levels during de-oxidization and phase transition process have shown that the strong Rh 4d-Fe 3d hybridization is responsible to the persistent FM order in B2 FeRh NPs where AF order could not be stabilized from epitaxy at interface with perovskite oxide substrate, due to finite size effects in alloyed nanomagnet. In addition, some other Operando X-ray absorption, natural linear and magnetic circular dichroism spectroscopy (XAS/XNLD/XMCD) measurements under synchrotron facilities will be presented on perovskite substrates.

Acknowledgments

The authors are very grateful to the ILMTECH platform for cluster synthesis at PLYRA and to SOLEIL staff for smoothly running the facility. Financial support is acknowledged from the International Research Network (IRN) / Groupement de Recherches International (GDRI) on Nanoalloys and from ANR to the ANR-19-CE09-0023 VOLCONANO project.

References

- [1] R. O. Cherifi, V. Ivanovskaya, L. C. Phillips, et al. [Electric-field control of magnetic order above room temperature](#). *Nature Materials* 13, 345–351 (2014).
- [2] Arnaud Hillion, A. Cavallin, S. Vlaic, et al. [Low Temperature Ferromagnetism in Chemically Ordered FeRh Nanocrystals](#). *Physical Review Letters* 110 (2013).
- [3] Guillermo Herrera, Anthony Robert, Véronique Dupuis, et al. [Chemical and magnetic order in mass-selected large FeRh nanomagnets embedded in a carbon matrix](#). *European Physical Journal: Applied Physics* 97, 32 (2022).
- [4] A. Reyes, G. Herrera, Pierre Capiod, et al. [Preferential orientations of FeRh nanomagnets deposited on a BaTiO₃ epitaxial thin film](#). *Physical Review B* 109, 245410 (2024).
- [5] A. X. Gray, D. W. Cooke, P. Krüger, et al. [Electronic Structure Changes across the Metamagnetic Transition in FeRh via Hard X-Ray Photoemission](#). *Physical Review Letters* 108 (2012).

Ab initio study of nanoscale skyrmions and bimerons in atomically thin van der Waals layers

Dongzhe Li^{1,*}, Moritz A. Goerzen¹, Soumyajyoti Haldar², and Stefan Heinze²

¹CEMES, Université de Toulouse, CNRS, France

²Institute of Theoretical Physics and Astrophysics, University of Kiel, Germany

*dongzhe.li@cemes.fr

Magnetic skyrmions – topologically protected quasi-particles with a whirling spin texture in real space – show great promise for spintronic applications. In recent years, the demand for device miniaturization in modern electronics has pushed the skyrmion playground from conventional transition-metal multilayers to 2D van der Waals (vdW) materials consisting of weakly bonded 2D layers [1, 2]. In this poster, we present our recent work on magnetic solitons in Fe_3GeTe_2 van der Waals (vdW) heterostructures, focusing on various aspects that are crucial for device applications, such as skyrmion nucleation, transformation, collapse mechanisms, and detection. First, using first-principles and atomistic spin simulations, we show how external stimuli can efficiently tune magnetic interactions in Fe_3GeTe_2 heterostructures [3]. In particular, the Dzyaloshinskii-Moriya interaction and magnetic anisotropy energy in this interface are highly tunable by strain, enabling the formation of zero-field sub-10 nm skyrmions [4]. Second, we predict the existence of multiple magnetic solitons in an all-magnetic vdW heterostructure $\text{Fe}_3\text{GeTe}_2/\text{Cr}_2\text{Ge}_2\text{Te}_6$ (see Fig. 1). We further demonstrate that, although skyrmions and bimerons are topologically equivalent, they exhibit very different localization behaviors. Skyrmions are isotropically localized, while bimerons exhibit anisotropic nonlocality, leading to strong finite-size effects [5]. Finally, we propose a novel approach to detect skyrmions using an electric current in vdW tunnel junctions with nonmagnetic electrodes. An exceptionally large noncollinear magnetoresistance near the Fermi energy is predicted for a graphite/ Fe_3GeTe_2 /germanene/graphite tunnel junction [6]. We trace the origin to the interplay between spin-mixing effect and orbital symmetry matching at the interface. This opens a new route to realize skyrmion racetrack memories based on atomically thin vdW materials with full-electrical writing/reading.

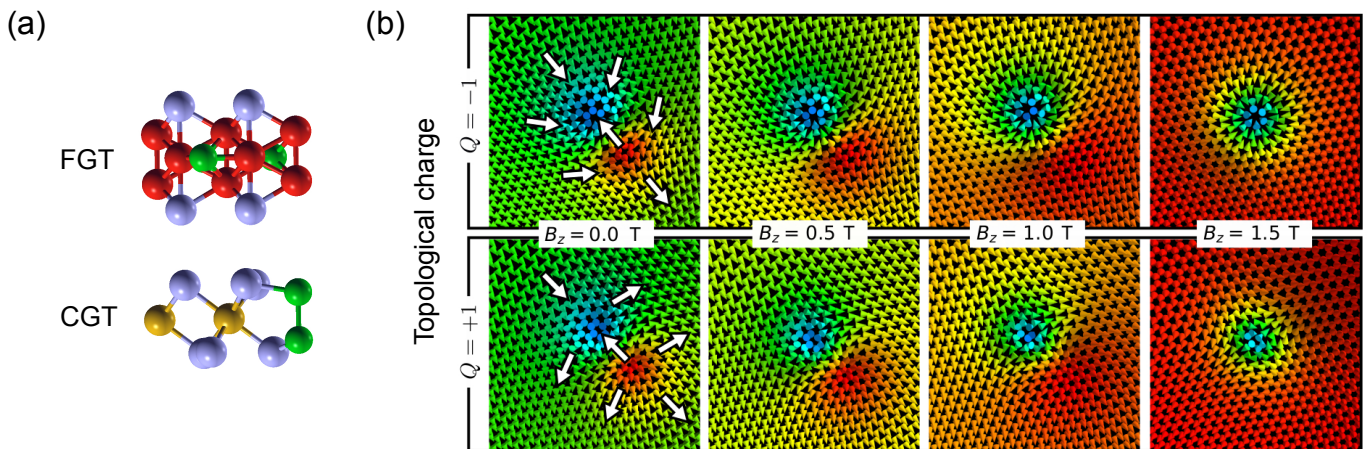


Figure 1: (a) Atomic structure of the $\text{Fe}_3\text{GeTe}_2/\text{Cr}_2\text{Ge}_2\text{Te}_6$ all-magnetic vdW heterostructure. (b) Coexisting zero-field bimerons ($Q = -1$) and antibimerons ($Q = 1$) and their transformation into skyrmions and antiskyrmions via external magnetic fields.

Acknowledgments

This study has been supported through the ANR Grant No. ANR-22-CE24-0019. This work has been (partially) supported through the grant NanoX no. ANR-17-EURE-0009 in the framework of the "Programme des Investissements d'Avenir". This work was performed using HPC resources from CALMIP.

References

- [1] B. Ding et al. [Observation of magnetic skyrmion bubbles in a van der Waals ferromagnet \$\text{Fe}_3\text{GeTe}_2\$](#) . *Nano Lett.* 20, 868–873 (2020).
- [2] Y. Wu et al. [Néel-type skyrmion in \$\text{WTe}_2/\text{Fe}_3\text{GeTe}_2\$ van der Waals heterostructure](#). *Nat. Commun.* 11, 3860 (2020).
- [3] D. Li et al. [Tuning the magnetic interactions in van der Waals \$\text{Fe}_3\text{GeTe}_2\$ heterostructures: A comparative study of *ab initio* methods](#). *Phys. Rev. B* 107, 104428 (2023).

- [4] D. Li et al. [Strain-driven zero-field near-10 nm skyrmions in two-dimensional van der Waals heterostructures](#). *Nano Lett.* 22, 7706–7713 (2022).
- [5] D. Li et al. [Stability and localization of nanoscale skyrmions and bimerons in an all-magnetic van der Waals heterostructure](#). *arXiv preprint arXiv:2408.15974* (2024).
- [6] D. Li et al. [Proposal for all-electrical skyrmion detection in van der Waals tunnel junctions](#). *Nano Letters* 24, 2496–2502 (2024).

Stability of high- Q topological spin textures beyond skyrmions in a van der Waals heterostructure

Shiwei Zhu^{1, *}, Moritz A. Goerzen¹, and Dongzhe Li¹

¹CEMES, Université de Toulouse, CNRS, France

*goodxdie@gmail.com

Magnetic skyrmions – stable, localized spin structures – hold great promise for future spintronic applications. The recent discovery of two-dimensional (2D) magnets opened new opportunities for topological spin structures in atomically thin van der Waals (vdW) materials [1, 2]. In this study, we investigate the stability and collapse mechanisms of high- Q topological spin textures beyond skyrmions in an all-magnetic van der Waals heterostructure, $\text{Fe}_3\text{GeTe}_2/\text{Cr}_2\text{Ge}_2\text{Te}_6$ – an experimentally feasible system [3]. By combining *ab initio* theory and atomistic spin simulations, we demonstrate that metastable high- Q bimerons and antibimerons can coexist at zero-field and be transformed into high- Q skyrmions and antiskyrmions by external stimuli. We analyze higher-order skyrmion transitions, collapse mechanisms, and lifetime by means of transition state theory.

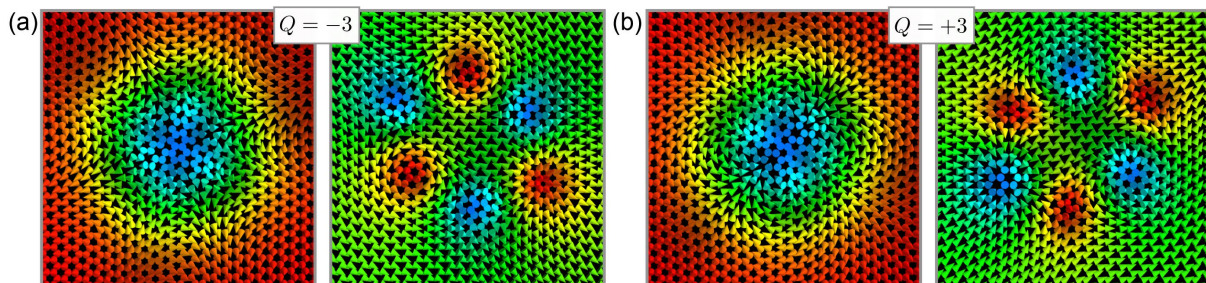


Figure 1: (a) Skyrmion and meron bound state with topological charge $Q = -3$ on a honeycomb lattice. Skyrmion and meron bound state with $Q = +3$ constructed similar to (a). Both bound states are metastable configurations with respect to the energy model of $\text{Cr}_2\text{Ge}_2\text{Te}_6$.

Acknowledgments

This work has been (partially) supported through the grant NanoX no. ANR-17-EURE-0009 in the framework of the “Programme des Investissements d’Avenir”. This work was performed using HPC resources from CALMIP.

References

- [1] B. Ding et al. [Observation of magnetic skyrmion bubbles in a van der Waals ferromagnet \$\text{Fe}_3\text{GeTe}_2\$](#) . *Nano Lett.* 20, 868–873 (2020).
- [2] Y. Wu et al. [Néel-type skyrmion in \$\text{WTe}_2/\text{Fe}_3\text{GeTe}_2\$ van der Waals heterostructure](#). *Nat. Commun.* 11, 3860 (2020).
- [3] Y. Wu et al. [A van der Waals interface hosting two groups of magnetic skyrmions](#). *Adv. Mater.* 34, 2110583 (2022).

Ultrafast dynamics of a spin-polarized electron gas

Benjamin Bakri^{1,*}, Giovanni Manfredi¹, Paul-Antoine Hervieux¹, Nicolas Crouseilles², and Xue Hong²

¹Université de Strasbourg, CNRS, Institut de Physique et Chimie des Matériaux de Strasbourg, UMR 7504, F-67000 Strasbourg, France

²Université de Rennes, Inria Rennes and IRMAR UMR CNRS 6625, F-35042 Rennes, France

*benjamin.bakri@ipcms.unistra.fr

Ultrafast magnetism is an actively explored research area in the general framework of ultrafast phenomena. For instance, the demagnetization of a thin magnetic layer by femtosecond laser pulses [1] and its fundamental origin are still under debate. Ultrafast magnetic phenomena are also crucial to devise and implement effective THz emitters.

In order to describe the coupled charge/spin dynamics in a ferromagnet, a great variety of models are available, going from the time-dependent spin density functional theory to quantum hydrodynamic models. An alternative approach consists in modelling the electrons with a phase-space approach similar to that used in plasma physics. In this approach, the electrons are described by a probability distribution function in the phase-space (x, v) [2]. For particles with spin, four distribution functions are required: one for the density of electrons in the phase space $f_0(x, v, t)$, and three for the spin density $f_i(x, v, t)$, where $i = (x, y, z)$ denotes the spin direction. These distribution functions obey an evolution equation similar to the Vlasov equation of plasma physics, coupled to a Poisson equation for the mean-field Coulomb potential [3, 4]. This constitute the itinerant part of the magnetism. In addition, the fixed-ion magnetism is described by the Landau-Lifschitz equation, coupled to the above spin-Vlasov equation through an exchange term of the Rundermann-Kittel-Kasuya-Yosida (RKKY) type. The overall model [5] is schematized in Fig. 1.

Our work is aimed at studying the dynamics of magnons in an infinite ferromagnetic material. In particular, we investigate the effect of the electron dynamics on the damping and propagation of the magnons. We observe that the magnon amplitude is modulated nonlinearly under strong excitation of the electron dynamics. Tuning the electron polarization at equilibrium η (e.g., through an external magnetic field) can affect the magnon's behavior, leading to either a demagnetization of the ferromagnet or a Gilbert damping of the magnon, depending on the value of η . Thanks to our model, one can have access to the threshold between these regimes. As a first result, we obtained the η -dependency of the magnon evolution.

For an electron polarization consistent with that of the fixed ions ($\eta > 0$ and above a certain threshold), the magnon amplitude decreases with time, in a sort of electron-induced Gilbert damping. In contrast, for low or negative η (corresponding to an "unnatural" polarization of the electrons induced by an external field) the magnon energy increases in time and leads to the demagnetization of the sample. These effects may be used for the ultrafast control of magnonic behaviours through the application of a femtosecond electromagnetic pulse.

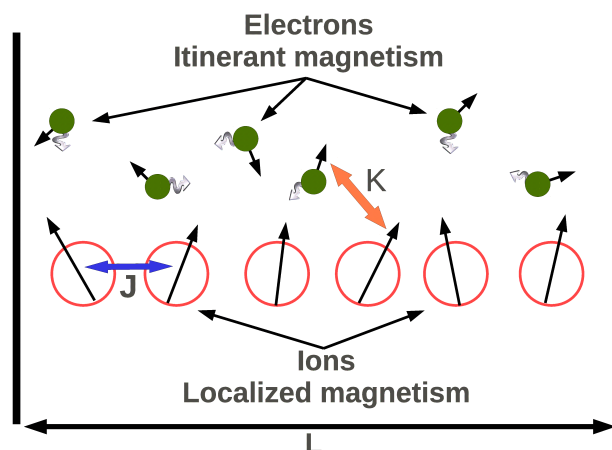


Figure 1: Schematic view of the model coupling the itinerant electron magnetism to the fixed electron magnetism. From [6].

Acknowledgments

This work is supported by France 2030 government investment plan managed by the French National Research Agency under grant reference PEPR SPIN – [SPINTHEORY] ANR-22-EXSP-0009. This work was partially funded by the French National Research Agency (ANR) through the Programme d'Investissement d'Avenir under contract ANR-11-LABX-0058-NIE and ANR-17-EURE-0024 within the Investissement d'Avenir program ANR-10-IDEX-0002-02.

References

- [1] Eric Beaurepaire, J-C Merle, A Daunois, and J-Y Bigot. Ultrafast spin dynamics in ferromagnetic nickel. *Physical review letters* 76, 4250 (1996).
- [2] Giovanni Manfredi. [How to model quantum plasmas](#). *arXiv: quant-ph/0505004* (2005).
- [3] Giovanni Manfredi, Paul-Antoine Hervieux, and Jérôme Hurst. Phase-space modeling of solid-state plasmas. *Reviews of Modern Plasma Physics* 3, 1–55 (2019).
- [4] Nicolas Crouseilles, Paul-Antoine Hervieux, Xue Hong, and Giovanni Manfredi. [Vlasov–Maxwell equations with spin effects](#). *Journal of Plasma Physics* 89, 905890215 (2023).
- [5] Jérôme Hurst, Paul-Antoine Hervieux, and Giovanni Manfredi. [Spin current generation by ultrafast laser pulses in ferromagnetic nickel films](#). *Phys. Rev. B* 97, 014424 (1 2018).
- [6] Benjamin Bakri, Nicolas Crouseilles, Paul-Antoine Hervieux, Xue Hong, and Giovanni Manfredi. [Ultrafast dynamics of a spin-polarized electron plasma with magnetic ions](#). *Journal of Plasma Physics* 91, E9 (2025).

Interlayer dipolar fields stabilize bimerons without Dzyaloshinskii-Moriya interaction in magnetic bilayers

Yuzhang Shi^{1, *}, Moritz A. Goerzen¹, and Dongzhe Li¹

¹*CEMES, Université de Toulouse, CNRS, France*

**shi.yuzhang@cemes.fr*

Bimerons are typically stabilized by interfacial Dzyaloshinskii-Moriya interaction (DMI). Here, we show that bimerons can form even in the absence of DMI in bilayers. This stabilization arises from interlayer dipolar fields, which induce opposite chiralities and mimic the effect of opposite-sign DMI. Using micromagnetic simulations and an analytical model, we quantify this effect and demonstrate its role in bimeron stability. Our work extends dipolar-induced chirality mechanisms to topological solitons in low-DMI systems.

Acknowledgments

This work has been (partially) supported through the grant NanoX no. ANR-17-EURE-0009 in the framework of the "Programme des Investissements d'Avenir". This work was performed using HPC resources from CALMIP.

Addressing bottlenecks in fabrication and reading/writing procedures for PSA-STT-MRAMs

N. Boscolo Meneguolo^{1,*}, J.-C. Toussaint², D. Gusakova¹, F. Disdier¹, E. Gautier¹, R. Sousa¹, L. Cagnon², L. D. Buda-Prejbeanu¹, I.L.Prejbeanu¹, and O. Fruchart¹

¹Univ. Grenoble Alpes, CEA, CNRS, Grenoble INP, SPINTEC, 38000 Grenoble, France

²Univ. Grenoble Alpes, CNRS, Institut Néel, 38000 Grenoble, France

*natalia.boscolomeneguolo@cea.fr

Nowadays, the microelectronic industry has to face two main challenges when developing new technologies for data storage: 1st) the requirement of a continuous downsizing of the devices and 2nd) the improvement of the energy efficiency of the same. The first obstacle becomes insurmountable for standard perpendicular magnetic tunnel junctions (p-MTJs) used as unit cells for MRAMs (Magnetic Random Access Memories). This is because of the physics underlying those structures, where interfacial anisotropy is the main contribution to energy of the system barrier allowing thermal stability. As a consequence, at very small diameters the stability decreases quadratically [1]. To provide a solution to this problem a new geometry for MTJs has been proposed: the PSA-STT-MTJ (Perpendicular Shape Anisotropy Spin Transfer Torque MTJ)[2-4]. In these devices, the free layer has a thickness equal to or larger than its diameter (figure 1). This configuration allows exploiting the volume contribution of the shape anisotropy for enhancing the stability of the system, enabling to target diameters below the 20nm.

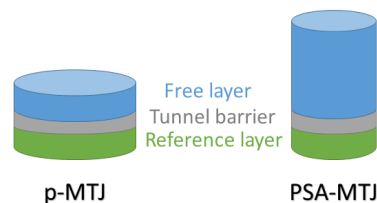


Figure 1: Schematics of a p-MTJ (left) and a PSA-STT-MTJ (right). The free-layer is thicker for the PSA-MTJ.

The work that we will present, concerns a detailed analysis of the PSA-STT-MRAM's free layer using Finite Element Method micromagnetic simulations paired with the local computation of the spin accumulation. Simulations represent a powerful tool when a system has to be optimized: indeed, our purpose is to understand better the physics of the PSA-STT-MRAM in such a way to be able afterwards to improve the switching times of the free layer and reduce the needed critical current to achieve the magnetisation reversal.

We show that several micromagnetic aspects arise specifically because we are considering a 3D nano-objects, while they do not take place in the thin layer of a standard MTJ. First, when dealing with a 3D nanostructure it is no longer possible to neglect the field-like component contribution to the Spin Transfer Torque (while it is a widespread assumption when working with p-MTJs [5]). Second, the magnetisation in a 3D nanopillar takes the configuration of the so-called flower state (i.e. it deviates from the main anisotropic axis at the edges of the structure). This specific configuration affects the dynamics of the system. At the edges, in consequence of the tilted magnetisation, a larger current-induced torque is expected. In our simulations, it is evident that excitation and magnetisation reversal typically begin at the edges of the structure. This aspect becomes more evident when higher electrical currents are used to trigger the magnetisation reversal (figure 2). A direct consequence of the flower state is the existence of non-uniform reversal modes for structures having dimensions close to the one of the dipolar exchange (also figure 2).

We may see that not only the reversal mode becomes of higher order for higher currents but also that the reversal speed becomes faster (the value is provided through the parameter $\tau_{90\%}$ that represents the time needed in order to allow the z-component of the normalized magnetisation to pass from a +1 state to a -0.9 state).

After having investigated theoretically the behaviour of the PSA-STT-MRAM, we wanted to explore the most suitable design of the free layer in order to optimize the energy efficiency through a decrease in needed critical switching current. For this reason, in parallel to the analysis based on micromagnetic simulations, we are working to implement experimentally these 3D nano-magnetic systems. The objective is to realize embedded in-via free layers with a top-deposited tunnel barrier and reference layer. In order to obtain the embedded free layer we etch a regular array of vias in SiO₂ layers. Afterwards, we aim to electrodeposit a ferromagnetic material inside those vias. The reference layer and the top metal contact are obtained through first a physical vapour deposition of the missing stack on the electrodeposited substrates that has been previously submitted to chemical-mechanical polishing. The full MTJ is obtained using a photolithographic process. The main advantage of this novel process flow consists into allowing obtaining denser sample arrays, which is not possible in processes based on ion-beam etching for the definition of the PSA, because it requires grazing-incidence steps and therefore a large separation between the pillars. This increment in throughput meets the first challenge of microelectronic industry: the downsizing.

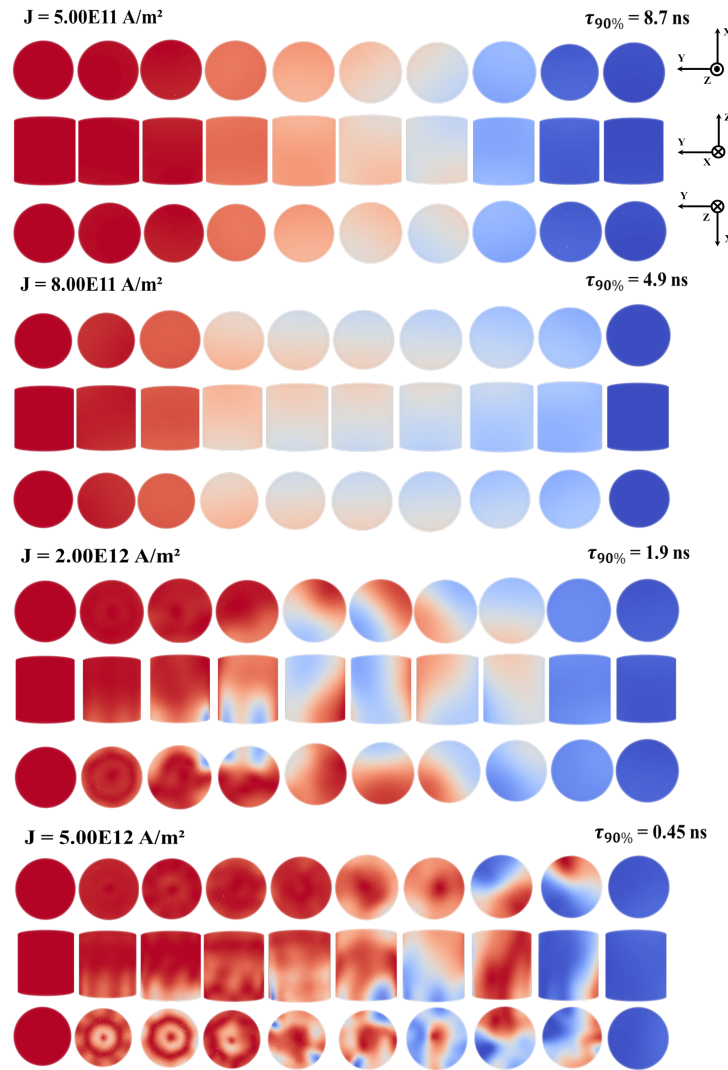


Figure 2: The evolution of the reversal mode is shown for pillars of 20nm diameter and 20nm thickness for a progressively higher injected electrical current density (J). Red color correspond with unit magnetisation m_z pointing along the z -axis upward while blue corresponds to m_z pointing along the z -axis downward.

References

- [1] H. Sato, E. C. I. Enobio, M. Yamanouchi, et al. [Properties of magnetic tunnel junctions with a MgO/CoFeB/Ta/CoFeB/MgO recording structure down to junction diameter of 11nm](#). *Applied Physics Letters* 105 (2014).
- [2] K. Watanabe, B. Jinnai, S. Fukami, H. Sato, and H. Ohno. [Shape anisotropy revisited in single-digit nanometer magnetic tunnel junctions](#). *Nature Communications* 9 (2018).
- [3] N. Perrissin, S. Lequeux, N. Strelkov, et al. [A highly thermally stable sub-20 nm magnetic random-access memory based on perpendicular shape anisotropy](#). *Nanoscale* 10, 12187–12195 (2018).
- [4] N. Caçoilo, S. Lequeux, B.M.S. Teixeira, et al. [Spin-Torque-Triggered Magnetization Reversal in Magnetic Tunnel Junctions with Perpendicular Shape Anisotropy](#). *Physical Review Applied* 16, 024020 (2021).
- [5] A. A. Timopheev, R. Sousa, M. Chshiev, L. D. Buda-Prejbeanu, and B. Dieny. [Respective influence of in-plane and out-of-plane spin-transfer torques in magnetization switching of perpendicular magnetic tunnel junctions](#). *Physical Review B* 92, 104430 (2015).

Altermagnetism from Orbital Ordering the Ruddelsden-Popper Chromates

Quintin N. Meier^{1,*}

¹*Institut Néel, CNRS, 25 av des Martyrs, Grenoble*

**quintin.meier@neel.cnrs.fr*

Altermagnets form a recently identified subclass of collinear antiferromagnets with zero net magnetization but broken time-reversal symmetry, realized through non-relativistic spin splitting of the electronic bands. Altermagnetism is symmetry-allowed if the operation connecting opposite magnetic sublattices is neither a simple translation nor an inversion; thus, its existence imposes restrictions on the crystal symmetry [1].

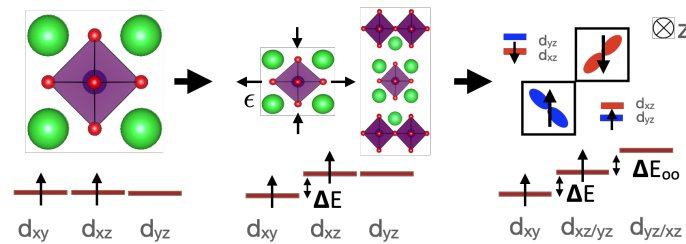


Figure 1: Orbital ordering in the Ruddlesden-Popper strontium chromates.

In the Ruddlesden-Popper $\text{Sr}_{n+1}\text{Cr}_n\text{O}_{3n+1}$ series, the Cr^{4+} ions exhibit an electronic configuration of $d_{xz}^1 d_{xz/yz}^1$, where the d_{xy} orbital is lowered in energy due to the layered geometry of the crystal structure. The doubly degenerate $d_{xz/yz}$ manifold has a tendency towards orbital ordering due to electronic interactions, leading to a state where electrons occupy either the d_{xz} or the d_{yz} orbital on neighboring chromium sites (see Figure 1). This orbital ordering triggers a metal-insulator transition in low- n members of the series [2].

Using first-principles calculations, we explore the interaction between orbital ordering and the antiferromagnetic order in these materials. We demonstrate that orbital ordering breaks the translational symmetry between the two magnetic sublattices, enabling an altermagnetic non-relativistic spin splitting even in the absence of structural distortion [3], an effect that had previously been demonstrated only in model systems [4].

In the layered structures, the distinct orbital ordering and antiferromagnetic patterns can either align or anti-align in adjacent layers, resulting in altermagnetic or compensated (anti-)altermagnetic behavior. In the latter case, the altermagnetic spin splitting has the opposite sign in adjacent layers; however, the layerwise spin splitting remains intact. The relative stability of the altermagnetic and anti-altermagnetic phases in these systems can be tuned through effective dimensionality and strain engineering [3].

References

- [1] Libor Šmejkal, Jairo Sinova, and Tomas Jungwirth. [Emerging Research Landscape of Altermagnetism](#). *Physical Rev X* 12, 040501 (2022).
- [2] Spencer Doyle, Lerato Takana, Margaret A. Anderson, et al. [Effects of Dimensionality on the Electronic Structure of Ruddlesden-Popper Chromates \$\text{Sr}_{n+1}\text{Cr}_n\text{O}_{3n+1}\$](#) . *Phys. Rev. Mater.* 8, L071602 (2024).
- [3] Quintin N. Meier, Alberto Carta, Claude Ederer, and Andres Cano. (Anti-)Altermagnetism from Orbital Ordering in the Ruddlesden-Popper Chromates $\text{Sr}_{n+1}\text{Cr}_n\text{O}_{3n+1}$. *Submitted* (2025).
- [4] Valentin Leeb, Alexander Mook, Libor Šmejkal, and Johannes Knolle. [Spontaneous Formation of Altermagnetism from Orbital Ordering](#). *Phys. Rev. Lett.* 132, 236701 (2024).

Engineering magnetic domain wall energies in multiferroic BiFeO₃ via epitaxial strain

Sebastian Meyer^{1,*}, Bin Xu^{2,3}, Laurent Bellaïche³, and Bertrand Dupé¹

¹TOM/Q-MAT, Université de Liège, B-4000 Sart Tilman, Belgium

²Jiangsu Key Laboratory of Thin Films, School of Physical Science and Technology, Soochow University, Suzhou 215006, China

³Physics Department and Institute for Nanoscience and Engineering, University of Arkansas, Fayetteville, Arkansas 72701, USA

*smeyer@uliege.be

Epitaxial strain has emerged as a powerful tool for tuning magnetic and ferroelectric properties in functional materials such as multiferroic perovskite oxides. Here, we use first-principles calculations to explore the evolution of magnetic interactions in the antiferromagnetic multiferroic BiFeO₃ (BFO), one of the most promising multiferroics for future technology. The epitaxial strain in BFO(001) oriented film is varied between $\varepsilon_{xx,yy} \in [-2\%, +2\%]$. Going from compressive to tensile strain, both exchange and Dzyaloshinskii-Moriya interaction decrease linearly, whereas uniaxial anisotropy prefers a $[11\bar{2}]$ magnetization direction for the calculated range of compressive strain and a $[1\bar{1}0]$ axis for tensile strain. Comparing the ratios of the three interactions, collinear G-type antiferromagnetic order in BiFeO₃ is strengthened for compressive strain due to a large increase of anisotropy by about 40% in accordance with experimental observations [1] (blue line and points of Fig. 1). For tensile strain our results show a similar magnetic ground state as for bulk BFO, where for a slight change in the ratios due to small distortions or impurities, also the collinear ground state can be favored (indicated by error bars in the tensile regime of Fig. 1) [2]. With the renormalization of the domain wall (DW) energy to our previous calculation in Ref. [3], we envision the region where isolated chiral magnetic texture might occur as a function of strain i.e. where the DW and the spin spiral energy are equal. This transition between -1.5% and -0.5% of strain should allow topologically stable magnetic states such as antiferromagnetic skyrmions and merons to occur [4].

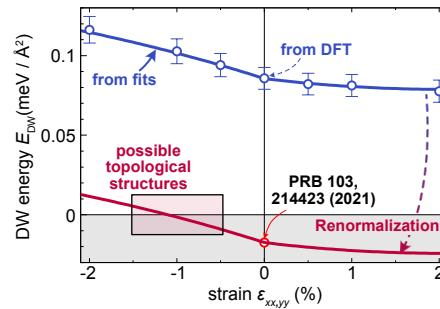


Figure 1: Domain wall energy E_{DW} as a function of applied strain. The blue points are derived from exchange, Dzyaloshinskii-Moriya interaction and uniaxial anisotropy values determined from density functional theory. The blue solid line shows the trend from fits of the respective trends. For large domain wall energies, collinear order is more favorable, for negative DW energies, non-collinear/cycloidal order is preferred. The red point shows the determined value for the R3c phase of according to Ref. [3] where the red line denotes the trend which is renormalized to that point.

References

- [1] H. Béa, M. Bibes, S. Petit, J. Kreisel, and A. Barthélémy. [Structural distortion and magnetism of BiFeO₃ epitaxial thin films: A Raman spectroscopy and neutron diffraction study](#). *Philosophical Magazine Letters* 87, 165–174 (3-4 2007).
- [2] A. Haykal, J. Fischer, W. Akhtar, et al. [Antiferromagnetic textures in BiFeO₃ controlled by strain and electric field](#). *Nature Communications* 11, 1704 (1 2020).
- [3] Bin Xu, Sebastian Meyer, Matthieu J. Verstraete, Laurent Bellaïche, and Bertrand Dupé. [First-principles study of spin spirals in the multiferroic BiFeO₃](#). *Phys. Rev. B* 103, 214423 (21 2021).
- [4] Sebastian Meyer, Bin Xu, Laurent Bellaïche, and Bertrand Dupé. [Engineering magnetic domain wall energies in BiFeO₃ via epitaxial strain: A route to assess skyrmionic stabilities in multiferroics from first principles](#). *Phys. Rev. B* 109, 184431 (18 2024).

Towards switchable magnetic tunnel junctions based on polyoxometalates monolayer

Emma Aoustin^{1,*}, Julie Lion¹, Florian Godel¹, Sophie Colin¹, Etienne Carre¹, Aymeric Vecchiola¹, Abdourahim Hammani², Anna Proust², Florence Volatron², Marie-Blandine Martin¹, Frederic Petroff¹, Pierre Seneor¹, and Richard Mattana¹

¹Laboratoire Albert Fert, CNRS, Thales, Université Paris Saclay, Palaiseau, France

²IPCM, Sorbonne Universités, Université Paris 06, Paris, France

*emma.aoustin@cnrs-thales.fr

Spintronics has revolutionized modern electronics by introducing new possibilities for data storage and magnetic sensing technologies. At its core are magnetic tunnel junctions (MTJs), which consist of two ferromagnetic electrodes separated by a thin insulating barrier. It has been demonstrated that molecules can be integrated into MTJs, leading to the emergence of molecular spintronics, which combines the principles of spintronics with the properties of organic molecules. Indeed, organic materials offer numerous advantages, such as variety, limitless functional possibilities, low cost, and flexibility.

Integrating molecules into MTJs is particularly attractive because it allows for the control of their properties through chemical design. Molecular engineering can be achieved by modifying the anchoring groups, the body, and the head of the molecules to independently adjust the coupling strength between the two ferromagnetic electrodes. Thanks to spin-dependent hybridization at the interfaces between ferromagnetic electrodes and molecules, spin polarization, and consequently tunnel magnetoresistance, can be tuned by the molecules inside a MTJ [1]. However, up to now, mainly passive molecules, such as alkane chains or aromatic rings, have been integrated into MTJs [2] [3]. Despite TMR signals showing the viability of such devices, the electronic properties of these hybrid interfaces cannot yet be controlled in-situ.

We aim to focus on MTJs incorporating more complex molecules, known as "active" molecules, which can be switched between different stable states in response to an external stimulus (such as light, pressure, or an electric field). The energy gap and coupling strength to the electrodes depend on the state of the molecule. Thus, modifying the molecule can lead to a modulation of the spin polarization at the interface. As a result, the properties of MTJs can potentially be tuned by switching the molecule's state. Among the wide variety of these "active" molecules [4], electrically addressable molecules are particularly promising for future applications.

In this study, we focus on polyoxotungstate ($PW_{11}O_{10}(SiC_3H_6SH)_2$) redox-switchable molecules, which belong to the polyoxometalate (POM) family. These molecules are composed of a POM complex with tungsten atoms, along with an alkane chain and a thiol group at the end, forming the anchoring group that creates a covalent bonding with the ferromagnetic electrode (see Fig. 1).

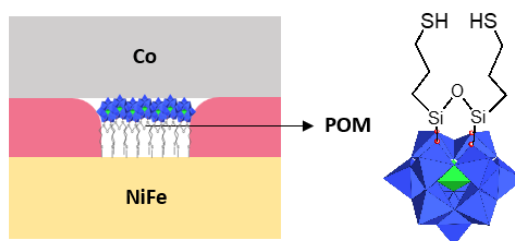


Figure 1: Representation of a magnetic tunnel junction (MTJ) integrating POM molecules

First, we need to confirm the grafting of molecules onto a ferromagnetic metal (NiFe). We have developed a protocol to form a self-assembled monolayer, and we verify it by doing XPS measurements. Next, we can focus on investigating the electrical switching of the molecules by performing CT-AFM measurements. This technique is used to measure current-voltage curves between an AFM tip and a substrate. In our system, the current is transmitted by tunnel effect through the molecular monolayer. A map of multiple current-voltage curves is shown in Fig. 2. We demonstrate that after applying a high voltage of 4V on the sample, the current increases, indicating a change in the resistance of the tunnel barrier, resulting in a modification of the molecule state. This is the first sign of commutation between two states by external electric stimulus.

The next objective is to integrate these molecules into a NiFe/POMs/Co MTJ. We will discuss the various challenges encountered during the device fabrication process and present the preliminary electrical characterization of the MTJ, which demonstrate that switchable polyoxometalate monolayer can be successfully integrated in MTJs. Finally, we were able to observe TMR signal in these junctions (see Fig. 3), demonstrating the spin-dependent transport in the MTJ. With the demonstration of the switching of POMs by applying voltage, and our ability to integrate them in a device, we are getting closer to developing multifunctional spintronic devices.

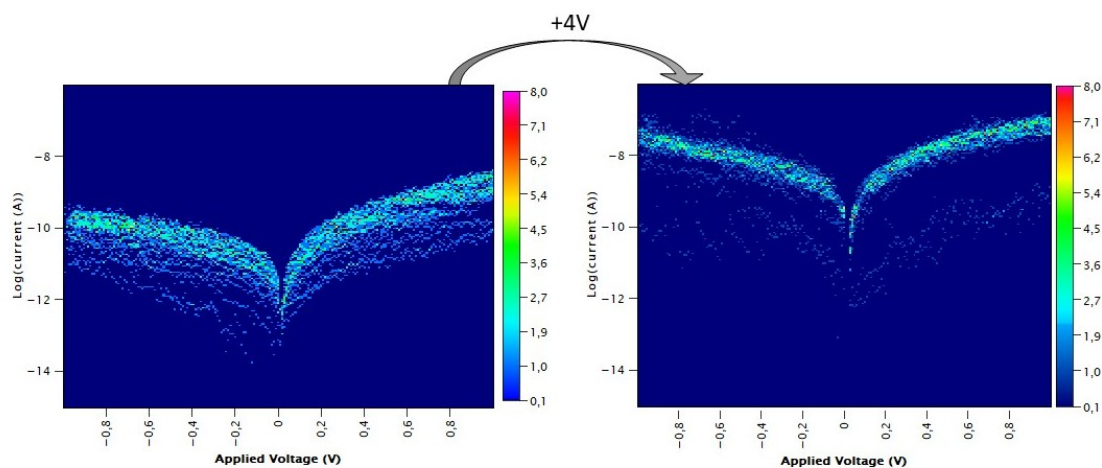


Figure 2: Map of current-voltage curves at initial state (left), and after applying +4V (right)

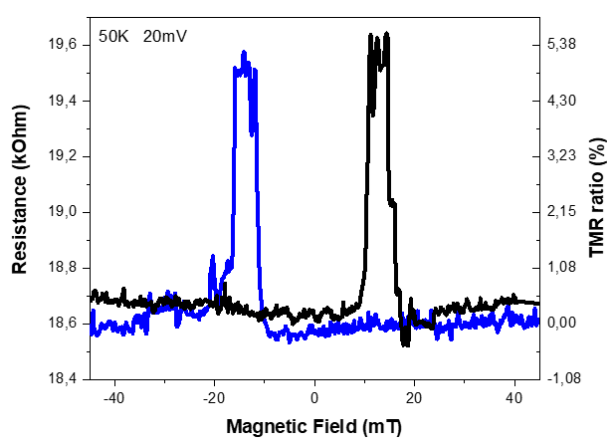


Figure 3: Magnetoconductance signal in a NiFe/POMs/Co MTJ measured at 50K and 20mV

References

- [1] Clément Barraud, Pierre Seneor, Richard Mattana, et al. [Unravelling the role of the interface for spin injection into organic semiconductors](#). *Nature Physics* 6, 615–620 (2010).
- [2] J. R. Petta, S. K. Slater, and D. C. Ralph. [Spin-Dependent Transport in Molecular Tunnel Junctions](#). *Physical Review Letters* 93 (2004).
- [3] Marta Galbiati, Clément Barraud, Sergio Tatay, et al. [Unveiling Self-Assembled Monolayers' Potential for Molecular Spintronics: Spin Transport at High Voltage](#). *Advanced Materials* 24, 6429–6432 (2012).
- [4] Wei Liu, Sha Yang, Jingtai Li, Guirong Su, and Ji-Chang Ren. [One molecule, two states: Single molecular switch on metallic electrodes](#). *WIREs Computational Molecular Science* 11 (2020).

Design of an arithmetic logic unit (ALU) using ferroelectric spin orbit (FESO) devices

Vincenzo Giannone¹, Paolo Sgarro¹, Chadi Al Khatib¹, Maxime Culot^{1,*}, Théo Frottier¹, Williams Savero-Torres², Lorena Anghel¹, Manuel Bibes^{2,3}, Guillaume Prenat¹, Louis Hutin⁴, Laurent Vila^{1,2}, and Jean-Philippe Attané^{1,2}

¹Spintec, UGA, CEA, CNRS, Grenoble, France

²Nellow, Grenoble, France

³Laboratoire Albert Fert, CNRS, Thales, UPS, Palaiseau, France

⁴LETI, UGA, CEA

*maxime.culot@spintec.fr

While transistor size and voltage scaling have allowed CMOS technology to offer a continuous increase in computing efficiency, it is now close to its technological limit. Indeed, the progressive increase of leakage attributed to the Boltzmann Tyranny has led to the end of Dennard's law. In this context, new spintronics based devices have recently been proposed as beyond CMOS candidates such as the MESO (MagnetoElectric Spin Orbit) device of Intel which exhibits memory and logic properties and has the potential to operate at the aJ scale [1]. These performances are possible thanks to a low power ferroelectric-based writing of the memory and a magnetoelectric coupling enabling a spin charge interconversion (SCI) based readout of the memory. This allows the device to work as a memory and produce an output charge current enabling logic. More recently, the FESO (FerroElectric Spin Orbit) device has been proposed by the Spintec laboratory with the same low power computing properties as the MESO device [2] (Fig. 1 (a)). However, it is a simpler concept that gets rid of the magnetoelectric element thanks to a direct control of the SCI by the ferroelectric state. In this work, we present a compact model for the FESO device (Fig. 1 (c)), simulated in the Cadence virtuoso environment. Using this model, we demonstrate the suitability of the FESO device for sequential and combinational logic and extract the required performance of the single FESO device for these applications. The FESO based basic elements for an ALU (majority gate illustrated in Fig. 1 (b), multiplexer, full adder, multiplier) are conceptualized and simulated to build a 4-bit FESO based ALU. The benefits in terms of area and energy consumption of the approach are evaluated. The expected area gains with respect to CMOS technology are summarised in table 1.

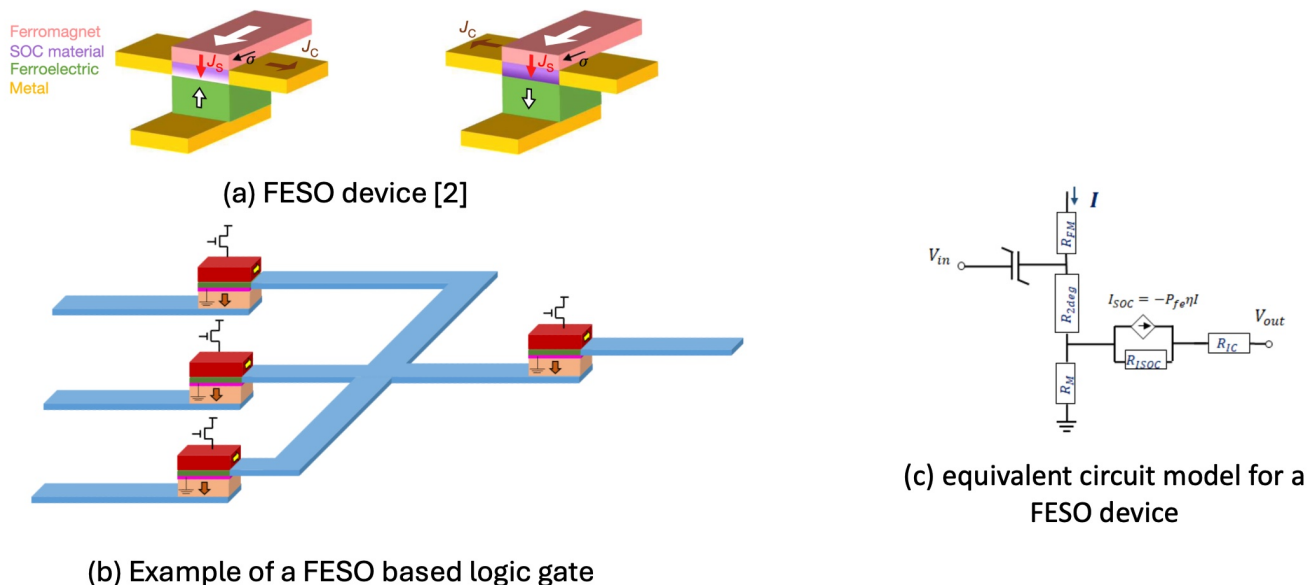


Figure 1: Modelling of FESO device

Acknowledgments

This work was supported by the ECOM project (ANR-22-PEEL-0009) and by the SPINFROST project (ANR-23-CE24-0010) from the Agence Nationale de la Recherche.

Circuits	N° of elements in FESO technology		N° of elements in CMOS technology	Potential area gain
	FESO device	Transistor		
NOT gate	1	2	2	2
Memory cell	1	2	6	3
D-latch	1	1	22	22
D-FlipFlop	1	2	32	16
3-input Majority gate	4	4	12	3
Full adder	10	10	28	2.8
Multiplier	14	14	34	2.43
Proposed 4-bit ALU	380	380	940	2.47

Table 1: Potential area gain of circuit elements realised with FESO with respect to CMOS Technologies

References

- [1] Sasikanth Manipatruni, Dmitri E. Nikonov, Chia-Ching Lin, et al. [Scalable Energy-Efficient Magnetoelectric Spin–Orbit Logic](#). *Nature* 565, 35–42 (2019).
- [2] Paul Noël, Felix Trier, Luis M. Vicente Arche, et al. [Non-Volatile Electric Control of Spin–Charge Conversion in a SrTiO3 Rashba System](#). *Nature* 580, 483–486 (2020).

Vortex gyrotropic mode excited by surface acoustic waves

R. Lopes Seeger^{1,2,*}, F. Millo¹, G. Soares², J.-V. Kim¹, A. Solignac², G. de Loubens², and T. Devolder¹

¹Centre de Nanosciences et de Nanotechnologies, CNRS, Université Paris-Saclay, 91120 Palaiseau, France

²SPEC, CEA, CNRS, Université Paris-Saclay, 91191 Gif-sur-Yvette, France

*rafaelseeger@gmail.com

One particularly interesting example of magnetization dynamics is found in magnetic vortices. These structures are an inhomogeneous magnetic texture that can be formed in magnetic nanodisks, featuring in-plane magnetization curling along the disk's perimeter and out-of-plane magnetization at the center, which defines the vortex core [1]. At remanence the vortex core is localized at the center of the disk. Resonant excitation by a microwave field induces gyrotropic dynamics of the vortex core [2]. Recently, it has been proposed by simulations that surface acoustic waves (SAWs) can excite the gyrotropic mode of the vortex state in a magnetic disk [3].

Here we report on experiments utilizing a magnetic resonance force microscope to investigate magnetization dynamics in CoFeB sub-micrometer disks in the vortex state, grown on a Z-cut LiNbO₃ substrate [4]. Our device design enables excitation of the gyrotropic mode either inductively, using an antenna on top of the disks, or acoustically via SAWs launched from an interdigital transducer (IDT) (Fig. 1, left). These experiments demonstrate the clear excitation of the vortex gyrotropic mode by magneto-acoustic excitation. Our modelling indicates that the lattice rotation ω_{xz} generates a localized magnetoacoustic field that displaces the vortex from the disk center (Fig. 1, right). Combined with the other non-vanishing strain terms (ϵ_{xx} and ϵ_{zz}) that results in an additional magnetoacoustic excitation field that allows driving the vortex gyrotropic mode.

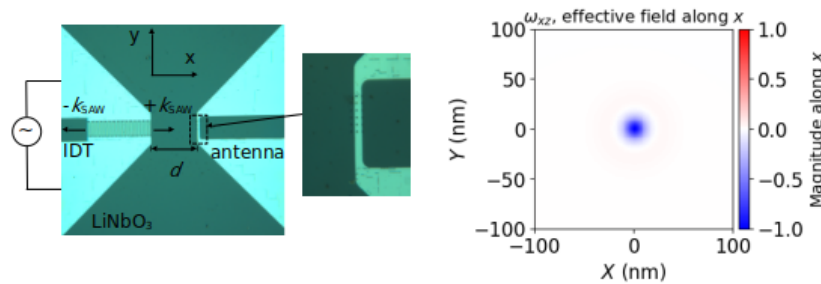


Figure 1: (left) Optical image of the experiment to detect the vortex gyration induced by SAWs. An IDT excites SAWs on a piezoelectric substrate towards a disk in the vortex state. The setup includes a top antenna for inductive excitation. (right) Normalized magnetoacoustic field (b_{eff}) distribution over the vortex due to the rotation ω_{xz} at zero applied field, with color coding indicating the x-direction field.

Acknowledgments

This work was supported by the Agence Nationale de la Recherche (ANR) under Contract No. ANR-20-CE24- 0025 (MAX-SAW), the “Investissements d’Avenir” program LabEx NanoSaclay, under Contract No. ANR- 10-LABX-0035 (SPICY), and the France2030 program PEPR SPIN, under Contract Nos. ANR-22-EXSP-0008 and ANR-22-EXSP-0004.

References

- [1] R. P. Cowburn, D. K. Koltsov, A. O. Adeyeye, M. E. Welland, and D. M. Tricker. [Single-Domain Circular Nanomagnets](#). *Phys. Rev. Lett.* 83, 1042–1045 (5 1999).
- [2] V. Novosad, F. Y. Fradin, P. E. Roy, et al. [Magnetic vortex resonance in patterned ferromagnetic dots](#). *Phys. Rev. B* 72, 024455 (2 2005).
- [3] A. Koujok, A. Riveros, D. R. Rodrigues, et al. [Resonant excitation of vortex gyrotropic mode via surface acoustic waves](#). *Applied Physics Letters* 123, 132403 (2023).
- [4] R. Lopes Seeger, F. Millo, G. Soares, et al. [Experimental observation of vortex gyrotropic mode excited by surface acoustic waves](#). 2024. arXiv: [2409.05998](https://arxiv.org/abs/2409.05998) [[cond-mat.mtrl-sci](#)].

Towards ultrafast deterministic switching in magnetic memory by laser excitation

Quoc Trung Trinh^{1,*}, David Salomoni¹, Yi Peng², Stéphane Auffret¹, Mouad Fattouhi¹, Gregory Malinowski², Stéphane Mangin², Ioan-Lucian Prejbeanu¹, Michel Hehn², Liliana Buda-Prejbeanu¹, and Ricardo Sousa¹

¹Université Grenoble Alpes, CEA, CNRS, Grenoble INP, SPINTEC, 38000 Grenoble, France

²Université de Lorraine, CNRS, IJL, F-54000 Nancy, France

*quoc-trung.trinh@cea.fr

Recent advances in ultra-fast switching in magnetic memory have been made possible by fs and ps pulse laser excitation of magnetic tunnel junctions (MTJs) integrated with Tb/Co multilayers [1, 2]. The underlying mechanism behind the magnetization reversal relies on the precessional motion of the ferromagnetic layer initiated by the demagnetization induced by the laser pulse. During the thermal demagnetization of the rare-earth metallic layer, the magnetic moment precesses around quickly, changing its effective anisotropy axis. Depending on the cooling time and the input energy of the laser beam, the magnetic moment moves along a trajectory that crosses the X-Y plane and subsequently relaxes back to its initial or to a reversed orientation along the perpendicular Z axis [3, 4]. Fabricated MTJ devices with tunnel magnetoresistance (TMR) up to 74% showed consistent all-optical switching (AOS) magnetization reversal under 50-fs laser pulses [5]. However, the dependence of the magnetization reversal on the precessional motion of the magnetic moment implies that the magnetic state cannot be deterministically defined from the point of view of memory storage. This leads to the biggest challenge for AOS-MTJs when applied in real memory applications due to its toggle switching under a laser pulse. Furthermore, current developments in the AOS-MTJs nanopillar devices are still limited by their low thermal budgets and electrical properties, notably by the low thermal annealing conditions and high resistance area values, somewhat limiting their compatibility with CMOS technology.

Our current work addresses a possible deterministic switching in AOS-MTJs devices by combining the ultrafast localized heating from the laser pulse with the spin-polarized current (Fig. 1a). Macrospin simulations have successfully indicated the possibility for the spin-polarized current to impact the optically induced magnetic switching of the ferromagnetic system. During the precessional motion of the free layer, the spin-polarized current exerts a torque on the magnetization, driving it to eventually relax in the desired magnetic state. These findings serve as an essential theoretical basis for conducting this experiment on manufactured nanopillar devices (Fig. 1b). Furthermore, the results from the model also show that the spin-transfer torque from the applied voltage not only reduces the threshold fluence for successive magnetic switching, but also assists the reversal resulting in a faster re-orientation of the magnetization during the precessional dynamics, hence, decreasing the switching time and energy required (Fig. 2).

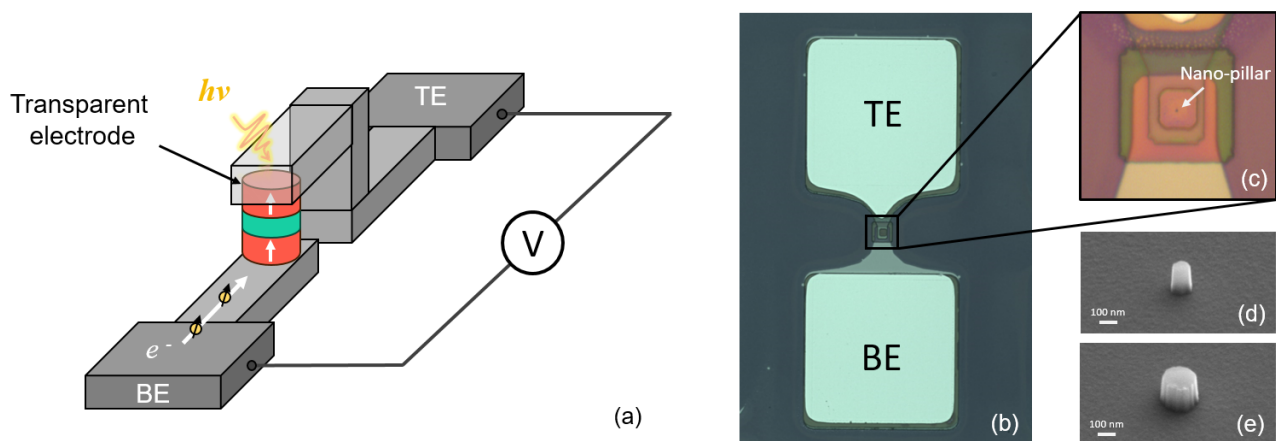


Figure 1: Schematic illustration of AOS-MTJ devices under the effect of laser excitation and spin-polarized current (a); Microscope image of the final patterned AOS-MTJs device (b); The close view of a fabricated window with an underlying nano-pillar (c); SEM images of nano-pillar devices with different diameters: 100 nm (d), and 200 nm (e).

In the AOS-MTJ stack structure, a thin MgO capping layer at the top of Tb/Co multilayers can also be used to increase the thermal endurance of the stack up to 350°C annealing temperature. Simultaneously, the oxidation conditions of the Mg layer were optimized to achieve both high anisotropy and thermal stability with a thin tunnel barrier. These improvements reduce the resistance area of the AOS-MTJs stack to levels compatible with spin-transfer torque effects assisting the magnetic switching during the precessional motion, as predicted by the simulation results.

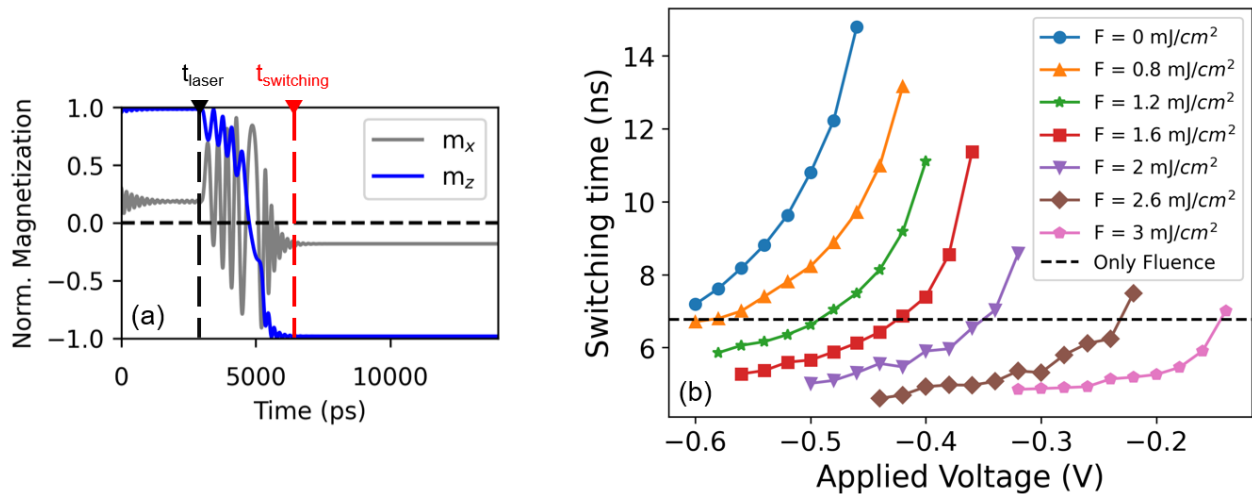


Figure 2: Example of time traces of m_x , m_z components under fluence and applied voltage ($F = 2 \text{ mJ/cm}^2$, $V = -0.4 \text{ V}$). The dashed lines represent the laser excitation moment (black), and the switching time of reversed magnetic moment at the relaxed state (red) (a); Effect of laser fluence and applied voltage on the switching time of the magnetic system (b).

References

- [1] L Avilés-Félix, L Álvaro-Gómez, G Li, et al. Integration of Tb/Co multilayers within optically switchable perpendicular magnetic tunnel junctions. *Aip Advances* 9 (2019).
- [2] L Avilés-Félix, Aurélien Olivier, Guanqiao Li, et al. Single-shot all-optical switching of magnetization in Tb/Co multilayer-based electrodes. *Scientific reports* 10, 5211 (2020).
- [3] Kshiti Mishra, Thomas GH Blank, CS Davies, et al. Dynamics of all-optical single-shot switching of magnetization in Tb/Co multilayers. *Physical Review Research* 5, 023163 (2023).
- [4] Y Peng, D Salomoni, G Malinowski, et al. In-plane reorientation induced single laser pulse magnetization reversal. *Nature Communications* 14, 5000 (2023).
- [5] D Salomoni, Y Peng, L Farcis, et al. Field-free all-optical switching and electrical readout of Tb/Co-based magnetic tunnel junctions. *Physical Review Applied* 20, 034070 (2023).

Study of skyrmions in ferromagnetic metallic superlattices using in situ Lorentz magnetic methods

Anaïs Fondet^{1,*}, Thomas Blon², Anne Bernard-Mantel¹, and Christophe Gatel¹

¹CEMES-CNRS, Toulouse, France

²LPCNO, Toulouse, France

*anaïs.fondet@cemes.fr

Magnetic skyrmions, which consist of local swirls of spins, are a prime example of topologically nontrivial spin textures. Nanoscale isolated skyrmions exist at low temperature in bulk chiral materials, while in thin films and multilayers, room temperature (RT) stable skyrmions exhibit intermediate sizes ranging between 50 nm to a few μm . Ferromagnetic metallic superlattices are materials which are promising for the development of RT nanoscale skyrmions due to the high tunability of their properties. There exist a large number of experimental studies reporting the observation of stripe domains and skyrmion bubbles in metallic multilayers, for example Pt/Fe/Ir[1] and Ta/Co/Pt[2]. It is well understood that these skyrmions and stripes are created by a combined action of the stray field effect and the Dzyaloshinskii-Moria interaction (DMI)[3]. These non-collinear spin structures can also be easily simulated numerically [2]. However, in a system with a high number of degrees of freedom, the quest remains open regarding how to optimize the parameters to obtain the most compact and stable skyrmion and the development of adequate analytical tools could lead to breakthrough and transform this quest from a random walk to a guided tour. Many experimental techniques have been used throughout the years in order to study skyrmions, including Magnetic Force Microscopy[4], soft-x-ray microscopy[1] and Magneto-Optical Kerr Effect (MOKE) microscopy [5] among others. However, quantitative nanoscale studies on the conditions of skyrmion nucleation remains of primary importance. In this study, we chose to study skyrmions in a classical $[\text{Pt}/\text{Co}/\text{Ta}]_n$ metallic superlattices system, n being the number of repetitions of the trilayer.

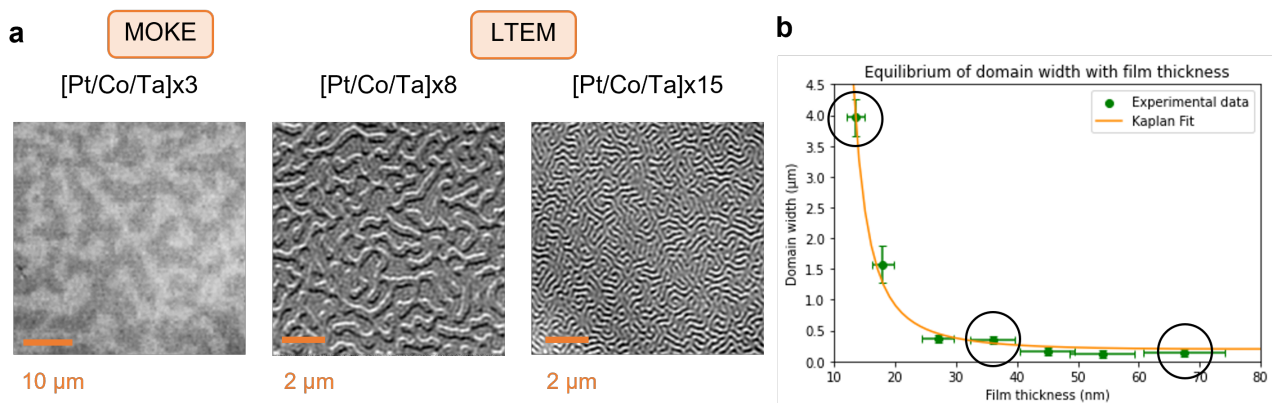


Figure 1: (a) MOKE and LTEM observations of stripe domains at zero applied field for different numbers of repetition n , and (b) the stripe domain width as a function of the multilayer thickness in $[\text{Pt}/\text{Co}/\text{Ta}]_n$ multilayers with circled points extracted from images of (a), fitted with Kaplan stripe domains model.

In this system, RT skyrmionic bubbles as small as 50 nm have been observed when the Co thickness was tuned close to the spin reorientation transition[2]. In our study, we fixed the Co thickness at 0.8 nm and we tuned the thickness of the total system by varying the number of repetitions n of the Pt/Co/Ta tri-layer. This allows us to tune selectively the effect of the stray field while keeping roughly constant the system intrinsic parameters (magneto-crystalline anisotropy, saturation magnetisation, DMI). We were able to image the magnetic micro-structures of $[\text{Pt}/\text{Co}/\text{Ta}]_n$ multilayers with various different number of repetitions in LTEM and MOKE (Figure 1a). In the first place, we conducted an experimental study of the stripe domain structures as a function of the multilayer total thickness, see Figure 1b. Moreover, when applying a magnetic field (using the objective lens), we studied the formation process of magnetic skyrmions, the stripe-skyrmion transition, and the presence of skyrmion lattice or isolated skyrmions in different samples. We could correlate the magnetic contrast observations with applied field to the magnetic hysteresis obtained from VSM measurements.

In addition, we studied the influence of temperature on the stripe pattern and on the formation of skyrmions, under LTEM, from which we could elaborate experimental phase diagrams coupled to theoretical diagrams, based on the skyrmionic bubble model (Figure 2). We will present our understanding of these diagrams obtained by combining the observations with the model and magnetometry measurements.

Finally, we performed EH experiments on these same samples, combining high spatial resolution with a dedicated Lorentz stage, direct electron detector with the K3 camera and long exposure time up to 4 mn thanks to the dynamical correction of instabilities and dedicated image treatment. We were able to recover the magnetic phase of the Néel type skyrmions up to few nanometers of spatial resolution, and to observe the detailed stripe-to-skyrmion transition with external applied magnetic field (Figure 3). We will detail the magnetic processes which has been deduced from such observations combined with simulations.

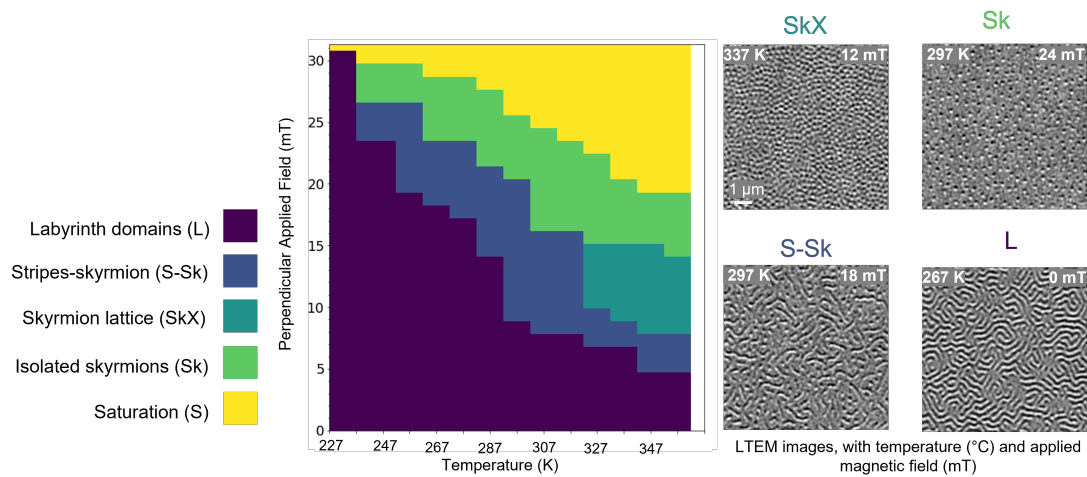


Figure 2: Experimental phase diagram (B-T) constructed from series of LTEM images for $[\text{Pt}/\text{Co}/\text{Ta}]_{\text{x}12}$. The LTEM images show the different phases observed and identified in the phase diagram.

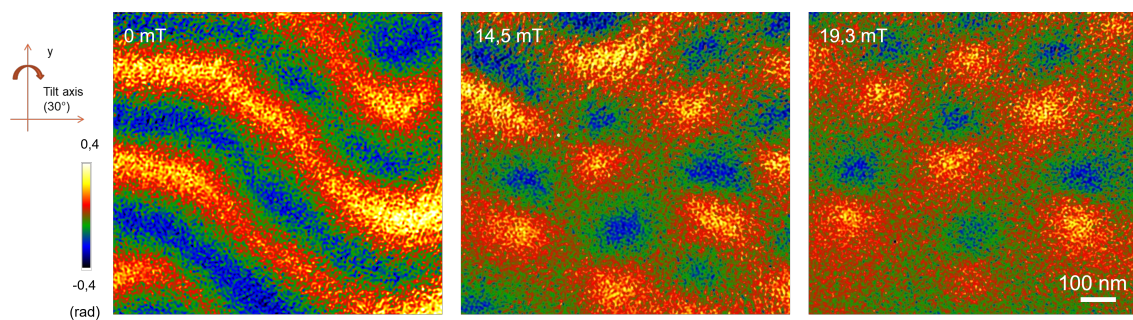


Figure 3: Magnetic phase images of $[\text{Pt}/\text{Co}/\text{Ta}]_{\text{x}10}$ sample extracted from respective holograms at different in-situ applied fields, with the sample tilted by 30° . A circular mask has been applied in Fourier space leading to 7 nm spatial resolution.

References

- [1] C. Moreau-Luchaire, C. Moutafis, N. Reyren, et al. [Additive interfacial chiral interaction in multilayers for stabilization of small individual skyrmions at room temperature](#). *Nature Nanotechnology* 11, 444–448 (2016).
- [2] Lei Wang, Chen Liu, Nasir Mehmood, et al. [Construction of a Room-Temperature Pt/Co/Ta Multilayer Film with Ultrahigh-Density Skyrmions for Memory Application](#). *ACS Applied Materials & Interfaces* 11, 12098–12104 (27, 2019).
- [3] Anne Bernard-Mantel, Lorenzo Camosi, Alexis Wartelle, et al. [The skyrmion-bubble transition in a ferromagnetic thin film](#). *SciPost Physics* 4, 027 (25, 2018).
- [4] A. Hrabec, J. Sampaio, M. Belmeguenai, et al. [Current-induced skyrmion generation and dynamics in symmetric bilayers](#). *Nature Communications* 8, 15765 (8, 2017).
- [5] Marine Schott, Anne Bernard-Mantel, Laurent Ranno, et al. [The Skyrmion Switch: Turning Magnetic Skyrmion Bubbles on and off with an Electric Field](#). *Nano Letters* 17, 3006–3012 (10, 2017).

Optimization of synthesis and growth of layered ferromagnetic oxides

Dorian Morley^{1,2,*}, David Spenato³, David Dekajevi³, Jean-Philippe Jay³, Alexandre Lebon⁴, Jean-Christophe Le Breton¹, Pascal Turban¹, and Valérie Demange²

¹*Institut de Physique de Rennes, Université de Rennes - CNRS, Rennes, France*

²*Institut des Sciences Chimiques de Rennes, Université de Rennes - CNRS, Rennes, France*

³*Laboratoire d'Optique et de Magnétique, Université de Brest, Brest, France*

⁴*Laboratoire de Chimie Électrochimie Moléculaires et Chimie Analytique, Université de Brest, Brest, France*

*dorian.morley@univ-rennes.fr

Spintronics is one of the promising ways to further develop electronic systems, in particular with the aim of greatly reducing energy consumption while maintaining growing performances. One of the present challenges for the development of 2D-based magnetic tunnel junctions is the synthesis of air-stable 2D ferromagnet with Curie point higher than room-temperature.

This presentation focuses on the development of synthesis of 2D-TFCO ($Ti_{0.8-x/4}Fe_{x/2}Co_{0.2-x/2}O_2$), doped-titanate oxide nanosheets, an original 2D oxide stable in ambient atmosphere which could have suitable magnetic properties at room temperature for spintronics uses[1]. TFCO oxide nanosheets are produced via the exfoliation of a bulk layered parent oxide of KTFCO ($K_{0.4}Ti_{0.8-x/4}Fe_{x/2}Co_{0.2-x/2}O_2$), synthesized by solid-state chemistry methods. Our recent advancements in the optimization of synthesis and growth have permitted us to obtain millimetric KTFCO single crystals (see Fig.1a), suitable for bulk properties analysis prior to the exfoliation of large area TFCO nanosheets.

Latest results on KTFCO crystals characterizations will be presented, especially their magnetic properties with Curie point above room temperature (see Fig.1b). Structural properties coupled with vibrational spectroscopies of the layered phase will also be presented. Finally, some of the early results of exfoliation of KTFCO crystals as TFCO-nanosheets will also be shown to demonstrate their possible use as nanometrically thin materials suitable in spintronics heterostructures.

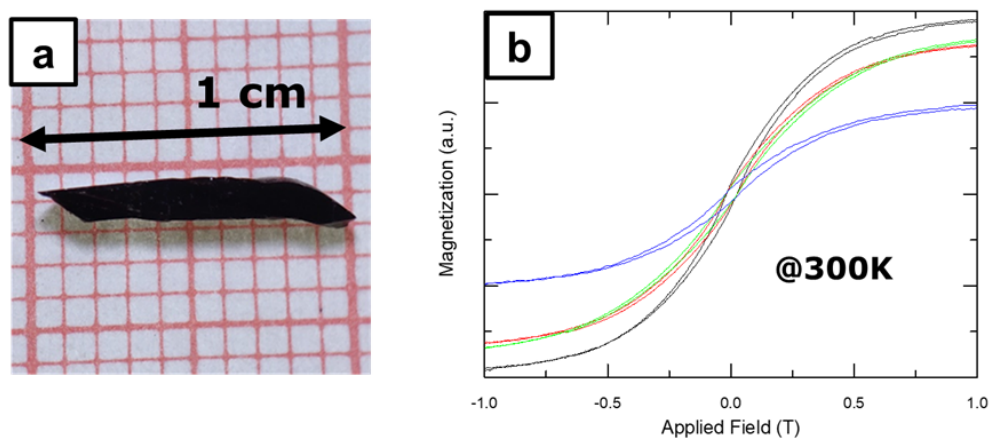


Figure 1: a) Picture of millimetric KTFCO layered crystal grown using molten salts method; b) Ferromagnetic hysteresis measured at 300K on a bulk crystal of KTFCO with field applied in-plane (black, red, green curves) and out-of-plane (blue curve) of titanate layers.

Acknowledgments

This work is financially supported by the French ANR (Agence Nationale de la Recherche) organization, in the framework of the ONSET project (ANR-22-CE09-0010) and the France 2030 PEPR SPINTRONIQUE program (ANR-22-EXSP 0007).

References

- [1] M. Osada, S. Yoguchi, M. Itose, et al. [Controlled doping of semiconducting titania nanosheets for tailored spinel electronic materials](#). *Nanoscale* 6, 14227–14236 (2014).

Polarization analysis of multi-magnon excitations in LaFeO₃ thin films using RIXS

Nora Lahmiti^{1,2}, Marcel Hennes², and Hebatalla Elnaggar¹

¹*Institute of Mineralogy, Physics of Materials and Cosmochemistry (IMPMC), Sorbonne University, Paris, France*

²*Institute of NanoSciences of Paris (INSP), Sorbonne University, Paris, France*
*nora.lahmiti@sorbonne-universite.fr

Using magnons, quasiparticles representing the fundamental units of collective magnetic oscillations, as information carriers yields significant advantages over classical approaches relying on electron transport. Recent studies have emphasized the potential of THz magnons for advanced information processing [1], as high-frequency magnons enable faster information transfer, aligning with current technological demands. In this context, a novel phenomenon in the field of THz-frequency magnons has been unveiled: high-energy magnon cascades in α -Fe₂O₃ [2], where a single photon excitation, within a 2-photon scattering process, generates multiple propagating magnons, called multi-magnons.

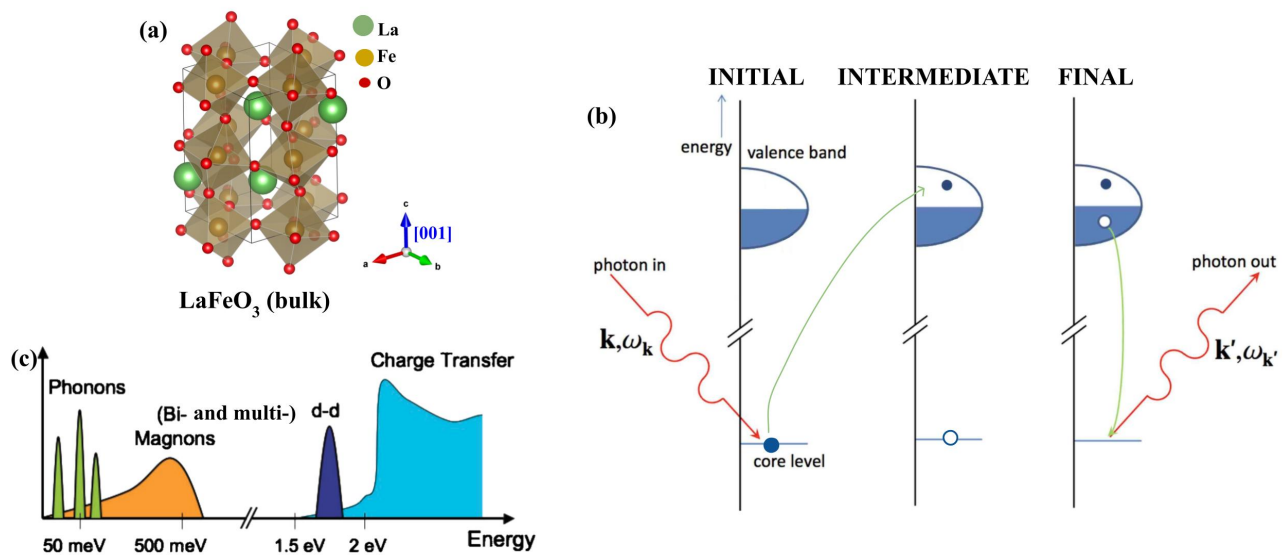


Figure 1: (a) Orthorhombic unit cell of LaFeO₃ (LFO). (b) Schematic representation of the Resonant Inelastic X-ray Scattering (RIXS) process [3]. A photon with energy $\hbar\omega_k$ excites an electron from the core level to a higher energy state. This excitation creates an intermediate state, with a core hole. Finally, a valence electron (not necessarily the excited one) fills the core hole, emitting a photon with energy $\hbar\omega_{k'}$. (c) Different elementary excitations that occur in materials and their corresponding energy scale[3].

To gain a better understanding of the mechanisms governing the behavior of multi-magnons, we conducted Resonant Inelastic X-ray Scattering (RIXS) experiments on orthorhombic, antiferromagnetic LaFeO₃/SrTiO₃(001) (LFO/STO) thin films (fig1.a) at the ESRF synchrotron in Grenoble. RIXS technique is a photon-in/photon-out technique, where an incoming photon (fig1.b-initial state) excites an electron to a higher energy level(fig1.b-intermediate state), and an outgoing photon results from a decay process in the material (fig1.b-final state). By analyzing the energy, momentum, and polarization differences between the incoming and outgoing photons, a multitude of excitations in the material can be probed, including multi-magnons, as shown in figure 1.c.

In this contribution, I will present our RIXS data and focus on the photon polarization analysis, which allowed us to derive selection rules for multi-magnon excitations. Furthermore, we investigated the possible role of phonon modes during multi-magnon excitation process. This study serves as an initial step to examine the primary characteristics of multi-magnon excitations in perovskite thin films and will pave the way for future multi-magnon "engineering" via substrate strain and doping.

Acknowledgments

We thank the staff of ID32 at the ESRF for their help with the data acquisition and analysis. We also thank Mr. M.Lazem and Dr. Y.Birkholzer for their help during the beamtime and for the sample preparation. We also thank the Institut de Science des Matériaux (IMAT) of the Alliance Sorbonne Université for funding this PhD.

References

- [1] Khalil Zakeri. [Terahertz magnonics: Feasibility of using terahertz magnons for information processing](#). *Physica C: Superconductivity and its Applications* 549, 164–170 (2018).
- [2] Hebatalla Elnaggar, Abhishek Nag, Maurits W. Haverkort, et al. [Magnetic excitations beyond the single- and double-magnons](#). *Nature Communications* 14 (2023).
- [3] Luuk J. P. Ament, Michel van Veenendaal, Thomas P. Devereaux, John P. Hill, and Jeroen van den Brink. [Resonant inelastic x-ray scattering studies of elementary excitations](#). *Reviews of Modern Physics* 83, 705–767 (2011).

Imaging Antiferromagnetic Texture in Epitaxial Mn_3Sn Thin Films with Scanning NV center Magnetometry

Elijah Wane^{1,*}, Carolin Schrader¹, Charles Guillemard², Matthieu Petit², Lisa Michez², Vincent Jacques¹, and Aurore Finco¹

¹Laboratoire Charles Coulomb, Université de Montpellier, CNRS, Montpellier, France

²CINAM, Université d'Aix Marseille, CNRS, Marseille, France

*elijah.wane@umontpellier.fr

Non-collinear antiferromagnets (AFMs) attract significant interest because of their novel magnetic orders, unique spin dynamics, and promising applications in energy-efficient spintronic devices. A key advantage of AFMs is their vanishingly small stray fields, which enhance stability against external magnetic perturbations, enabling high data retention and the potential for high-density memory integration. To harness these advantages in practical magnetic devices, a deeper understanding of AFM spin structures and dynamics is crucial. Mn_3Sn , a non-collinear antiferromagnet, exhibits a slightly distorted kagome lattice structure in which magnetic moments form an inverse triangular configuration, see Fig 1. This unique arrangement leads to a small remnant magnetic moment due to only one of the three moments in each Mn triangle being parallel to the local easy-axis, breaking perfect antiferromagnetic compensation. It has also been demonstrated that Mn_3Sn exhibits a large anomalous Hall effect (AHE) at room temperature. Unlike the AHE observed in ferromagnets, which arises from net magnetization, the AHE in Mn_3Sn originates from its chiral spin texture and Berry curvature effects in momentum space. The exotic spin properties of Mn_3Sn make it a model material for exploring unconventional magnetic textures [1].

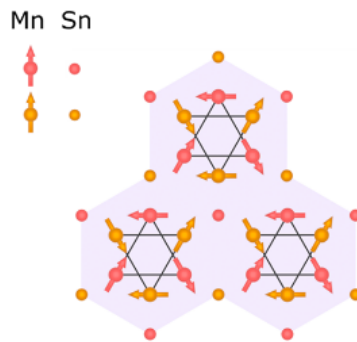


Figure 1: Magnetic structure of Mn_3Sn , top view of the ab plane [2].

This work focuses on characterizing magnetic domains in $\text{Mn}_{3-x}\text{Sn}_{1+x}$ thin films, with particular attention to the effects of crystallinity and stoichiometry, using state-of-the-art scanning NV magnetometry. In polycrystalline Mn_3Sn films, previous studies have demonstrated the existence of multidomain magnetic textures. These films, grown via magnetron sputtering, exhibit domain sizes that scale with film thickness, as determined by scanning NV magnetometry experiments [2]. However, the influence of epitaxial growth on the magnetic domain configuration has not yet been explored. To address this question, we investigated 5 nm thick epitaxial $\text{Mn}_{3-x}\text{Sn}_{1+x}$ films of different stoichiometries (Mn_3Sn , $\text{Mn}_{2.9}\text{Sn}_{1.1}$, $\text{Mn}_{2.8}\text{Sn}_{1.2}$), grown using molecular beam epitaxy on $\text{MgO}(111)$ substrates with intermediate metallic layers. Our results reveal that our epitaxial films exhibit significantly smaller magnetic domains than previously studied polycrystalline samples, as expected for thinner films. The observed domain structures were not significantly affected by stoichiometry or substrate type. The weak remnant magnetization in Mn_3Sn , attributed to its chiral antiferromagnetic state, was corroborated by low stray field amplitudes of around 0.1 mT detected across all the samples, see Fig 2. We validated these findings with the help of multiple measurements, and comparison with simulations of expected stray field. The observed behavior agrees with the theoretical expectations of Mn_3Sn 's weak ferromagnetic moment and supports its suitability for additional exploration as a novel antiferromagnet for future spintronics applications. Furthermore, this study highlights the potential of scanning NV magnetometry as a powerful tool to investigate complex magnetic textures in non collinear antiferromagnets, paving the way for deeper insights into their nanoscale magnetic phenomena.

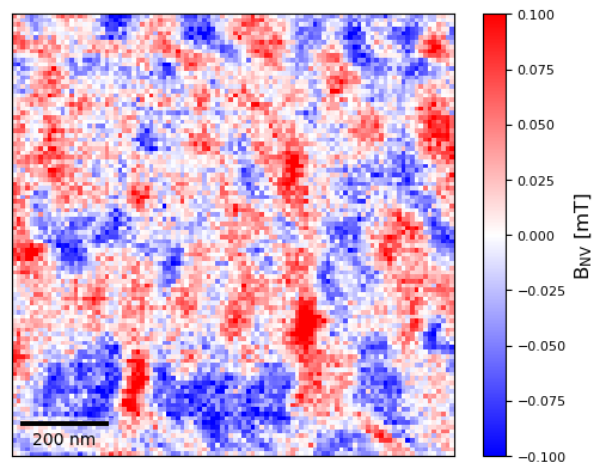


Figure 2: Scanning NV magnetometry image of the stray field produced by antiferromagnetic domains in Mn₃Sn.

References

- [1] Satoru Nakatsuji, Naoki Kiyohara, and Tomoya Higo. [Large Anomalous Hall Effect in a Non-Collinear Antiferromagnet at Room Temperature](#). *Nature* 527, 212–215 (2015).
- [2] Senlei Li, Mengqi Huang, Hanyi Lu, et al. [Nanoscale Magnetic Domains in Polycrystalline Mn₃Sn Films Imaged by a Scanning Single-Spin Magnetometer](#). *Nano Letters* 23, 5326–5333 (2023).

Probing the antiferromagnetic to ferromagnetic transition in FeRh using surface acoustic waves

C. Gourdon^{1,*}, A. Vythelingum¹, D. Nguyen¹, E. Dandeu¹, V. Laude², and L. Thevenard¹

¹*Sorbonne Université, CNRS, Institut des Nanosciences de Paris, INSP, F-75005 Paris, France*

²*Université de Franche-Comté, CNRS, Institut FEMTO-ST, F-25000 Besançon, France*

*catherine.gourdon@insp.jussieu.fr

Bulk acoustic waves in the form of ultrasonic pulses have long been recognized as a very sensitive tool for probing phase transitions, whether structural, magnetic, or electronic [1]. The modification of either or both the mass density and the elastic constants leads to detectable changes of the sound velocity, which provide a clear signature of the phase transition. The acoustic pulse attenuation, although less often probed, arises as a fingerprint of the time relaxation of the order parameter coupled to the strain components. Only a few of them investigate first order transitions, in which the two phases can coexist over a large temperature range [2, 3].

Here we probe the first-order antiferromagnetic (AFM) to ferromagnetic (FM) phase transition of the equiatomic FeRh alloy, a versatile material attractive for information storage [4, 5] or its multicaloric properties [6]. This transition is isostructural but accompanied by a $\approx 1\%$ volume increase. The AFM-FM transition of bulk FeRh was long ago probed by longitudinal and transverse acoustic waves [7]. Here we use a more appropriate acoustic wave for probing an FeRh layer, namely a Rayleigh surface acoustic waves (SAW). It probes a 270 nm thick polycrystalline FeRh layer grown by DC sputtering on a GaAs substrate and a 100 nm Ta buffer (Fig. 1(a)) [8]. Recently it was shown that a SAW of high amplitude can irreversibly induce a partial AFM-to-FM (FM-to-AFM) transition upon heating (cooling) [9]. Here we observe a clear signature of the transition in the SAW velocity and attenuation changes in the mixed AFM-FM phase. The main results can be summarized as follows: (i) the SAW velocity variation follows the same temperature dependence as the magnetization. Hence it can be used to determine the FM fraction versus temperature, (ii) the SAW attenuation contains two contributions, one from SAW-induced ferromagnetic resonance (SAW-FMR), which can be suppressed by operating at a sufficiently high field and the other resulting from the coupling of the SAW-induced strain and the FM fraction modulated at the SAW frequency with a relaxation time.

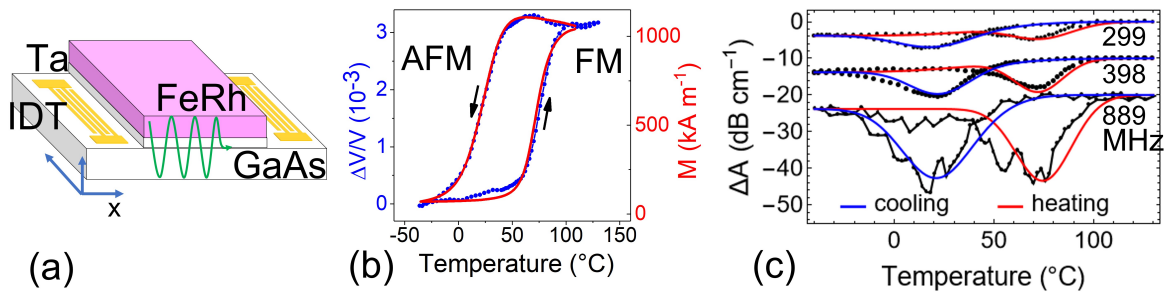


Figure 1: (a) Schematics of the experiment. The SAW is generated using the piezoelectricity of the GaAs substrate by applying a radio-frequency pulse on the left IDT. It is detected by the induced voltage on the right IDT fed to an oscilloscope. (b) Velocity variation obtained from the phase variation of the detected voltage and magnetization obtained from vibrating sample magnetometry, showing similar hysteretic behaviors at the AFM-FM first-order transition of FeRh. (c) Variation of the SAW transmitted amplitude for the 3 available SAW frequencies, down-shifted for clarity, showing large absorption in the middle of the heating/cooling transition. The data are taken under a magnetic field of 50 mT in order to suppress the SAW-FMR contribution. The red and blue full curves are the calculated curves.

SAW pulses of carrier frequency $f_1=299$, $f_2=398$ and $f_3=889$ MHz and pulse length 200 ns were excited and detected using interdigitated transducers (IDT) (Fig. 1(a)). The oscilloscope trace of the central part of the detected SAW pulses was fitted with an $A\sin(2\pi f t + \phi)$ function. From the phase variation, we obtained the velocity variation $\frac{\Delta V}{V} = \frac{V_R - V_{R,ref}}{V_{R,ref}}$, with V_R the Rayleigh velocity of the stack and $V_{R,ref}$ its value at $T_{ref} = -40^\circ\text{C}$ (Fig. 1(b)). Its hysteretic temperature behavior closely follows that of the magnetization, making $\frac{\Delta V}{V}$ a measure of the temperature dependent FM fraction $f(T)$. We first show that the opening of the cycle (a few 10^{-3}) arises from the different Rayleigh velocities in the AFM and FM phases, mainly originating from different elastic constants in the two phases. Solving the SAW propagation equation in a 2-layers-on-substrate model and using the FeRh elastic constants determined in [10] we obtain the Rayleigh velocity as a function of the SAW frequency, in good agreement with experimental data.

The variation of SAW transmitted amplitude is experimentally obtained as $\Delta A = \frac{20}{L} \log\left(\frac{A}{A_{ref}}\right)$ where L is the length of the delay line between the two IDTs (Fig. 1(c)). The SAW attenuation is the largest in the middle of the heating and cooling

transitions. It has a much stronger variation with frequency than the velocity variation, as seen in many ultrasonic studies of phase transitions [1].

We model the SAW attenuation using a very simple model. We consider only the longitudinal displacement of the SAW $U_x = U_0 \exp(i(\omega t - kx))$ where ω is the angular frequency of the SAW, k the wave vector, and we neglect its in-depth z -dependence. The FM fraction is taken as $f = f_0(T) + \delta f$ where T is the temperature. Assuming a relaxation time τ for the SAW-induced variation δf , which proceeds through AF-FM domain wall displacements, we have $\frac{\partial \delta f}{\partial t} = -\frac{\delta f}{\tau} - \frac{\partial f_0}{\partial T} \frac{\partial T_m}{\partial \epsilon} \frac{\partial \epsilon}{\partial t}$ where T_m is the mid-transition mid-temperature and $\epsilon = \frac{\partial U_x}{\partial x}$ the strain. We further assume a coupling energy of the form $\Delta g = \frac{\partial g_{AFM}}{\partial \epsilon} \epsilon (1 - f) + \frac{\partial g_{FM}}{\partial \epsilon} \epsilon f$, where g_{AFM} (g_{FM}) are the Gibbs energies of the AFM (FM) phases, and inject it into the SAW propagation equation. We then solve the coupled equations for U_x and δf and calculate the SAW attenuation as $-\text{Im}(k)$. The calculated variation of the transmitted SAW amplitude ΔA is then

$$\Delta A = \frac{20}{\ln(10)} \left(-\frac{\left| \frac{\partial(g_{FM} - g_{AFM})}{\partial \epsilon} \frac{\partial T_m}{\partial \epsilon} \right|}{2C_{11}(T) V_R(T)} \frac{\omega^2 \tau}{1 + \omega^2 \tau^2} \frac{\partial f_0}{\partial T}(T) + \frac{1}{L} \ln \left(\frac{\epsilon(T)}{\epsilon(T_{\text{ref}})} \right) \right). \quad (4)$$

The first term in the parenthesis of Eq.4 arises from the coupling of the SAW strain and the FM fraction. The temperature dependence is dominated by the Gaussian-like shape of the derivative $\frac{\partial f_0}{\partial T}(T)$. C_{11} is an effective elastic constant obtained from the Rayleigh velocity and the mass density of FeRh. The second term takes into account the variation of the SAW amplitude with temperature since the IDT generation and detection efficiency at the operating frequency slightly depends on temperature. The calculated curves are shown in Fig. 1(c) in red (blue) for the heating (cooling) branch. They are in good agreement with the experimental ones. The $\frac{\partial T_m}{\partial \epsilon}$ factor is taken as $7.43 \cdot 10^3$ K using the dependence of the transition temperature on pressure from [11]. The best fit for the three frequencies is found for values of the parameters $\left| \frac{\partial(g_{FM} - g_{AFM})}{\partial \epsilon} \right| = 1.34 \cdot 10^5$, a value somewhat smaller than the one used by Wu *et al.* in [9], and $\tau = 0.25$ ns. τ is not very much smaller than the SAW period leading to a sub- ω^2 behavior of the amplitude variation.

Finally we will present and discuss the variation of the SAW amplitude attenuation at zero applied magnetic field, where two contributions are present: from the FM phase modulation and from the SAW-FMR close to the coercive field.

Acknowledgments

This work has been partly supported by the French Agence Nationale de la Recherche (ANR ACAF 20-CE30-0027).

References

- [1] Walther Rehwald. [The study of structural phase transitions by means of ultrasonic experiments](#). *Advances in Physics* 22, 721–755 (1973).
- [2] R.R. Hemphill. “Effect of a Thin-Film Phase-Transition Material on Surface Acoustic Wave Propagation”. *IEEE 1984 Ultrasonics Symposium*. IEEE, 1984, 1006–1002.
- [3] András L. Szabó, Mark H. Fischer, and Manfred Sigrist. [Effects of nucleation at a first-order transition between two superconducting phases: Application to CeRh₂As₂](#). *Physical Review Research* 6 (2024).
- [4] X. Marti, I. Fina, C. Frontera, et al. [Room-temperature antiferromagnetic memory resistor](#). *Nature Materials* 13, 367–374 (2014).
- [5] Antonio B. Mei, Yongjian Tang, Jennifer L. Grab, et al. [Structural, magnetic and transport properties of Fe_{1-x}Rh_x/MgO\(001\) films grown by molecular-beam epitaxy](#). *Applied Physics Letters* 113 (2018).
- [6] Enric Stern-Taulats, Antoni Planes, Pol Lloveras, et al. [Barocaloric and magnetocaloric effects of bulk Fe₄₉Rh₅₁](#). *Physical Review B* 89 (2014).
- [7] S. B. Palmer, P. Dentschuk, and D. Melville. [Elastic Properties of an Iron-Rhodium Alloy](#). *Physica Status Solidi (a)* 32, 503–508 (2 1975).
- [8] D. Nguyen Ba, G. Olivetti, T. Tremblais, et al. [Origin of low-field microwave absorption in metallic magnetic films evidenced in FeRh/Ta/GaAs](#). *to appear in Phys. Rev. B* (2025).
- [9] Huiliang Wu, Qingfang Liu, Runliang Gao, et al. [Acoustic Wave-Induced FeRh Magnetic Phase Transition and Its Application in Antiferromagnetic Pattern Writing and Erasing](#). *ACS Nano* 18, 12134–12145 (19 2024).
- [10] D. Ourdani, A. Castellano, A. K. Vythelingum, et al. [Experimental determination of the temperature- and phase-dependent elastic constants of FeRh](#). *Physical Review B* 110 (2024).
- [11] AI Zakharov, AM Kadomtseva, RZ Levitin, and EG Ponyatovskii. Magnetic and magnetoelastic properties of a metamagnetic iron-rhodium alloy. *Sov. Phys. JETP* 19, 1348–1353 (1964).

THz emission from topological spintronics elements probed by electro-optic sampling (EOS)

Filip Miljevic^{1,*}, Mudit Jain^{1,2}, Sylvain Massabeau¹, Romain Lebrun¹, Frédéric Leroy³, Jean-Marie George¹, and Henri Jaffres¹

¹Laboratoire Albert Fert, CNRS, Thales, Université Paris-Saclay, Palaiseau, France

²Centre for Nanoscience and Nanotechnology, CNRS, Université Paris-Saclay, Palaiseau, France

³Aix Marseille Univ, CNRS, CINAM, AMUTECH, Marseille, France

*filip.miljevic@cnrs-thales.fr

Introduction and motivations

In the field of orbitronics and spinorbitronics, probing fundamental material properties, such as spin and orbital generation, propagation and spin relaxation in the time domain, is today mandatory for the development of a new generation of magnetoelectronic devices as spintronic THz emitters [1]. These represents a novel technology of electromagnetic emission broadband source up to 30 THz. The spectrum of problems brings the need for variety of different emitters. Depending on the need, the emitters may be required to produce waves in specific ranges, intensities and bandwidths. Controlling these parameters and constructing reliable devices is a challenging problem both from practical and theoretical point of view. Indeed, one of the most common devices used for THz generation are made actually of photo-conducting antennas based on III-V semiconducting materials suffering from the phonon absorption in the 4-8 THz window. Other technology involves optical rectification such as ZnTe. Here, broken inversion symmetry at surfaces leads to the asymmetric charge displacement under the influence of intense electromagnetic field and results in THz generation.

Modern physical phenomena involving spin (and possibly orbital) degree of freedom, involving specific band structure like Rashba states, or topological surface states. The principle is the conversion of an ultrafast spin-current into a transient charge current *via* the spin-charge conversion phenomena induced by either spin Hall effects (SHE) or Rashba-Edelstein effects (REE) at interfaces. Standard conventional THz spintronic emitters consist then of of heterostructures made of metallic magnetic materials and non magnetic materials (e.g. 5d heavy metals) characterized by large spin-orbit coupling. By shining femtosecond laser pulses onto the heterostructures, photons absorption can generate ultrafast demagnetisation and spin-polarized hot electrons in the ferromagnet. This leads to a picosecond spin-current that can be converted into a charge current through large spin orbit coupling at Rashba interfaces or in the bulk of materials via the inverse spin-Hall effect. Those phenomenon open new horizons towards optimized THz generation. By using novel spintronic materials/heterostructures with limited optical absorption in the THz spectrum, emitters covering frequencies 1-30 THz can be then developed.

THz-TDS Experimental setup

General description of the optical bench

On Figure 1a we show our experimental setup we are working on at the laboratory and I am personally using in my master 2 internship. A source is a pulsed laser that consists of the Main oscillator, OPA (Optical Parameter Amplifier) and a Compressor. The available frequencies lay in two ranges; NIR that takes values between 640 nm and 940 nm, and Idler that ranges from 1159 nm to 2745 nm. The generated signal is split into two beams: pump and probe.

The pump is directed towards the sample and is presented in blue color on the figure. On the way to the sample, the pump first passes through half wave-plate and polarizer, which purpose is to control the intensity while maintaining fixed linear polarization. Next, it passes through mechanical chopper connected to lock-in amplifier and whose purpose is to modulate the signal in order to perform a lock-in detection. After the chopper the pump hits the sample and the THz signal is emitted in forward and backward direction with detection made in transmission geometry. THz signals generated are collected by a parabolic mirror, and focus it through a series of 4 mirrors on an electro-optical (EO) signal. Our focus is the front propagating signal. Two IR blockers are set between the parabolic mirrors to isolate THz signal from the pump. Electro-motor is used to rotate the emitter so the detection can be observed for different angles of the sample.

Detection technique by Electro-optical sampling (EOS)

In order to describe the detection method, we assume that the optical beam is propagating inside a birefringent material material of thickness d along the x -axis. We note n_y and n_z the indices or refraction of interest. We decompose the propagating field into y and z components, which travel optical paths of different lengths. As a result, the phase shift is induced:

$$\Delta\phi = \frac{2\pi d}{\lambda} (|n_y - n_z|) \quad (5)$$

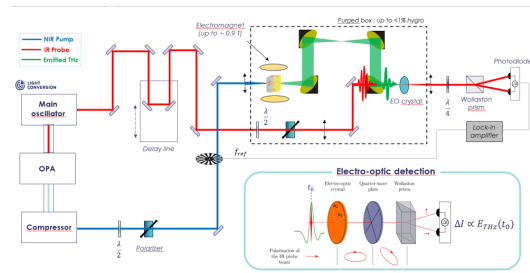


Figure 1: Illustration of the experimental setup used in Laboratoire Albert Fert (main figure) used in this work and during my M2 internship and the schematic representation of the EO sampling (bottom right inset)

In our work the THz signal acts as a slow varied electric field, modifying the optical index of the material for an optical probing pulse. The birefringent material is ZnTe EO detector. In practice, temporal duration of THz pulse is of order of 10 ps and of NIR pulse is of order 100 fs. For that reason, the THz beam can be considered quasi-static for the entire duration of probe's passing through detector. By measuring the change of polarization of the probe, we can deduce the intensity of THz field for the given temporal position [2][3]. On the bottom right inset of Fig. 1a we illustrate the detection part of the setup. Lower intensity NIR probe pulse is directed towards the EO detector, where the THz-induced non-linear optical effects affect the probe's polarization. A delay line is used to control the optical path of the probe, which is necessary for THz TDS (Time Domain Spectroscopy). Finally, after the use of a quarter wave-plate and wollaston prism, the two components of the NIR beam along ordinary and extraordinary axes are measured using balanced photo-diodes. The photo-diodes are connected to lock-in amplifier where the THz intensity is computed.

Spintronics emission: Experiments and data analyses.

At this conference, I will present the following:

- The technique of EOS adapted to spintronics THz-TDS and its calibration from the derivation of electro-optic sampling equations for the detection of THz waves, along with the description of the experimental setup.
- Results of spintronic THz emission from bulk and interface Rashba-Edelstein effects generated from heterostructures made of topological insulators (this is the focus on another presentation of the group, see M. Jain et al.).
- Preliminary results obtained on ferroelectric Rashba semiconductor as *e.g.* *GeTe* used as a Rashba spin-charge converter in epitaxial Fe/*GeTe*/Si(111) systems[4]. We studied the emission for different thicknesses, analyzed the uniformity of the sample at different manufacturing conditions with the help of X-ray diffraction and related it to the material conductivity.
- Preliminary results obtained on wavelength-dependent THz generation in various Heusler compounds[5] used as highly efficient spin-reservoir with almost full spin-polarization, and seeking the correlation with existence and energy of the band-gap. THz emission was demonstrated for both NIR (640nm-940nm) and Idler (1159nm-2400nm) wavelength ranges. The peak-to-peak intensity was compared with reference emitter $\text{Al}_2\text{O}_3//\text{W}/\text{CFB}/\text{Pt}$.

References

- [1] T. Seifert, S. Jaiswal, U. Martens, et al. [Efficient metallic spintronic emitters of ultrabroadband terahertz radiation](#). *Nature Photonics* 10, 483–488 (2016).
- [2] Paul C. M. Planken, Han-Kwang Nienhuys, Huib J. Bakker, and Tom Wenckebach. [Measurement and calculation of the orientation dependence of terahertz pulse detection in ZnTe](#). *J. Opt. Soc. Am. B* 18, 313–317 (2001).
- [3] G. Gallot and D. Grischkowsky. [Electro-optic detection of terahertz radiation](#). *J. Opt. Soc. Am. B* 16, 1204–1212 (1999).
- [4] Boris Croes, Fabien Cheynis, Salia Cherifi-Hertel, et al. [Polarization structure of nanostrip domain intersections in GeTe films](#). *Phys. Rev. B* 109, 024103 (2024).
- [5] Yoichi Ando. [Topological Insulator Materials](#). *Journal of the Physical Society of Japan* 82, 102001 (2013). eprint: <https://doi.org/10.7566/JPSJ.82.102001>.

Level attraction in a quasiclosed cavity: Antiresonance in magnonic devices

G. Bourcin^{1,2}, M. P. Avicena^{1,2,*}, A. Gardin^{1,2,3}, J. Bourhill⁴, V. Vlaminck^{1,2}, and V. Castel^{1,2}

¹IMT Atlantique, Technopole Brest-Iroise, CS 83818, Brest Cedex 3 29238, France

²Lab-STICC (UMR 6285), CNRS, Technopole Brest-Iroise, CS 83818, Brest Cedex 3 29238, France

³School of Physics, The University of Adelaide, Adelaide, SA 5005, Australia

⁴Quantum Technologies and Dark Matter Labs, Department of Physics, University of Western Australia, 35 Stirling Hwy, Crawley, Western Australia 6009

*mufti.avicena@imt-atlantique.fr

Contrary to resonant systems in open cavities, which are more well understood, the physical basis of level attraction between resonant systems in quasi-closed cavities, has for so long, remained an open question. Further, it is also of interest to the development of microwave and quantum devices as level attraction offers two useful features, exceptional points (EPs) and bound states in the continuum (BICs). Both enables several appealing applications such as topological energy transfer [1], and enhancement of device sensitivity for EPs and applications in slow-light devices, sensing, and quantum memory technologies leveraging the long lifetimes of these BICs [2–4].

In this work, we utilize the input-output theory [5] to discriminate between the repulsive and attractive aspect of this coupling. By understanding the nature of the phase-jump between resonances and antiresonances, we can describe the behavior of antiresonance coupling and its relation to the position of ferrimagnet within the cavity. We start by deriving the S-matrix computed using the input-output theory and then consider two different pathways antiresonance may occur. To validate our results, we perform finite element method simulations and show that both are in agreement with each other [6].

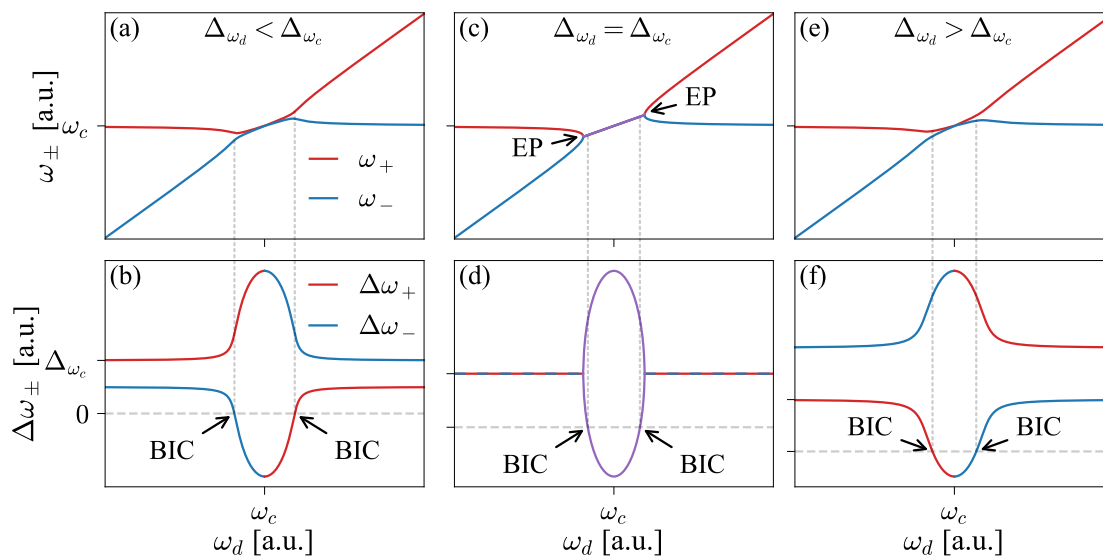


Figure 1: Light-matter dissipative coupling at eigenfrequencies (a), (c), and (e) and linewidths (b), (d), and (f). The dissipative nature of the coupling gives rise to exceptional points (EPs) that relates to the convergence of polaritonic frequencies; and bound states in continuum (BICs) that corresponds to real eigenvalues with no imaginary components [6].

Acknowledgments

We acknowledge financial support from Brest Métropole for the PhD funding of Guillaume Bourcin. This work is part of the research program supported by the European Union through the European Regional Development Fund (ERDF), by the Ministry of Higher Education and Research, and Brittany region, through the CPER SpaceTech DroneTech, and the ANR projects ICARUS and MagFunc. Jeremy Bourhill is funded by the Australian Research Council Centre of Excellence for Engineered Quantum Systems, CE170100009 and the Centre of Excellence for Dark Matter Particle Physics.

References

- [1] H. Xu, D. Mason, Luyao Jiang, and J. G. E. Harris. [Topological energy transfer in an optomechanical system with exceptional points](#). *Nature* 537, 80–83 (2016).
- [2] Jan Wiersig. [Enhancing the Sensitivity of Frequency and Energy Splitting Detection by Using Exceptional Points: Application to Microcavity Sensors for Single-Particle Detection](#). *Physical Review Letters* 112, 203901 (2014).
- [3] Xufeng Zhang, Kun Ding, Xianjing Zhou, Jing Xu, and Dafei Jin. [Experimental Observation of an Exceptional Surface in Synthetic Dimensions with Magnon Polaritons](#). *Physical Review Letters* 123, 237202 (2019).
- [4] Yunshan Cao and Peng Yan. [Exceptional magnetic sensitivity of \$PT\$ -symmetric cavity magnon polaritons](#). *Physical Review B* 99, 214415 (2019).
- [5] C. W. Gardiner and M. J. Collett. [Input and output in damped quantum systems: Quantum stochastic differential equations and the master equation](#). *Physical Review A* 31, 3761–3774 (1985).
- [6] Guillaume Bourcin, Alan Gardin, Jeremy Bourhill, Vincent Vlamincq, and Vincent Castel. [Level attraction in a quasi-closed cavity: Antiresonance in magnonic devices](#). *Physical Review Applied* 22 (2024).

Unraveling temperature-dependent spin-polarized electron transport in Fe via spin-wave Doppler shift

José Solano^{1,*}, Quentin Rossi¹, Jérôme Robert², Marc Lenertz², Yves Henry², Benoît Gobaut², David Halley², and Matthieu Bailleul²

¹*Institute of Physics of the Czech Academy of Sciences, Prague, Czech Republic*

²*Institut de physique et de chimie des matériaux de Strasbourg, Strasbourg, France*

*jose.solano@fzu.cz

Although central for spintronics, the interplay between magnetism and transport in metallic ferromagnets remains incompletely understood. Unfortunately, the inherent complexity of this many-body problem (electrons, phonons, magnons) has hindered both experimental and theoretical advances in this topic. Only until recently, the finite-temperature resistivity of elemental Fe, Co, Ni could be modeled using sophisticated ab initio methods [1]. Yet still, the spin-polarization of underlying scattering mechanisms and role of interactions (spin-orbit coupling, correlations, etc) remain unclear.

In this work, we experimentally address this problem in epitaxial Fe thin films grown on MgAl₂O₄/MgO. We use the recently developed current-induced spin-wave Doppler shift technique [2]: we pattern Fe strips that serve as conduits for a spin-polarized electric current j , and for coherent spin waves of a given wave vector k [Fig. 2 (a)]. The bulk spin-polarized current transfers torque to the spin waves producing a shift of their resonance magnetic field (spin-wave Doppler shift) [Fig. 2 (b)]. Measuring precisely the shifts for counterpropagating spin waves as a function of temperature [Fig. 2 (c)], we extract the temperature dependence of the degree of spin-polarization of the electrical current $P = (\rho_{\downarrow} - \rho_{\uparrow}) / (\rho_{\downarrow} + \rho_{\uparrow})$. This is found to increase from 75% up to 85% when cooling the sample from 300 K down to 10 K [Fig. 2 (d)]. Our observation contradicts early considerations, which, based on its global density of states, predict a weak spin-polarization for Fe [3]. On the contrary, we believe the spin-polarization of the current is dictated by the scattering mechanisms with a majority electron channel that is much less affected by scattering compared to minority electrons [Fig. 2 (d)].

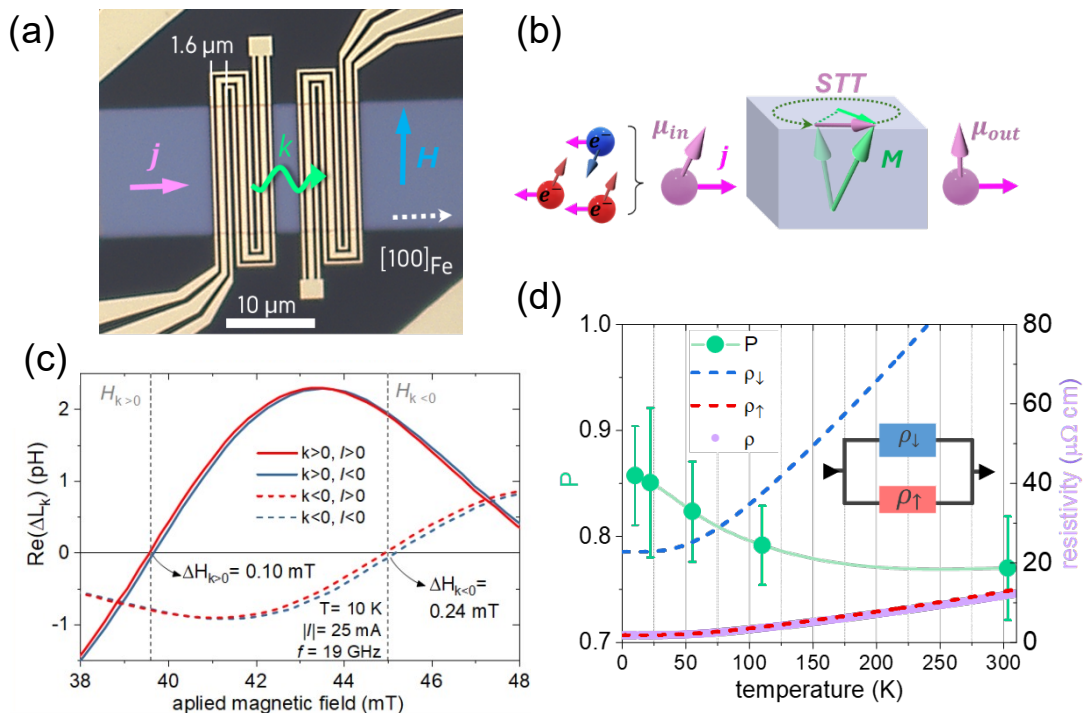


Figure 1: (a) Microscope picture of the device for current-induced Doppler shift: two antennas patterned on top of a 14 μm wide and a 20 nm thick Fe (001) strip. (b) Sketch of the spin-transfer torque process between a spin-polarized current and the magnetization. (c) Measured mutual inductance between antennas as function of the applied magnetic field displaying field shifts for different configurations. (d) Temperature dependence of degree of spin-polarization of the current and resistivity in our devices.

Furthermore, combining our polarization estimate with resistivity measurements, we create a relatively simple two-current resistivity model with contributions from film surfaces, phonons and thermal magnons. Finally, as an independent check, we validated the magnitude of the latter through independent measurements of magnon magnetoresistance [4] performed on the same system.

Acknowledgments

We thank Arnaud Boulard, Benoît Leconte, Daniel Spor, Jérémy Thoraval and Fares Abiza for their support in assembling and testing the broadband FMR and PSWS setup; Romain Bernard, Sabine Siegwald and Hicham Majjad for technical support during nanofabrication at STnano platform; Sergiy Mankovsky, Benjamin Bacq-Labreuil and François Gautier for theoretical support and discussion.

References

- [1] H. Ebert, S. Mankovsky, K. Chadova, et al. [Calculating linear-response functions for finite temperatures on the basis of the alloy analogy model](#). *Phys. Rev. B* 91, 165132 (16 2015).
- [2] Vincent Vlaminck and Matthieu Bailleul. [Current-Induced Spin-Wave Doppler Shift](#). *Science* 322, 410–413 (2008). eprint: <https://www.science.org/doi/pdf/10.1126/science.1162843>.
- [3] A. Fert I. A. Campbell and R. Pomeroy. [Evidence for two current conduction iron](#). *The Philosophical Magazine: A Journal of Theoretical Experimental and Applied Physics* 15, 977–983 (1967). eprint: <https://doi.org/10.1080/14786436708221641>.
- [4] B. Raquet, M. Viret, E. Sondergard, O. Cespedes, and R. Mamy. [Electron-magnon scattering and magnetic resistivity in 3d ferromagnets](#). *Phys. Rev. B* 66, 024433 (2 2002).

Nonreciprocal spin waves in adaptive Bi-YIG nanomagnonic devices utilizing domain walls

Hanadi Mortada¹, Philipp Pirro¹, Roman Verba², and Alexandre Abbass Hamadeh^{3,*}

¹Fachbereich Physik and Landesforschungszentrum OPTIMAS, Rheinland-Pfälzische Technische Universität Kaiserslautern-Landau, 67663 Kaiserslautern, Germany

²Institute of Magnetism, Kyiv 03680, Ukraine.

³Université Paris-Saclay, Centre de Nanosciences et de Nanotechnologies, CNRS, 91120, Palaiseau, France
*alexandre.hamadeh@universite-paris-saclay.fr

The advancement of CMOS technology is facing significant limitations, prompting the exploration of alternative approaches to address scaling and performance challenges. **Magnonics** offers a promising solution due to its tunability and energy efficiency, making it an attractive option for future data processing systems. Challenges remain in miniaturizing magnonic devices, understanding spin-wave behavior in nanostructured environments in which the classical theories fail at the nanoscale, and integrating discrete magnonic signal processing units into a **coherent magnonic circuit**[1]. In this context, leveraging micromagnetic simulations and analytical theory, we propose a novel approach that exploits the dipolar interaction between two adjacent nanoscale waveguides composed of bismuth-doped yttrium iron garnet (Bi-YIG)[2], envisioning applications in next-generation data processing. We introduce an adaptable spin-wave directional coupler at the nanoscale, capable of functioning as a waveguide crossing element, tunable power splitter, and frequency multiplexer (refer to Fig. 1a). The coupler's operational principle relies on the interference of spin-wave modes, modulated by various system parameters, thereby facilitating a range of linear and nonreciprocal magnonic functionalities.

A controllable phase shifter constitutes an essential building block for the development of spin-wave-based logic devices. Thus, we also present an innovative phase-shifter device that exploits the positional tunability of magnetic DWs and the dipolar coupling between two closely spaced waveguides to achieve precise phase modulation at low excitation frequencies, obviating the need for an external bias magnetic field. We model a nanoscale self-biased spin-wave waveguide with a bent configuration coupled to a half-ring-shaped waveguide (refer to Fig. 1b). Numerical analyses reveal that exchange-dominated, isotropic magnetostatic forward-volume-like spin waves propagating within the device accumulate a systematically varying phase, contingent on the DW's position. A pronounced phase shift is observed when the spin waves traverse the dipolar coupling region containing a DW, as compared to the configuration without a DW. The device's functionality is predicated on the dynamic positional flexibility of the DW, enabling a reconfigurable and tunable mechanism for phase modulation. This enhanced control over spin-wave propagation holds substantial promise for the realization of advanced spin-wave-based logic circuits, representing a pivotal advancement in the field of magnonics. Moreover, we emphasize the scalability of the device to nanometer dimensions and its significant nonreciprocal properties, providing flexibility in reconfiguring the device's operations.

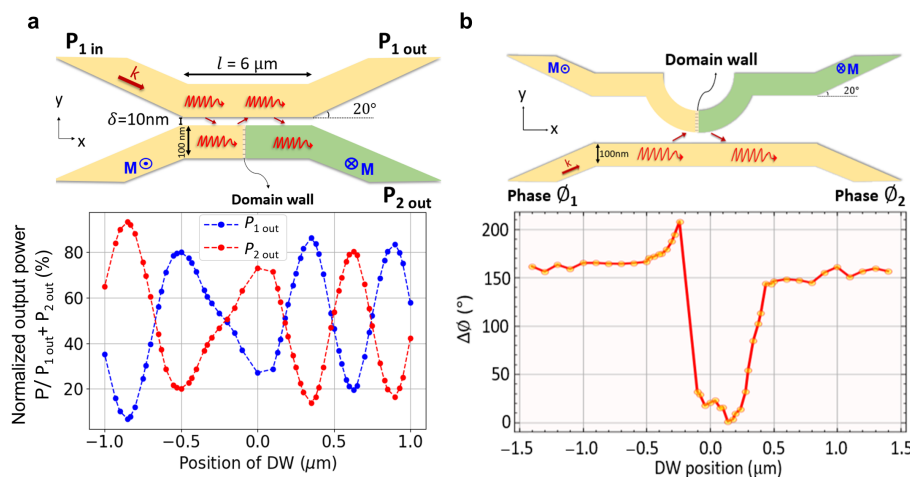


Figure 1: **Domain Wall modulating parameter of device's functionality.** (a) The DW position dependence of the normalized power at the two output beam passes of the directional coupler. (b) The corresponding DW position dependence of the input-output SWs-phase shift.

References

- [1] Q Wang, P Pirro, R Verba, et al. Reconfigurable nanoscale spin-wave directional coupler. *Science advances* 4, e1701517 (2018).
- [2] Y Fan, M J Gross, T Fakhru, et al. Coherent magnon-induced domain-wall motion in a magnetic insulator channel. *Nature Nanotechnology* 18, 1000–1004 (2023).

Engineering Spin Wave dispersion and Surface Acoustic Wave-driven FMR in Fe thin films by N-implantation

Anupam Sharma^{1,*}, Louis Christienne¹, Pauline Rovillain¹, Laura Thevenard¹, Catherine Gourdon¹, Mahmoud Eddrief¹, Franck Fortuna², Abdelmadjid Anane³, and Massimiliano Marangolo¹

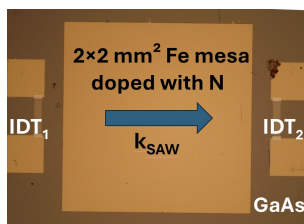
¹Sorbonne Université, CNRS, Institut des Nanosciences de Paris, INSP, F-75005 Paris, France

²Université Paris-Saclay, CNRS, Institut des Sciences Moléculaires d'Orsay, 91405 Orsay, France

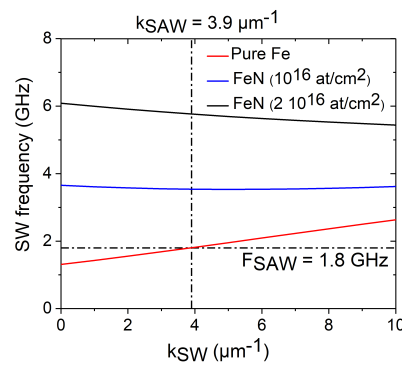
³Laboratoire Albert Fert, CNRS, Thales, Université Paris-Saclay, Palaiseau, France

*anupam.sharma@insp.upmc.fr

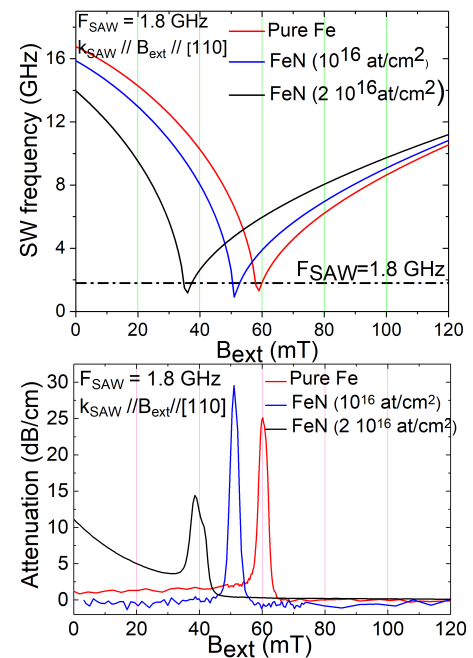
Magnonics has emerged as a new and exciting field that uses spin waves, or magnons, as information carriers that can propagate with minimal energy dissipation and at high frequencies, offering an alternative to traditional electronics. In the quest for future magnonic devices, the engineering of spin wave (SW) spectra is deemed to be crucial to manipulate local propagation modes, enabling the control of SW propagation. One of the promising techniques to modify the local spin wave propagation is through ion implantation in magnetic films which is the subject of our study.



(a) Sample under study. Surface acoustic waves are excited electrically by the input IDT₁ and detected by the receiving IDT₂. These IDTs are deposited on the surface of the piezoelectric GaAs (001).



(b) Calculated spin wave dispersion relations for pure Fe film and doped Fe films. A horizontal line at the working SAW frequency of 1.8 GHz intersects the spin wave (SW) dispersion curve for pure Fe film. These dispersion relations are plotted for $B_{ext} = 58.4$ mT which is the resonant field for pure Fe film (Figure 1c). This indicates that, at this field, the SAW frequency is in resonance with the SW precession frequency of pure Fe. No such resonance occurs at 58.4 mT for doped Fe films.



(c) The SW frequencies as a function of external magnetic field magnitude calculated for $k_{SW} = k_{SAW} = 3.9 \mu\text{m}^{-1}$, with B_{ext} aligned parallel to k_{SAW} along the [110] hard axis of Fe. The equations used for this calculation are extracted from [1]. The red curve represents the SW frequency versus B_{ext} for a pure Fe sample, while the blue and black curves correspond to Fe films doped with 1.0×10^{16} N/cm² and 2.0×10^{16} N/cm², respectively (top figure). Experimental SAW attenuation curves as a function of the external field magnitude as it propagates through the magnetic layer (bottom figure).

Figure 1: Depiction of the sample, and analysis of spin wave dispersion and SAW-driven ferromagnetic resonance, illustrating resonance characteristics and their shifts in pure and doped Fe films.

Surface acoustic waves (SAWs), traveling elastic waves on the surface of piezoelectric materials, are of extreme importance in magnonics for their ability to interact with magnons, and to induce magnetization dynamics, making them ideal for scalable magnonic devices [2]. It has been established that a SAW interacts with the magnetization via two mechanisms: magnetoelastic and magneto-rotation coupling [3] [4]. The softening of magnetization precession frequency allows it to couple resonantly with the SAW frequency as experimentally demonstrated in the past [5]. Our study deals with the propagation of SAW on a piezoelectric GaAs (001) substrate, with a Fe thin film deposited on it via molecular beam epitaxy (MBE), and subsequently etched into a $(2 \times 2) \text{mm}^2$ mesa (Figure 1a). The Fe mesa has been doped using an accelerator

with N atoms at low dosage in order to preserve the epitaxy conditions and the low SW damping of pure Fe films [6]. In particular, the magnetocrystalline anisotropies are slightly modified by ion implantation with moderate yet controlled variation of the SW dispersion (Figure 1b).

We have observed that the resonant magnetic field, at which the attenuation and velocity variation of the SAW are maximized, is slightly shifted compared to the pure Fe sample (Figure 1c). This resonant field corresponds to the external field magnitude at which the SW frequency matches the SAW frequency, enabling SAW-FMR (Figure 1c (top)). This resonant field value, marked by the minimum of each curve, shifts distinctly towards lower fields with the nitrogen doping level in Fe. At SAW-FMR coupling, the interaction between the SAW and the magnetization reaches its maximum, leading to a maximum attenuation of the SAW as it propagates through the magnetic layer. The SAW attenuation also shifts with the doping levels, which is consistent with the resonant field shift with doping (Figure 1c (bottom)). This shift validates the effectiveness of the ion implantation approach for finely engineering the interaction between SAWs and SWs. Furthermore, we anticipate that the ion implantation would alter the so-called non-reciprocal SAW propagation, i.e., the dependence of the propagation characteristics with the direction of the SAW-wave vector (k_{SAW}) with respect to the static magnetization orientation.

Integrating these findings reveals a pathway to control SW emission by desired modification of the spin wave spectra through ion implantation which alters the magnetic anisotropy of the magnetic thin film, and in turn, the SAW-SW interaction. This interaction is anticipated to be locally controlled by implanting N atoms using a Focused Ion Beam (FIB) technique.

Acknowledgments

This research was supported by the French ANR-22-CE24-0025 SACOUMAD and the European Union within the HORIZON-CL4-2021-DIGITAL-EMERGING-01, PEPR SPIN projects ANR 22 EXSP 0008 and ANR 22 EXSP 0004.

References

- [1] Pauline Rovillain, Jean-Yves Duquesne, Louis Christienne, et al. Impact of spin-wave dispersion on surface-acoustic-wave velocity. *Physical Review Applied* 18, 064043 (2022).
- [2] Anjan Barman, Gianluca Gubbiotti, Sam Ladak, et al. The 2021 magnonics roadmap. *Journal of Physics: Condensed Matter* 33, 413001 (2021).
- [3] Mingran Xu, Kei Yamamoto, Jorge Puebla, et al. Nonreciprocal surface acoustic wave propagation via magneto-rotation coupling. *Science advances* 6, eabb1724 (2020).
- [4] Alberto Hernández-Mínguez, F Macià, JM Hernández, J Herfort, and PV Santos. Large nonreciprocal propagation of surface acoustic waves in epitaxial ferromagnetic/semiconductor hybrid structures. *Physical Review Applied* 13, 044018 (2020).
- [5] J-Y Duquesne, P Rovillain, C Hepburn, et al. Surface-acoustic-wave induced ferromagnetic resonance in Fe thin films and magnetic field sensing. *Physical Review Applied* 12, 024042 (2019).
- [6] Ibrahima Sock Camara, S Tacchi, Louis Charles Garnier, et al. Magnetization dynamics of weak stripe domains in Fe-N thin films: a multi-technique complementary approach. *Journal of Physics: Condensed Matter* 29, 465803 (2017).

Revealing the three-dimensional nature of the field-driven movement of magnetic topological defects

Marisel Di Pietro Martínez^{1,2*}, Luke Alexander Turnbull^{1,2}, Jeffrey Neethirajan¹, Max Birch³, Simone Finizio⁴, Jörg Raabe⁴, Edouard Lesne¹, Anastasios Markou^{1,5}, María Vélez^{6,7}, Aurelio Hierro-Rodríguez^{6,7}, Marco Salvalaglio^{8,9}, and Claire Donnelly^{1,2}

¹Max Planck Institute for Chemical Physics of Solids, Noethnitzer Str. 40, 01187 Dresden, Germany

²International Institute for Sustainability with Knotted Chiral Meta Matter (WPI-SKCM²), Hiroshima University, Hiroshima 739-8526, Japan

³RIKEN Center for Emergent Matter Science (CEMS) Wako 351-0198, Japan

⁴Swiss Light Source, Paul Scherrer Institut, Forschungsstrasse 111 5232 PSI Villigen, Switzerland

⁵Physics Department, University of Ioannina, 45110 Ioannina, Greece

⁶Departamento de Física, Universidad de Oviedo, 33007, Oviedo, Spain

⁷CINN (CSIC-Universidad de Oviedo), 33940, El Entrego, Spain

⁸Institute of Scientific Computing, TU Dresden, 01062 Dresden, Germany

⁹Dresden Center for Computational Materials Science (DCMS), TU Dresden, 01062 Dresden, Germany

*Marisel.DiPietro@cpfs.mpg.de

Understanding the processes of creation, propagation, and annihilation of topological defects is key to gaining control over the different processes they mediate. In magnetism, for instance, magnetic switching is mediated by domain wall motion while vortex core reversal is driven by Bloch point singularities. Here, we focus on magnetic dislocations in stripe domains and their role in the field-driven continuous rotation of the stripes. By harnessing both 2D and 3D magnetic imaging, specifically combining 3D soft X-ray magnetic vectorial imaging with *in situ* magnetic fields, as shown in Figure 1 (a), not only we characterize the motion of these defects, but also understand how their underlying 3D configuration influences their behavior (Figure 1 (b)). These advances establish the necessary capabilities to study the behavior of topological textures in 3D, opening the door to insights into the field-driven behavior of buried three-dimensional magnetic textures.

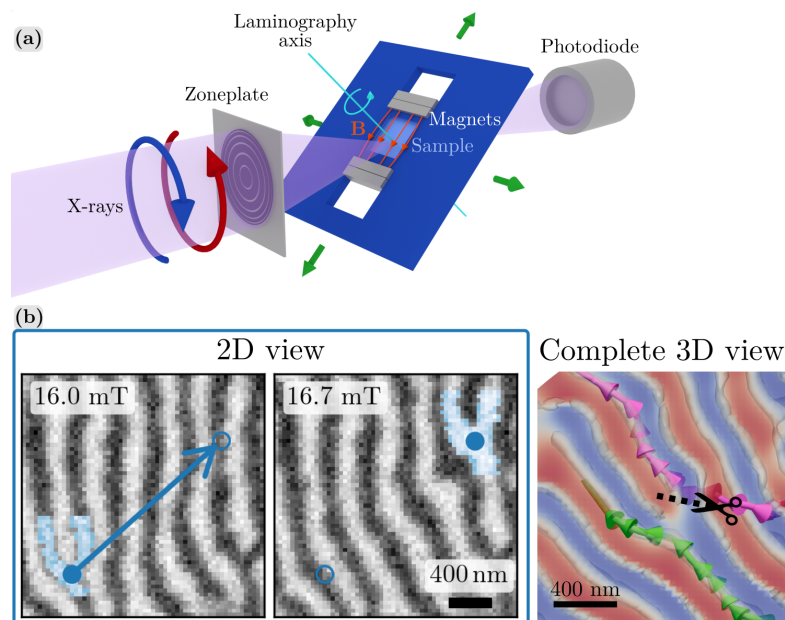


Figure 1: (a) 3D magnetic imaging with *in situ* magnetic fields: The sample is moved in the direction of the green arrows to perform scanning transmission X-ray microscopy (STXM). By rotating the sample around the laminography axis a set of 2D STXM images is obtained that can be used to reconstruct the magnetization vector field. To measure laminography while applying *in situ* magnetic fields, a special sample holder with stacking permanent magnets is used. (b) The movement of dislocations driven by an external magnetic field as seen by 2D (left) and 3D imaging (right): the inner magnetic structure revealed by 3D imaging, highlighted in pink and green, is involved in the mechanism for the movement of the dislocations.

Unconventional flat lifetimes of solitons in 2D easy-plane magnets

Moritz A. Goerzen^{1,2}, Soumyajyoti Haldar², Tim Drevelow², Hendrik Schrautzer^{2,3}, Stefan Heinze^{2,4}, and Dongzhe Li¹

¹*CEMES, Université de Toulouse, CNRS, 29 rue Jeanne Marvig, F-31055 Toulouse, France*

²*Institute of Theoretical Physics and Astrophysics, University of Kiel, Leibnizstraße 15, 24098 Kiel, Germany*

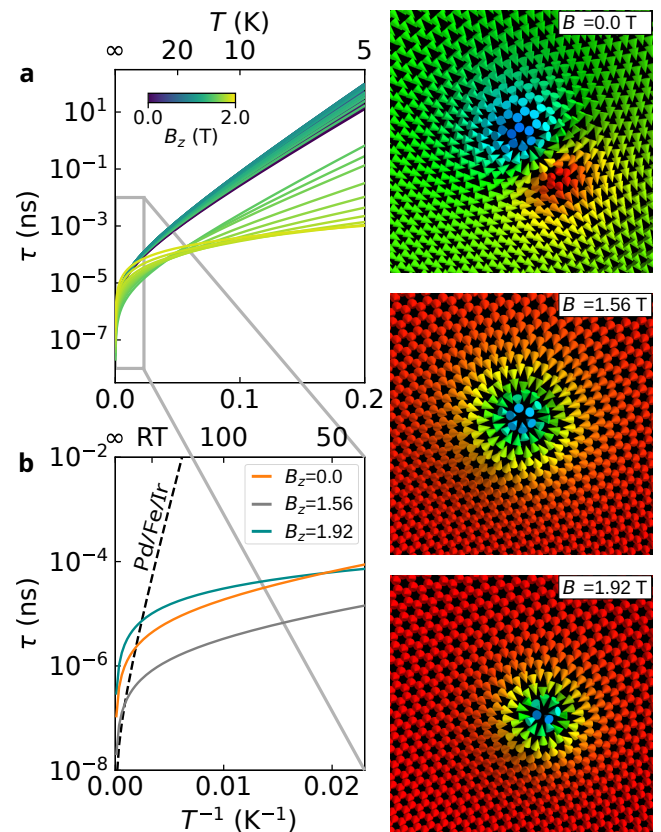
³*Science Institute and Faculty of Physical Sciences, University of Iceland, VR-III, 107 Reykjavík, Iceland*

⁴*Kiel Nano, Surface, and Interface Science (KiNSIS), University of Kiel, 24118 Kiel, Germany*

*moritz.goerzen@cemes.fr

In state-of-the-art spintronic devices, the activation energy for switching a magnetic bit is usually bound by $\Delta E > 50k_B T$ at room temperature. This ensures the thermal stability of stored information. However, high activation energies also cause an exponentially increased sensitivity to temperature deviations due to the Arrhenius-law-like lifetime of magnetic bits. To overcome this issue for reliable future spintronic devices, we investigate the entropy-dominated lifetime of magnetic solitons in a van der Waals heterostructure $\text{Fe}_3\text{GeTe}_2/\text{Cr}_2\text{Ge}_2\text{Te}_6$, an experimental feasible system [1]. Using first-principles and atomistic spin simulations, we demonstrate the coexistence of bimerons and antibimerons in the easy-plane $\text{Cr}_2\text{Ge}_2\text{Te}_6$ -layer at zero-field and the (anti)bimeron-(anti)skyrmion switching. We further quantify their resistivity against thermal and magnetic disturbance by means of transition state theory [2], which allows for the identification of the important degrees of freedom that are responsible for the stability of both classes of solitons. Our findings [3] illustrate that the richness of solitons in easy-plane magnets fundamentally exceeds those in usually discussed easy-axis magnets and are thus promising platforms for spintronic devices that demand highly nonlinear soliton interactions.

Figure 1: **Lifetime of solitons in CGT.** **a** The average lifetime τ of magnetic solitons with topological charge $Q = -1$ is displayed over inverse temperature. The line color indicates the strength of the externally applied magnetic field, reaching from bimerons at $B_z = 0$ T (violet) to skyrmions $B_z > 1.54$ T (yellow). **b** Zoom on the region indicated in **a**. The lifetime of specific solitons in $\text{Cr}_2\text{Ge}_2\text{Te}_6$, which are illustrated on the right with respect to the applied magnetic field, is compared to those in the experimentally well-studied ultrathin film system $\text{fcc-Pd/Fe/Ir}(111)$ at $B_z = 3.9$ T.



Acknowledgments

This work is supported by France 2030 government investment plan managed by the French National Research Agency under grant reference PEPR SPIN – [SPINTHEORY] ANR-22-EXSP-0009. This work was performed using the HPC resources provided by CALMIP (Grant 2022/2024-[P21008]).

References

- [1] Y. Wu et al. [A van der Waals interface hosting two groups of magnetic skyrmions](#). *Adv. Mater.* 34, 2110583 (2022).
- [2] P. Bessarab et al. [Harmonic transition-state theory of thermal spin transitions](#). *Phys. Rev. B* 85, 184409 (2012).
- [3] D. Li et al. [Stability and localization of nanoscale skyrmions and bimerons in an all-magnetic van der Waals heterostructure](#). *arXiv preprint arXiv:2408.15974* (2024).

Carbon Doping Effects on MgO Tunneling Barriers and Their Influence on Magnetic Tunnel Junction Noise

Mariana Caseiro^{1,*}, Rohit Pachat¹, Martin Bowen², Michel Hehn³, Daniel Lacour³, and Myriam Pannetier-Lecoecur¹

¹*SPEC, CEA, CNRS, Université Paris-Saclay, CEA Saclay 91191 Gif-sur-Yvette, France*

²*Institut de Physique et Chimie des Matériaux de Strasbourg, CNRS, Université de Strasbourg, 67034 Strasbourg, France*

³*Institut Jean Lamour, CNRS, Université de Lorraine, 54506 Vandoeuvre les Nancy, France*

*mariana-isabel.finocaseiro@cea.fr

Magnetic tunnel junctions (MTJs) are highly sensitive magnetic field sensing devices with a wide range of applications: non-volatile memories (MRAM), spintronic nanoscillators (STNO), neuromorphic computing or current sensing. This area of spintronics is very active not only for its practical uses but also for its interesting fundamental mechanisms such as tunneling, spin-orbit torque, or noise to name a few. The most important advance in this field comes from the prediction and demonstration of coherent spin-dependent tunneling in Fe(100)/MgO(100)/Fe(100) MTJs [1]. The large values (>100%) of tunneling magnetoresistance (TMR) found at room temperature are due to the lower tunneling barrier height for electrons in the Δ_1 band state when compared to Δ_5 electrons [2]. However, transport across the MgO barrier gets significantly more complex when dealing with defects, vacancies or doping, that is, when there are changes to the electronic structure of the interface or barrier. Defect-mediated tunnelling in the oxide can promote or hinder magnetotransport depending on the defect type [3]. Additionally, it has been demonstrated that carbon doping in the Fe/MgO interface can lead to asymmetric TMR versus bias [4]. Thus, by engineering the structure of the MTJ, different transport mechanisms can be probed.

In this work, the effect of carbon doping on the noise spectrum of MTJs is studied for different positions along the MgO. We investigate the Hooke factor and the presence of RTN in CoFeB/MgO/CoFeB MTJs, with and without carbon doping, as a function of magnetic configuration, applied bias and polarity. The success of this study can yield a promising candidate for a resilient and efficient spin engine [5].

The samples were deposited by magnetron sputtering under UHV, with base pressure 5.1×10^{-9} mBar and work pressure 5.1×10^{-3} mBar, on SiO₂ substrates with the following structure: [Ta 3/Pt 5]_{x3}/IrMn 8/CoFeB 4/I/CoFeB 6/Ta 3/Pt 5 (nm). The barrier I is divided into 4 different types: (a) MgO 2.1 (without doping), (b) C 0.2/MgO 2.1, (c) MgO 0.3/C 0.2/MgO 1.8 and (d) MgO 0.6/C 0.2/ MgO 1.5. After deposition, the samples were annealed at 200°C during 30 min with a magnetic field of 1T to pin the hard layer IrMn 8/CoFeB 4 into the sensitivity axis direction (0°) and to obtain a good crystallization of the CoFeB barrier interfaces. To perform noise measurements, the sensors were assembled on a half Wheatstone bridge in order to filter out the DC component before amplification. The sensor signal passed through a bandpass filter (SR360) and was captured by an acquisition card which then applied a fast Fourier transform (FFT) to obtain the spectrum. To

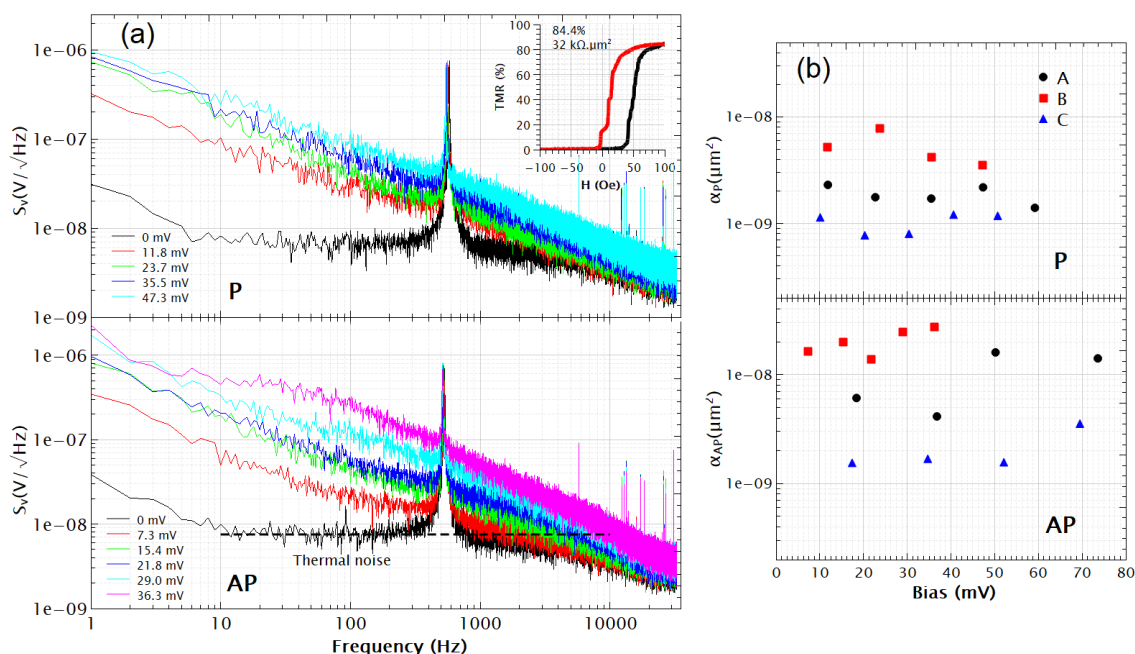


Figure 1: (a) Voltage noise as a function of applied bias voltage for sensor type B in the P (top panel) and AP (bottom panel) magnetization states. Top panel inset: TMR curve of the measured sensor. (b) Hooke factor in the P (top panel) and AP (bottom panel) magnetization states for sensor types A, B and C. All data correspond to circular pillars of 3 μm diameter.

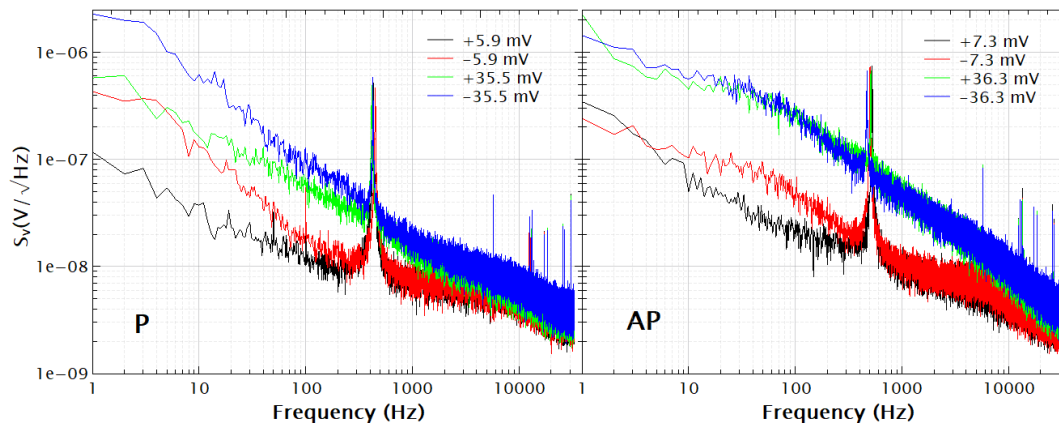


Figure 2: Voltage noise as a function of applied bias voltage and polarity for sensor type B in the P (left panel) and AP (right panel) magnetization states.

avoid external interference, both the bandpass filter and Wheatstone bridge were fed by a battery while inside a mu-metal shielded room.

The highest TMR measured was around 100% for sensor types A, B and C with a RA product value ranging from $31 \text{ k}\Omega\mu\text{m}^2$ to $0.57 \text{ M}\Omega\mu\text{m}^2$. All sensors of type D were found to have very low TMR ($<1\%$) and resistance, which was also seen to partially occur on sensors of type B and C. It is likely that the presence of carbon in the oxide leads to the creation of pinholes across the barrier. We show here data from devices with circular pillars of $3 \mu\text{m}$ diameter. An example of a typical TMR curve measured is shown on the inset of Fig.1(a). The voltage noise of a sensor of type B in both parallel (P) and antiparallel (AP) magnetization states as a function of applied bias voltage is depicted in Fig.1(a). The frequency-independent component of the noise floor is attributed to the thermal and shot noise, whereas the $1/f$ noise and RTN dominate the low-frequency range. In addition, the spectra present a peak at around 500 Hz that derives from an external perturbation and not from any response from the sensor. In the AP state, the voltage noise clearly depicts the presence of RTN above a bias of 29 mV that is not seen in the P state. To investigate the $1/f$ noise, the Hooge factors were extracted from the noise measurements for all sensor types using $\alpha = fAS_V(f)/V^2$, where A is the junction area and V is the DC voltage applied to a single junction. The results are shown in Fig.1(b) for both magnetic configurations. It is interesting to note that sensor type C displayed the lowest noise despite the presence of carbon doping, whereas an increase was observed for sensor type B. Lastly, Fig.2 shows the voltage noise of sensor type B as a function of bias polarity. For a negative bias, both P and AP states present a RTN signal that exists at lower voltages and only begins to appear at positive bias between 29 to 36 mV. The asymmetry of this feature is possibly a reflection of the asymmetry of the bottom and top CoFeB/MgO interfaces as it does not appear on any other sensor types as of yet. More measurements are currently underway exploring other types of experiments such as I-V curves, TMR as a function of voltage and $\Delta I/I(T)$ measurements in order to evaluate if more information on these structures can be probed and to determine the nature of the observed features.

Acknowledgments

This work is a collaboration with Institut Jean Lamour who were responsible for the sample depositions. The work is supported by France 2030 government investment plan managed by the French National Research Agency under grant reference PEPR SPIN –ADAGE ANR-22-EXSP-0006.

References

- [1] Stuart SP Parkin, Christian Kaiser, Alex Panchula, et al. Giant tunnelling magnetoresistance at room temperature with MgO (100) tunnel barriers. *Nature materials* 3, 862–867 (2004).
- [2] WH Butler, X-G Zhang, TC Schulthess, and JM MacLaren. Spin-dependent tunneling conductance of Fe| MgO| Fe sandwiches. *Physical Review B* 63, 054416 (2001).
- [3] F Schleicher, U Halisdemir, Daniel Lacour, et al. Localized states in advanced dielectrics from the vantage of spin-and symmetry-polarized tunnelling across MgO. *Nature communications* 5, 4547 (2014).
- [4] C Tiusan, M Sicot, Michel Hehn, et al. Fe/ MgO interface engineering for high-output-voltage device applications. *Applied physics letters* 88 (2006).
- [5] K Katcko, E Urbain, B Taudul, et al. Spin-driven electrical power generation at room temperature. *Communications Physics* 2, 116 (2019).

Étude de textures magnétiques générées par impulsion laser sur couches minces

L. Petitdemange^{1,*}, M. Hehn¹, G. Malinowski¹, and D. Lacour¹

¹Institut Jean Lamour UMR7198, Nancy, France

*leo.petitdemange@univ-lorraine.fr

Dans la matière condensée, l'étude des textures magnétique concilie la recherche fondamentale et l'innovation technologique, avec des applications potentielles dans des domaines variés tels que l'informatique, l'énergie et la physique fondamentale. Ces textures complexes peuvent être générées par impulsion laser, favorisant alors l'émergence des systèmes de stockage d'informations ultra-rapide à faible consommation d'énergie. [1]

Notre étude s'inspire des travaux de Zhang *et al.* [2] et est effectuée sur des films minces à anisotropie perpendiculaire. Nos mesures de rotation Kerr montrent qu'en diminuant l'épaisseur d'un film mince de CoFeGd de 8.5 à 7 nm l'état d'aimantation passe d'une configuration magnétique homogène à inhomogène en champ nul (Fig. 2.b). Avant la transition, il est possible de préparer le système dans un état métastable en champ nul. L'utilisation d'une impulsion laser femtoseconde peut alors fournir suffisamment d'énergie localement pour franchir la barrière de potentiel qui sépare l'état métastable de celui de plus basse énergie. Il s'ensuit un changement de la configuration magnétique (Voir Fig. 2.a)).

Dans ce poster, nous allons présenter nos résultats sur CoFeGd en film mince sur un substrat monocristallin de Si/SiO, élaboré par PVD (Physical Vapor Deposition) sous ultraviolet dans le tube DAUM à l'Institut Jean Lamour. Une étude du signal Kerr en fonction de l'épaisseur de la couche témoigne de la transition homogène/inhomogène (Voir Fig. 2.b)). Après une impulsion laser de 30 fs sur un échantillon de CoFeGd d'épaisseur de 8.5 nm, nous avons observé l'apparition d'une texture magnétique composée de domaines par microscopie MOKE et MFM (Voir Fig. 2.c)). Des mesures non invasives par magnétométrie à balayage à centre NV [3] effectuées sur ce système mais aussi sur d'autres alliages en films minces (multicouches de PtCoAl, CoDy...) sont en cours et seront également présentées.

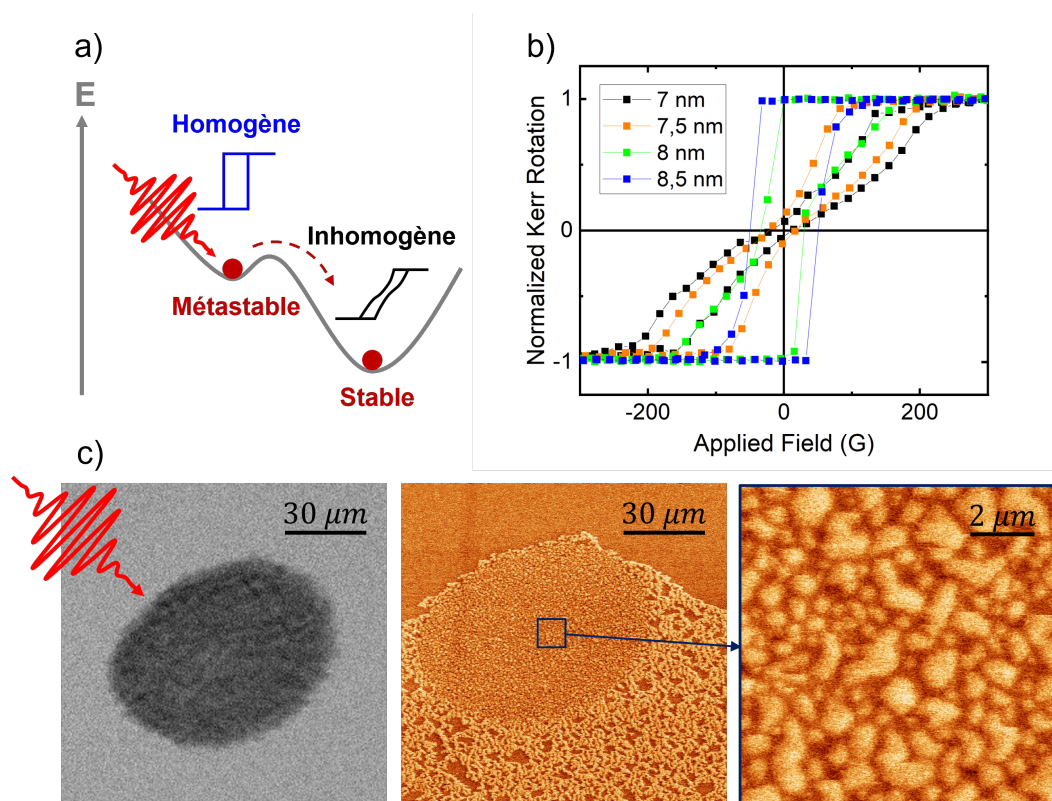


Figure 1: a) Mécanisme de transition. b) Rotation Kerr en fonction du champ magnétique pour différentes épaisseurs de couche mince de CoFeGd. c) Images de microscopie MOKE et MFM des textures magnétiques après une impulsion laser (30 fs) sur CoFeGd pour une épaisseur de 8.5 nm.

References

- [1] Hamed Vakili, Wei Zhou, Chung T. Ma, et al. [Computing and Memory Technologies based on Magnetic Skyrmions](#). *Journal of Applied Physics* 130, 070908 (2021).

- [2] Wei Zhang, Tian Xun Huang, Michel Hehn, et al. [Optical Creation of Skyrmions by Spin Reorientation Transition in Ferrimagnetic CoHo Alloys](#). *ACS Applied Materials & Interfaces* 15, 5608–5619 (2023).
- [3] Jean-Philippe Tetienne. “Un microscope de champ magnétique basé sur le défaut azote-lacune du diamant : réalisation et application à l’étude de couches ferromagnétiques ultraminces”. PhD thesis. Ecole Normale Supérieure de Cachan, 2014.

Étude de la désaimantation ultrarapide des alliages et multicouches CoPt par dichroïsme circulaire magnétique des rayons X

Lola Chamot^{1,*}, Nora Lahmiti¹, Moundji Hemili¹, Juliette Dubois^{1,2}, Matthias Riepp¹, Adriana Valerio³, Emanuele Pedersoli³, Matteo Pancaldi³, Marcel Hennes⁴, Jan Lüning⁵, Clemens Von Korff Schmising⁶, Flavio Capotondi³, Boris Vodungbo¹, and Emmanuelle Jal¹

¹*Sorbonne Université, CNRS, Laboratoire de Chimie Physique Matière et Rayonnement, LCPMR, 75005 Paris, France*

²*Laboratoire d'Optique Appliquée, ENSTA ParisTech, CNRS, École Polytechnique, Institut Polytechnique de Paris, 6 7 828 Bd des Maréchaux, 91702 Palaiseau, France*

³*Elettra-Sincrotrone Trieste SCpA, 34149 Basovizza, Trieste, Italy*

⁴*Sorbonne Université, CNRS, Institut des NanoSciences de Paris, INSP, UMR7588, F-75005 Paris, France*

⁵*Helmholtz-Zentrum Berlin für Materialien und Energie, 14109 Berlin, Germany*

⁶*Max Born Institut für Nichtlineare Optik und Kurzzeitspektroskopie, 12489 Berlin, Germany*

*lola.chamot-alory@sorbonne-universite.fr

L'étude et le contrôle de l'aimantation des matériaux présentent un grand intérêt pour la recherche fondamentale et les applications technologiques, en particulier dans le contexte du stockage de données. Dans ce contexte, la découverte de la désaimantation ultrarapide en 1996 par Beaurepaire et al. [1], révélant qu'une excitation laser de quelques femtosecondes pouvait entraîner une désaimantation à l'échelle de la picoseconde, a suscité un vif intérêt au sein de la communauté scientifique internationale.

Cependant, malgré des décennies de recherche, un consensus sur les phénomènes microscopiques à l'origine de cette désaimantation reste absent [2]. La question centrale est de savoir comment le moment angulaire de l'état ferromagnétique est transféré hors du système de spin du métal de transition à cette échelle de temps. Les études montrent une même tendance mais peuvent diverger sur les temps caractéristiques, les amplitudes de désaimantations et les mécanismes expliquant les observations expérimentales. Par exemple, concernant les alliages et multicouches de Cobalt Platine, les résultats et les interprétations physiques font débat. D'un côté, une modification de l'énergie d'échange dues à des effets locaux ou non-locaux est mis en avant [2-4]. D'un autre, des études ont révélé que des excitations transversales de type Heisenberg, telles que l'inclinaison du moment magnétique due à des fluctuations thermiques, ou des excitations collectives comme les magnons influencent la désaimantation ultrarapide.[5]

La question reste de savoir si ces différences proviennent des propriétés intrinsèques des matériaux (comme leur stœchiométrie ou leur structure) ou des techniques de caractérisation utilisées. En effet, les différentes techniques de caractérisation du magnétisme sondent des aspects distincts des propriétés des matériaux. Pour mieux comprendre la contribution et l'importance des différents phénomènes microscopiques intrinsèques et de distinguer les apports spécifiques des techniques utilisées, nous avons entrepris une étude systématique des systèmes CoPt. Dans ce cadre, nous avons réalisé des mesures de dichroïsme circulaire magnétique des rayons X (XMCD) au laser à électrons libres de rayons X (XFEL) à Elettra FERMI sur des multicouches et alliages de CoPt.

Le XMCD repose sur la différence d'absorption des rayons X en fonction de la polarisation circulaire de la lumière et de la direction d'aimantation de l'échantillon. Pour explorer la dynamique d'aimantation, il est nécessaire d'adopter une configuration expérimentale pompe-sonde permettant des mesures résolues en temps. Nous avons donc adapté l'expérience de XMCD afin de la rendre compatible avec cette approche.

L'expérience pompe-sonde a été conçue pour répondre à deux objectifs principaux: établir un dispositif offrant un très bon signal sur bruit dans une fenêtre temporelle de l'ordre de quelques picosecondes ($\Delta t = 2,7$ ps), et permettre, de sonder simultanément le Cobalt et le Platine dans les échantillons de CoPt, en utilisant deux énergies de rayons X distinctes, l'une au seuil d'absorption du Platine O_3 et l'autre au seuil $M_{2,3}$ du Cobalt.

Pour cela, l'expérience utilise une lentille à zone de Fresnel (FZP) hors axe, qui permet des mesures résolues en temps à l'échelle des picosecondes (Figure 1). La sonde est un rayon X focalisé sur l'échantillon, et la pompe est une impulsion laser infrarouge (800 nm). Comme montrée sur la figure 1, la FZP introduit des décalages temporels grâce à la différence de chemin optique entre les rayons passant par les différentes zones de la lentille. L'absorption est ensuite détectée par une caméra CCD, qui, grâce à la différence de chemin optique, associe chaque délai temporel de la désaimantation à une position spatiale distincte sur une image 2D [7]. Pour sonder simultanément le Cobalt et le Platine, deux FZP aux longueurs identiques et adaptées à des énergies distinctes ont été employées [6].

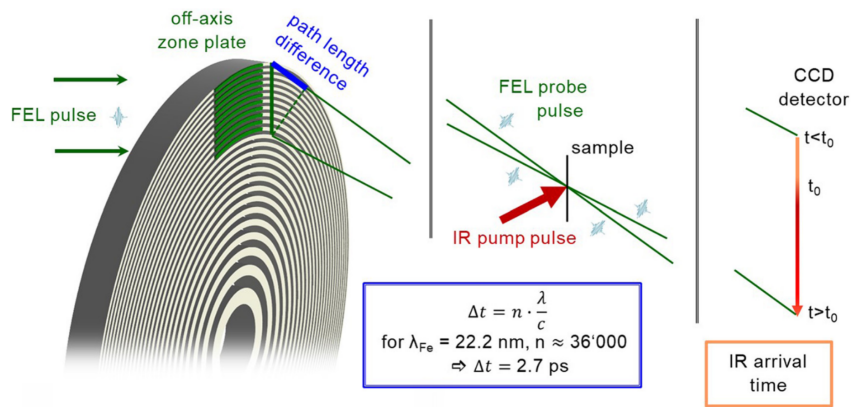


Figure 1: Illustration du principe expérimental d'une FZP [6]. Une impulsion lumineuse incidente est diffractée par une zone hors axe d'une lentille à zone de Fresnel (FZP) qui correspond au rectangle vert sur la lentille. Cette dernière va induire une différence de chemin optique et entraîner un retard temporel, Δt , qui est précisément défini par la vitesse de la lumière, le nombre de paires de zones n , et la longueur d'ondes des rayons X incidents λ . Le rectangle bleu représente une application numérique type. Dans le plan de l'échantillon les faisceaux sont focalisés au même endroit que l'on vient exciter par une impulsion infrarouge (IR). Dans le plan de la caméra CCD, les faisceaux arrivent à des temps différents: avant la pompe $t < t_0$ pour les faisceaux arrivant en haut de la caméra et après la pompe $t > t_0$ pour les rayons X arrivant en bas de la CCD.

Je détaillerai dans mon poster cette technique expérimentale en montrant comment celle-ci permet d'accéder à la dynamique d'aimantation du CoPt. Je présenterai ensuite la méthode d'analyse et les résultats obtenues au cours de ce temps de faisceau. Par ailleurs, j'exposerai l'influence des différentes intensités de pompes, compositions et structures d'échantillons, ainsi que longueurs d'ondes des rayons X sur la dynamique d'absorption mesurée.

References

- [1] E. Beaurepaire, J.-C. Merle, A. Daunois, and J.-Y. Bigot. [Ultrafast Spin Dynamics in Ferromagnetic Nickel](#). *Physical Review Letters* 76, 4250–4253 (1996).
- [2] Philippe Scheid, Quentin Remy, Sébastien Lebègue, Gregory Malinowski, and Stéphane Mangin. [Light induced ultrafast magnetization dynamics in metallic compounds](#). *Journal of Magnetism and Magnetic Materials* 560, 169596 (2022).
- [3] Shree Ram Acharya, Volodymyr Turkowski, G. P. Zhang, and Talat S. Rahman. [Ultrafast Electron Correlations and Memory Effects at Work: Femtosecond Demagnetization in Ni](#). *Physical Review Letters* 125 (2020).
- [4] Phoebe Tengdin, Wenjing You, Cong Chen, et al. [Critical behavior within 20 fs drives the out-of-equilibrium laser-induced magnetic phase transition in nickel](#). *Science Advances* 4 (2018).
- [5] Steffen Eich, Moritz Plötzing, Markus Rollinger, et al. [Band structure evolution during the ultrafast ferromagnetic-paramagnetic phase transition in cobalt](#). *Science Advances* 3 (2017).
- [6] Benedikt Rösner, Boris Vodungbo, Valentin Chardonnet, et al. [Simultaneous two-color snapshot view on ultrafast charge and spin dynamics in a Fe-Cu-Ni tri-layer](#). *Structural Dynamics* 7 (2020).
- [7] Marcel Hennes, Benedikt Rösner, Valentin Chardonnet, et al. [Time-Resolved XUV Absorption Spectroscopy and Magnetic Circular Dichroism at the Ni M2, 3-Edges](#). *Applied Sciences* 11, 325 (2020).

A step forward with 3D spintronics: electrical control of cocoons

Jhon J. Chilibingua^{1,*}, Matthieu Grelier^{1,2}, R. Battistelli³, W. Bouckaert¹, K. Puzhekadavil Joy^{3,4}, S. Collin¹, F. Godel¹, K. Bouzehouane¹, A. Vecchiola¹, A. Fert¹, F. Büttner^{3,4}, H. Popescu⁵, N. Jaouen⁵, V. Cros¹, and Nicolas Reyren¹

¹Laboratoire Albert Fert, CNRS, Thales, Université Paris-Saclay, Palaiseau, France

²Spin-ion Technologies, Palaiseau, France

³Helmholtz-Zentrum Berlin, Berlin, Germany

⁴Institut für Physik, Universität Augsburg, Augsburg, Germany

⁵Synchrotron SOLEIL, L'Orme des Merisiers, Gif-sur-Yvette, France

*jhon.chilibingua-jacome@cnrs-thales.fr

Topological magnetic textures have been rigorously studied as they could represent an asset for the development of next-generation spintronics devices, for example, for neuromorphic computing [1]. Chiral magnets and magnetic multilayers allow for the stabilization of two-dimensional (2D) textures, like the magnetic skyrmion. Beyond these 2D textures, research interest has expanded to more complex three-dimensional (3D) textures that vary structurally across their thickness.

Recently, we have reported a new type of 3D textures called skyrmionic cocoon [2, 3]. They were found in Pt/Co/Al-based aperiodic multilayers with variable Co thickness. Interestingly, these multilayers have also demonstrated the capability to host multiple objects, such as columnar skyrmions together with cocoons. Figure 1 shows an X-ray laminography reconstruction of such a system. On the other hand, new HERALDO (Holography with Extended Reference by Autocorrelation Linear Differential Operator) data were acquired, and we aim to perform a 3D reconstruction with an enhanced spatial resolution.

However, these stacks were optimized for 3D imaging using large thicknesses, several times the vertical resolution of the probe. This feature makes them unsuitable for current-induced motion of magnetic objects, since high currents are required. Even more, cocoons in these multilayers show no displacement under current pulses due to changes in rotation sense along their structure.

To overcome the problems related to thickness, we aim to reduce the number of repetitions in these stacks. This approach will make it easier to increase the current density in the tracks while making the deposition and patterning processes time- and cost-efficient. Additionally, the detection of the new textures via MFM (Magnetic Force Microscopy) will be easier due to their depth in the track. We also investigate approaches to nucleate and move cocoons through electrical currents, potentially advancing 3D spintronics applications.

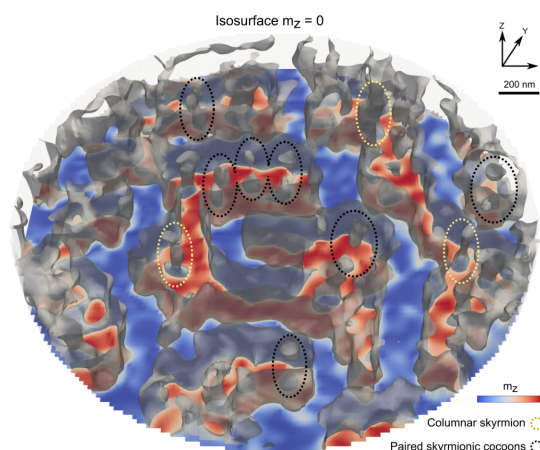


Figure 1: Laminography reconstruction showing columnar skyrmions and paired cocoons (circled). Isosurfaces $m_z = 0$ are displayed to show the transition between domains. The out-of-plane magnetization texture of the bottom layer is color-coded.

Acknowledgments

The authors acknowledge financial support from the EU project SkyANN (reference: 101135729) and from a France 2030 government grant managed by the French National Research Agency (ANR-22-EXSP-0002 PEPR SPIN CHIREX) and French ANR TOPO3D (ANR-22-CE92-0082).

References

- [1] Tristan da Câmara Santa Clara Gomes, Yanis Sassi, Dédalo Sanz-Hernández, et al. [Neuromorphic weighted sums with magnetic skyrmions](#). *Nature Electronics* (2025).
- [2] Matthieu Grelier, Florian Godel, Aymeric Vecchiola, et al. [Three-dimensional skyrmionic cocoons in magnetic multilayers](#). *Nature Communications* 13, 6843 (2022).
- [3] M. Grelier, F. Godel, A. Vecchiola, et al. [X-ray holography of skyrmionic cocoons in aperiodic magnetic multilayers](#). *Phys. Rev. B* 107, L220405 (22 2023).

Entropy-Assisted Nanosecond Stochastic Operation in Perpendicular Superparamagnetic Tunnel Junctions

L. Desplat^{1,2,*}, L. Soumah¹, N.-T. Phan¹, A. Sidi El Valli¹, A. Madhavan^{3,4}, F. Disdier¹, S. Auffret¹, R. C. Sousa¹, U. Ebels¹, and P. Talatchian¹

¹Univ. Grenoble Alpes, CEA, CNRS, Grenoble INP, SPINTEC, 38000 Grenoble, France

²Nanomat/Q-mat/CESAM, Université de Liège, B-4000 Sart Tilman, Belgium

³Associate, Physical Measurement Laboratory, NIST, Gaithersburg, Maryland 20899, USA

⁴Institute for Research in Electronics and Applied Physics, University of Maryland, College Park, Maryland 20742, USA

*louise.desplat@cea.fr

Magnetic tunnel junctions (MTJs) are now well established building blocks for nonvolatile magnetic memory, for which information retention at the scale of years is required. More recently, superparamagnetic MTJs, in which thermal noise induces the magnetization to fluctuate rapidly between two metastable states—parallel (P) and antiparallel (AP) (Fig. 1(a)), have emerged as highly appealing for numerous low-energy, unconventional and bioinspired computing applications [1, 2]. For the latter, reducing the mean dwell times between reversals is a way to increase efficiency.

In this work [3], we demonstrate a good agreement between mean dwell times measured in 50 nm diameter, perpendicularly magnetized superparamagnetic tunnel junctions, and theoretical predictions based on Langer's theory [4]. Due to a large entropic contribution, the theory yields Arrhenius prefactors in the femtosecond range for the measured junctions, in stark contrast to the typically assumed value of 1 ns. Thanks to the low prefactors, and fine-tuning of the perpendicular magnetic anisotropy, we report measured mean dwell times as low as 2.7 ns under an in-plane magnetic field at negligible bias voltage (Fig. 1(c))—a timescale thus far only reported in junctions magnetized in plane [5]. Under a perpendicular magnetic field, we predict a case of the Meyer-Neldel compensation rule, whereby the prefactor scales like an exponential of the activation energy [6], in line with the exponential dependence of the measured dwell time on the field (Fig. 1(d)). We further predict the occurrence of (sub)nanosecond dwell times as a function of effective anisotropy and junction diameter at zero bias voltage.

These findings pave the way towards the development of ultrafast, low-power, unconventional computing schemes operating by leveraging thermal noise in perpendicular SMTJs, which can be scaled down below 20 nm.

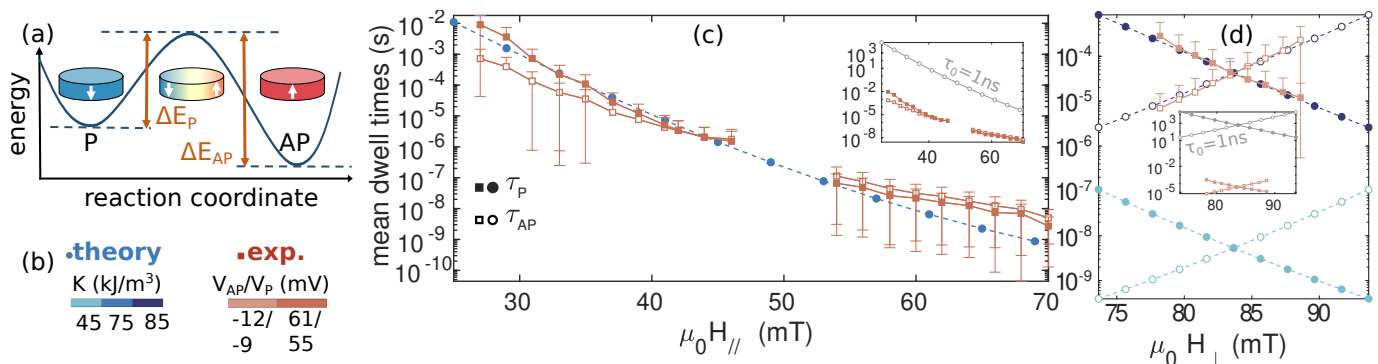


Figure 1: (a) Sketch of the energy profile along the reaction coordinate for parallel (P) and antiparallel (AP) states. (b) General legend for (c, d), where K is the effective perpendicular anisotropy, and V_{AP}/V_P is the voltage inside the MTJ. (c, d) Experimental and theoretical mean dwell times as a function of applied (c) in-plane and (d) out-of-plane field. The insets in (c, d) show a comparison with dwell times computed with a prefactor τ_0 of 1 ns.

Acknowledgments

This work was supported by NSF grant number CCF-CISE-ANR-FET-2121957, the NSF-ANR grant StochNet Project ANR-21-CE94-0002-01, the Carnot project PRIME SPOT ANR P-22-03813, and the French RENATECH network. L. D. acknowledges funding from the University of Liège under Special Funds for Research, IPD-STEMA Programme.

References

- [1] A. Mizrahi, T. Hirtzlin, A. Fukushima, et al. [Neural-like computing with populations of superparamagnetic basis functions](#). *Nat. Commun.* 9, 1533 (2018).

- [2] W. A. Borders, A. Z. Pervaiz, S. Fukami, et al. [Integer factorization using stochastic magnetic tunnel junctions](#). *Nature* 573, 390–393 (2019).
- [3] L. Soumah, L. Desplat, N.-T. Phan, et al. [Nanosecond stochastic operation in perpendicular superparamagnetic tunnel junctions](#). *arXiv preprint arXiv:2402.03452* (2024).
- [4] J. S. Langer. [Statistical theory of the decay of metastable states](#). *Ann. of Phys.* 54, 258–275 (1969).
- [5] K. Hayakawa, S. Kanai, T. Funatsu, et al. [Nanosecond random telegraph noise in in-plane magnetic tunnel junctions](#). *Phys. Rev. Lett.* 126, 117202 (2021).
- [6] L. Desplat and J.-V. Kim. [Entropy-reduced Retention Times in Magnetic Memory Elements: A Case of the Meyer-Neldel Compensation Rule](#). *Phys. Rev. Lett.* 125, 107201 (10 2020).

Eigenmode following for magnetic lifetime calculations beyond harmonic approximation

Stephan von Malottki^{1,2,3,4,*}, Moritz Goerzen¹, Hendrik Schrautzer^{1,2}, Pavel F. Bessarab^{2,5}, and Stefan Heinze^{1,6}

¹*Institute of Theoretical Physics and Astrophysics, University of Kiel, Kiel, Germany*

²*Science Institute, University of Iceland, Reykjavík, Iceland*

³*Thayer School of Engineering, Dartmouth College, Hanover, USA*

⁴*UCLouvain, Institute of Condensed Matter and Nanosciences, Louvain-la-Neuve, Belgium*

⁵*Department of Physics and Electrical Engineering, Linnaeus University, Kalmar, Sweden*

⁶*Kiel Nano, Surface, and Interface Science (KiNSIS), University of Kiel, Germany*

*stephan.von.malottki@uclouvain.be

The stability of phases and states is an important property for almost every technological application of solid state physics. It is often described by an Arrhenius law,

$$\nu = \nu_0 e^{-\beta \Delta E}, \quad (6)$$

where ν is the average transition rate, ν_0 the pre-exponential factor containing dynamical and entropic effects, ΔE the energy barrier and $k_B T$ the thermal energy. In magnetism, a recent example for extensive studies of stability are magnetic skyrmions, which are desired to be simultaneously small, deterministic and room temperature stable [1]. It has been demonstrated that not only energy barriers but also entropic effects, i. e. the prefactor, can strongly affect average skyrmion lifetimes [2].

In many fields, the application of transition state theory is the standard way to calculate prefactors. In most cases, this is made possible by applying an harmonic approximation to the energy in order to solve the Boltzmann integral over all states in the system. While the harmonic approximation is certainly powerful, it has some shortcomings, namely the assumed decoupling of eigenmodes and the assumption that the energy curve of each degree of freedom is parabolic. While the harmonic approximation is applied widely, naturally, these conditions are not always true. For magnetic skyrmions, this is the case for the rotation mode of the chimera skyrmion transition state [3, 4] as well as the rotation mode of skyrmions in the presence of weak Dzyaloshinskii-Moriya interaction [5].

Here, we present the eigenmode following (EMF) method for direct entropy calculation. In EMF, the potential energy landscape around a selected state is explored along chosen eigenvectors by iteratively updating and partially diagonalizing the Hessian matrix along the path (see Fig. 1). The Boltzmann factor along the energy curve is integrated numerically, yielding the partial partition function, and hence, the entropy contributions of the followed eigenmodes.

The EMF method comes with increased computational cost compared to the harmonic approximation due to repeated diagonalization of the Hessian matrix. However, by only treating the lowest few eigenmodes of a state with EMF while keeping the rest in harmonic approximation it is feasible to improve the description of these most important eigenmodes while still treating realistic systems.

In this presentation, first, the concept of the method and a sketch of its algorithm are introduced. This is followed by some toy model examples to illustrate EMF and make a comparison with the harmonic and zero mode approximation. Finally, real applications in skyrmionics are shown in which the traditional approaches via harmonic approximation were inadequate and the calculation of mean lifetimes has been enabled by EMF (see Fig. 2).

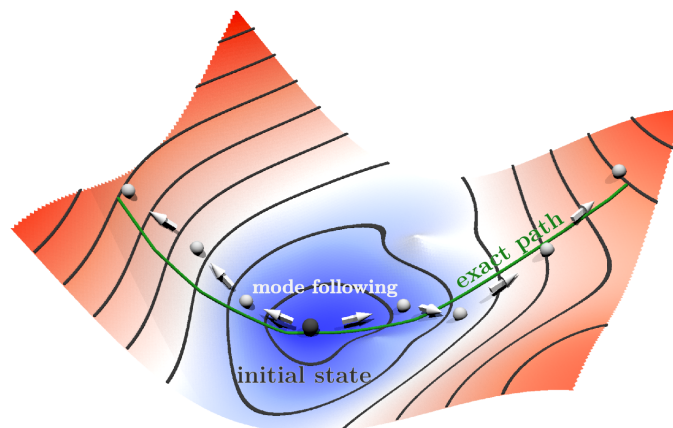


Figure 1: **Illustration of the eigenmode following method.** An arbitrary energy potential with a local minima is illustrated by the shape and colour of a 2D surface. The EMF method translates the initial state (black) iteratively along the selected eigenvector (arrows). The eigenvector is recalculated after each step, yielding an approximated path of the eigenmode.

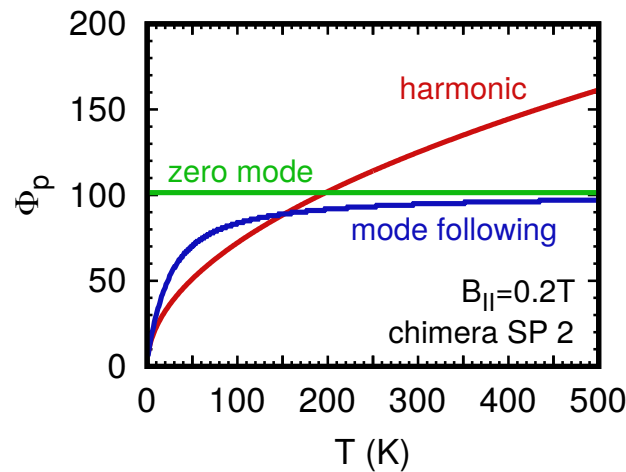


Figure 2: **Value of the partition function of the second Chimera transition state over temperature.** The partition function, Φ_p , has been calculated in harmonic approximation, zero mode approximation and with eigenmode following. The second eigenmode of the Chimera transition state corresponds to a rotation around the Bloch-like point and has been calculated in the fcc-Pd/Fe/Ir(111) system with 0.2 T of magnetic field applied in in-plane direction. Figure adapted from Ref. [4]

Acknowledgments

S.v.M. gratefully acknowledges funding of the Deutsche Forschungsgemeinschaft (DFG) via a Walter Benjamin-Stipendium with project number 523127890 as well as funding from the Fonds National de la Recherche Scientifique (FNRS) under project number 1.B.504.24. H.S. gratefully acknowledges financial support from the Icelandic Research Fund (Grant No. 239435). P.F.B. gratefully acknowledges financial support from the Icelandic Research Fund (Grants No. 217750 and 2410333), the University of Iceland Research Fund (Grant No. 15673), the Swedish Research Council (Grant No. 2020-05110), and the Crafoord Foundation (Grant No. 20231063). M.G. and S.H. gratefully acknowledge financial support from the DFG through SPP2137 “Skyrmionics” (Project No. 462602351). We thank Dr. Johannes Steinmetzer and Prof. Henrik Grönbeck for helpful discussions.

References

- [1] Börge Göbel, Ingrid Mertig, and Oleg A Tretiakov. Beyond skyrmions: Review and perspectives of alternative magnetic quasiparticles. *Physics Reports* 895, 1–28 (2021).
- [2] Johannes Wild, Thomas NG Meier, Simon Pöllath, et al. Entropy-limited topological protection of skyrmions. *Science advances* 3, e1701704 (2017).
- [3] Florian Muckel, Stephan von Malottki, Christian Holl, et al. Experimental identification of two distinct skyrmion collapse mechanisms. *Nature Physics* 17, 395–402 (2021).
- [4] Stephan von Malottki. “Stability of magnetic skyrmions in ultrathin films”. PhD thesis. Christian-Albrechts-Universität zu Kiel, 2021.
- [5] Moritz A Goerzen, Stephan von Malottki, Sebastian Meyer, Pavel F Bessarab, and Stefan Heinze. Lifetime of coexisting sub-10 nm zero-field skyrmions and antiskyrmions. *npj Quantum Materials* 8, 54 (2023).

Growth, characterization and THz time-domain spectroscopy of $\text{Bi}_{1-x}\text{Sb}_x/\text{Co}$

Mudit Jain^{1,2*}, Filip Miljevic², Sylvain Massabeau², Rodrigo Torrão², Luis Moreno Vicente-Arche², Ludovic Largeau¹, Nathaniel Findling¹, Henri Jaffres², Aristide Lemaitre¹, and Jean-Marie George²

¹*Centre for Nanoscience and Nanotechnology, CNRS, Université Paris-Saclay, Palaiseau, France*

²*Laboratoire Albert Fert, CNRS, Thales, Université Paris-Saclay, Palaiseau, France*

*mudit.jain@cnrs.fr

The development of energy-efficient spintronic devices is a significant focus in condensed matter physics and nanotechnology, with a primary challenge being the efficient conversion of spin currents into charge currents or vice versa for memory and logic applications. This is typically achieved using heterostructures comprising ferromagnetic (FM) layers and heavy metals [1]. In one direction, a charge current flowing through the heavy metal generates a spin current via the spin Hall effect, which diffuses into the FM layer and exerts a torque on its magnetization, enabling magnetic state manipulation. Conversely, the FM layer can inject a spin current into the heavy metal, which is then converted into a measurable charge current via the inverse spin Hall effect. To further enhance spin-to-charge conversion (SCC) efficiency, topological materials such as Bismuth-Antimony ($\text{Bi}_{1-x}\text{Sb}_x$) alloys have emerged as promising candidates [2]. These materials exhibit robust surface states with perpendicular spin-momentum locking, making them ideal for efficient spin transport and conversion. However, their integration poses challenges. The surface states in topological insulators (TI) are protected by time-reversal symmetry, which is broken by exchange coupling with the FM layer, potentially degrading their functionality. Therefore, achieving reliable and efficient SCC requires addressing key issues, such as optimizing the growth of high-quality BiSb thin films, preserving their surface states and minimizing the impact of exchange coupling when integrating them with FM layers.

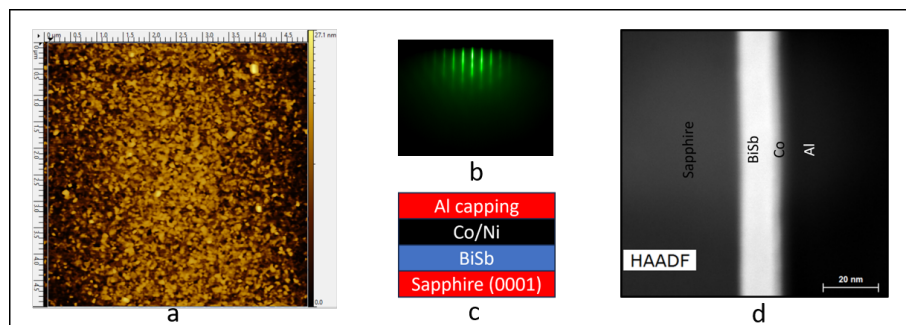


Figure 1: In **a**) is shown an *ex-situ* atomic force microscopy map of 10 nm BiSb grown on a sapphire substrate with crystallographic orientation (0001). In **b**) is shown the reflection high energy electron diffraction image of the same sample. In **c**) is the schematic of the heterostructure used to measure the spin-to-charge conversion and in **d**) is the STEM scan image of the heterostructure.

In the current study, we grow $\text{Bi}_{0.89}\text{Sb}_{0.11}$ (x nm)/Co (2 nm)/Al (2.5 nm) heterostructures via RF magnetron sputtering on sapphire (0001) substrates, where aluminum acts as a capping layer to prevent cobalt oxidation. To disentangle surface versus bulk contributions, we varied the thickness of BiSb and performed different pre-annealing and post-annealing treatments. As thickness increases, bulk contributions grow while surface contributions remain fixed. The BiSb composition was determined using Vegard's law in conjunction with XRD data. BiSb growth is highly sensitive to the -5.3% lattice mismatch with sapphire, resulting in morphology challenges: thinner films have incomplete coverage (holes), whereas thicker films exhibit vertical columnar growth. Significant efforts were made to optimize growth conditions for high-quality, near-epitaxial bilayers. Systematic investigations of thickness and annealing effects using atomic force microscopy (AFM) revealed complete films (without holes or pillars) in the 7.5–15 nm range, achieved with pre-annealing at 600–1280 °C for 9 hours and post-annealing at 225–275 °C for 180 minutes. Representative AFM images (Figure 1a) confirm an atomically flat, fully covering surface, and streaky Reflection high-energy electron diffraction (RHEED) patterns observed during growth demonstrate the bidimensional growth of BiSb layers (Figure 1b).

Alternating gradient force magnetometry (AGFM) measurements were performed to evaluate the Co magnetic configuration. By varying the magnetic field in-plane and out-of-plane while measuring sample magnetization, it was confirmed that all samples exhibited an in-plane magnetic easy axis. As spin-orbit torque (SOT) generation primarily arises at the TI/FM interface, ensuring the interface quality is crucial. Scanning transmission electron microscopy (STEM), shown in Figure 1d, confirmed the structural integrity and uniformity of the interface, reinforcing the high quality of the samples.

After achieving a satisfactory growth optimization, we used terahertz time-domain spectroscopy (THz-TDS) to investigate the SCC. The results reveal that BiSb sample with thickness of 7.5 nm, post-annealed at 275°C, and grown on pre-annealed sapphire substrates at 1100°C, exhibited the highest SCC efficiency (see Figure 2). Comparing this result value

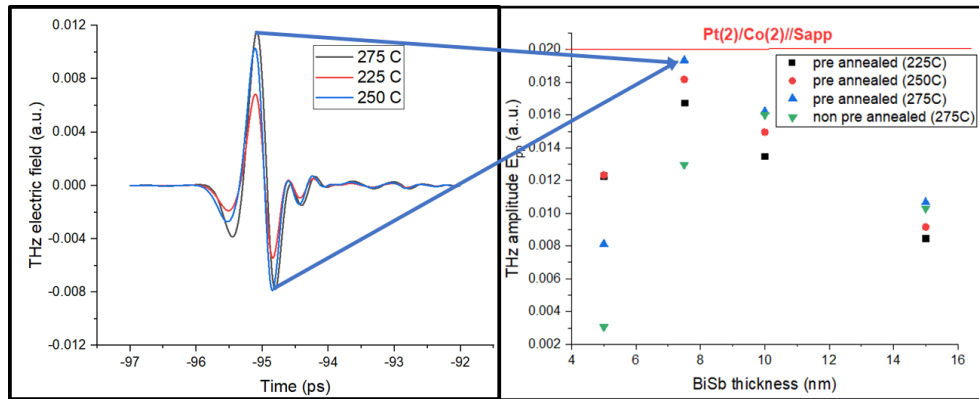


Figure 2: **Left:** THz emission of a 7.5 nm BiSb film with different post annealing temperature. **Right:** THz electric field peak-to-peak value for different conditions.

with the Pt/Co, known to be one of the best SCC convertor, we are able to achieve almost the same conversion efficiency using sputtered BiSb.

Despite the promising SCC results, significant challenges remain. For instance, distinguishing the contributions of surface and bulk states to SCC requires both optical and structural insights, necessitating further measurements and analysis to fully understand the conversion mechanism. Another key aspect is the impact of the FM proximity effect on BiSb surface states. To address this, we plan to introduce spacer layers (Pt, W, Ti, Ag) of varying thickness between Co and a 10 nm BiSb film, mitigating exchange coupling and preserving topological surface states [3], enabling a deeper understanding of surface state roles. Additionally, recent theoretical studies show that Ni exhibits enhanced orbital effects [4], making it a promising ferromagnetic layer for orbital-to-charge current conversion studies, as the orbital counterpart effect is expected to be at least an order of magnitude higher than spin current.

Acknowledgments

This work was supported by the French Agence Nationale de la Recherche under the program ESR/EquipEx+ (Grant No. ANR-21-ESRE-0025) 2D-Mag, ANR-22-EXSP-0003 TOAST, ANR-22-EXSP-0007 SPINMAT and the French RENATEC network.

References

- [1] Tuo Fan, Nguyen Huynh Duy Khang, Soichiro Nakano, and Pham Nam Hai. [Ultrahigh efficient spin orbit torque magnetization switching in fully sputtered topological insulator and ferromagnet multilayers](#). *Scientific Reports* 12 (2022).
- [2] Nguyen Huynh Duy Khang, Yugo Ueda, and Pham Nam Hai. [A conductive topological insulator with large spin Hall effect for ultralow power spin-orbit torque switching](#). *Nature Materials* 17, 808–813 (2018).
- [3] Kang Wang, Lijuan Qian, See-Chen Ying, and Gang Xiao. [Manipulation of the interlayer exchange coupling in perpendicular magnetized thin films via tunable magnetic-layer and spacer thicknesses](#). *Physical Review B* 102 (2020).
- [4] Yong Xu, Fan Zhang, Albert Fert, et al. [Orbitronics: light-induced orbital currents in Ni studied by terahertz emission experiments](#). *Nature Communications* 15 (2024).

Inverse Rashba Edelstein THz emission modulation induced by ferroelectricity in van der Waals heterostructures

Sylvain Massabeau^{1,*}, Oliver Paull¹, Armando Pezo¹, Filip Miljevic¹, Martin Mičica², Arnaud Grisard³, Pascal Morfin², Romain Lebrun^{3,1}, Henri Jaffrès¹, Sukdheep Dhillon², Jean-Marie George¹, Matthieu Jamet⁴, and Manuel Bibes¹

¹Laboratoire Albert Fert, CNRS, Thales, Université Paris-Saclay, 91767 Palaiseau, France

²Laboratoire de Physique de l'Ecole Normale Supérieure, ENS, Université PSL, CNRS, Sorbonne Université, Université Paris Cité, F-75005 Paris, France

³Thales Research & Technology, 91767 Palaiseau, France

⁴Univ. Grenoble Alpes, CEA, CNRS, Grenoble INP, IRIG-SPINTEC, F-38000 Grenoble, France

*sylvain.massabeau@cnrs-thales.fr

Spintronic Terahertz emitters, based on optically triggered spin-to-charge conversion (SCC) processes, have recently emerged as novel route towards compact and efficient THz sources. Yet, the next challenge for further technologically-relevant devices remains to modulate the emission, with low-energy consumption operation. To this aim, ferroelectric materials coupled to active spin-orbit layers such as two-dimensional transition metal dichalcogenides are potential candidates. In this work, we present the realization of a large area heterostructure of CoFeB/PtSe₂/MoSe₂ on a bidomain LiNbO₃ substrate and propose to elucidate the SCC mechanisms at work using THz time-domain spectroscopy together with density functional theory calculations.

Samples were first prepared from a LiNbO₃ wafer with pre-poled out-of-plane polarization areas along opposite directions, and cut into 10x10 mm² coupons, with half the area hosting a polarization pointing up (up area) and half pointing down (down area). The 2D layers constituting the MoSe₂/PtSe₂ van der Waals heterostructure were grown using molecular beam epitaxy on a Mica substrate and transferred onto the ferroelectric substrate in an aqueous environment [1]. Finally, a 3 nm-thick ferromagnetic layer made of CoFeB was deposited by sputtering without breaking vacuum, followed by 4 nm of Al to prevent oxidation, defining the heterostructure depicted in Fig. 1a.

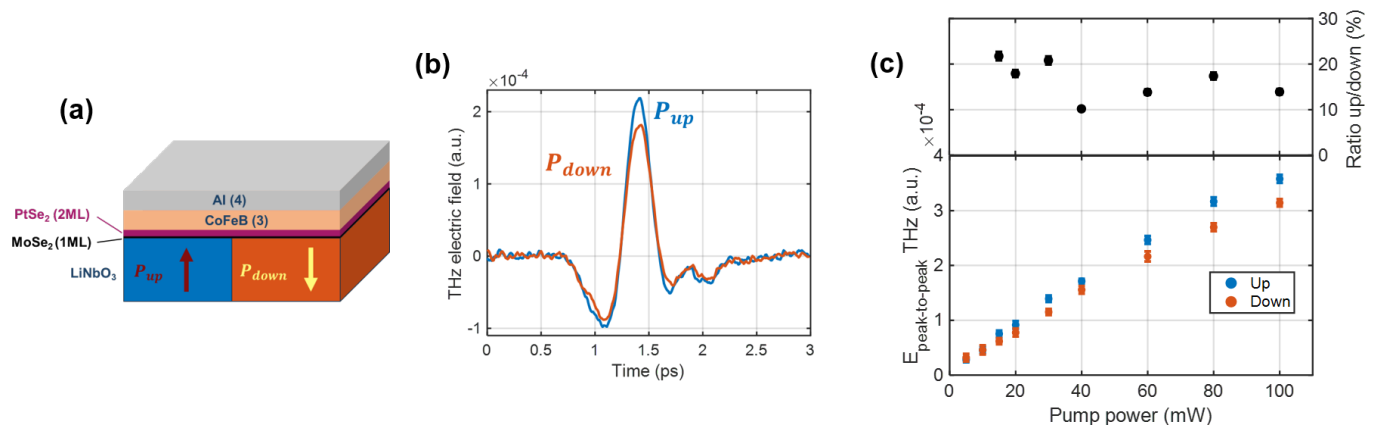


Figure 1: (a) Schematic of the full heterostructure. Numbers in parentheses express the number of monolayers (thickness in nm) for 2D (bulk) materials, respectively. (b) Temporal traces of magnetic THz contribution for up and down areas. (c) Down panel: Peak-to-peak amplitude of the magnetic contribution for up and down areas, as a function of the incident infrared pump power. Upper panel: Calculated ratio between the peak-to-peak amplitudes in up polarized and down polarized areas in % (ratio up/down) as a function of incident pump power.

The THz emission properties of the system were probed using standard THz time-domain spectroscopy technique in transmission mode. Samples were excited from the substrate side (LiNbO₃) at normal incidence by linearly polarized 80 fs-long pulses centered at 800 nm (photon energy ~ 1.55 eV) while applying a small in-plane magnetic field (~ 20 mT). We probed up and down ferroelectric areas for two opposite directions of the magnetic field, allowing to extract the magnetic contribution to the THz emission by performing the difference of the time traces [2]. We observe that both THz signatures are of the same positive phase, with a sizable increase of the THz emission in the up-poled area compared to the down one (Fig. 1c). This result shows that the ultrafast spin current generated in the FM layer under illumination is efficiently converted into a charge current into adjacent layers, in the vicinity of LiNbO₃/2D interface. Interestingly, we also observe that the THz emission remains always higher for the up area over a large range of pump power excitation (see Fig. 2a)

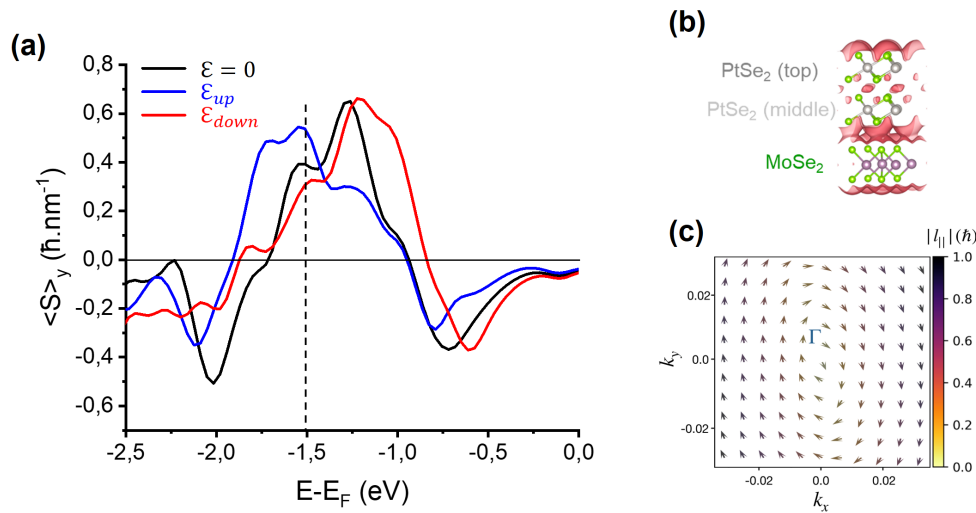


Figure 2: (a) Spin accumulation as a function of the energy for the trilayer, at equilibrium (black) and while applying an external electric field $\mathcal{E}=0.25$ V/Å pointing up (blue) and down (red). (b) Charge density for the trilayer at the isosurface 0.01 e/Å³, displaying the strong hybridization between MoSe₂ and PtSe₂. (c) Spin texture at an energy cut of $E=E_F-1.5$ eV (vertical dashed line in (a)) showing Rashba states.

corroborating the influence of ferroelectricity direction on SCC efficiency. We evaluate the induced ferroelectric modulation on SCC to be about 15-20%.

We now turn to Density Functional Theory of SCC phenomena in these systems. We evaluate in Fig. 2a the spin accumulation response, related to the Rashba Edelstein tensor and thus THz emission, at equilibrium and for an electric field \mathcal{E} pointing either up or down, in agreement with our experiment. In the absence of any additional polarization field ($\mathcal{E}=0$), a strong and positive spin accumulation is observed in the valence band. In the presence of an electric field pointing up (down), the spin accumulation remains positive and is shifted towards lower energy (higher energy), resulting in a total energy shift of about 0.32 eV, in agreement with previous experimental observation in similar systems [1]. At an energy cut of $E=E_F-1.5$ eV (vertical dashed line in Fig. 2a), corresponding to the photon energy of our pump laser, the spin up accumulation becomes larger than the down one, in qualitative agreement with our experimental results. The charge density map (Fig. 2b) highlights the conversion location in the heterostructure, showing a strong hybridization between MoSe₂ and PtSe₂ layers. Since MoSe₂ takes part to the inversion symmetry breaking, it lifts the degeneracy present in PtSe₂, leading to Rashba states (Fig. 2c) as already reported in the case of PtSe₂/Gr bilayers [3], in which SCC also occurs in the valence band. We thus interpret the observed THz emission change in up and down areas to arise from SCC mediated by Inverse Rashba-Edelstein effect at the interface between MoSe₂ and PtSe₂, and modulated by ferroelectricity.

Acknowledgments

The authors acknowledge funding from European Union's Horizon 2020 research and innovation program under grant agreement No 964735 (FET-OPEN EXTREME-IR). The French National Research Agency (ANR) is acknowledged for its support through the ANR-21-CE24-0011 TRAPIST, ANR-22-EXSP-0003 TOAST, ANR-22-EXSP-0009 SPINTHEORY and ESR/EQUIPEX+ ANR-21-ESRE-0025 2D-MAG projects. The authors also thanks F. Ibrahim, V. Libor and M. Chshiev from SPINTEC for their fruitful help into the calculation of electric field polarization in the 2D materials.

References

- [1] Raphaël Salazar, Sara Varotto, Céline Vergnaud, et al. [Visualizing Giant Ferroelectric Gating Effects in Large-Scale WSe₂/BiFeO₃ Heterostructures](#). *Nano Letters* 22, 9260–9267 (2022).
- [2] E. Rongione, S. Fragkos, L. Baringthon, et al. [Ultrafast Spin-Charge Conversion at SnBi₂Te₄/Co Topological Insulator Interfaces Probed by Terahertz Emission Spectroscopy](#). *Advanced Optical Materials* 10, 2102061 (2022).
- [3] Khasan Abdukayumov, Martin Mičica, Fatima Ibrahim, et al. [Atomic-Layer Controlled Transition from Inverse Rashba–Edelstein Effect to Inverse Spin Hall Effect in 2D PtSe₂ Probed by THz Spintronic Emission](#). *Advanced Materials* 36, 2304243 (2024).

Detection of magnetic textures via 3-Terminal MRAM devices

Rodrigo Guedas Garcia^{1,*}, Ilaria Di Manici¹, Anike Purbawati¹, Stéphane Auffret¹, Florian Disdier¹, Markus Weigan², Sebastian Wintz², Bruno Fernandez³, Gilles Gaudin¹, and Olivier Boulle¹

¹Univ. Grenoble Alpes, CEA, CNRS, Grenoble INP, SPINTEC, 38000 Grenoble, France

²Helmholtz-Zentrum Berlin für Materialien und Energie GmbH, Germany

³Univ. Grenoble Alpes, CNRS, Institut Néel, 38042 Grenoble, France

*rodrigo.guedasgarcia@cea.fr

Magnetic Skyrmions are nanometric topological spin textures that have attracted a large interest owing to their promising applicability for non-volatile memories, logic devices or non-conventional computing. Their stabilization at room temperature and current-induced motion in ferromagnetic thin films have recently been demonstrated, making them interesting candidates as information carriers [1]. Moreover, the possibility of electrically nucleating and annihilating them in basic MRAM units, Magnetic Tunnel Junctions (MTJ) [2, 3] via Voltage Controlled Magnetic Anisotropy (VCMA) and Spin Transfer Torque (STT) points them closer to commercial devices. Recently, due to their already mentioned particle-like properties and non-linearity, were proposed as possible candidates for non-conventional computing [4]. However, the low signal extracted from conventional electric measurements such as Anomalous Hall Effect (AHE) have opened the path to explore different detection methods, mainly via Tunneling Magnetoresistance (TMR) within MTJs [5] due to their large signal. Unfortunately, the use of MTJs to detect single skyrmions in a magnetic track is still a challenge, and no demonstration of TMR readout accompanied by magnetic texture imaging has been done to the moment.

The purpose of this work is to demonstrate the full electrical read and write operation of skyrmion-based devices using 3-terminal devices, an important milestone for low power consumption applications. This device consists of a magnetic track that hosts skyrmions and on top of it an MTJ to detect them (see Fig. 1a). To deterministically show skyrmion imprinting in the Free Layer of the MTJ, we simultaneously performed images using Scanning Tunneling Magnetic Microscopy (STXM) experiments and magneto-transport measurements to track the TMR by fabricating the devices on top of SiN ultrathin membranes. These techniques allow us a high spatial resolution of the spin texture and unambiguous electrical detection. The magnetic stack of the track and the FL of the MTJ are optimized to be in the spin-reorientation transition to enhance skyrmion nucleation (see Fig. 1b) with high Spin Orbit Coupling (SOC). Nanosecond current pulses are delivered through the track, displacing the skyrmions towards the detectable area below the MTJ. The TMR readout increment it is proportional to the number of skyrmions imprinted in the FL (see Fig. 1b).

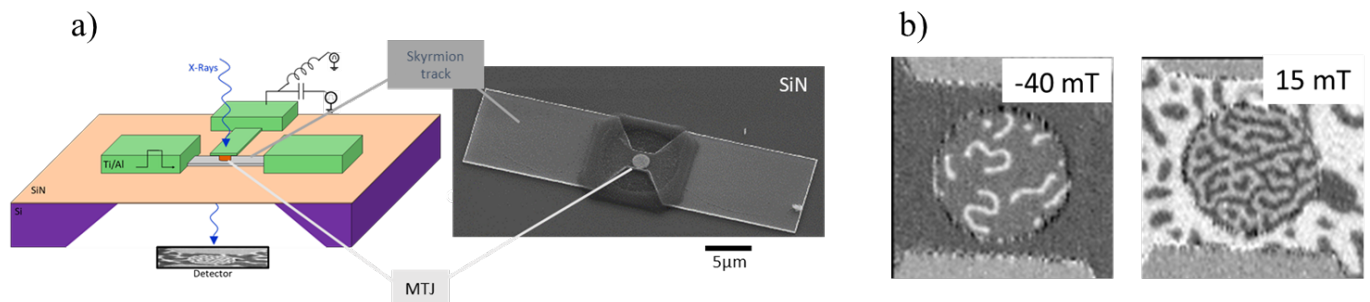


Figure 1: a) Diagram and SEM image of the 3 terminal device and b) magnetic textures in track and FL for different magnetic fields.

References

- [1] Albert Fert, Vincent Cros, and João Sampaio. [Skyrmions on the track](#). *Nature Nanotechnology* 8, 152–156 (2013).
- [2] Joseba Urrestarazu Larrañaga, Naveen Sisodia, Rodrigo Guedas, et al. [Electrical Detection and Nucleation of a Magnetic Skyrmion in a Magnetic Tunnel Junction Observed via Operando Magnetic Microscopy](#). *Nano Letters* 24, 3557–3565 (2024).
- [3] Shaohai Chen, James Lourembam, Pin Ho, et al. [All-electrical skyrmionic magnetic tunnel junction](#). *Nature* 627, 522–527 (2024).
- [4] Tomoyuki Yokouchi, Satoshi Sugimoto, Bivas Rana, et al. [Pattern recognition with neuromorphic computing using magnetic field-induced dynamics of skyrmions](#). *Science Advances* 8 (2022).
- [5] Grisca Beneke, Thomas Brian Winkler, Klaus Raab, et al. [Gesture recognition with Brownian reservoir computing using geometrically confined skyrmion dynamics](#). *Nature Communications* 15 (2024).

Strategies to measure picoTesla magnetic fields in space

T. Brun^{1,2,*}, S. Manceau^{1,2}, C. Ducruet¹, P. Sabon¹, L. Prejbeanu¹, J. Fischer¹, C. Cavoit², G. Jannet², H. Béa^{1,3}, M. Kretzschmar², and C. Baraduc¹

¹SPINTEC, Univ. Grenoble Alpes, CNRS, CEA, 17 avenue des Martyrs, Grenoble, France

²LPC2E, CNRS & Université d'Orléans, 3 avenue de la recherche scientifique, Orléans, France

³Institut Universitaire de France (IUF)

*thomas.brun@cea.fr

Magnetic tunnel junctions (MTJs) are widely employed as magnetic field sensors because of their exceptional sensitivity relative to their size. By applying a magnetic field along the hard axis direction of the free magnetic layer, its magnetization rotates coherently. Thanks to the tunnel magnetoresistance (TMR) effect and the presence of a reference magnetic layer, insensitive to this applied field, a linear variation in the junctions resistance is achieved. This resistance change is thus used to measure the amplitude of the applied field.

Our objective is to develop an integrated magnetic field sensor, based on MTJ technology, capable of detecting picotesla magnetic fields across a broad frequency band, from DC to 10 kHz. With the rise of nanosatellites (cubesat), miniaturized magnetic field sensors with such performance are essential to replace conventional bulky magnetic sensors commonly employed in space missions, such as search coils or flux gates [1]. To improve the limit of detection, or detectivity, defined by the ratio of the sensor noise over its sensitivity, increasing the sensitivity and simultaneously decreasing noise are required.

In pursuit of this objective, we first increased the MTJs sensitivity, i.e. the variation of the TMR value related to the applied magnetic field. By adding a 7 μm thick Permalloy flux concentrator (FC) grown by electrodeposition, we achieved an enhancement of the sensitivity from 3.6 %/mT to 1600 %/mT [2]. Recently, sensitivities of the order of 18 %/mT were demonstrated in optimized MTJ stacks with an inversion of the free and reference layers as compared to usual stacks [3]. By including these inverted magnetic stacks within our sensor design, we reached high sensitivities of 9.5 %/mT. The combination with our single stage flux concentrator with a gain of 440 should thus lead to 4200 %/mT.

Approaching picotesla detectivity at low frequencies also requires to minimize the noise of magnetic origin, which varies like the inverse of frequency and is thus large in our frequency range of interest. Increasing the magnetic volume is a well-known way to reduce the $1/f$ noise. However, it requires a wider and longer air-gap of the flux concentrator to accommodate larger junctions, which results in a decrease of the FC gain. We show here an optimal design (Fig. 1), resulting from a trade-off between increasing the size and number of MTJs and lessening the gain of the flux concentrator. This is achieved for 61 MTJs of 9 μm . With this optimized FC geometry and MTJ design, we estimate that we can improve the detectivity of the previously mentioned junctions with concentrators by a factor of 7. This will bring the estimated detectivity to 60 $\text{pT}/\sqrt{\text{Hz}}$.

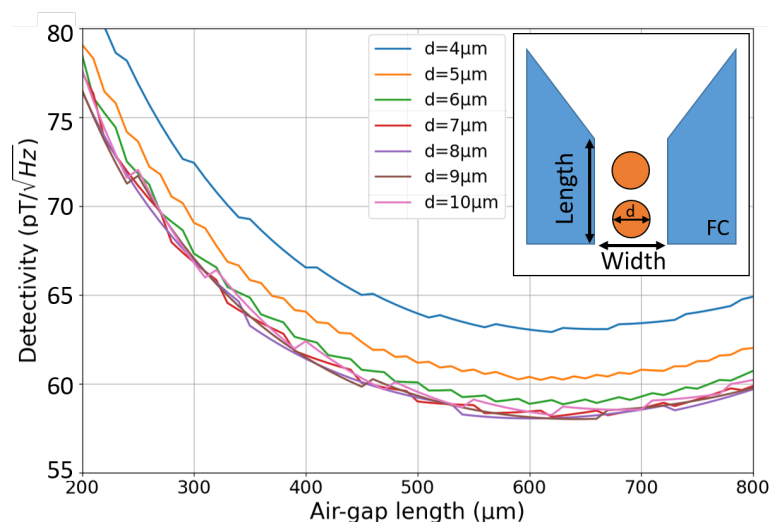


Figure 1: Estimated detectivity as a function of the air-gap length for multiple junction's diameter d . The inset represent a scheme of the air-gap with N junctions inside. The minimum is reached for 61 MTJs of 9 μm of diameter. The steps of the curve are linked with the discrete number of junctions in the air-gap.

Finally, to ultimately reach the (sub-)picotesla detectivity at low frequencies we propose to implement a magnetic modulation scheme based on magnetic flux chopping by coupling a piezoelectric and a ferromagnetic material [4]. This ongoing development is expected to lead to a magnetic sensor able to detect variations of the order of 1 pT at low frequencies (10Hz and below).

Acknowledgments

This work has been supported by CNES R&T and ANR-22-CE42-0020 project MAROT.

References

- [1] G. Jannet, T. Dudok de Wit, V. Krasnoselskikh, et al. [Measurement of Magnetic Field Fluctuations in the Parker Solar Probe and Solar Orbiter Missions](#). *Journal of Geophysical Research: Space Physics* 126, e2020JA028543 (2021).
- [2] Samuel Manceau, Thomas Brun, Johanna Fischer, et al. [Large amplification of the sensitivity of symmetric-response magnetic tunnel junctions with a high gain flux concentrator](#). *Applied Physics Letters* 123, 082405 (2023).
- [3] Tomoya Nakatani, Hirofumi Suto, Prabhanjan D. Kulkarni, Hitoshi Iwasaki, and Yuya Sakuraba. [Tunnel magnetoresistance sensors with symmetric resistance-field response and noise properties under AC magnetic field modulation](#). *Applied Physics Letters* 121, 192406 (2022).
- [4] Long Pan, Mengchun Pan, Jiafei Hu, et al. [Novel Magnetic Field Modulation Concept Using Multiferroic Heterostructure for Magnetoresistive Sensors](#). *Sensors* 20, 1440 (2020).

Passive microwave rectification in perpendicular magnetic tunnel junctions for wireless sensor networks

S. Panigrahy^{1,*}, L. Soumah¹, A. Purbawati¹, A. Sidi El Valli¹, F. Disdier¹, L. D. Buda-Prejbeanu¹, P. Talatchian¹, and U. Ebels¹

¹Univ. Grenoble Alpes, CEA, CNRS, Grenoble INP, SPINTEC, 38000 Grenoble, France

*Sujit-kumar.panigrahy@cea.fr

The rapid expansion of the global IoT market raises concerns about the energy consumption that goes along with the massive use of IoT devices. In particular, for wireless sensor networks, as part of IoT, reducing the energy consumption of its constituting components and warranting autonomous operation are two important issues. These can be tackled by concepts such as wake-up receivers and RF energy harvesting or wireless RF power transfer. Within this framework, spintronic-based devices emerge as a unique and promising solution [1]. Nanoscale magnetic tunnel junctions (MTJs) form the foundation of most spintronic-based information communication technology (ICT) devices. Over the past decade, they have been extensively demonstrated in memory and sensor applications [2]. Recently, promising results have also emerged for RF-to-DC rectification [3–6]. When the rectification signal is narrowband, it can be used for the detection of RF signals within wake-up receivers [4] and when it is broadband it can be used for RF energy harvesting or RF power transfer [5, 6]. However, since ambient RF power levels are typically low - below -30 dBm - and concentrated in frequency bands around 2.4 and 5.2 GHz, there is a critical need to develop high-efficiency devices operating at the desired frequencies without the need for a DC bias and external magnetic field. This work focuses on the investigation of such devices.

Results will be presented for the narrowband and broadband RF-to-DC signal conversion using perpendicular magnetic tunnel junctions (pMTJs) (see Fig. 1(a)). The rectified DC voltage originates from the non-linear coupling between an injected RF current and the dynamic resistance of the device, due to resonance excitations of the magnetization. A peak in the detected DC voltage is observed when the frequency of the injected current approaches the intrinsic ferromagnetic resonance (FMR) frequency of either the free layer (FL) or the reference layer (RL) of the pMTJ. A key feature of pMTJs is that their internal fields can be tuned by adjusting the device dimensions, such as the diameter and thickness of the magnetic layers. For example, by varying the FL thickness around the spin reorientation transition, it is possible to induce a transition from in-plane (IP) to out-of-plane (OOP) magnetization orientations. We examined pMTJ devices with FL thicknesses between 1.2 and 1.9 nm, covering transitions from OOP to IP orientations. A prior study from our group by Valli et al. [4] demonstrated that IP-FL configurations produce the best narrowband RF-to-DC detection signals (in the mV range) under an IP magnetic field. Such signals were observed in devices with small effective anisotropy and small nominal diameter (20 nm), which improved spin-transfer torque efficiency. Building on this work, we now demonstrate the ability to tune the rectified DC voltage using OOP magnetic fields. One notable advantage of magnetization dynamics characterization under OOP fields is that these fields can be more easily generated via internal biasing, either by incorporating a biasing ferromagnet [7] or optimizing the thickness of the synthetic antiferromagnet (SAF) layers. Our results show that applying an OOP field opposite to the RL magnetization direction consistently enhances the rectified DC voltage across devices for all FL thicknesses (Fig. 1 (c)). We achieved a maximum output voltage of 16 mV at -5 dBm input power, exceeding the performance of IP field measurements. Static magnetoresistance (MR) measurements reveal that higher OOP fields cause tilting of the magnetization of the SAF (and consequently the RL), creating a non-zero angle between the RL and FL (Fig. 1 (b)). This angular misalignment, which increases with field strength, leads to the observed improvement in the rectified DC voltage. First measurements were realized with an electromagnet whose field is limited to 170 mT; further studies using magnets up to 1 T are underway that will reveal the limit of the RF-DC signal strength. To analyze the dynamics of the different layers at larger fields, we performed macrospin simulations solving the coupled LLG equations for a four-block model representing the two layers of the SAF and the RL and FL layers. The exchange and dipolar interaction between the different layers can be adjusted, and current-induced effects such as spin transfer torque and Joule heating are included. The simulations closely match our experimental results and show that the output DC voltage initially increases with field, as in the experiment, before decreasing to zero at higher fields due to parallel alignment of the FL and RL at large OOP field values (Fig. 1 (c)).

A further observation of experimental and simulation studies is that when the magnetic field is applied in a direction opposing the RL magnetization (negative field in Fig. 1 (d) and (e)), the FMR frequencies for the RL and FL show opposite trends. In particular, the FMR frequency of the RL decreases with field, whereas the FL FMR frequency increases (Fig. 1 (e)). In devices, where the FL is close to the IP-to-OOP transition, when these two frequencies are close to each other, a large broadband rectification signal has been observed (Fig. 1 (f)). This high-frequency broadband range is tunable and lies in the range of 2.5-6.5 GHz. Another broadband rectification signal with opposite voltage is also observed in the range of 0-3 GHz (Fig. 1 (f)). These frequency ranges, which fall inside the IEEE wireless LAN standards for the 2.4, 5 and 6 GHz bands could be used in energy harvesting modules to recover wasted RF energy. To conclude, our findings show the prospect of utilizing pMTJs for narrowband microwave detectors suitable for wake-up receivers, and broadband energy harvesting.

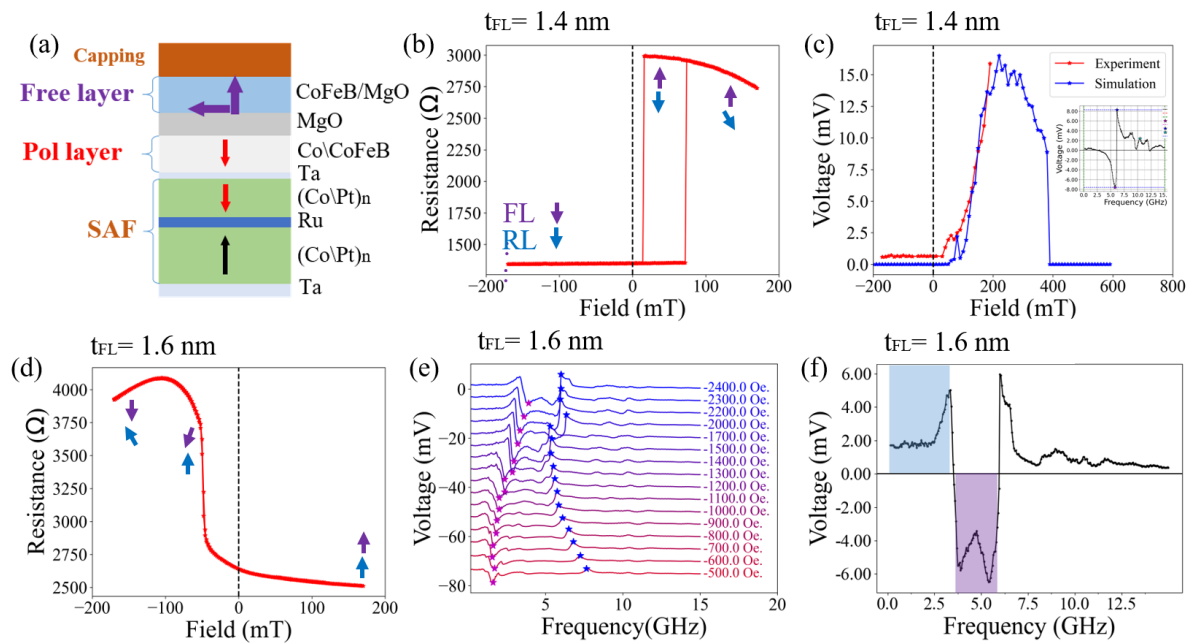


Figure 1: (a) A simplified schematic of the pMTJ stack. (b) OOP MR loop for a pMTJ with a free layer (FL) thickness of 1.4 nm, a nominal diameter of 40 nm. (c) Experimental and simulation results for Maximum rectified DC voltage for the device mentioned in (b) under an injected RF power of -5 dBm. Magnetic field swept from negative to positive. The inset shows a typical signal in this device. (d) MR loop for a pMTJ with FL thickness of 1.6 nm, a nominal diameter of 40 nm. (e) Frequency response of the rectified DC voltage at different magnetic field values for the device mentioned in (d). (f) Example of low frequency and high frequency broadband rectification (marked by regions in filled colors) in the device from (e) under a magnetic field of -230 mT.

Acknowledgments

The authors acknowledge support from the Horizon Europe project Swan-on-chip (N° 101070287) and by the France 2030 government investment plan managed by the French National Research Agency under grant reference PEPR SPIN –SPINCOM ANR-22-EXSP-0005. This work was supported by the French RENATECH Network and the Upstream Technological Platform (PTA).

References

- [1] G. Finocchio, R. Tomasello, B. Fang, et al. [Perspectives on spintronic diodes](#). *Applied Physics Letters* 118 (2021).
- [2] N. Locatelli, V. Cros, and J. Grollier. [Spin-torque building blocks](#). *Nature Materials* 13, 11–20 (2013).
- [3] A. A. Tulapurkar, Y. Suzuki, A. Fukushima, et al. [Spin-torque diode effect in magnetic tunnel junctions](#). *Nature* 438, 339–342 (2005).
- [4] A. Sidi El Valli, V. Iurchuk, G. Lezier, et al. [Size-dependent enhancement of passive microwave rectification in magnetic tunnel junctions with perpendicular magnetic anisotropy](#). *Applied Physics Letters* 120 (2022).
- [5] Raghav Sharma, Rahul Mishra, Tung Ngo, et al. [Electrically connected spin-torque oscillators array for 2.4 GHz WiFi band transmission and energy harvesting](#). *Nature Communications* 12 (2021).
- [6] Raghav Sharma, Tung Ngo, Eleonora Raimondo, et al. [Nanoscale spin rectifiers for harvesting ambient radiofrequency energy](#). *Nature Electronics* 7, 653–661 (2024).
- [7] Artem Litvinenko, Ahmed Sidi El Valli, Vadym Iurchuk, et al. [Ultrafast GHz-Range Swept-Tuned Spectrum Analyzer with 20 ns Temporal Resolution Based on a Spin-Torque Nano-Oscillator with a Uniformly Magnetized “Free” Layer](#). *Nano Letters* 22, 1874–1879 (2022).

Reconfiguring Tunnel Magnetoresistance sensors with Spin-Orbit Torque

Rohit Pachat^{1,*}, Manar Fiat², Rémy Soucaille¹, Aurélie Solignac¹, Claude Fermon¹, and Myriam Pannetier-Lecoecur¹

¹*SPEC, CEA, CNRS, Université Paris-Saclay, CEA Saclay, 91191 Gif-sur-Yvette Cedex, France*

²*Université Paris-Saclay, 91120 Palaiseau, France*

*rohit.pachat@cea.fr

Spin-orbit torque (SOT) is an energy-efficient tool to manipulate magnetization dynamics in spintronic devices. SOT is facilitated by the transfer of angular momentum of electrons from the lattice to the spin system, i.e., when a charge current flows parallel to an interface with broken inversion symmetry, spin-orbit coupling generates a spin density at the interface and/or generates transverse pure spin current in the nonmagnetic metal layer, exerting torque on the adjacent magnetic layer. Depending on its origin, the exerted torque could be field-like or damping-like, enabling various manipulations of magnetization dynamics.

The emergence of SOT has shown fast and low power magnetization switching in magnetic tunnel junctions, offering a potential alternative for cache memory applications [1, 2], current-induced magnetization dynamics such as skyrmion motion [3, 4], chiral domain wall motion [5, 6], and oscillation [7]. In addition, the three dimensional detection of magnetic fields without the need for multiple sensors has been enabled by a single SOT-magnetic field sensor [8]. Therefore, SOT emerges as a promising energy-efficient methodology for advancing spintronic devices.

In this work, SOT is used to carefully tune the magnetization dynamics of the free magnetic layer in an in-plane Ta/CoFeB/MgO/CoFeB-based tunnel magnetoresistance (TMR) sensor (see Fig. 1). Our results show that the influence of distinct SOT components, fieldlike and dampinglike torques, the magnitudes of which can be precisely regulated through the optimization of materials and heterostructures, addresses important TMR sensor challenges such as offset drifts over time, stray fields and sensing range. This innovative approach is envisaged to enable energy-efficient, reconfigurable TMR sensors.

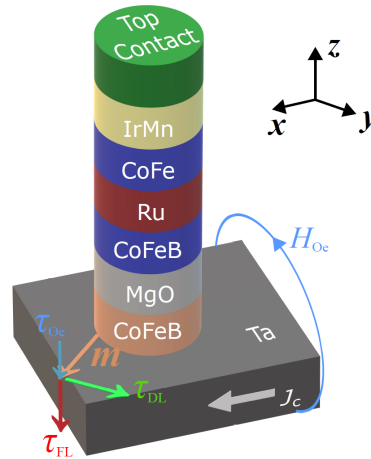


Figure 1: A schematic representation of the stack showing a charge current flowing through the Ta layer (current density J_c), generating an Oersted field H_{Oe} and the corresponding torque τ_{Oe} , as well as the distinct SOT components: fieldlike (τ_{FL}) and dampinglike (τ_{DL}) torques that act on the magnetization m of the CoFeB free layer.

Acknowledgments

We gratefully acknowledge the financial support from France 2030 government investment plan managed by the French National Research Agency under grant reference PEPR SPIN –ADAGE ANR-22-EXSP-0006 and by ANR grant STORM (ANR-22-CE42-0013-02).

References

- [1] Ioan Mihai Miron, Kevin Garello, Gilles Gaudin, et al. [Perpendicular switching of a single ferromagnetic layer induced by in-plane current injection](#). *Nature* 476, 189–193 (2011).
- [2] Murat Cubukcu, Olivier Boulle, Marc Drouard, et al. [Spin-orbit torque magnetization switching of a three-terminal perpendicular magnetic tunnel junction](#). *Applied Physics Letters* 104, 042406 (2014).
- [3] Wanjun Jiang, Pramey Upadhyaya, Wei Zhang, et al. [Blowing magnetic skyrmion bubbles](#). *Science* 349, 283–286 (2015).
- [4] Seonghoon Woo, Kai Litzius, Benjamin Krüger, et al. [Observation of room-temperature magnetic skyrmions and their current-driven dynamics in ultrathin metallic ferromagnets](#). *Nature Materials* 15, 501–506 (2016).
- [5] Satoru Emori, Uwe Bauer, Sung-Min Ahn, Eduardo Martinez, and Geoffrey S. D. Beach. [Current-driven dynamics of chiral ferromagnetic domain walls](#). *Nature Materials* 12, 611–616 (2013).
- [6] Kwang-Su Ryu, Luc Thomas, See-Hun Yang, and Stuart Parkin. [Chiral spin torque at magnetic domain walls](#). *Nature Nanotechnology* 8, 527–533 (2013).
- [7] Luqiao Liu, Chi-Feng Pai, Y. Li, et al. [Spin-Torque Switching with the Giant Spin Hall Effect of Tantalum](#). *Science* 336, 555–558 (2012).
- [8] Ruofan Li, Shuai Zhang, Shijiang Luo, et al. [A spin-orbit torque device for sensing three-dimensional magnetic fields](#). *Nature Electronics* 4, 179–184 (2021).

Spin-wave and mechanical modes of suspended YIG microdisks

G. de Loubens^{1,*}, G. Soares¹, R. Lopes Seeger¹, H. Merbouche¹, J. Ben Youssef², N. K. P. Babu³, S. O. Valenzuela³, S. W. Kurfman⁴, G. Schmidt⁴, G. Olivetti^{5,6}, B. Pigeau⁵, T. Valet⁶, and O. Klein⁶

¹*SPEC, CEA, CNRS, Université Paris-Saclay, Gif-sur-Yvette, France*

²*LabSTICC, CNRS, Université de Bretagne Occidentale, Brest, France*

³*Catalan Institute of Nanoscience and Nanotechnology (ICN2), CSIC and BIST, Bellaterra, Spain*

⁴*Martin Luther Universität Halle-Wittenberg - Institut für Physik, Halle, Germany*

⁵*Institut Néel, CNRS, Université Grenoble Alpes, Grenoble, France*

⁶*Université Grenoble Alpes, CEA, CNRS, Grenoble INP, Spintec, Grenoble, France*

*gregoire.deloubens@cea.fr

The magneto-elastic interaction couples the magnetic and elastic degrees of freedom, allowing spin waves and ultrasonic waves to hybridize [1]. Yttrium iron garnet (YIG) is well known by the magnonics community because of its extremely low spin-wave damping. It also exhibits very low acoustic losses and moderate magnetoelasticity [2], which results in strong magnon-phonon coupling in single-crystalline samples [3].

With recent advances in the nanofabrication of YIG nanoresonators [4], it can now be envisioned to couple spin-wave dynamics to mechanics in such systems. An interesting practical aspect is to efficiently actuate the mechanical modes of YIG microstructures in the gigahertz range by inductively driving specific spin-wave modes in them. A longer-term perspective would be to achieve the strong coupling regime between microwave photons, magnons, and phonons, which would allow for broadband and coherent frequency conversion using this type of magnetomechanical transducer [5].

In this work, we present the mechanical and magnetic characterizations in the microwave range of suspended YIG microdisks obtained by two distinct methods to integrate these suspended YIG structures with on-chip waveguide elements. In the first one, inductive elements are patterned near and around existing micrometer-sized suspended YIG microdisks without damage to the YIG structures (see Fig. 1(a,b)), while in the second one, focused ion beam (FIB) manufactured YIG micro-rings are transferred directly into existing inductive antennas on arbitrary substrates (see Fig. 1(c)). These two distinct methods provide alternative and complementary means, the former being a “bottom-up” approach while the latter is effectively “top-down” fabrication, to produce high-quality devices necessary for these goals.

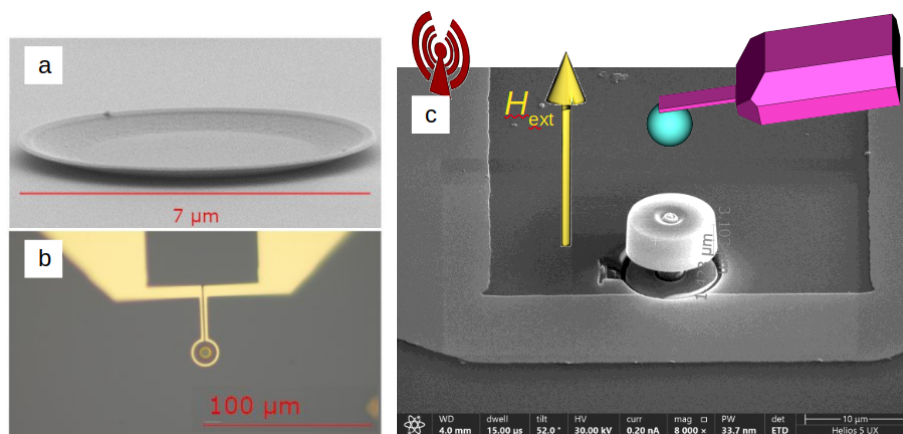


Figure 1: (a) SEM picture of a YIG disk patterned on a GGG substrate, with a thickness of 100 nm and a diameter of 7 μm (1.5 μm suspended on each side). (b) Optical picture of the same microdisk surrounded by an omega shaped microwave antenna used to excite its mechanical modes, which are monitored thanks to a homemade scanning interferometry set-up. (c) Schematics of the MRFM measurement of a YIG ring of thickness 3 μm and diameter 8.5 μm (inner diameter 2 μm). The SEM image also shows the nearby microwave antenna deposited on sapphire which provides the rf field to drive the magnetization dynamics. A cantilever with a cobalt magnetic nanosphere attached to its end is placed above the YIG microstructure to perform its spin-wave spectroscopy.

To characterize the mechanical modes of these suspended YIG microstructures, we use a homemade laser Michelson interferometer to detect mechanical vibrations. The laser probe is focused with a 100x microscope objective that can be precisely scanned over the sample with a spatial resolution of 300 nanometers. The interference signal is detected with a high-speed photodiode giving the measurement a bandwidth of 1 GHz and a displacement resolution around the picometer. To detect acoustic modes in these structures, the experiment consists in sending a microwave excitation in the antenna at a given frequency while measuring the mechanical displacement under the laser spot by demodulating the interferometric signal at the same frequency. Sweeping the excitation frequency, we access the amplitude and phase spectrum of the

mechanical vibrations. It turns out that the non-resonant magnetostriction is strong enough in YIG to transfer energy into acoustic modes. Many of them can be detected from 50 to 1000 MHz, and identified by mapping their spatial profile using the scanning capabilities of our set-up. They can be labeled with radial and azimuthal indices and understood in the framework of their total angular momentum. The smoothness and regularity of the amplitude as well as the phase profiles highlight the quality of the YIG crystal. Moreover, the vibration profiles close to the disk edges are smooth, which is a signature of clean surfaces with low roughness. As a matter of fact, the different mechanical modes exhibit quality factors of around 1000 at ambient temperature and pressure; they are expected to increase tremendously in vacuum.

To perform the spin-wave spectroscopy of the suspended YIG disks and rings, we employ a magnetic resonance force microscope (MRFM) [6], whose schematics is shown in Fig. 1(c). A magnetic probe attached at the end of a soft cantilever monitors the dipolar force with the underlying magnetic sample under microwave irradiation. When a spin-wave mode is resonantly excited in the sample, a corresponding reduction of the averaged magnetization yields the MRFM signal. The micrometer-sized YIG ring shown on the figure exhibits a rich spin-wave spectrum when it is saturated out-of-plane by the applied dc magnetic field. It is composed of three main groups of densely packed peaks, which correspond to different spatial localization of standing spin-wave modes within the spatially non-uniform internal field in the ring. A good agreement with mumax3 micromagnetic simulations and a homemade axi-symmetric eigen solver is found. To estimate the damping in this structure, we measure the linewidth of a few isolated peaks at high field. The FWHM is found to lie between 2 and 2.5 Oe at 20 GHz, yielding an upper bound of $2 \cdot 10^{-4}$ to the damping coefficient. This low value indicates that the top-down fabrication process does not introduce too much damage to the YIG ring, which was extracted by FIB from a high quality 12 μm thick film grown by liquid phase epitaxy.

Acknowledgments

This work is supported by the EU project HORIZON-EIC-2021-PATHFINDEROPEN PALANTIRI-101046630.

References

- [1] C. Kittel. [Interaction of Spin Waves and Ultrasonic Waves in Ferromagnetic Crystals](#). *Phys. Rev.* 110, 836–841 (1958).
- [2] R.C. LeCraw and R.L. Comstock. “4 - Magnetoelastic Interactions in Ferromagnetic Insulators”. *Lattice Dynamics*. Ed. by Warren P. Mason. Vol. 3. Physical Acoustics. Academic Press, 1965, 127–199.
- [3] K. An, A. N. Litvinenko, R. Kohno, et al. [Coherent long-range transfer of angular momentum between magnon Kittel modes by phonons](#). *Phys. Rev. B* 101, 060407 (2020).
- [4] F. Heyroth, C. Hauser, P. Trempler, et al. [Monocrystalline Freestanding Three-Dimensional Yttrium-Iron-Garnet Magnon Nanoresonators](#). *Phys. Rev. Applied* 12, 054031 (2019).
- [5] F. Engelhardt, V.A.S.V. Bittencourt, H. Huebl, O. Klein, and S. Viola Kusminskiy. [Optimal Broadband Frequency Conversion via a Magnetomechanical Transducer](#). *Phys. Rev. Applied* 18, 044059 (2022).
- [6] O. Klein, G. de Loubens, V. V. Naletov, et al. [Ferromagnetic resonance force spectroscopy of individual submicron-size samples](#). *Phys. Rev. B* 78, 144410 (2008).

Coercivity-driven surface acoustic wave ferromagnetic resonance

L. Thevenard^{1,*}, T. Tremblais¹, A. Vythelingum¹, D. Nguyen¹, E. Dandeu¹, V. Laude², and C. Gourdon¹

¹Sorbonne Université, CNRS, Institut des Nanosciences de Paris, INSP, F-75005 Paris, France

²Université de Franche-Comté, CNRS, Institut FEMTO-ST, F-25000 Besançon, France

*laura.thevenard@insp.jussieu.fr

For the past decade, great progress has been made in understanding how spin waves, or magnons, interact with bulk and surface acoustic wave (SAWs) via magnetoelasticity[1]. Acoustic waves are an interesting non-thermal and adjustable lever with which to actuate on a magnetic system, in particular when they are *resonant* with magnetic eigenfrequencies. Such SAW-driven ferromagnetic resonance (SAW-FMR) experiments were initially done on nickel and GaMnAs[2, 3], but very general features of this interaction, in particular the importance of the static magnetization position were put to light in cobalt, YIG, FeMnSi, or Fe[4]. In parallel to this work within the ferromagnetic resonance community, devices, models and systems were being developed by the magnetic field sensor community[5], using the same physics but treating it from an acoustic perspective. Measuring a field through the variation of elastic constants, even very far from the magnetic resonance has indeed been found to be an interesting alternative to traditional field sensors based on magnetoresistive or Hall effects, with the potential benefit of a wireless operation mode. For both sides of this same coin - harnessing magnetoelasticity to either actuate on the magnetization or to measure a field via acoustic properties - magnetic hysteresis is at best avoided, or at worst a real issue to be dealt with. In this work, we show that coercivity is in fact a viable route to reach the SAW FMR regime.

Using electrically excited SAWs (Fig. (a)), we evidence for the first time SAW FMR in FeRh, an atypical material, which we choose for its easily tunable coercivity. This equiatomic alloy exhibits upon cooling a first-order transition from a ferromagnetic (FM) state to an antiferromagnetic (AFM) state, during which it sees its coercivity diverge (Fig. b). Working on a FeRh(270nm)/Ta(100nm)/GaAs sample and performing positive/negative field sweeps, we find the SAW FMR to be hysteretic (Fig. c), with a coercivity perfectly matching that of the static magnetization at all temperature (Figs. (b,d)). The data is modeled well when considering the SAW to induce an effective magneto-acoustic field, which forces the precession of the magnetization [2]. The resonance field corresponds to the one for which the eigenfrequency matches the SAW frequency. This condition is validated at the coercivity, when field and magnetization are anti-aligned, and the applied field exactly compensates the anisotropy field $B_u = \frac{2K_u}{M_s}$, thus softening the eigenfrequency down to f_{SAW} (Eq. 7 with $\phi_{eq}=0$ or π depending on the field history) (Fig. (b) and [4]).

$$\omega_0(H) = \frac{\gamma}{M_s(1+\alpha^2)} \sqrt{2K_u \cos 2\phi_{eq} + \mu_0 H M_s \cos \phi_{eq}} \sqrt{\mu_0 H M_s \cos \phi_{eq} + 2K_u \cos^2 \phi_{eq} + \mu_0 M_s^2 (1 - P_{00}(k))} \quad (7)$$

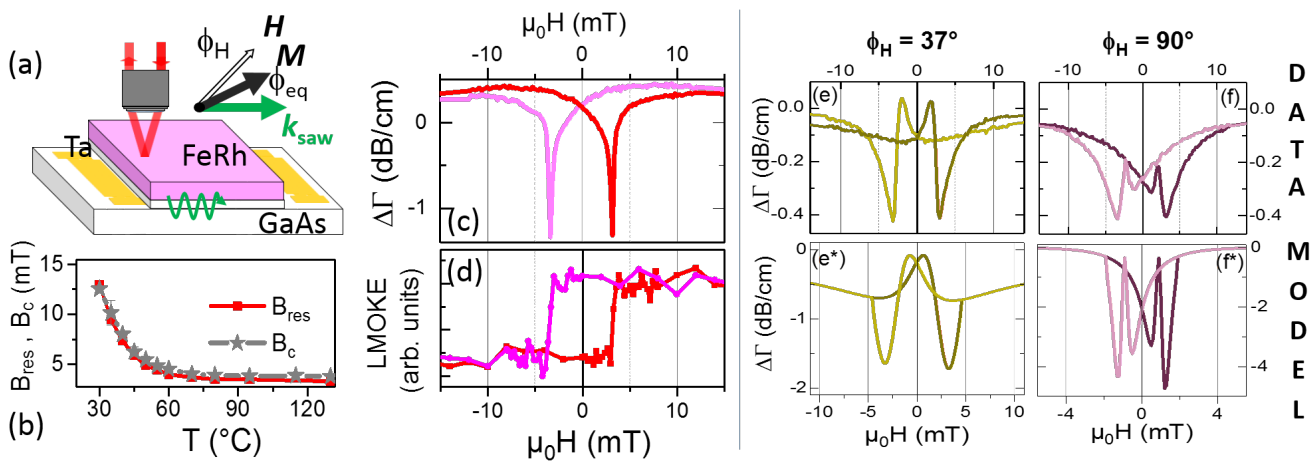


Figure 1: (a) A $f_{SAW}=299$ MHz SAW is excited along the [110] direction of GaAs substrate and travels on a FeRh/Ta/GaAs stack grown by a graded composition technique[6]. (c) Hysteretic SAW amplitude variations at 130°C with the resonance field matching the static coercivity of the sample measured by longitudinal microscopy at the same temperature (d), a feature observed at all temperatures coming down from the fully ferromagnetic phase (b). (e), (e*), (f) and (f*) SAW amplitude variations for different in-plane field angles, data (top curves) and model using a hysteretic SAW-FMR model (bottom).

Varying the field angle of the applied field, unusual hysteretic shapes are observed (Fig. (d,e)). Again the SAW-FMR model including hysteresis, *i.e.* with M and H allowed to be anti-aligned in the Landau-Lifshitz equation, reproduces qualitatively well the observed features. Here we will show that peaks not only come from a softening of the eigenfrequency

(Eq. 7), but also of the canceling of the magneto-elastic field for specific positions of the static magnetization. To conclude, hysteretic SAW-FMR has been observed and a clear correlation between resonance and coercive fields demonstrated. The effect has been tracked down to the lowering of the eigenfrequency at the coercivity. Using a combination of isotropic depinning energy and uniaxial anisotropy, this model was extended to explain the field angle dependency of the SAW-FMR. Looking towards SAW-based applications such as field sensors, resonators and magnetic delay lines, for which clever solutions have been devised to avoid hysteresis, such a model could now be used to harness this hysteresis to obtain a large, resonant response of these devices at very moderate fields.

Acknowledgments

This work has been partly supported by the French Agence Nationale de la Recherche (ANR ACAF 20-CE30-0027), and the PEPR SPIN project: ANR 22 EXSP 0008 and ANR 22 EXSP 0004. We acknowledge D. Hrabovsky (MPBT - Mesures Physiques à Basses Températures-Physical Properties Low-Temperature Facility of Sorbonne University) for help with the magnetometry experiments.

References

- [1] Per Delsing, Andrew N Cleland, Martin J A Schuetz, et al. [The 2019 surface acoustic waves roadmap](#). *Journal of Physics D: Applied Physics* 52, 353001 (2019).
- [2] M. Weiler, L. Dreher, C. Heeg, et al. [Elastically Driven Ferromagnetic Resonance in Nickel Thin Films](#). *Physical Review Letters* 106 (2011).
- [3] L. Thevenard, C. Gourdon, J. Y. Prieur, et al. [Surface-acoustic-wave-driven ferromagnetic resonance in \(Ga, Mn\)\(As, P\) epilayers](#). *Physical Review B* 90 (2014).
- [4] Pauline Rovillain, Jean-Yves Duquesne, Louis Christienne, et al. [Impact of Spin-Wave Dispersion on Surface-Acoustic-Wave Velocity](#). *Physical Review Applied* 18 (2022).
- [5] V. Polewczyk, K. Dumesnil, D. Lacour, et al. [Unipolar and Bipolar High-Magnetic-Field Sensors Based on Surface Acoustic Wave Resonators](#). *Physical Review Applied* 8 (2017).
- [6] D. Nguyen Ba, G. Olivetti, T. Tremblais, et al. [Origin of low-field microwave absorption in metallic magnetic films evidenced in FeRh/Ta/GaAs](#). *to appear in Phys. Rev. B* (2025).

Non-reciprocal caustic spin-wave beams in extended ferromagnetic film

Dinesh Wagle¹, Daniel Stoeffler², Loic Temdie³, Vincent Castel³, Hicham Majjad², Romain Bernard², Yves Henry², Matthieu Bailleul², Matthias Benjamin Jungfleisch¹, and Vincent Vlaminck^{3,*}

¹Department of Physics and Astronomy, University of Delaware, Newark, DE 19716, USA

³Institut de Physique et Chimie des Matériaux de Strasbourg (IPCMS), UMR 7504, UDS, CNRS, 23 rue du Loess, BP 43, 67034, Strasbourg, France

²IMT Atlantique, Dpt. MO, Lab-STICC - UMR 6285 CNRS, Technopole Brest-Iroise CS83818, 29238 Brest Cedex 03, France

*vincent.vlaminck@imt-atlantique.fr

The control of spin waves beamforming and near-field interferences at the sub-micron scale is central for the development of wave-based computing applications such as reservoir computing [1], holographic memory, or spectral analysis [2]. The complexity of spin dynamics, inherently due to its dependence to numerous parameters, and the intricacy of magnon-magnon interactions, requires heavy computational methods, which can limit the scope of study. In this context, we developed an efficient tool to study the near-field diffraction (NFD) patterns of spin-wave in homogeneous out-of-plane magnetized thin films for arbitrary distribution of excitation fields [3, 4]. In this communication, we present the adaptation of our NFD model to in-plane magnetized thin films, and reveal how non-reciprocal caustic spin-wave beams can be directly emitted from a sharply constricted stripline [5]. In particular, we draw on the importance of assessing the microwave field distribution in nanostructured antennas using Comsol simulations, which are subsequently used as input for the micromagnetic and NFD simulations. Using spatially resolved micro-focused Brillouin light spectroscopy on various constriction sizes, we satisfyingly verify our predictions, and explore further the steerability as well as the caustic beams properties. These findings showcase the potential for two-dimensional magnonic devices like magnon circulators, advancing scalable spin-wave-based information processing technologies.

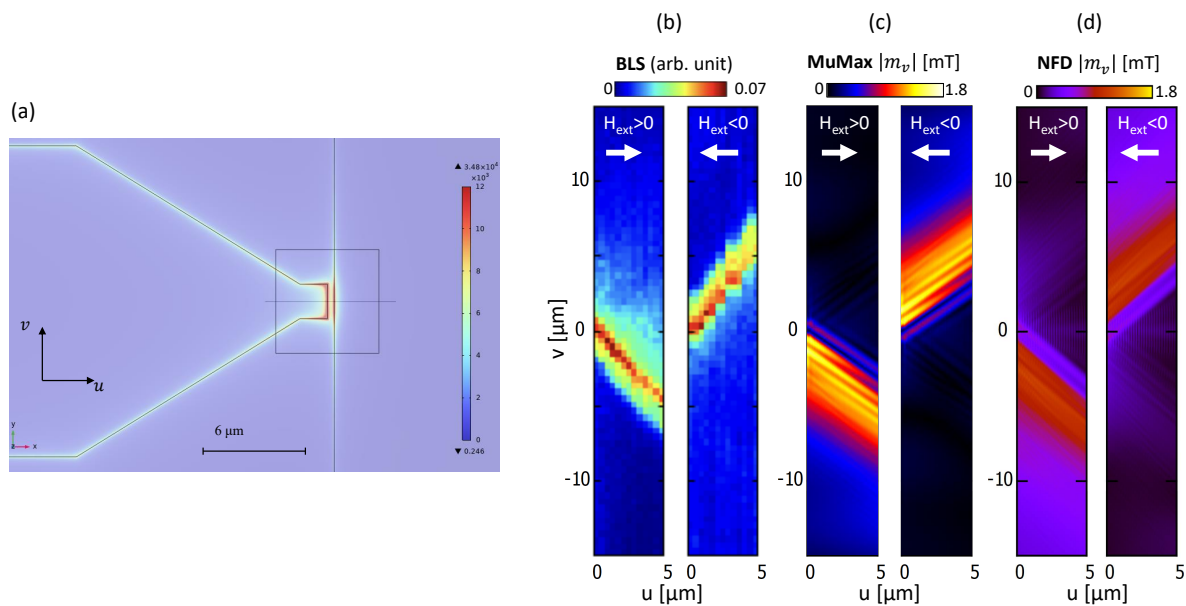


Figure 1: (a) Comsol simulation of the microwave field distribution in a nanoconstricted stripline. (b) BLS measurement at 7.5 GHz, and a +188 mT (left) and -188 mT (right) bias field applied along u . (b) Corresponding MuMax3, and (c) NFD simulations for both bias field polarities.

Acknowledgments

We acknowledge the financial support from the French National research agency under the projects *MagFunc*/ANR-20-CE91-0005, and also France 2030 program under project ANR-22-EXSP-0004 SWING. We also thank the High Performance Computing Center of the University of Strasbourg for supporting this work by providing scientific support and access to computing resources. Research at the University of Delaware was supported by the U.S. Department of Energy, Office of Basic Energy Sciences, Division of Materials Sciences and Engineering under Award DE-SC0020308.

References

- [1] [Ádám Papp, Wolfgang Porod, and Gyorgy Csaba. Nanoscale neural network using non-linear spin-wave interference. *Nature Communications* 12 \(2021\).](#)
- [2] [Ádám Papp, Wolfgang Porod, Árpád I. Csurgay, and György Csaba. Nanoscale spectrum analyzer based on spin-wave interference. *Scientific Reports* 7 \(2017\).](#)
- [3] [V. Vlaminc, L. Temdie, V. Castel, et al. Spin wave diffraction model for perpendicularly magnetized films. *Journal of Applied Physics* 133 \(2023\).](#)
- [4] [L. Temdie, V. Castel, M.B. Jungfleisch, et al. Probing Spin Wave Diffraction Patterns of Curved Antennas. *Physical Review Applied* 21 \(2024\).](#)
- [5] [Dinesh Wagle, Daniel Stoeffler, Loic Temdie, et al. *Shaping non-reciprocal caustic spin-wave beams*. 2024.](#)

Spin Hall magnetoresistance at the altermagnetic insulator/Pt interface

Miina Leiviskä^{1,*}, Reza Firouzmandi², Kyo-Hoon Ahn¹, Peter Kubaščík³, Zbynek Soban¹, Satya Prakash Bommanaboyena¹, Christoph Müller¹, Dominik Kriegner¹, Sebastian Sailler⁴, Michaela Lammel⁴, Kranthi Kumar Bestha^{2,5}, Libor Šmejkal^{6,7,1}, Jakub Zelezny¹, Anja U. B. Wolter², Monika Scheufele^{8,9}, Johanna Fischer¹⁰, Matthias Opel⁸, Stephan Geprägs⁸, Matthias Althammer⁸, Bernd Büchner^{2,11,12}, Tomas Jungwirth^{1,13}, Lukáš Nádvořník³, Sebastian T. B. Goennenwein⁴, Vilmos Kocsis², and Helena Reichlova¹

¹*Institute of Physics, Czech Academy of Sciences, Prague, Czechia*

²*Institut für Festkörperforschung, Leibniz IFW Dresden, Dresden, Germany*

³*Faculty of Mathematics and Physics, Charles University, Prague, Czechia*

⁴*Department of Physics, University of Konstanz, Konstanz, Germany*

⁵*Institute of Solid State and Materials Physics, TU Dresden, Dresden, Germany*

⁶*Max Planck Institute for the Physics of Complex Systems, Dresden, Germany*

⁷*Max Planck Institute for Chemical Physics of Solids, Dresden, Germany*

⁸*Walther-Meißner-Institut, Bayerische Akademie der Wissenschaften, Garching, Germany*

⁹*Technical University of Munich, TUM School of Natural Sciences, Physics Department, Garching, Germany*

¹⁰*Université Grenoble Alpes, CEA, CNRS, Spintec, Grenoble, France*

¹¹*Institute of Solid State and Materials Physics and Würzburg-Dresden Cluster of Excellence ct.qmat, Technische Universität Dresden, Dresden, Germany*

¹²*Center for Transport and Devices, Technische Universität Dresden, Dresden, Germany*

¹³*School of Physics and Astronomy, University of Nottingham, Nottingham, UK*

*leiviska@fzu.cz

Spin Hall magnetoresistance (SMR) is a magnetoresistive effect present in magnetic insulator (MI) and heavy metal (HM) bilayers [1, 2]. As illustrated in Figure 2a, it relies on the concerted action of spin Hall (SHE) and inverse spin Hall effects (ISHE), and spin accumulation dissipation at the interface: when a current (\mathbf{j}_c) is driven in the HM layer, a spin current (\mathbf{j}_s) and a spin accumulation (μ_s) at the HM|MI interface is generated via SHE and depending on the spin transparency of this interface \mathbf{j}_s can flow into the MI ($\mathbf{j}_s^{\text{abs}}$) while the back-reflected spin current ($\mathbf{j}_s^{\text{ref}}$) is re-converted to a charge current via ISHE. Rotating the (sublattice) magnetic moment direction (\mathbf{m}) will modulate the resistivity of the HM layer as the spin current transparency of the interface is sensitive to \mathbf{m} . Typically, $\mu_s \parallel \mathbf{m}$ facilitates the spin current reflection at the HM|MI interface giving a low-resistance state, while $\mu_s \perp \mathbf{m}$ facilitates the spin current absorption by the MI giving a high-resistance state. The relative resistance difference between these two states, known as the SMR ratio, is usually of the order of 0.01% in MI/Pt heterostructures [3–5].

Altermagnets are a new class of collinear compensated magnets with a unique anisotropic spin ordering with characteristic spin-degenerate nodes and alternating even-parity spin polarization that breaks the time-reversal symmetry [6]. Their various unconventional properties, such as the pure spin-current generation [7–10] and anisotropic chirality-split magnon dispersion [11, 12], are potentially advantageous for spintronics and magnonics. In addition, also the record SMR ratio (0.25 %) has been observed in heterostructures of Pt and the insulating altermagnetic candidate α -Fe₂O₃ [5], considerably surpassing the SMR ratio in heterostructures incorporating ferrimagnetic insulators, such as yttrium ion garnet (YIG) (0.16 %) [3], and antiferromagnetic insulators, such as NiO (0.08 %) [4].

In this work, we present a set of SMR measurements in heterostructures of Pt and an insulating and ferroelectric altermagnet candidate Ba₂CoGe₂O₇ (BCGO). We will first detail the fabrication of devices for SMR experiments on bulk crystals of BCGO, and then discuss characteristic SMR features of the BCGO/Pt heterostructures. Notably, we show that the SMR ratio is unexpectedly large and shows anisotropy depending on in which crystal direction the current is applied as shown in Figure 2b. We systematically rule out device-to-device variations, magnetic domains, magnetocrystalline anisotropy, and electric polarization as the main origin of this current-direction anisotropy of the SMR ratio. Finally, we will suggest mechanisms through which the crystal symmetries that characterize the altermagnetic phase of BCGO could give rise to the observed anisotropy.

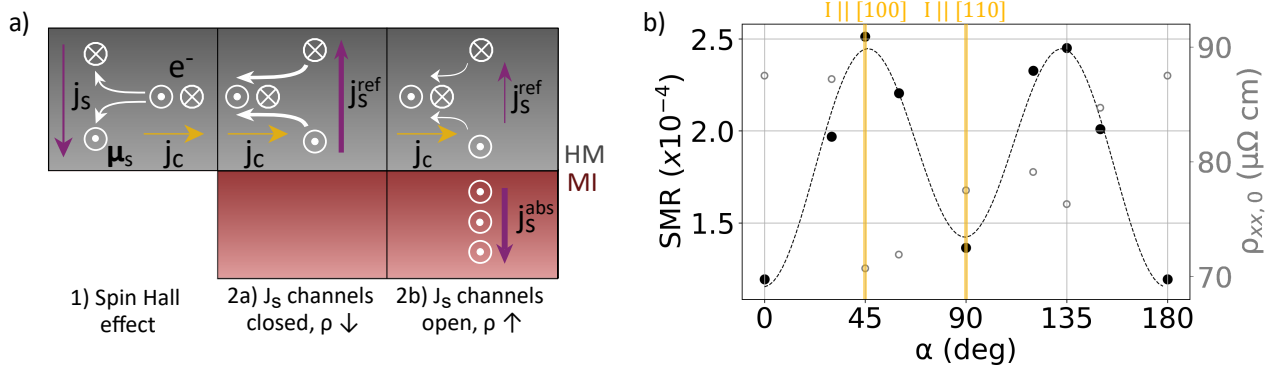


Figure 1: a) Spin Hall magnetoresistance modulates the resistivity of the HM in HM/MI heterostructures. (1) A charge current (j_c) generates a spin current (j_s) and consequently a spin accumulation μ_s at the HM|MI interface. (2) j_s can be either reflected (j_s^{ref}) or absorbed (j_s^{abs}) at the interface depending on the available spin current channels across the interface. (2a) When there are no available channels the spin current is reflected and converted back to charge current and (2b) when the channels are open the spin current is absorbed by the MI. b) The SMR ratio (closed symbols) depends on the crystal direction of the current channel (α is the angle between the current and the $[1\bar{1}0]$ crystal axis) while the same trend is not observed in the longitudinal resistivity of Pt ($\rho_{xx,0}$) (open symbols).

Acknowledgments

The work was supported by the Grant Agency of the Czech Republic Grant No. 22-17899K, the Dioscuri Program IV23025 funded by MPG and MEYS, TERA FIT - CZ.02.01.01/00/22_008/0004594 funded by OP JAK, call Excellent Research, the Deutsche Forschungsgemeinschaft (DFG, German Research Foundation) via projects 445976410 and 490730630, as well as via Project-ID No. 446571927 and the SFB 1432, Project-ID No. 425217212, and the Grant Agency of the Charles University through grants No. 166123 and SVV-2024-260720. We also gratefully acknowledge technical support and advice by the nano.lab facility of the University of Konstanz. V. K. was supported by the Alexander von Humboldt Foundation.

References

- [1] H. Nakayama, M. Althammer, Y.-T. Chen, et al. [Spin Hall Magnetoresistance Induced by a Nonequilibrium Proximity Effect](#). *Phys. Rev. Lett.* 110, 206601 (2013).
- [2] Yan-Ting Chen, Saburo Takahashi, Hiroyasu Nakayama, et al. [Theory of spin Hall magnetoresistance](#). *Phys. Rev. B* 87, 144411 (2013).
- [3] Matthias Althammer, Sibylle Meyer, Hiroyasu Nakayama, et al. [Quantitative study of the spin Hall magnetoresistance in ferromagnetic insulator/normal metal hybrids](#). *Phys. Rev. B* 87, 224401 (2013).
- [4] Johanna Fischer, Olena Gomonay, Richard Schlitz, et al. [Spin Hall magnetoresistance in antiferromagnet/heavy-metal heterostructures](#). *Phys. Rev. B* 97, 014417 (2018).
- [5] Johanna Fischer, Matthias Althammer, Nynke Vlietstra, et al. [Large spin Hall magnetoresistance in antiferromagnetic \$\alpha\$ -Fe₂O₃/Pt Heterostructures](#). *Phys. Rev. Appl.* 13, 014019 (2020).
- [6] Libor Šmejkal, Jairo Sinova, and Tomas Jungwirth. [Beyond Conventional Ferromagnetism and Antiferromagnetism: A Phase with Nonrelativistic Spin and Crystal Rotation Symmetry](#). *Phys. Rev. X* 12, 031042 (2022).
- [7] Rafael González-Hernández, Libor Šmejkal, Karel Výborný, et al. [Efficient Electrical Spin Splitter Based on Nonrelativistic Collinear Antiferromagnetism](#). *Phys. Rev. Lett.* 126, 127701 (2021).
- [8] Arnab Bose, Nathaniel J. Schreiber, Rakshit Jain, et al. [Tilted spin current generated by the collinear antiferromagnet ruthenium dioxide](#). *Nature Electronics* 5, 267–274 (2022).
- [9] Shutaro Karube, Takahiro Tanaka, Daichi Sugawara, et al. [Observation of Spin-Splitter Torque in Collinear Antiferromagnetic RuO₂](#). *Phys. Rev. Lett.* 129, 137201 (2022).
- [10] H. Bai, Y. C. Zhang, Y. J. Zhou, et al. [Efficient Spin-to-Charge Conversion via Altermagnetic Spin Splitting Effect in Antiferromagnet RuO₂](#). *Phys. Rev. Lett.* 130, 216701 (2023).
- [11] Libor Šmejkal, Alberto Marmodoro, Kyo-Hoon Ahn, et al. [Chiral Magnons in Altermagnetic RuO₂](#). *Phys. Rev. Lett.* 131, 256703 (2023).
- [12] Qirui Cui, Bowen Zeng, Ping Cui, Tao Yu, and Hongxin Yang. [Efficient spin Seebeck and spin Nernst effects of magnons in altermagnets](#). *Phys. Rev. B* 108, L180401 (2023).

Direct CVD graphene integration for Spintronics

J. Perrin^{1,*}, V. Zatzko¹, S. Dubois³, J. Daniel¹, S. Vergara¹, H. Wei¹, F. Brunnett¹, E. Aoustin¹, J. Peiro², F. Godel¹, F. Petroff¹, J.C. Charlier³, M.B. Martin¹, B. Dlubak¹, and P. Seneor¹

¹Laboratoire Albert Fert, CNRS, Thales, Université Paris-Saclay, Palaiseau, France

²Thales Research and Technology, Palaiseau, France

³Institute of Condensed Matter and Nanosciences (IMCN), Université Catholique de Louvain, B-1348 Louvain-la-Neuve, Belgium
*jeremy.perrin@cnsr-thales.fr

Spin-based electronics, recently highlighted as a leading candidate for highly efficient and ultrafast embedded memories (such as MRAMs) and post-CMOS unconventional electronics strategies (including spin logics, stochastic, neuromorphic and quantum computing), has experienced considerable growth. Beyond the intrinsic spin transport properties of graphene, 2D materials have unlocked a wealth of previously unexplored opportunities for spintronic devices.

We will present results concerning the integration of graphene in vertical Magnetic Tunnel Junctions. We will show that a thin graphene passivation layer, directly integrated by low temperature catalyzed chemical vapor deposition (CVD) [1–3], allows to preserve a highly surface sensitive spin current polarizer/analyzer behavior and adds new enhanced spin filtering properties. Here, the graphene layer prevents the oxidation of the ferromagnet enabling the use of novel processes for spintronics devices. [4, 5].

Comprehensive characterizations of complete spin valves making use of graphene grown by CVD will be presented. First, we will illustrate the protection property of graphene by demonstrating the use of ozone-based ALD processes for fabricating efficient spin valves protected with graphene. Following this, we will discuss the experimental spin signals in the context of highly efficient bulk band structure spin filtering effect (reminding MgO symmetry filtering). Additionally, we will also highlight the critical role of interfacial hybridization for spin selection (a.k.a spinterface) for spin selection. Notably, we will reveal spin polarizations exceeding 98% in Magnetic Tunnel Junctions (MTJ), with ab-initio calculations in support. [6, 7]. We will further discuss potential toward scaling of 2D materials based spin devices, and integration into applications. [8] The different presented experiments unveil promising uses of 2D materials for spintronics.

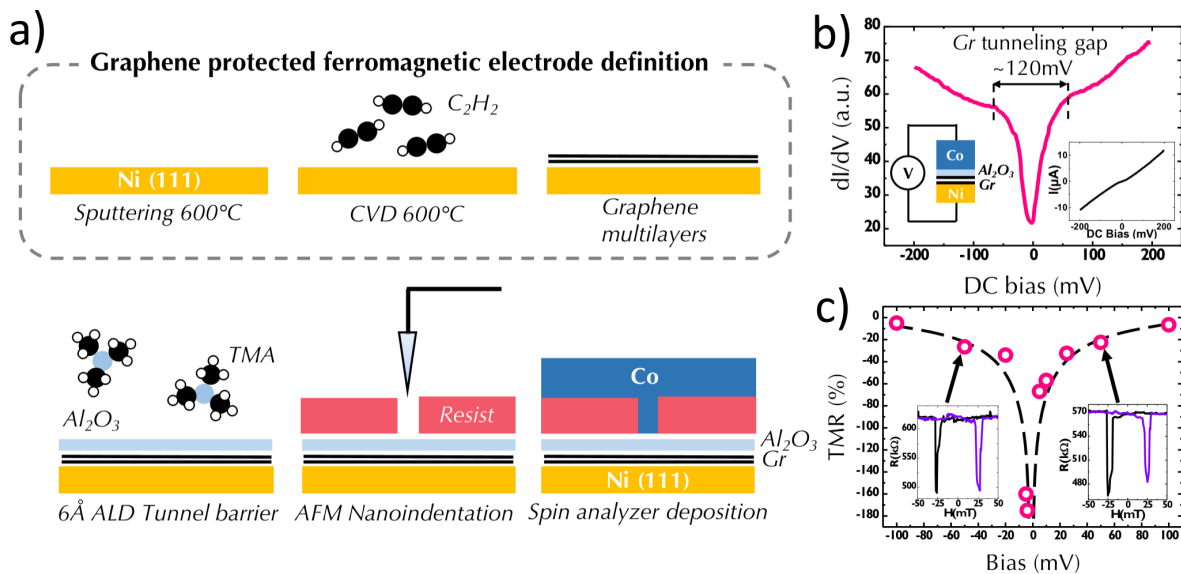


Figure 1: a) Schematic process flow for the fabrication of epitaxial multilayer graphene-based MTJs b) Conductance measurement recorded at 2 K on the graphene-based spin valve. c) TMR dependency with respect to the DC bias applied in the junction with pink circles being experimental TMR measured at different biases.

References

- [1] Bruno Dlubak, Marie-Blandine Martin, Robert S. Weatherup, et al. [Graphene-Passivated Nickel as an Oxidation-Resistant Electrode for Spintronics](#). *ACS Nano* 6, 10930–10934 (2012).
- [2] H. Naganuma, V. Zatzko, M. Galbiati, et al. [A perpendicular graphene/ferromagnet electrode for spintronics](#). *Applied Physics Letters* 116, 173101 (2020).
- [3] Maëlis Piquemal-Banci, Regina Galceran, Marie-Blandine Martin, et al. [2D-MTJs: introducing 2D materials in magnetic tunnel junctions](#). *Journal of Physics D: Applied Physics* 50, 203002 (2017).

- [4] Marie-Blandine Martin, Bruno Dlubak, Robert S. Weatherup, et al. [Sub-nanometer Atomic Layer Deposition for Spintronics in Magnetic Tunnel Junctions Based on Graphene Spin-Filtering Membranes](#). *ACS Nano* 8, 7890–7895 (2014).
- [5] Pascal Martin, Bruno Dlubak, Richard Mattana, et al. [Combined spin filtering actions in hybrid magnetic junctions based on organic chains covalently attached to graphene](#). *Nanoscale* 14, 12692–12702 (35 2022).
- [6] Maëlis Piquemal-Banci, Regina Galceran, Simon M.-M. Dubois, et al. [Spin filtering by proximity effects at hybridized interfaces in spin-valves with 2D graphene barriers](#). *Nature Communications* 11 (2020).
- [7] Victor Zatko, Simon M.-M. Dubois, Florian Godel, et al. [Almost Perfect Spin Filtering in Graphene-Based Magnetic Tunnel Junctions](#). *ACS Nano* 16, 14007–14016 (2022).
- [8] Hyunsoo Yang, Sergio Valenzuela, Mairbek Chshiev, et al. [Two-dimensional materials prospects for non-volatile spintronic memories](#). *Nature* 606, 663–673 (2022).

Depth-resolved magnetization dynamics in Fe thin films after ultrafast laser excitation

Valentin Chardonnet¹, Marcel Hennes², Romain Jarrier¹, Renaud Delaunay¹, Nicolas Jaouen³, Marion Kuhlmann⁴, Cyril Leveillé³, Clemens von Korff Schmising⁵, Daniel Schick⁵, Kelvin Yao⁵, Xuan Liu³, Gheorghe S. Chiuzbaian¹, Jan Lüning⁶, Boris Vodungbo^{1,*}, and Emmanuelle Jal¹

¹Sorbonne Université, CNRS, Laboratoire de Chimie Physique – Matière et Rayonnement, LCPMR, Paris 75005, France

²Sorbonne Université, Institut des NanoSciences de Paris, INSP, CNRS UMR 7588, Paris 75005, France

³Synchrotron SOLEIL, L'Orme des Merisiers Saint-Aubin, BP48, 91192 Gif-sur-Yvette, France

⁴Deutsches Elektronen-Synchrotron, 22607 Hamburg, Germany

⁵Max Born Institut für Nichtlineare Optik und Kurzzeitspektroskopie, 12489 Berlin, Germany

⁶Helmholtz-Zentrum Berlin für Materialien und Energie, 14109 Berlin, Germany

*emmanuelle.jal@sorbonne-universite.fr

During the last two decades, a variety of models have been developed to explain the ultrafast quenching of magnetization following femtosecond optical excitation [1–3]. These models can be classified into two broad categories, relying either on a local or a non-local transfer of angular momentum [3, 4]. To distinguish those local and non-local effects we can measure the magnetization depth profile with femtosecond resolution, thanks to time-resolved x-ray resonant magnetic reflectivity [5, 6]. In this presentation, I will show how, from our experimental results gathered at the free electron laser FLASH, we can unravel the dynamics of the transient inhomogeneous depth magnetic profile of an Fe layer after optical excitation.

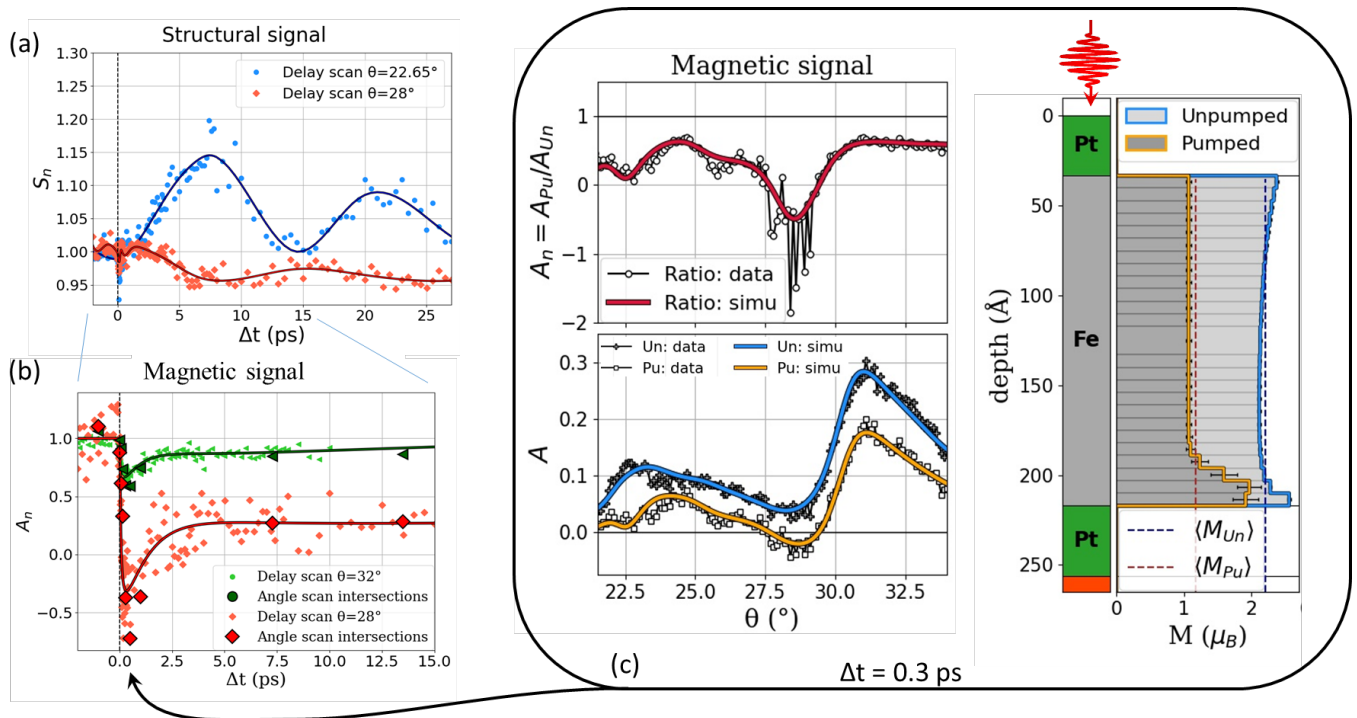


Figure 1: Delay scans for the (a) structural signal S_n and (b) magnetic signal A_n extracted from x-ray magnetic reflectivity as a function of the delay Δt between the pump and the probe for two different reflectivity angles θ . (c) Magnetic signal as a function of the reflectivity angle θ for a delay $=\Delta t = 0.3$ ps and its fit for the magnetic asymmetry Pumped and Unpumped (Pu - orange and Up - blue respectively) and their ratio (A_n - red). The depth magnetic profile derived from these fits is shown in the right panel for unpumped data (without optical excitation, blue) and 300 fs after an optical excitation (Pumped, orange). The vertical axis corresponds to the sample depth with the different layers indicated on the left while the horizontal axis corresponds to the magnetization in μ_B .

First our experiment on a polycrystalline Fe sample reveals two distinct dynamics at different time scales for the structure and the magnetization [Fig. 1 (a) and (b)]. Until one picosecond, the magnetic signal is quickly evolving while the structural one stays more or less constant. After that, the magnetic signal is slowly coming back to equilibrium while the structural one changes periodically. For this structural signal, we observe a maximum dilation of 0.2 nm followed by a coherent damped oscillation of the thickness of the sample [Fig. 1 (a)]. This dynamic is due to stresses that are generated by the rapid increase in temperature and might be enhanced via magnetostrictive effects.

Second, the quantitative analysis of our magnetic reflectivity data allows us to retrieve the inhomogeneous depth magnetic profile for different delays after the optical excitations. As shown in Fig. 1 (c), close to the bottom interface, there is an overall reduction of the demagnetization. When comparing this result to simulation we can directly show that both local and non-local phenomena [7] take place at the same time scale and that there is probably a contribution from spin currents that could carry the magnetization beyond the magnetic layer [8].

References

- [1] M. Battiato, K. Carva, and P. M. Oppeneer. [Superdiffusive Spin Transport as a Mechanism of Ultrafast Demagnetization](#). *Physical Review Letters* 105, 027203 (2010).
- [2] B. Koopmans, G. Malinowski, F. Dalla Longa, et al. Explaining the paradoxical diversity of ultrafast laser-induced demagnetization. *Nature Materials* 9, 259–265 (2010).
- [3] G. P. Zhang, Y. H. Bai, Tyler Jenkins, and Thomas F. George. [Laser-induced ultrafast transport and demagnetization at the earliest time: first-principles and real-time investigation](#). *Journal of Physics: Condensed Matter* 30, 465801 (2018).
- [4] P. Scheid et al. [Light induced ultrafast magnetization dynamics in metallic compounds](#). *Journal of Magnetism and Magnetic Materials* 560, 169596 (2022).
- [5] Emmanuelle Jal, Víctor López-Flores, Niko Pontius, et al. [Structural dynamics during laser-induced ultrafast demagnetization](#). *Physical Review B* 95, 184422 (2017).
- [6] Valentin Chardonnet, Marcel Hennes, Romain Jarrier, et al. [Toward ultrafast magnetic depth profiling using time-resolved x-ray resonant magnetic reflectivity](#). *Structural Dynamics* 8, 034305 (2021).
- [7] J. Wiczorek, A. Eschenlohr, B. Weidtmann, et al. [Separation of ultrafast spin currents and spin-flip scattering in Co/Cu\(001\) driven by femtosecond laser excitation employing the complex magneto-optical Kerr effect](#). *Phys. Rev. B* 92, 174410 (2015).
- [8] A. Eschenlohr, M. Battiato, P. Maldonado, et al. [Ultrafast spin transport as key to femtosecond demagnetization](#). *Nature Materials* 12, 332–336 (2013).

Proximity effect between 2D ferromagnetic and 2D ferroelectric materials

Cyriack Jego^{1,*}, Quentin Guillet¹, Gaétan Verdier¹, Rayan Jamil⁴, Oliver Paull², Elzbieta Gradauskaite², Rahul Sharma¹, Isabelle Gomes de Moraes¹, Van-Hoan Le⁴, Hanako Okuno⁴, Nicolas Gauthier⁴, Alain Marty¹, Jean François Jacquot³, and Matthieu Jamet¹

¹Université Grenoble Alpes, CEA, CNRS, IRIG-Spintec, 38000 Grenoble, France

²Laboratoire Albert Fert, CNRS, Thales, Université Paris-Saclay, 91767, Palaiseau France

³Université Grenoble Alpes, CEA, CNRS, IRIG-SYMMES, 38000 Grenoble, France

⁴Université Grenoble Alpes, CEA-LETI, 38000 Grenoble, France

*cyriack.JEGO@cea.fr

Recently, molecular beam epitaxy (MBE) has become a powerful tool to grow high-quality 2D materials on large areas, opening a new route for their integration in spintronics or electronic devices. As an example, the MBE growth of 2D Van der Waals ferromagnets has been achieved with perpendicular magnetic anisotropy [1] and room temperature Curie temperature (T_c) [2]. Those materials are made of atomically thin monolayers weakly bound to each other by a van der Waals interaction. In such materials, the number of layers is a key parameter in controlling the magnetic properties. Post-growth annealing constitutes another method of adjusting magnetic properties by controlling the annealing temperature and duration [3]. Our primary candidate for exploring this effect is Cr₂Te₃, a 2D vdW ferromagnet. After the growth on graphene, we can modify the Curie temperature (approximately 100 K increase) with in situ annealing while maintaining a similar atomic structure but different stoichiometry[4]. We also found that using a stable capping layer (alumina) allows us to increase the Curie temperature even higher (up to room temperature) by annealing the film in air (see Fig.1). Another promising family of materials are 2D ferroelectrics. One recent example is the 2D layered α -In₂Se₃ material with polarization both in and out of plane and showing a T_c above room temperature (see Fig.2). Moreover, this material also has other phases (β and γ) with the same stoichiometry but different electronic properties, which is of great interest for the development of new memory devices. This combination of knowledge on 2D vdW ferromagnetic and ferroelectric materials with high T_c leads us toward the development of a synthetic multiferroic heterostructure (2D ferromagnet/2D ferroelectrics) working at room temperature, by taking advantage of the proximity effects between the two materials. Our goal is to control magnetic properties with ferroelectric polarization. The main challenge would be to maintain the desired properties necessary for the proximity effect while succeeding in the growth of the heterostructure by MBE, especially since the ferromagnet is grown in a Te-rich chamber while the ferroelectric is grown in a Se-rich chamber.

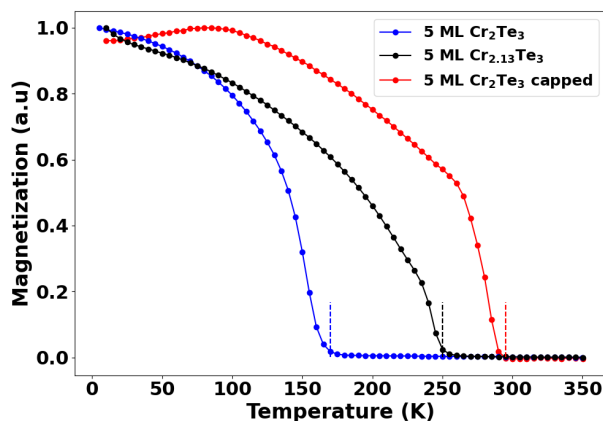


Figure 1: SQUID measurements of the remanence magnetization as a function of temperature to determine the Curie temperature of Cr₂Te₃;

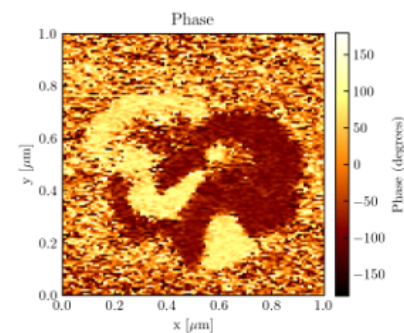


Figure 2: Piezo force microscopy (PFM) image of 10 nm In₂Se₃.

Acknowledgments

The French National Research Agency (ANR) is acknowledged for its support through the ANR-18-CE24-0007 MAGIC-VALLEY and ESR/EQUIPEX+ ANR-21-ESRE-0025 2D-MAG projects. The LANEF framework (No. ANR-10-LABX-0051) is acknowledged for its support with mutualized infrastructure.

References

- [1] Quentin Guillet, Libor Vojáček, Djordje Dosenovic, et al. Epitaxial van der Waals heterostructures of Cr₂Te₃ on two-dimensional materials. *Physical Review Materials* 7, 054005 (2023).
- [2] M Ribeiro, G Gentile, A Marty, et al. “Large-scale epitaxy of two-dimensional van der Waals room-temperature ferromagnet Fe₅GeTe₂. npj 2D Mater”. *Appl.* Vol. 6. 2022, 1038.
- [3] Yuita Fujisawa, M Pardo-Almanza, Jennifer Garland, et al. Tailoring magnetism in self-intercalated Cr_{1+δ}Te₂ epitaxial films. *Physical Review Materials* 4, 114001 (2020).
- [4] Quentin Guillet, Hervé Boukari, Fadi Choueikani, et al. Magnetic evolution of Cr₂Te₃ epitaxially grown on graphene with post-growth annealing. *Applied Physics Letters* 124 (2024).

Epitaxial growth of $(\text{LaVO}_3)_n/(\text{PrVO}_3)_m$ superlattices for emerging multiferroicity

Adrian Bénédict-Cardenas^{1,*}, Ludovic Pasquier¹, Jaafar Ghanbaja¹, Sylvie Migot¹, Karine Dumesnil¹, and Olivier Copie¹

¹Institut Jean Lamour, CNRS, Université de Lorraine, 54000 Nancy, France

*adrian-alberto.benedict-cardenas@univ-lorraine.fr

The increasing demand for faster digital technologies drives the development of advanced memory materials. Modern memory processing involves the dynamics of reading and writing in various storage types. Magnetic memories are highly reliable for long-term data retention but consume significant energy during the writing process. Conversely, electric memories are energy-efficient during writing but suffer from volatility, posing challenges for long-term stability.

Recent innovations have introduced hybrid memories that combine the advantages of electric and magnetic properties. These systems leverage an electric field for writing and magnetic order for stable information retention, offering a promising pathway towards fast and efficient memory technologies [1][2][3]. Such advancements have fuelled the exploration of multiferroic materials that exhibit coupled magnetic and electric properties.

In the last decade, a novel multiferroic material was theoretically predicted. This material is structured as a perovskite superlattice of rare earth oxides as represented in figure 1. At low temperatures, the superexchange interaction causes an antiferromagnetic behaviour that, at the same time, may be coupled with improper ferroelectric behaviour [4] where the Jahn-Teller distortions and orbital ordering play a significant role. This study presents the synthesis of superlattices, in the form of epitaxial thin films, composed of repeating motifs of $(\text{LaVO}_3)_n/(\text{PrVO}_3)_m$, where n and m represent the number of unit cells for each compound per motif.

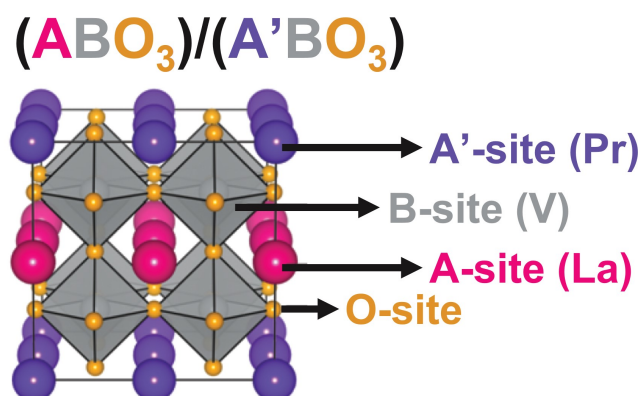


Figure 1: Superlattice structure for achieving multiferroic properties. Atoms of vanadium are located at the B site. Oxygen atoms are located at the vertices of the octahedron. The A site is filled by a rare earth element and the A' site by another. In this work the A and A' rare earth used were lanthanum and praseodymium respectively

The $(\text{LaVO}_3)_n/(\text{PrVO}_3)_m$ superlattices were deposited using Molecular Beam Epitaxy (MBE), with an ozone source acting as the oxygen provider. Two distinct deposition strategies were employed to achieve the desired structures. In the co-deposition approach, vanadium and rare earth atoms simultaneously arrive at the substrate, allowing the materials to self-arrange into the target structure. Alternatively, the atomic layer-by-layer (ALL) deposition method involves sequential arrival of vanadium and rare earth atoms at the substrate. This process enforces a controlled growth sequence, regulated by successive openings of effusion cell shutters. ALL allows for the formation of sharper interfaces inside the superlattice [5].

Monitoring of the growth process is performed using Reflection High-Energy Electron Diffraction (RHEED). For that purpose, oscillations of the intensity of the 01 streak along the $[110]$ azimuth are registered in real time. For the co-deposition approach, one oscillation corresponds to the deposition of one unit cell. In the case of ALL deposition, the RHEED intensity increases during the arrival of rare earth atoms and decreases during vanadium deposition (see figure 2). The precise timing of the shutter openings is critical for achieving the correct doses for the AO and VO_2 planes.

After deposition, the structure and epitaxy of the superlattices were examined using a variety of analytical techniques. Reciprocal space mapping, performed by X-ray diffraction (XRD), allowed a comparison of in-plane lattice parameters between the substrate and the superlattice. The in-plane lattice parameter decreases while the out-of-plane parameter increases. The former adjusts to match with the substrate lattice parameter and forces the latter to increase. High resolution transmission electron microscopy (HR-TEM), particularly high-angle annular dark-field scanning transmission electron microscopy (HAADF-STEM), provided validation of the epitaxial growth in agreement with RHEED and XRD.

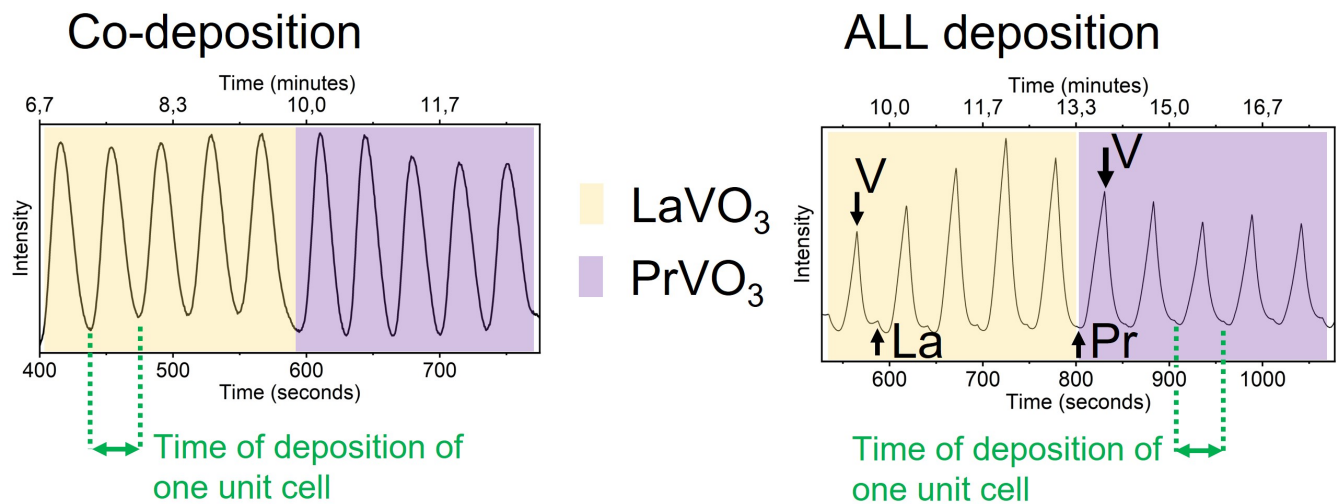


Figure 2: RHEED oscillation monitoring superlattice growth on co-deposition and atomic layer-by-layer (ALL) regimes. On both cases, one oscillation corresponds to the deposition of one unit cell. Regions in yellow and purple correspond to deposition of LaVO_3 and PrVO_3 respectively. On ALL deposition, arrows indicate the moment each cell's shutter is opened during one oscillation. Each shutter is closed just before the opening of the next one. Intensity increases (decreases) during the arrival of rare earth (vanadium) atoms.

The successful synthesis of $(\text{LaVO}_3)_n/(\text{PrVO}_3)_m$ superlattices with $n = m$ was achieved, with a total thickness maintained at 40 nm. Satellite peaks observed in XRD Bragg-Brentano configuration diffractograms confirmed the formation of periodic superlattices for both co-deposition and ALL methods. Additionally, electron energy loss spectroscopy (EELS) probed the composition of each atomic layer and confirmed that there was no interdiffusion.

References

- [1] Marian Vopsaroiu, John Blackburn, and Markys G Cain. [A new magnetic recording read head technology based on the magneto-electric effect](#). *Journal of Physics D: Applied Physics* 40, 5027–5033 (2007).
- [2] Marian Vopsaroiu, John Blackburn, A. Muniz-Piniella, and Markys G. Cain. [Multiferroic magnetic recording read head technology for 1Tbit.in.2 and beyond](#). *Journal of Applied Physics* 103 (2008).
- [3] J. F. Scott. [Multiferroic memories](#). *Nature Materials* 6, 256–257 (2007).
- [4] Julien Varignon, Nicholas C. Bristowe, Eric Bousquet, and Philippe Ghosez. [Coupling and electrical control of structural, orbital and magnetic orders in perovskites](#). *Scientific Reports* 5 (2015).
- [5] J.H. Haeni, C.D. Theis, and D.G. Schlom. [RHEED Intensity Oscillations for the Stoichiometric Growth of \$\text{SrTiO}_3\$ Thin Films by Reactive Molecular Beam Epitaxy](#). *Journal of Electroceramics* 4, 385–391 (2000).

Contribution of non-uniform magnetization states to the initial susceptibility of soft magnetic materials

Anne-Lise Adenot-Engelvin¹ and Mélissa Marchi^{1,*}

¹CEA-DAM Le Ripault, BP 16, 37260 Monts, France

*Melissa.MARCHI@cea.fr

The initial permeability of sintered soft ferrites plays a critical role in the design of many magnetic devices. For a given composition, many experimental data report the variation of the initial permeability with the average grain size. This was first interpreted by the contribution of a domain wall relaxation to the permeability, in accordance with microwave permeability measurements [1]. Globus has then expressed various grain size dependences depending on the field regime of the domain wall (Globus type model) [2]. An other idea suggested by [3] was to assume a non-magnetic phase (located at the grain boundary), whose volume fraction depends on the grain size. The “Non-Magnetic Grain Boundary” model was shown to successfully describe the initial permeability of MnZn ferrite on a wide range of grain size. Many relevant experimental results are published in a recent keynote paper of van der Zaag [4] and are questioned, for example, with in-depth microstructural characterizations of the grain boundary composition, and neutron depolarization experiments for determination of the volume domain size versus the grain size in various samples. In a soft NiZnCo ferrite, these data clearly show a critical grain size for a transition between a uniform magnetization state or monodomain state (MD) to a bi-domain (BD) magnetization state.

Using an effective medium theory approach, we have been able to extend the Brown model for the critical radius (R_C) of this magnetic state transition established for an isolated soft magnetic sphere to the case of a dense polycrystalline soft magnetic material. The computed value of R_C is in good accordance with the one determined experimentally by the neutron depolarization data. A striking feature of magnetic properties (coercive field, initial susceptibility, and volume domain size) is that a discontinuity is observed at the critical size. This means that the grains in the sample are then all in the MD state or in the BD state. We propose a mechanism explaining such a fact, showing an analogy with a nucleation with a phase transition mechanism.

Then, we have extended the Globus model, in which the magnetostatic energy does not take into account the interaction with the neighbouring particles, to the case of a full dense polycrystalline medium, using the effective medium theory. We then successfully retrieve the initial susceptibility dependence on the grain size for various compositions of ferrites.

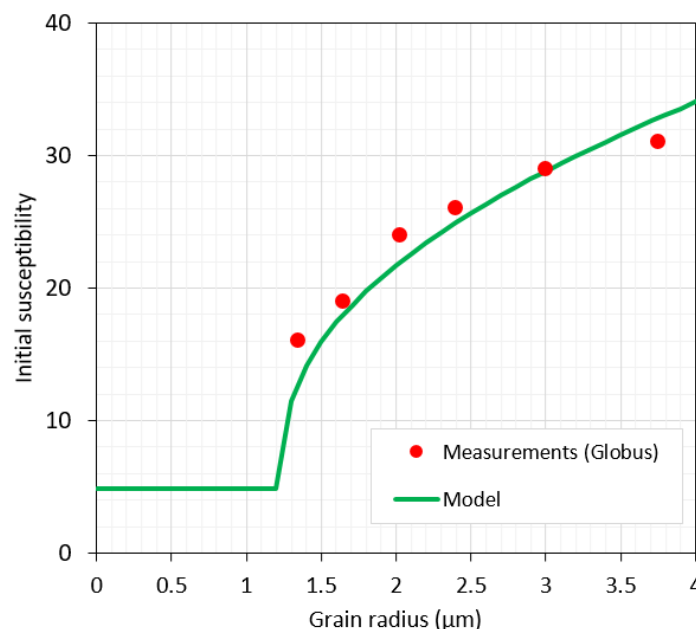


Figure 1: Comparison between initial susceptibility measured by Globus and the one determined by the extended model

References

- [1] G. T. Rado. [On the Inertia of Oscillating Ferromagnetic Domain Walls](#). *Physical Review* 83, 821–826 (1951).
- [2] A. Globus and P Duplex. [Size of Bloch Wall and Parameters of the Magnetic Susceptibility in Ferrimagnetic Spinels and Garnets](#). *Physica Status Solidi (a)* 3, 53–61 (1970).

- [3] M. T. Johnson and E. G. Visser. [A coherent model for the complex permeability in polycrystalline ferrites](#). *IEEE Transactions on Magnetics* 26, 1987–1989 (1990).
- [4] P. J. van der Zaag. [\(Keynote Paper\) Mono-Domain Ferrites and Their Implications](#). *IEEE Transactions on Magnetics* 56 (2020).

Dissipation properties of altermagnetic versus ferromagnetic Hall devices

V. Desbuis^{1,*}, D. Lacour², M. Hehn², S. Geiskopf², L. Michez³, J. Rial⁴, V. Baltz⁴, and J-E. Wegrowe¹

¹Laboratoire des Solides Irradiés, Ecole polytechnique, CNRS, CEA, Institut Polytechnique de Paris, F 91128 Palaiseau, France

²Institut Jean Lamour, UMR 7198 CNRS, Université de Lorraine, Vandoeuvre-lès-Nancy, France

³Aix-Marseille University, CNRS, CINaM, Marseille France

⁴Univ. Grenoble Alpes, CNRS, CEA, Grenoble INP, IRIG-SPINTEC, Grenoble, France

*valentin.desbuis@polytechnique.edu

The Hall current is often assumed dissipationless because it is normal to the driving field, or in other terms because it is produced by a curl-force (in relation to gauge invariance and geometrical phase), or again in other words, because it is due to time-reversal symmetry breaking at the microscopic scales in relation with antireciprocal Onsager relations. In the case of electric transport in magnetic systems, both the anomalous Hall effect (AHE), and the Planar Hall effect (PHE) can be measured [1]. The former effect is described by an antisymmetric conductivity matrix, while the latter is described by a symmetric conductivity matrix. Both AHE and PHE effects can then be considered as archetype of Onsager reciprocity relations, because the dissipative properties of reciprocal vs. non-reciprocal relations can be studied on equal footing [2]. Since seventy years [1], the study of AHE has been the object of deep and fundamental theoretical developments, especially since the description of the magnetic field generated in the momentum space by the Berry curvature.

In the last years, the studies about AHE focused on the different possible origin of the effect, pointing-out the qualitative difference between extrinsic and intrinsic mechanisms. The extrinsic mechanisms for AHE being related to spin-dependent scattering (skew scattering and side-jump scattering), while the intrinsic mechanisms are related to non-dissipative geometrical phase (i.e. Berry curvature). The last property is today intensively studied in new topological materials like Heusler alloys, topological semimetals, or altermagnetic materials [3].

Yet, as shown in a recent experimental work [4], the electric power carried by the anomalous Hall-current can be measured from the Joule power dissipated in a load circuit (which is connected in place of the Hall voltmeter: see Fig.1). In this configuration, the maximum power is shown to be approximately proportional to the square of the Hall angle, and depends on the load resistance in agreement with phenomenological predictions based on the second law of thermodynamics for the stationary regime [2,5]. However, the observations about GdCo ferrimagnetic Hall-device reported in reference [4] were non-conclusive from the point of view of the role played by the geometric phase, because extrinsic scattering mechanisms could dominate in GdCo, even at low temperature. Furthermore, the typical profile observe was also a-priori compatible with a more conventional anisotropic conduction, like that observed in the planar Hall effect [1,2].

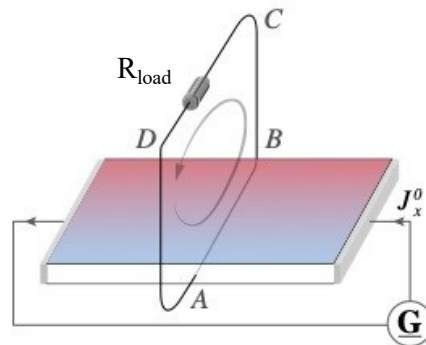


Figure 1: Illustration of a Hall bar connected to a load circuit with resistance R_{load}

The goal of the present work is to extend these observations to various magnetic materials, including the altermagnet Mn_5Si_3 (thin single crystal layer) that generates intrinsic AHE [3] (i.e. related to the Berry curvature of its band structure). Indeed, the measurements performed on the altermagnetic material are compared to that performed on GdCo and NiFe Hall bars of identical geometry and measured under the same experimental protocol. The NiFe (thin polycrystalline layer) plays here the role of yardstick for the conventional dissipation, as it has a strong anisotropic magnetoresistance - hence a strong Planar Hall effect - together with negligible AHE.

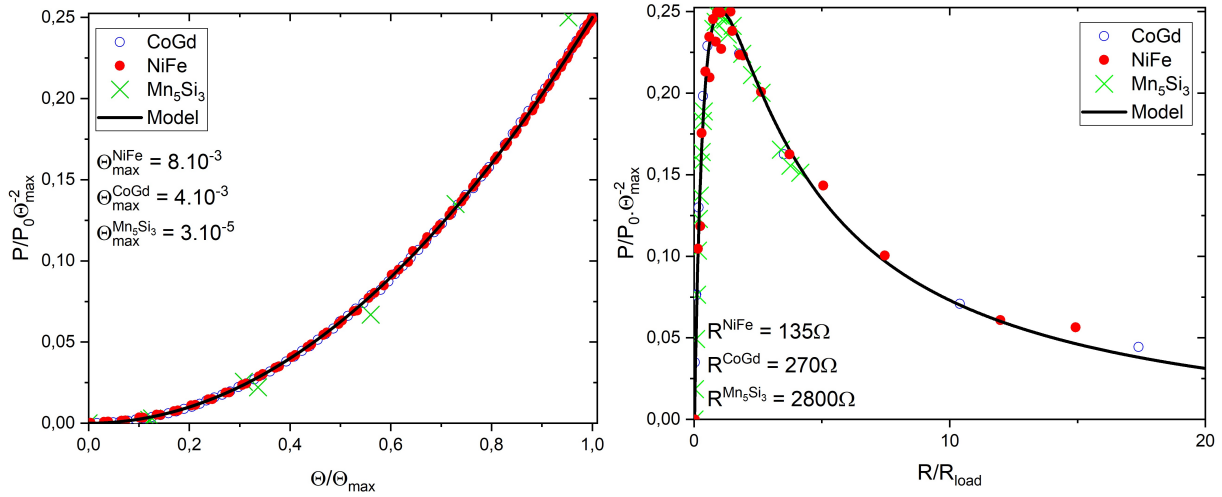


Figure 2: Normalized dissipated power in the load resistance as a function of normalized Hall angle (left) and normalized load resistance (right) for the three materials: NiFe, CoGd and Mn_5Si_3 . Continuous black line indicates variation for both dependencies predicted by Eq.8. Hall angle and load resistance corresponding to the maximum dissipated values in both figures are indicated for all materials.

The observations show that the profiles of the power dissipation as a function of the load resistance R_{load} and as a function of the Hall angle Θ can be superimposed (see Fig.2), at the leading order in the Hall angle Θ . The maximum power dissipated is approximately proportional to Θ^2 , and obeys the maximum power transfer theorem (maximum for the resistance matching). These observations are in agreement with the phenomenological theory based on dissipative transport developed in reference [2] and summarized in the expression of the power dissipated in the load resistance:

$$P(\Theta, R_{load}) = P_0 \frac{\Theta^2}{1 \pm \Theta^2} \frac{\frac{R^i}{R_{load}}}{\left(1 + \frac{R^i}{R_{load}}\right)^2} \quad (8)$$

where P_0 is the power injected in the Hall bar, R^i is the film resistance corresponding to $i = \{\text{NiFe}, \text{CoGd}, \text{Mn}_5\text{Si}_3\}$. In the denominator of Eq.(1), the sign (+) corresponds to AHE while the sign (−) corresponds to PHE.

Spin-wave circulation in unbounded ferromagnetic film

Jan Klíma¹, Loic Temdie², Daniel Stoeffler³, Roberto Fenollosa⁴, Aurélie Solignac⁵, Carsten Dubs⁶, Yves Henry³, Matthieu Bailleul³, and Vincent Vlaminck^{2,*}

¹*Institute of Physical Engineering, Faculty of Mechanical Engineering, Brno University of Technology, Technická 2, 616 69 Brno, Czech Republic*

²*IMT Atlantique, Dpt. MO, Lab-STICC - UMR 6285 CNRS, Technopole Brest-Iroise CS83818, 29238 Brest Cedex 03, France*

³*Institut de Physique et Chimie des Matériaux de Strasbourg (IPCMS), UMR 7504, UDS, CNRS, 23 rue du Loess, BP 43, 67034, Strasbourg, France*

⁴*Instituto de Tecnología Química, Consejo Superior de Investigaciones Científicas, Universitat Politècnica de València, Avenida de los Naranjos s/n, 46022 Valencia, Spain*

⁵*SPEC, CEA, CNRS, Université Paris-Saclay, CEA Saclay, 91191 Gif-sur-Yvette Cedex, France*

⁶*INNOVENT e.V. Technologieentwicklung, Pruessingstrasse 27B, 07745 Jena, Germany*
*vincent.vlaminck@imt-atlantique.fr

A key challenge in spin-wave computing is steering spin waves through circuits without wave distortion or reflections [1–3]. This often results in 1D propagation scenarios, which hinder applicability in 2D magnonic circuits. We demonstrate a novel approach using a hard-magnetic spherical microparticle to guide spin waves in an unbounded YIG film as sketched in Figure 1(a). The particle's stray field induces a radially symmetric magnetization landscape, which was confirmed with micromagnetic simulations shown in Figure 1(b). Thus, this radial Magnetic order creates a circular path for the spin waves propagation. We present an experiment conducted on a 55 nm-thin YIG film using RF antennas at 180° for which homogeneous order prevents any spin wave transmission. Approaching the spherical particle above the antenna results in significant spin-wave transmission spectra consistently with the particle position and its resulting stray field (cf Figure 1(c)). Furthermore, the spin-wave spectra display extinction features that are reminiscent of multi-path interference spectra, suggesting that the spin-wave loops around itself. In parallel, we conducted micromagnetic simulations using MuMax3 reproducing the experimental conditions at the same scale as shown in Figure 1(d). These simulations confirmed the formation of spin-waves packet circulating several times around the particle. Nevertheless, it also shows an increasing spread due to the magnitude inhomogeneities of the particle stray field away from the center. This work demonstrates the possibility to steer spin-wave onto a circular path using inhomogeneous magnetic landscape, showcasing the potential for two-dimensional magnonic devices like magnon circulators, advancing scalable spin-wave-based information processing technologies.

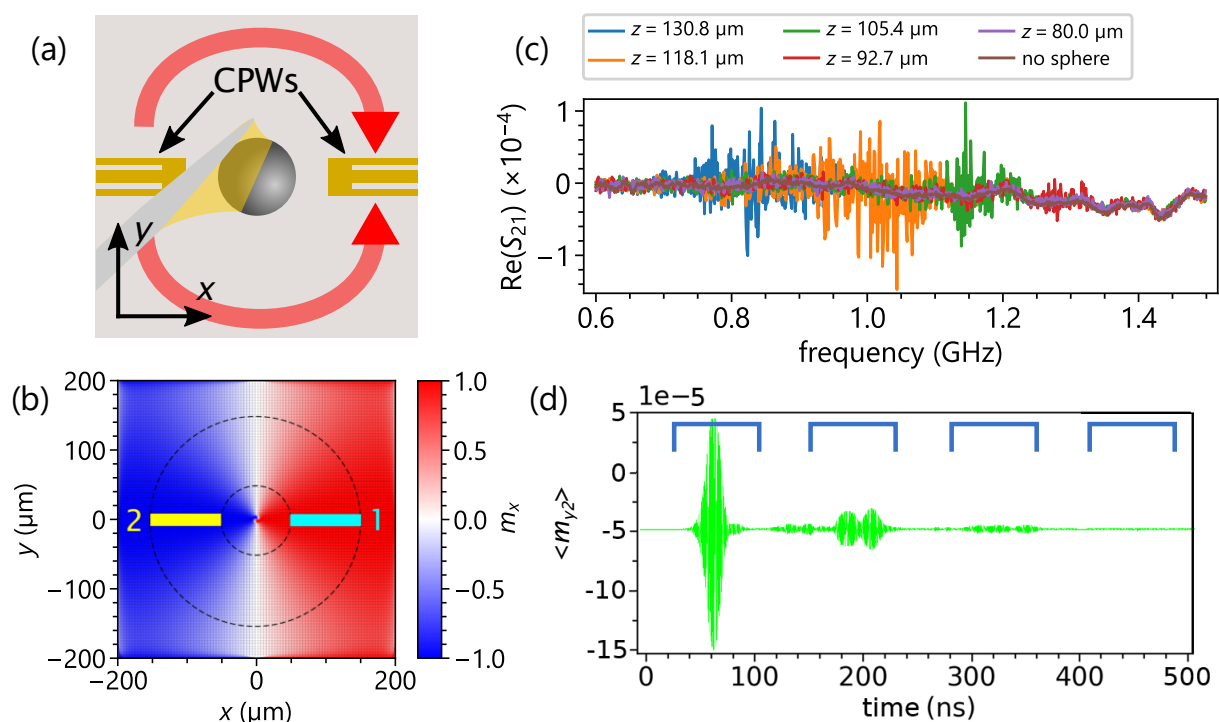


Figure 1: (a) Sketch of the propagating-spin-wave spectroscopy experiment in the presence of a magnetic sphere magnetized in the $-\hat{z}$ direction. (b) Micromagnetic simulation of the static magnetization in the YIG film subjected to a $70\mu\text{m}$ -diameter sphere located at $80\mu\text{m}$ above the YIG film. (c) VNA measurement with the sphere at different heights. (d) Micromagnetic showing the time evolution in region 2 from a pulse launched in region 1.

Acknowledgments

We acknowledge the financial support from the French National research agency under the projects *MagFunc*/ANR-20-CE91-0005, and also France 2030 program under project ANR-22-EXSP-0004 SWING.

References

- [1] Jan Klíma, Ondřej Wojewoda, Václav Roučka, et al. [Zero-field spin wave turns](#). *Applied Physics Letters* 124 (2024).
- [2] Dinesh Wagle, Daniel Stoeffler, Loic Temdie, et al. *Shaping non-reciprocal caustic spin-wave beams*. 2024.
- [3] L. Temdie, V. Castel, M.B. Jungfleisch, et al. [Probing Spin Wave Diffraction Patterns of Curved Antennas](#). *Physical Review Applied* 21 (2024).

Spin charge conversion with Homo and Hetero bilayers of TMDs : 1H/1T and 1T/1T case study

Rahul Sharma^{1,*}, Soumya Mukherjee², Martin Micica², Fatima Ibrahim¹, Libor Vojacek¹, Mairbek Chshiev¹, Sukhdeep Dhillon², and Matthieu Jamet^{1,*}

¹Université Grenoble Alpes, CEA, CNRS, IRIG-SPINTEC, 38000 Grenoble, France

²Laboratoire de Physique de l'Ecole Normale Supérieure, ENS, Université PSL, CNRS, Sorbonne Université, Université de Paris, Paris, 75005 France

*rahul.sharma@cea.fr; matthieu.jamet@cea.fr

Transition metal dichalcogenides (TMDs) have emerged as a versatile class of materials, offering promise for nanoelectronics, optoelectronics, and spintronics. Their electronic, optical, and magnetic properties can be finely tuned by varying layer thickness, stacking configurations, and inherent symmetries.[1, 2] Based on symmetry properties, TMDs are generally categorized into two primary phases. The 1T phase, with its octahedral coordination, maintains inversion symmetry, while the 1H phase features trigonal prismatic coordination and broken inversion symmetry.[1] These structural distinctions directly affect the electronic band structure and, in conjunction with TMDs' notable spin-orbit coupling (SOC), underpin their utility in spin-charge conversion (SCC). This phenomenon lies at the core of spintronics, enabling the mutual conversion of spin and charge currents.

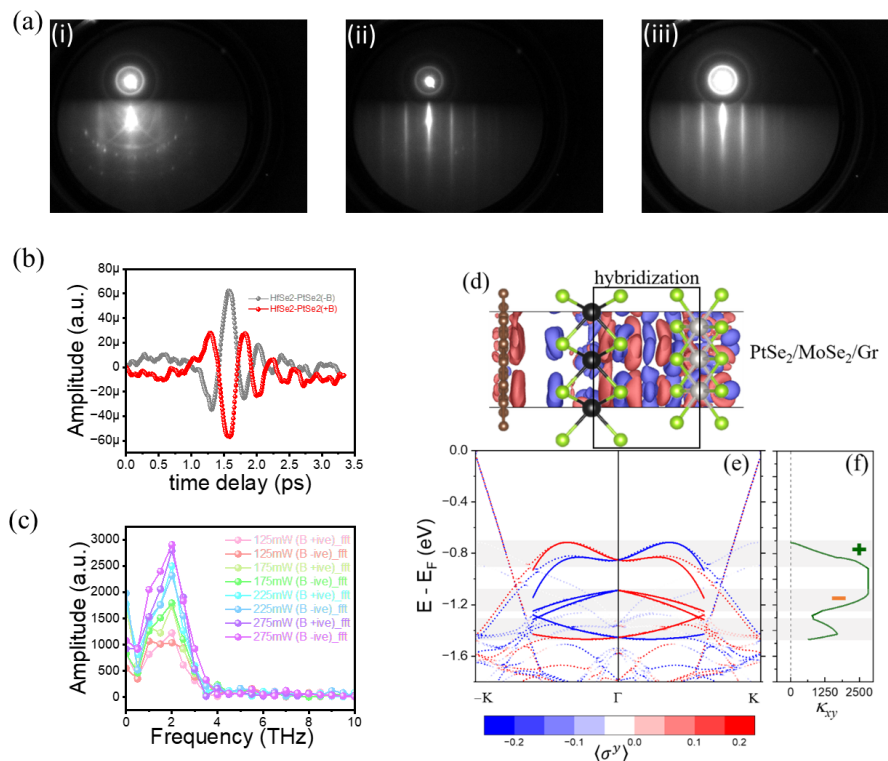


Figure 1: Figure 1: (a) RHEED images of (i) epitaxial Graphene/SiC Substrate (ii) WSe₂ monolayer and (ii) HfSe₂ monolayer on WSe₂ monolayer along [100] confirming heterostructure. (b) THz electric field as a function of time delay and magnetic field direction for HfSe₂/HfSe₂ heterostructure. The external magnetic field (strong enough to saturate the Co magnetization) is applied along an azimuthal angle of 0° (red) and 180° (Grey) showing a clear magnetic contribution due to SCC. (c) Fourier transform of Figure b and other power dependent measurements. (d) Crystal structure and calculated charge density in PtSe₂/MoSe₂/Gr heterostructures (e) The dotted lines are the DFT calculated bands whereas the solid lines are the fitted ones using the free-electron model. (f) The SCC efficiency is quantified by the calculated κ_{yx} tensor in arbitrary units where its cumulative profile is displayed. The negative sign corresponds to the SCC sign of Co/Pt.[3]

Despite their potential in spintronics, the influence of structural symmetries and symmetry-based heterostructures on SCC remains largely unexplored. In particular, the SCC properties of 1T/1T and 2H/1T heterostructures, which offer diverse stacking sequences and interlayer interactions, have not yet been systematically studied. These architectures could unlock novel spintronic behaviors governed by the interplay of symmetry and phase-specific features.

In this work, we focus on molecular beam epitaxy (MBE) grown HfSe₂, WSe₂, and PtSe₂ as representative TMDs to examine how structural symmetries and heterostructures shape SCC. Using spintronic terahertz emission spectroscopy and density functional theory (DFT), we investigate the SCC characteristics of TMD bilayers in both 1T/1T and 2H/1T configurations,

paying particular attention to the role of stacking sequence. Our findings provide fresh insights into the relationship between symmetry and stacking in TMDs, paving the way for the design of next-generation materials for advanced spintronic applications.

Acknowledgments

The French National Research Agency (ANR) is acknowledged for its support through the ANR-18-CE24-0007 MAGIC-VALLEY and ESR/EQUIPEX+ ANR-21-ESRE-0025 2D-MAG projects. The LANEF framework (No. ANR-10-LABX-0051) is acknowledged for its support with mutualized infrastructure

References

- [1] Biao Qin, Chaojie Ma, Quanlin Guo, et al. [Interfacial epitaxy of multilayer rhombohedral transition-metal dichalcogenide single crystals](#). *Science (New York, N.Y.)* 385, 99–104 (2024).
- [2] Juan F Sierra, Jaroslav Fabian, Roland K Kawakami, Stephan Roche, and Sergio O Valenzuela. [Van der Waals heterostructures for spintronics and opto-spintronics](#). *Nature Nanotechnology* 16, 856–868 (2021).
- [3] Khasan Abdukayumov, Martin Mičica, Fatima Ibrahim, et al. [Atomic-Layer Controlled Transition from Inverse Rashba–Edelstein Effect to Inverse Spin Hall Effect in 2D PtSe₂ Probed by THz Spintronic Emission](#). *Advanced Materials* 36, 2304243 (2024).

Spin and orbital Rashba effects at the Ni/HfO₂ interface

Armando Pezo¹, Andrés Saul², Aurélien Manchon², and Rémi Arras^{3,*}

¹Laboratoire Albert Fert, CNRS, Thales, Université Paris-Saclay, 91767, Palaiseau, France

²Aix-Marseille Université, CNRS, CINaM, Marseille, France

³CEMES, Université de Toulouse, CNRS, 29 rue Jeanne Marvig, F-31055, Toulouse, France

*remi.arras@cemes.fr

The design of extrinsic multiferroics, formed by the association of a ferroelectric material with a ferromagnet in heterostructures, has been a subject of intense research aiming to obtain large magnetoelectric couplings. Indeed, switching the magnetization through spin-orbit torques (SOT), by applying an electric field, represents an extraordinary opportunity to reduce the power consumption of magnetic memory devices [1–3]. In these devices, spin-orbit coupling plays a central role as it governs the spin-charge or orbital-charge interconversion phenomena. Ferroelectric compounds can substantially boost these mechanisms by altering the crystal structure in a non-volatile manner. However, the use of ferroelectric compounds in miniaturized devices faces several challenges, such as the disappearance of the electric polarization below a layer critical thickness or the growth incompatibility with CMOS technologies. Of these observations, the recent discovery of ferroelectricity in doped hafnia (HfO₂) films [4], which do not suffer from the aforementioned issues, has been welcomed with enthusiasm for the design of ferroelectric-based applications or memories involving resistive-switching processes.

We predict the giant ferroelectric control of interfacial properties of Ni/HfO₂, namely, (i) the magnetocrystalline anisotropy and (ii) the inverse spin and orbital Rashba effects [5]. Using a combination of *ab initio* simulations and transport calculations, we demonstrate that reversing the electric polarization modulates the interface magnetocrystalline anisotropy from in-plane to out-of-plane. This modulation compares favorably with recent reports obtained upon electromigration induced by ionic gating. In addition, we find that the current-driven spin and orbital densities at the interface can be modulated by about 50% and 30%, respectively. This giant modulation of the spin-charge and orbit-charge conversion efficiencies opens appealing avenues for voltage-controlled spin- and orbitronics devices.

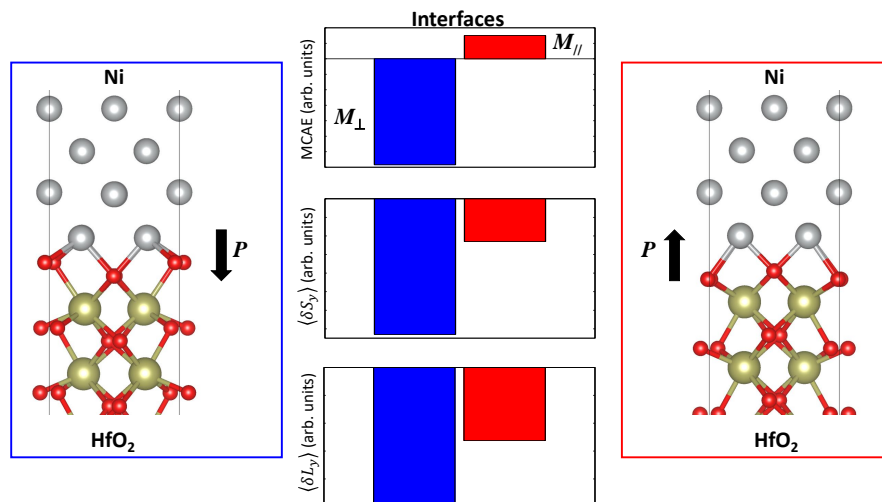


Figure 1: Manipulation of the magnetocrystalline-anisotropy energy (MCAE), the spin $\delta\langle S_y \rangle$ and orbital $\delta\langle L_y \rangle$ accumulation at the Ni/HfO₂ interface through a reversal of the electric polarization P .

Acknowledgments

This work was supported by the ANR ORION project, grant ANR-20-CE30-0022-01 of the French Agence Nationale de la Recherche, by the Excellence Initiative of Aix-Marseille Université-A*Midex, a French "Investissements d'Avenir" program, by the France 2030 government grants managed by the French National Research Agency PEPR SPIN [SPINMAT] ANR-22-EXSP-0007 and [SPINTHEORY] ANR-22-EXSP-0009 and by the EIC Pathfinder OPEN grant 101129641 "OBELIX". This work was granted access to the HPC resources of CALMIP (Allocations No. 2022-2024/P19004 and P1229) and CINES (Allocation AD010915807R1).

References

- [1] S. Manipatruni, D. E. Nikonov, C.-C. Lin, et al. [Scalable energy-efficient magnetoelectric spin-orbit logic](#). *Nature* 565, 35 (2019).

- [2] A. Manchon, J. Železný, I. M. Miron, et al. [Current-induced spin-orbit torques in ferromagnetic and antiferromagnetic systems](#). *Rev. Mod. Phys.* 91, 035004 (3 2019).
- [3] N. Paul, F. Trier, L. M. Vicente Arche, et al. [Non-volatile electric control of spin–charge conversion in a SrTiO₃ Rashba system](#). *Nature* 580, 483 (2020).
- [4] T. S. Böscke, J. Müller, D. Bräuhäus, U. Schröder, and U. Böttger. [Ferroelectricity in hafnium oxide thin films](#). *Appl. Phys. Lett.* 99, 102903 (2011).
- [5] A. Armando Pezo, A. Saul, A. Manchon, and R. Arras. [Spin and Orbital Rashba effects at the Ni/HfO₂ interface](#). *arXiv* 2412.04927 (2024).

Magnetic imaging under high pressure with a spin-based quantum sensor integrated in a van der Waals heterostructure

Z. Mu¹, J. Fraunié², A. Durand¹, S. Clément¹, A. Finco¹, J. Rouquette³, A. Hadj-Azzem⁴, N. Rougemaille⁴, J. Coraux⁴, J. Li⁵, T. Poirier⁵, J. H. Edgar⁵, I. C. Gerber², X. Marie^{2,6}, B. Gil¹, G. Cassabois^{1,6}, C. Robert², and V. Jacques^{1,*}

¹Laboratoire Charles Coulomb, Université de Montpellier and CNRS, 34095 Montpellier, France

²Université de Toulouse, INSA-CNRS-UPS, LPCNO, 135 Avenue Rangueil, 31077 Toulouse, France

³Institut Charles Gerhardt, Université de Montpellier and CNRS, 34095 Montpellier Cedex, France

⁴Université Grenoble Alpes, CNRS, Grenoble INP, Institut NEEL, 38000 Grenoble, France

⁵Tim Taylor Department of Chemical Engineering, Kansas State University, Kansas 66506, USA

⁶Institut Universitaire de France, 75231 Paris, France

*vincent.jacques@umontpellier.fr

Pressure is a powerful thermodynamic parameter for tuning the magnetic properties of van der Waals magnets owing to their weak interlayer bonding [1–3]. However, local magnetometry measurements under high pressure still remain elusive for this important class of emerging materials. Here we introduce a method enabling *in situ* magnetic imaging of van der Waals magnets under high pressure with sub-micron spatial resolution. Our approach relies on a quantum sensing platform based on boron-vacancy (V_B^-) centers in hexagonal boron nitride (hBN), which can be placed in atomic contact of any type of two-dimensional (2D) material within a van der Waals heterostructure [4–7]. We first show that the V_B^- center can be used as a magnetic field sensor up to pressures of a few GPa, a pressure range for which the properties of a wide variety of van der Waals magnets are efficiently altered. We then use V_B^- centers in a thin hBN layer to perform magnetic imaging of a van der Waals magnet under pressure. To illustrate the performances of the method, we image the pressure-dependent magnetization in micrometer-sized flakes of 1T-CrTe₂ (see Fig 1), whose evolution is explained by a shift of the Curie temperature [8]. Besides providing a new path for studying pressure-induced phase transitions in van der Waals magnets, this work also opens up interesting perspectives for exploring the physics of 2D superconductors under pressure via local measurements of the Meissner effect [9, 10].

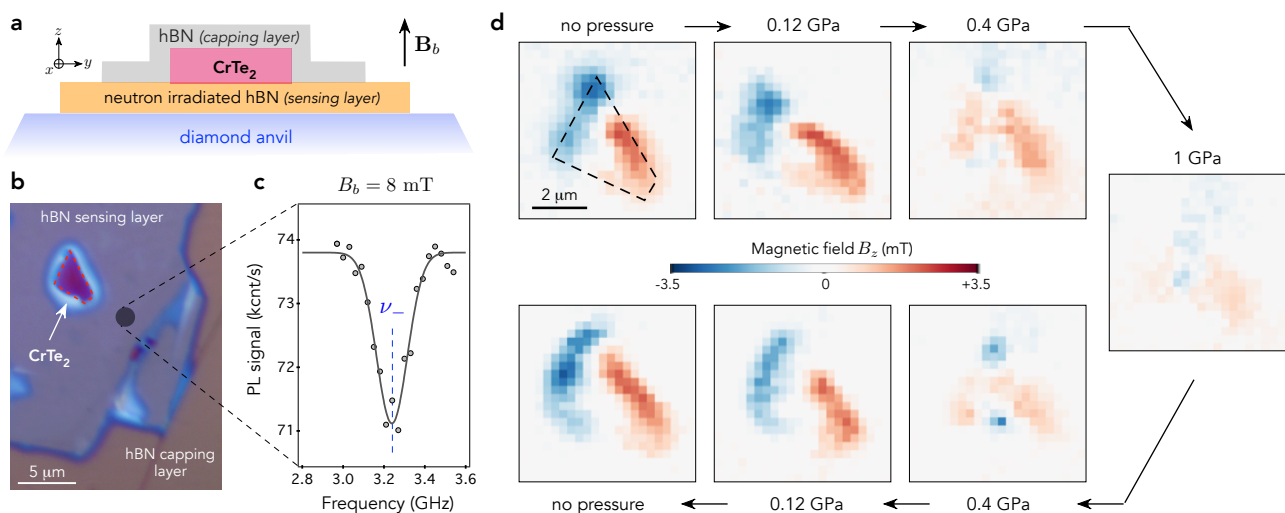


Figure 1: Magnetic imaging under pressure with V_B^- centers integrated in a van der Waals heterostructure. (a) Sketch and (b) optical image of the heterostructure deposited in the high-pressure chamber of a diamond anvil cell (DAC). (c) Spectrum of the low-frequency magnetic resonance of the V_B^- center recorded far from the CrTe₂ flake at zero external pressure with a bias field $B_b = 8$ mT. (d) Images of the magnetic field component B_z produced by the CrTe₂ flake for increasing (top) and decreasing (bottom) pressure. For all images, the pixel size is 300×300 nm² and the acquisition time per pixel is 60 s.

References

- [1] Tiancheng Song, Zaiyao Fei, Matthew Yankowitz, et al. [Switching 2D magnetic states via pressure tuning of layer stacking](#). *Nature Materials* 18, 1298–1302 (2019).

- [2] Tingxin Li, Shengwei Jiang, Nikhil Sivadas, et al. [Pressure-controlled interlayer magnetism in atomically thin CrI₃](#). *Nature Materials* 18, 1303–1308 (2019).
- [3] Amit Pawbake, Thomas Pelini, Ivan Mohelsky, et al. [Magneto-Optical Sensing of the Pressure Driven Magnetic Ground States in Bulk CrSBr](#). *Nano Letters* 23, 9587–9593 (2023).
- [4] Andreas Gottscholl, Mehran Kianinia, Victor Soltamov, et al. [Initialization and read-out of intrinsic spin defects in a van der Waals crystal at room temperature](#). *Nature Materials* 19, 540–545 (2020).
- [5] Mengqi Huang, Jingcheng Zhou, Di Chen, et al. [Wide field imaging of van der Waals ferromagnet Fe₃GeTe₂ by spin defects in hexagonal boron nitride](#). *Nature Communications* 13, 5369 (2022).
- [6] P. Kumar, F. Fabre, A. Durand, et al. [Magnetic Imaging with Spin Defects in Hexagonal Boron Nitride](#). *Phys. Rev. Appl.* 18, L061002 (2022).
- [7] A. J. Healey, S. C. Scholten, T. Yang, et al. [Quantum microscopy with van der Waals heterostructures](#). *Nature Physics* 19, 87–91 (2023).
- [8] Z. Mu, J. Fraunié, A. Durand, et al. [Magnetic imaging under high pressure with a spin-based quantum sensor integrated in a van der Waals heterostructure](#) (2025). Preprint arXiv: 2501.03640.
- [9] Dong Qiu, Chuanhui Gong, SiShuang Wang, et al. [Recent Advances in 2D Superconductors](#). *Advanced Materials* 33, 2006124 (2021).
- [10] Matthew Yankowitz, Shaowen Chen, Hryhoriy Polshyn, et al. [Tuning superconductivity in twisted bilayer graphene](#). *Science* 363, 1059–1064 (2019).

Exploring Interconversion of Charge Current to Spin Current in Sputter-Deposited Topological Insulating Materials

Damián Melo^{1,2,*}, Paul Carvajal¹, Melissa Yactayo^{2,3}, Laurent Badie², Sebastien Petit-Watlot², Carlos García¹, and J. Carlos Rojas-Sánchez²

¹*Departamento de Física, Universidad Técnica Federico Santa María, 2390123 Valparaíso, Chile*

²*Institut Jean Lamour, Université de Lorraine, UMR 7198 CNRS, 54011 Nancy, France*

³*Facultad de Ciencias Físicas, Universidad Nacional Mayor de San Marcos, P.O.-Box 14-0149, Lima 14, Peru.*

*damian.melo@usm.cl

Advancements in spintronics demand energy-efficient and high-performance materials for next-generation technologies, such as non-volatile random access memory and spin-caloric devices. Topological insulators (TI) have garnered significant attention due to their unique spin-momentum locking, a result of strong spin-orbit coupling, which enables highly efficient charge-to-spin current conversion [1]. To fully harness their potential, it is essential to understand how key material properties, such as layer thickness and interface engineering, affect spin transport and magnetization dynamics. This study addresses these challenges by exploring charge-to-spin current conversion in thin films of the TI Bi_2Te_3 , the FM Co and non-magnetic materials as Pt , Cu and Al fabricated via magnetron sputtering, providing valuable insights into their performance and applicability in advanced spintronic devices.

Direct contact between a topological insulator (TI), such as Bi_2Se_3 , and a ferromagnetic metal (FM), such as Ni or Co, is theoretically predicted to disrupt the helical spin structure of the TI [2]. Furthermore, significant interdiffusion between polycrystalline FM and TI layers has been observed [3], altering the chemical composition and reducing the spin-to-charge conversion efficiency (SCCC). However, the strong spin-orbit coupling (SOC) inherent in Bi and Te enables compounds like Bi_2Te_3 to retain high SCCC. To address these challenges, we propose interface engineering by introducing 2 nm thick spacer layers (LM) between the Bi_2Te_3 and FM layers, to prevent interdiffusion and preserve helical spin texture of the TI. Despite the polycrystalline nature of the samples, we aim to investigate whether interfacial contributions—such as the Edelstein Effect or Inverse Edelstein Effect—coexist alongside the bulk contributions dominated by strong SOC. To this end, we also conducted a thickness dependence study on the Bi_2Te_3 layer, also enabling us to estimate its spin diffusion length (SDL).

This research employs two complementary experimental approaches to investigate and optimize the spin-to-charge conversion efficiency of sputtered Bi_2Te_3 . First, in-plane magnetized systems with 5 nm Co layers in structures like $Bi_2Te_3/LM/Co/Al$ were developed for spin pumping FMR and spin torque FMR measurements. Second, systems featuring 0.6 nm Co layers with perpendicular magnetic anisotropy (PMA), such as $Bi_2Te_3/LM/Pt/Co/Pt$, were designed to enhance spin-orbit torque (SOT)-induced magnetization switching. For both studies, the TI layer thickness was varied across 3, 5, 8, 10, and 20 nm to characterize the bulk contributions to SCCC. To mitigate interdiffusion between the TI and Co layers and to preserve the helical spin structure of the TI, we introduced nonmagnetic spacer layers (LM) such as Cu, Ag, Ru, Ti, and Au. Magnetic and spin-charge interconversion properties were systematically compared with those of analogous devices based on heavy metals like Pt , these comparisons included systems like FM/Al and $Pt/Co/Al$ for in-plane magnetized structures, as well as $Pt/Co(0.6\text{ nm})/AlO_x$ for systems with PMA.

To analyze the magnetic properties of the deposited thin films, advanced characterization techniques were employed. These included Magneto-Optical Kerr Effect (MOKE) magnetometry, Vibrating Sample Magnetometry (VSM) (Fig. 1), and Ferromagnetic Resonance (FMR). Additionally, structural characterization was performed using X-ray Diffraction (XRD) to determine the structural properties of the samples, along with X-ray Reflectivity (XRR) to accurately measure the film thickness.

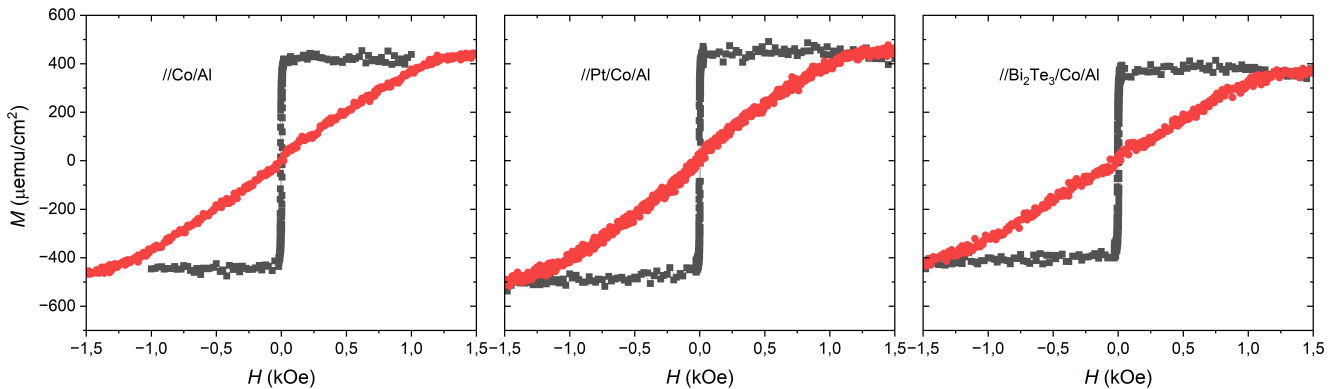


Figure 1: Magnetization normalized by the sample area (M) versus magnetic field (H) curves are presented for three multilayer systems: $Co(5nm)/Al(3nm)$, $Pt(5nm)/Co(5nm)/Al(3nm)$, and $Bi_2Te_3(3nm)/Co(5nm)/Al(3nm)$. Each system is evaluated in in-plane (IP, black) and out-of-plane (OOP, red) orientations. The results demonstrate an hard magnetization axis in the OOP orientation and a easy magnetization in the IP orientation.

Device fabrication was performed using standard optical lithography to enable proper measurements of spin-to-charge conversion efficiency. Characterization of in-plane magnetized systems was carried out using Spin Pumping FMR (SP-FMR) [4] and Spin Torque FMR (ST-FMR) [5] measurements. For PMA systems, SOT-switching experiments [6] were conducted to evaluate their performance in magnetization switching.

Acknowledgments

D. M. acknowledges the financial support provided by the Beca Doctorado USM, the ANID FONDECYT/Regular 1241918 (Chile) and the European Union's Horizon 2020 research and innovation program under the Marie Skłodowska-Curie Grant Agreement No. 101007825 (ULTIMATE-I project). We also acknowledge support from the ERC CoG project MAGNETALLIEN grant ID 101086807, and the project "Lorraine Université d'Excellence" reference ANR-15-IDEX-04-LUE.

References

- [1] Albert Fert and Frédéric Nguyen Van Dau. Spintronics, from giant magnetoresistance to magnetic skyrmions and topological insulators. *Comptes Rendus. Physique* 20, 817–831 (2019).
- [2] Jia Zhang, Julian P Velez, Xiaoqian Dang, and Evgeny Y Tsymlal. Band structure and spin texture of Bi 2 Se 3 3 d ferromagnetic metal interface. *Physical Review B* 94, 014435 (2016).
- [3] Isabel C Arango, Alberto Anadón, Silvestre Novoa, et al. Spin-to-charge conversion by spin pumping in sputtered polycrystalline Bi x Se 1- x. *Physical Review Materials* 7, 075402 (2023).
- [4] J.-C. Rojas-Sánchez, S. Oyarzún, Y. Fu, et al. Spin to Charge Conversion at Room Temperature by Spin Pumping into a New Type of Topological Insulator: α -Sn Films. *Phys. Rev. Lett.* 116, 096602 (9 2016).
- [5] Yi Wang, Dapeng Zhu, Yang Wu, et al. Room temperature magnetization switching in topological insulator-ferromagnet heterostructures by spin-orbit torques. *Nature communications* 8, 1364 (2017).
- [6] Hao Wu, Yong Xu, Peng Deng, et al. Spin-orbit torque switching of a nearly compensated ferrimagnet by topological surface states. *Advanced Materials* 31, 1901681 (2019).

Static macromagnetic modelling of multilayers applied to spin-orbit torque characterization

Rémy Soucaille^{1,*}, Rohit Pachat¹, Manar Fiat², Aurélie Solignac¹, Claude Fermon¹, and Myriam Pannetier-Lecoecur¹

¹*SPEC, CEA, CNRS, Université Paris-Saclay, CEA Saclay, 91191 Gif-sur-Yvette Cedex, France*

²*Université Paris-Saclay, 91120 Palaiseau, France*

*remy.soucaille@cea.fr

Spin Orbit Torques (SOT) are effects in which an electric current flowing in a non-magnetic material exhibiting spin-orbit (SO) interaction (typically a heavy metal) is converted into a transverse spin current capable of acting through a transfer of spin angular momentum on the magnetization of an adjacent layer (e.g. Co, CoFeB or NiFe). This transfer of spins leads to effective magnetic torques exerted on the ferromagnetic layer, which changes its magnetization. These effects can be used in variety of devices, such as MRAMs, but can also be good candidates for TMR sensors in which SOT can tune the properties. The archetypical structure is a Magnetic Tunnel Junction (MTJ) incorporating SOT material, in a 3 or 4 terminal device (see Inset Fig 1). A proper characterization of all the magnetic interactions in such device is very relevant for understanding the response of the device and predicting the best configurations. However, as the structure of magnetic layers becomes more complex and even in the case of a simpler macromagnetic approach, other interactions –such as the Oersted field– can mask the effect of spin orbit-interaction.

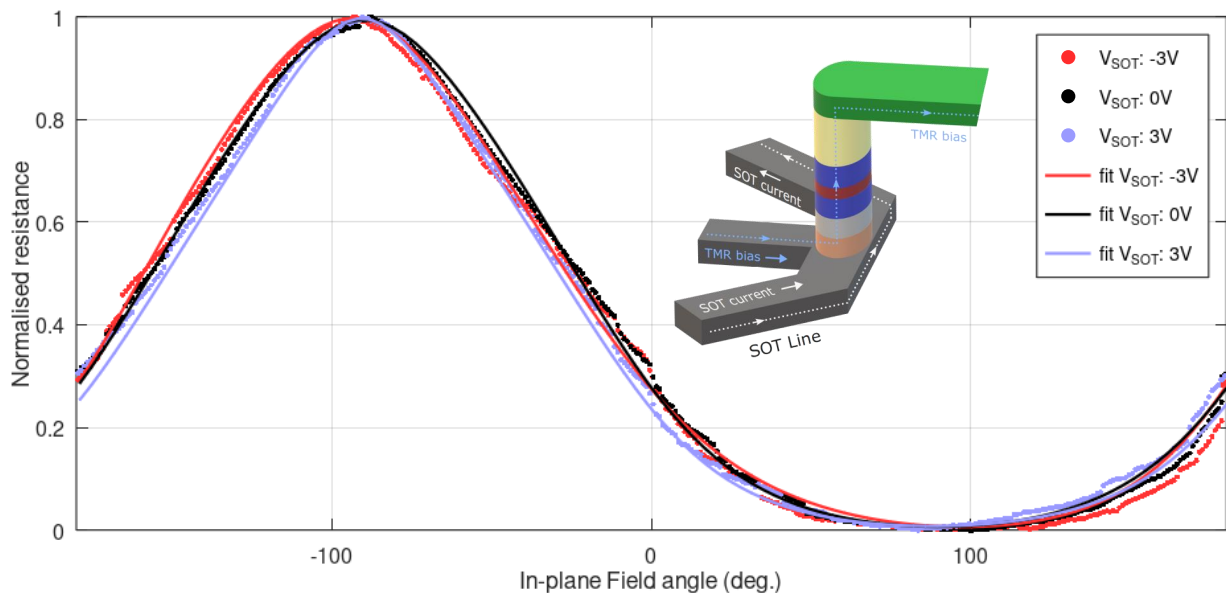


Figure 1: Normalized voltage versus in-plane field angle measurement, the amplitude of the in-plane field being 10 mT. Dot: experimental data, solid line: fitting. Inset: scheme of the characterized device with two separated path. The SOT line width is 10 μm and is composed of Ta(3nm)/Pt(7nm). A voltage V_{SOT} is connected at the SOT line terminal. The TMR pillar on top of the SOT line is biased with a constant current: 3 μA . The TMR pillar stack is, from bottom to top: CoFeB(2nm)/MgO(2nm)/CoFeB(2.6nm)/Ru(0.85nm)/CoFe(2.1nm)/IrMn(9nm).

The characterization of spin-orbit torques is usually performed on a simplified stack containing a single magnetic layer in contact with a heavy metal layer. One can then retrieve torques applied onto the magnetization by disentangling the various contribution of the spin hall voltage [1]. For magneto-resistive sensor application used with spin-orbit torque effect, the stack contains at least four different layers: two ferromagnetic layers, a spacer and a current line. In a more realistic case, there are almost twice as many layers when the reference layer is pinned.

We have developed [2] a tool to simulate the static magnetic configuration in xMR stacks (x: Giant or Tunnel), using macromagnetic framework. The static configuration comes from the local minimization of the total energy [3], so it can be used to extract the amplitude of the various interactions. We can feed this code with experimental data (resistance, or magnetic moment) as a function of the field amplitude in any direction, or as a function of a rotating in-plane field.

To integrate the SOT, we start from the Landau-Lifshitz-Gilbert equation and find an energy term that will lead to the proper equivalent torque after derivation:

$$\frac{d\mathbf{m}}{dt} = -\gamma\mathbf{m} \times \mathbf{H}_{\text{eff}} + \alpha\mathbf{m} \times \frac{d\mathbf{m}}{dt} + \tau_{FL}\mathbf{m} \times \mathbf{p} + \tau_{DL}\mathbf{m} \times (\mathbf{m} \times \mathbf{p}) \quad (9)$$

We show here that while the integration of the field-like torque is straightforward (it can be directly described as a field applied along the spin polarization) the damping-like torque must be adapted, as it does not derive from a potential. The advantage of this method is that we can easily take into account for changes in the static configuration from all layers and one can disentangle the contribution of the Oersted field coming from the current flowing inside the layers.

We have applied this method to the measurement of $R(\theta)$ on the four-terminal device presented in inset of figure 1. The stack is composed of Si/SiO₂/Ta(3nm)/Pt(7nm)/CoFeB(2nm)/MgO(2nm)/CoFeB(2.6nm)/Ru(0.85nm)/CoFe(2.1nm)/IrMn(9nm). The TMR pillar is polarized with a current of 3 μ A under a constant rotating field of 10 mT. We can then fit the experimental data with respect to the field angle. As a result, we can deduce the amplitude and the sign of the field-like torque as well of the Oersted field contribution. We plan to apply this method for other SOT materials (such as Ta, W...). This approach can be extended to other types of multilayer stacks including PMA structures.

Acknowledgments

This work has benefited from a government grant operated by the French National Research Agency as part of the France 2030 program, reference «ANR-22-EXSP-0006» and by ANR grant STORM (ANR-22-CE42-0013-02).

References

- [1] Kevin Garello, Ioan Mihai Miron, Can Onur Avci, et al. [Symmetry and magnitude of spin-orbit torques in ferromagnetic heterostructures](#). *Nature Nanotechnology* 8, 587–593 (2013).
- [2] A. Solignac *et al.* Macrospin modelling combined with experimental approach for magnetic sensor stack optimization. *ICM 2024-Bologna* (2024).
- [3] Yanjun Xu, Yumeng Yang, Ziyang Luo, Baoxi Xu, and Yihong Wu. [Macro-spin modeling and experimental study of spin-orbit torque biased magnetic sensors](#). *Journal of Applied Physics* 122, 193904 (2017).

Exploring NbN-based stacks for superconducting spintronics

T. Courtois^{1,*}, Y Leverge-Serandour¹, J.-X Lin¹, C. Pfaff¹, M. Hehn¹, S. Andrieu¹, S. Mangin¹, J. Ghanbaja¹, S. Migot¹, K. Dumesnil¹, and T. Hauet¹

¹Institut Jean Lamour, Université de Lorraine, 2 allée André Guinier, 54011 Nancy, France

*theo.courtois@univ-lorraine.fr

The interplay between magnetism and superconductivity has been heavily studied during the past 35 years in X/S bilayers, where S was mostly a thick niobium or aluminum layer with critical temperatures (T_c) of the order of few Kelvin and X was either a normal metal (NM) or a uniformly magnetized ferromagnetic layer (F) [1]. Since the 2010s, stacks with thinner S layer, non-uniformly magnetized F layer and more complex hybrids stackings revealed new phenomena opening the way to mix superconductivity and spintronics [2]. On the one hand, paramagnetism was observed for superconducting films thinner than 100 nm [3, 4] whose origin is still under debate. On the other hand, generation of spin-polarized equal spin-triplet Cooper pairs has been evidenced [5] but their reliable and efficient generation, as well as techniques to detect and manipulate them are still pursued. To tackle these 2 questions, we have studied the growth, the magnetic properties and spin-injection through ferromagnetic resonance (FMR) of various stacks based on epitaxial NbN thin films.

The growth of epitaxial NbN and X/NbN/Y/Py films with X,Y=Cu, Pt, Ta at room temperature using physical vapor deposition (PVD). The NbN crystal, characterized by x-ray diffraction (XRD), x-ray reflectivity (XRR), and transmission electron microscopy (TEM, see Fig. 1(b)), is strongly influenced by the chamber pressure and nitrogen percentage during deposition [6]. The best T_c is obtained at 9.8% N₂ for NbN on MgO and 7% for NbN on Pt[100]. Despite the absence of substrate heating, the NbN films exhibit critical temperatures around 15 K for a NbN thickness greater than 25 nm as shown in Fig 1(a) while T_c decreases rapidly for thicknesses below 25 nm when NbN is capped with Pt and below 10nm for MgO. This allows to disentangle the different origins of the decrease: inverse proximity effect, coherence length and structural defect. Electrical transport and magnetic measurements, based on the BCS model, reveal a typical coherence length of approximately 6.5 nm for 90 nm thick films, and around 5.5 nm for 15 nm thick films at the 0 K limit.

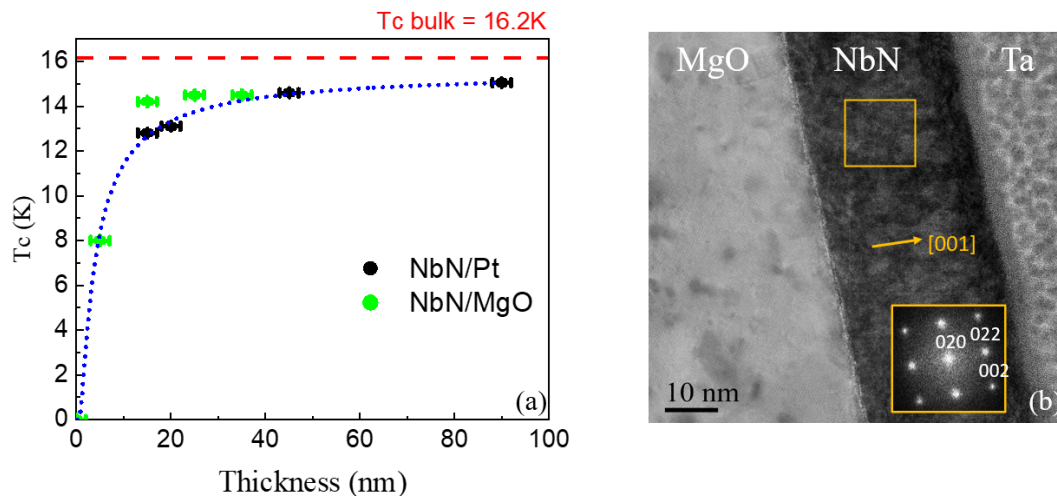


Figure 1: (a) Critical temperature as a function of thin film thickness of NbN with MgO and Pt capping, the blue dashed curve corresponds to an exponential function fit similar to the Cooper model [7]. (b) High resolution TEM micrograph of a MgO[100]/MgO/NbN/Ta epitaxial structure.

As recently observed for MgB₂ thin films [4], for sufficiently thin film, high field and large temperature, the magnetization versus field loop of NbN in the superconducting state consist in an "inverted" loop as shown in Fig.2 (a), as compared to the usual $M(H)$ loop described by the Bean or Kim-Ji models [8, 9]. NbN has a coherence length similar to MgB₂ but a much higher penetration depth [10, 11]. We observed that under measurement conditions identical to those used for MgB₂, this inverted effect was more pronounced in NbN. We propose that the inverted cycle could be a manifestation of a phase transition in the vortex lattice, gradually shifting from a classical Abrikosov lattice to a liquid-like vortex lattice [12]. Based on this hypothesis, the role of vortex pinning and edge field was experimentally investigated and quantified.

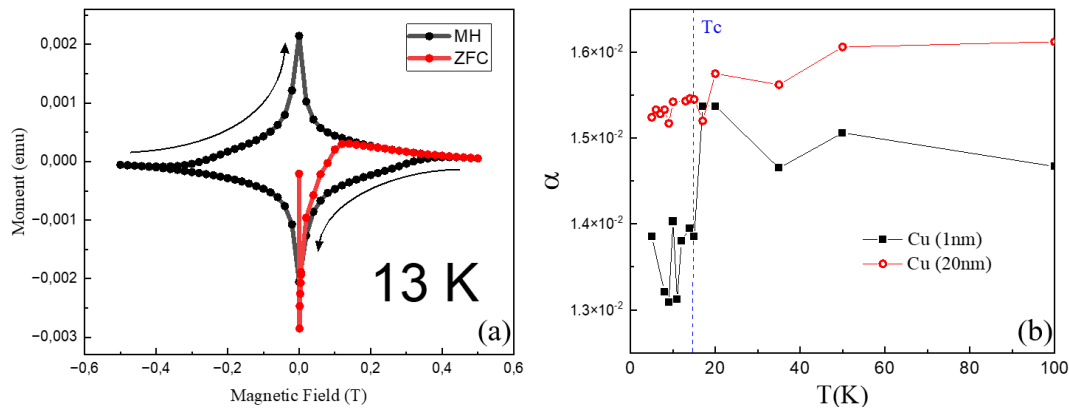


Figure 2: (a) SQUID-VSM measurement of an epitaxial NbN thin film (45nm) with a magnetic field applied perpendicular to the film plane. Measurements are done with a field sweeping rate of 1 mT/s. At 13 K, The red curve corresponds to the ZFC (Zero Field Cooling) curve, which measures the magnetization of a material when it is cooled in the absence of an external magnetic field. The black curve represents the variation of the field after ZFC ($H_{\max} \rightarrow H_{\min}$ and $H_{\min} \rightarrow H_{\max}$). The cycle is traversed in the reverse direction compared to a bulk superconductor (Kim-Ji model). (b) Temperature dependence of Gilbert damping for NbN/Cu/Py stacks.

Additionally, X/NbN/Y and X/NbN/Y/Py stacks were synthesized to explore the influence of X,Y = Cu, Ta, Pt on NbN T_c , as well as to test the influence of NbN and of X,Y = Cu, Ta, Pt on permalloy (Py) damping. As observed in previous studies on Nb/Py [1] and NbN/Py [13], the momentum loss channel in the NbN (50 nm) layer is partially suppressed by the opening of the superconducting gap below T_c . This leads to a reduction of the damping parameter below T_c (Fig. 2 (b)). The amplitude of the damping reduction changes as a function of the Y interlayer thickness for Y = Cu as shown in Fig.2 (b).

References

- [1] C. Bell, S. Milikisyants, M. Huber, and J. Aarts. [Spin Dynamics in a Superconductor-Ferromagnet Proximity System](#). *Phys. Rev. Lett.* 100, 047002 (4 2008).
- [2] Jacob Linder and Jason W. A. Robinson. [Superconducting spintronics](#). *Nature Physics* 11, 307–315 (2015).
- [3] A. K. Geim, S. V. Dubonos, J. G. S. Lok, M. Henini, and J. C. Maan. [Paramagnetic Meissner effect in small superconductors](#). *Nature* 396, 144–146 (1998).
- [4] C. Pfaff, T. Courtois, M. R. Koblischka, et al. [Magnetic moment of thin film superconductors: When thickness matters](#). *Phys. Rev. B* 110, 094502 (9 2024).
- [5] J. W. A. Robinson, J. D. S. Witt, and M. G. Blamire. [Controlled Injection of Spin-Triplet Supercurrents into a Strong Ferromagnet](#). *Science* 329, 59–61 (2010). eprint: <https://www.science.org/doi/pdf/10.1126/science.1189246>.
- [6] Zhen Wang, A. Yamamoto, S. Nishiyama, and J. Ishiyama. [Superconducting properties and crystal structures of single-crystal niobium nitride thin films deposited at ambient substrate temperature](#). *Journal of Applied Physics* 79, 7837–7842 (1996).
- [7] Stuart A. Wolf, James J. Kennedy, and Martin Nisenoff. [Properties of superconducting rf sputtered ultrathin films of Nb](#). *Journal of Vacuum Science and Technology* 13, 145–147 (1976). eprint: https://pubs.aip.org/avs/jvst/article-pdf/13/1/145/12087140/145_1_online.pdf.
- [8] C. P. Bean. [Magnetization of Hard Superconductors](#). *Phys. Rev. Lett.* 8, 250–253 (6 1962).
- [9] D.-X. Chen and R. B. Goldfarb. [Kim model for magnetization of type-II superconductors](#). *Journal of Applied Physics* 66, 2489–2500 (1989).
- [10] M. Belogolovskii, M. Poláčková, E. Zhitlukhina, and et al. [Competing length scales and 2D versus 3D dimensionality in relatively thick superconducting NbN films](#). *Scientific Reports* 13 (2023).
- [11] A. Carrington and F. Manzano. [Magnetic penetration depth of MgB2](#). *Physica C: Superconductivity* 385, 205–214 (2003).
- [12] Rishabh Duhan, Subhamita Sengupta, Ruchi Tomar, et al. [Structure and dynamics of a pinned vortex liquid in a superconducting \$a\text{-Re}_0\text{Zr}\$ thin film](#). *Phys. Rev. B* 108, L180503 (18 2023).
- [13] M. Müller, L. Liensberger, L. Flacke, et al. [Temperature-Dependent Spin Transport and Current-Induced Torques in Superconductor-Ferromagnet Heterostructures](#). *Phys. Rev. Lett.* 126, 087201 (8 2021).

Three terminal devices for improved efficiency

Corrado C. M. Capriata^{1, *}, M. Biagi¹, C. Bouchard², L. Hutin², B. Viala², R. Sousa¹, and K. Garello¹

¹Université Grenoble Alpes, CEA, CNRS, Grenoble-INP, SPINTEC, Grenoble 38000, France

²CEA LETI, Grenoble 38000, France

*corrado-carlomaria.capriata@cea.fr

Spin orbit torques (SOT) based magnetic tunnel junctions (MTJ) hold great promise for embedded non-volatile memories application. In fact, they feature ultra-fast dynamics (sub-ns), large endurance (10^{12-16}) and low power operation (sub-pJ) [1]. The working mechanism of SOT-MTJ is summarized in Fig. 1. In such a structure, a charge current flowing through a non-magnetic material, usually a heavy metal (HM), is converted into a spin current source, mediated by the Spin Hall effect (SHE) and the Rashba-Edelstein effect (REE) [2]. Such spin current, in turn applies a torque on the adjacent magnetic layer, the free layer (FL) that stores information, Fig. 1(a).

A key challenge that has to be resolved for SOT-MRAMs technology is reducing the write current I_{write} , which is directly related to the charge-to-spin current conversion ratio parameter ξ , that describes the SOT material efficiency. β -tungsten is the state-of-the-art conversion layer [1], but recent studies suggest making use of orbital physics to further enhance ξ [3]. Various materials such as Cr, Ti, Al, and Ru were shown to have potential in this. Although various materials (Cr, Ti, Al, Ru) have shown promise, experimental demonstration of a clear improved switching in SOT-MTJs with these elements is still lacking [4], .

In this poster, I will present a material study incorporating Ru as orbital source, and the current effort undertaken to realize three terminal (3-T) structures such as benchmarking these emerging solutions aiming at improving ξ . Our approach begins with simplified stacks patterned as Hall-bars, Fig. 2(a), to investigate how the efficiency varies when inserting different materials and thicknesses of the conversion layers Fig. 2(c). This first phase of the study allows us to select the most promising material systems, separate the origin of different contributions, and evaluate the impact of the annealing step necessary for MRAM technology.

In a second part, promising stacks were transferred to full SOT-MTJ devices with diameters down to 50 nm, Fig. 2(b). We will present their electrical characterization and compare different material systems Fig. ???. The preliminary results hint at an improved conductivity, but this does not translate into an equivalent improvement in ξ .

This study aims at clarifying whether orbital-to-spin conversion can improve the current SOT-MRAM technology, and further opens the way to multipillar SOT-MRAMs.

Acknowledgments

This work was partly supported by the French RENATECH network, implemented at the Upstream Technological Platform in Grenoble PTA (ANR-22-PEEL-0015), by France 2030 government investment plan managed by the French National Research Agency under grant reference PEPR Electronique (ANR-22-PEEL-0009).

References

- [1] Viola Krizakova, Manu Perumkunnil, Sébastien Couet, Pietro Gambardella, and Kevin Garello. [Spin-orbit torque switching of magnetic tunnel junctions for memory applications](#). *Journal of Magnetism and Magnetic Materials* 562, 169692 (2022).
- [2] Sachin Krishnia, Yanis Sassi, Fernando Ajejas, et al. [Large Interfacial Rashba Interaction Generating Strong Spin–Orbit Torques in Atomically Thin Metallic Heterostructures](#). *Nano Letters* 23, 6785–6791 (2023).
- [3] Dongwook Go and Hyun-Woo Lee. [Orbital torque: Torque generation by orbital current injection](#). *Physical Review Research* 2, 013177 (20, 2020).
- [4] Rahul Gupta, Chloé Bouard, Fabian Kammerbauer, et al. [Harnessing orbital Hall effect in spin-orbit torque MRAM](#). *Nature Communications* 16, 130 (2, 2025).

Multistate MTJs crossbar arrays as hardware AI co-processors: coping with non-idealities

Anatole Moureaux^{1,*}, Anthony Lopes Temporao¹, Lindiomar Borges de Avila Jr¹, and Flavio Abreu Araujo¹

¹Neuromorphic Engineering Group, Institute of Condensed Matter and Nanosciences, Université catholique de Louvain, Louvain-la-Neuve, Belgium

*anatole.moureaux@uclouvain.be

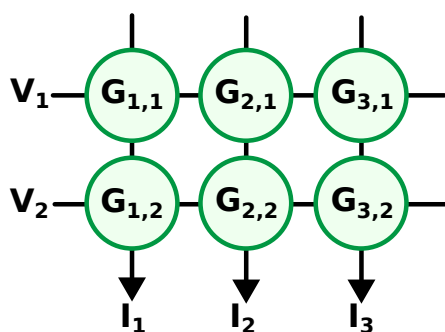
During the past few years, evidences of the concerning amount of energy consumed by data storage and processing systems has been put to light [1, 2]. The increasing use of the internet of things (IoT) and the recent surge in the AI applications development reinforce the need for energy-efficient data processing techniques. In the meantime, neuromorphic engineering has begun to address these issues by focusing on the development of analog and brain-inspired computing systems. These techniques rely on running specialized computing schemes on dedicated low-power hardware, by leveraging specific features of physical systems. Magnetic tunnel junctions (MTJ) are choice candidates for implementing such hardware. Indeed, the dynamics of spin-torque vortex oscillators (STVO) has already been successfully used as a nonlinear activation function in different kinds of neural networks relying on random nonlinear transformations for data classification and timeseries forecasting [3, 4].

However, nonlinear transformations are only one of the two main operations occurring in neural networks, the second one being the weighted sum of a set of inputs. The so-called multiply-and-accumulate (MAC) operation essentially consists in multiplying an input vector \mathbf{x} by a weight matrix \mathbf{W} to produce an output vector \mathbf{y} (Eq. 10).

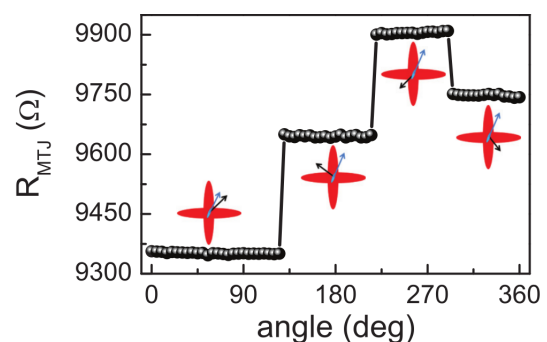
$$\mathbf{y} = \mathbf{W}\mathbf{x} \Leftrightarrow y_i = \sum_j W_{i,j}x_j \quad (10)$$

$$I_i = \sum_j G_{i,j}V_j \quad (11)$$

Some works have already showcased the use of magnetic systems for performing the so-called multiply-and-accumulate (MAC) operation such spin-torque oscillators operated with the spin-diode effect [5], or even skyrmions [6]. It can also be performed directly in the hardware using a crossbar array of cells presenting a set of distinct conductance levels. The input, which is encoded into a voltage vector \mathbf{V} applied to the gates of the cells, is *multiplied* by the weight encoded in the conductance level $G_{i,j}$ of each cell through Ohm's law. The resulting currents are then *accumulated* along each row using Kirchoff's current law to produce the output current vector \mathbf{I} , effectively implementing the weighted sum (see Fig. 1a and Eq. 11). Previous works already showcased MAC operations performed with a crossbar array of binary state memristive



(a) An input voltage vectors \mathbf{V} is multiplied with the conductance matrix \mathbf{G} to produce an output current vector \mathbf{I} .



(b) Each memristive cell contains a MTJ able to store 4 distinct states depending on the magnetization of the free layer (black arrow). The fixed layer magnetization is represented by the blue arrow. Extracted from [7].

Figure 1: A crossbar array of multistate MTJs can be used to perform the MAC operation efficiently in the hardware.

cells [8], or the dynamics of field-effect transistors for multibit operations [9]. In this work, we consider MTJs presenting 4 distinct conductance levels (Fig. 1b), allowing to perform analog MAC operations with unprecedented speed and scalability. These levels can be obtained in each cell by setting the magnetization of the MTJ free layer in a specific nonvolatile state through external field or spin-orbit torque [7].

However said states are not linearly distributed, which is an ideal case crucial for performing MAC operations reliably. Using simulations, we investigate the impact of the non-ideality of the MTJ states and derive a lower bound for the expected error. The scaling of this intrinsic error with the dimensions of the matrix \mathbf{W} is assessed. The impact of the MTJ non-idealities

is shown independent from the number of output channels in the crossbar array, but increasing with the number input channels. By considering the signal-to-noise ratio of the output signal, we show that the array is optimized for multiplying large input vectors and wide matrices, which is precisely the case in random nonlinear projection techniques. The simulated non-ideal crossbar array is hence finally used to demonstrate the classification of the MNIST dataset in the framework of extreme learning machines (ELM) [4].

Acknowledgments

Disclaimer: Funded by the European Union. Views and opinions expressed are however those of the author(s) only and do not necessarily reflect those of the European Union, the European Innovation Council or the SMEs Executive Agency (EISMEA). Neither the European Union nor the granting authority can be held responsible for them.

References

- [1] V. K. Sangwan and M. C. Hersam. [Neuromorphic nanoelectronic materials](#). *Nature Nanotechnology* 15, 517–528 (2020).
- [2] A. S. Luccioni, Y. Jernite, and E. Strubell. [Power Hungry Processing: Watts Driving the Cost of AI Development?](#) *arXiv preprint 2311.16863* (2023).
- [3] F. Abreu Araujo, M. Riou, J. Torrejon, et al. [Role of non-linear data processing on speech recognition task in the framework of reservoir computing](#). *Scientific Reports* 10, 328 (2020).
- [4] Moureaux A., C. Chopin, S. de Wergifosse, Jacques L., and F. Abreu Araujo. [Spintronics for image recognition: Performance benchmarking via ultrafast data-driven simulations](#). *arXiv preprint 2308.05810* (2023).
- [5] N. Leroux, F. Mizrahi, D. Marković, et al. [Hardware realization of the multiply and accumulate operation on radio-frequency signals with magnetic tunnel junctions](#). *Neuromorphic Computing and Engineering* 1, 011001 (2021).
- [6] T. da Câmara Santa Clara Gomez, Y. Sassi, Sanz-Hernández D., et al. [Neuromorphic weighted sums with magnetic skyrmions](#). *Nature Electronics*, 1–11 (2025).
- [7] S. Das, A. Zaig, M. Schultz, et al. [A four-state magnetic tunnel junction switchable with spin-orbit torques](#). *Applied Physics Letters* 117, 072404 (2020).
- [8] S. Jung, H. Lee, S. Myung, et al. [A crossbar array of magnetoresistive memory devices for in-memory computing](#). *Nature* 601, 211–216 (2022).
- [9] T. Soliman, S. Chatterjee, N. Laleni, et al. [First demonstration of in-memory computing crossbar using multi-level Cell FeFET](#). *Nature Communications* 14, 6348 (2023).

Magnetic properties of $\text{YCo}_{12}\text{B}_6$ compound studied with neutrons, X-rays and macroscopic characterization techniques

Baptiste Vallet-Simond^{1,*}, Léopold V. B. Diop², Fabrice Wilhelm¹, Andrei Rogalev¹, and Olivier Isnard³

¹European Synchrotron Radiation Facility, Grenoble, France

²Institut Jean Lamour (CNRS), Nancy, France

³Université Grenoble-Alpes - Institut Néel (CNRS), Grenoble, France

*baptiste.vallet-simond@esrf.fr

$\text{YCo}_{12}\text{B}_6$ is a fascinating compound for study in the context of itinerant electron magnetism and spin fluctuations. With a Curie temperature T_C close to 152 K and an average magnetic moment per Co atom of approximately $0.45 \mu_B$ [1], $\text{YCo}_{12}\text{B}_6$ offers a possibility to get new insights into the magnetism of intermetallic compounds. Indeed, despite its high Co content, both the magnetic moment and the ordering temperature are remarkably low. This is a common feature of all $\text{RCo}_{12}\text{B}_6$ compounds, with R being a rare earth. These compounds belong to the $\text{SrNi}_{12}\text{B}_6$ structure type (space group $R\bar{3}m$), and they have the peculiarity of having two very similar but inequivalent crystal sites, 18g and 18h, for the Co atoms. The interplay between itinerant electrons and localized magnetic moment in this compound provides insight into the mechanisms driving magnetic ordering and fluctuations. Here, we will focus on a combined approach using local probes and macroscopic characterization techniques to investigate the properties of $\text{YCo}_{12}\text{B}_6$, be they structural, magnetic, or magneto-responsive.

First, the structure and the chemical composition were studied in details though X-ray diffraction (XRD) and scanning electron microscopy (SEM) combined with energy dispersive spectroscopy (EDS). Through this, we confirmed the high quality of $\text{YCo}_{12}\text{B}_6$ crystalline samples (for polycrystalline samples or single crystals).

In a second part, the macroscopic magnetic properties were studied through the scope of mainly three theoretical models:

- The critical exponents and the associated Landau coefficients related to the phase transition at $T = T_C$ were studied through Landau's theory of phase transitions using the Inoue-Shimizu model [2, 3].
- The temperature dependence of spontaneous magnetization has been analyzed through the physical model described in refs. [4–7]. The strength of this model is that it allows the determination of the spin wave stiffness for a ferromagnetic (or ferri) compound.
- The delocalization degree of 3d electrons in $\text{YCo}_{12}\text{B}_6$ has been evaluated with the theory of spin fluctuations by Takahashi [8].

Finally, we have exploited the different local probes to study magnetic properties of $\text{YCo}_{12}\text{B}_6$. Neutron diffraction experiments at ILL (D1B diffractometer) allowed for direct observation of magnetic structures and moment arrangements. The solved magnetic structure of $\text{YCo}_{12}\text{B}_6$ can be seen on Figure 1.

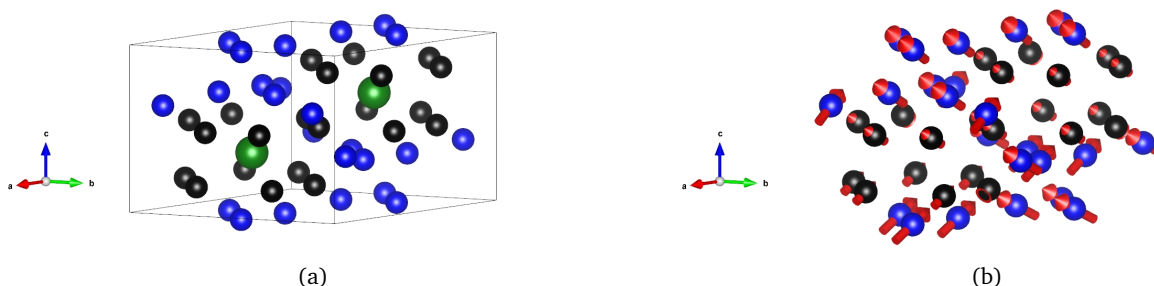


Figure 1: (a) Atomic environment of 3d transition metal atoms at sites 18g (black) and 18h (blue). The Y atoms (in green) at the four vertices of the unit cell, as well as all the B atoms, have been removed for an easier visualisation. (b) Representation of a fraction of the magnetic structure corresponding to two crystallographic unit cells along the c axis. Only the magnetic atoms are shown here (red arrow to represent the magnetic moment).

In order to provide element selective information on the electronic structure and magnetic moments, we have carried out X-ray magnetic circular dichroism (XMCD) on single crystals at the ESRF - ID12 beamline. Experiments have been performed at the Co-K edge and $\text{Y-L}_{2,3}$ edges. Using the magneto-optical sum rules, we have determined the spin and orbital magnetic moment of the 4d states of Y.

Despite the fact that Y is usually considered to be "non-magnetic", we have found a sizeable XMCD signal at the $\text{Y-L}_{2,3}$ edges, reflecting a magnetic polarization of Y due to 4d(Y)-3d(Fe) hybridization, as displayed on Figure 2. The induced total magnetic moment of Y ($\mu_0 H = 7 \text{ T}$) is found to be antiparallel to the magnetic field (the orbital moment m_o and m_s

are parallel for $\mu_0 H // c$), i.e. antiferromagnetically coupled to Co magnetic sublattices. However, with \vec{k} and $\mu_0 H$ along the a -axis, the orbital and spin moments are now opposite (the orbital moment m_o and m_s are antiparallel), with a spin moment much stronger than the orbital one. The total magnetic moment is once again antiparallel to the applied magnetic field. We also performed theoretical calculations, using LMTO and FDMNES, confirming the induced magnetic polarization of Y-4d states, therefore showing the role of Y in the magnetic properties of $\text{YCo}_{12}\text{B}_6$.

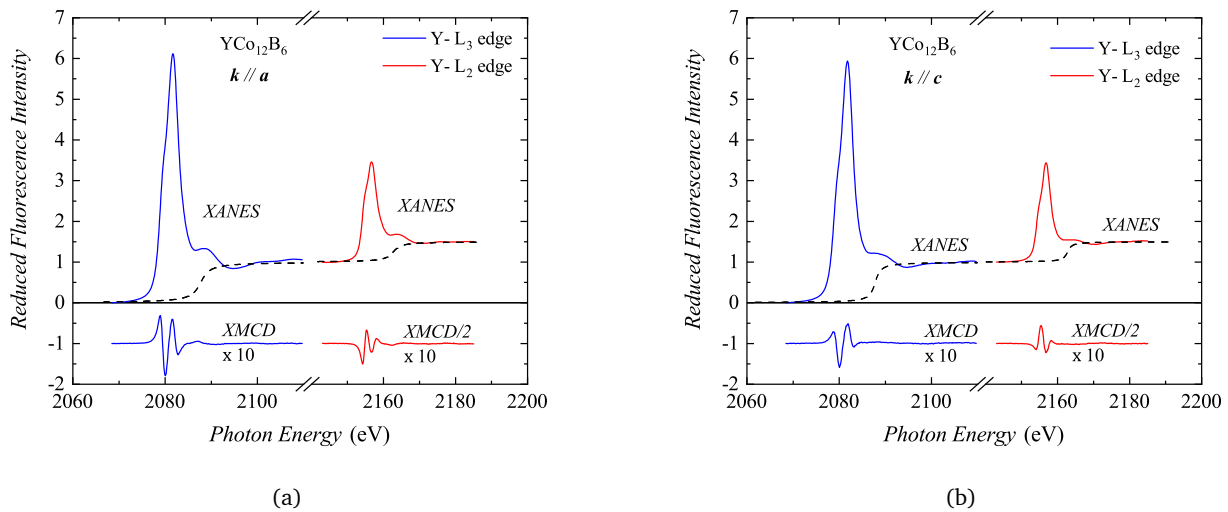


Figure 2: X-ray Absorption Near Edges (XANES) spectra and the associated X-ray Magnetic Circular Dichroism (XMCD) for the $L_{2,3}$ edges of Y measured on $\text{YCo}_{12}\text{B}_6$ single crystals. (a) The propagation vector of the X-rays \vec{k} is aligned with the \vec{a} axis of the crystal. (b) The propagation vector of the X-rays \vec{k} is aligned with the \vec{c} axis of the crystal.

References

- [1] M. Rosenberg, M. Mittag, and K. H. J. Buschow. Magnetic properties of $\text{YCo}_{12}\text{B}_6$ and $\text{GdCo}_{12}\text{B}_6$ intermetallics. *Journal of Applied Physics* 63 (3586-3588).
- [2] J. Inoue and M. Shimizu. Volume dependence of the first-order transition temperature for RCO_2 compounds. *Journal of Physics F : Metal Physics* 12 (1982).
- [3] P. E. Brommer. A GENERALIZATION OF THE INOUE-SHIMIZU MODEL. *Physica B* 154, 197–202 (1989).
- [4] M. D. Kuz'min. Shape of Temperature Dependence of Spontaneous Magnetization of Ferromagnets: Quantitative Analysis. *Physical Review Letters* 94 (2005).
- [5] M. D. Kuz'min and A. Tishin. Temperature dependence of the spontaneous magnetization of ferromagnetic insulators: Does it obey the law? *Physics Letters A* 341, 240–243 (2005).
- [6] M. D. Kuz'min, M. Richter, and A. N. Yaresko. Factors determining the shape of the temperature dependence of the spontaneous magnetization of a ferromagnet. *Physical Review B* 73 (2006).
- [7] M. D. Kuz'min, K. P. Skokov, L. V. B. Diop, I. A. Radulov, and O. Gutfleisch. Exchange stiffness of ferromagnets. *European Physical Journal Plus* 135 (2020).
- [8] Yoshinori Takahashi. *Spin Fluctuation Theory of Itinerant Electron Magnetism*. Springer Berlin, Heidelberg, 2013.

Micromagnetic analysis of skyrmion trajectories in weak Dzyaloshinskii-Moriya interaction system

Capucine Gueneau^{1,*}, Charles-Elie Fillion¹, Johanna Fischer¹, Olivier Boulle¹, Gilles Gaudin¹, Laurent Ranno², Claire Baraduc¹, and H el ene B ea¹

¹ Univ. Grenoble Alpes, CEA, CNRS, Spintec, Grenoble, France

² Univ. Grenoble Alpes, CNRS, N el Institute, Grenoble, France

*capucine.gueneau@cea.fr

Magnetic skyrmions are two dimensional chiral spin textures stabilized by the antisymmetric exchange interaction called Dzyaloshinskii-Moriya interaction (DMI) [1],[2]. They have many interesting properties: they can be small, their size is usually between the nano and the microscale [3]; they are stable at room temperature [4], they can be created and annihilated using a gate voltage [5] and furthermore, they are efficiently manipulated with a current [6]. All these characteristics make skyrmions promising for many applications, such as skyrmions racetrack memories [7],[8] and skyrmions based logic devices [8] but also for neuromorphic computing [9]. However, we need to understand and control the physics of skyrmions and particularly their trajectory under an applied current. While this has been widely studied, both experimentally and theoretically [10], these studies usually focus on N el type skyrmions, in systems with a relatively large DMI strength. Recent experimental observations on the control of the helicity and chirality by material tuning or gate voltage [11],[12],[13] allow easy reaching of all intermediate states between Bloch and N el skyrmions. We thus need to better understand the behaviour under current of the intermediate skyrmions found in these weak DMI systems.

Here we will present an analytical and micromagnetic analysis of the skyrmion trajectory under current in systems with weak DMI. In particular, we will focus on the influence of the DMI strength and damping. The micromagnetic study was performed using the software Mumax3.10 [14]. The physics of the motion of skyrmions under an electric current in Heavy Metal(HM)/ Ferromagnet(FM)/ Metal Oxide tri-layer system relies on a transverse spin current created by the spin Hall effect when a current is injected into the HM layer. This results in a spin accumulation at the HM/FM interface, whose polarization is determined by the spin Hall angle of the HM. At the interface between the HM and FM layers, the angular momentum of the accumulated spins is transferred to those within the FM layer, generating a spin-orbit torque (SOT) which, in turn, generates the motion of the spin textures.

Under this current, the skyrmion trajectory is expected to be a straight line, deflected from the current direction by an angle φ_{traj} . Following the thiele equation,[15], we can analytically derive a trajectory angle :

$$\varphi_{traj} = \arctan\left(\frac{-p\delta_{DW}}{\alpha R}\right) - \xi = \varphi_{SkHE}\left(\frac{R}{\delta_{DW}}\right) - \xi \quad (12)$$

with p the polarity of the skyrmion (orientation of its core), α the damping parameter, δ_{DW} the width of the domain wall (DW), R the radius of the skyrmion and ξ his helicity, the angle between the spin in the domain wall and the radial unit vector as defined in Fig. 1 (a).

The first term in the equation, φ_{SkHE} , represents the well-known skyrmion hall angle, which arises from the Skyrmion Hall Effect (SkHE). This angle represents the deflection of the skyrmion's trajectory from the one induced by the force exerted by the spin-orbit torque (SOT), expressed in the second term as directly proportional to the helicity.

In fig. 1 (b), we see that the trajectory angles simulated (colored crosses) show a discrepancy from the linear analytical behaviour expected if φ_{SkHE} is constant (red dotted line), especially close to $\xi = \frac{\pi}{2}$. In fact, φ_{SkHE} is not constant for varying helicities as it is directly related to the radius of the skyrmions and therefore to the value of the DMI coefficient. To determine φ_{SkHE} using the simulation, we remove the helicity term from the trajectory angle.

We now explore the influence of the damping parameter, from 0 to 1. In fig. 1.(c), the colored lines correspond to the analytic plot of $\varphi_{SkHE}\left(\frac{R}{\delta_{DW}}\right)$, while the colored crosses correspond to the values obtained from the micromagnetic simulations. The results demonstrate a good agreement between our simulations and the analytical formula 12 for three values of damping used for the simulations (0.05, 0.5 and 1).

Through simulations, we validated an analytical model that accurately predicts skyrmion trajectories based on their structural characteristics (R , δ_{DW} , ξ , p) and material parameters such as α . Specifically, we show that the skyrmion trajectory depends linearly on helicity and that φ_{SkHE} depends on $\frac{R}{\delta_{DW}}$, while also noting the impact of the damping parameter on the trajectories of skyrmions. Importantly, by tuning the DMI, for instance via gate voltage control, it is possible to adjust skyrmion helicity and radius, thereby impacting the skyrmion's motion. This study underscores the significance of coupling material engineering and external control mechanisms, such as voltage gating [11], to finely tune skyrmion properties, an essential step toward realizing advanced spintronic applications.

Acknowledgments

The authors acknowledge funding by the French ANR (ADMIS n ANR-19-CE24-0019) and CHIREX (ANR-22-EXSP-0002).

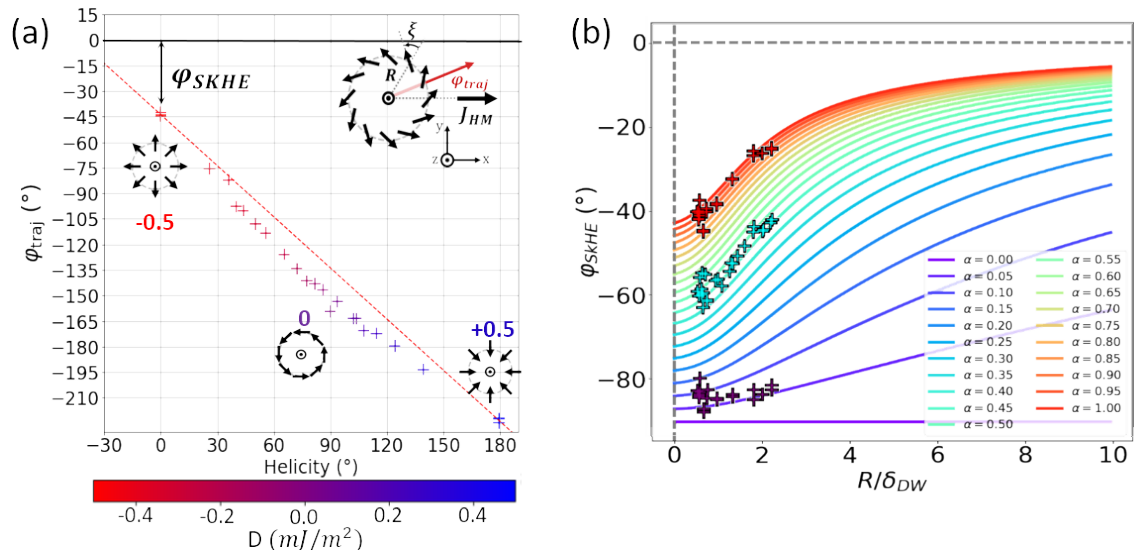


Figure 1: (a) Trajectory of the skyrmions stabilized with different values of DMI $\in [-0.5, 0.5] J/m^2$ plotted according to the helicity ξ . The simulated results are displayed using the colored crosses and the red dotted line correspond to the linear behavior $\varphi_{SKHE} - \xi$, with φ_{SKHE} constant. The insert is a scheme of a skyrmion with φ_{traj} the angle corresponding to the trajectory of the skyrmion and ξ the helicity (c) Plot of the skyrmion Hall angle φ_{SKHE} according to the ratio $\frac{R}{\delta_{DW}}$ for different values of damping $\alpha \in [0, 1]$. The lines correspond to the analytic formula 12 meanwhile the crosses correspond to the simulation results.

References

- [1] I. Dzyaloshinsky. [A Thermodynamic Theory of “Weak” Ferromagnetism of Antiferromagnetics](#). *Journal of Physics and Chemistry of Solids* 4, 241–255 (1958).
- [2] Tôru Moriya. [Anisotropic Superexchange Interaction and Weak Ferromagnetism](#). *Phys. Rev.* 120, 91–98 (1960).
- [3] C. Moreau-Luchaire, C. Moutafis, N. Reyren, et al. [Additive Interfacial Chiral Interaction in Multilayers for Stabilization of Small Individual Skyrmions at Room Temperature](#). *Nature Nanotech* 11, 444–448 (2016).
- [4] Olivier Boulle, Jan Vogel, Hongxin Yang, et al. [Room-Temperature Chiral Magnetic Skyrmions in Ultrathin Magnetic Nanostructures](#). *Nature Nanotech* 11, 449–454 (2016).
- [5] Marine Schott, Anne Bernand-Mantel, Laurent Ranno, et al. [The Skyrmion Switch: Turning Magnetic Skyrmion Bubbles on and off with an Electric Field](#). *Nano Lett.* 17, 3006–3012 (2017).
- [6] Seonghoon Woo, Kai Litzius, Benjamin Krüger, et al. [Observation of Room-Temperature Magnetic Skyrmions and Their Current-Driven Dynamics in Ultrathin Metallic Ferromagnets](#). *Nature Mater* 15, 501–506 (2016).
- [7] Albert Fert, Vincent Cros, and João Sampaio. [Skyrmions on the Track](#). *Nature Nanotech* 8, 152–156 (2013).
- [8] Xichao Zhang, G. P. Zhao, Hans Fangohr, et al. [Skyrmion-Skyrmion and Skyrmion-Edge Repulsions in Skyrmion-Based Racetrack Memory](#). 2015. arXiv: 1403.7283 [cond-mat].
- [9] D. Pinna, F. Abreu Araujo, J.-V. Kim, et al. [Skyrmion Gas Manipulation for Probabilistic Computing](#). *Phys. Rev. Applied* 9, 064018 (2018).
- [10] Roméo Juge, Soong-Geun Je, Dayane de Souza Chaves, et al. [Current-Driven Skyrmion Dynamics and Drive-Dependent Skyrmion Hall Effect in an Ultrathin Film](#). *Phys. Rev. Applied* 12, 044007 (2019).
- [11] Charles-Elie Fillion, Johanna Fischer, Raj Kumar, et al. [Gate-Controlled Skyrmion and Domain Wall Chirality](#). *Nat Commun* 13, 5257 (2022).
- [12] R. Kumar, C.E. Fillion, B. Lovery, et al. [Control of Skyrmion Chirality in Ta / Fe - Co - B / Ta O x Trilayers by Ta O x Oxidation and Fe - Co - B Thickness](#). *Phys. Rev. Applied* 19, 024064 (2023).
- [13] Bingqian Dai, Di Wu, Seyed Armin Razavi, et al. [Electric Field Manipulation of Spin Chirality and Skyrmion Dynamic](#). *Sci. Adv.* 9, eade6836 (2023).
- [14] Arne Vansteenkiste, Jonathan Leliaert, Mykola Dvornik, et al. [The Design and Verification of MuMax3](#). *AIP Advances* 4, 107133 (2014).
- [15] A. A. Thiele. [Steady-State Motion of Magnetic Domains](#). *Phys. Rev. Lett.* 30, 230–233 (1973).

Efficiency of Spin Transfer Torque and Characteristic Switching Times in Unconventional Double-MgO Magnetic Memories

Hanna Karaoui^{1,*}, Bruno Teixeira¹, Louis Farcis¹, David Salomoni¹, Stéphane Auffret¹, Kevin Garello¹, and Ricardo C. Sousa¹

¹Spintec, CEA, Grenoble, France

*hanna.karaoui@cea.fr

MRAM efficiency can be defined as the amount of energy required to write one cell into the high- or low-resistance state and the energy barrier to overcome during the corresponding magnetization reversal. The retention time is determined by the thermal stability factor Δ corresponding to the ratio between the energy barrier and the thermal energy. This work investigates two different methods to assess the efficiency of a spin-transfer torque (STT) magnetic memory. The investigated stack has a main and a capping MgO barrier creating two magnetic-oxide interfaces to increase the perpendicular magnetic anisotropy. These methods are then used to find optimized magnetic stacks, by creating two orthogonal FeCoB thickness wedges on the same wafer and comparing their device properties.

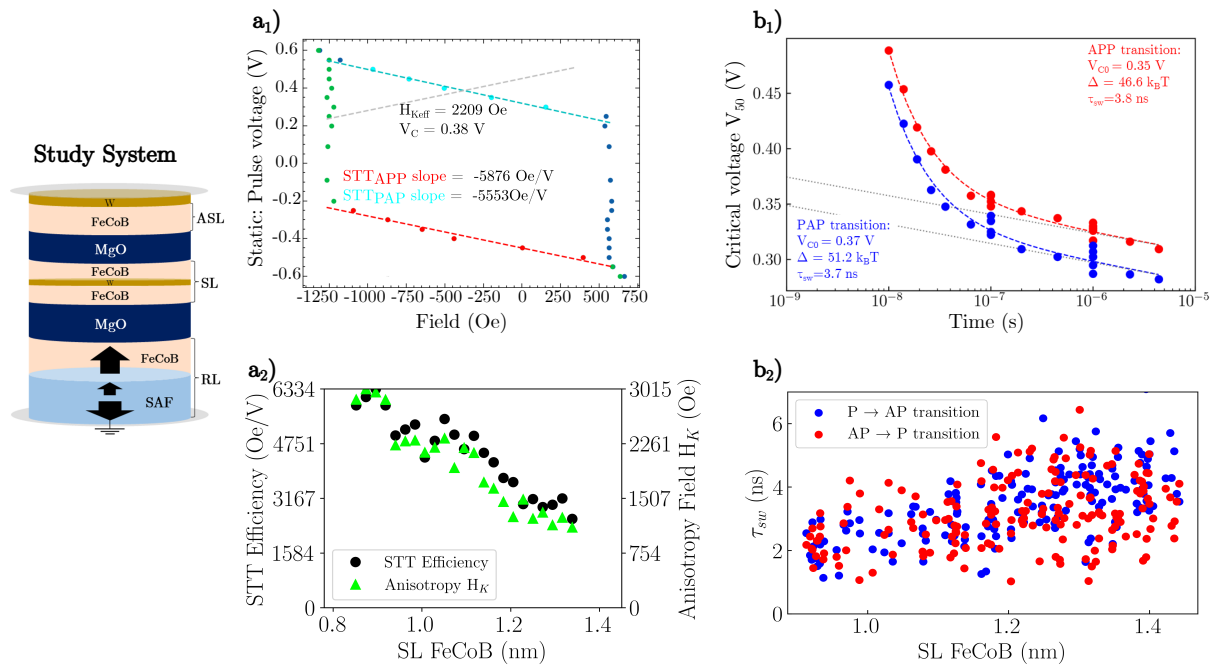


Figure 1: Evaluation of spin transfer torque efficiency through quasi-static measurements and magnetization switching times through WER measurements in the showcased study system featuring dual MgO tunneling barriers and three FM layers of FeCoB: one in the reference layer (RL) in which the magnetization is fixed by a Co/Pt multilayer synthetic anti-ferromagnet (SAF), storage layer (SL) and assistance layer (ASL) in which the magnetizations are free. **a₁)**: Pulse voltage variation as a function of applied field extracted from a field phase diagram of a single device, using pulses applied during a field sweep [1] to extract the effective anisotropy field $H_{Keff} = 2209$ Oe, and a critical switching voltage $V_{50} = 0.38$ V, to evaluate the STT efficiency from the boundary slope for both parallel to anti-parallel (PAP) and anti-parallel to parallel (APP) transitions, respectively 5876 Oe/V and 5553 Oe/V. **a₂)**: STT efficiency and the anisotropy field H_K evolution as a function of the storage layer FeCoB at a fixed thickness of ASL layer (0.7 nm). **b₁)**: The relationship between critical switching voltage V_{50} and pulse width is analyzed for PAP and APP transitions within the thermally activated regime for durations up to 10^{-6} seconds and the precessional regime for pulses shorter than 100^{-9} seconds. **b₂)**: The change in characteristic magnetization switching time τ_{sw} is examined relative to the storage layer FeCoB thickness for both PAP and APP transitions.

The first method involves applying 100 ns current pulses during quasi-static field sweep measurements. The resulting phase state diagram shows the variation in the critical switching voltage as a function of the external applied field as presented in Figure a₁). These diagrams are used to extract parameters such as the effective anisotropy field and the critical switching voltage. One way to evaluate the efficiency of the spin transfer torque (STT) using the above method is to calculate the ratio between the anisotropy field and the minimum critical switching, as discussed in a previous study [1]. An initial evaluation employing this efficiency metric was conducted to optimize the layer thickness of the magnetic stack. A significant

relationship is observed between the STT efficiency and the thickness of the ferromagnetic layers. As shown in Figure a₂) we observe a higher STT efficiency, up to more than 6000 Oe/V at lower FM thicknesses of 0.84 nm in the FeCoB storage layer and at 0.65 nm of the assistance layer (ASL FeCoB).

The second method used to evaluate the efficiency is based on Write Error Rate (WER) measurements. Investigating the switching probability of each device over more than 1000 writing attempts for different pulse widths and voltage amplitudes. Moreover, this method allows us to investigate pulse widths as short as 7ns, addressing both the thermally activated and the precessional reversal regimes. A unified model was used to fit the data simultaneously over the whole pulse width as described in [2]. The thermally activated regime allows us to extract the thermal stability factor (Δ). The precessional regime, when the critical switching voltage increases inversely proportional to the pulse width, typically extends up to 100 ns. A characteristic time in this regime is represented by the magnetization switching time τ_{sw} , which corresponds to the time at which the reversal energy is minimized. We investigated its various dependencies in both parallel (P)-to-antiparallel (AP) transitions (in blue) and vice versa (AP-to-P transitions, in red). One significant finding, illustrated in figure b₂) demonstrates a clear dependence of magnetization switching time on the storage layer thickness. Faster switching times (1-4 ns) occur for thinner FeCoB (0.8-1.1 nm), while thicker FeCoB (1.15-1.45 nm) results in slower switching times (4-6.5 ns).

A key question is how the dependencies observed in spin-transfer torque efficiency, as evaluated from 100 ns pulses in quasi-static measurements, are correlated with the characteristic times in the precessional regime. A preliminary comparison of the dependencies of STT efficiency and switching times on the FeCoB storage layer thickness suggests a correlation where higher STT efficiency and faster switching times are observed for thin storage layer thicknesses. It is important to examine the influence of additional physical parameters, such as the diameter of the device, taking into account variations in the thermal stability between devices. The stability is also affected by the ferromagnetic coupling between the storage and assistance layers of the stack. Addressing these complexities is the focus of our ongoing studies.

References

- [1] AA Timopheev, R Sousa, M Chshiev, LD Buda-Prejbeanu, and B Dieny. Respective influence of in-plane and out-of-plane spin-transfer torques in magnetization switching of perpendicular magnetic tunnel junctions. *Physical review B* 92, 104430 (2015).
- [2] Laura Rehm, Georg Wolf, Bartek Kardasz, Mustafa Pinarbasi, and Andrew D Kent. [Sub-nanosecond spin-torque switching of perpendicular magnetic tunnel junction nanopillars at cryogenic temperatures](#). *Applied Physics Letters* 115 (2019).

Low-temperature epitaxial magnetic garnet thin films for quantum magnonics II

William Legrand^{1,2*}, Hanchen Wang², Davit Petrosyan², Francesca Zanichelli², Pietro Gambardella², Richard Schlitz³, Michaela Lammel³, Jamal Ben Youssef⁴, and Myriam H. Aguirre⁵

¹CNRS, Institut Néel, Université Grenoble Alpes, Grenoble, France

²Department of Materials, ETH Zürich, Switzerland

³Department of Physics, University of Konstanz, Germany

⁴LabSTICC, CNRS, Université de Bretagne Occidentale, Brest, France

⁵Department of Condensed Matter Physics, University of Zaragoza, Spain

*william.legrand@neel.cnrs.fr

Magnetically ordered systems sustain collective dynamical excitations in which all magnetic moments precess coherently, known as spin waves. Spin waves are prime candidates for encoding information that can be processed, propagated and converted in other types of signals, enabling various technological applications. At temperatures that are low enough for quantification to occur, these concepts are promising for quantum information applications based on the generation of magnons in the quantum regime [1, 2].

Yttrium iron garnet (YIG, $\text{Y}_3\text{Fe}_5\text{O}_{12}$) is the magnetic material known to feature the lowest magnon losses in bulk and epitaxial thin film forms, and has been the most studied platform in the context of magnonics. In the past decade, the synthesis of nm-thick epitaxial films of iron garnets by physical vapor deposition has opened up exciting opportunities for the on-chip generation and processing of microwave signals encoded in magnons. Nevertheless, extrinsic magnetic losses are commonly observed at cryogenic temperatures, owing to the ubiquitous use of a paramagnetic substrate, gadolinium gallium garnet (GGG, $\text{Gd}_3\text{Ga}_5\text{O}_{12}$). Recently, YIG has been purposely grown on lattice-mismatched yttrium scandium gallium garnet (YSGG, $\text{Y}_3\text{Sc}_2\text{Ga}_3\text{O}_{12}$), a commercially available substrate that is nominally free of paramagnetic species, either directly as a substrate [3] or as an intermediate layer between YIG and GGG [4]. However, iron garnet thin films still suffer from demanding lattice-matching and stoichiometry requirements. This calls for renewed synthesis methods and substrate/film combinations including suitably substituted iron garnet systems.

This poster is a follow-up to the results presented in 2023 in Sète, and is intended to support further discussion on the broad topic of magnonic thin films for cryogenic applications. Using magnetron sputtering, we grow perfectly epitaxial ultrathin iron garnet films (thicknesses from 3 to 90 nm) with controlled magnetic anisotropy and low damping. We will present our most recent updates on YIG, off-stoichiometric Y-doped YIG and Bi-doped YIG grown on GGG and YSGG with:

- an innovative approach to control garnet film stoichiometry, based on the co-sputtering of binary oxides [5]
- lattice-matched substituted garnets on YSGG to reduce paramagnetic losses in cryogenic conditions [5]
- measurements of a hybrid magnon–photon system in thin film geometry using a loop-gap resonator [6]
- an investigation of orbital pumping in Bi-doped YIG [7]

References

- [1] Yutaka Tabuchi, Seiichiro Ishino, Atsushi Noguchi, et al. [Coherent coupling between a ferromagnetic magnon and a superconducting qubit](#). *Science* 349, 405–408 (2015).
- [2] H. Y. Yuan, Yunshan Cao, Akashdeep Kamra, Rembert A. Duine, and Peng Yan. [Quantum magnonics: When magnon spintronics meets quantum information science](#). *Phys. Rep.* 965, 1–74 (2022).
- [3] Side Guo, Daniel Russell, Joseph Lanier, et al. [Strong on-Chip Microwave Photon–Magnon Coupling Using Ultralow-Damping Epitaxial \$\text{Y}_3\text{Fe}_5\text{O}_{12}\$ Films at 2 K](#). *Nano Lett.* 23, 5055–5060 (2023).
- [4] Side Guo, Brendan McCullian, P. Chris Hammel, and Fengyuan Yang. [Low damping at few-K temperatures in \$\text{Y}_3\text{Fe}_5\text{O}_{12}\$ epitaxial films isolated from \$\text{Gd}_3\text{Ga}_5\text{O}_{12}\$ substrate using a diamagnetic \$\text{Y}_3\text{Sc}_{2.5}\text{Al}_{2.5}\text{O}_{12}\$ spacer](#). *J. Magn. Magn. Mater.* 562, 169795 (2022).
- [5] William Legrand, Yana Kemna, Stefan Schären, et al. Lattice-tunable substituted iron garnets for low-temperature magnonics. *arXiv:2407.06850* (2024). arXiv: <http://arxiv.org/abs/2407.06850v1> [cond-mat.mtrl-sci].
- [6] Francesca Zanichelli, Davit Petrosyan, Hanchen Wang, et al. Loop-gap resonators for strong coupling to magnetic insulator thin films. *under review* (2025).
- [7] Hanchen Wang, Min-Gu Kang, Davit Petrosyan, et al. Observation of Orbital Pumping in Ferrimagnetic Insulators. *under review* (2025).

Posters session 2

(Mis)estimation of spin-orbit torques in the presence of current-induced magnon creation and annihilation

Paul Noel^{1,2,*}, Emir Karadža¹, Richard Schlitz¹, Pol Welter³, Charles-Henri Lambert¹, Luca Nesi^{1,4}, Federico Binda¹, Christian L. Degen³, and Pietro Gambardella¹

¹Department of Materials, ETH Zurich, CH-8093 Zurich, Switzerland

²Institut de Physique et Chimie des Matériaux de Strasbourg, UMR 7504 CNRS, Université de Strasbourg, 23 Rue Du Loess, BP 43, 67034 Strasbourg Cedex 2, France

³Department of Physics, ETH Zurich, CH-8093 Zurich, Switzerland

⁴Dipartimento di Fisica, Politecnico di Milano, Via G. Colombo 81, 20133 Milano, Italy

*paul.noel@ipcms.unistra.fr

Materials with high spin-orbit torque (SOT) efficiency are essential for the development of new spin-orbitronic devices that enable storage and logic technologies that are fast, nonvolatile, and enduring. The proper metrology of these SOTs is pivotal for the technological development and for the understanding of their underlying physical mechanisms. Several techniques have been developed to quantify the SOTs [1], but there appear to be recurrent inconsistencies in the reported results on the SOT efficiency suggesting that the understanding of the involved processes is incomplete, even for the most studied Pt-based systems [2].

Harmonic Hall resistance measurements are widely used to evaluate SOT effects, and more particularly the efficiency of the dampinglike (DL) torque and the fieldlike (FL) torque in normal metal (NM)/ferromagnet (FM) bilayers [3]. The usual harmonic Hall resistance analysis assumes a constant magnetization, unaffected by the current and magnetic field. However, this reasoning does not hold in general, as the creation or annihilation of magnons induced by the spin current affects the magnetization [4]. The excitation of magnons by an interfacial spin accumulation depends on the relative direction of the accumulated spins and the magnetization. Spin-flip scattering leads to the creation (annihilation) of magnons when the magnetization M is parallel (antiparallel) to the spin accumulation, as depicted in Fig. 2. In turn, the modification of the magnon population by a spin current leads to a change of the magnetization.

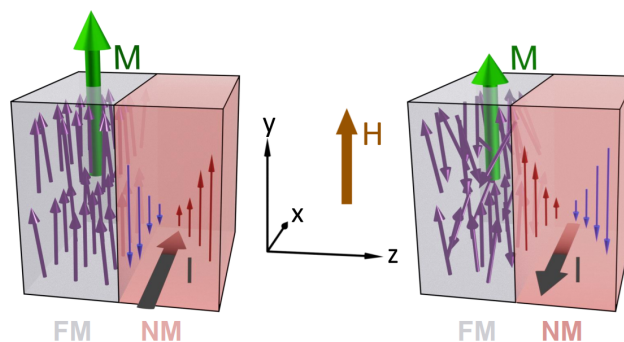


Figure 1: Schematic of the annihilation and creation of magnons in a FM due to current-induced spin accumulation in the NM. The local magnetic moments are shown as purple arrows, the spin moments are shown as thin red and blue arrows. The spin magnetic moment is opposite to the spin moment. Figure adapted from [5].

All magnetoresistances that depend on the magnitude of the magnetization, such as the anisotropic magnetoresistance, spin Hall magnetoresistance, planar Hall effect, and anomalous Hall effect, thus have a nonlinear contribution that depends on the current density. The change of magnon population due to spin currents in NM/FM bilayers give rise to transverse and longitudinal nonlinear magnetoresistances due to magnon creation or annihilation. We call this set of nonlinear magnetoresistances the magnon creation-annihilation magnetoresistances ($m\dot{m}$ MRs) [5, 6]. In particular, the transverse magnetoresistances due to the nonlinear planar Hall effect ($m\dot{m}$ PHE) and nonlinear anomalous Hall effect ($m\dot{m}$ AHE) were previously not accounted for in the harmonic Hall resistance measurements. Due to their similar symmetry to the SOT contributions, the $m\dot{m}$ PHE and $m\dot{m}$ AHE can lead to a strong misestimation of the torques. Consequently, the widespread harmonic Hall resistance measurement technique that has been used to study heavy metals should include the $m\dot{m}$ MRs to provide a correct estimation of the torque efficiency [7].

In this work we present a comprehensive approach combining both longitudinal and transverse second harmonic resistance measurements to evaluate the $m\dot{m}$ MRs and SOT contributions in NM/FM bilayers. Accounting for the $m\dot{m}$ MRs, we provide a corrected estimate of the SOTs in different NM/FM material. Specifically, we show that the $m\dot{m}$ PHE, when unaccounted for, can lead to strong misestimation of both the DL and FL SOTs in NM/FM bilayers with in-plane magnetization.

To evidence this misestimation, we compare, on the same device, the DL torque estimated by the usual harmonic Hall resistance technique with the one estimated using a calibrated magneto-optical Kerr effect (MOKE) technique. This comparison reveals a discrepancy of the DL torque, which is overestimated by 30% in Pt/CoFeB (and up to 100% in W/CoFeB) when using the uncorrected harmonic Hall resistance method compared to the MOKE measurement and corrected harmonic Hall method as shown in Fig. 3.

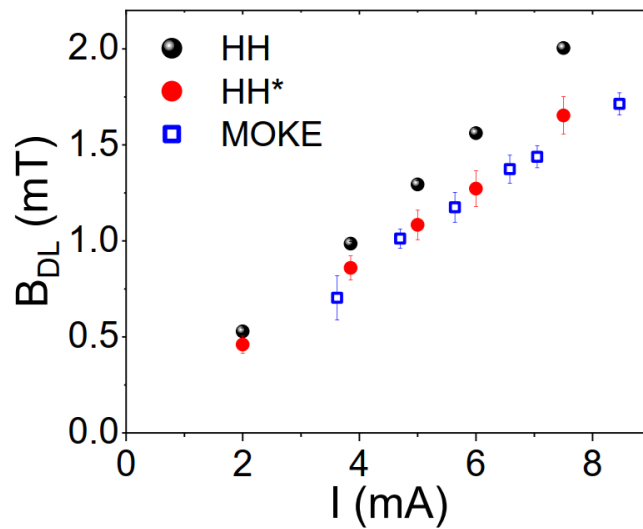


Figure 2: Comparison between the DL torque obtained at different currents from MOKE and the harmonic Hall resistance analysis with (HH*) and without (HH) magnon correction. Figure adapted from [7].

Acknowledgments

This work was supported by the Swiss National Science Foundation (Grant No. 200020 200465). P.N. acknowledges the support of the ETH Zurich Postdoctoral Fellowship Program 19-2 FEL- 61.

References

- [1] A. Manchon, J. Železný, I. M. Miron, et al. [Current-induced spin-orbit torques in ferromagnetic and antiferromagnetic systems](#). *Reviews of Modern Physics* 91, 035004 (9, 2019).
- [2] Lijun Zhu, Daniel C. Ralph, and Robert A. Buhrman. [Maximizing spin-orbit torque generated by the spin Hall effect of Pt](#). *Applied Physics Reviews* 8, 031308 (13, 2021).
- [3] Can Onur Avci, Kevin Garello, Mihai Gabureac, et al. [Interplay of spin-orbit torque and thermoelectric effects in ferromagnet/normal-metal bilayers](#). *Physical Review B* 90, 224427 (31, 2014).
- [4] Can Onur Avci, Johannes Mendil, Geoffrey S. D. Beach, and Pietro Gambardella. [Origins of the Unidirectional Spin Hall Magnetoresistance in Metallic Bilayers](#). *Physical Review Letters* 121, 087207 (24, 2018).
- [5] Paul Noël, Richard Schlitz, Emir Karadža, et al. [Nonlinear longitudinal and transverse magnetoresistances due to current-induced magnon creation-annihilation processes](#). 12, 2024. arXiv: [2411.07991](#) [cond-mat].
- [6] Haripriya Madathil, Pranav Pradeep, Paul Noël, and Saül Vélez. [Large enhancement of spin-flip scattering efficiency at Y3Fe5O12/Pt interfaces due to vertical confinement](#). 26, 2024. arXiv: [2412.19247](#) [cond-mat].
- [7] Paul Noël, Emir Karadža, Richard Schlitz, et al. [Estimation of spin-orbit torques in the presence of current-induced magnon creation and annihilation](#). 12, 2024. arXiv: [2411.07999](#) [cond-mat].

Method of analysis of the spectra obtained by microfocused Brillouin light scattering

N. Benaziz^{1,*}, J-P. Adam¹, and T. Devolder¹

¹Centre des Nanosciences et des Nanotechnologies, Université Paris-Saclay, CNRS, 91120 Palaiseau, France

*nessrine.benaziz@universite-paris-saclay.fr

Spin waves (SW) are the elementary excitations in magnetic material. One popular technique to characterize them is Brillouin light Scattering (BLS) [1]. BLS is an inelastic scattering between photons and magnons that occurs through two types of interaction. A magnon can be annihilated, increasing the photon energy in an antiStokes (AS) process, or created, decreasing the photon energy in a Stokes (S) process. In this technique, the light is focused on the sample using a quasi-parallel beam, where only SW wavevectors $k = \frac{4\pi}{\lambda} \sin \theta$ can be probed (with θ being the incident angle). To access different wavevectors, the scattering geometry must be changed. Focusing the light through a high numerical aperture lens instead, allows mapping a wide range of in-plane SW wavevectors in a single acquisition. This technique is called microfocused Brillouin light scattering (μ -BLS). This results in complex spectra that need to be analyzed and interpreted. Here, we develop a physically transparent method to help interpret the μ -BLS signal as only a few models have been reported [2].

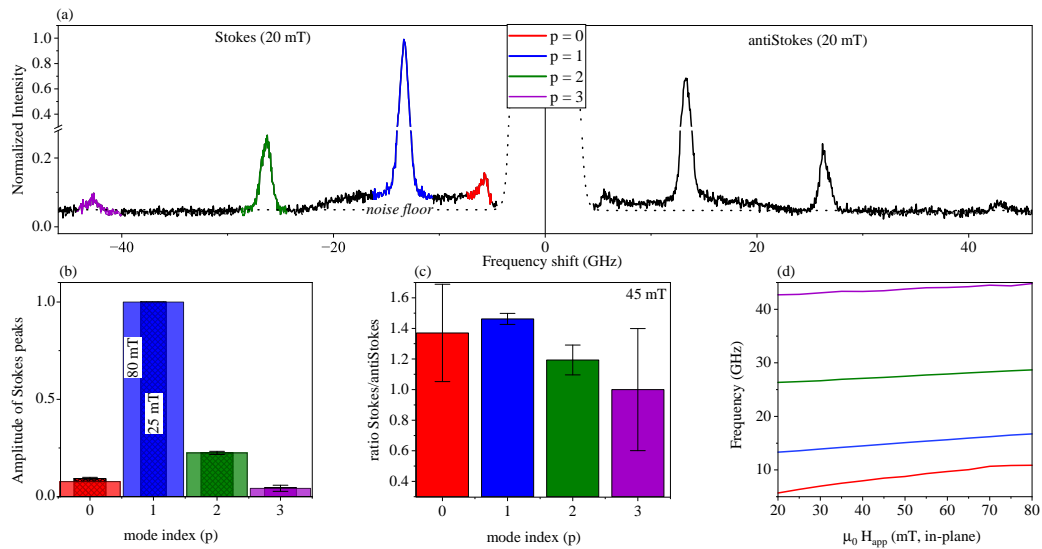


Figure 1: Experimental results: (a) microfocused BLS spectrum recorded for an applied field of $\mu_0 H_{\text{app}} = 20$ mT. (b) Noise-floor-corrected intensity maxima of the Stokes peaks corresponding to different modes for $\mu_0 H_{\text{app}} = 25$ mT (shaded narrow bars) and $\mu_0 H_{\text{app}} = 80$ mT (wide bars). The error bars correspond to 25 mT. (c) ratios of the Noise-floor-corrected maxima of intensity of the S versus AS parts of the spectra for the 4 modes at $\mu_0 H_{\text{app}} = 45$ mT. (d) Field dependence of the frequencies of the maxima of the spectra.

We first started by investigating the thermally excited SW from a 50 nm thick CoFeB film by μ -BLS. These spectra exhibited four distinct modes which we identify as the uniform modes ($p = 0$) and the first three perpendicular standing spin wave (PSSW) modes ($p = 1, 2, 3$). These spectra show unique features such as peak shapes not being Lorentzian [Fig 1](a), a non monotonic intensity [Fig 1(b)] and a S/AS intensity asymmetry [Fig 1(c)]. The model we develop to understand those results is the following,

$$F_{\text{bils}}(\omega) = \sum_{\Psi_k} \eta(\Psi_k) R(\vec{k}) I(\Psi_k) L(\omega - \omega_{\Psi_k}) \quad (13)$$

where $\eta(\Psi_k)$ is the population of the Ψ_k magnon, $R(\vec{k})$ is an instrumental function related to the light diffraction (Rayleigh criterion), $I(\Psi_k)$ is the intensity scattered by each magnon and $L(\omega - \omega_{\Psi_k})$ is a Lorentzian function accounting for the finite lifetime of the magnon and the finite instrumental width. To calculate these contributions, we only need the following parameters, which can be classified into two categories: magnetic and optical inputs. The magnetic inputs are the equilibrium magnetization, SW wavevector, SW frequency, SW population, SW linewidth, dynamic magnetization. To generate these inputs, we used the numerical solver TetraX [3, 4]. As for the optical input, it only consists on the permittivity tensors of the magnetic material.

To get a better understanding of the μ -BLS, we performed a first fictitious μ -BLS experiment where we only consider that the "Backward Volume" (BV) waves are the sole present in the system [Fig. 2(a)] and the second is when only the

"Damon-Eshbach" (DE) waves are present in the system [Fig. 2(b)]. This is done by restricting the sum in Eq. 13 to the corresponding orthogonal line scans in wavevector space.

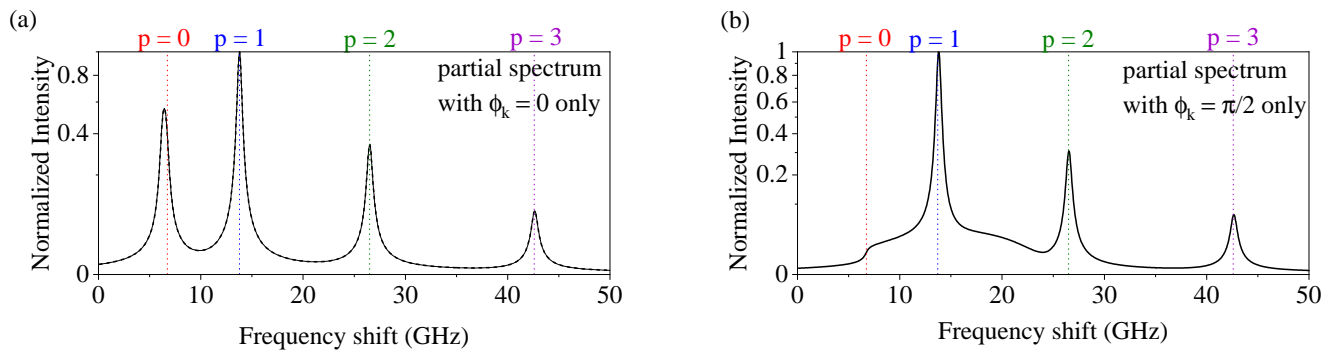


Figure 2: AntiStokes part of the modeled microfocused BLS spectra that would be obtained if the only spin waves populated in the material would be (a) the backward volume waves ($\phi_k=0$, black, dashed lines) or (b) the Damon-Eshbach waves ($\phi_k=\frac{\pi}{2}$, black lines). The dotted lines correspond to the frequencies of the FMR mode and the PSSW 1,2 and 3 modes. The spectral intensities are scaled in a square root manner to better evidence the low intensity features. Each spectrum is normalized to the $p = 1$ mode.

When the sole BV SW are considered, the spectrum [Fig. 2(a)] contains 4 narrow peaks that are positioned at frequencies very near the frequencies of the FMR and the PSSW 1, 2 and 3 modes. In contrast in the second experiment [Fig. 2(b)], only 3 peaks are present. The shape of the two lowest SW branches ($p = 0$ and $p = 1$) spread over a wide frequency interval (6-25 GHz), giving a small asymmetric shallow hill skewed to the high frequency side. For both spectra, the $p = 1$ mode gives the most intense peak in the spectrum.

From this observation, we can expect the following features from the real μ -BLS spectra. For all the modes, the amplitudes of the peaks will result from their thermal population –approximately inversely proportional to their frequencies– and the interplay between their thickness profile and the light penetration profile within the magnetic material. In addition, the lowest frequency peak $p = 0$ will have a rather small amplitude and a composite shape, appearing to result from the sum of a rather narrow peak approximately placed at the absolute bottom of the dispersion relation, plus a shallow asymmetric hill offset to larger frequencies and extending up to 25 GHz, as indeed observed experimentally [Fig. 1(a)]. As for the linewidth of each peak in a μ -BLS, it does not correspond to the damping but rather reflects the dispersion of the spin waves within the interval of wavevectors sensed by the experimental setup.

The present formalism offers a physically transparent and direct method to interpret microfocused BLS spectra.

Acknowledgments

This work was supported by the French National Research Agency (ANR) as part of the “Investissements d’Avenir” and France 2030 programs. This includes the SPICY project of the Labex NanoSaclay: ANR-10-LABX-0035, the MAXSAW project ANR-20-CE24-0025 and the PEPR SPIN projects ANR 22 EXSP 0008 and ANR 22 EXSP 0004.

References

- [1] Thomas Sebastian, Katrin Schultheiss, Björn Obry, Burkard Hillebrands, and Helmut Schultheiss. [Micro-focused Brillouin light scattering: imaging spin waves at the nanoscale](#). *Frontiers in Physics* 3 (2015).
- [2] Ondřej Wojewoda, Martin Hrtoň, and Michal Urbánek. *Modeling of the micro-focused Brillouin light scattering spectra*. 2024.
- [3] Lukas Körber, Gwendolyn Quasebarth, Alexander Hempel, et al. *TetraX: Finite-Element Micromagnetic-Modeling Package*. 2022.
- [4] L. Körber and A. Kákay. [Numerical reverse engineering of general spin-wave dispersions: Bridge between numerics and analytics using a dynamic-matrix approach](#). *Physical Review B* 104, 174414 (2021).

High-resolution X-ray spectroscopy of highly charged ions for magnetic surface investigation

E. M. Tosi^{1,*}, C. V. Ahmad¹, E. Lamour¹, C. Prigent¹, S. Steydli¹, M. Werl², R. A. Wilhelm², D. Vernhet¹, and M. Trassinelli¹

¹*Institut des NanoSciences de Paris, CNRS, Sorbonne Université, Paris, France*

²*Institute of Applied Physics, TU Wien, Vienna, Austria*

³*Polifab, Politecnico di Milano, Milan, Italy*

*elena-maria.tosi@insp.upmc.fr

To detect surface magnetism, a technique using highly charged ions (HCIs) as probe and X-ray spectroscopy of HCIs has been developed in recent years by our team [1]. Such a detection is chosen suitable as, amongst others, it gives spin information from the sample of the very first atomic layer in a non-destructive way and with no need to apply external fields.

Experiments proving the feasibility of the technique have been recently done [2][3] on a monocrystalline Ni (110) sample using 170 keV Ar¹⁷⁺ ions at grazing incidence in a range of different temperatures with low-resolution detection. The observed asymmetric broadening at higher temperature of the acquired emission peak, unresolved in its electron composition, provides an evidence of the phase change from the ferromagnetic to the paramagnetic phase. The outcome motivated the need for high-resolution detection to resolve precisely the spin-dependent population of the sample's first atomic layer, and thus the possibility to detect antiferromagnetic phases.

For this purpose, a Bragg spectrometer has been designed and predisposed combining a Highly Oriented Pyrolytic Graphite crystal with a time- and space- resolved pixel detector (ASI Technology) [4][5]. Here we present the preliminary characterization of such a detector with respect to a calibrated detector on benchmark targets with and without a diffraction crystal. Moreover, we will present the preliminary results on the new measurement campaign that will take place in Spring 2025 on Ni and FeRh samples. The latter is particularly interesting because of the possibility to study the double magnetic transition antiferro-/ferromagnetic and ferro-/paramagnetic with the same sample.

The X-ray spectrometer, permitting to perform also coincidence measurements, open the possibility to resolve surface magnetism. After the development of calibration in well-characterized samples, the aim is to use the technique also on more exotic materials, such as 2D materials, which will be specifically fabricated and characterized at Polifab.

References

- [1] M. Trassinelli et al. *J. Atoms*. 10 (2022).
- [2] P. Dergham et al. In preparation for *Phys. Rev. Lett.* (Forthcoming).
- [3] P. Dergham. "PhD Dissertation". PhD thesis. Sorbonne Université, 2023.
- [4] E. Lamour et al. *J. Phys. B: At. Mol. Opt. Phys.* 48, 144016 (2015).
- [5] ASI Technology Resources. *ASI Technology resources*. <https://www.amscins.com/resources/technology/>.

Magneto-Ionic Control of Magnetic Anisotropy in Pt/Co/Al Multilayers

Xinyuan Yang^{1,*}, H. Singh², A. Durnez¹, S. Collin², J. Grollier², V. Cros², N. Reyren², and L. Herrera Diez¹

¹Centre de Nanosciences et de Nanotechnologies, CNRS, Université Paris-Saclay, 91120 Palaiseau, France

²Laboratoire Albert Fert, CNRS, Thales, Université Paris-Saclay, Palaiseau, France

*xinyuan.yang@universite-paris-saclay.fr

The manipulation of magnetic anisotropy and Dzyaloshinskii-Moriya interactions (DMI) is of great research interest in modern spintronics, with the goal of developing devices that feature non-volatility, high access speeds, and low power consumption. In particular, Pt/Co/Al multilayers have emerged as an ideal platform for tuning interfacial properties, such as DMI and perpendicular magnetic anisotropy (PMA). Magneto-ionic gating is a powerful technique for precisely tuning the properties of the topmost magnetic layer in multilayer stacks. By applying a gate voltage through an ionic liquid, a previous study demonstrated that the magnetic anisotropy in the top Co layer of Pt/Co/Al multilayers can be changed from PMA to in-plane magnetic anisotropy (IPMA) [1]. These results indicate that magneto-ionic control of the anisotropy in a single layer can effectively manipulate the magnetic properties of coupled multilayer systems. Although ionic liquid devices are robust and easy to fabricate, solid-state devices are more compatible with practical applications and miniaturization.

Here, we report the magneto-ionic gating effect on Pt/Co/Al multilayers, using HfO₂ as gating material. Figure 1a shows a schematic of the multilayer and Hall bar structure. The stack is composed of Ta/Pt/[Co/Al/Pt]₄/Co/Al/AIO_x, grown by magnetron sputtering on a SiO₂ substrate. HfO₂ serves as the source of oxygen species, altering the Al / AIO_x front with the application of a gate voltage [2]. Indium Tin Oxide (ITO) is on top of the HfO₂ and used as one electrode. Figure 1b shows the Hall resistance of this stack in the as-grown state and after application of gate voltages. In the as-grown situation, the stack exhibits a complete PMA state. After applying a +5V gate voltage for 120 seconds, the anomalous Hall resistance decreases to four-fifths of its saturation value. Further +9V gating for 60 seconds induces a complete transition from PMA to IPMA in the top Co layer, which can be fully reversed, restoring the stack to its original state by applying -9V gating for 60 seconds. These results demonstrate that the magneto-ionic control of anisotropy from PMA to IPMA can be effectively transferred from ionic liquid to solid-state devices.

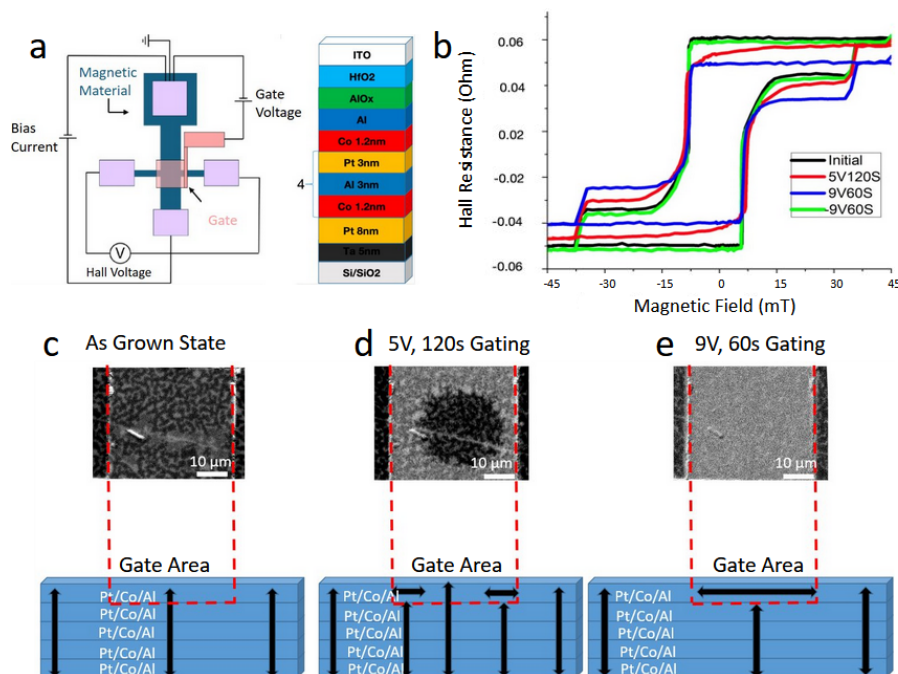


Figure 1: (a) Multilayer and Hall bar structure. (b) Hall resistance under different gating conditions. (c) Kerr microscopy images of the domain motion in an as grown state. (d) Kerr microscopy images of the domain motion after a +5V gating for 120 seconds. (e) Kerr microscopy images of the domain motion after a +9V gating for 60 seconds.

Figure 1c, 1d and 1e illustrate Kerr microscopy images of the magnetization switching induced by an out-of-plane magnetic field. Below each microscopy image, there is a corresponding side view of the five Pt/Co/Al repetitions with their magnetic properties (PMA or IPMA) indicated. Vertical black arrows represent the PMA state, while horizontal black arrows represent the IPMA state. In the as grown state shown in Figure 1c, the domains in five layers are coupled and then propagate smoothly without any pinning effects as they move under the area covered by the electrode.

In Figure 1d, after applying a +5V gate voltage for 120 seconds, the top Co layer beneath the ITO remains PMA state at the center, while the edges exhibit IPMA, as proved by the gray scale contrast displayed in the Kerr microscopy image. This inhomogeneous gating effect may promote the formation of chiral magnetic domains, which could be manipulated for domain generation, movement, and annihilation. Figure 1e shows the domain configuration after applying a +9V gating for 60 seconds. In this case, the top Co layer under the electrode exhibits only IPMA, while the four underlying Co layers remain PMA. This transition can pin the domain motion when it moves from the as-grown region to the gated area, meaning a higher out-of-plane magnetic field is required to continue the switching once the domain front achieves the gated area.

In conclusion, this work demonstrates that solid HfO₂ can be used to control the magnetic property of the top Co layer in multilayers, advancing the understanding of the anisotropy and magnetic domains manipulation via gating. The transition from PMA to IPMA in the top layer also enables control of the domain motion beneath it, with potential applications for the control of magnetization in 3D magnetic multilayer systems.

Acknowledgments

We acknowledge funding from a France 2030 government grant managed by the French National Research Agency (grant no. ANR-22-EXSP-0002 PEPR SPIN CHIREX) and from EU project SkyANN (reference no. 101135729).

References

- [1] S. A. Wolf, D. D. Awschalom, R. A. Buhrman, et al. [Spintronics: A Spin-Based Electronics Vision for the Future](#). *Science* 294, 1488–1495 (2001).
- [2] Sachin Krishnia, Libor Vojáček, Tristan Da Câmara Santa Clara Gomes, et al. *Interfacial spin-orbitronic effects controlled with different oxidation levels at the Co|Al interface*. 2024. arXiv: [2409.10685 \[cond-mat.mtrl-sci\]](#).

Gate controlled magnetoresistances on antiferromagnetic semiconductor 2D material

Davy Borowski^{1,*}, Mohamed Soliman¹, Arnaud Glippe¹, and Jean-François Dayen¹

¹Institut de physique et de chimie des matériaux de Strasbourg (IPCMS), DMONS, CNRS, 67200 Strasbourg, France

*davy.borowski@ipcms.unistra.fr

Atomically thin van der Waals semiconductor magnetic materials (2D) display behaviors resulting from the interplay between semiconducting and magnetic properties, those being absent in other material systems. This combination of magnetic and semiconducting transport properties enables the control of charge and spin carriers so that one can show complete spin polarization of conduction electrons. These considerations are more so significant while considering the realization of field-effect transistors (FET), therefore enabling gate-tunable transport measurements. In this regard, C_rSB_r is a layered A-type antiferromagnetic material of choice featuring intralayer ferromagnetic order and interlayer antiferromagnetic coupling [1]. In order to conduct this study, we consider a field-effect transistor geometry fabrication forming, in this manner, a Si bottom-gate and a graphite top-gate. Nanofabrication of all the exfoliated materials including C_rSB_r is performed using the dry transfer method in a glove box to protect the air sensitive magnetic material from oxidation and furthermore in the objective of ensuring good quality interfaces between the 2D magnetic and insulating layers.

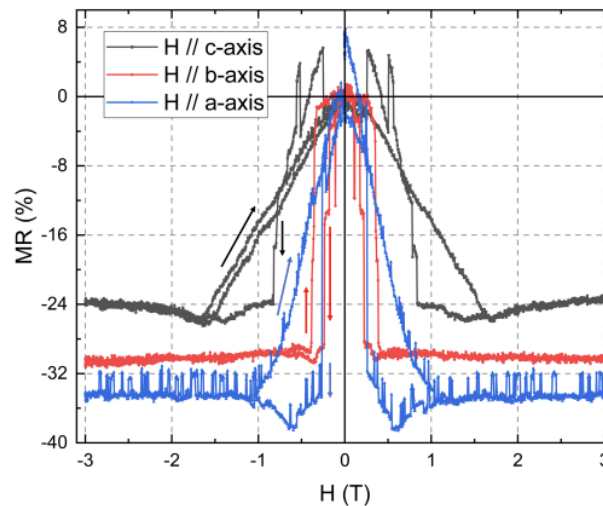


Figure 1: field anisotropy MR measurements at 10K

By following the FET architecture principals, this work is focusing on the effect of the doping induced by the two gates as well as the influence of the electric field generated [2]. The study of the magnetic field anisotropy and the conduction anisotropy is achieved thanks to our fabrication process and enables us to observe magnetoresistance (MR) switches from -60% to 60%. A complete modification from negative to positive magnetoresistance never observed before with this material. As a general statement, this study highlights very novel results that are providing a new understanding for the theoretical interpretation of the magneto-transport properties and behaviors of C_rSB_r .

References

- [1] Evan J. Telford, Avalon H. Dismukes, Raymond L. Dudley, et al. [Coupling between magnetic order and charge transport in a two-dimensional magnetic semiconductor](#). *Nature Materials* 21, 754–760 (2022).
- [2] Fan Wu, Ignacio Gutiérrez-Lezama, Sara A. López-Paz, et al. [Quasi-1D Electronic Transport in a 2D Magnetic Semiconductor](#). *Advanced Materials* 34 (2022).

Epitaxial growth of $\text{Mn}_5(\text{Si}_x\text{Ge}_{1-x})_3$ thin films on Ge(111) substrate by MBE: from ferro- to alter-magnetism?

S. Kang¹, V. Heresanu¹, C. Guillemard¹, L. Michez^{1,*}, M. Petit¹, E. Jedryka², R. Kalvig², and M. Wojcik²

¹Aix-Marseille Univ., CNRS, CINaM, AMUtech, Marseille, France

²Institute of Physics, Polish Academy of Sciences, Aleja Lotników 32/46, PL-02668 Warsaw, Poland

*lise.michez@univ-amu.fr

We present the controlled and epitaxial growth of $\text{Mn}_5(\text{Si}_x\text{Ge}_{1-x})_3$ thin films on Ge(111) substrate by Molecular beam epitaxy method (co-deposition), as well as characterizations of their structural and magnetic properties by X-ray diffraction (XRD), Atomic force microscopy (AFM), Transmission electron microscopy (TEM), and Nuclear magnetic resonance (NMR).

Mn_5Ge_3 and Mn_5Si_3 are two compounds exhibiting hexagonal $D8_8$ structure (space group $P6_3/mcm$) and they can be grown epitaxially on Ge(111) substrates [1]. However, they exhibit very different magnetic behavior. Mn_5Ge_3 is a metallic ferromagnet that presents a high spin polarization of the conduction electrons at the Fermi level, a Curie temperature of 296 K and a strong uniaxial magnetocrystalline anisotropy along the hexagonal c axis [1]. On the other hand, Mn_5Si_3 thin films exhibit a complex magnetic structure that is both temperature- and field- dependent: it is non-collinear antiferromagnetic below 65 K and collinear antiferromagnetic up to 100 K [2]. It can also be driven altermagnetic by growth engineering [3, 4].

The electrical and magnetic properties of the bulk $\text{Mn}_5(\text{Si}_x\text{Ge}_{1-x})_3$ materials have only been studied in the bulk phase by few research groups, however no studies were carried out on the thin films. XRD shows the correlation between Si concentration and lattice structural parameter deformation and crystallinity. Magnetic measurements ($M(T)$ and ^{55}Mn NMR) reveal the changes of local magnetic properties over Si concentrations [5, 6].

References

- [1] L-A Michez, A Spiesser, M Petit, et al. [Magnetic reversal in \$\text{Mn}_5\text{Ge}_3\$ thin films: an extensive study](#). *Journal of Physics: Condensed Matter* 27, 266001 (2015).
- [2] Christoph Sürgers, Thomas Wolf, Peter Adelman, et al. [Switching of a large anomalous Hall effect between metamagnetic phases of a non-collinear antiferromagnet](#). *Scientific Reports* 7, 42982 (2017).
- [3] Ismaïla Kounta, Helena Reichlova, Dominik Kriegner, et al. [Competitive actions of MnSi in the epitaxial growth of \$\text{Mn}_5\text{Si}_3\$ thin films on Si\(111\)](#). *Physical Review Materials* 7, 024416 (2023).
- [4] Helena Reichlova, Rafael Lopes Seeger, Rafael González-Hernández, et al. [Observation of a spontaneous anomalous Hall response in the \$\text{Mn}_5\text{Si}_3\$ d-wave altermagnet candidate](#). *Nature Communications* 15, 4961 (2024).
- [5] R. Kalvig, E. Jędryka, S. Kang, et al. [Magnetic interactions in epitaxial films of \$\text{Mn}_5\(\text{Ge}_{1-x}\text{Si}_x\)_3/\text{Ge}\(111\)\$: \$^{55}\text{Mn}\$ NMR study](#). *Journal of Magnetism and Magnetic Materials* 600, 172120 (2024).
- [6] Sueyeong Kang, Matthieu Petit, Vasile Heresanu, et al. [Epitaxial growth and magnetic properties of \$\text{Mn}_5\(\text{Si}_x\text{Ge}_{1-x}\)_3\$ thin films](#). *Thin Solid Films* 797, 140338 (2024).

Spin-torque nano-oscillators for unconventional computing and wireless communication applications

Elli Georgopoulou Kotsaki^{1,*}, Léna Le Roux-Kadhi¹, Leandro Martins¹, Abderrazak Hakam¹, Anike Purbawati¹, Florian Disdier¹, Artem Litvinenko¹, Alex Jenkins², Ricardo Ferreira², Philippe Talatchian¹, and Ursula Ebels¹

¹Univ. Grenoble Alpes, CEA, CNRS, Grenoble INP, SPINTEC, 38000 Grenoble, France

²International Iberian Nanotechnology Laboratory (INL), 4715-31 Braga, Portugal

*elli.georgopouloukotsaki@cea.fr

Energy consumption is one of the major issues that semiconductor electronics and computing systems have to face alongside with scalability. This is in particular the case when running brain inspired algorithms on conventional von Neuman architectures for which processing and storage units are physically separated. This results in increased energy consumption when moving large amount of data sets between them. Novel approaches for computing architectures and computing hardware are thus intensively searched for. Spintronics provides promising solutions [1]: spin-based devices require no standby power for memory operation, they are compatible with CMOS technology, they operate at room temperature, they are multifunctional, acting as memory, logic, sensor and microwave devices and at the hardware level they can act as artificial neurons and synapses. In this context, it has been demonstrated that spin-torque nano-oscillators (STNOs), based on magnetic tunnel junctions, can emulate the oscillatory behavior of neurons and perform spoken digit recognition or classification tasks [2]. The rich dynamics of STNOs, along with their non-linear properties is also of interest for wireless communication applications [3], [4] and fast frequency analysis [5]. Optimization of the microwave properties of STNOs for these different applications is hence an essential task including the realization of high quality STNO devices and the characterization of their spin torque driven magnetization dynamics. Two different STNO configurations are considered in this study: vortex-state (STVO) and uniformly magnetized STNOs with perpendicular magnetic anisotropy (PMA) called pbias-STNO (see Fig. 2).

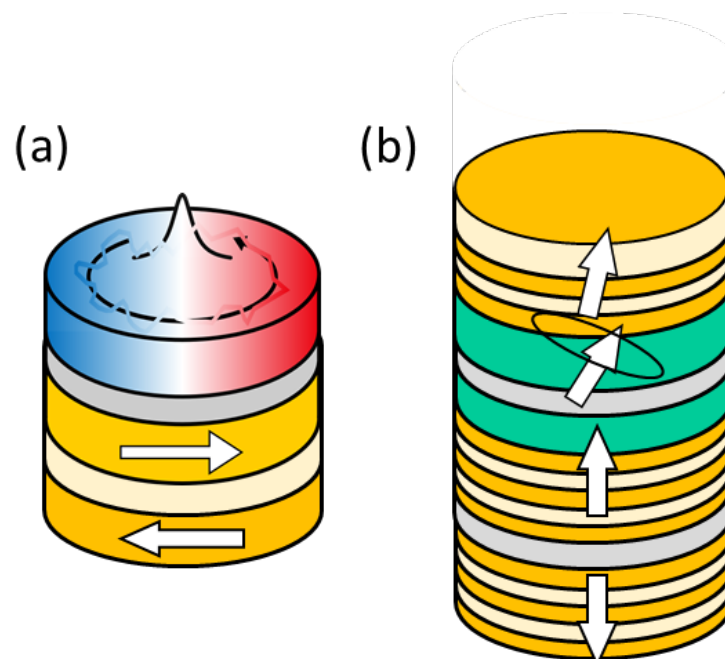


Figure 1: Schematic representation of the (a) vortex and (b) pbias STNO configuration

In the STVO, a magnetic vortex is stabilized in the free layer and steady state oscillations occur in the frequency range of 200 – 600 MHz. The pbias-STNO is based on perpendicular magnetized memory devices, for which the free layer is biased by an additional PMA layer. The corresponding frequencies lie in the 2-10 GHz range [5]. For the generation of true random numbers [6] and Ising-model based unconventional computing (Hopfield networks, Ising machines) [7], [8] the understanding and control of the phase dynamics of single and coupled STNO devices is essential. Phase control is achieved when the spin torque driven self-oscillations are locked to an external microwave signal. The phase is then described by the Adler equations [4]. When the frequency of the control signal is close to twice the natural STNO frequency (called here $2f$ synchronization), the STNO phase can take two distinct values 0 and π . In a previous study, this phase binarization has been well demonstrated for vortex STNOs and it was shown that it will be suitable for unbiased random number generation. Here we investigate the phase binarization for pBias-STNOs. Further control of the phase is achieved

when adding to the 2f-synchronisation signal a 1f synchronization signal that breaks the symmetry and leads to a biased random number generation [6]. Here we investigate the phase binarization for pBias-STNOs. Further control of the phase is achieved when adding to the 2f-synchronisation signal a 1f perturbation signal that breaks the symmetry and leads to a biased random number generation. Here we analyze the biasing via the 1f signal as a function of the frequency mismatch with the external RF source, the STNO configuration as well as the operating point (DC current, applied magnetic field), to determine best operational conditions and annealing strategies for Hopfield networks and Ising machines.

Acknowledgments

This work was supported in part by the French National Research Agency under grant reference ANR-22-CE24-0004 (SpinIM), the « France 2030 government investment plan » managed by the French National Research Agency under grant reference PEPR SPIN – SPINCOM ANR-22-EXSP-0005, the CEA under the programme FOCUS “Numérique Frugal”, as well as IRGA-MIAI program from the Univ. Grenoble Alpes. This work was supported by the French RENATECH Network and the Upstream Technological Platform (PTA).

References

- [1] G. Finocchio, R. Tomasello, B. Fang, et al. [Perspectives on spintronic diodes](#). *Applied Physics Letters* 118 (2021).
- [2] Miguel Romera, Philippe Talatchian, Sumito Tsunegi, et al. [Vowel recognition with four coupled spin-torque nano-oscillators](#). *Nature* 563, 230–234 (2018).
- [3] Hyun Seok Choi, Sun Yool Kang, Seong Jun Cho, et al. [Spin nano–oscillator–based wireless communication](#). *Scientific Reports* 4 (2014).
- [4] A. Litvinenko, P. Sethi, C. Murapaka, et al. [Analog and Digital Phase Modulation and Signal Transmission with Spin-Torque Nano-Oscillators](#). *Physical Review Applied* 16 (2021).
- [5] Artem Litvinenko, Ahmed Sidi El Valli, Vadym Iurchuk, et al. [Ultrafast GHz-Range Swept-Tuned Spectrum Analyzer with 20 ns Temporal Resolution Based on a Spin-Torque Nano-Oscillator with a Uniformly Magnetized “Free” Layer](#). *Nano Letters* 22, 1874–1879 (2022).
- [6] Nhat-Tan Phan, Nitin Prasad, Abderrazak Hakam, et al. [Unbiased random bitstream generation using injection-locked spin-torque nano-oscillators](#). *Physical Review Applied* 21 (2024).
- [7] Dagur Ingi Albertsson, Mohammad Zahedinejad, Afshin Houshang, et al. [Ultrafast Ising Machines using spin torque nano-oscillators](#). *Applied Physics Letters* 118 (2021).
- [8] Nitin Prasad, Prashansa Mukim, Advait Madhavan, and Mark D Stiles. [Associative memories using complex-valued Hopfield networks based on spin-torque oscillator arrays](#). *Neuromorphic Computing and Engineering* 2, 034003 (2022).

Self-learning physical neural networks utilising superparamagnetic tunnel junctions

Jonathan Peters^{1,*} and Philippe Talatchian¹

¹Univ. Grenoble Alpes, CEA, CNRS, Grenoble INP, SPINTEC, Grenoble, France

*jonathan.peters@cea.fr

Deep neural networks have been responsible for the rise of artificial intelligence (AI) technologies in the modern era. However, network structures fail to map easily to conventional von Neumann computing architectures, which consist of separated units responsible for memory and processing. This separation causes drastic energy usage required for edge-AI applications, since vast quantities of data are shuffled between memory and processor, expending energy every time a computation requires memory access [1]. Neuromorphic computing architectures, inspired by the interconnectivity of the brain, avoid such issues since simple memory (synapse) and processing (neuron) units are intertwined. We focus on how such novel architectures could learn specific AI tasks, since the process of learning requires a significant amount of data shuffling and rewriting. Self-learning physical networks, which don't require separated units, promise to dramatically reduce the energy consumption of AI technology [2].

An increasing portion of recent research efforts investigates radically changing the computational architectures on which AI is performed. Such a paradigm shift to network-inspired architectures will require devices that can perform memory and processing capabilities at the nanoscale. This is because today's neural networks have a huge number of neurons and synapses (approaching $10^{11} - 10^{15}$). Emulating such large networks on a realistic-sized chip requires very small neurons and synapses.

Magnetic tunnel junctions (MTJs) are excellent CMOS-compatible nanoscale candidates for emulating both neurons and synapses in hardware [3]. Their non-volatile property, extensively used for memory applications, is a great opportunity to emulate low-energy non-volatile synapses. On the other hand, the same device, through trivial geometry variations or changing the applied field or current operating regimes, can emulate a large variety of neural dynamics such as oscillations, spikes, and stochastic switching.

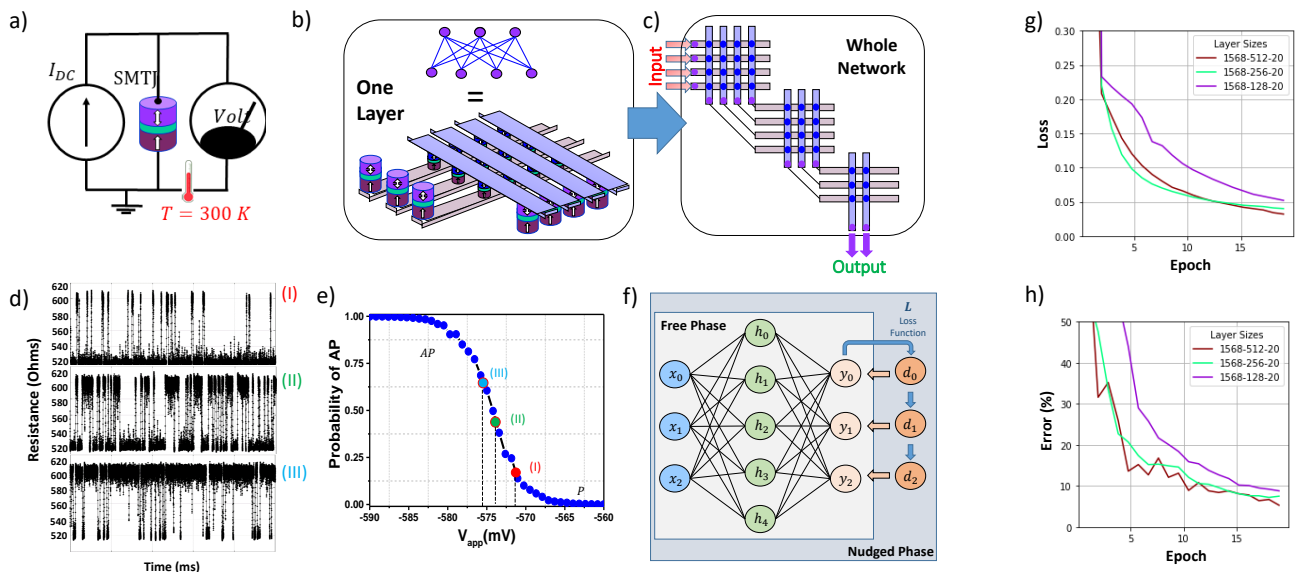


Figure 1: a) A single superparamagnetic tunnel junction (SMTJ), whose free layer magnetization switching probability can be changed through the voltage applied across the device. b) One layer of c) a multi-layer deep neural network of SMTJs (purple nodes). d) Example resistance fluctuation of an SMTJ. The voltages of the three depicted examples are labelled on e) showing the sigmoidal relation between the voltage across the SMTJ and the anti-parallel (AP) state probability. Adapted from [4]. f) Depiction of the two phases of learning through Equilibrium Propagation (EP). The second, or nudged, phase alters the network state from the previous free phase by comparing the current (y) and expected (d) network outputs. g) and h) show simulation results for the loss and testing error when training networks on the MNIST dataset. The layer sizes represent the size of the input, hidden, and output layers for our deep networks. Increasing the hidden layer improves our testing accuracies.

One important aspect of neural networks is the presence of non-linearities, allowing complex mappings of inputs to outputs. For physical MTJ-based networks, we propose to use superparamagnetic tunnel junctions (SMTJs) as non-linear processors at each network node. SMTJs can be seen as unstable MTJs where the energy barrier separating the two stable

configurations (P and AP) is sufficiently small, typically of the order of a few kT , where k is the Boltzmann constant, and $T = 300$ K is the room temperature. Such small energy barriers are sufficient for thermal fluctuations at room temperature to switch SMTJ's magnetization between the P and AP states in a stochastic manner, on a timescale ranging from a few ms to ns (see Figure 1) [5]. State switching probabilities can be deterministically biased by the voltage V (representing the network node value) across the device. The evolution of the corresponding probability with the applied voltage follows a sigmoid dependence for a sufficiently large number of taken statistics.

By construction, SMTJ-based networks we envision mimic the dynamics of a specific type of machine learning model, known as an energy-based model (EBM). EBMs are described by a scalar 'energy' function across the network. The gradient of this energy potential then determines the dynamics of the network over time. Minima of the energy function correspond to long-term network solutions. EBMs require the weight matrices between layers to be symmetric. Since electrical currents, described by Kirchhoff's laws, govern the information transferred through the physical networks, this condition is satisfied.

For local supervised learning compatible with EBMs, we propose to use the Equilibrium Propagation (EP) algorithm. EP describes how network parameters need to be changed for the model to learn successfully [6]. Figure 1 depicts EP visually. The benefit of EP compared to other learning algorithms, such as the popular backpropagation algorithm, is that the information required when updating the parameters can be accessed locally. This is in contrast to backpropagation, which requires global knowledge of the network and, therefore, large amounts of data shuffling every time a parameter is updated. Whilst EP was formulated for supervised learning on deterministic Hopfield-like networks, our physical implementation introduces stochasticity to the algorithm through SMTJs. The potential benefits of stochasticity within network activation functions has been previously shown [7].

In this work, we assess the capability of a physical SMTJ-based neural network to learn classification tasks by itself. We define self-learning to mean the capability of the network to learn how to change its parameters (weights and biases) to provide the correct input-to-output mapping for the task using local dynamics, without the need for external processing. We leave solving the task of updating the network parameters physically for future work.

Here, *in silico*, we show for the first time the ability of EP to reliably learn and update network parameters for a given task, when the system dynamics are noise-dependent. We demonstrate this on a realisable nanoscale physical network that utilises the spintronic technology of MTJs.

Our results, in Figure 1, show the ability of a physical network to learn the correct input-to-output mapping for the MNIST image recognition dataset. We show that the network weights converge over time up to a 96% recognition rate on MNIST. Excluding input nodes, which we define as constant input voltages, the network consists of three interconnected layers of SMTJs, respectively. We varied the size of the hidden layer during our investigation. The size of the hidden layer can alter the mapping accuracy by several percent, as seen in our results.

This work provides an opportunity to prove accurate mappings can still be achieved for more complex datasets, both using conventional network structures explored here, as well as more modern structures such as convolutional networks. Experimental demonstrations of networks composed of MTJs and SMTJs, working up to harder tasks such as those described here, are a further long-term research goal that we will actively tackle in future studies.

Acknowledgments

This work was supported by a public grant overseen by the French National Research Agency (ANR) as part of the 'PEPR IA France 2030' program (Emergences project ANR-23-PEIA-0002), and by NSF-ANR via grant StochNet Projet ANR-21-CE94-0002-01.

References

- [1] Sasha Luccioni, Yacine Jernite, and Emma Strubell. "Power hungry processing: Watts driving the cost of AI deployment?" *The 2024 ACM Conference on Fairness, Accountability, and Transparency*. 2024, 85–99.
- [2] Benjamin Scellier, Maxence Ernoult, Jack Kendall, and Suhas Kumar. Energy-based learning algorithms for analog computing: a comparative study. *Advances in Neural Information Processing Systems* 36 (2024).
- [3] Julie Grollier, Damien Querlioz, KY Camsari, et al. Neuromorphic spintronics. *Nature electronics* 3, 360–370 (2020).
- [4] Ahmed Sidi El Valli. "La détection des signaux radiofréquence et la génération des nombres aléatoires avec les jonctions tunnel magnétique perpendiculaire". PhD thesis. Université Grenoble Alpes, 2022.
- [5] L. Soumah, L. Desplat, N.-T. Phan, et al. [Nanosecond stochastic operation in perpendicular superparamagnetic tunnel junctions](#). *arXiv preprint arXiv:2402.03452* (2024).
- [6] Benjamin Scellier and Yoshua Bengio. Equilibrium propagation: Bridging the gap between energy-based models and backpropagation. *Frontiers in computational neuroscience* 11, 24 (2017).
- [7] Fabing Duan, François Chapeau-Blondeau, and Derek Abbott. Optimized injection of noise in activation functions to improve generalization of neural networks. *Chaos, Solitons & Fractals* 178, 114363 (2024).

TMD Engineering of 2D-Magnetic Tunnel Junctions – From Barriers to Electrodes

J. Daniel^{1,*}, F. Brunnett¹, S.M. -M. Dubois², H. Wei¹, J. Peiro¹, J. Perrin¹, S. Vergara¹, V. Zatzko¹, M. Galbiati¹, F. Godel¹, E. Carré¹, C. Carretero¹, A. Vecchiola¹, M. Och³, C. Mattevi³, F. Fossard⁴, J-S. Merot⁴, A. Loiseau⁴, J-C. Charlier², M-B. Martin¹, B. Dlubak¹, and P. Seneor¹

¹Laboratoire Albert Fert, Université Paris-Saclay, Palaiseau, France

²Institute of Condensed Matter and Nanosciences (IMCN), Belgium

³Imperial College - Department of Materials, United Kingdom

⁴Laboratoire d'Etude des Microstructures - ONERA, France

*jane.daniel@cnrs-thales.fr

Spintronics has revolutionized data storage, notably through the development of highly sensitive hard-drive read-heads based on Giant Magnetoresistance (GMR), and later Tunnel Magnetoresistance (TMR) technologies. These are at the core of Magnetic Tunnel Junctions (MTJs), nowadays composing the latest generation of ultra-fast and low power Magnetic Random Access Memories (MRAMs) and fueling post-CMOS unconventional electronics strategies (including spin logics, stochastic, neuromorphic and quantum computing). In this direction 2D materials [1], [2] have unleashed a multitude of previously unexploited possibilities for spintronic devices. As such, graphene has already demonstrated impressive performance, achieving record spin polarization of up to -98 % in a MTJ [3]. But more recently, a new class of materials, 2D ferromagnets, have emerged as particularly promising for spintronics, as they could pave the way to gate-controllable 2D magnetic tunnel junction (2D-MTJ) spin valve devices. However, a 2D ferromagnet efficiently working at room temperature remains a clear challenge. In this work, we focus on the development of room temperature 2D ferromagnets and their integration as electrode into 2D-MTJs. Specifically, we have engineered 2D ferromagnets based on Fe₄GeTe₂. To achieve this, we have recently developed novel in-situ processes based on large-scale pulsed laser deposition (PLD) techniques to allow the growth and heterostacking of different 2D materials [4], [5]. We will discuss how to reach one step further with the large-scale integration of these materials into tailored 2D heterostructures.

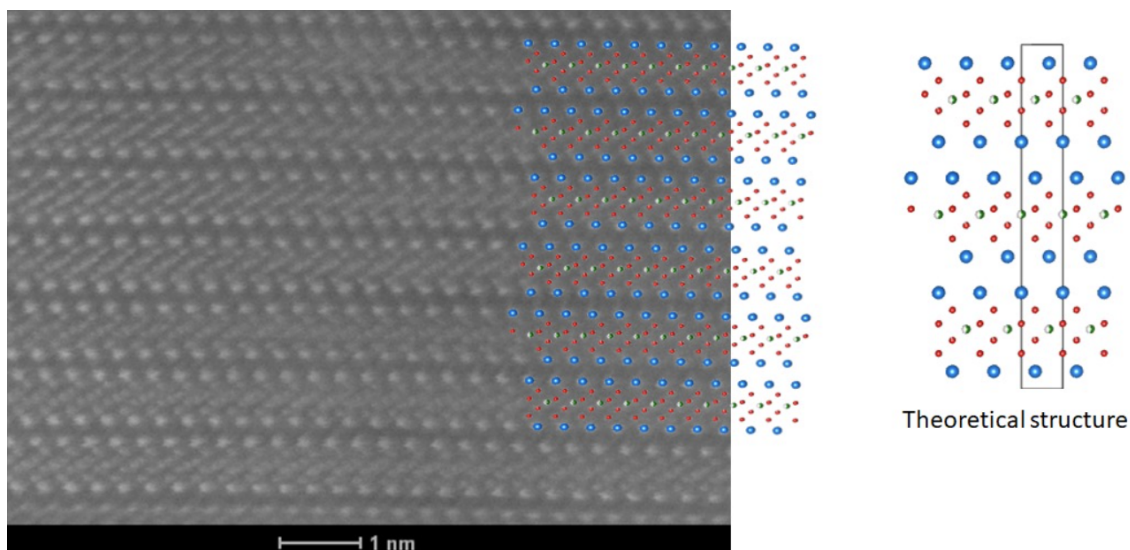


Figure 1: HAADF image of PLD-grown Fe₄GeTe₂ with simulated crystal structure.

References

- [1] Maëlis Piquemal, Regina Galceran, Marie-Blandine Martin, et al. [2D-MTJs: Introducing 2D materials in magnetic tunnel junctions](#). *Journal of Physics D: Applied Physics* 50, 203002 (2017).
- [2] Hyunsoo Yang, Sergio Valenzuela, Mairbek Chshiev, et al. [Two-dimensional materials prospects for non-volatile spintronic memories](#). *Nature* 606, 663–673 (2022).
- [3] Victor Zatzko, Simon M.-M. Dubois, Florian Godel, et al. [Almost Perfect Spin Filtering in Graphene-Based Magnetic Tunnel Junctions](#). *ACS Nano* 16, 14007–14016 (2022).
- [4] Victor Zatzko, Simon Mutien-Marie Dubois, Florian Godel, et al. [Band-Gap Landscape Engineering in Large-Scale 2D Semiconductor van der Waals Heterostructures](#). *ACS Nano* 15, 7279–7289 (2021).
- [5] Hao Wei, Simon Dubois, Frederic Brunnett, et al. [Large-Area Artificial van der Waals “Mille-Feuille” Superlattices](#). *Advanced Materials Interfaces* 11 (2024).

Deterministic modelling of ultrafast demagnetization in 3d ferromagnetic elements

Mouad Fattouhi^{1,*}, Pascal Thibaudeau², and Liliana D.Buda-Prejbeanu¹

¹Univ. Grenoble Alpes, CNRS, CEA, SPINTEC, F-38000, Grenoble, France

²CEA, DAM, Le Ripault, F-37260, Monts, France

*mouad.fattouhi@cea.fr

Controlling magnetization dynamics through light interactions has become a major focus of research, attracting extensive attention from both theoretical and experimental perspectives. This interest stems from its promising potential to enable new, energy-efficient paradigms for spintronic applications. Modeling the interaction between light and magnetization is commonly achieved using stochastic Landau-Lifshitz-Gilbert (sLLG) equation coupled with two- or three-temperature models (2TM/3TM) [1]. This approach involves solving the sLLG equation alongside the 2TM/3TM for multiple realizations, then obtaining the final result by averaging over these realizations. While this method provides reliable results, it is computationally intensive and less efficient in terms of processing time.

Here, we study the ultrafast demagnetization of 3d ferromagnetic materials (Nickel, Iron, and Cobalt) using deterministic atomistic spin dynamics (ASD) and femtosecond laser heating. This method involves solving the dynamical Landau-Lifshitz-Bloch (dLLB) equation for each spin in a multi-spin system [2, 3].

Initially, the Curie temperature T_C of these ferromagnets is determined using dLLB equation with a classical fluctuation dissipation relation (CFDR) [1], which overestimates T_C due to the mean-field approximation (MFA) of the exchange interaction as can be observed from Fig.1(a) (red symbols). To correct this, a linear adjustment to the MFA exchange constant is applied, mimicking second-order fluctuations. We find that dLLB with CFDR does not accurately capture the magnetization behavior at lower temperatures [4, 5]. This issue was addressed by using information from the magnon band structure, which can be measured experimentally or computed, to better model energy transfers [6]. This approach employs a quantum fluctuation dissipation relation (QFDR) based on Bose-Einstein statistics instead of the Maxwell-Boltzmann statistics used in CFDR.

By simulating the ultrafast demagnetization of Ni, Fe, and Co with femtosecond laser heating using dLLB and QFDR, the energy exchange between different reservoirs is accurately modeled, and we find that the results match the experimental data, which can be seen from Fig.1(b). This demonstrates that dLLB equation can efficiently model all-optical switching mechanisms, avoiding the need for multiple statistical realizations required in methods based on the stochastic Landau-Lifshitz-Gilbert equation [5].

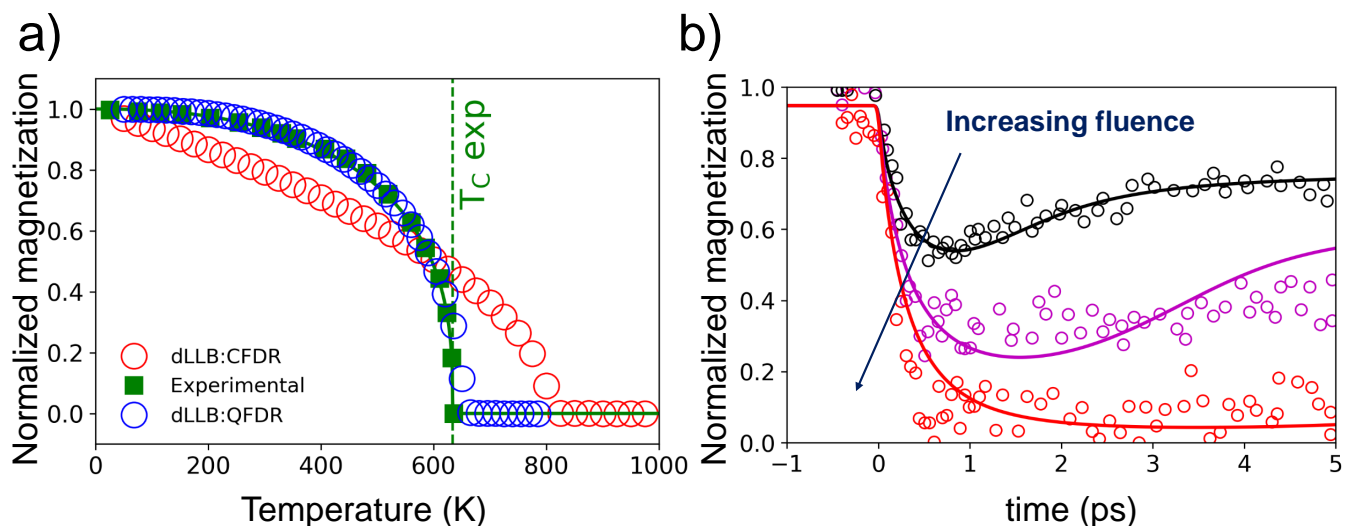


Figure 1: a) Magnetization versus temperature curve of Nickel computed from dLLB with both CFDR and QFDR compared to experimental data from [7]. b) Laser induced ultrafast demagnetization of Nickel. Experimental data are adapted from [8].

In conclusion, deterministic atomistic spin simulations based on the dynamic Landau-Lifshitz-Bloch equation have proven to be highly efficient tools for modeling thermal effects in spintronics. These equation is powerful enough to effectively simulate not just simple, but also complex structures and realistic devices, such as those based on Tb/Co which are often used in advanced all-optical switching schemes [9].

Acknowledgments

This work is supported partly by France 2030 government investment plan managed by the French National Research Agency under grant reference PEPR SPIN – [SPINTHEORY] ANR- 22-EXSP-0009, and CEA Exploratory Program, Bottom-Up 2023 ref.59 [THERMOSPIN].

References

- [1] Richard Francis Llewelyn Evans, Unai Atxitia, and Roy W Chantrell. Quantitative simulation of temperature-dependent magnetization dynamics and equilibrium properties of elemental ferromagnets. *Physical Review B* 91, 144425 (2015).
- [2] Julien Tranchida, Pascal Thibaudeau, and Stam Nicolis. Colored-noise magnetization dynamics: from weakly to strongly correlated noise. *IEEE Transactions on Magnetics* 52, 1–4 (2016).
- [3] Julien Tranchida, Pascal Thibaudeau, and Stam Nicolis. Hierarchies of Landau-Lifshitz-Bloch equations for nanomagnets: A functional integral framework. *Physical Review E* 98, 042101 (2018).
- [4] MD Kuz'min. Shape of Temperature Dependence of Spontaneous Magnetization of Ferromagnets: Quantitative Analysis. *Physical review letters* 94, 107204 (2005).
- [5] Olle Eriksson, Anders Bergman, Lars Bergqvist, and Johan Hellsvik. *Atomistic spin dynamics: foundations and applications*. Oxford university press, 2017.
- [6] ED Thompson and JJ Myers. Magnon Energy of Nickel. *Physical Review* 153, 574 (1967).
- [7] J Crangle and GM Goodman. The magnetization of pure iron and nickel. *Proceedings of the Royal Society of London. A. Mathematical and Physical Sciences* 321, 477–491 (1971).
- [8] B Koopmans, Grégory Malinowski, F Dalla Longa, et al. Explaining the paradoxical diversity of ultrafast laser-induced demagnetization. *Nature materials* 9, 259–265 (2010).
- [9] D Salomoni, Y Peng, L Farcis, et al. Field-free all-optical switching and electrical readout of Tb/Co-based magnetic tunnel junctions. *Physical Review Applied* 20, 034070 (2023).

Magnetic properties of epitaxial Mn_4N films doped with non-magnetic elements

Tomohiro Yasuda^{1,2,*}, Rodrigo Guedas¹, Ilaria Di Manici¹, Gilles Gaudin¹, Takashi Suemasu², Stefania Pizzini³, and Olivier Boule¹

¹Spintec, Université Grenoble Alpes, CEA, CNRS, Grenoble, France

²University of Tsukuba, Tsukuba, Japan

³Institut Néel, Université Grenoble Alpes, CNRS, Grenoble, France

*ytrp108@gmail.com

Anti-perovskite Mn_4N is a ferrimagnet with a perpendicular magnetic anisotropy (magnetic anisotropy constant: $K_u \sim 0.1 \text{ MJ m}^{-3}$) and a small saturation magnetization ($M_s \sim 80 \text{ kA m}^{-1}$)[1]. In addition, Mn_4N films exhibit magnetic compensation (MC) composition if Mn atoms are replaced by other elements [2], allowing faster magnetization dynamics. For example, STT-driven DW motion of $v_{DW} \sim 3 \text{ km s}^{-1}$ was demonstrated in $\text{Mn}_{4-x}\text{Ni}_x\text{N}$ tracks at room temperature (RT)[3]. To achieve faster and more efficient magnetization control, we fabricated new materials by doping Mn_4N films with other non-magnetic elements, and investigated their magnetic properties. 10-nm-thick $\text{Mn}_{4-x}\text{Z}_x\text{N}$ ($Z = \text{Cu, Ag or Au}$) films were formed on $\text{SrTiO}_3(001)$ substrates by molecular beam epitaxy. The substrate temperature was set at $450 \text{ }^\circ\text{C}$ during deposition. All samples were capped with 3-nm-thick SiO_2 to prevent oxidation. The crystalline quality was evaluated by reflection high-energy electron diffraction (RHEED) along the $\text{SrTiO}_3[100]$ azimuth and by $2\theta/\omega$ X-ray diffraction (XRD). The magnetization curves were obtained by using a vibrating sample magnetometer (VSM).

Figures 1(a) and 1(b) show $2\theta/\omega$ XRD profiles and the RHEED images of samples with a composition of $x = 0.3$, respectively. Peaks and fringes around the SrTiO_3 002 reflection originate from $\text{Mn}_{4-x}\text{Z}_x\text{N}$ crystals. Streaky patterns in the RHEED images suggest that the crystals are also oriented in-plane. Similar results were obtained for $x \leq 0.3$. This demonstrates the epitaxial growth of these samples. Figures 1(c) and 1(d) show the composition dependence of the saturation magnetizations M_s and the coercive fields $\mu_0 H_c$ measured by VSM at RT. Regardless of the dopant, the presence of a minimum M_s and a maximum $\mu_0 H_c$ was confirmed. The composition corresponding to this M_s close to 0 and this $\mu_0 H_c$ maximum corresponds to the MC point. Other profiles will be detailed during our presentation. To study the current-induced domain wall motion, we patterned the samples into tracks contacted to metallic electrodes using a standard nanofabrication process. Results of the current-induced domain wall dynamics for various doping compositions will be presented.

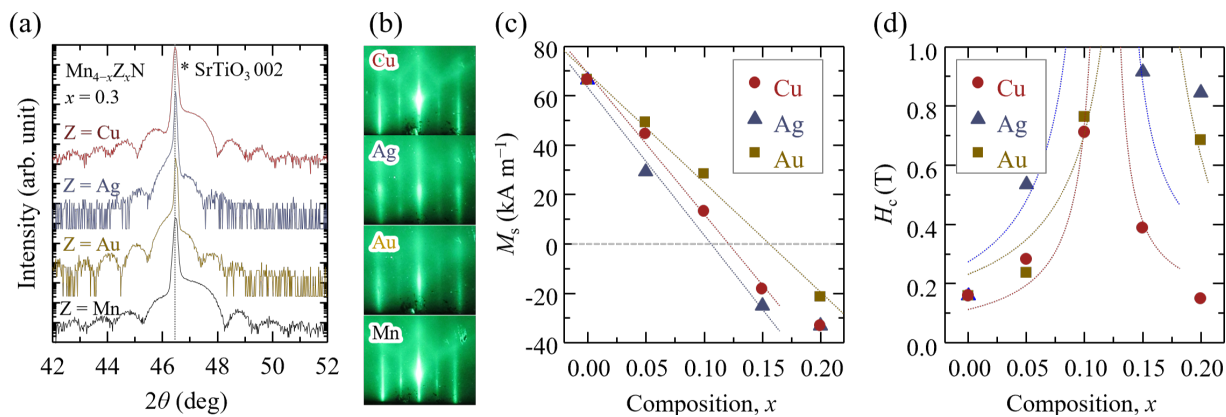


Figure 1: (a) $2\theta/\omega$ XRD profiles and (b) RHEED images of $\text{Mn}_{4-x}\text{Z}_x\text{N}$ ($Z = \text{Cu, Ag or Au}$) films with $x = 0.3$. (c) Saturation magnetization M_s and coercive fields $\mu_0 H_c$. Dotted lines show the fitted profiles around MC compositions.

References

- [1] Takashi Suemasu, Laurent Vila, and Jean-Philippe Attané. [Present Status of Rare-earth Free Ferrimagnet \$\text{Mn}_4\text{N}\$ and Future Prospects of \$\text{Mn}_4\text{N}\$ -based Compensated Ferrimagnets](#). *Journal of the Physical Society of Japan* 90, 081010 (2021).
- [2] Yi Zhang, Yi Deng, Yinan Lin, et al. [Oscillator-Network-Based Ising Machine](#). *Micromachines* 13, 1016 (2022).
- [3] Sambit Ghosh, Taro Komori, Ali Hallal, et al. [Current-Driven Domain Wall Dynamics in Ferrimagnetic Nickel-Doped \$\text{Mn}_4\text{N}\$ Films: Very Large Domain Wall Velocities and Reversal of Motion Direction across the Magnetic Compensation Point](#). *Nano Letters* 21, 2580–2587 (2021).

Effets d'épaisseur et de température sur les propriétés magnétiques des systèmes à base de Ir/FeV

W.A Fotso Sindze^{1,*}, D.Ourdani¹, Y. Roussigné¹, S. M. Chérif¹, M. S. Gabor², and M. Belmeguenai¹

¹Université Sorbonne Paris Nord, LSPM, CNRS, UPR 3407, F-93430 Villetaneuse, FRANCE.

²Center for Superconductivity, Spintronics and Surface Science, Physics and Chemistry Department, Technical University of Cluj-Napoca, Str. Memorandumului No. 28 RO-400114 Cluj-Napoca, ROMANIA

*wilfried.fotso@lspm.cnrs.fr

Afin d'obtenir des dispositifs spintroniques plus rapides, plus denses et plus efficaces avec une consommation d'énergie réduite, les propriétés des matériaux magnétiques doivent être bien définies et ajustées en fonction de l'application souhaitée. L'amortissement magnétique α , qui est l'un des paramètres les plus critiques des matériaux, joue un rôle important dans de nombreuses applications spintroniques, car il affecte fortement l'énergie requise et la vitesse à laquelle un dispositif spintronique peut fonctionner. Par conséquent, les matériaux magnétiques ayant à la fois un faible amortissement et une faible aimantation à saturation (M_s) sont fortement souhaitables pour un fonctionnement économe en énergie. En effet, la densité de courant critique pour écrire dans une cellule de mémoire magnétique à accès aléatoire à base du couple de transfert de spin est proportionnelle à la fois à M_s et à α [1]. D'autres parts, une M_s modérée produit un champ de fuite réduit, ce qui permet d'obtenir des structures plus denses car le couplage entre les bits est faible. L'utilisation des alliages de fer-vanadium (FeV) permet d'obtenir des valeurs d'amortissement plus faibles. En effet, il a été rapporté que le FeV est l'un des meilleurs candidats pour une réduction efficace de l'aimantation à saturation, ainsi qu'une diminution de l'amortissement [2]. En outre, les systèmes composés d'une interface matériau ferromagnétique/ métal lourd sont extrêmement importants pour la spintronique. Cette interface est à l'origine de nombreux phénomènes tels que le pompage de spin et l'effet Hall de spin (SHE) [3], qui peuvent être utilisés pour la commutation de l'aimantation par l'intermédiaire du couple de spin orbite, et l'interaction Dzyaloshinskii-Moriya d'interface (iDMI) [4], donnant lieu à de nouvelles configurations magnétiques telles que les skyrmions. L'objectif de ce travail est donc d'étudier l'amortissement, l'anisotropie magnétique perpendiculaire (PMA) et l'iDMI dans les systèmes à base d'Ir/FeV. L'idée est de contrôler leur intensité en optimisant la qualité de l'interface par la variation de l'épaisseur du FeV, l'utilisation de différentes couches de recouvrement (Cu et MgO) et en variant la température de mesure.

Afin de mener cette étude à terme, des mesures par diffusion Brillouin de la lumière (BLS) et par résonance ferromagnétiques (FMR), complétées par des mesures statiques de l'aimantation par magnétométrie à échantillon vibrant (VSM) ont été faites. Les mesures par VSM ont révélé des valeurs similaires de M_s et de l'épaisseur de la couche morte (t_d) pour les échantillons recouverts de Cu et de MgO ($M_s = 1100 \pm 20 \text{ kA/m}$ et $t_d = 0.39 \pm 0.04 \text{ nm}$). Cette couche morte magnétique pourrait être due à l'oxydation du FeV pendant le dépôt de la couche de MgO et à l'interdiffusion aux interfaces Ir/FeV et FeV/Cu. Cependant, la valeur similaire de t_d pour les deux systèmes suggère une oxydation ou une interdiffusion négligeable aux interfaces FeV/MgO et Fe/Cu, confirmant l'immiscibilité du Fe et du Cu. La valeur M_s est nettement inférieure à celle du Fe pur (1700 kA/m) et du Co en massif : 1422 kA/m pour le Co hcp et 1450 kA/m pour le Co fcc, ce qui renforce l'intérêt du FeV pour les dispositifs basés sur le couple de transfert de spin. L'analyse des mesures BLS et FMR révèle l'existence d'une anisotropie magnétique uniaxiale perpendiculaire d'interface qui montre une légère dépendance de la couche de recouvrement mais il est difficile de déterminer avec précision l'interface induisant une telle PMA puisque les deux interfaces FeV/Cu et FeV/MgO pourraient contribuer à cette anisotropie en plus de l'interface Ir/FeV. Toutefois, on peut s'attendre à ce que la contribution de l'interface supérieure avec FeV dans les deux systèmes soit négligeable, en particulier celle de FeV/MgO où les liaisons Fe-O, qui sont une source de PMA d'interface, sont censées se produire. Cela suggère que V pourrait réduire de manière significative les liaisons Fe-O à l'interface FeV/MgO, empêchant ainsi toute contribution à la PMA. Cette hypothèse pourrait être élucidée en étudiant les systèmes Cu/FeV/Cu. En revanche, la constante PMA du second ordre, qui pourrait résulter de la distribution inhomogène et des fluctuations spatiales à l'échelle nanométrique de la PMA uniaxiale à l'interface, est significativement plus forte pour le système Ir/FeV/Cu.

Les mesures FMR de la largeur de raie sous champ magnétique appliqué dans le plan et perpendiculairement ont permis de conclure à une constante d'amortissement de Gilbert relativement faible de FeV ($\alpha_{FeV} = 1,7 \cdot 10^{-2}$) et d'identifier les inhomogénéités et les contributions de la diffusion de deux magnons. Alors que la largeur de raie à fréquence nulle (ΔH_0) dans le plan résulte principalement de la diffusion de deux magnons pour les deux systèmes, ΔH_0 dans la configuration perpendiculaire est due à des inhomogénéités interfaciales. Une augmentation significative de l'amortissement a été observée et attribuée au pompage de spin à l'interface Ir/FeV. Nous avons également étudié l'iDMI dans les deux systèmes, qui peut être déterminée par l'investigation du décalage de fréquence entre les fréquences des ondes de spin correspondant aux lignes Stokes et anti-Stokes. La dépendance en épaisseur de la constante effective de l'iDMI a été mesurée et a permis de séparer les contributions des différentes interfaces. Nos résultats montrent que les interfaces Ir/FeV et FeV/MgO induisent une faible iDMI de signe opposé conduisant à une contribution supplémentaire à l'iDMI totale.

La dépendance de ces propriétés magnétiques par rapport à la température constitue un moyen efficace d'étudier leurs relations et pourrait être utilisée pour mieux comprendre leurs origines physiques. Par conséquent, l'effet de la mesure de la température sur le PMA et l'amortissement de ces deux systèmes a été étudié in situ à l'aide d'un système, intégré dans un dispositif de résonance ferromagnétique. À cette fin, la température a été variée de la température ambiante à 250°C et les spectres FMR sous un champ magnétique appliqué dans le plan ont été enregistrés. Pour chaque température, le chauffage, l'équilibre thermique et l'acquisition de spectre durent approximativement 2h et les dépendances en épaisseur de l'aimantation effective et du coefficient d'amortissement ont été utilisées pour déterminer les constantes de PMA et la conductance par mixage de spin, représentées sur la figure 1 en fonction de la température. Comme notre VSM ne permet pas d'effectuer des mesures en fonction de la température, les mesures VSM ont été menées seulement sur les échantillons n'ayant subi aucun chauffage et sur ceux qui ont été soumis à un cycle de chauffage complet (variation de la température de mesure de l'ambiante à 250°C). Le moment magnétique de saturation par unité de surface est ensuite déterminé et utilisé pour obtenir M_s et t_d pour chaque système. Les valeurs de M_s et t_d avant chauffage ont été utilisées pour analyser les données en fonction de la température. Les dépendances de la température ont révélé une augmentation des constantes PMA de volume (K_v) et d'interface (K_s) et la conductance par mixage de spin ($g_{eff}^{\uparrow\downarrow}$) et une diminution de l'amortissement intrinsèque (α_0) et avec l'augmentation de la température comme le montre la figure 1.

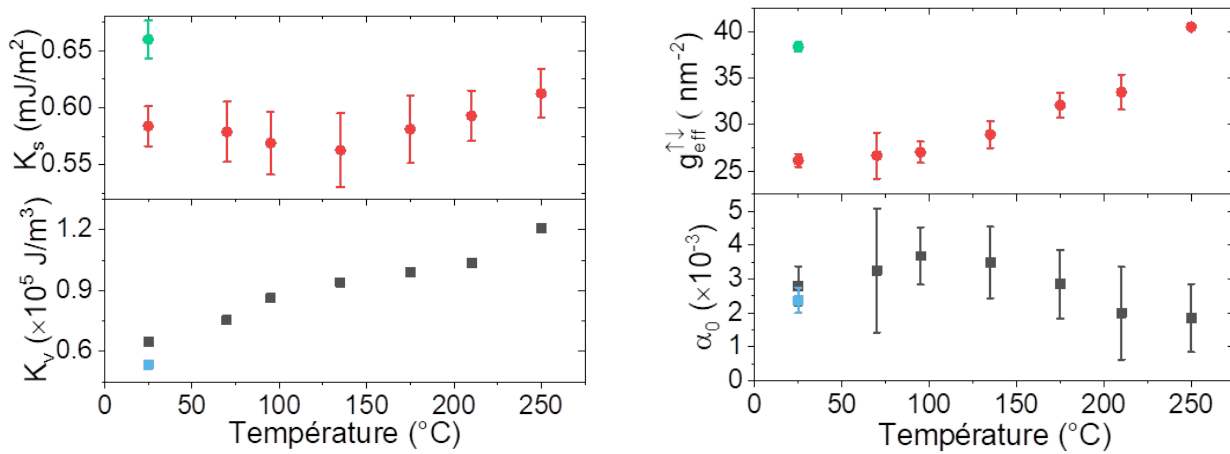


Figure 1: Dépendance en température de mesure des constantes d'anisotropie perpendiculaire de volume (K_v) et de surface (K_s), de l'amortissement intrinsèque (α_0) et la conductance par mixage de spin ($g_{eff}^{\uparrow\downarrow}$) pour systèmes à base de Ir/FeV/MgO. Les symboles bleus et verts représentent les valeurs obtenues après un cycle complet de mesure en température.

References

- [1] Stuart S. P. Parkin, Masamitsu Hayashi, and Luc Thomas. [Magnetic Domain-Wall Racetrack Memory](#). *Science* 320, 190–194 (2008).
- [2] Jairo Sinova, Sergio O. Valenzuela, J. Wunderlich, C. H. Back, and T. Jungwirth. [Spin Hall effects](#). *Rev. Mod. Phys.* 87, 1213–1260 (2015).
- [3] A. Crépieux and C. Lacroix. [Dzyaloshinsky–Moriya interactions induced by symmetry breaking at a surface](#). *J. Magn. Mater.* 182, 341–349 (1998).
- [4] Huanglin Yang, Shuai Hu, Meng Tang, et al. [Spin–orbit torque and Dzyaloshinskii–Moriya interaction in perpendicularly magnetized heterostructures with iridium](#). *Appl. Phys. Lett.* 118, 062409 (2021).

Growth and Characterisation of the Non-Collinear Antiferromagnet Mn_3Sn

Elias Abboubi^{1,*}, Gwenael Acheson¹, Jérôme Faure-Vincent¹, Olivier Boulle¹, and Vincent Baltz¹

¹Univ. Grenoble Alpes, CNRS, CEA, SPINTEC, 38054 Grenoble, France

*elias.abboubi@cea.fr

Antiferromagnets (AF) have been capturing interest in spintronics over the last decades due to their fast dynamics and their vanishing stray field, compared to ferromagnets (F), paving the way for low-power and fast devices [1]. Using AFs for practical applications remains challenging due to their vanishing magnetization, making it difficult to detect the magnetic order from electrical or optical signals. Among non-collinear antiferromagnets (NCAF), there is a specific subclass that breaks time-reversal symmetry [2], leading to observable effects typically associated with F (e.g., the anomalous Hall effect (AHE) [3] or magneto-optical Kerr effect [4]), despite having zero net magnetization. This class of materials combines the advantages of both AF and F making them suitable for use as spin-active layers in devices. A long-term objective is to stabilize spin textures in NCAF and control them by current to use them as information carriers. Therefore, the growth of pure NCAF is crucial. Here, a method for the growth of polycrystalline Mn_3Sn , a triangular NCAF material (Fig. 1), and various ways of characterising the material are presented.

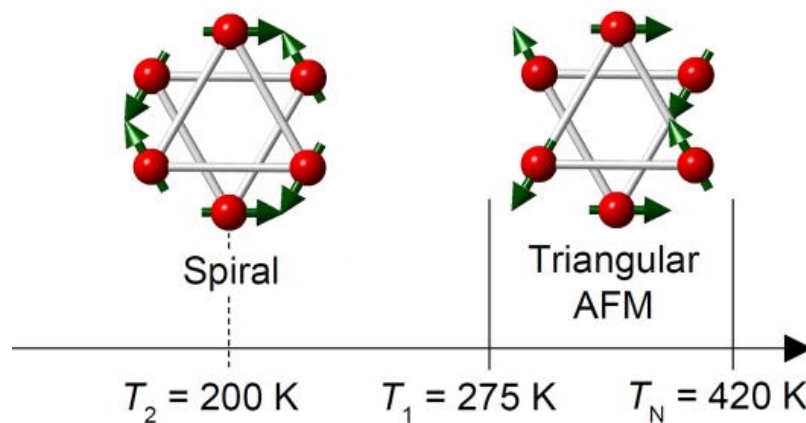


Figure 1: Crystal and spin structure of Mn_3Sn , showing the triangular NCAF configuration above 275 K and the helical arrangement below 275 K. Adapted from [5] with permission from AIP.

Mn_3Sn has been deposited on a SiO_2 substrate via magnetron co-sputtering. To improve the crystal quality, it is expected that annealing the samples will favor the diffusion and organization of atoms into an ordered state. Annealed and non-annealed samples were then compared. To characterize the material, a diffractometer working with Co X-ray tubes was used. To study the electronic properties, a physical property measurement system was used to analyse the transport properties of the material under various magnetic fields and temperatures. In particular, the field dependence of the transversal resistivity allows us to recover the AHE.

X-rays data (Fig. 2) show that annealing favors the formation of a crystalline phase. The obtained diffractogram demonstrates that some peaks match properly with Mn_3Sn , but not all of them, making it clear that there are crystalline impurities composed of other materials, likely Mn_2Sn or Mn_3Sn_2 . The evolution of the transversal resistivity under a magnetic loop shows a non-zero Hall effect even at zero magnetic excitation (Fig. 3), indicating a F or a symmetry-breaking AF phase after annealing, while it was linear before, confirming the role of annealing. A way to ensure that the grown material is Mn_3Sn is to study the magnetic phase transition at 275 K. Below this temperature, it adopts a helical spin configuration (Fig. 1) where symmetries do not allow for AHE [5]. It was confirmed that there is a drop in AHE, showing the prominence of a Mn_3Sn phase, but it does not reach zero, indicating that the crystalline impurities are probably F materials such as Mn_2Sn or Mn_3Sn_2 . To get a pure NCAF crystal, studies on stoichiometric control during the deposition need to be done.

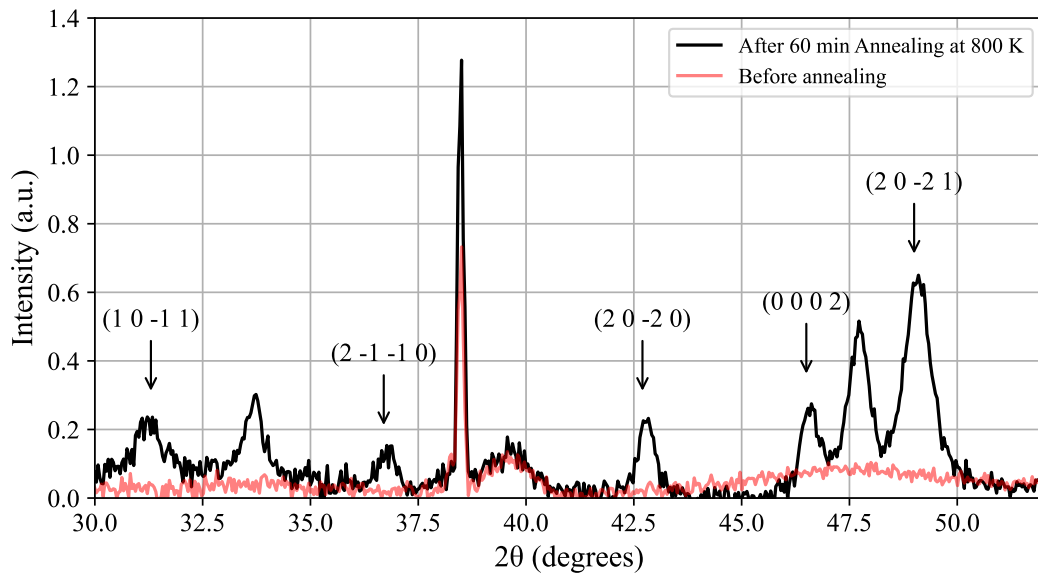


Figure 2: X-ray diffractograms at 300 K, comparing annealed (black) and non-annealed (red) Mn_3Sn films grown by co-sputtering. The peaks corresponding to the crystal planes of Mn_3Sn are indicated. The other peaks are likely to be attributed to Mn_2Sn or Mn_3Sn_2 phases.

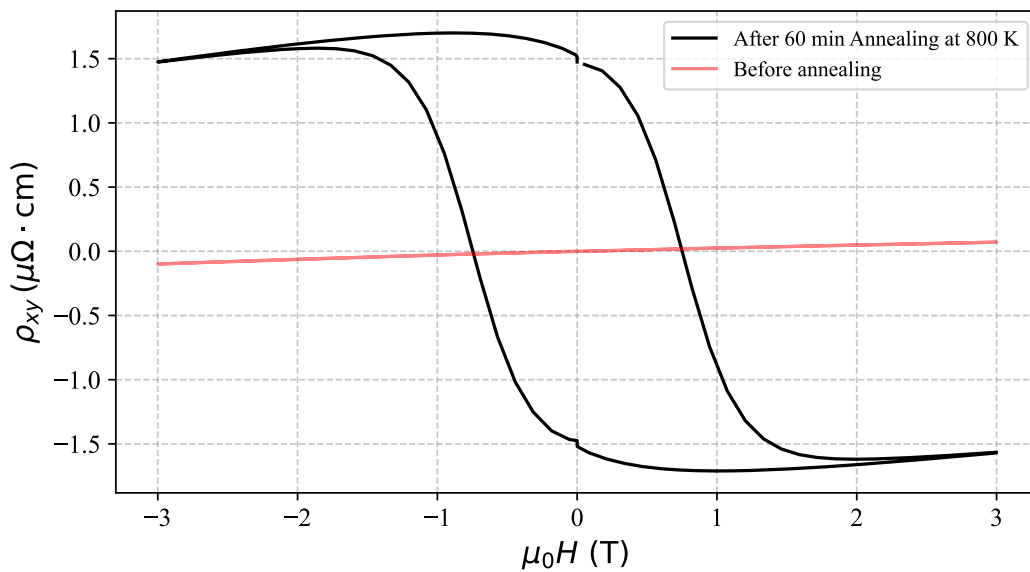


Figure 3: Transversal resistivity of Mn_3Sn films (annealed vs. non-annealed) as a function of magnetic field, at 300 K.

References

- [1] V. Baltz, A. Manchon, M. Tsoi, et al. [Antiferromagnetic spintronics](#). *Rev. Mod. Phys.* 90, 015005 (2018).
- [2] B. H. Rimmler, B. Pal, and S. P. Parkin. [Non-collinear antiferromagnetic spintronics](#). *Nature Reviews Materials* (2024).
- [3] T. Higo and S. Nakatsuji. [Thin film properties of the non-collinear Weyl antiferromagnet \$\text{Mn}_3\text{Sn}\$](#) . *Journal of Magnetism and Magnetic Materials* 564, 170176 (2022).
- [4] T. Higo, H. Man, D. B. Gopman, et al. [Large magneto-optical Kerr effect and imaging of magnetic octupole domains in an antiferromagnetic metal](#). *Nature Photonics* 12 (2018).
- [5] N. H. Sung, F. Ronning, J. D. Thompson, and E. D. Bauer. [Magnetic phase dependence of the anomalous Hall effect in \$\text{Mn}_3\text{Sn}\$ single crystals](#). *Applied Physics Letters* 112, 132406 (2018).

All-inductive observation of linear dynamics and nonlinear processes of spin waves in synthetic antiferromagnets

A. Mouhoub^{1,*}, C. Chappert¹, J.-V. Kim¹, A. Solignac², and T. Devolder¹

¹Université Paris-Saclay, CNRS, Centre de Nanosciences et de Nanotechnologies, 91120 Palaiseau, France

²SPEC, CEA, CNRS, Université Paris-Saclay, 91191 Gif-sur-Yvette, France

*asma.mouhoub@universite-paris-saclay.fr

Spin waves are the eigen-excitations of magnetic materials. They exhibit specific properties such as nonlinearity [1, 2]. This property makes them potentially suitable for applications in neuromorphic computing and magnonic logic devices [3]. Synthetic antiferromagnets (SAFs), composed of two ferromagnetic layers separated by a non-magnetic layer that favors antiparallel magnetizations, are particularly effective for studying the nonlinearity of spin waves [4]. A comprehensive understanding of the magnetic properties of SAFs is essential before exploring their nonlinear properties.

The interlayer coupling is a degree of freedom that confers a large tunability to SAFs, which allows their customization in several spintronics applications. The efficient use of this magnetic configuration requires an in-depth understanding of the magnetic properties and their correlation with the material structure. We established a reliable procedure to quantify the interlayer exchange coupling and the intralayer exchange stiffness in SAF. We applied this procedure to the ultrasmooth and amorphous $\text{Co}_{40}\text{Fe}_{40}\text{B}_{20}$ (t_{mag})/Ru (0.7 nm)/CoFeB (t_{mag}) structure [5]. The complex interplay between the two exchange interactions results in a gradient of the magnetization orientation across the thickness of the stack, which alters the hysteresis and the spin wave eigenmodes of the stack in a nontrivial way. We measured the frequency-field dependence of the first four spin waves confined within the thickness of the stack. We modeled these frequencies and the corresponding thickness profiles of these spin waves using micromagnetic simulations. The comparison with the experimental results allows us to deduce the magnetic parameters that best account for the sample behavior. The exchange stiffness is $A_{\text{ex}} = 16 \pm 2$ pJ/m, independent of the film thickness. The interlayer exchange coupling starts from -1.7 mJ/m² for the thinnest layers and it can be maintained above -1.3 mJ/m² for CoFeB layers that are as thick as 40 nm.

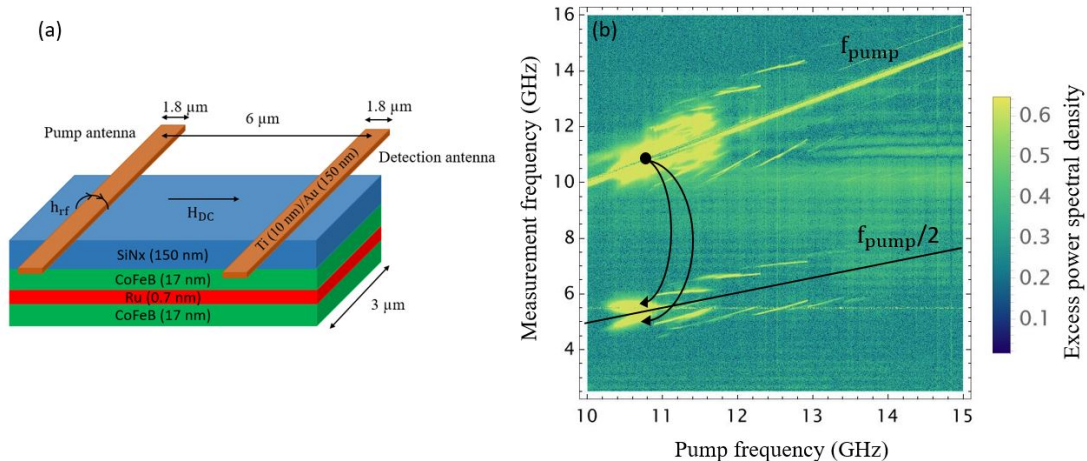


Figure 1: a) Scheme of the experimental configuration. In practice, 4 well separated $\text{Co}_{40}\text{Fe}_{40}\text{B}_{20}$ microstrips are positioned under the antennas to improve the signal-to-noise ratio. b) Spectra of excess power spectral density versus pump frequency at excitation power arriving at the sample 11 dBm and $H_{\text{DC}}=20$ mT, for a SAF with 2×17 nm of CoFeB.

Frequency-field dependence allows the identification of conditions that exhibit nonlinear interactions. For specific configurations of the applied static magnetic field H_{DC} the frequency of the acoustic magnon mode (f_{ac}) becomes half of the optical magnon mode frequency (f_{op}), a favorable condition to investigate nonlinear phenomena in SAF.

We developed an experimental setup shown in Fig 1.a that is based on propagating spin wave spectroscopy. We investigated the nonlinear processes inductively by varying the applied field H_{DC} , the pumping frequency and the microwave power arriving at the sample. Two phenomena are observed (see Fig 1.b): the doublets near $f_{\text{pump}}/2$ evidence a three-magnon process where one optical magnon at f_{pump} split into two acoustic magnons at $f_{\text{pump}}/2 - \delta$ and $f_{\text{pump}}/2 + \delta$. 2). A strong halo around f_{pump} could be a four-magnon scattering process, in which two optical magnons at f_{pump} annihilate and create two new optical magnons.

We focused on the three-magnon splitting process on a device patterned by optical lithography, featuring a $1.8 \mu\text{m}$ wide single-wire antenna. We showed that the population of the created magnons varies exponentially with the amplitude of the rf excitations above a certain threshold, which is 1.8 mT. Furthermore, to explore the dynamics of magnon creation, we

apply rf pulses with various durations. We developed an analytical model that we compared to the experiment to effectively determine the growth rate of the population of the acoustic mode.

To investigate spin waves in confined nanometric geometries, we fabricated new devices using electron beam lithography that feature 100 nm and 150 nm wide U-shaped antennas on top of magnetic conduits. This enables the excitation over a large range of wavevectors $\Delta k = 10 \text{ rad}/\mu\text{m}$ corresponding to a frequency interval of $\Delta f = 4.13 \text{ GHz}$ as shown in Fig 2. In contrast to the $1.8 \mu\text{m}$ wide antenna, which excites a narrower range of wavevectors $\Delta k = 2 \text{ rad}/\mu\text{m}$ corresponding to $\Delta f = 0.64 \text{ GHz}$.

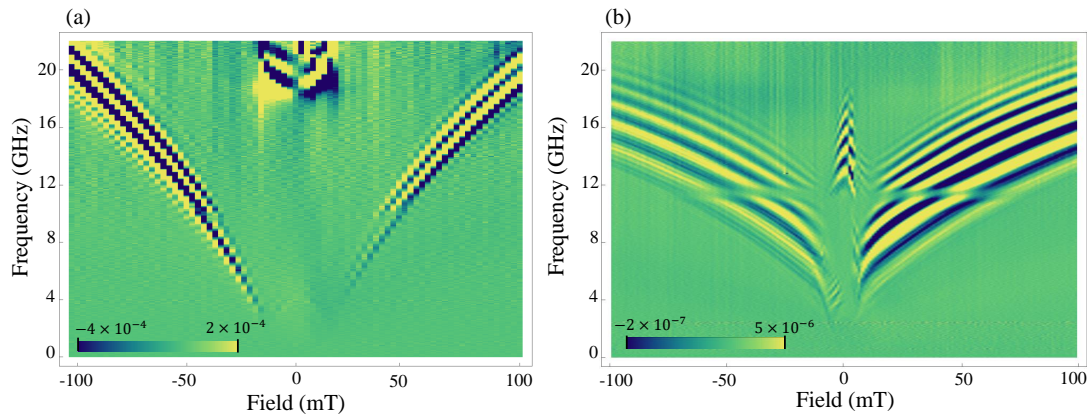


Figure 2: The field-derivative of the microwave transmission S21 between two stripelines for a $5 \mu\text{m}$ magnetic bus. a) A SAF with 17 nm of CoFeB and a $1.8 \mu\text{m}$ wide antenna on top. b) A SAF with 22 nm of CoFeB and a 150 nm wide antenna on top.

Acknowledgments

We acknowledge financial support from the EOBE doctoral school of Paris-Saclay University. This work was done within the C2N micro nanotechnologies platforms and partly supported by the RENATECH network and the General Council of Essonne.

References

- [1] Roman Verba, Lukas Körber, Katrin Schultheiss, et al. Theory of three-magnon interaction in a vortex-state magnetic nanodot. *Physical Review B* 103, 014413 (2021).
- [2] H Schultheiss, K Vogt, and B Hillebrands. Direct observation of nonlinear four-magnon scattering in spin-wave microconduits. *Physical Review B* 86, 054414 (2012).
- [3] Lukas Körber, Christopher Heins, Tobias Hula, et al. Pattern recognition in reciprocal space with a magnon-scattering reservoir. *Nature Communications* 14, 3954 (2023).
- [4] A Kamimaki, S Iihama, KZ Suzuki, Natsuhiko Yoshinaga, and S Mizukami. Parametric amplification of magnons in synthetic antiferromagnets. *Physical Review Applied* 13, 044036 (2020).
- [5] A Mouhoub, J-V Kim, J Létang, and A Solignac. Exchange energies in CoFeB/Ru/CoFeB synthetic antiferromagnets. *Physical Review Materials* 7, 044404 (2023).

Electric field effects on the spin/orbital conversion into charge

André Grailhon^{1,*}, Jean-Yves Chauleau¹, and Michel Viret¹

¹*SPEC, CEA, CNRS, Université Paris-Saclay, 91191 Gif-sur-Yvette, France*

**andre.grailhon@cea.fr*

The Rashba interaction is an effective spin-orbit interaction (SOI) linear in momentum that can lead to the conversion of a spin density into a charge current, also known as the spin galvanic effect [1]. One of the most interesting aspects of Rashba SOI is its tunability by a gate voltage which has been demonstrated in Rashba systems such as the 2D electron gas existing between LAO and STO [2], [3]. Recently the existence of Rashba-split states at the interface between CoFeB and MgO has been observed by measuring spin-to-charge conversion [4]. Interestingly, these interface states often allow for a large sensitivity to the application of an electric field. The present work aims to investigate this effect in a top-gate geometry in metallic-oxide multilayer structures.

The samples studied in this work, Glass|CoFeB|MgO|HfO₂, Glass|CoFeB|Cu|MgO|HfO₂ and Glass|CoFeB|Pt|MgO|HfO₂, were deposited by magnetron sputtering (see Fig. 1). They present different contributions from both spin and orbital angular momentum converted into charge. A few micrometers thick polyimide is spun on top of the sample to reduce current leakage when a gate voltage is applied. Spin injection is carried out through the spin Seebeck effect which requires a thermal gradient applied normal to the ferromagnetic layer, achieved by shining high intensity 465 nm blue light on the samples. The Spin Seebeck effect is accompanied by a spurious signal coming from anomalous Nernst voltage parallel to the spin/charge conversion signal and directly proportional to the thermal gradient inside the ferromagnet and its magnetization [5]. To better interpret our results, we simulate the thermal gradient by finite elements' calculations incorporating the light's absorption profile simulated by the transfer matrix method. This innovative approach is envisaged to enhance the conversion of angular momentum into charge by applying a gate voltage to discriminate interface from bulk effects and possibly spin and orbital contributions. Mastering this is key for faster and more enduring low-consumption spin/orbit-based memories [6].

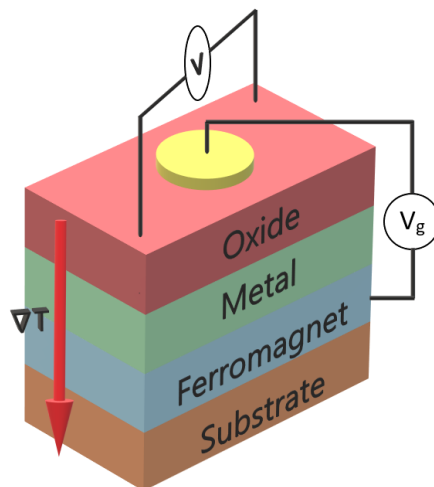


Figure 1: Schematic of the device under a temperature gradient ∇T and gate voltage V_g

Acknowledgments

We acknowledge funding from the ANR ORION (grant ANR-20-CE30-0022-01) and the EIC Pathfinder OPEN grant 101129641 “OBELIX”. We also wish to acknowledge Aurélie Solignac for her assistance with sample fabrication.

References

- [1] Aurelien Manchon, Hyun Cheol Koo, Junsaku Nitta, Sergey M Frolov, and Rembert A Duine. New perspectives for Rashba spin-orbit coupling. *Nature materials* 14, 871–882 (2015).
- [2] N Reyren, M Bibes, E Lesne, et al. Gate-controlled spin injection at LaAlO₃/SrTiO₃ interfaces. *Physical Review Letters* 108, 186802 (2012).
- [3] Anas El Hamdi, Jean-Yves Chauleau, Margherita Boselli, et al. Observation of the orbital inverse Rashba–Edelstein effect. *Nature Physics* 19, 1855–1860 (2023).

- [4] Olivier Rousseau, Cosimo Gorini, Fatima Ibrahim, et al. Spin-charge conversion in ferromagnetic Rashba states. *Physical Review B* 104, 134438 (2021).
- [5] Hiroto Adachi, Ken-ichi Uchida, Eiji Saitoh, and Sadamichi Maekawa. Theory of the spin Seebeck effect. *Reports on Progress in Physics* 76, 036501 (2013).
- [6] Yihong Wu, Yanjun Xu, Ziyang Luo, et al. Charge–spin interconversion and its applications in magnetic sensing. *Journal of Applied Physics* 129 (2021).

Neuro-Inspired Computing in k-Space: Harnessing Spin Wave Dynamics in YIG Microdisks

David Zehner^{1,*}, Isabella Boventer¹, Ping Che¹, Jamal Ben Youssef², Manuel Muñoz³, Romain Lebrun¹, Dédalo Sanz Hernández¹, Vincent Cros¹, Paolo Bortolotti¹, and Abdelmadjid Anane¹

¹Laboratoire Albert Fert, CNRS, Thales, Université Paris-Saclay, Palaiseau, France

²LabSTICC, CNRS, Université de Bretagne Occidentale, Brest, France

³Instituto de Tecnologías Físicas y de la Información (CSIC), Madrid, Spain

*david.zehner@cnrs-thales.fr

Neuromorphic devices promise new perspectives for the next generation of hardware technologies. Bypassing conventional CMOS architectures and exploiting nontrivial physical effects may offer lightweight and energy-efficient computation solutions. We present here an approach based on the nonlinear spin wave interactions in YIG micro-structures as a versatile platform for nontrivial calculation and classification tasks. Unlike other physical neuromorphic systems that rely on discrete interconnected building blocks composed of neurons and synapses, interconnectivity in our approach occurs intrinsically in the reciprocal or k-space of the spin wave excitation spectrum, eliminating the need for hardwired interconnections. This concept has been successfully demonstrated in other magnetic microstructures [1].

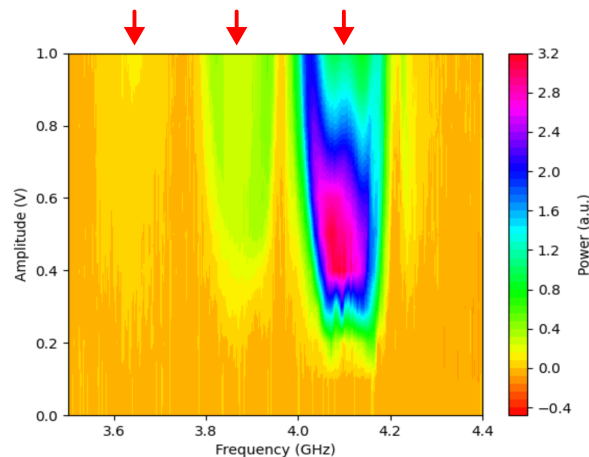


Figure 1: Three parametrically excited modes of an array of $\varnothing 1 \mu\text{m}$ and 55 nm thick LPE YIG disks, detected inductively using a spectrum analyzer, with varying excitation frequency and amplitude.

When considering a YIG microstructure such as a $1 \mu\text{m}$ disk, finite-size effects impose quantization, resulting in a discrete spin wave spectrum. The corresponding magnon modes have been identified by micromagnetic simulations and experimentally observed using Brillouin light scattering (BLS) [2]. Figure 1 demonstrates that several modes can be independently parametrically excited and inductively detected at excitation frequencies in the accessible range (3.5 GHz – 4.5 GHz) of our setup. These nonlinear excitation processes exhibit a threshold behavior, a key feature for enabling neuromorphic computation. In addition, the population of one magnon mode can induce (de-)populations of other modes, where the interaction strengths vary for each mode pair. Hence, the YIG disk can be formally modeled as a fully interconnected recurrent neural network (RNN), where spin wave modes are the neurons and their coupling through non-linear modes interactions are the synapses, the synaptic weights being the strength of those interactions that are directly related to the individual modes population.

An illustrative example of a network representation with four modes (n_1 to n_4) is shown in Figure 2. In this model, the modes function as neurons, whose output values (populations) are nonlinearly dependent on their inputs. The finite line widths of the modes result in the broadening of their response in frequency space, leading to multitone input and output signals being given by continuous spectra rather than discrete frequency peaks. Furthermore, it is possible to crossover from a reservoir-computing-like architecture to a programmable neural network by adding a programming signal to the input redefining the dynamical state at will. This approach dynamically biases each neuron and shifts its threshold value, enabling the reconfigurability of the RNN response.

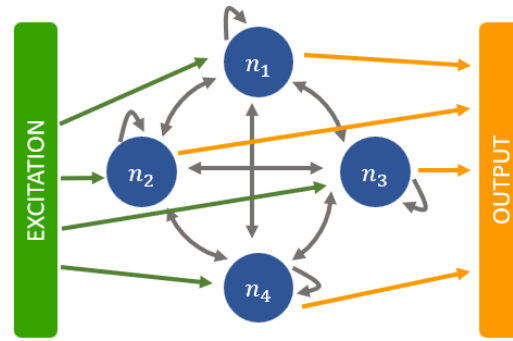


Figure 2: Recurrent neural network of interacting magnon modes in k-space.

Our experimental setup (Figure 1a) consists of 20 identical Yttrium Iron Garnet (YIG) disks, each with a thickness of 55 nm and a diameter of 1 μm . The magnetization of these disks is saturated by applying a 27 mT in-plane static magnetic field. Spin waves are excited using a coplanar waveguide with a 2 μm wide signal line, which generates a time-varying magnetic field at a 45° angle relative to the static field. We use an arbitrary waveform generator (AWG) to shape the input signal. The system's response is measured using a spectrum analyzer, capturing the frequency-resolved magnetization response at half the excitation frequency.

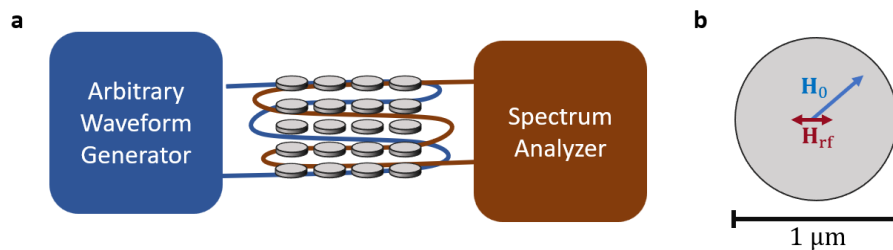


Figure 3: **a** Setup for spin wave excitation and detection using an AWG and spectrum analyzer. **b** YIG microdisk with in-plane static and time-varying magnetic field at a 45° angle.

We investigate the potential of this platform through a speech classification task using the Google Speech Commands dataset [3]. The initial focus is on binary classification, identifying the occurrence of a specific word. To process audio data, the frequency range relevant for speech recognition ($\approx 300 \text{ Hz} - 3.5 \text{ kHz}$) is mapped to our setup's excitation range. To mitigate overfitting while preserving the structural integrity of the sound signal, we apply a combination of frequency scaling and shifting in the frequency domain, directly mapping the audible spectrum to the excitation range.

We parametrize the programming signal as a superposition of a small number (≈ 10) of sinusoidal components, each characterized by amplitude, frequency, phase shift, and onset and cutoff times relative to the resampled speech signal. The model parameters are then refined using optimization techniques, such as gradient-based algorithms and global minimizers, to minimize the loss function of the recognition task. Upon progressing with the binary classification task, the gained understanding of the relevant parameter space will provide insights into the potential capabilities and limitations of the current neural network, thereby laying the groundwork for adapting the system to more complex tasks.

Acknowledgments

This work is supported by the Horizon 2020 Framework Program of the European Commission under contract number 899646 (k-Net) and has benefited from a government grant operated by the French National Research Agency as part of the France 2030 program, reference ANR-22-EXSP-0004 (SWING).

References

- [1] Lukas Körber, Christopher Heins, Tobias Hula, et al. [Pattern recognition in reciprocal space with a magnon-scattering reservoir](#). *Nature Communications* 14 (2023).
- [2] T. Srivastava, H. Merbouche, I. Ngouagnia Yemeli, et al. [Identification of a Large Number of Spin-Wave Eigenmodes Excited by Parametric Pumping in Yttrium Iron Garnet Microdisks](#). *Phys. Rev. Appl.* 19, 064078 (6 2023).
- [3] Pete Warden. *Speech Commands: A Dataset for Limited-Vocabulary Speech Recognition*. 2018. arXiv: [1804.03209](#).

Oersted field driven dynamics in spin-torque vortex oscillators

Simon de Wergifosse^{1,*}, Tristan da Câmara Santa Clara Gomes², Anatole Moureaux¹, Chloé Chopin³, Ursula Ebels³, and Flavio Abreu Araujo¹

¹*Institute of Condensed Matter and Nanosciences, UCLouvain, Louvain-la-Neuve, Belgium*

²*INESC Microsistemas e Nanotecnologias, Lisbon, Portugal*

³*Univ. Grenoble Alpes, CNRS, CEA, SPINTEC, Grenoble, France*

*simon.dewergifosse@uclouvain.be

Spin-torque vortex oscillators (STVOs) are compact spintronic devices characterized by their highly nonlinear dynamics. These devices typically consist of a magnetic tunnel junction (MTJ) stack structure, in which the free layer exhibits a vortex magnetization configuration. Over the years, STVOs have gained considerable interest for a wide range of applications, particularly in the emerging field of neuromorphic computing, where their ability to mimic certain aspects of biological neural networks offers potential advantages in terms of energy efficiency and computational power. [1] The operating principle of these devices relies on the injection of a current into the system, which triggers the excitation of the gyrotropic mode of the vortex. This gyrotropic motion of the vortex magnetization results in an oscillatory behavior, allowing for the generation of a corresponding alternating voltage through magnetoresistance effects. Such a measurable signal is directly linked to the dynamics of the vortex. In practice, this out-of-plane current injection can also be combined with other excitation methods, such as magnetic fields.

For future on-chip integration, it is anticipated that multiple oscillators will be arranged to interact and form highly dense networks. When spin-torque vortex oscillators are placed in close proximity to one another, they can communicate via dipolar interactions. This type of coupling has been widely studied in the literature, both experimentally and by theoretical means. [2, 3] However, the influence of the Oersted magnetic field generated by one oscillator on its neighbors has, to the best of our knowledge, not yet been thoroughly considered. In this study, we focus specifically on the effect of this Oersted field (see Fig. 1a), deliberately excluding dipolar interactions from our analysis. We demonstrate that this nonuniform, planar field has a significant effect on the dynamics of a vortex by altering the magnetic energy landscape (see Fig. 1b). The presence of this field introduces additional complexity to the system, influencing the motion of the vortex core in ways that can not be attributed to dipolar interactions alone. Given these findings, we suggest that incorporating the Oersted field into future studies of STVO arrays would provide a more comprehensive understanding of their collective dynamics and could lead to more optimized designs for practical applications.

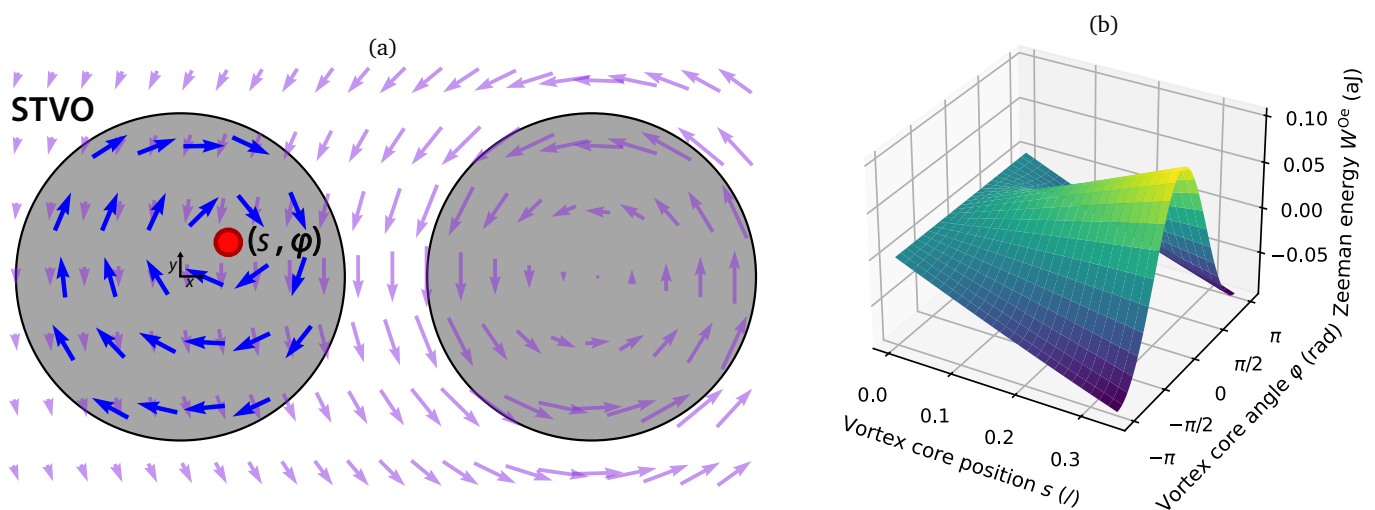


Figure 1: a) Schematic of the system under study. The free layer of an STVO, which exhibits a vortex magnetization (in blue), is excited by an out-of-plane spin-polarized current, its core (in red) oscillates at a position (s, φ) (in cylindrical coordinates). If a conducting wire (which could be a neighboring STVO in a dense STVO network) is located close (~ 100 nm) to this STVO, the Oersted field generated modifies the Zeeman energy of the system and influences the dynamics. b) Theoretical calculation of the Zeeman energy W^{Oe} associated with an external Oersted field, with respect to the vortex core orbit s and its phase φ .

In practice, the influence of a local stationary Oersted field, modeled as emitted from a simple conductive wire, on a vortex magnetic structure has been thoroughly investigated. An analytical expression for the Zeeman energy associated with this field was derived and confirmed through numerical simulations, [4] providing a clear understanding of the interaction

between the field and the magnetic structure. The study then examined the effects of an oscillating Oersted field, revealing resonance phenomena and demonstrating how the frequency of the excitation field affects the trajectory of the vortex core, as already studied for uniform fields by Lee & Kim. [5] These findings offer valuable insights into the dynamics of vortex oscillators and their response to external fields. The results of this work are expected to present implications for applications involving dense oscillator networks, such as neuromorphic computation, frequency detection, and RF signal generation. The ability to control and manipulate these interactions opens up new possibilities for the design of efficient and versatile spintronic devices for future technologies.

Acknowledgments

Computational resources have been provided by the Consortium des Equipements de Calcul Intensif (CECI), funded by the Fonds de la Recherche Scientifique de Belgique (F.R.S.-FNRS) under Grant No. 2.5020.11 and by the Walloon Region. F.A.A. is a Research Associate and S.d.W. is a FRRIA grantee, both of the F.R.S.-FNRS. T.d.C.S.C.G. is an ERA fellow. Funded by the European Union. Views and opinions expressed are however those of the authors only and do not necessarily reflect those of the European Union or the European Research Executive Agency (REA). Neither the European Union nor the granting authority can be held responsible for them.

References

- [1] Jacob Torrejon, Mathieu Riou, Flavio Abreu Araujo, et al. Neuromorphic computing with nanoscale spintronic oscillators. *Nature* 547, 428–431 (2017).
- [2] Nicolas Locatelli, Abbass Hamadeh, Flavio Abreu Araujo, et al. Efficient synchronization of dipolarly coupled vortex-based spin transfer nano-oscillators. *Scientific Reports* 5, 17039 (2015).
- [3] Leandro Martins, Alex S Jenkins, Jérôme Borme, et al. Second harmonic injection locking of coupled spin torque vortex oscillators with an individual phase access. *Communications Physics* 6, 72 (2023).
- [4] A. Vansteenkiste, J. Leliaert, M. Dvornik, et al. The design and verification of MuMax3. *AIP advances* 4 (2014).
- [5] Ki-Suk Lee and Sang-Koog Kim. Two circular-rotational eigenmodes and their giant resonance asymmetry in vortex gyrotropic motions in soft magnetic nanodots. *Physical Review B* 78, 014405 (2008).

Structural and magnetic characterization of $\text{Mn}_{100-x}\text{Sn}_x$ chiral antiferromagnets epitaxial films

C. Guillemard^{1,*}, M. Petit¹, V. Heresanu¹, and L. Michez¹

¹Aix-Marseille Univ., CNRS, CINaM, Marseille, France

*charles.guillemard@cnrs.fr

Non-collinear chiral AntiFerroMagnets (AFM) of the Mn_3X ($\text{X} = \text{Sn}, \text{Ga}, \text{Ge}$) family of intermetallic compounds have attracted a lot of attention recently since the discovery of a significant Anomalous Hall Effect (AHE) and Anomalous Nernst Effect (ANE) [1], normally observed only in ferromagnetic materials. The chirality emerges from the triangular spin lattice carried by Mn atoms and gives rise to a non-vanishing Berry phase of the electronic states responsible for this AHE and ANE, as well as the predicted Weyl semi-metallic nature of their band structure. Furthermore, it has been shown recently that chiral AFMs were able to carry spin-triplet Cooper pairs over long distances in Josephson junctions [2], opening the way toward superconducting spintronic applications. Combining the AFM stability toward stray fields, the manipulation of the magnetic state with currents via the AHE and the vast number of phenomena associated to the magnetic chirality, Mn_3X compounds are very promising for future spintronic devices and an excellent playground to study the physics associated to magnetic topological phases of matter.

In this study, we have tested the epitaxial growth of $\text{Mn}_{100-x}\text{Sn}_x$ compounds with a large range of stoichiometry, $x \in [20; 50]$, i.e. from equiatomic MnSn to Mn_4Sn , by molecular beam epitaxy. Surprisingly, a single-crystalline phase is maintained throughout the stoichiometry range, as demonstrated by the Reflection High Energy Electron Diffraction (RHEED) patterns in figure 1. This result is particularly interesting since MnSn was not found in any crystallographic databases. Atomic Force Microscopy and RHEED confirmed a drastic change in the surface morphology, with an increase of the roughness as a function of the Mn content. The structure of the $\text{Mn}_{100-x}\text{Sn}_x$ epitaxial layers is investigated using X-Ray Diffraction and a non-monotonous evolution of the lattice spacings is observed, in agreement with a structural transition that still needs to be determined. The magnetic properties are being studied using magnetometry and X-ray magnetic circular dichroism.

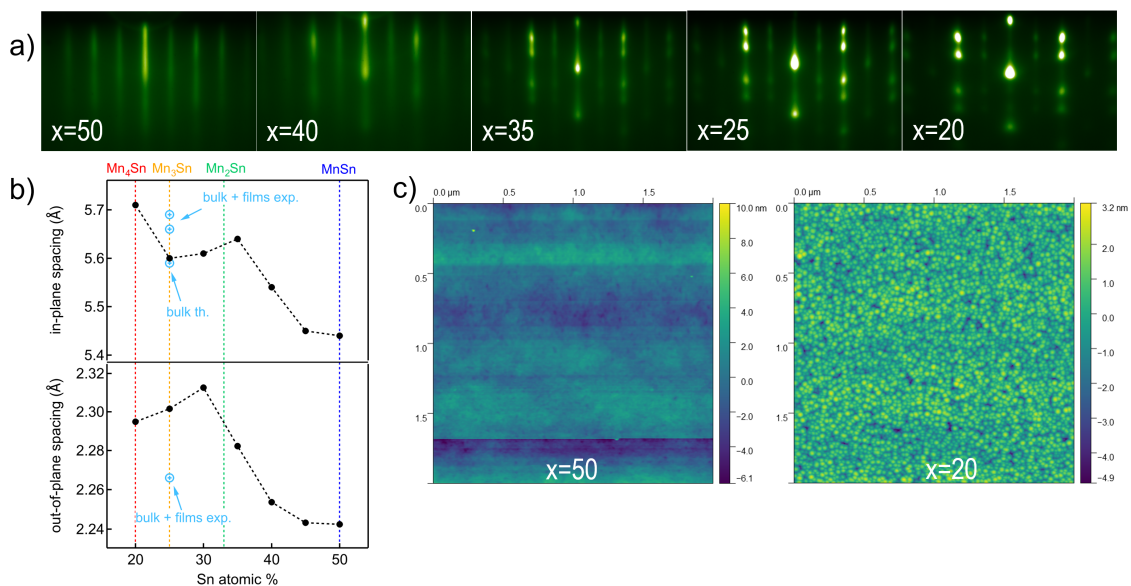


Figure 1: a) RHEED patterns of selected $\text{Mn}_{100-x}\text{Sn}_x$ epitaxial layers. b) lattice spacings obtained from XRD and RHEED. c) AFM images showing islands for Mn rich samples.

References

- [1] Satoru Nakatsuji, Naoki Kiyohara, and Tomoya Higo. [Large anomalous Hall effect in a non-collinear antiferromagnet at room temperature](#). *Nature* 527, 212–215 (2015).
- [2] Kun-Rok Jeon, Binoy Krishna Hazra, Jae-Keun Kim, et al. [Chiral antiferromagnetic Josephson junctions as spin-triplet supercurrent spin valves and d.c. SQUIDS](#). *Nature Nanotechnology* 18, 747–753 (2023).

Periodic nanostructures subjected to mechanical stress: Experimental and numerical study of spin waves mode

S. Chirolì^{1,2,*}, D. Faurie¹, A. O. Adeyeye^{3,4}, and F. Zighem¹

¹LSPM-CNRS UPR3407, Université Sorbonne Paris Nord, Villetaneuse, France

²Laboratoire Albert Fert UMR137, CNRS-Thales, Palaiseau, France

³Department of Electrical and Computer Engineering, ISML, NUS, Singapore

⁴Department of Physics, Durham University, United Kingdom

*stephane.chirolì@cnrs-thales.fr

This work explores the field of magnonics and magnetoelastic couplings, focusing on the control of spin wave frequencies in nanostructured films through the application of mechanical stress. Part of this work involves finite element simulations of such phenomena using Comsol Multiphysics®. These simulations couple the effects of mechanical deformations on magnetic properties (indirect coupling) as well as the effect of magnetization on mechanical properties (direct effect) through the magneto elastic energy:

$$F_{me} = \underline{\underline{\varepsilon}}^{el} : \underline{\underline{C}} : \underline{\underline{\varepsilon}}^{el} = \varepsilon_{ij}^{el} \sigma_{ij} \quad (14)$$

where :

$$\underline{\underline{\varepsilon}}^m = \frac{3}{2} \left[\lambda_{100} \begin{pmatrix} m_x^2 - \frac{1}{3} & m_x m_y & m_x m_z \\ m_x m_y & m_y^2 - \frac{1}{3} & m_y m_z \\ m_x m_z & m_y m_z & m_z^2 - \frac{1}{3} \end{pmatrix} + (\lambda_{111} - \lambda_{100}) \begin{pmatrix} 0 & m_x m_y & m_x m_z \\ m_x m_y & 0 & m_y m_z \\ m_x m_z & m_y m_z & 0 \end{pmatrix} \right] \quad (15)$$

They enable us to account for the temporal evolution of magnetic properties, the dispersive characteristics of spin waves, and even predict magnon-phonon couplings that may arise in certain systems. We studied Both numerically with Comsol and experimentally by FMR and BLS the behavior of spin waves modes in such strained systems in order to observe magnetoelastic and geometrical effects induced mechanically.[1-3]

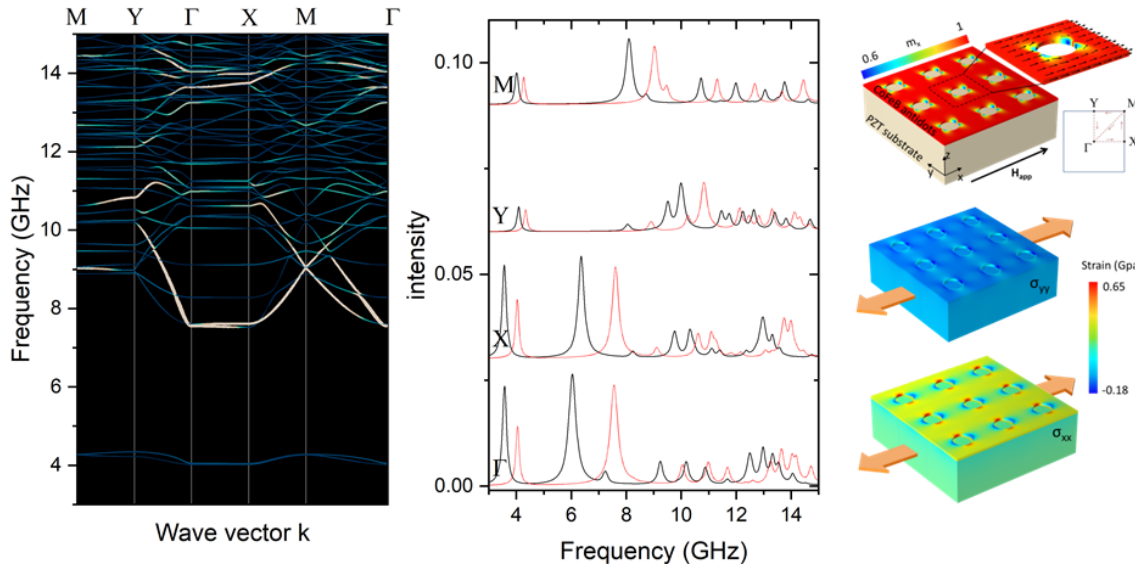


Figure 1: (Left) Simulation of spin wave dispersion in a square lattice of holes in $\text{Co}_{40}\text{Fe}_{40}\text{B}_{20}$ under 0.2% strain. (Middle) Simulated spectra for 0% strain (black) and 0.2% strain (red). (Right) Simulated profiles of the static magnetization configuration and the σ_{xx} and σ_{yy} components of the stress tensor.

References

- [1] S. Chirolì, D. Faurie, M. Haboussi, A. O. Adeyeye, and F. Zighem. [Magnetization dynamics of elastically strained nanostructures studied by coupled micromagnetic-mechanical simulations](#). *Physical Review B* 108, 024406 (2023).

- [2] S. Chiroli, M. Faurie, A. O. Adeyeye, and F. Zighem. [Impact of thickness and saturation direction over magnetostatic mode energies and profiles in Ni80Fe20 antidots](#). *Journal of Physics D: Applied Physics* 58, 015001 (2023).
- [3] N. Challab, A. D. Aboumassound, F. Zighem, D. Faurie, and M. Haboussi. [Micromagnetic modeling of nanostructures subject to heterogeneous strain fields](#). *Journal of Physics D: Applied Physics* 52, 355004 (2023).

Terahertz emission using the spin and orbital Hall effect

Anakha Anil^{1,*}, Michel Hehn², Christophe Coudert¹, Mircea Vomir¹, Matthieu Bailleul¹, and Paul Noël¹

¹IPCMS, CNRS, University of Strasbourg, France

²Jean Lamour Institute, CNRS, University of Lorraine, Nancy, France

*anakha.anil@ipcms.unistra.fr

Terahertz waves bridging the gap between microwave and infrared radiation, offer a wide range of applications in investigating material properties, telecommunication, medical imaging etc. The rise in frequency compared with current telecommunications in the GHz range gives the possibility to an even faster data transfer rate and the ability of THz waves to penetrate through plastic and coatings is advancing the field of non-destructive screening. Despite having a wide range of potential scientific and industrial applications the emission and detection of THz waves is still challenging and the emitters and detectors have limited performances: this is known as the THz gap [1]. The conventional emission techniques of THz involve nonlinear optical methods such as optical rectification, higher harmonic generation and semiconductor-based approaches [2]. In this work, we explore the THz emission using spintronic mechanisms [3]. The aim of this work is to realise the emission of the THz waves in ferromagnet/normal metal bilayers by taking advantage of the inverse spin Hall effect (ISHE) and orbital Hall effect (IOHE). The ultrafast laser pulse excitation induces a demagnetisation in the ferromagnetic (FM) layer which leads to the generation of a spin (orbital) current propagating to the normal metal where it is converted into a charge current via the ISHE or IOHE. The transient charge current radiates as an electromagnetic wave of THz frequency in free space namely the THz waves. This mechanism of conversion of the spin current (J_S) induced by the femtosecond laser pulse (fs-pump) into a transverse charge current (J_C) in a heterostructure giving THz waves is illustrated in Fig.1. Typically, the ISHE is observed in heavy metals like Pt or W and the IOHE in light metal like Ti or oxidised Cu (CuO_x) [4, 5]. The measurement of the emitted THz wave is performed using electro-optic sampling in a ZnTe crystal. The heavy metal based spintronic emitters typically outperform most laser driven semiconductor THz emitters using spintronic mechanisms [4]. Notably the ISHE and IOHE can also be used for THz detection too making spintronics a potential versatile platform for THz emission and detection.

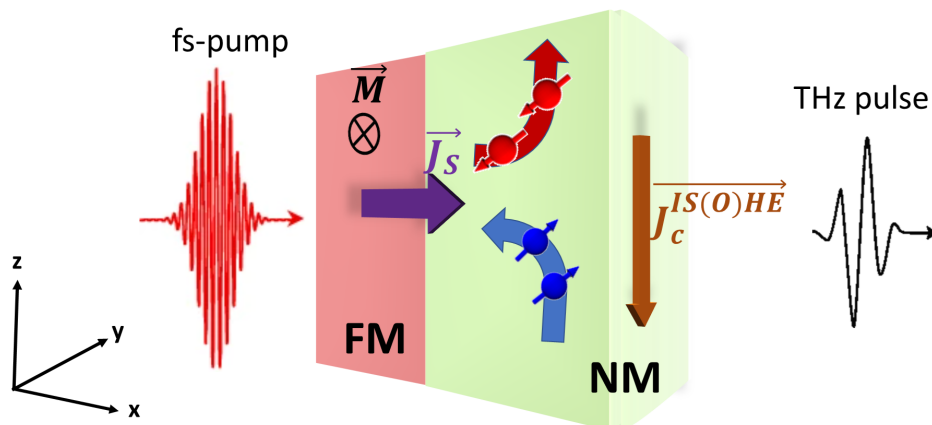


Figure 1: The schematic of the heterostructure depicting the inverse spin Hall effect (ISHE) and orbital Hall effect (IOHE). The ultra-fast demagnetisation caused by the femtosecond laser pulse will produce a spin (orbital) current in the ferromagnetic layer (FM). This spin (orbital) current (J_S) would convert into a transient charge current (J_C) via IS(O)HE in the normal metal and radiates as an electromagnetic wave of THz frequency range into the free space.

In this work, we used multilayer heterostructures comprising of a heavy/light metal and a ferromagnetic metal deposited on intrinsic FZ-Si by magnetron sputtering and integrated them within a THz time-domain system. In particular, we studied Co/Pt and CoFeB/Pt bilayers and compared the efficiency of the THz emission with Co/Cu and CoFeB/Cu using either Cu with 3 nm Al capping and Cu without a capping layer. In all these samples we could detect THz emission and we confirmed the spin (orbital) origin of the signal by reversing the magnetic field. As expected the samples with Cu gives a much smaller signal than the heavy metal Pt samples. Surprisingly oxidised Cu, which is expected to have a large orbital Hall effect comparable to the spin Hall effect in Pt [6] gives an even smaller THz emission signal than unoxidised Cu (See figure 2). These results indicate an apparent discrepancy between the large direct orbital Hall effect measured using spin orbit torque measurement and the small THz signal associated with the inverse orbital Hall effect. This “non-reciprocity” could be explained by the small orbital-to-spin magnetisation ratio in Co and CoFeB, leading to an inefficient orbital current injection [7].

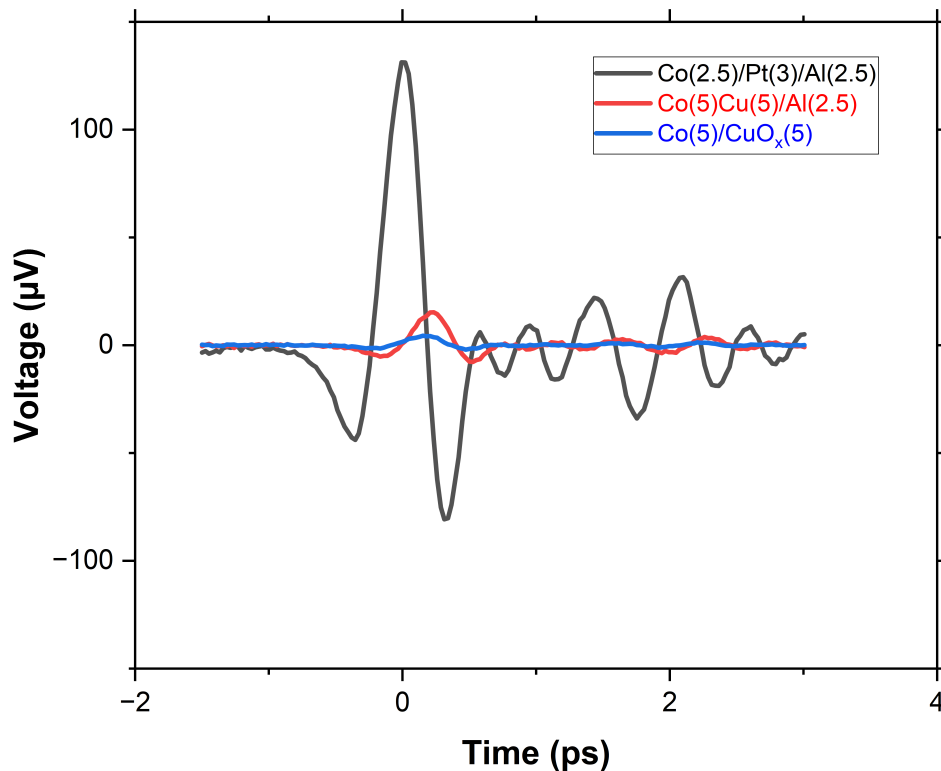


Figure 2: Signal comparison of time-domain THz emission from different heterostructures of Co(2.5)/Pt(3)/Al(2.5), Co(5)/Cu(5)/Al(2.5) and Co(5)/CuO_x(5), the numbers in parentheses correspond to the thickness in nm.

Acknowledgments

This work is funded by the French national research PEPR SPIN program through project ANR-22-EXSP-0003 TOAST

References

- [1] Evangelos Th. Papaioannou and René Beigang. [THz spintronic emitters: a review on achievements and future challenges](#). *Nanophotonics* 10, 1243–1257 (2020).
- [2] Katsuyoshi Aoki, Janne Savolainen, and Martina Havenith. [Broadband terahertz pulse generation by optical rectification in GaP crystals](#). *Applied Physics Letters* 110 (2017).
- [3] Jiayu Zhao. Principle of Terahertz Time-Domain Spectroscopy. *arXiv preprint arXiv:2308.08503* (2023).
- [4] T. Seifert, S. Jaiswal, U. Martens, et al. [Efficient metallic spintronic emitters of ultrabroadband terahertz radiation](#). *Nature Photonics* 10, 483–488 (2016).
- [5] Yong Xu, Fan Zhang, Albert Fert, et al. Orbitronics: light-induced orbital currents in Ni studied by terahertz emission experiments. *Nature Communications* 15, 2043 (2024).
- [6] Daegeun Jo, Dongwook Go, and Hyun-Woo Lee. Gigantic intrinsic orbital Hall effects in weakly spin-orbit coupled metals. *Physical Review B* 98, 214405 (2018).
- [7] Dongwook Go, Kazuya Ando, Armando Pezo, et al. Orbital pumping by magnetization dynamics in ferromagnets. *arXiv preprint arXiv:2309.14817* (2023).

Inductive magnon noise spectroscopy of thermally excited magnons

Richard Schlitz^{1,*}, Luise Siegl¹, Jamal Ben Youssef², Christian Runge¹, Akashdeep Kamra³, William Legrand⁴, Hans Huebl^{5,6,7}, Michaela Lammel¹, and Sebastian T.B. Goennenwein¹

¹Department of Physics, University of Konstanz, 78457 Konstanz, Germany

²LabSTICC, CNRS, Université de Bretagne Occidentale, 29238 Brest, France

³Department of Physics, Rheinland-Pfälzische Technische Universität (RPTU) Kaiserslautern-Landau, 67653 Kaiserslautern, Germany.

⁴Université Grenoble Alpes, CNRS, Institut Néel, 38042 Grenoble, France

⁵Walther-Meißner-Institut, Bayerische Akademie der Wissenschaften, 85748 Garching, Germany

⁶TUM School of Natural Sciences, Technische Universität München, 85748 Garching, Germany

⁷Munich Center for Quantum Science and Technology (MCQST), 80799 München, Germany

*richard.schlitz@uni-konstanz.de

The identification of non-classical magnon states relies on the ability to reference the states fluctuations to the thermal or vacuum fluctuations. We show that thermal magnetization fluctuations of a ferromagnetic thin film can be sensitively probed using inductive magnon noise spectroscopy (iMNS, see Fig. 1). Our broadband approach allows to detect the microwave emission of the equilibrium magnetization fluctuations relative to a cold microwave background by utilizing a coplanar waveguide and a spectrum analyzer. Modeling the response of the whole microwave system and comparing it quantitatively with low-power broadband ferromagnetic resonance (FMR) measurements in linear response yields excellent agreement, which verifies the equilibrium character of the iMNS. Therewith, our work establishes purely inductive broadband access to the equilibrium properties of magnetization fluctuations [1].

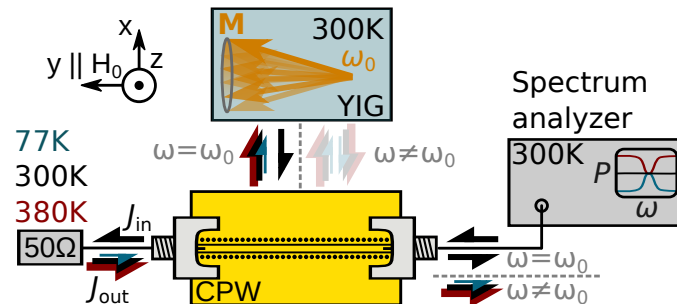


Figure 1: Sketch of the inductive magnon noise spectroscopy setup and measurement principle.

References

- [1] Luise Siegl, Richard Schlitz, Jamal Ben Youssef, et al. [Inductive noise spectroscopy of thermally excited magnons](#). *Physical Review Applied* 22, 054036 (2024).

Metallised 3D printed plastic resonator demonstrates superconductivity below 4 K

J. Bourhill¹, J. Haumant², V. Vlaminck^{3,4}, A. Manchec⁵, and V. Castel^{3,4,*}

¹Quantum Technologies and Dark Matter Labs, Department of Physics, University of Western Australia, 35 Stirling Hwy, 6009 Crawley, Western Australia

²Elliptika (GTID) 2 Rue Charles Jourde, 29200 Brest, France

³IMT Atlantique, Technopole Brest-Iroise, CS 83818, 29238 Brest Cedex 3, France

⁴Lab-STICC (UMR 6285), CNRS, Technopole Brest-Iroise, CS 83818, 29238 Brest Cedex 3, France

⁵THALES, 10 Av. 1ère DFL, 29200 Brest, France

*vincent.castel@imt-atlantique.fr

We report the first observation of a superconducting transition in a 3D printed, metalized-plastic device. A resonant TE microwave mode at 13.41 GHz is observed to reduce its losses by an order of magnitude once it is cooled below 3.72 K; the superconducting transition temperature of tin, with the mode's Q factor increasing from 2.7×10^4 to 4.0×10^5 .

Plastic resin 3D printing has been demonstrated to be an extraordinarily portable technology, with the ability to move a printer from one location to another without the need for arduous set-up and pack-down procedures, or overly cumbersome printing units – a typical printer weighs on the order of 20 kg. This fact makes them an intriguing technology to explore for their applications to defence and space exploration wherein manufacturing from the same device may be required at changing locations with short lead times. It has been previously demonstrated that microwave resonant cavities with equivalent performance to their traditionally manufactured counterparts can be produced by plastic 3D SLA printing followed by metallisation [1]. This result has opened up the possibility of rapid, low cost, and highly reproducible production of a wide variety of microwave devices; such as filters, isolators, RF and magnetic field shielding, and more complicated systems for coupling microwave photonics to additional degrees of freedom to form a hybrid system.

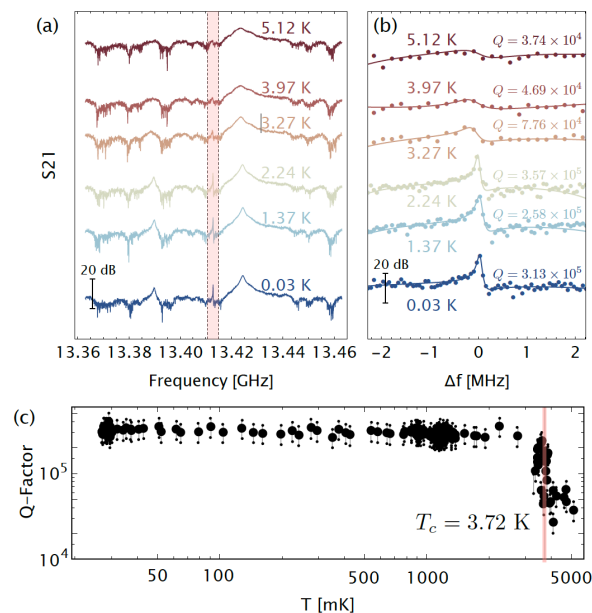


Figure 1: (a) S21 transmission spectra over a 100 MHz span at various temperatures with the central highlighted region zoomed in (b). (c) Q factor of the mode extracted from fitting as a function of temperature with the superconducting transition temperature of Sn labelled in red.

A hollow cylinder is first 3D printed with a stereolithography 3D printer. This printer has a resolution of $25 \mu\text{m}$ for the vertical axis. The internal diameter and height of the cavity were both designed to be 30 mm, with radial wall thickness 7 mm. A conventional 3-D metallization procedure of plastic elements has been adapted to produce a full metallization of the plastic cavity with copper and tin (Sn). The Sn layer is made thicker to ensure that it acts as a bulk superconductor, well above the percolation limit [2]. The cavity has a rubidium oxide temperature sensor mounted to its base, ensuring direct measurement of the real cavity surface temperature, and together they are mounted to the mixing chamber (MXC) plate of a dilution refrigerator. Data is recorded during the condense procedure of the dilution fridge, in which the temperature of the MXC changes from 5 K to 20 mK, an ideal window to observe the superconducting transition of Sn.

A sample of the S21 transmission spectra recorded at different temperatures is displayed in Fig. 1 (a) and (b). It can be observed from the first figure that within the observed 100 MHz frequency span there exists 3 modes, each of which becomes

more resolved as the temperature decreases; a direct result of the increase in conductivity of the conducting boundaries. The mode of interest is the central, high Q TE₀₁₁ mode with frequency $\omega/2\pi=13.413$ GHz. It is determined from finite element simulation (COMSOL Multiphysics) that this is indeed the mode we are looking at. A zoomed in picture of the mode is shown in Fig. 1 (b) as well as theoretical fits using a Fano model [3] and the resulting calculated Q factor. It is clear that an increase in Q as well as peak transmission is associated with a decrease in temperature. By plotting the fitted Q values against temperature in Fig. 1 (c), we observe that a jump in Q occurs around $T_c = 3.72$ K; the superconducting transition for Sn. Over an order of magnitude improvement in Q factor is achieved; rising from a 2.7×10^4 to 4.0×10^5 .

In conclusion, our study marks a decisive advance in the combination of superconductivity and additive manufacturing. We have successfully demonstrated the first ever superconducting transition in a 3D-printed metallized plastic device.

Acknowledgments

This work was jointly funded by the Région Bretagne through the project OSCAR-SAD18024, by the UWA Research COLLABORATION AWARDS (RCA) grant "Investigation of 3D printed microwave cavities at cryogenic temperature", and by the Australian Research Council Centre of Excellence for Engineered Quantum Systems, CE170100009 and the Centre of Excellence for Dark Matter Particle Physics, CE200100008.

References

- [1] Jeremy Bourhill, Vincent Castel, Alexandre Manchec, and Gwendal Cochet. [Universal characterization of cavity–magnon polariton coupling strength verified in modifiable microwave cavity](#). *Journal of Applied Physics* 128, 073904 (2020).
- [2] M. H. Beutel, N. G. Ebersperger, M. Thiemann, et al. [Microwave study of superconducting sn films above and below percolation](#). *Superconductor Science and Technology* 29 (2016).
- [3] U. Fano. [Effects of Configuration Interaction on Intensities and Phase Shifts](#). *Phys. Rev.* 124, 1866–1878 (1961).

Using Artificial Intelligence to Explore Magnetic Topological Structures

Xavier Bosch^{1,*}, Sebastian Meyer^{1,2}, and Bertrand Dupé^{1,2}

¹TOM group, Q-Mat Research Unit, Université de Liège, 19 Allée du 6 août, 4000 Liège, Belgium

²FRS-FNRS, 5 Rue d'Egmont, 1000 Bruxelles, Belgium

*x.bosch@uliege.be

Skyrmions are particle-like magnetic non-collinear textures. Skyrmions are characterized by an integer called skyrmion number, such as -1 for an anti-skyrmion, 1 for a skyrmion, and 0.5 for a vortex or meron. The skyrmion number is given by:

$$Q = \frac{1}{4\pi} \int_S \mathbf{n} \cdot \left(\frac{\partial \mathbf{n}}{\partial x} \times \frac{\partial \mathbf{n}}{\partial y} \right) dS \quad (16)$$

Where S is the surface of the topological textures and \mathbf{n} is the unitary vector field collinear to the magnetization field. A non-zero topological charge ensures an energy barrier between collinear long-range and topological short-range states, preventing spontaneous collapse. This stability makes skyrmions especially promising for applications in spintronics. Skyrmion-based spintronics could drive significant advances in communication technologies [1], with potential for increased storage density due to skyrmions' sub-10 nm size, compared to the ~ 30 nm limit of domain walls, neuromorphic computing due to their non-trivial dynamics combined with their peculiar transport properties [1]. Additionally, skyrmions can be moved with a low current density in different directions depending on their skyrmion number and even more dynamical properties have been predicted [2, 3]. These innovations could counteract the slowdown in Moore's law and significantly reduce the energy consumption of electronic and spintronic devices [4].

One challenge in skyrmion-based spintronics is to identify the internal structures of topological objects. As the topological charge is a non-local property that requires the definition of a boundary, opposite topological structures with opposite charges, like a skyrmion and an anti-skyrmion, will cancel each other's charge when evaluated collectively [5]. Therefore, distinguishing the number, type and spatial extension of these structures within a sample is complex but essential. Developing such methods is critical for advancing research on the creation, annihilation, and topological protection of skyrmions, enabling systematic simulations even at high temperatures.

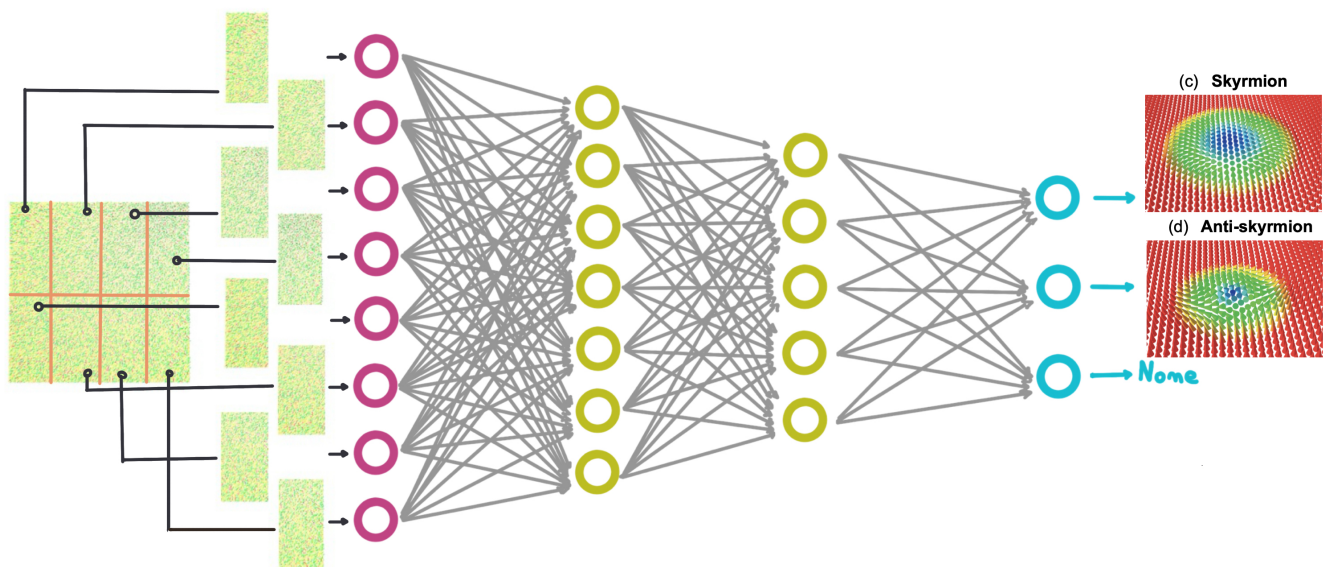


Figure 1: Simulation results showing a disordered spin texture. In our implementation, the vector field could be the magnetization field, the gauge field or the displacement field. To each vector component corresponds a neuron in the input layer. Then several hidden layer of different size may be defined. As an output, the NN can give information about the chiral nature of the magnetic texture as well as its boundary. In this particular example, we show in our preliminary result that a skyrmion or an antiskyrmion may be recognized. This approach can be used to recognized topological textures *in-situ*.

To tackle these challenges, our work relies on three core elements. The first is the generation of dynamics for magnetic topological structures. This is achieved through the implementation of algorithms within the Matjes program developed at TOM research unit [6]. The second element is the automation of the creation of the database required for the training of neural networks. This enables us to train different types of network. The last element is the development of optimized neural networks, both in terms of intrinsic structural design and architectural configuration, within Matjes.

The three core elements are connected to each other as represented in Fig. 1. The atomistic simulations provides us vector field samples as the one on the left of the figure 1. The information within the samples is divided into parts that serve as input for the first layer (purple neurons) of the neural network. The neural network applies its trained artificial intelligence when the information goes from the left to the right of the network. The last layer, composed of the blue neurons, provides the output of the network. In this case, the output is a skyrmion as represented on the right of Fig. 1. Our neural network is able to classify the topological magnetic structure inside the sample.

Acknowledgments

S.M. is a Postdoctoral Researcher (CR) of the Fonds de la Recherche Scientifique - FNRS (FR.S.-FNRS no. CR 1.B.324.24F). This work is supported by Excellence of Science project CONNECT number 40007563 funded by FWO and FNRS.

References

- [1] Albert Fert, Nicolas Reyren, and Vincent Cros. [Magnetic skyrmions: advances in physics and potential applications](#). *Nature Reviews Materials* 2, 17031 (2017).
- [2] Ulrike Ritzmann, Stephan von Malottki, Joo-Von Kim, et al. [Trochoidal motion and pair generation in skyrmion and antiskyrmion dynamics under spin-orbit torques](#). *Nature Electronics* 1, 451–457 (2018). eprint: [1803.00534](#).
- [3] Ulrike Ritzmann, Louise Desplat, Bertrand Dupé, Robert E Camley, and Joo-Von Kim. [Asymmetric skyrmion-antiskyrmion production in ultrathin ferromagnetic films](#). *Physical Review B: Condensed Matter and Materials Physics* 102, 174409 (2020). eprint: [2007.10749](#).
- [4] Christian H. Back, Vincent Cros, Hubert Ebert, et al. [The 2020 Skyrmionics Roadmap](#). *Journal of Physics. D, Applied Physics* 53 (2020).
- [5] Bertrand Dupé, Christian Kruse, Tobias Dornheim, and Stefan Heinze. *How to reveal metastable skyrmionic spin structures by spin-polarized scanning tunneling microscopy*. 2016.
- [6] P.M. Buhl, L. Desplat, M. Boettcher, S. Meyer, & B. Dupé. *Matjes*. Version 1.1.0. 2024.

Convergence: A Flexible Tool for Developing Materials at SPINTEC

Gwenaël Atcheson^{1,*}, Miguel Rubio-Roy¹, Md-Rejaul Karim¹, Stéphane Auffret¹, and Jérôme Faure-Vincent¹

¹Univ. Grenoble Alpes, CNRS, CEA, SPINTEC, Grenoble, France

*gwenael.atcheson@cea.fr

Spintronics research is built upon materials. The humble magnetic tunnel junction (MTJ) has seen decades of study [1], from subtle improvements through tweaking of compositions and layer dimensions, to leaps in performance made possible through the development of new materials (such as Heuslers [2-4]) and material combinations (such as the Fe/MgO interface [5]). Spintronics and magnetics research has been the driver of the big-data revolution, and continues to push increased connectivity and performance in all areas of information technology and science. The future of spintronics includes low-energy MRAM [6] and in-memory computing, as well as breakthrough neural network systems [7], all of which requires building a foundation for the exploitation of properties that new and novel materials can bring to our research. This depends not only on understanding of the materials themselves, but also the ability to produce and develop such materials in a flexible environment, where fast prototyping is key.

Due to its scalability, sputtering is the standard physical vapour deposition (PVD) technique for depositing a variety of materials and devices, ranging from hard coatings to complex multilayer active devices. Co-sputtering allows for the precise control of film stoichiometry by controlling the deposition rate of each target, either elemental or an alloy. Other properties such as structure and morphology are controlled by a complex interplay of sputter power, chamber pressure, deposition temperature and post-annealing steps. Optimising films for application means balancing between ideal properties of single films and the requirements of device structures, as well as further developing standard industry processes to be compatible with new materials.

With increased performance requirements from MTJs and spintronics research, the team at SPINTEC developed the Convergence tool, shown in Fig 1, to meet the needs of future research and explore new material systems. Based on a confocal design, the system is capable of sputtering from eight targets, and up to four simultaneously, on 100 mm wafers. Deposition across the wafer can be uniform, or with a wedge in any arbitrary direction. Using MEIVAC MAK2 magnetrons, the system is capable of depositing magnetic and non-magnetic materials, dielectrics via RF power, as well as reactive sputtering with oxygen and nitrogen gas. The custom design allows for expansion and modification of the system's capabilities, including a new high-power heater currently under construction, for oxygen-compatible high-temperature depositions. Using a robotic distribution chamber also permits expansion to include extra process chambers, allowing us to further increase the capabilities of the system.

As a co-sputter tool, the Convergence is key in the development of materials for emerging topics in SPINTEC, in particular for anti-ferromagnetic and altermagnetic materials, including Mn_3Sn , Mn_5Si_3 , and other Mn-based materials, as well as Heusler alloys (Co_2MnSi), and hard magnetic materials ($\text{L1}_0/\text{L1}_2$ CoPt, FePt). In addition, the system allows fast prototyping of multi-layer systems with atypical materials which can be transferred to systems with mature MTJ growth capabilities.

Acknowledgments

The Convergence was funded by CNRS and Grenoble INP (Univ. Grenoble Alpes).

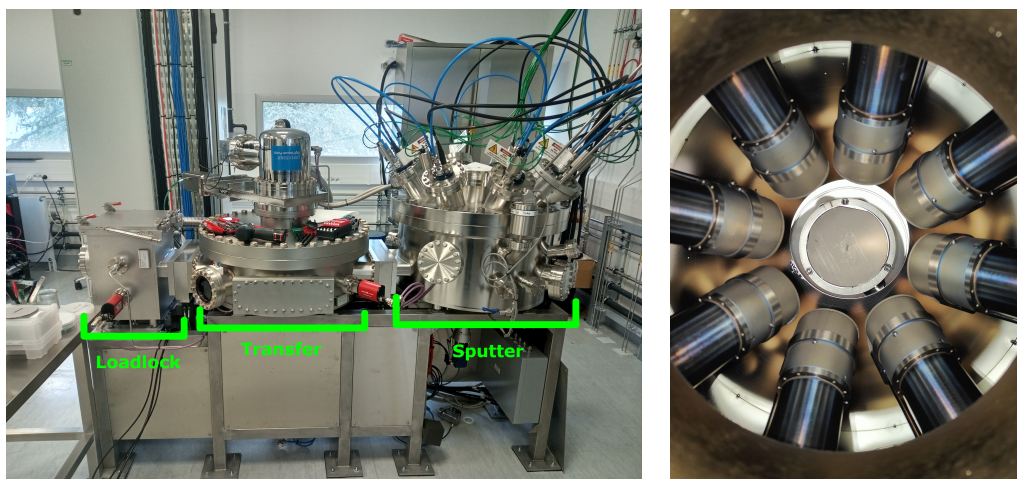


Figure 1: Left: The Convergence deposition platform, with the different chambers indicated
Right: View inside the chamber from above the sample

References

- [1] S. A. Wolf, D. D. Awschalom, R. A. Buhrman, et al. [Spintronics: A Spin-Based Electronics Vision for the Future](#). *Science* 294, 1488–1495 (2001).
- [2] Takayuki Ishikawa, Hong-xi Liu, Tomoyuki Taira, et al. [Influence of film composition in Co₂MnSi electrodes on tunnel magnetoresistance characteristics of Co₂MnSi/MgO/Co₂MnSi magnetic tunnel junctions](#). *Applied Physics Letters* 95, 232512 (2009).
- [3] Benjamin Balke, Sabine Wurmehl, Gerhard H. Fecher, Claudia Felser, and Juergen Kuebler. [Rational design of new materials for spintronics: Co₂FeZ \(Z = Al, Ga, Si, Ge\)](#). *SCIENCE AND TECHNOLOGY OF ADVANCED MATERIALS* 9 (2008).
- [4] H. Kurt, K. Rode, M. Venkatesan, P. Stamenov, and J. M. D. Coey. [Mn_{3-x}Ga \(0 ≤ x ≤ 1\): Multifunctional thin film materials for spintronics and magnetic recording](#). *physica status solidi (b)* 248, 2338–2344 (2011).
- [5] S. Yuasa and D. D. Djayaprawira. [Giant tunnel magnetoresistance in magnetic tunnel junctions with a crystalline MgO\(001\) barrier](#). *JOURNAL OF PHYSICS D-APPLIED PHYSICS* 40, R337–R354 (2007).
- [6] Sabpreet Bhatti, Rachid Sbiaa, Atsufumi Hirohata, et al. [Spintronics based random access memory: a review](#). *MATERIALS TODAY* 20, 530–548 (2017).
- [7] J. Grollier, D. Querlioz, K. Y. Camsari, et al. [Neuromorphic spintronics](#). *NATURE ELECTRONICS* 3, 360–370 (2020).

Graphene/CoFeB-Based Heterostructures : Influence of Direct and Oxide-Separated Interfaces on Dynamic Magnetic Properties

Imane BERRAI^{1,*}, Wafa Alimi¹, Mohamed Belmeguenai¹, Yves Roussigné¹, P. A. Dainone², Hyunsoo Yang³, Yuan Lu², Samir Farhat¹, and Salim Mourad Chérif¹

¹*Université Sorbonne Paris Nord, Laboratoire des Sciences des Procédés et des Matériaux, CNRS, LSPM-LPR 3407, 99 Avenue J.-B. Clément, 93430 Villetaneuse, France*

²*Institut Jean Lamour, Université de Lorraine, CNRS UMR 7198, Campus ARTEM, 2 Allée André Guinier, BP 50840, 54011 Nancy, France*

³*Department of Electrical and Computer Engineering, National University of Singapore, 117576, Singapore*

**imane.berrai@lspm.cnrs.fr*

The integration of graphene (Gr) in spintronic devices has been shown to be effective in modulating the magnetic properties of ferromagnetic (FM) films as demonstrated by research conducted over the last decade [1]. In this work, the dynamic magnetic properties of graphene-based heterostructures in two geometries have been studied: (i) SiO₂/Gr/CoFeB/Cu : in this case the monolayer graphene (MLGr) is interfaced with the FM layer, and (ii) SiO₂/Gr/Oxide/CoFeB/Ta where MLGr is separated from the FM layer by an oxide barrier. We have shown in this study that the influence of MLGr on the given system persists in both cases, mainly through its intrinsic ripples, regardless of direct contact or oxide separation.

The structural properties of the heterostructures were investigated by Raman spectroscopy and HR TEM was used to analyze the interface quality. Dynamic magnetic properties have been studied using Brillouin Light Scattering (BLS) and Ferromagnetic Resonance (FMR) techniques. In SiO₂/Gr/CoFeB/Cu heterostructures, an increase in surface Perpendicular Magnetic Anisotropy (PMA) of about 23 % was observed (Figure 1-a). This enhancement is due to the following two mechanisms: a proximity effect (hybridization at the Gr/FM interface) and a geometric effect (ripples inherent to Gr). Conversely, in SiO₂/Gr/Oxide/CoFeB/Ta multilayers, where the Gr is separated from the FM by MgO or Al₂O₃ barriers, the PMA enhancement is mainly attributed to interface structural effects. An increase in the effective PMA constant by approximately 30 % was noted, as deduced from the decrease in BLS frequencies in the presence of Gr (Figure 1-b).

In SiO₂/Gr/CoFeB/Cu heterostructures, FMR measurements showed a significant increase in magnetic damping due to the contribution of two-magnon scattering (TMS), while no evidence of spin pumping contribution was observed. The TMS effect was found to be enhanced by a factor of three in the presence of graphene (see figure 2-a). In the presence of an oxide barrier, a notable increase in the damping constants, more pronounced with MgO, is also observed, suggesting a stronger influence of heterogeneities in the presence of MLGr (see figure 2-b). This finding is consistent with Raman and HRTEM results (see figure 2-c, 2-d et 2-e). Crucially, it is shown how the rippling of Gr plays an important role in determining the properties of these heterostructures. Furthermore, the frequency asymmetry of spin waves measured through BLS was weak, and an effective DMI constant of about 0.04 mJm⁻² in both cases was determined, indicating a weak interfacial DMI even in the presence of graphene [2].

This study establishes that the effect of Gr on the dynamic magnetic properties of FM films persists regardless of whether it is in direct contact or separated by an oxide barrier. The results thus provide an important insight into the engineering of Gr/FM interfaces for improved performance in spintronic devices.

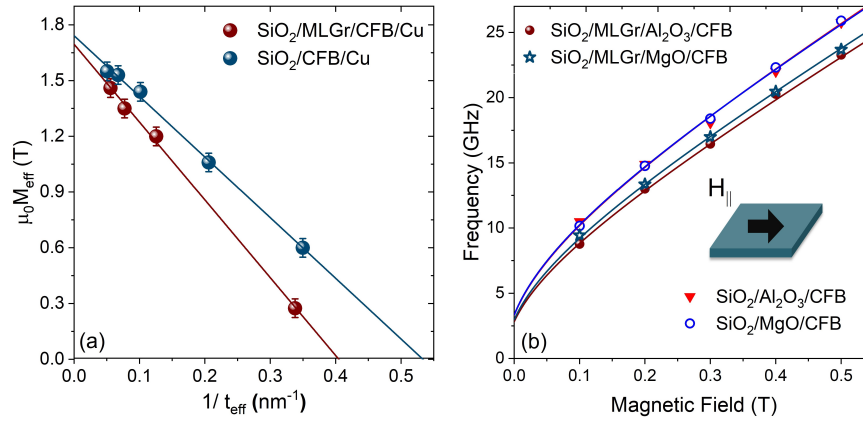


Figure 1: (a) Effective magnetization ($\mu_0 M_{\text{eff}}$) vs t_{eff}^{-1} of CoFeB films with or without Gr, (b) Field dependence of frequencies of Si/SiO₂/MLGr/oxide/CFB-based heterostructures.

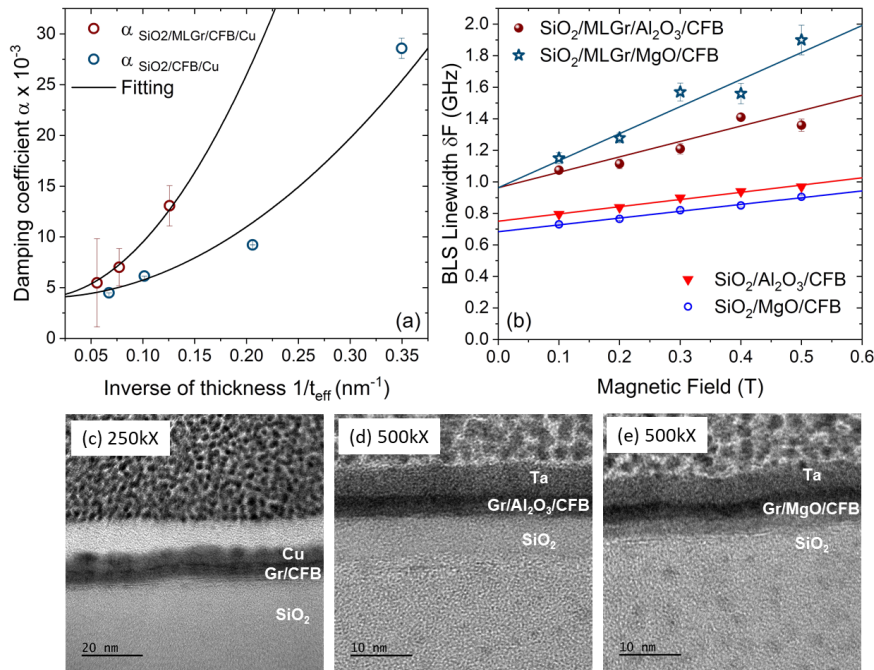


Figure 2: (a) Damping for SiO₂/CFB and MLGr/CFB plotted as a function of t_{eff}^{-1} ; and fitting curves with parabolic function as expected for TMS, (b) In-plane applied field-dependent BLS linewidth of the SiO₂/MLGr/OxB/CFB/Ta samples and their references, and Comparative HRTEM Imaging of (c) Si/SiO₂/MLGr/CFB, (d) Si/SiO₂/MLGr/Al₂O₃/CFB, and (e) Si/SiO₂/MLGr/MgO/CFB heterostructures.

References

- [1] Gaojie Zhang, Hao Wu, Li Yang, et al. [Graphene-based spintronics](#). *Applied Physics Reviews* 11 (2024).
- [2] Imane Berrai, Kyusup Lee, Mohamed Belmeguenai, et al. [Magnetic properties of CoFeB films grown on a single-layer graphene underlayer](#). *Physical Review Materials* 8 (2024).

Stochastic phase dynamics of an array of coupled, injection-locked spin-torque nano-oscillators

Matéo Ibarra Gomez¹, Arthur Courberand¹, Abderrazak Hakam¹, Chloé Chopin¹, Philippe Talatchian¹, Ursula Ebels¹, and Liliana D. Buda-Prejbeanu^{1,*}

¹Univ. Grenoble Alpes, CEA, CNRS, Grenoble INP, SPINTEC, Grenoble, France

*liliana.buda@cea.fr

The phase dynamics of coupled and/or injection locked arrays of spin torque nano-oscillators (STNO) can be harnessed for novel hardware concepts within unconventional computing schemes [1] or for smart communication applications [2]. Here we address the case of an array of weakly coupled STNOs that are simultaneously injection locked to an RF signal whose frequency is close to two times the free running STNO frequency. This $2f$ -injection-locking leads to a phase binarization (π -periodic values of the oscillator phase) that can be exploited as a binary spin to implement an Ising machine (IM) for solving combinatorial optimization problems (COP) [3]. For this purpose, the problem is mapped on the Ising Hamiltonian $\mathcal{H}_{Ising} = -\sum_{i,j} J_{ij} \sigma_i \sigma_j - \sum_i h \sigma_i$ that describes a 2D lattice of binary-valued spins σ_i, σ_j and where the coupling constants J_{ij} encode a given problem. The inherent convergence towards the global energy minimum can then be used as an algorithm to determine the solution of the COP.

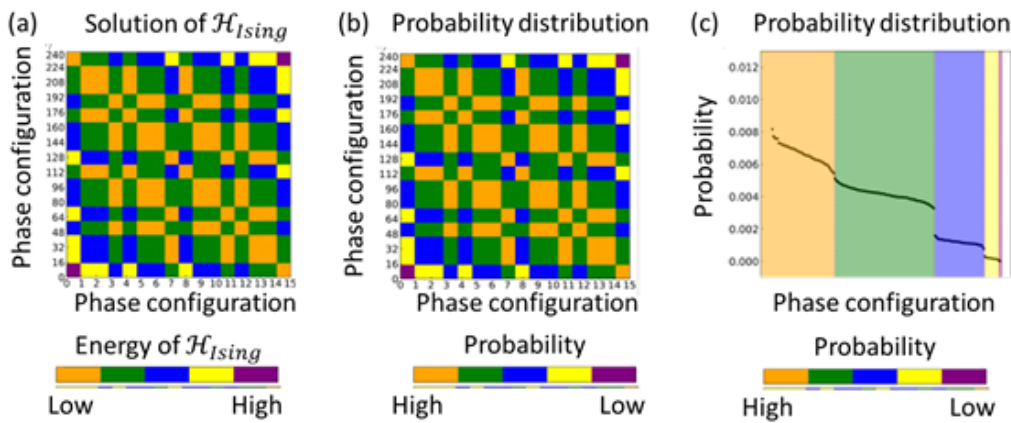


Figure 1: Comparison of the solution of (a) the Ising Hamiltonian \mathcal{H}_{Ising} for $N = 8$ spins, with 256 highly degenerate spin states, resulting in only 5 different energy levels indicated by the color code and (b) the probability distribution for $N = 8$ coupled identical STNOs for $V_{DC} = 1.5V$, RF source frequency $9.618GHz$ and a ratio of detuning to locking range $\delta/\Delta\Omega = 0.6$. The total simulation time is $200\mu s$ and the temperature $T = 50K$. The probabilities are grouped into five levels, given by the color code, according to (c), where the states of highest to lowest probability are plotted. Although in each group the probability is not the same, there are distinct jumps in the value of the probability that allows identification of the corresponding energy level. There is good agreement between (a) and (b). However, when changing the detuning sign, operating point (V_{DC}) or coupling constant, the agreement is less good. In (a) and (b) the 256 levels are arranged in a matrix with each line representing 16 levels, that are counted from left to right and continue in the next line, going from bottom to top.

To explore the stochastic phase dynamics within an Ising system based on in-plane magnetized STNOs, the coupled Landau-Lifshitz-Gilbert-Slonczewski equations including thermal fluctuations have been solved numerically. Combining these numerical simulations with analytical models provided by the non-linear auto-oscillator theory [4] allows one to extract the instantaneous phase of single and N coupled STNOs ($N \geq 2$). Due to thermal fluctuations, the phase of each STNO jumps stochastically between its two binary states and, therefore, phase state probabilities and phase correlations between different STNOs are extracted. For a single oscillator, both phase states are equiprobable in the isolated and coupled case. However, the probabilities of the 2^N collective phase states are unequal when the coupling between STNOs is activated. The probability distribution of the phase states of all coupled STNOs is analyzed as a function of the coupling parameters (strength, sign, type of coupling), frequency mismatch and operational point in order to determine the parameter range that provides the solution to an optimisation problem. Results are illustrated for the MaxCut problem ($J_{ij} = K < 0$) for which the energy levels of the corresponding Ising Hamiltonian \mathcal{H}_{Ising} are determined for all possible phase state combinations Fig. 1a. The phase states with lowest energy are expected to correspond to the phase states of highest probability Fig. 1b. We first present results for identical STNOs and then address the important question of non-identical STNOs to guide experimental implementations of an Ising machine and evaluate the feasibility of the concept.

Acknowledgments

This work was supported in part by the France 2030 government investment plan managed by the French National Research Agency under grant reference « PEPR SPIN – SPINTHEORY ANR-22-EXSP-0009 », by the French National Research Agency project SpinIM ANR-22-CE24-0004 and by the CEA project PTC-MINOS. Mateo Ibarra Gomez acknowledges financial support from the French Space Agency (CNES) and the European Union’s Horizon 2020 research and innovation programme under grant agreement No 800945 — NUMERICS — H2020-MSCA-COFUND-2017.

References

- [1] J. Grollier, D. Querlioz, K. Y. Camsari, et al. [Neuromorphic spintronics](#). *Nature Electronics* 3, 360–370 (2020).
- [2] A. Litvinenko, P. Sethi, C. Murapaka, et al. [Analog and Digital Phase Modulation and Signal Transmission with Spin-Torque Nano-Oscillators](#). *Physical Review Applied* 16 (2021).
- [3] T. Wang and J. Roychowdhury. [OIM: Oscillator-Based Ising Machines for Solving Combinatorial Optimisation Problems](#). *Unconventional Computation and Natural Computation* 11493, 232–256 (2019).
- [4] A. Slavin and V. Tiberkevich. [Nonlinear Auto-Oscillator Theory of Microwave Generation by Spin-Polarized Current](#). *IEEE Transactions on Magnetics* 45, 1875–1918 (2009).

Singulus advanced thin-film deposition sputtering system: Capabilities and Applications

Md Rejaul KARIM^{1,*}, Clarisse DUCRUET¹, Miguel RUBIO-ROY¹, Patrick WARIN¹, and Jérôme FAURE-VINCENT¹

¹Univ. Grenoble Alpes, CNRS, CEA, SPINTEC, Grenoble, France

*md-rejaul.karim@cea.fr

The evolution of thin-film deposition technologies has significantly transformed material science and device fabrication enabling the substantial development of next-generation spintronic devices. The Singulus sputtering system, equipped with 24 targets across two deposition modules, represents a cutting-edge solution for precise, scalable, and versatile thin-film deposition. Designed to handle 200mm wafers, the tool allows for the deposition of up-to 24 different materials in total (see Fig. 1) and is fully automated, featuring at least one loading slot capable of accommodating 25-wafer cassettes. In its final configuration, the system will incorporate dedicated oxidation-etching and thermal annealing chambers. This advanced system provides exceptional flexibility for depositing complex multilayer structures, supporting the integration of various materials such as metals, oxides, nitrides, and alloys within a single processing cycle. Capabilities like simultaneous co-sputtering, sequential deposition, and gradient layer formation enable precise control over film properties, including composition, thickness uniformity, and interface quality. The tool also enables the integration of heavy metals, antiferromagnet and oxides for advanced spintronic functionalities, such as perpendicular magnetic anisotropy and efficient spin current generation, etc. This poster highlights the sputtering system's applications in spintronics, including the deposition of films for magnetic tunnel junctions, spin valves, spin-orbit torque devices, magnetoresistive random-access memory, and high-performance memory and logic devices.

The tool ensures high reproducibility and uniformity (within wafer and wafer to wafer), making it ideal for both fundamental research and industrial-scale applications. This tool is also open for collaborations with academics and industrial partners.



Figure 1: The Singulus tool with two modules (left and right) and the transfer chamber (center) installed at Spintec.

Acknowledgments

Auvergne-Rhône-Alpes region (FEDER, CPER), Grenoble Alpes Métropole, EQUIPEX Nanofutur, PEPR SPIN, PEPR Electronique, Univ. Grenoble Alpes, CEA and CNRS.

Integration of new materials with strong spin-orbit coupling (van der Waals tellurides) for SOT-MRAM memories

Lucas Badeau^{1,2,*}, Alain Marty¹, Matthieu Jamet¹, Kévin Garello¹, and Bérangère Hyot²

¹Spintec, Grenoble, France

²CEA-Leti, Grenoble, France

*lucas.badeau@cea.fr

In the objective of decreasing the energy consumption of electronic devices, “spinorbitronics” appears as an interesting research field. In the last years, a new technology of non-volatile memories has emerged, called SOT-MRAM. It uses spin-orbit torque (SOT) to reverse the magnetic orientation of a ferromagnetic (FM) material in a magnetic tunnel junction, which stores the information 0 or 1. SOT-MRAM presents fast operation time and high endurance [1]. However, this technology faces many challenges, including the optimisation of charge-spin conversion in order to reduce the current required to achieve magnetization switching. A new class of materials, namely topological insulators (TI), appears as promising candidates to enhance energy efficiency of SOT-MRAM [2], due to their strong spin-orbit coupling caused by the presence of topological surface states in which it is possible to generate important spin accumulation.

The aim of this PhD work is to study the integration of tellurides-based topological insulators (Bi_2Te_3 , Sb_2Te_3 and $(\text{Bi}_x\text{Sb}_{1-x})_2\text{Te}_3$) in SOT devices. We will deposit ferromagnetic materials on sputtering-grown topological insulators, and study the magnetic and spin-orbit torques in these stacks. The CEA-Leti is developing TI growth by the industrial-friendly magnetron sputtering method over large area up to 300 mm.

The first part of this work consists in optimizing the surface quality of the topological insulators, before the deposition of the ferromagnet. The TI and ferromagnet being grown in two different sputtering machines, the samples have to be transported in air from one machine to the other. To keep the TI surface quality, the films are capped with protecting layers which need to be removed without damaging the TI layer, by annealing, ion beam etching or both. The crystallographic structure of the stack and surface quality are monitored in-situ by reflection high-energy electron diffraction (RHEED) (Fig. 1), and we perform material characterizations such as X-ray diffraction and atomic force microscopy to control the quality of the topological insulator and its surface morphology.

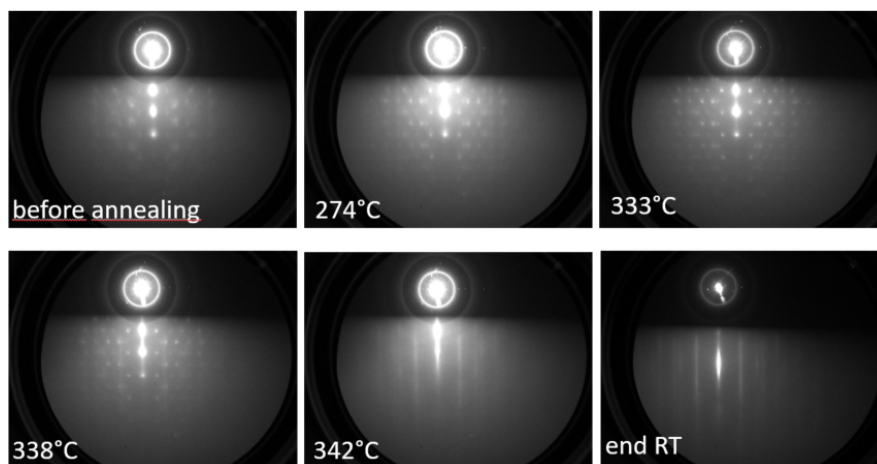


Figure 1: in-situ RHEED, during the evaporation of the capping layer. When the annealing temperature increases, we observe the diffraction pattern turning into vertical lines, which is the signature of a smooth crystal surface of the TI layer.

References

- [1] V. D. Nguyen, S. Rao, K. Wostyn, and S. Couet. [Recent progress in spin-orbit torque magnetic random-access memory.](#) *npj Spintronics* 2, 1–15 (2024).
- [2] Yi Wang and Hyunsoo Yang. [Spin–Orbit Torques Based on Topological Materials.](#) *Accounts of Materials Research* 3, 1061–1072 (2022).

Interference effects in the parametric excitation of spin waves in confined geometry

M. Massouras^{1,*}, G. Soares², R. Lopes-Seeger², S. Pierna³, J-P. Adam¹, T. Srivastava¹, T. Devolder¹, M. d'Aquino³, C. Serpico³, H. Merbouche³, G. de Loubens³, and J-V. Kim¹

¹Centre de Nanosciences et de Nanotechnologies, CNRS, Université Paris-Saclay, Palaiseau, France

²SPEC, CEA, CNRS, Université Paris-Saclay, Gif-sur-Yvette, France

³Università degli Studi di Napoli Federico II, Naples, Italy

*maryam.massouras@c2n.upsaclay.fr

Parametric excitation using radiofrequency fields allows populating specific spin wave modes in magnetic microstructures. In the context of unconventional computing using nonlinear spin wave dynamics [1, 2], it is essential to understand how excited modes influence the generation of other modes and whether transients dynamics play a role. We examine this question in simulation for 1- μm -diameter 50-nm-thick YIG disks [Fig. 1(a)] at 300K using the MuMAX3 code [3]. The system is under parametric excitation in parallel pumping configuration: both static field $B_0 = 50$ mT and sinusoidal radio-frequency b_{rf} field are applied along the same direction [Fig. 1(a)]. Using mode-filtering method projected onto precomputed eigenmode profiles [4, 5], we track the time evolution of any mode both population and power spectrum. Figure shows the main features for modes $\kappa = 11$ and 18 with eigenfrequencies $\nu_{11} = 2.885$ GHz and $\nu_{18} = 3.139$ GHz and critical threshold of $b_{\text{rf},\kappa,11} = b_{\text{rf},\kappa,18} = 0.70$ mT. We monitor the populated modes when excited parametrically first separately [Figs. 1(b-c)] then toggled with 500 ns delay in between [Figs. 1(g-h)]. On one hand, pumping at $\nu_{\text{rf}} = 2\nu_{11}$ with $b_{\text{rf}} = 1.05$ mT [Fig. 1(b)], targeted mode ψ_{11} is populated along with modes ψ_{17} and ψ_7 . Modes reach their saturation values (n_{κ}^{sat}) simultaneously with n_{11}^{sat} about two order of magnitude higher than n_{17}^{sat} and n_7^{sat} . When the pumping frequency is detuned [Fig. 1(d)] steady state values follow a sawtooth shape expected from the parametric excitation. On the other hand, pumping at $2\nu_{18}$ with same field [Fig. 1(c)], targeted mode ψ_{18} is populated along with mode ψ_{19} , modes that are close in eigenfrequencies ($\nu_{19} - \nu_{18} = 4$ MHz). Here the two modes have similar saturation values, n_{18}^{sat} and n_{19}^{sat} , but the latter reaches it after the former. Their steady values have sawtooth shape with different trends when frequency is detuned [Figs. 1(e-f)]. The goal after, is to determine whether modes associated with a second pump can be populated when a family of modes preexists in the system [Figs. 1(g-h)]. When $2\nu_{11}$ is pumped first, thus populating modes ψ_{11} , ψ_{17} and ψ_7 , additional pump $2\nu_{18}$ populates mode ψ_{18} and inhibits mode ψ_{19} while preexisting modes carry on. When the sequence is reversed, additional pump $2\nu_{11}$ populates all modes affiliated while preexisting mode ψ_{18} maintains its value and mode ψ_{19} is annihilated. The mode spectrogram also reveals that the annihilation is accompanied by the transient mode creation of two modes ψ_{12} and ψ_{29} . While mode power spectra can account for mode creations (we have $\nu_{11} + \nu_{29} = 2\nu_{18}$ and the negative frequency shift of mode ψ_{12} of a few MHz), the presence/absence of modes associated with the additional frequency can be explained by the mutual nonlinear frequency shift imposed by the first frequency. It is possible to estimate the frequency shift related to this quantity and predict the n_{κ}^{sat} values of the modes intended to populate. For modes $\kappa = 18, 19$ when exciting at $2\nu_{11}$ have a negative frequency shift of 1 MHz and 9 MHz respectively [shaded curves in Figs. 1(e-f)]. At $2\nu_{18}$, $n_{18}^{\text{sat, shifted}}$ yields non-zero value and $n_{19}^{\text{sat, shifted}}$ below thermal level value, explaining why mode ψ_{11} is populated mode ψ_{19} is inhibited. When exciting at $2\nu_{18}$, mode ψ_{11} has a negative frequency shift of 2 MHz, at $2\nu_{11}$ we have $n_{11}^{\text{sat, shifted}}$ yielding non-zero value again explaining why mode ψ_{11} is populated [Fig. 1(d)]. Toggling these nonlinear excitations goes beyond mode selection: full inhibition, annihilation and complete coexistence of modes and their satellites have been observed depending on pumping frequencies, sequence and supercriticality. Observations are similar for created modes, beyond the transient creation: created modes can take over for inhibited ones or follow stimulated 4-magnon scattering rules. This strong bearing on the overall dynamics can also be tuned by taking into account the characteristics of the nonlinear excitation either detuning or field amplitude which could be promising for information processing.

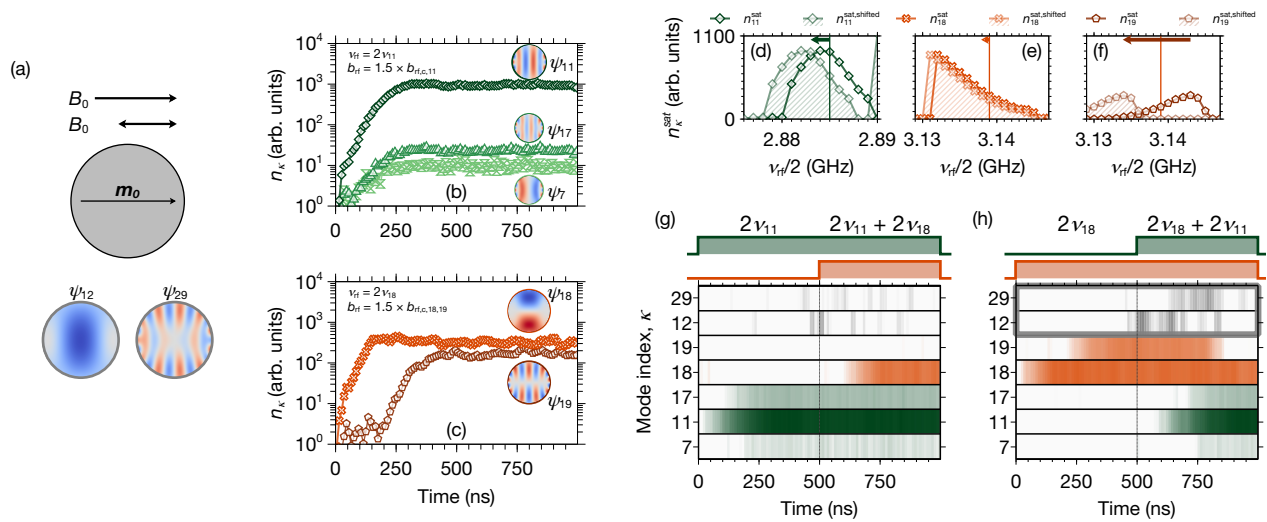


Figure 1: (a) Geometry and eigenmode profiles. Populated modes when pumping at (b) $\nu_{rf} = 2\nu_{11}$ and (c) $\nu_{rf} = 2\nu_{18}$ with $b_{rf} = 1.05$ mT. Evolution of saturation values with detuning under same field of (d) n_{11}^{sat} at $2\nu_{11}$ (solid filling) and $n_{11}^{sat, shifted}$ when pumping at $2\nu_{18}$ (shaded filling), (d) n_{18}^{sat} and $n_{18}^{sat, shifted}$, (d) n_{19}^{sat} and $n_{19}^{sat, shifted}$ at $2\nu_{18}$ (solid filling) and shifted in presence of $2\nu_{11}$ (shaded filling). (c) Populated modes when excitations are toggled under sequence defined by a first excitation applied for 500 ns followed by the addition of a second pump for another 500 ns (see sketches) with (g) $2\nu_{11}$, $2\nu_{11} + 2\nu_{18}$ and reversed sequence (h) $2\nu_{18}$, $2\nu_{18} + 2\nu_{11}$.

Acknowledgments

This work is supported by the Horizon2020 Framework Programme of the European Commission under contract number 899646 (k-Net).

References

- [1] Lukas Körber, Christopher Heins, Tobias Hula, et al. Pattern recognition in reciprocal space with a magnon-scattering reservoir. *Nature Communications* 14, 3954 (2023).
- [2] Joo-Von Kim and Hugo Merbouche. Stimulated magnon scattering by non-degenerate parametric excitation. *Applied Physics Letters* 125, 122401 (2024).
- [3] A. Vansteenkiste, J. Leliaert, M. Dvornik, et al. The design and verification of MuMax3. *AIP advances* 4 (2014).
- [4] Maryam Massouras, Salvatore Perna, Massimiliano d'Aquino, Claudio Serpico, and Joo-Von Kim. Mode-resolved micromagnetics study of parametric spin wave excitation in thin-film disks. *Physical Review B* 110, 064435 (2024).
- [5] Massimiliano d'Aquino, Claudio Serpico, Giovanni Miano, and Carlo Forestiere. A novel formulation for the numerical computation of magnetization modes in complex micromagnetic systems. *Journal of Computational Physics* 228, 6130–6149 (2009).

Embedded nano-magnets for thermoelectric applications

Joseph Moreau^{1,*}, Stéphane Pailhès¹, Olivier Boisron¹, Régis Debord¹, Agnès Piednoir¹, Alice Berthelot¹, and Florent Tournus¹

¹*institut Lumière Matière, Université Claude Bernard Lyon 1, Villeurbanne, France*

**joseph.moreau@univ-lyon1.fr*

In a context of energetic crisis, significant efforts are being devoted to developing new solutions for energy generation and recuperation. In this context, thermoelectricity stands its ground by bringing reliable, noiseless and compact devices on the table. Still, fundamental limitations in the efficiency persist, coming from the inherent physical properties of the materials. Indeed, when it comes to characterizing performances of thermoelectric materials, one quickly gets in touch with the thermoelectric figure of merit $zT = \frac{\sigma S}{\kappa}$, imposing very small conversion yields for usual materials. Recently, experimental and theoretical progress in the synthesis and comprehension of low dimensionality materials gave hopes to investigate this new horizon with unconventional materials to propose systems taking advantage of low dimensional effects and nano-structuration. Among these systems, the inclusion of metallic nanoparticles allows optimization of the materials on different fronts [1], [2].

In the meantime, the idea of adding the spin degree of freedom to the optimization of thermoelectric material has become a hot topic [3], [4]. Taking advantage of these two trends, Zhao et al. [3] demonstrated experimentally that the inclusion of magnetic nanoparticles within a thermoelectric matrix could significantly enhance performances, suggesting in the same time that the magnetic state of the nanoparticle assembly may provide a means to control the thermoelectric properties of such complex materials. Despite these experimental findings, this topic remains largely unexplored, with no clear trend predicting which thermoelectric properties benefit from magnetic nanoparticle inclusions [2], and this work takes place in the global effort to rationalize these effects, by introducing a new model system to investigate them.

The nano-composite system we propose is composed of a semiconducting matrix (thin-film of amorphous or nano-crystalline germanium) into which nanoparticles of transition metals (Co or Co based alloys) are co-deposited using the Low Energy Cluster Beam Deposition method (LECBD [5]) under ultrahigh vacuum conditions. With this original set-up, we are able to synthesize with a physical route nanoparticles of very precise sizes and controlled concentration (i.e. a controlled interparticle distance) inside the e-beam evaporated matrix. This provides an ideal platform for the in-depth study of the effects of the magnetic nano-inclusions on the transport properties of thin semi-conductor films of various crystallinity.

As a first step, significant effort has been dedicated to the reproducible synthesis of a germanium matrix using e-beam evaporation, with well controlled crystallinity, surface morphology and segregation between nanoparticles and matrix. This last point is mandatory as it allows the existence of second phase magnetic material inside of a non magnetic matrix, which has been confirmed by SQUID magnetometry and STEM-EDX, see Fig. 1.

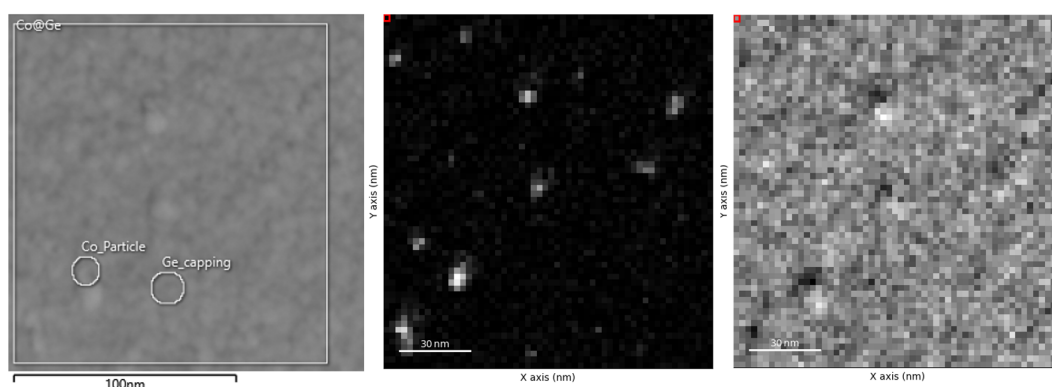


Figure 1: From left to right : Scanning Transmission Electron Microscopy of our system. Energy Dispersive X-ray Spectroscopy, for cobalt and germanium.

Besides, we have characterized the electronic transport properties of the Ge matrix by resistivity and Hall measurements. Other structural characterizations will be discussed, utilizing complementary experimental methods such as X-ray diffraction and reflectivity, Raman and Brillouin spectroscopy, Atomic Force Microscopy, Transmission and Scanning Electron Microscopy to ensure confidence in the control of the synthesis process. Ongoing transport measurements (thermopower, temperature dependant electrical conductivity and capacitive characterization), will also be presented, with a huge focus

on reproducibility of samples and measurements. The first results are showing tremendous increase in electrical conductivity and thermopower for doped samples.

To conclude, we will have a look at perspectives about systematic characterization of thermal conductivity by time-resolved thermoreflectance and field dependence of transport properties which is still lacking in the community for this kind of nanostructured systems.

References

- [1] Jessy Paterson, Sunanda Mitra, Yanqing Liu, et al. [Thermal conductivity reduction due to phonon geometrical scattering in nano-engineered epitaxial germanium](#). *Applied Physics Letters* 124, 181902 (2024).
- [2] Sebastian Sailer, Ruben Bueno Villoro, Samaneh Bayesteh, et al. [Grain boundary chemistry and increased thermoelectric performance in Bi₂Se₃-Fe₃O₄ nanocomposites](#). *Materials Today Physics* 46, 101477 (2024).
- [3] Wenyu Zhao, Zhiyuan Liu, Zhigang Sun, et al. [Superparamagnetic enhancement of thermoelectric performance](#). *Nature* 549, 247–251 (2017).
- [4] Weinan Zhou, Kaoru Yamamoto, Asuka Miura, et al. [Seebeck-driven transverse thermoelectric generation](#). *Nature Materials* 20, 463–467 (2021).
- [5] V. Dupuis, A. Hillion, A. Robert, et al. [Bottom-up strategies for the assembling of magnetic systems using nanoclusters](#). *Journal of Nanoparticle Research* 20, 128 (2018).

Propagation of spin waves in magnetic non-uniform textures

Greeshmani Doddi^{1,*}, Ping Che¹, Diane Gouéré¹, Nicolas Reyren¹, Wafa Ballouch¹, Sarah Manton¹, Imtiaz Noor Bhatti¹, Romain Lebrun¹, Vincent Cros¹, and Abdelmadjid Anane¹

¹Labaratoire Albert Fert, CNRS, Thales, Université Paris-Saclay, Palaiseau, France

*greeshmani.doddi@cnrs-thales.fr

Magnonics focuses on the study and manipulation of spin waves (SWs), which are collective excitations of electron spins in ordered magnetic materials. Devices based on Spin Waves encode data through their phase and amplitude and enable information transmission and processing over micrometer-scale distances without charge transport, effectively eliminating Joule heating. Their tunability through magnetic phase diagrams, controlled by external fields, magnetic anisotropy, or material compositions, makes them ideal for magnon-based reconfigurable signal processor and logic circuits.

Yttrium iron garnet (YIG) has been the main material platform for magnonics because of its ultra low magnetic damping $\alpha \approx 10^{-5}$ [1]. It has been shown that perpendicular magnetic anisotropy (PMA) induced by Bismuth doping [2] can stabilize magnetic textures such as worm-like domains or magnetic bubbles, making Bi-YIG an optimal candidate for reconfigurable magnonic devices [3] [4] (see Fig. 1). In this work, we investigated the propagation of SWs in Bi-YIG films with thickness ~ 20 nm, using simultaneously - magneto-Optical Kerr effect (MOKE) imaging and vector network analyzer (VNA)-based propagating spin wave spectroscopy (PSWS) between two inductive antennas (Fig. 2). A vectorial in-plane ($\mu_0 H_{ip}$) and out-of-plane ($\mu_0 H_{oop}$) fields are applied simultaneously and controlled independently to tune the magnetic phases. Polar-MOKE was used to image the out-of-plane components of the magnetization.

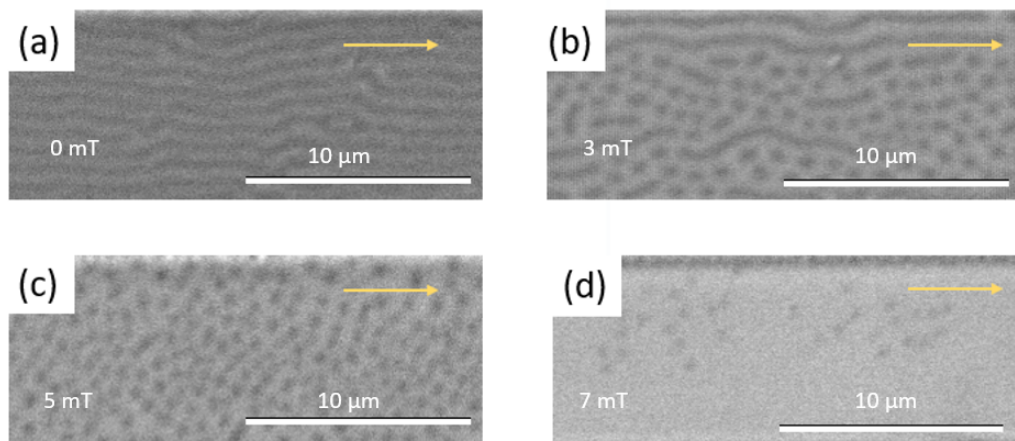


Figure 1: Magnetic imaging of BiYIG at zero in-plane (IP) field and at different out-of-plane fields (OOP). The domains are initialized by cycling from high IP field (60 mT) to -60 mT at a fixed OOP field. Due to this field history, even at 0 mT, a well-defined distribution of domains can be seen. Wide variety of magnetic states are observed: (a) Domains at $\mu_0 H_{oop} = 0$ mT, (b) Domains + bubbles at $\mu_0 H_{oop} = 3$ mT, (c) Bubble lattice at $\mu_0 H_{oop} = 5$ mT and (d) Isolated bubbles at $\mu_0 H_{oop} = 7$ mT. The yellow arrow indicates the direction of the initial in-plane field.

Different magnetic textures were observed - magnetic bubbles or domains or a mixture of both depending on the strengths of the in-plane (IP) field, out-of-plane (OOP) fields and the angle at which the in-plane field is applied (as displayed in Fig. 1). Using VNA-based PSWS, we characterized spin wave transmission, showing forbidden frequency band gaps in Fig. 2 (red frames) as a function of IP fields for the various OOP fields. The position of the band gaps is observed to vary depending on the strength of the OOP field. The group velocity of the SWs was also extracted from the phase data obtained from the imaginary part of S-parameters of VNA and compared to the Kalinikos-Slavin model [5].

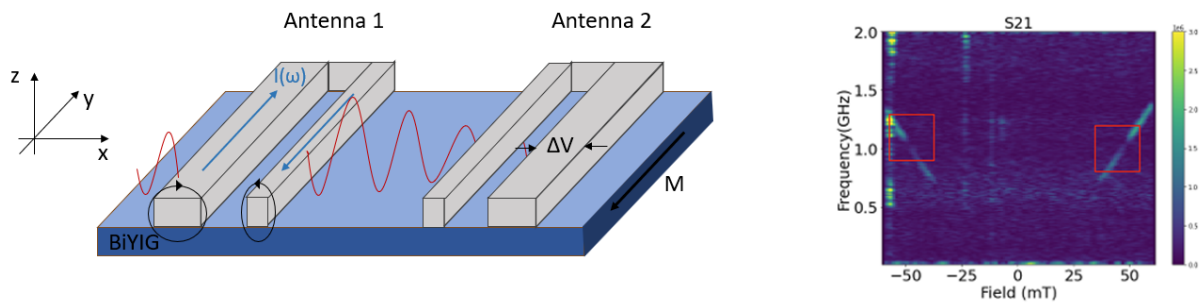


Figure 2: (a) Schematic illustration of propagating spin wave spectroscopy (PSWS): When microwave current $I(\omega)$ is injected to the antenna, a dynamic RF magnetic field is induced, which excites the spin wave. The SWs then propagate to the second antenna, where they are detected through voltage variation ΔV because of the varying magnetic field induced; (b) S_{21} magnitude of transmission spectrum for in-plane field spanning from -60 mT to 60 mT at zero out-of-plane field. The red frames show the bandgaps.

We compare the results with micromagnetic simulations using Mumax3 [6] software to unravel the SW propagation, magnetic domain behavior, and the interactions between magnetic textures and spin wave dynamics in different states in order to bridge the gap between experimental results and theoretical predictions.

Acknowledgments

This work has benefited from a government grant operated by the French National Research Agency as part of the France 2030 program, reference ANR-22-EXSP-0004 (SWING) and partially supported by Projet-ANR-22-CE30-0014 (DEMURGE).

References

- [1] V. Cherepanov, I. Kolokolov, and V. L'vov. [The saga of YIG: Spectra, thermodynamics, interaction and relaxation of magnons in a complex magnet](#). *Physics Reports* 229 (1993).
- [2] Lucile Soumah. "Pulsed Laser Deposition of Substituted thin Garnet Films for Magnonic Applications". PhD thesis. Université Paris-Saclay, 2019.
- [3] L. Soumah, N. Beaulieu, L. Qassym, et al. [Ultra-low damping insulating magnetic thin films get perpendicular](#). *Nat. Commun.* 9 (2018).
- [4] Y. Fan, M.J. Gross, T. Fakhrul, et al. [Coherent magnon-induced domain-wall motion in a magnetic insulator channel](#). *Nat. Nanotechnol.* 18 (2023).
- [5] B. A. Kalinikos, M. P. Kostylev, N. V. Kozhus, and A. N. Slavin. [The dipole-exchange spin wave spectrum for anisotropic ferromagnetic films with mixed exchange boundary conditions](#). *J. Phys.: Condens. Matter* 2 (1990).
- [6] A. Vansteenkiste, J. Leliaert, M. Dvornik, et al. [The design and verification of mumax3](#). *AIP Adv.* (2014).

Optimisation de la sensibilité de capteurs AMR $\text{La}_{1-x}\text{Sr}_x\text{MnO}_3$ sur substrat vicinal SrTiO_3 par intégration de concentrateurs de flux magnétique

Tagi Tagiyev¹, Thomas Brun², Victor Pierron¹, H  l  ne B  a², Claire Baraduc², St  phane Flament¹, and Laurence M  chin¹

¹Universit   de Caen, ENSICAEN, CNRS, Normandie Univ, GREYC (UMR 6072) - Caen, France

²Commissariat    l'  nergie atomique et aux   nergies alternatives, Spintec, Grenoble, France

*tagi.tagiyev@unicaen.fr , sflament@ensicaen.fr

Les capteurs    magn  toresistance anisotrope (AMR) r  alis  s    base de couches minces de manganite $\text{La}_{1-x}\text{Sr}_x\text{MnO}_3$ (LSMO) font partie des capteurs de champs magn  tiques comp  titifs, au m  me titre que les GMR et les TMR, en raison de leur faible bruit intrins  que [1]. La manganite LSMO est ferromagn  tique pour des concentrations de dopant de Sr comprises entre 0.25 et 0.5 et pour la fabrication de capteurs une couche mince   pitaixale d  pos  e par PLD (Pulsed Laser Deposition) est requise. Afin d'obtenir une r  ponse magn  tique sans hyst  r  sis, une anisotropie uniaxiale est induite dans le plan de la couche mince et le champ magn  tique    d  tecter est appliqu   selon la direction difficile d'aimantation. L'anisotropie magn  tique uniaxiale est induite dans la couche mince par l'utilisation d'un substrat vicinal de SrTiO_3 (STO) pr  sentant un angle vicinal de 4  . L'axe facile magn  tique est align   selon les bords des marches [2] [3]. La figure 1 montre deux configurations de capteurs dispos  s en pont de Wheatstone.

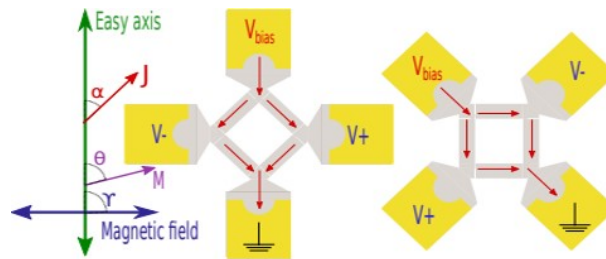


Figure 1: Capteur AMR LSMO dispos  s en ponts de Wheatstone

Le bruit basse fr  quence de ces couches minces de LSMO suit le mod  le empirique de Hooge [4]. Il s'av  re particuli  rement faible ce qui permet d'obtenir une bonne d  tectivit  . Ainsi pour un dopage $x=0.3$ (conduisant    une temp  rature de Curie d'environ 360K [5] nettement sup  rieure    la temp  rature ambiante), la meilleure d  tectivit   obtenue atteint $1.4 \text{ nT} \cdot \text{Hz}^{-1/2}$    1Hz et $240 \text{ pT} \cdot \text{Hz}^{-1/2}$    1kHz, pour une tension de polarisation de 20V [1].

Afin d'am  liorer la d  tectivit  , et donc le rapport signal sur bruit, l'int  gration de concentrateurs de flux magn  tique (MFC) est ici   tudi  e. Ces concentrateurs vont amplifier la densit   de flux magn  tique vue par le capteur. Ils sont r  alis  s par   lectrod  p  t dans un bain   lectrolytique, de couches de permalloy (NiFe) de 7  m, d'  paisseur d  pos  es sur un seed layer conducteur [6]. Afin de d  finir la g  om  trie optimale de ces concentrateurs, des simulations utilisant la m  thode des   l  ments finis,    l'aide du logiciel COMSOL, ont   t   men  es. Plusieurs g  om  tries ont   t     tudi  es. Diff  rentes tailles de concentrateurs et du gap s  parant les concentrateurs au milieu desquels se trouve le capteur, ont   t     tudi  es ainsi que diff  rentes formes visant    am  liorer la focalisation de la densit   de flux vers le capteur. Les r  sultats obtenus pour certaines g  om  tries ont   t   compar  es    des r  sultats de litt  rature [6] [7], ce qui a permis de valider la m  thode. De mani  re compl  mentaire, une   tude de l'homog  n  it   du champ appliqu   au capteur par les concentrateurs a   t   men  e.

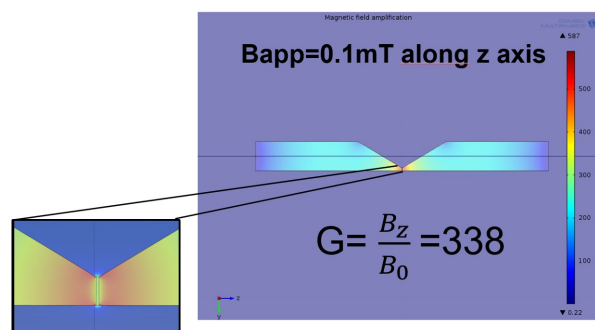


Figure 2: Simulation Comsol montrant une amplification du champ magn  tique de 338 fois pour cette structure

A titre d'exemple de résultat, pour un concentrateur de 10mm de longueur par 1 mm de largeur, un gain théorique de 340 est attendu pour une largeur de gap de 30 μ m (cf figure 2), tandis qu'un gain de 150 est attendu pour un capteur en pont de Wheastone de 15 μ m de coté et une largeur de gap de 10 μ m.

La réalisation de ces concentrateurs de flux est en cours. La caractérisation expérimentale visera à vérifier ces facteurs de concentration et étudier une éventuelle contribution de bruit basse fréquence supplémentaire de la part des concentrateurs. Il s'agira enfin d'évaluer si la détectivité en basse fréquence des capteurs suit bien la loi ci dessous (Eq 1), où D , S et Ω désignent respectivement la détectivité, la sensibilité et le volume du capteur, D_0 , S_0 et Ω_0 étant la détectivité, la sensibilité et le volume d'un capteur de référence de 300 μ m de coté, dépourvu de concentrateur.

$$\frac{D}{D_0} = \frac{S_0}{S} \sqrt{\frac{\Omega_0}{\Omega}} \quad (17)$$

Acknowledgments

Ce travail est soutenu par le plan d'investissement gouvernemental France 2030 géré par l'Agence nationale de la recherche française sous la référence PEPR SPIN -ADAGE ANR-22-EXSP-0006.

References

- [1] L. Enger, S. Flament, I. Bahtti, O. Rousseau, B. Guillet, et al. [Key Parameters for Detectivity Improvement of Low Noise Anisotropic Magnetoresistive Sensors Made of \$\text{La}_{2/3}\text{Sr}_{1/3}\text{MnO}_3\$ Single Layers on Vicinal Substrates](#). *ACS Applied Electronic Materials* 5, 125–132 (2023).
- [2] P. Perna, D. Maccariello, F. Ajejas, et al. [Engineering Large Anisotropic Magnetoresistance in \$\text{La}_{0.7}\text{Sr}_{0.3}\text{MnO}_3\$ Films at Room Temperature](#). *Advanced Functional Materials* 27, 1700664 (2017).
- [3] S K Chaluvadi, P Perna, F Ajejas, et al. [Thickness and angular dependent magnetic anisotropy of \$\text{La}_{0.67}\text{Sr}_{0.33}\text{MnO}_3\$ thin films by Vectorial Magneto Optical Kerr Magnetometry](#). *Journal of Physics: Conference Series* 903, 012021 (2017).
- [4] C. Barone, S. Pagano, L. Méchin, B. Guillet, and J.-M. Routoure. [Comment on "A case study on the scaling of 1/f noise: \$\text{La}_{2/3}\text{Sr}_{1/3}\text{MnO}_3\$ thin films"](#)[*J. Appl. Phys.* 113, 094901 (2013)]. *Journal of Applied Physics* 115 (2014).
- [5] J. Hemberger, A. Krimmel, T. Kurz, et al. [Structural, magnetic, and electrical properties of single-crystalline LSMO](#). *Physical Review B* 66, 094410 (2002).
- [6] Samuel Manceau, Thomas Brun, Johanna Fischer, et al. [Large amplification of the sensitivity of symmetric-response magnetic tunnel junctions with a high gain flux concentrator](#). *Applied Physics Letters* 123 (2023).
- [7] Xiaoming Zhang, Yu Bi, Guobin Chen, et al. [Influence of size parameters and magnetic field intensity upon the amplification characteristics of magnetic flux concentrators](#). *AIP Advances* 8 (2018).

Room temperature detectivity of anisotropic magnetoresistive sensors patterned in $\text{La}_{2/3}\text{Sr}_{1/3}\text{MnO}_3$ and in Cr_4Te_5 thin films

Tagi Tagiyev^{1,*}, Sandeep Kumar Chaluvadi², Pasquale Orgiani², Stéphane Flament¹, and Laurence Méchin¹

¹Université de Caen, ENSICAEN, CNRS, Normandie Univ., GREYC (UMR 6072) - Caen, France

²CNR-IOM – Istituto Officina dei Materiali, Consiglio Nazionale delle Ricerche, 34149, Trieste, Italy

*tagi.tagiyev@unicaen.fr

Anisotropic magnetoresistances (AMR) sensors use the change in electrical resistance of a ferromagnetic material when its magnetization is rotated relative to the current direction[1]. AMR sensors generally have lower sensitivity than Giant MagnetoResistance (GMR) and Tunnel MagnetoResistance (TMR) sensors but they are easier to fabricate since they need only one active layer. So far the most popularly used material for AMR sensors is Permalloy, an alloy of iron and nickel. We previously demonstrated that high sensitive AMR sensors can be fabricated using $\text{La}_{2/3}\text{Sr}_{1/3}\text{MnO}_3$ thin films. Detectivity as low as $200 \text{ pT}\cdot\text{Hz}^{-1/2}$ at 1 kHz and $1 \text{ nT}\cdot\text{Hz}^{-1/2}$ at 1 Hz could be measured at 310 K in 45 nm thick LSMO thin films deposited on vicinal SrTiO_3 (001) substrate of vicinal angle 4° [2]. Among other possible room temperature ferromagnetic candidates Cr_4Te_5 compounds have great potentials. It has been reported that Cr_4Te_5 epitaxial films showing ferromagnetic-metallic character at room-temperature could be deposited on Al_2O_3 (0001) substrates by Pulsed Laser Deposition (PLD) using a KrF laser with wavelength 248 nm [3], [4] or by PLD using a first harmonic Nd:YAG solid-state laser with wavelength 1064 nm [5].

Here we will present magnetoresistance and low frequency noise measurements measured in Wheatstone bridges patterned in 75 nm thick Cr_4Te_5 thin films deposited on Al_2O_3 (11-20) substrates. PLD using a first harmonic Nd:YAG solid-state laser with wavelength 1064 nm was used. The films were deposited at a temperature of 570°C under ultra-high vacuum (UHV) conditions ($<10^{-7}$ mbar), with a substrate-to-target distance of 8 cm and a laser repetition rate of 2 Hz. In contrast to the isotropic magnetic anisotropy that was obtained on Al_2O_3 (0001) substrates, magnetization versus magnetic field loops measured at room temperature by magneto-optical Kerr effect indicated that an uniaxial magnetic anisotropy could be obtained. We deposited gold layer and patterned the $\text{Cr}_4\text{Te}_5/\text{Al}_2\text{O}_3$ (11-20) film using laser lithography and ion beam etching using argon to define Wheatstone bridge with arm of width $100 \mu\text{m}$ and length $300 \mu\text{m}$. Figure 1 shows the voltage of the Wheatstone bridge as a function of magnetic field at 300 K for different bias voltages. Detectivity of about $5 \text{ nT}\cdot\text{Hz}^{-1/2}$ at 1 kHz and $1000 \text{ nT}\cdot\text{Hz}^{-1/2}$ at 1 Hz could be measured at 5V. Even if these values are still higher than the detectivity measured at 5V in LSMO Wheatstone bridges of the same dimensions at 310 K ($800 \text{ pT}\cdot\text{Hz}^{-1/2}$ at 1 kHz and $2 \text{ nT}\cdot\text{Hz}^{-1/2}$ at 1 Hz) these results are very promising. Further studies are needed to be performed versus film thickness, Wheatstone bridge dimensions and temperature and will be compared with results obtained in NiFe and LSMO.

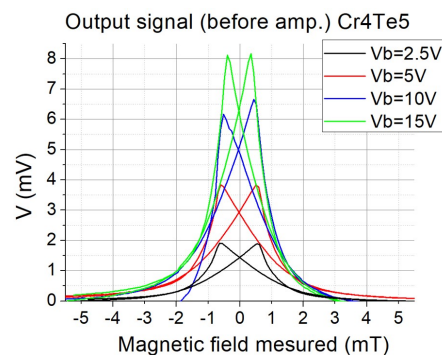


Figure 1: Wheatstone bridge voltage versus applied magnetic field at 300 K for various bias voltages

Acknowledgments

This work is supported by France 2030 government investment plan managed by the French National Research Agency under grant reference PEPR SPIN –ADAGE ANR-22-EXSP-0006.

References

- [1] McGuire T.R. and Potter R.L. [Anisotropic magnetoresistance in ferromagnetic 3d alloys](#). *IEEE Trans. Magn.* 11, 1018–1038 (1975).
- [2] Enger L.G., Flament S., Bhatti I.N., et al. [Key Parameters for Detectivity Improvement of Low Noise Anisotropic Magnetoresistive Sensors Made of \$\text{La}_{2/3}\text{Sr}_{1/3}\text{MnO}_3\$ Single Layers on Vicinal Substrates](#). *ACS Applied Materials and Interfaces* 5, 729–739 (2023).
- [3] Wang J., Wang W., Fan J., et al. [Epitaxial growth and room-temperature ferromagnetism of quasi-2D layered \$\text{Cr}_4\text{Te}_5\$ thin film](#). *J. Phys. D: Appl. Phys.* 55, 165001 (2022).
- [4] Wang W., Fan J., Liu H., et al. [Fabrication and magnetic–electronic properties of van der Waals \$\text{Cr}_4\text{Te}_5\$ ferromagnetic films](#). *CrystEngComm* 24, 674 (2022).
- [5] Chaluvadi S.K., Chalil S.P., Jana A., et al. [Pulsed Laser Deposited \$\text{Cr}_4\text{Te}_5\$ thin films: a quasi-two-dimensional ferromagnetic material](#). *2023 IEEE Nanotechnology Materials and Devices Conference (NMDC)*, 463–464 (2023).

Magnetolectric coupling reprogrammed magnonic waveguides in multiferroic/ferromagnetic heterostructure

Ping Che^{1,*}, Amr Abdelsamie¹, Sali Salama², André Thiaville³, Romain Lebrun¹, Karim Bouzehouane¹, Stéphane Fusil¹, Vincent Garcia¹, Agnès Barthélémy¹, Aymeric Vecchiola¹, Jean-Paul Adam², Vladislav Demidov⁴, Paolo Bortolotti¹, Abdelmadjid Anane¹, and Isabella Boventer¹

¹Laboratoire Albert Fert, CNRS, Thales, Université Paris-Saclay, 91767 Palaiseau, France

²Centre de Nanosciences et de Nanotechnologies, CNRS, Université Paris-Saclay, 91120, Palaiseau, France

³Laboratoire de Physique des Solides, Université Paris-Saclay, CNRS UMR 8502, Orsay, France

⁴Institute of Applied Physics, University of Muenster, Corrensstrasse 2-4, 48149, Muenster, Germany

*ping.che@cnrs-thales.fr

To date, the ever-increasing use of computers and especially the advent of new tools using artificial intelligence (AI) lead to an exponential increase in the world's power consumption. Additionally, classical semiconductor technology (CMOS) is reaching its limits in terms of performance and size. At the core of any conventional computing device are logical circuits and, therefore, new approaches for logic devices are required. Magnons, the quanta of spin waves, are the associated quasiparticles of collective excitations in a magnetically ordered material. The information is encoded and processed using rather the spin than the electronic charge, thus Joule heating is significantly reduced especially in magnetic insulators [1]. Therefore, magnonic logic devices have been identified as promising candidates to provide solutions in terms of performance and efficiency while scaling down to the nanoscale and operating across a wide frequency range from the GHz to the THz for the next-generation computing devices, e.g. magnonic logic devices. Such devices have been already successfully realized, ranging from magnon majority gates, magnonic directional couplers to magnon transistors and inversely designed magnonic demultiplexers [2-5]. However, to date, the realization of fully reconfigurable, voltage-controlled and programmable on-chip magnonic devices is compulsory to fully harness the immense potential of magnonic logic and neuromorphic computing devices.

With our findings, we suggest to employ the impact of the magnetolectric (ME) coupling on the spin wave propagation in nanometer thick multiferroic/ferromagnetic heterostructures. We use a heterostructure from 34 nm-thick multiferroic BiFeO₃ grown on 21 nm-thick La_{0.67}Sr_{0.33}MnO₃ on a NdGaO₃ (NGO) (001)_o orthorhombic substrate (illustrated in Fig. 1a). By controlling the applied voltage to change the orientation of the ferroelectric polarization state (in-plane and out-of-plane) for different customized geometries by means of piezoresponse force microscopy (PFM) (10 nm resolution) (Fig. 1b and c), it was shown that the spin wave dispersion can be altered [6]. In this work, we investigated the origin of the changes in spin wave dispersion and took it a step further by tailoring these changes, e.g. frequency and wavelength. We achieved the design of spin waveguides merely by carefully imprinting areas of identical ferroelectric polarization in the multiferroic layer into the desired geometry. We used Brillouin light scattering (BLS) spectroscopy to image both incoherent and coherent spin wave tuned by ME coupling. The study of the thermal magnons shows that the ME coupling changes the effective internal magnetization and hence leads to a frequency difference of 150 MHz for opposite ferroelectric polarization (Fig. 1e). Coherently excited magnon propagation along the defined waveguide is also observed. Controlled spin wave propagations in Damon-Eshbach configuration along tailored waveguides formed by the ME coupling to the multiferroic layer are evidenced. This allows us to control the spin wave propagation and opens further means for more complex magnonic structures for logic in this specific system in the future.

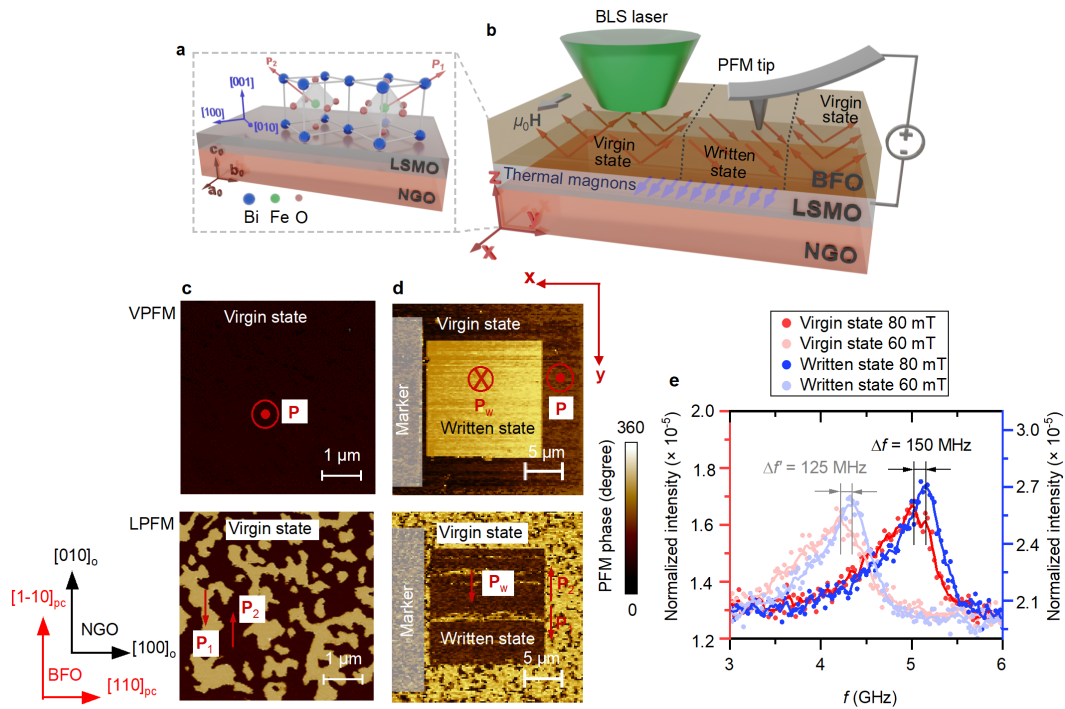


Figure 1: **a** and **b** Schematics of the BFO/LSMO heterostructure and the writing principle of the ferroelectric polarization state in BFO via piezoresponse force microscopy (PFM). Micro-focus BLS was utilized to detect the thermal magnon (green laser) and RF-excited magnons (blue laser). **c** and **d** PFM images of a written area compared to the virgin state both for the out-of-plane (upper) and the in-plane (bottom) component. **e** Thermal spectra of magnons in LSMO in the region corresponding to written and virgin states in **d**. All spectra are averaged scan over 4 locations normalized to the elastic peaks of each BLS scan.

Acknowledgments

We acknowledge the support from Horizon2020 Research Framework Programme of the European Commission under grant no. 899646 (k-NET), ANR TATOO (ANR-21-CE09-0033), and European Horizon 2020 TSAR (No. 964931) projects.

References

- [1] B. Flebus, D. Grundler, B. Rana, et al. [The 2024 magnonics roadmap](#). *J. Phys.: Condens. Matter* 36 (2024).
- [2] A. V. Chumak, Alexander A. S., and Burkard H. [Magnon transistor for all-magnon data processing](#). *Nat. Commun.* 5 (2014).
- [3] T. Fischer, M. Kewenig, Bozhko D. A., et al. [Experimental prototype of a spin-wave majority gate](#). *Appl. Phys. Lett.* 110 (2017).
- [4] Zidong Wang, Minghua Guo, Heng-An Zhou, et al. [Thermal generation, manipulation and thermoelectric detection of skyrmions](#). *Nature Electronics* 3, 672–679 (2020).
- [5] Shaohai Chen, James Lourembam, Pin Ho, et al. [All-electrical skyrmionic magnetic tunnel junction](#). *Nature* 627, 522–527 (2024).
- [6] H. Merbouche, I. Boverter, V. Haspot, et al. [Voltage-Controlled Reconfigurable Magnonic Crystal at the Sub-micrometer Scale](#). *ACS Nano* 15, 9775–9781 (2021).

Bi:YIG garnet thin films for spintronics

Jan Hnilica^{1,*}, E. Mossang¹, S. Grenier¹, S. Pizzini¹, W. Legrand¹, and L. Ranno¹

¹*Institut Néel, CNRS et Université Grenoble Alpes, Grenoble, France*

**jan.hnilica@neel.cnrs.fr*

Ferrimagnetic garnets such as $Y_3Fe_5O_{12}$ and its derivatives are materials with lowest magnetic damping α , allowing spin-wave propagation for very long distances. Implementing pure spin-injection in ferrimagnetic insulating oxides (YIG, Bi:YIG) is of interest because of their insulator properties. This can be realized by adding Pt electrodes, which allow spin injection into garnet films through the Spin-Hall Effect (SHE) [1]. Spin-orbit torque (SOT) induced magnetization reversal mediated by domain-wall (DW) motion has been recently shown by S. Hussain et al. [2] in TmIG garnet films. It is in general assumed that DW with a Néel component stabilized by Dzyaloshinskii–Moriya interaction (DMI) can be driven by SHE-SOT, however recent studies shows weak or no evidence of this effect in Pt/ garnet bilayers [3]. Thiaville et al. [4] have recently shown that DWs in garnet films with cubic symmetry are not of pure Bloch type and therefore can be driven by SHE-SOT.

Our objective is to demonstrate the presence of cubic anisotropy and determine its value for further SOT-induced DW motion measurements by studying in-plane (IP) Bi: YIG layers and perpendicularly magnetized YIG/Bi: YIG multilayers with tunable anisotropy.

Using a two-step synthesis (RF magnetron sputtering at room temperature followed by post-annealing), single and bilayers are prepared in the 5 - 100 nm thickness range. We have optimized $Bi_{1.5} : Y_{1.5}Fe_5O_{12}$ garnet fabrication, figure 1, a shows thermal dependence of the magnetization which agrees with the mean-field model of the Bi: YIG [5]. The material has the expected magnetic properties with respect to the model.

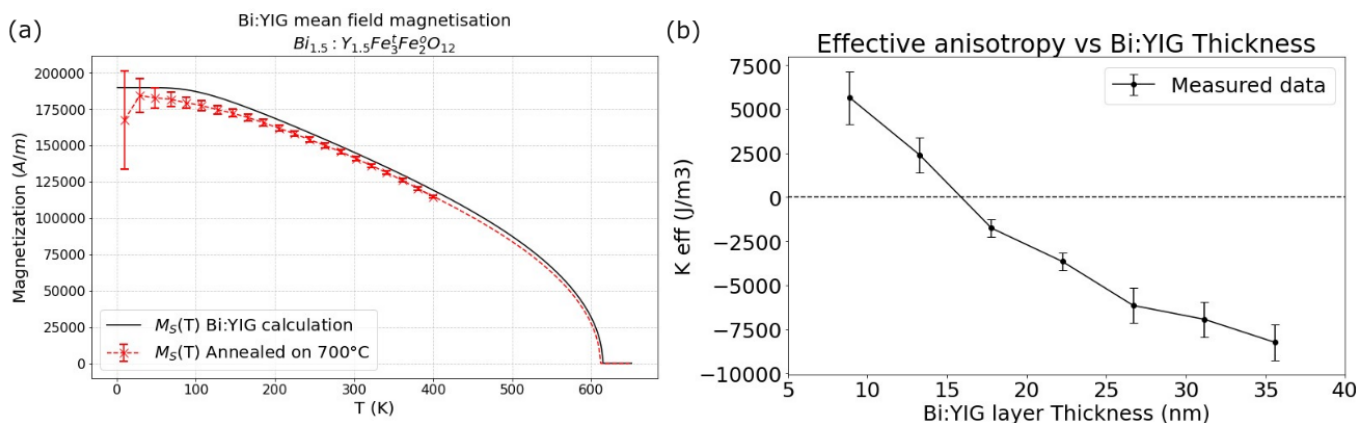


Figure 1: Figure 1: a) VSM-SQUID measured magnetization at different temperatures of 35 nm Bi:YIG/ sGGG plotted with a Mean-Field model. b) Dependence of effective anisotropy on Bi: YIG layer thickness.

Using sGGG substrates, heteroepitaxy is achieved with strained ferrimagnetic garnet. Magnetoelastic anisotropy related to lattice mismatch allowed us to fabricate an IP easy magnetization axis single layer, here Bi:YIG/ sGGG(111) and an Out-Of-Plane (OOP) one YIG/ sGGG(111). Growing (x nm) Bi: YIG/ (13 nm) YIG/ sGGG bilayers produce an effective material, which evidences an Out-Of-Plane to In-Plane reorientation close to 13.7 nm Bi: YIG as shown in Fig. 1, b. By tuning the Bi: YIG thickness it is thus possible to tune effective anisotropy.

5-nm thick Pt electrodes grown by magnetron sputtering, patterned using UV lithography allowed us to measure transport properties in the Hall and Magnetoresistance configurations evidencing spin-injection, on top of that in a Kerr microscope with 3D magnetic field (Fig. 2, a). Here we would like to address the role of cubic anisotropy in the OOP magnetized bilayers close to OOP-IP transition studied using P-MOKE and Spin-Magnetoresistance (SMR). Transversal SMR measurement at +/-10 mT IP field showing dominant 2-fold symmetry originating in spin absorption/ reflection into the transversal direction (Fig. 2, b). The amplitude saturates at 35 mT corresponding to the sample saturation field in the IP direction (Fig. 2, c). The Fourier transformation of the SMR signal with + 10 mT IP field shows dominant 2-fold symmetry originating from SMR and minor 3-fold symmetry frequency originating in the cubic anisotropy (Fig. 2, d).

To conclude, using a multilayer approach, the effective anisotropy could be tuned to a low value. This allows to evidence 3-fold symmetry originating in the cubic anisotropy term.

Work is on the way to model quantitatively and extract K_1 value of the cubic anisotropy and check the expected [001] orientations. Secondly, we would like to measure and quantify SOT acting on the garnet multilayers.

Acknowledgments

QuanG and MSCA co-funded PhD grant for these studies.

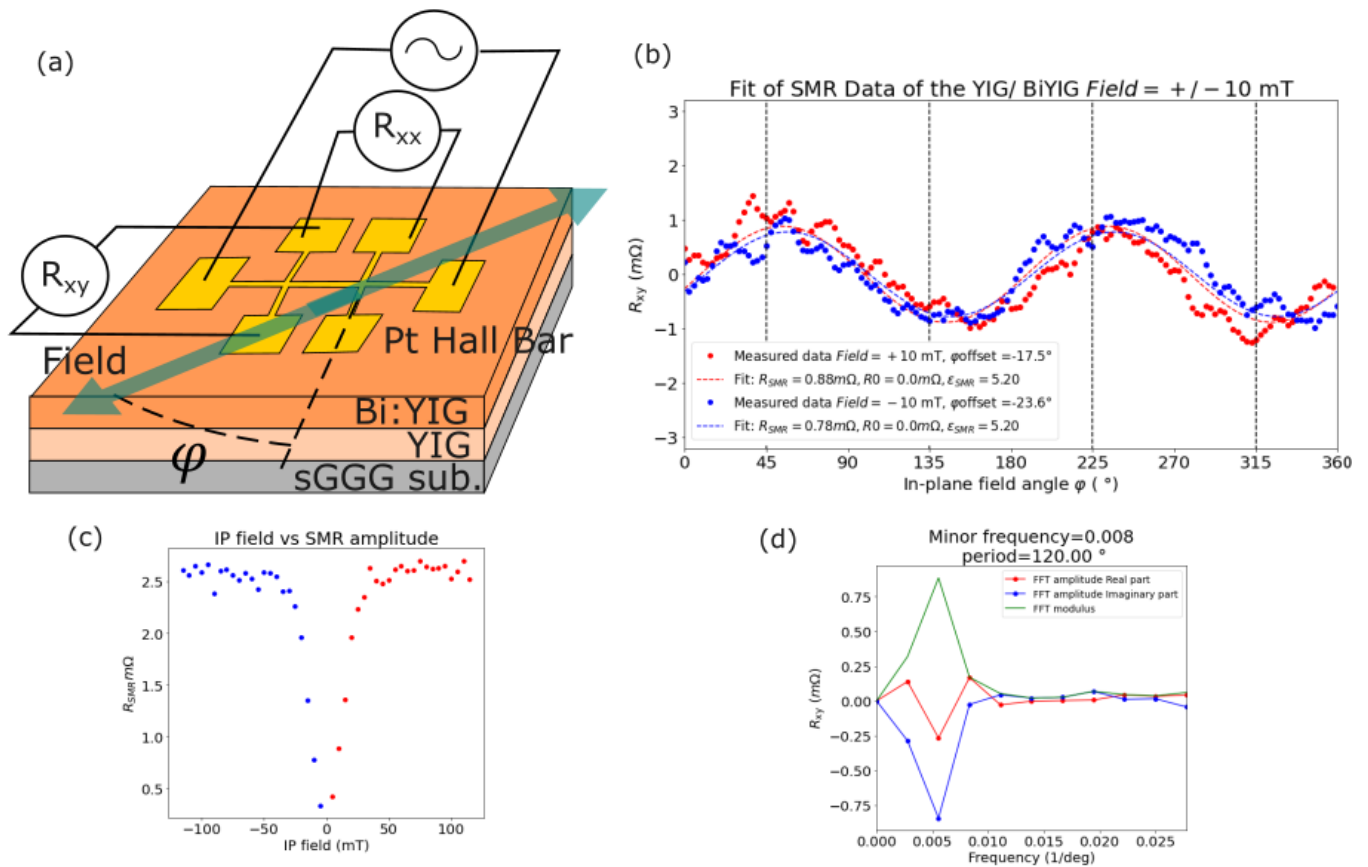


Figure 2: Figure 2: a) Scheme of the Spin-Magnetoresistance experiment in longitudinal (R_{xx}) and transversal (R_{xy}) geometry performed on Pt-Hall bar on OOP magnetized Bi: YIG/YIG/sGGG bilayer. b) Transversal SMR measurement performed at ± 10 mT IP applied magnetic field evidencing spin injection. c) SMR amplitude scaling with an applied IP field. d) Fourier transformation of Transversal SMR signal at +10 mT shows dominant 2-fold symmetry of SMR and minor 3-fold symmetry due to cubic anisotropy.

References

- [1] Christian Hahn, Grégoire De Loubens, Olivier Klein, et al. Comparative measurements of inverse spin Hall effects and magnetoresistance in YIG/Pt and YIG/Ta. *Physical Review B—Condensed Matter and Materials Physics* 87, 174417 (2013).
- [2] Sajid Husain, Nicholas F Prestes, Olivier Fayet, et al. Field-free switching of perpendicular magnetization in an ultrathin epitaxial magnetic insulator. *Nano Letters* 24, 2743–2750 (2024).
- [3] Hanchen Wang, Jilei Chen, Tao Liu, et al. Chiral spin-wave velocities induced by all-garnet interfacial Dzyaloshinskii-Moriya interaction in ultrathin yttrium iron garnet films. *Physical review letters* 124, 027203 (2020).
- [4] André Thiaville and Jacques Miltat. Spin-orbit torque driven domain wall motion in the absence of Dzyaloshinskii-Moriya interactions. *Europhysics Letters* (2024).
- [5] P Hansen, K Witter, and W Tolksdorf. Magnetic and magneto-optic properties of lead-and bismuth-substituted yttrium iron garnet films. *Physical Review B* 27, 6608 (1983).

Anomalous thermal drift of skyrmions in frustrated magnets under spin-orbit torques

Joo-Von Kim^{1,*} and Louise Desplat²

¹*Centre de Nanosciences et de Nanotechnologies, CNRS, Université Paris-Saclay, 91120 Palaiseau*

²*SPINTEC, CEA, CNRS, Université Grenoble Alpes, Grenoble INP, 38054 Grenoble*

**joo-von.kim@cnrs.fr*

Skyrmions are topological spin textures that exhibit particle-like dynamics under current-driven forces such as spin-orbit torques (SOT). In frustrated magnets, competing exchange interactions and the Dzyaloshinskii-Moriya interaction (DMI) can stabilize textures of different topologies, such as skyrmions and antiskyrmions [1]. These textures exhibit distinct motion under SOT, such as trochoidal trajectories and skyrmion-antiskyrmion pair generation, in addition to the usual rectilinear motion. This behaviour arises from a departure from the frozen-core limit, where the (anti)skyrmion helicity couples to the core position [2].

Here, we discuss the role of thermally-driven helicity dynamics in the Brownian motion of skyrmions [3]. Under weak DMI and SOT, the magnitude of the DMI, which governs the strength of the restoring force experienced by the helicity, relative to $k_B T$, significantly influences the thermal drift of the skyrmion core compared to its deterministic trajectories under weak SOT at zero temperature. This behaviour stems from the thermal drift and diffusion of the helicity under SOT, which is analogous to the well-known problem of Brownian motion in a tilted washboard potential. In this scenario, the helicity plays the role of an oscillator phase in a periodic potential with a linear force term.

Under weak SOT or strong DMI, we observe a “phase-locked” solution in which the helicity is pinned, resulting in rectilinear drift. Conversely, under strong SOT or weak DMI, we find a “free-running” solution, where the helicity varies continuously in time (akin to the Walker regime in domain wall motion) and results in an amplified Brownian diffusion of the skyrmion core. In between these two regimes, thermally-activated hopping of the helicity between energy minima occurs.

These results highlight the importance of helicity dynamics and may have bearing on dipole-stabilized bubbles for which drive-dependent skyrmion Hall angles [4] and low drift velocities have been reported [5].

Acknowledgments

This work was partially supported by the Agence Nationale de la Recherche under contract no. ANR-22-CE30-0014 (DeMI-uRGe).

References

- [1] Shi-Zeng Lin and Satoru Hayami. [Ginzburg-Landau theory for skyrmions in inversion-symmetric magnets with competing interactions](#). *Physical Review B* 93, 064430 (2016).
- [2] Ulrike Ritzmann, Stephan von Malottki, Joo-Von Kim, et al. [Trochoidal motion and pair generation in skyrmion and antiskyrmion dynamics under spin-orbit torques](#). *Nature Electronics* 1, 451–457 (2018).
- [3] Jacques Miltat, Stanislas Rohart, and André Thiaville. [Brownian motion of magnetic domain walls and skyrmions, and their diffusion constants](#). *Physical Review B* 98, 020405 (2018).
- [4] Kai Litzius, Jonathan Leliaert, Pedram Bassirian, et al. [The role of temperature and drive current in skyrmion dynamics](#). *Nature Electronics* 3, 30–36 (2020).
- [5] W Jiang, P Upadhyaya, W Zhang, et al. [Blowing magnetic skyrmion bubbles](#). *Science* 349, 283–286 (2015).

Magnetization dynamics in Bismuth-doped Yttrium Iron Garnet Films

Titiksha Srivastava^{1,*}, Jean-Paul Adam¹, Jamal Ben Youssef², Thibaut Devolder¹, and Joo-Von Kim¹

¹Centre de Nanosciences et de Nanotechnologies, CNRS, Université Paris-Saclay, 91120 Palaiseau, France

²LabSTICC, CNRS, Université de Bretagne Occidentale, Brest, France

*titiksha.srivastava@c2n.upsaclay.fr

Spin waves (SW) are collective oscillations in magnetic materials with their associated quantum of excitation called magnons (as phonons are to lattice vibrations). Nonuniform magnetic textures have been explored for generating and manipulating spin waves and generally offer an opportunity to expand the range of useful phenomena for applications. Such textures can appear spontaneously at the micro- and nanoscale in magnetic materials as a result of the competing interactions, namely, exchange, dipolar, and anisotropy. Magnetic textures like bubbles, stripes, and vortices have been shown to exhibit a rich diversity of magnetization dynamics[1]. However, the observation of their dynamics is quite challenging as it is difficult to stabilize these structures in materials with low damping.

In this regard, ferrimagnetic insulators such as Yttrium Iron Garnet (YIG) and Bismuth-substituted YIG (BiYIG) are well-known low damping materials for studying linear and non-linear magnetization dynamics. These garnets can also host magnetic textures[2] and can therefore facilitate the study of regimes that cannot be achieved in metallic systems.

In this study, we explore the magnetization dynamics of BiYIG films grown by Liquid Phase Epitaxy (LPE) on GGG substrates with thicknesses in the range of 120-180 nm. These films have an effective small out-of-plane anisotropy in the range of 3 mT to 12 mT as a result of an optimization of the growth conditions. In these samples, we first characterize the static properties using Polar-Kerr Microscopy (PMOKE) where we observe well defined stripe domains with a period of around 600 nm at near-zero fields as shown in Fig. 1(a). The observed stripe domain alignment depends on the history of the applied field direction.

For the dynamics, we performed microfocussed Brillouin Light Spectroscopy (BLS) measurements on BiYIG film as a function of in-plane magnetic field. The sample is saturated at 140 mT where we observe the Kittel mode and many other modes parallel to it. As we decrease the in-plane field, we see a softening of the Kittel mode and subsequent parallel modes, as shown in Fig. 1(b). Strikingly, we also see the appearance of new modes with optical characteristics (i.e. negative slope), resulting in a complex crossing of many modes in the frequency-field dispersion map. We performed BLS spectroscopy on different parts of the sample and observed that the sample was quite homogenous in the in-plane direction. X-Ray diffraction measurements on the sample indicated the same. We will discuss the origin of these multiple modes that seem to have acoustic and optical characteristics and interpret the observed complex dynamics using micromagnetic simulations.

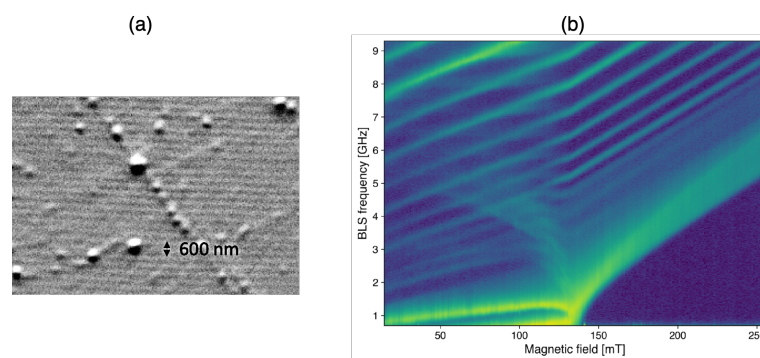


Figure 1: (a) Polar Kerr Microscopy image of stripe domains in BiYIG sample. (b) BLS spectra

Acknowledgments

This work was partially supported by the Agence Nationale de la Recherche (ANR) under Grant No. ANR 22HR2652 (DeMIuRGe)

References

- [1] T. Srivastava, Y. Sassi, F. Ajejas, et al. [Resonant dynamics of three-dimensional skyrmionic textures in thin film multilayers](#). *APL Materials* 11, 061110 (2023).
- [2] N. Vukadinovic, M. Labrune, J. Ben Youssef, et al. [Ferromagnetic resonance spectra in a weak stripe domain structure](#). *Phys. Rev. B* 65, 054403 (2001).

Enhancement of the current-induced torque by orbital torque

Greis Cipi^{1,*} and Stanislas Rohart¹

¹Laboratoire de Physique des Solides, Université Paris-Saclay, CNRS UMR 8502, 91405 Orsay Cedex, France

*greis.cipi@universite-paris-saclay.fr

Spin-orbit coupling has transformed our understanding of magnetism by giving rise to new emerging phenomena [1]. Of particular interest is the generation of spin currents from charge currents, for example using the Spin Hall effect (SHE). In a heavy metal (HM)/ferromagnetic (FM) stack, the spin accumulation at the interface exerts a torque on the magnetic layer, called spin-orbit torque (SOT), able to manipulate its magnetization. Recently, significant current-induced torques have been observed in systems featuring light metal [2]. Given the weak spin-orbit coupling (SOC) in light metals, this effect is more closely associated with the orbital moment of the electrons. Orbital current generation can arise from two mechanisms: the orbital Hall effect (OHE) and the orbital Rashba-Edelstein effect (OREE) [3]. The former originates through momentum-space orbital texture at the Fermi level, whereas the latter from inversion symmetry breaking, naturally present at surfaces and interfaces. As the orbital angular momentum cannot directly act on the magnetization, the orbital current arose by a charge current needs to be converted into spin current in a intermediate layer with strong SOC. Our objective is to explore this physics by investigating the materials that are source of orbital current, and the material used to convert the orbital current to a spin current.

In this study, we engineered stacks of Pt(2)/Co(1)/Ta(t)/Cu*(3) (nm), where Cu* represents the naturally oxidised Cu layer. Here, Cu is the light metal at the origin of orbital current: 3 nm is sufficiently enough to not completely oxidize the Cu layer, giving rise to a vertical oxidation profile. The Ta layer provides a layer with strong SOC to convert the orbital current into spin current. Its thickness varies between 2 nm and 6 nm in order to see when the orbital current is efficiently converted and injected into the FM layer below. The bottom Pt layer is a seed layer that promotes a (111) texture required to obtain a perpendicular magnetization of the Co layer. Its thickness is minimized to avoid a significant SOT contribution. The samples are grown by evaporation in ultra-high vacuum conditions at room temperature.

Detection of the magnetization can be done through transport measurements, using the Anomalous Hall effect (AHE). When current flows in the sample, a transverse voltage V_{AHE} arises, allowing to probe the perpendicular component of the magnetization m_z . Moreover, the applied current also induces changes in the magnetization direction from its equilibrium position, allowing the quantification of the current-induced torques. The equilibrium magnetization direction gives a signal proportional on the applied current. Instead, the current-induced magnetization changes scale as the square of the current. To differentiate these two contributions, an alternating current (AC) at low-frequency ω is used. This approach enables the observation of equilibrium properties at ω and current-induced effects at 2ω [4]. When an in-plane field is applied to the sample the static magnetization direction varies, enhancing the visibility of the current-induced perturbations at fields close to magnetic anisotropy field H_k .

Different current densities are sent to the samples, which were optically patterned into Hall crosses of 5 nm-width channels. Through a double lockin amplifier, the signal corresponding to the two harmonics are recorded. In Figure 1 the signals at different current densities are shown as shades of blue dots, and the orange line represents the fit performed, and represented as a function of the applied magnetic field. In Figure 1(a) the ω -signal is normalised by the current density, evaluated assuming a homogeneous flow through all the layers composing the stack. Under the assumption of the macrospin model, it is possible to extract the magnetic anisotropy field H_k , together with the AHE signal amplitude. In Figure 1(b) the 2ω -signal is normalised by the square of the current, as it is linked to the effect of its perturbations. The influence of the current is the strongest for applied fields close to H_k , with the peak amplitude predominantly influenced by the damping-like component of the torque H_{DL} .

The behaviour of H_{DL} as a function of the thickness of the Ta layer is shown in Figure 2. When the torque is generated by uniquely SOT, the damping-like torque is expected to monotonous increase until saturation for thicknesses greater than the spin diffusion length [2]. The orbital current is responsible of the peak for 5 nm of Ta, where a more efficient conversion of orbital current into spin current, and efficient injection in the FM layer occur. In addition, as compared to the literature where the orbital to spin conversion is performed using Pt, we obtain an opposite H_{DL} sign due to the opposite SOC signs of the two heavy metals. This thus corroborates the scenario where the orbital current needs to be converted into spin current through SOC.

This study highlights the importance of orbital effects in light metals on the manipulation of magnetization, and the effect of the heavy metals on its conversion. Additional works are on-going to better investigate the efficiency of this effect by exploring alternative light metals, like Ti, V and Cr.

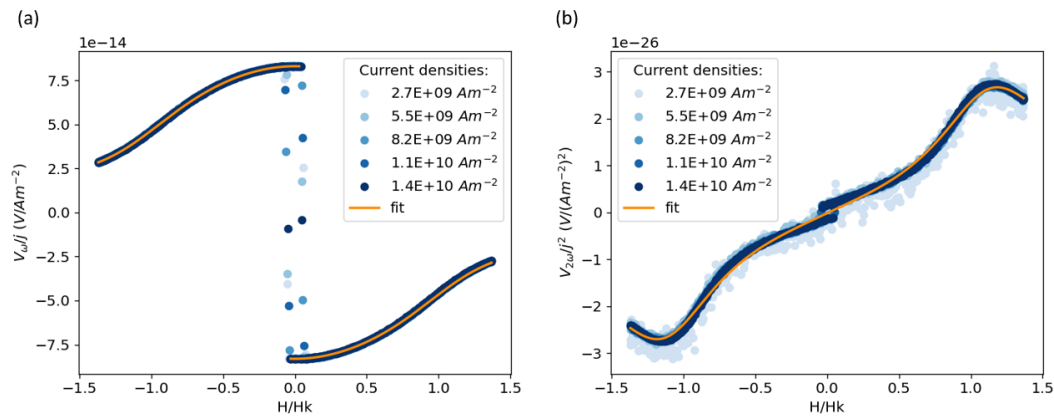


Figure 1: Normalized first (a) and second (b) harmonic signals (blue dots) for different current densities in damping-like configuration, and corresponding fits (orange line).

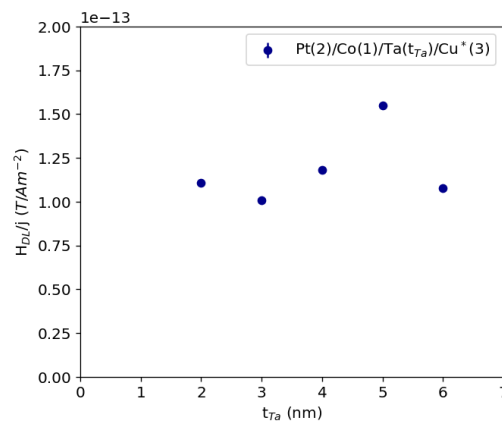


Figure 2: Damping-like field behaviour as a function of the Ta thickness. For 5 nm of Ta the orbital torque is efficiently converted into spin current and injected into the Co layer.

Acknowledgments

We acknowledge funding by France 2030 (moonshot project Chirex PEPR SPIN ANR-22-EXSP-0002).

References

- [1] Anjan Soumyanarayanan, Nicolas Reyren, Albert Fert, and Christos Panagopoulos. [Emergent phenomena induced by spin-orbit coupling at surfaces and interfaces](#). *Nature* 539, 509–517 (2016).
- [2] S. Krishnia, B. Bony, E. Rongione, et al. [Quantifying the large contribution from orbital Rashba-Edelstein effect to the effective damping-like torque on magnetization](#). *APL Materials* 12 (2024).
- [3] Dongwook Go, Daegeun Jo, Hyun-Woo Lee, Mathias Kläui, and Yuriy Mokrousov. [Orbitronics: Orbital currents in solids](#). *EPL (Europhysics Letters)* 135, 37001 (2021).
- [4] Masamitsu Hayashi, Junyeon Kim, Michihiko Yamanouchi, and Hideo Ohno. [Quantitative characterization of the spin-orbit torque using harmonic Hall voltage measurements](#). *Physical Review B* 89 (2014).

SOT- and Magnetic Field-Driven Domain Wall Dynamics

Ettore Angeli^{1,*}, Imtiaz N. Bhatti², André Thiaville¹, Abdelmadjid Anane², and Vincent Jeudy¹

¹Laboratoire de Physique des Solides, Université Paris Saclay, 91405 Orsay Cedex, France

²Laboratoire Albert Fert, CNRS, Thales, Université Paris Saclay, 91767 Palaiseau, France

*ettore.angeli@universite-paris-saclay.fr

The controlled manipulation of magnetic textures such as domain walls in thin films is important for the development of spintronic devices, like magnetic memories and logic. In this context, the study of DW driven by various torques [1] (magnetic field, Spin-Orbit Torque, Spin-Transfer Torque...) in materials with very low interaction between domain walls and disorder is particularly interesting. Recent results indicate how ultra-thin iron garnet films are characterized by depinning magnetic field which stands orders of magnitude lower than other classic ferromagnetic materials. In this work, we present a preliminary comparison between magnetic field- and Spin-Orbit Torque-driven DW dynamics on *BiYIG* (Bismuth substituted Yttrium Iron Garnet) ultra-thin films [2]; the study is focused on the possible link between the low-drive dynamical regimes (creep regime and depinning transition) for the two driving forces, with particular attention on how to model DW velocity accounting for possible spurious effects, as Joule heating.

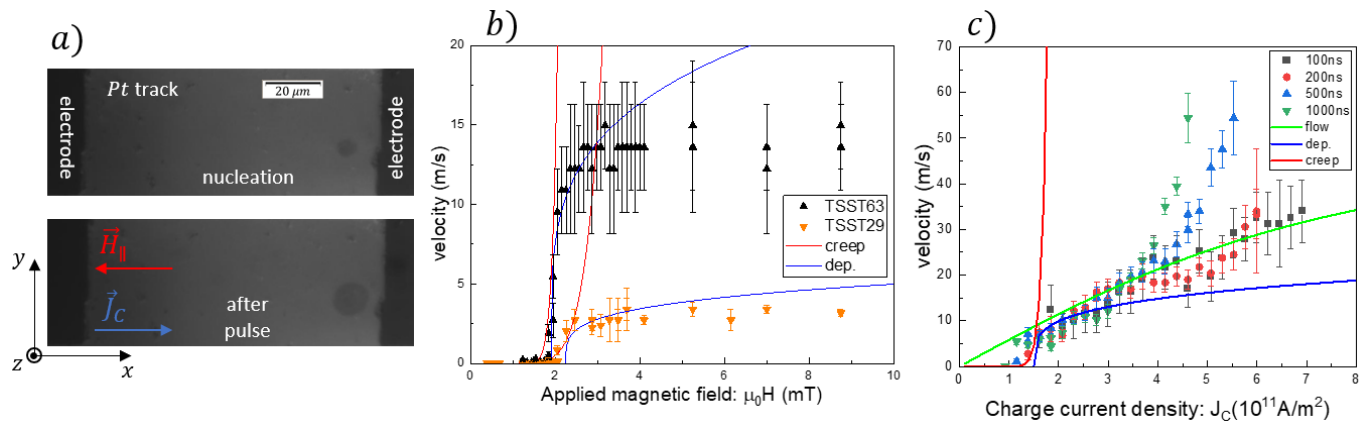


Figure 1: a) MOKE acquisitions showing nucleation and propagation of a circular domain wall by SOT. DW displacement is calculated as the distance Δx travelled by the DW during the charge current pulse duration Δt . b) DW velocity as function of applied magnetic field for two *BiYIG* ultra-thin samples with similar depinning fields. Highlight on creep regime and depinning transition. c) DW velocity as function of charge current pulse for one of the previous sample (TSST29), with different modelled dynamical behaviors. Highlight on the role of Joule heating at high drives.

In thin films, domain walls present a wide variety of dynamical behaviors, that depend on both the nature and magnitude of the driving force acting on them [3][4][5]. At high drive, domain walls are expected to follow strongly non-linear dissipative regimes, for which velocity depends on time evolution of the DW internal magnetization. The high-velocity regimes are generally difficult to reach, because of domain walls pinning by ubiquitous defects of magnetic materials. At low drive, the interaction between domain wall and defects is dominant. Dynamics is the result of the interplay between domain walls elasticity, interaction with disorder, and thermal activation. DW dynamics present universal behaviors, similar to those encountered in a large variety of other phenomena (contact lines in wetting, domain walls in ferroelectric materials, propagation of fractures in earthquakes...), which are described in the generic theoretical framework of disordered elastic systems. Pinned dynamics is characterized by two regimes [6]. For a driving force lower than depinning force f_d , DW velocity follows a thermally activated creep, with velocity scaling as an Arrhenius-like law $v \sim \exp(-\Delta E/k_b T)$, where $\Delta E \sim f^{-1/4}$. Approaching the depinning, the pinning barrier heights become comparable to thermal activation energy, and the effect of disorder starts to weaken. For $f \gtrsim f_d$, velocity follows a polynomial law $v \sim f^{1/4}$, which is smoothed by thermal rounding. A self-consistent model, developed in Ref. [6], allows to define a set of material dependent parameters which quantify the role of pinning in the material: depinning force, f_d , average pinning barrier height, $k_b T_d$ and depinning velocity v_d . Above depinning, domain walls enter the flow regime, for which pinning no longer contributes to DW dynamics.

DW dynamics produced by SOT and magnetic field pulses is reported in Fig. 1. In Fig. 1a) we show MOKE acquisitions of *BiYIG/Pt* bilayer. On the side are visible the two electrodes, that send charge current pulses in the *Pt* track. By Spin Hall Effect, along with an in plane magnetic field, it is possible to nucleate and displace DW (expansion & contraction). Subsequently, DW velocity is defined as the ratio between the displacement, Δx , and the current pulse duration Δt . In Fig. 1b), we present field-driven DW motion. The comparison with predictions of the self-consistent model allows us to identify the creep regime and depinning transition, as well as the dissipative regime corresponding to the velocity plateau. Both samples have low depinning field, $\mu_0 H_d \approx 2mT$. In Fig. 1c), we show SOT-driven motion, for different current pulses duration

(from 100ns up to 1μs). The different curves evidence Joule heating effect on DW dynamics. The curves for shorter pulse duration (100–200ns) can be superimposed, indicating no strong Joule heating. By increasing the pulse duration, velocity starts instead to strongly increase. Let us discuss the depinning current J_d . The curve obtained for 100–200ns present good agreement with the predictions for the creep regime and depinning transition, which allows to obtain $J_d = 1.5 \cdot 10^{11} A/m^2$. Assuming the Spin Hall angle to be given by $\theta_{SH} = (H_d 4e\mu_0 M_s t) / (J_d \hbar \pi)$, we obtain $\theta_{SH} = 0.06 \pm 0.10$, which is close to the value reported in the literature [7]. Moreover, the shape of the curves is in agreement with the prediction for the flow [8]. Further analysis are needed to better understand the contribution of the internal magnetization of DW on SOT-driven free and pinned dynamics.

Acknowledgments

This work has been supported by the French National Research Agency under the project 'DeMIuRGe' ANR-22-CE30-0014.

References

- [1] Saül Vélez, Jakob Schaab, Martin S. Wörnle, et al. [High-speed domain wall racetracks in a magnetic insulator](#). *Nature Communications* 10 (2019).
- [2] Lucile Soumah, Nathan Beaulieu, Lilia Qassym, et al. [Ultra-low damping insulating magnetic thin films get perpendicular](#). *Nature Communications* 9 (2018).
- [3] V. Jeudy, A. Mougín, S. Bustingorry, et al. [Universal Pinning Energy Barrier for Driven Domain Walls in Thin Ferromagnetic Films](#). *Physical Review Letters* 117 (2016).
- [4] R. Díaz Pardo, W. Savero Torres, A. B. Kolton, S. Bustingorry, and V. Jeudy. [Universal depinning transition of domain walls in ultrathin ferromagnets](#). *Physical Review B* 95 (2017).
- [5] R. Díaz Pardo, N. Moisan, L. J. Albornoz, et al. [Common universal behavior of magnetic domain walls driven by spin-polarized electrical current and magnetic field](#). *Physical Review B* 100 (2019).
- [6] V. Jeudy, R. Díaz Pardo, and W. Savero Torres. [Pinning of domain walls in thin ferromagnetic films](#). *Physical Review B* 98 (2018).
- [7] J. C. Rojas-Sánchez, N. Reyren, P. Laczkowski, et al. [Spin pumping and inverse spin Hall effect in Platinum and other 5d metals: The essential role of spin-memory loss and spin-current discontinuities at interfaces](#). *SPIE NanoScience* 9167 (2014).
- [8] André Thiaville, Stanislas Rohart, Émilie Jué, Vincent Cros, and Albert Fert. [Dynamics of Dzyaloshinskii domain walls in ultrathin magnetic films](#). *Europhysics Letters* 100 (2012).

Influence of applied deformation on magnetic properties: ferromagnetic $Ni_{60}Fe_{40}$ thin films deposited on polymeric substrate.

A. Toledano Povedano^{1,*}, P. O. Renault¹, A. Michel¹, P. Godard¹, D. Thiaudière², P. Joly², C. Mocuta², N. Girodon-Boulandet³, D. Faurie³, F. Zighem³, and E. Haltz³

¹Institut Pprime, Université de Poitiers - CNRS - ENSMA, Futuroscope Cedex, France

²Synchrotron SOLEIL, Gif-sur-Yvette, France

³LSPM, Université Sorbonne Paris Nord - CNRS UPR3407, Villetaneuse, France

*alejandro.toledano.povedano@univ-poitiers.fr

Metallic ferromagnetic thin films are key components in devices including sensors, data storage, and signal processing systems. With the rise of flexible electronics, understanding the relationship between magnetic properties and mechanical deformations in the low and high strain regimes is critical [1]. These deformations induce not only homogeneous elastic strains, but also strain heterogeneities due to crystalline defects and cracks, impacting the magnetic properties of films through dipolar interactions and magnetostriction [2]. The research aims to reveal the relationship between controlled microstructural changes (residual stress, film thickness [3]) and magnetic properties, from initial strain to crack onset and subsequent propagation. To investigate these effects, a unique setup has been developed at Synchrotron SOLEIL (DiffAbs beamline) (fig.1). It combines four techniques to study, in situ, the crystalline and magnetic properties of the films subjected to controlled biaxial deformation: Digital Image Correlation (DIC) to measure macroscopic strains, X-Ray Diffraction (XRD) to monitor the lattice strain, electrical square resistivity measurements (R_{\square}) to reveal the crack onset and longitudinal Magneto-Optical Kerr Effect (L-MOKE) to follow the magnetic reversal.

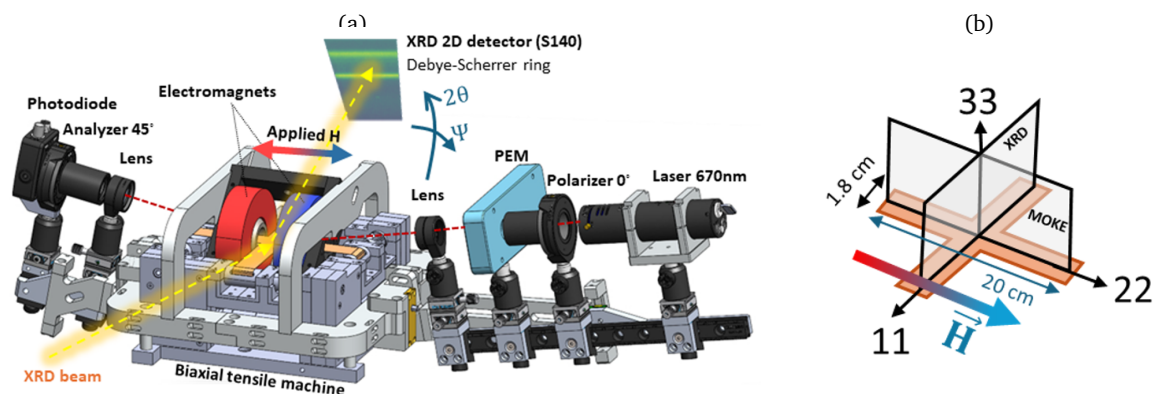


Figure 1: Experimental setup at DiffAbs beamline in Synchrotron SOLEIL. Fig.1a shows the optical bench attached to the tensile machine which is itself installed on the diffractometer. Fig.1b illustrates the cruciform PI sample with the planes of the X-Ray beam and the L-MOKE laser beam. Applied magnetic field \vec{H} is along 22 direction.

Magnetostrictive ($\lambda = 14 \cdot 10^{-6}$) $Ni_{60}Fe_{40}$ thin films have been elaborated by physical vapor deposition (direct ion beam sputtering) and deposited on 75 μm polyimide (PI) flexible substrates with a 20 nm Mo buffer layer. Two modes of mechanical loading have been performed: equibiaxial and sequenced uniaxial until high strain regimes, creating different crack patterns. Two different $Ni_{60}Fe_{40}$ thicknesses (20 and 200 nm) have been analysed, to determine the importance of plasticity. Fig.2 depicts data of the four techniques from PI/Mo(20 nm)/ $Ni_{60}Fe_{40}$ (20 nm) samples subjected to three different loading paths: an equibiaxial tensile test (fig.2a) and two sequenced uniaxial tensile tests (figs.2b, 2c), followed by unloading, as a function of time. (DIC): the first line of graphs show the macroscopic strain of the substrate (ϵ^{DIC}), which reached up to 7% in the first sample, 8% in the second and 10% in the third one. (XRD): this macroscopic strain applied directly to the substrate is transmitted to the thin film, resulting in three mechanical behaviors: an elastic regime (I), a microcracking/plastic regime followed by a multi-cracking regime (II), and unloading (III), reaching a maximum of transmitted elastic strain of 0.7% (for the first sample) and 1% (for the other two). When loading is applied equibiaxially (fig.2a), the film experiences in plane isotropic tensile stress, creating a mud crack pattern (refer to the inset optical microscope image). For fig.2b, the sequenced uniaxial loading firstly applies tension in the 22 direction (fig.1b) (loading 1), which leads to the formation of straight, parallel cracks perpendicular to the applied magnetic field. At 3.8 hours, the strain is applied along 11 direction (loading 2), an array of secondary cracks forms. In contrast, for fig.2c, primary straight cracks form parallel to \vec{H} (loading 1). After loading 2, a brick crack pattern is created. The third line of graphs (R_{\square}): an increase of 10% with respect to the initial value is considered to be the ending of plastic regime and the crack onset. For all three samples presented, this is reached slightly after the maximum of elastic strain underwent by the alloy. (L-MOKE): magnetic

features were obtained from the analysis of hysteresis loops throughout the experiment. For each experiment, the coercive field $\mu_0 H_c$ and the saturation field $\mu_0 H_{sat}$ are shown. A similar starting point is observed for the three samples ($\mu_0 H_c \sim 5$ mT and $\mu_0 H_{sat} \sim 5,9$ mT). When loading is applied equibiaxially (fig.2a), the magnetoelastic coupling effects are cancelled out, resulting in no significant variation in the linear elastic regions (I). Heterogeneities of stress are generated in regime (II), leading to small changes of the MOKE loops. Then, a plateau is formed when there is a relaxation of stress thanks to the propagation of cracks. During the unloading in regime (III), the saturation field reduces even more due to the decrease of internal stresses. The greater variations of the hysteresis loops are shown in figs.2b, 2c. It is associated to a huge increase of $\mu_0 H_{sat}$ when the tensile stress increases in the 11 direction. This happens with or without cracks. For all samples, the initial square-loops are almost recovered at the end of the unloading, despite the presence of cracks.

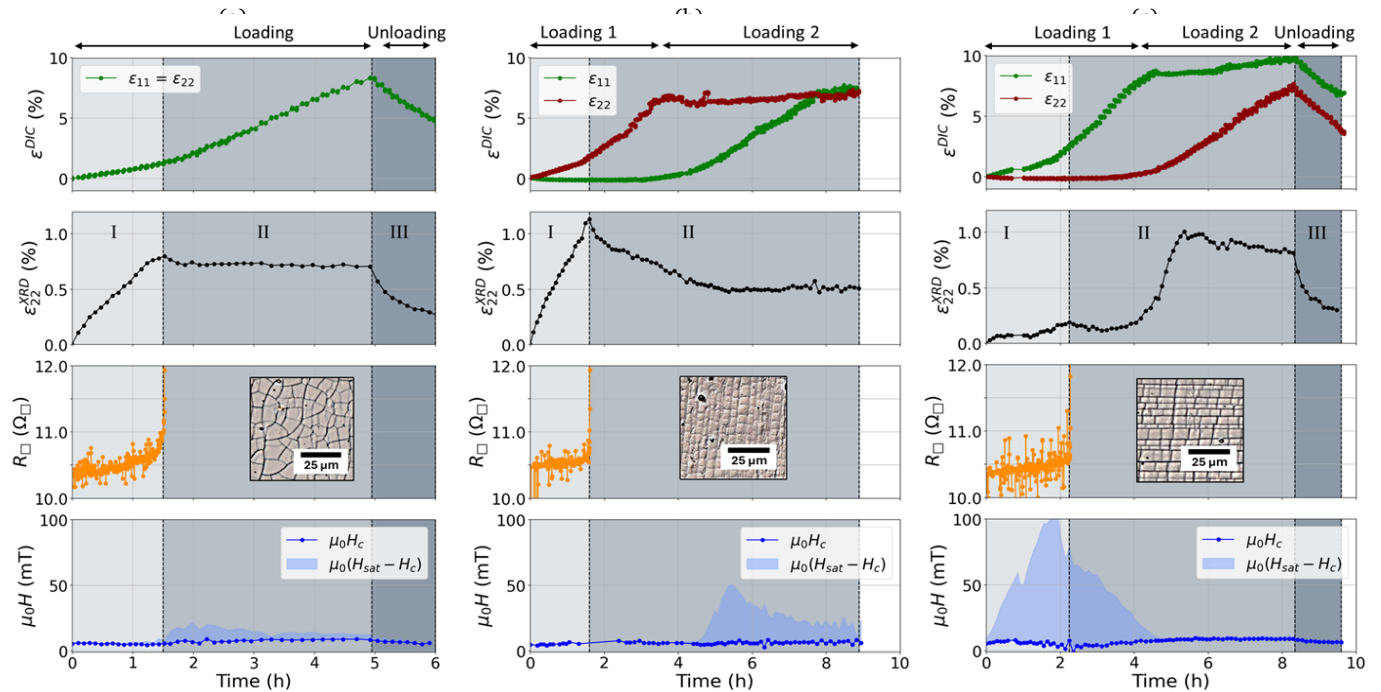


Figure 2: Magneto-mechanical characterization of PI/Mo(20 nm)/Ni₆₀Fe₄₀(20 nm) samples. Fig.2a equibiaxial loading tensile test and figs.2b,2c a complex sequenced uniaxial loading (respectively 22 then 11; and 11 then 22). All figures show (from top to bottom) the macroscopic in-plane deformation of the substrate (DIC), the elastic behavior of the NiFe (111) plane (XRD), the electrical square resistance of the film (R_{\square}), and the evolution of the magnetic reversal where the coercive field $\mu_0 H_c$ and the saturation field $\mu_0 H_{sat}$ allow to depict the width and squareness of the magnetic hysteresis loops (L-MOKE). An inset of optical microscopy images of *post mortem* samples show the final crack configuration.

Other measurement campaigns have been carried out with different magnetic thicknesses and magnetostrictive responses (by changing the Ni/Fe ratio). Findings show how crack density (which varies with thickness) and fragmentation modes influence the material's magneto-mechanical properties. Further research will investigate more in detail the magnetic reversal process and show how crack patterns, that differ between fragile and ductile materials, may influence the shape, distribution, and orientation of magnetic domains.

Acknowledgments

This work was supported by the French government program EUR INTREE, reference ANR-18-EURE-0010 and DAMMAG project, reference ANR-22-CE08-0032.

References

- [1] F Zighem and D Faurie. A review on nanostructured thin films on flexible substrates: links between strains and magnetic properties. *Journal of Physics: Condensed Matter* 33, 233002 (2021).
- [2] H Ben Mahmoud, D Faurie, P-O Renault, and F Zighem. Tensile properties of ferromagnetic nanofilms on stretchable substrates: Links between multi-cracking and magnetic properties. *Applied Physics Letters* 122 (2023).
- [3] P Godard, A Guillot, F Zighem, et al. Strain ratio and thickness effects on plasticity and crack patterns of Nickel thin films. *Scripta Materialia* 213, 114638 (2022).

Dzyalonskii-Moriya interaction in Fe_5GeTe_2 epitaxial thin films

J. Sampaio^{1,*}, A. Mougin¹, A. Pascaud¹, E. Quero¹, A. Thiaville¹, V. Polewczyk², A. Marty², and F. Bonell²

¹Laboratoire de Physique des Solides, CNRS, Univ. Paris-Saclay

²SPINTEC, Univ. Grenoble Alpes/CNRS/CEA

*joao.sampaio@cnrs.fr

Ferromagnetic van der Waals (vdW) materials present an interesting new class of materials for the study of nanomagnetism. In particular, the Fe_xGeTe_2 family stands out as a potential system for spintronics applications due to their high Curie temperature, metallic character, and large magneto-transport effects. Moreover, there have been reports of observations of chiral magnetic structures in films of this family [1, 2], which suggest that these films can host a significant Dzyalonskii-Moriya interaction (DMI), and are thus suitable for applications based on skyrmions and chiral domain walls. However, it is difficult to characterise the DMI and its origin from the observation of chiral magnetic textures alone.

In this work, we measure the static and dynamic magnetic properties of thin, epitaxially-grown Fe_5GeTe_2 films, capped to prevent oxidation (Fig. 1a), by Brillouin light scattering (BLS) spectroscopy (Fig. 1b). We directly measure the DMI in these films, demonstrating unambiguously the presence of a significant DMI.

The Fe_5GeTe_2 films ($t = 12, 8$ and 3 nm) were epitaxially grown on Al_2O_3 (0001). The 12-nm-thick film studied here was characterised in depth by Ribeiro et al. [3], and all films were grown following the protocol reported in that work. The films were capped by 3 nm of Al deposited at room temperature, then naturally oxidized in air. This capping layer prevents the oxidation of the film and guarantees symmetric top and bottom interfaces (Fig. 1a).

The spin wave dispersion was studied using BLS spectroscopy. The Stokes and anti-Stokes peaks in the BLS spectrum (Fig. 1c) correspond to cycloidal spinwaves of opposite rotation sense (Fig. 1b), and are subject to an opposite energy contributions from the DMI. In the limit of thin films ($kt \ll 1$), as is the case here, the difference in frequency between the Stokes and anti-Stokes peaks ($\Delta f \equiv |f_{\text{Stokes}}| - |f_{\text{anti-Stokes}}|$) can be used to determine the magnitude of the DMI effect D :

$$D = \frac{M_s \Delta f}{2\gamma k}, \quad (18)$$

where k is the wave vector of the spinwave (determined by the incidence angle of the light in the BLS measurement.) Several spectra were measured and the the slope of $\Delta f(k)$ (which we dub v_{DMI}) was determined. Fig. 1d shows the measured $\Delta f(k)$ for the 3, 8 and 12 nm films (at 150 K). We observe that there is clearly a linear slope and thus a finite D in all three films. All three show a slope, and thus a DMI, of the same sign.

The calculated D parameters (using eq. 18) are about 0.037 mJ/m^2 , a value comparable to other systems studied in spintronics. Significantly, they do not vary as $1/\text{thickness}$ and show an approximately constant dependence on the film thickness. This indicates that the DMI is not interfacially-induced, but instead arises from a mechanism present in the bulk of the material.

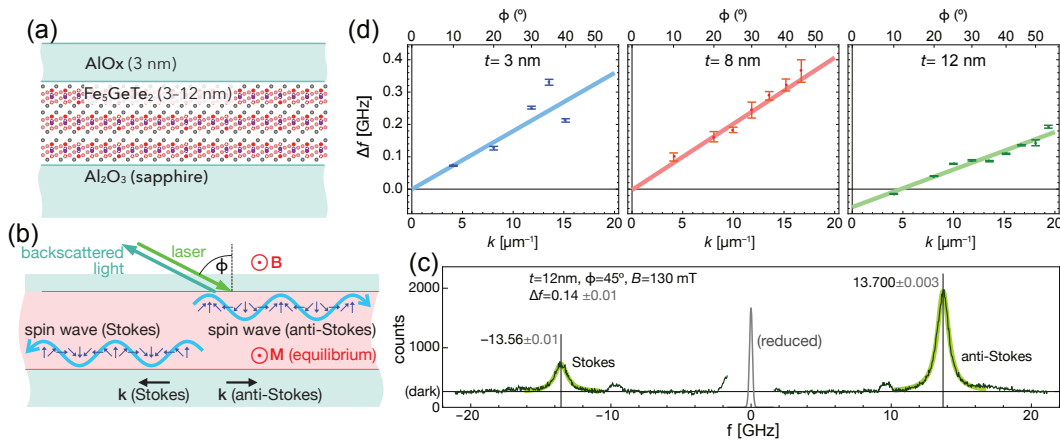


Figure 1: a) Schematic of the studied Fe_5GeTe_2 epitaxial films. b) Schematic of the BLS measurement. c) BLS spectrum of 12nm-thick film showing the Stokes and anti-Stokes peaks. d) Stokes/anti-Stokes frequency difference versus wave vector for three films.

These results confirm that Fe_5GeTe_2 can host a significant DMI and suggest that the reported magnetic textures in Fe_5GeTe_2 are likely chiral in nature. We propose that the bulk mechanism at the source of the DMI may be enhanced by adjusting the growth conditions, and complemented by interfacial-induced DMI. This makes of Fe_5GeTe_2 a promising material for exploring the dynamics of chiral magnetic textures and for chiral spintronic applications.

Acknowledgments

The authors thank V. Jeudy for his support with cryogenic measurements and Mr. E. Rivière at ICMMO (CNRS) for SQUID measurements. This work was supported by the French National Research Agency (ANR) through the projects ELMAX (ANR-20-CE24-0015), NEXT (ANR-23-CE09-0034), the FLAG-ERA grant MNEMOSYN (ANR-21-GRF1-0005-01), and the LANEF framework for mutualized infrastructure (ANR-10-LABX-51-01).

References

- [1] M. Yang, Q. Li, R. V. Chopdekar, et al. [Creation of skyrmions in van der Waals ferromagnet Fe₃GeTe₂ on \(Co/Pd\)_n superlattice](#). *Science Advances* 6 (2020).
- [2] Maurice Schmitt, Thibaud Denneulin, András Kovács, et al. [Skyrmionic spin structures in layered Fe₅GeTe₂ up to room temperature](#). *Communications Physics* 5 (2022).
- [3] M. Ribeiro, G. Gentile, A. Marty, et al. [Large-scale epitaxy of two-dimensional van der Waals room-temperature ferromagnet Fe₅GeTe₂](#). *npj 2D Materials and Applications* 6 (2022).

Spin-Orbit Torque Magnetic Tunnel Junctions at Cryogenic Temperatures

K. Subham Senapati^{1,*}, Kaiquan Fan², Laurent Vila¹, Aurelie Kandazoglou¹, Marco Biagi¹, Corrado Capriata¹, Aymen Fassatoui¹, Gilles Gaudin¹, Siddharth Rao², Gouri Sankar Kar², Sebastien Couet², and Kevin Garello¹

¹Univ. Grenoble Alpes, CEA, CNRS, Grenoble INP, SPINTEC, 38000 Grenoble, France

²imec, Kapeldreef 75, 3001 Leuven, Belgium

*kintali.senapati@cea.fr

There is a growing interest in evaluating the behavior of memories at cryogenic temperatures (223K, 77 K, 4 K) for high-performance, spatial, and quantum computing applications [1, 2]. Within the memory landscape, magnetoresistive RAM (MRAM) is gaining traction for embedded applications due to its lower power consumption, high speed, scalability, and endurance. Therefore, it is of interest to evaluate MRAM properties as a function of temperature to build predictive compact models for technology design and to further engineering MRAM stack such as minimizing power dissipation at operating temperatures.

MRAM building blocks are magnetic tunnel junctions (MTJs), which are read via the tunnel magnetoresistance (TMR) effect. Various methods can be employed for writing, including spin transfer torque (STT) and toggle MRAM, which are commercially available, and spin-orbit torque (SOT) MRAM, currently at the research stage. While STT is limited to operation times greater than 10 ns for reliability, SOT-MTJ demonstrates sub-ns writing speeds with large endurance, making it a promising candidate for future fast and energy-efficient embedded memory solutions [3]. Although there are reports on STT-MRAM [4, 5], the behavior of SOT-MRAM at low temperatures is under-explored and limited to 4 K [6].

In this presentation, we report on the cryogenic properties of 300 nm integrated W-based SOT-MTJs, initially designed for room temperature memory behavior. First, we introduce the main characteristics of the magnetic tunnel junction (TMR, B_c , B_k , B_{off} , Δ , R_{SOT}) and their variations with temperature down to 50 K for MTJ diameters ranging from 50 to 100 nm. Figure 1(a) shows a typical $R-H$ curve at 50 K and 300 K, clearly demonstrating the expected increase in coercivity (B_c) and TMR when dedcreasing T , consistent with the inelastic electron tunneling model [7].

Additionally, we present the temperature and field dependence of the SOT DC critical switching current down to 11 K, as shown in Figure 1(b). We also present preliminary switching studies using pulsed currents as fast as 250 ps down to 77 K. This analysis allows us to study the intrinsic critical switching current and energy conservation parameters versus temperature, which will be crucial for benchmarking SOT-MTJ systems [8].

Our study aims to develop a comprehensive compact model of SOT-MTJ behavior that includes low-temperature behaviors, and to establish an initial benchmark for SOT-MTJ operations in cryogenic applications. This will help to identify solutions to leverage SOT physics in low-temperature environments.

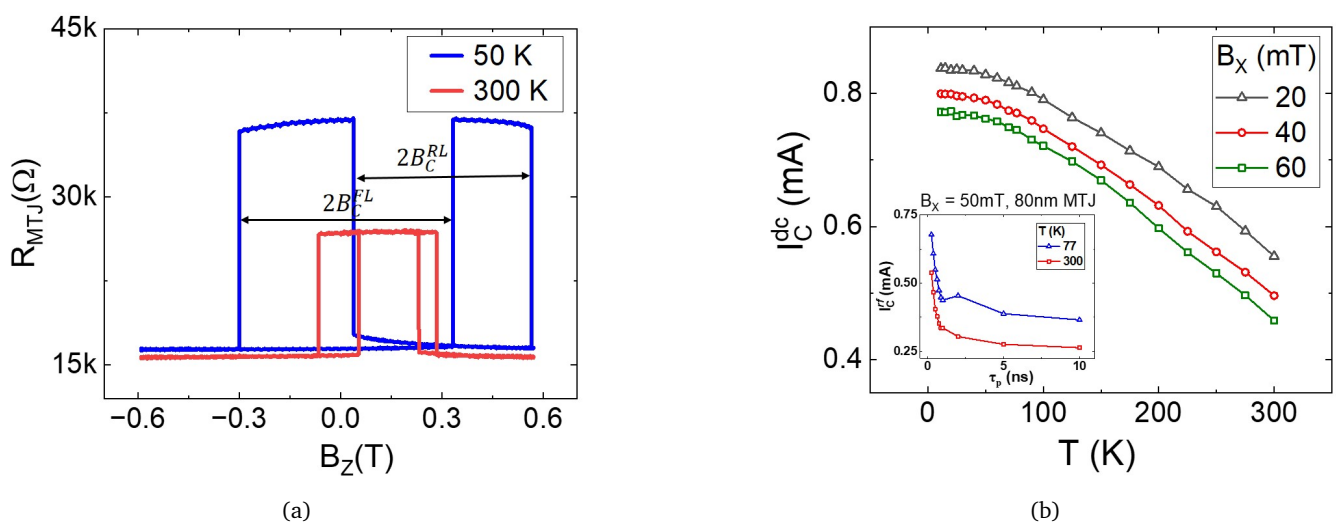


Figure 1: (a) $R-H$ loops obtained from 60nm based MTJ at 300K and 50K. (b) Critical switching current (DC) versus temperature for an 80nm based SOT-MTJ at varied external fields. Inset shows critical switching current (rf) versus pulse width curves down to 250ps pulses for an 80nm based SOT-MTJ at $T = 300K$ and $77K$

Acknowledgments

This work was partly supported by France 2030 government grant EMCOM (ANR-22-PEEL-0009), MAPS project (Pack Ambition Recherche N°19-009938-01, Région Auvergne-Rhône-Alpes), and by imec's industrial affiliation program on MRAM devices.

References

- [1] Arnout Beckers, Alexander Grill, Arvind Sharma, et al. "Cold CMOS for Sustainable Datacenters". 2024, 229–232.
- [2] Shamiul Alam, Md Shafayat Hossain, Srivatsa Rangachar Srinivasa, and Ahmedullah Aziz. [Cryogenic memory technologies](#). *Nature Electronics* 6, 185–198 (2, 2023).
- [3] K. Garello, F. Yasin, S. Couet, et al. "SOT-MRAM 300MM Integration for Low Power and Ultrafast Embedded Memories". *2018 IEEE Symposium on VLSI Circuits*. IEEE, 2018.
- [4] L. Rehm, G. Wolf, B. Kardasz, M. Pinarbasi, and A. D. Kent. [Sub-nanosecond spin-torque switching of perpendicular magnetic tunnel junction nanopillars at cryogenic temperatures](#). *Applied Physics Letters* 115, 182404 (2019). eprint: https://pubs.aip.org/aip/apl/article-pdf/doi/10.1063/1.5128106/13221485/182404_1_online.pdf.
- [5] H. L. Chiang, J. F. Wang, T. C. Chen, et al. "Cold MRAM as a Density Booster for Embedded NVM in Advanced Technology". *2021 Symposium on VLSI Technology*. 2021, 1–2.
- [6] Minh-Hai Nguyen, Guilhem J. Ribeill, Martin V. Gustafsson, et al. [Cryogenic Memory Architecture Integrating Spin Hall Effect based Magnetic Memory and Superconductive Cryotron Devices](#). *Scientific Reports* 10, 248 (14, 2020).
- [7] Y. Wang, H. Cai, L.A.B. Naviner, et al. [Compact thermal modeling of spin transfer torque magnetic tunnel junction](#). *Microelectronics Reliability* 55, 1649–1653 (2015).
- [8] Viola Krizakova, Manu Perumkunnil, Sébastien Couet, Pietro Gambardella, and Kevin Garello. [Spin-orbit torque switching of magnetic tunnel junctions for memory applications](#). *Journal of Magnetism and Magnetic Materials* 562, 169692 (2022).

Symmetry of the dissipation of surface acoustic waves by ferromagnetic resonance

Florian Millo^{1,*}, Rafael Lopes Seeger¹, Claude Chappert¹, Aurélie Solignac², and Thibaut Devolder¹

¹C2N - Université Paris-Saclay, Palaiseau 91120, France

²SPEC, CEA, Gif-sur-Yvette 91190, France

*florian.millo@university-paris-saclay.fr

The coupling between surface acoustic waves (SAWs) and ferromagnetic resonance (FMR) has garnered significant attention in recent years due to its potential for advancing the next generation radio-frequency and spintronic devices. The mechanism enabling the SAW-FMR coupling is the magnetoelasticity present in heterostructures comprised of thin magnetic films deposited on top of a piezoelectric substrates. For heterostructures with isotropic magnetic films, the SAW-FMR coupling is found to occur at four evenly spaced field orientations i.e., 4-fold symmetry [1]. However, in more realistic systems, the anisotropy of the magnetic film plays a significant role in the symmetry of SAW-FMR coupling.

In this work, we investigate the symmetry of SAW-FMR coupling in a CoFeB / LiNbO₃ heterostructure exhibiting uniaxial anisotropy which impacts the behavior of the symmetry of SAW-FMR coupling. We use a SAW device where the magnetic film is placed in-between two interdigitated transducers (IDTs) [see Fig. 1(a)]. The SAWs are excited at first port of a Vector Network Analyzer and the transmission is collected at the second port. The measurements are done for applied in-plane dc fields $\mu_0|\vec{H}_0| \in [-10, 10]$ mT of variable orientations $\psi \in [0^\circ, 360^\circ]$ [see Fig. 1(a)]. The SAW-FMR coupling is examined through the variation in amplitude of the forward transmission parameter (ΔS_{21}) defined as,

$$\Delta S_{21}(H_0, \psi, f) = 20 \log_{10} \left(\frac{|S_{21}(H_0, \psi, f)|}{|S_{21}(H_{\text{ref}}, \psi, f)|} \right) \quad \text{in [dB]}, \quad (19)$$

where f is the working frequency and $\mu_0 H_{\text{ref}} = -10$ mT is a reference dc field chosen far from the SAW-FMR resonance fields. Fig. 1(b) shows the hysteretic behaviour of the SAW-FMR coupling that is maximal at $\mu_0|\vec{H}_0| \approx \pm 3.5 - 4$ mT, and leads to an extra loss of 4 dB. The maximum of the extra loss depends on the field orientation (ψ) with respect to the SAW wavevector (\vec{k}_{SAW}) direction.

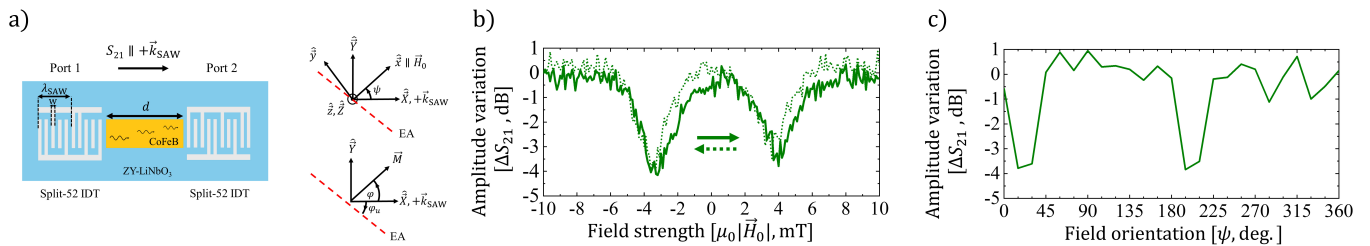


Figure 1: a) Experimental setup and geometry. The IDTs periodicity is $\lambda_{\text{SAW}} = 9 \mu\text{m}$ and the finger width is $w = 0.9 \mu\text{m}$. A CoFeB rectangle of length $d = 800 \mu\text{m}$ is placed between the IDTs. $\{xyz\}$ is the reference frame of the in-plane dc field $\vec{H}_0 \parallel \hat{x}$, and $\{XYZ\}$ is the reference frame of the LiNbO₃ crystal. EA stands for easy axis. b) Field dependence of ΔS_{21} at $\psi = 15^\circ$ and at $f_{\text{SAW}} = 1.72$ GHz. The arrows sketch the field sweeping direction. c) Measured maximum (negative) value of ΔS_{21} at $\mu_0|\vec{H}_0| = 4$ mT and $f_{\text{SAW}} = 1.72$ GHz versus the orientation of the applied field.

A 2-fold symmetry of the SAW-FMR coupling is depicted in Fig. 1(c) where the SAW energy is significantly absorbed only at two field orientations $\psi = 15^\circ$ and $\psi = 195^\circ$. What is the origin of this 2-fold symmetry of SAW-FMR coupling?

We turn now to the theoretical aspects to understand the 2-fold symmetry of SAW-FMR coupling in the system. In other words, we intend to calculate curves that reproduces Fig. 1(c). To do so, we employed a simplistic yet insightful model that considers only the following contributions: Zeeman energy, dipolar energy and uniaxial anisotropy. We calculate the magnetic susceptibility tensor ($\overleftrightarrow{\chi}$) associated with the ferromagnetic resonance, which serves as a critical parameter in characterizing the response of the system to external excitations. Furthermore, we restrict our study to the in-plane magnetoelastic field (h_{rf}) which will be dependent on the magnetoelastic coupling constant (B_1), the elastic strain (ϵ_{XX}), the magnetization state (φ) and field orientation (ψ).

To quantify the SAW-FMR coupling and study its symmetry, we use the time-averaged power transmitted to the magnetic film [2],

$$\Delta P = -\frac{\mu_0 \omega t}{2} \text{Im} \left(h_{\text{rf}}^\dagger \cdot \overleftrightarrow{\chi} \cdot h_{\text{rf}} \right) \Big|_{\varphi=\varphi_0} \quad \text{in } [\text{W/m}^2], \quad (20)$$

where the dagger symbol means transpose-conjugate, $\omega = 2\pi f_{\text{SAW}}$ is the SAW frequency and t is the thickness of the magnetic film. Eq. 20 is evaluated at the magnetization ground state (φ_0). We show in Fig. 2 our theoretical results. In Fig. 2(a), when the uniaxial anisotropy is zero we obtain the previously known 4-fold symmetry of the SAW-FMR coupling as in ref. [1]. For small anisotropy fields (i.e., $H_u < H_0$), the maximum coupling occurs in between the previous $\pi/4 + n\pi/2$ orientations and the hard axis of the anisotropy. The coupling is maximal for anisotropy fields of typically 2 mT. At anisotropy fields much larger than the applied dc field [see last panel in Fig. 2(a)] the maximum coupling finally tends to align with the hard axis. In general, as soon as a weak magnetic uniaxial anisotropy is present in the sample and whatever its orientation [see Fig. 2(b)], the symmetry of SAW-FMR is reduced to 2-fold and the coupling tends towards the hard axis of anisotropy.

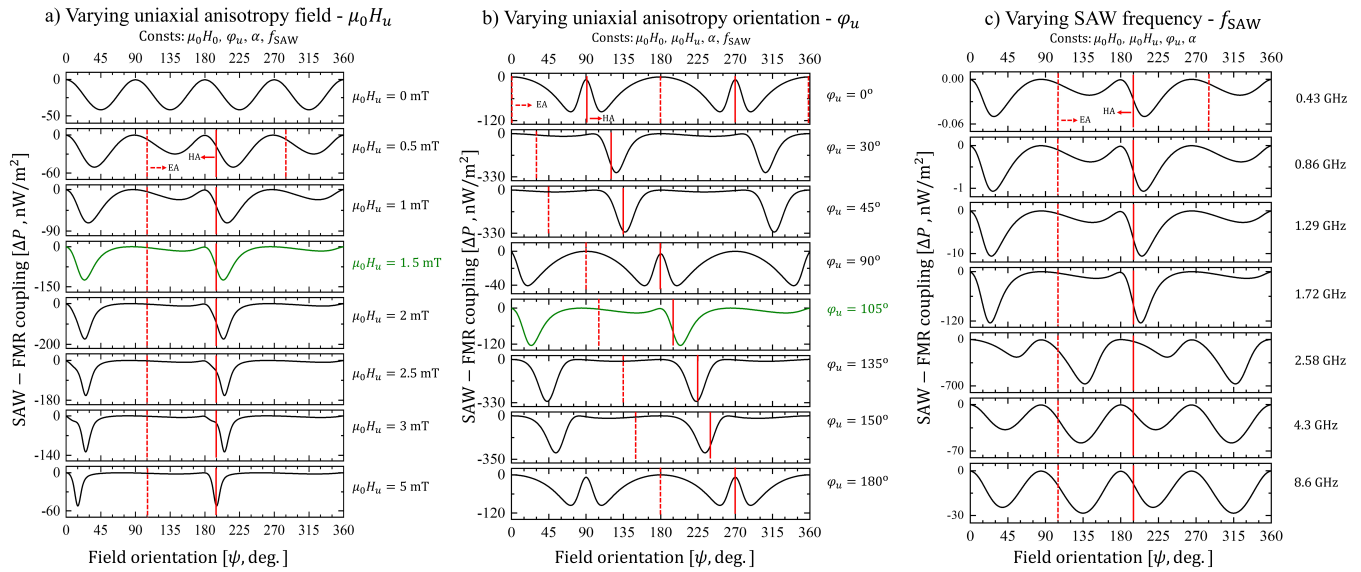


Figure 2: Angular dependence of SAW-FMR coupling when: a) varying $\mu_0 H_u$ and keeping constants uniaxial anisotropy angle $\varphi_u = 105^\circ$, and SAW frequency $f_{\text{SAW}} = 1.72$ GHz. b) varying φ_u and keeping constants $\mu_0 H_u = 1.5$ mT, and $f_{\text{SAW}} = 1.72$ GHz. c) varying f_{SAW} and keeping constants $\mu_0 H_u = 1.5$ mT, and $\varphi_u = 105^\circ$. The vertical lines represent the easy and hard axes (EA, HA). Global constants: $\mu_0 |\vec{H}_0| = 4$ mT, $\alpha = 0.01$. The green curve is the best fit of the measurements.

The SAW working frequency also plays a role to the symmetry of the SAW-FMR coupling [see Fig. 2(c)]: when going from lower to higher working frequencies the magnitude of the SAW-FMR coupling decreases but still retains the 2-fold symmetry, however at the highest working frequency the 4-fold symmetry is almost recovered. We emphasize that the green curves of Fig. 2 serve as a qualitative description of the 2-fold symmetry of SAF-FMR coupling shown in Fig. 1(c).

In a nutshell, our experimental and theoretical results demonstrate that the 2-fold symmetry of SAW-FMR coupling is originating from the uniaxial anisotropy present within the magnetic film [3].

Acknowledgments

The authors acknowledge the French National Research Agency (ANR) project under contract N° ANR-20-CE24-0025 (MAX-SAW). This work was done within the C2N micro nanotechnologies platforms and partly supported by the RENATECH network and the General Council of Essonne. FM acknowledges project under contract N° ANR-22-CE24-0015 (SACOUMAD) for financial support.

References

- [1] M. Weiler, L. Dreher, C. Heeg, et al. [Elastically Driven Ferromagnetic Resonance in Nickel Thin Films](#). *Phys. Rev. Lett.* 106, 117601 (2011).
- [2] R. Lopes Seeger, L. La Spina, V. Laude, et al. [Symmetry of the coupling between surface acoustic waves and spin waves in synthetic antiferromagnets](#). *Phys. Rev. B* 109, 104416 (2024).
- [3] Florian Millo, Rafael Lopes Seeger, Claude Chappert, Aurélie Solignac, and Thibaut Devolder. [Symmetry of the dissipation of surface acoustic waves by ferromagnetic resonance](#). 2024. arXiv: 2412.10847 [cond-mat.mtrl-sci].

Experimental and numerical study of dipolar interactions in complex magnetic fluids

Malika Khelfallah^{1,*}, Claire Carvallo¹, Vincent Dupuis², Dario Taverna¹, Sophie Neveu², Enzo Bertuit², Ekaterina V. Novak³, Andrey Kuznetsov⁴, Deniz Mostarac⁴, Sofia S. Kantorovich⁴, and Amélie Juhin¹

¹*Institut de Minéralogie, de Physique des Matériaux et de Cosmochimie, Sorbonne Université, Muséum National d'Histoire Naturelle, UMR CNRS 7590, IRD, 75005 Paris, France*

²*PHENIX, UMR 8234, Sorbonne Université, CNRS, F-75005 Paris, France*

³*Ural Federal University, Lenin Av. 51, Ekaterinburg 620000, Russian Federation*

⁴*Faculty of Physics, University of Vienna, Boltzmanngasse 5, 1090 Vienna, Austria*

*malika.khelfallah@gmail.com

Magnetic fluids, or ferrofluids, are colloidal suspensions of magnetic nanoparticles in a liquid solvent, stabilized by surfactants or ligands. These systems, characterized by their dipolar interactions, provide an ideal environment for studying fundamental aspects of self-assembly processes and magnetic interactions at the nanoscale. In the absence of an external magnetic field, magnetic nanoparticles can self-assemble into chains, rings, and branches, forming a complex topology with different magnetic states, including closed loops, head-to-tail coupling, and networked structures. When exposed to a magnetic field, these assemblies align into long, micrometer-sized chains that exhibit strong magnetic coupling between particles. This provides a unique opportunity to study the interplay between nanoparticle interactions and their macroscopic magnetic properties. Magnetic fluids have potential applications in diverse fields such as magnetic hyperthermia for targeted cancer treatment, MRI contrast agents, drug targeting and high-density data storage devices.

Binary ferrofluids, formed by mixing two ferrofluids with nanoparticles of different size, shape, or composition, represent a further extension of this system. These mixed systems introduce new degrees of freedom for controlling magnetic properties, as variations in particle size, shape, or composition can induce different ranges of magnetic moments or anisotropies, resulting in different magnetic behaviors. Notably, binary magnetic fluids give rise to intriguing effects such as the "poisoning effect", wherein smaller nanoparticles inhibit the magnetic behavior of larger ones by preventing or modifying the field-induced chaining process [1]. This effect highlights the importance of understanding magnetic interactions in binary ferrofluids, as their modular properties can provide a straightforward method for tuning magnetic behavior, particularly for applications like magnetic hyperthermia.

For example, a recent study [2] examined a unique magnetic fluid created by mixing iron oxide nanoparticles of different shapes, specifically elongated and spherical particles. This approach significantly improved the performance of magnetic hyperthermia, with the mixed samples exhibiting higher heating efficiencies than would be expected from a simple summation of the efficiencies measured for the single-phase nanoparticles. Similarly, another investigation [3] of MnFe_2O_4 and CoFe_2O_4 nanospheres revealed that the magnetization curves of binary magnetic fluids deviate from a simple average of their single-phase counterparts. Element-sensitive magnetometry was used to disentangle the contributions from each type of nanoparticle, highlighting the critical role of magnetic interactions in shaping the macroscopic properties of these binary ferrofluids.

In our study, we investigate the behavior of binary magnetic fluids composed of CoFe_2O_4 (a hard magnetic material) and MnFe_2O_4 (a soft magnetic material) in the presence and absence of an external magnetic field. Cryogenic transmission electron microscopy (cryo-TEM) is used to directly observe the spatial arrangement of nanoparticles in the magnetic fluid, providing a snapshot of their positions in real space. Although cryo-TEM has been applied to magnetic fluids before [4], our work is the first to perform a statistical analysis of the observed assemblies, providing deeper insights into the nature of self-assembled structures. This technique, combined with other more bulk-sensitive methods such as small-angle X-ray scattering, allows us to obtain both nanoscale and macroscopic information about the system.

Electron holography, a challenging and technically demanding technique, allows direct visualization of magnetic properties at the nanoscale. It uniquely reveals the behavior of individual nanoparticles and their interactions within assemblies, providing unparalleled insight that complements the macroscopic information obtained from bulk-sensitive methods.

Magnetometry and First-Order Reversal Curve (FORC) diagrams are employed to study the distributions of magnetic coercivity and of interaction fields within the magnetic fluids. Simulated FORC diagrams further enhance the analysis by providing deeper insights into the mechanisms underlying observed behaviors. In addition, advanced element-sensitive techniques such as liquid-cell X-ray spectroscopy, energy-dispersive X-ray spectroscopy, and scanning transmission X-ray microscopy (STXM) allow precise characterization of nanoparticle composition and magnetic interactions.

Molecular dynamics simulations based on experimentally obtained parameters are used to explain the observed experimental behavior, providing predictive insights into the interactions and properties of magnetic fluids while advancing our understanding of the mechanisms governing self-assembly and magnetic interactions in both single-phase and binary ferrofluids. These results emphasize the critical role of magnetic anisotropy, a parameter often simplified as uniaxial in simulations, demonstrating the necessity of incorporating its complexities into theoretical models.

In single-phase magnetic fluids, we present the first detailed observation of self-assembly in a CoFe_2O_4 nanoflower magnetic fluid, with quantification of the types of assemblies formed, in agreement with previous numerical predictions.

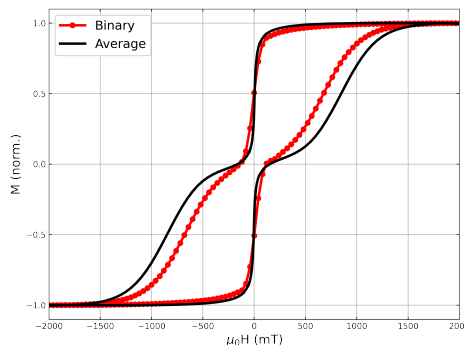


Figure 1: Magnetization curve of a binary ferrofluid (red) and the average magnetization curve obtained from both single phase-ferrofluid (black).

The results highlight the importance of magnetic anisotropy in driving magnetic interactions and organizing the nanoparticle assemblies [5]. In binary magnetic fluids, the magnetic properties of the MnFe_2O_4 component are significantly modified by the presence of CoFe_2O_4 nanoparticles, even in the absence of an applied field. Interestingly, this effect is asymmetric, as the CoFe_2O_4 component remains largely unaffected by the presence of MnFe_2O_4 . When an external magnetic field is applied, both types of nanoparticles form long, anisotropic chains (Fig. 2). The MnFe_2O_4 nanoparticles appear to "poison" the CoFe_2O_4 nanoparticles by introducing periodic disruptions within the chains, reducing the coercivity of the CoFe_2O_4 component and altering its magnetic properties within the assembly (Fig. 1).



Figure 2: Composite image obtained by STXM measured at the edge of Fe, Co and Mn. The cobalt ferrites nanoparticles are in green and the manganese ferrite in red. Scale bar = 200 nm

In summary, this study provides a comprehensive analysis of self-assembly and magnetic interactions in both single-phase and binary magnetic fluids. Our results highlight the crucial role of magnetic anisotropy and dipolar interactions in determining the macroscopic properties of magnetic fluids. These insights contribute to the broader understanding of magnetic anisotropy and offer valuable guidance for designing magnetic fluids with tunable properties for applications such as magnetic hyperthermia.

Acknowledgments

References

- [1] Sofia S. Kantorovich. [Chain Aggregate Structure in Polydisperse Ferrofluids: Different Applications](#). *Journal of Magnetism and Magnetic Materials*. Proceedings of the 10th International Conference on Magnetic Fluids 289, 203–206 (1, 2005).
- [2] Jesus G. Ovejero, Federico Spizzo, M. Puerto Morales, and Lucia Del Bianco. [Mixing Iron Oxide Nanoparticles with Different Shape and Size for Tunable Magneto-Heating Performance](#). *Nanoscale* 13, 5714–5729 (25, 2021).
- [3] Niéli Daffé, Jovana Zečević, Kalliopi N. Trohidou, et al. [Bad Neighbour, Good Neighbour: How Magnetic Dipole Interactions between Soft and Hard Ferrimagnetic Nanoparticles Affect Macroscopic Magnetic Properties in Ferrofluids](#). *Nanoscale* 12, 11222–11231 (2020).
- [4] Mark Klokkenburg, Chantal Vonk, Eva M. Claesson, et al. [Direct Imaging of Zero-Field Dipolar Structures in Colloidal Dispersions of Synthetic Magnetite](#). *Journal of the American Chemical Society* 126, 16706–16707 (1, 2004).
- [5] Malika Khelfallah, Claire Carvallo, Vincent Dupuis, et al. [Structural and Magnetic Properties of Ferrofluids Composed of Self-Assembled Cobalt Ferrite Nanoflowers: A Multiscale Investigation](#). *The Journal of Physical Chemistry C* (2024).

Magnetic textures and dynamics in ultra-thin bidimensionnal ferromagnets Fe_xGeTe_2

Edgar Quero^{1, *}, Joao Sampaio¹, André Thiaville¹, and Alexandra Mougin¹

¹IDMAG, Laboratoire de Physique des Solides, Université Paris Saclay, UMR CNRS 8502, Bâtiment 510, 91405 Orsay, France

*edgar.quero@universite-paris-saclay.fr

The ever-expanding field of 2D materials started in 2005 with the Nobel prize winning exfoliation of graphene. It has sparked significant discoveries in all fields of condensed matter physics [1] and notably the community of magnetism in 2017 with the emergence of 2D magnets [2]. These materials have unique properties and are particularly well suited to the study of interfacial effects because of their layered nature. By themselves or combined into stacks, they are widely researched today.

My Ph-D project focuses on Fe_xGeTe_2 compounds, namely Fe_3GeTe_2 and Fe_5GeTe_2 whose Curie temperature are 200 K and 300 K, respectively. Fe_3GeTe_2 is notable for its strong perpendicular magnetic anisotropy, which is essential for manipulating magnetic textures. Fe_5GeTe_2 exhibit an in-plane magnetic anisotropy but its complex structure may allow the existence of Dzyaloshinskii-Moriya interaction, as reported in calculations [3–5]. This makes Fe_5GeTe_2 a strong candidate for hosting skyrmions [5]. Results on this matter obtained in the group on Fe_5GeTe_2 epitaxial thin films are presented in another poster [6]. The respective crystalline structure of Fe_3 - and Fe_5GeTe_2 compounds are shown in Figure 1. Fe_3GeTe_2 displays a centrosymmetric structure. Fe_5GeTe_2 posses a split site for one of it's Fe atoms that induces a shift in the neighbouring Ge atom. This structure can be either centrosymmetric or acentric depending on the position occupied by the split site Fe atom.

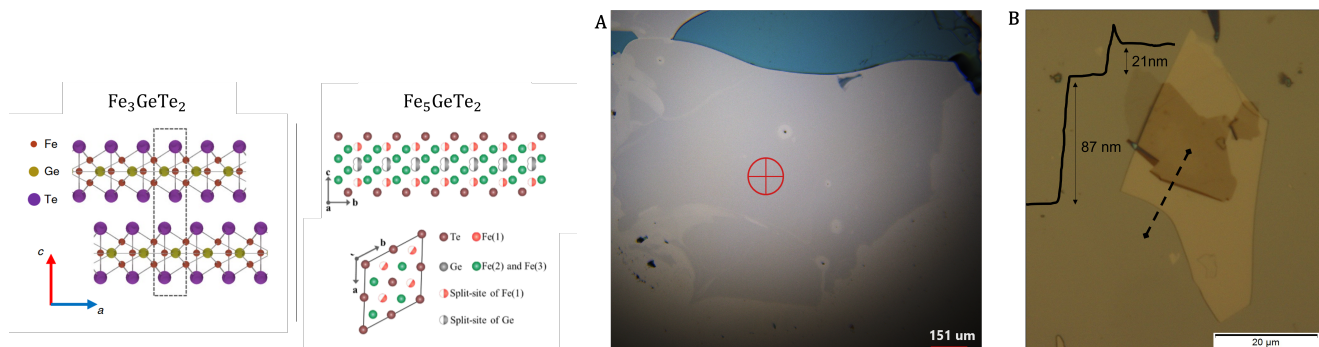


Figure 1: Left) Crystalline structure of Fe_3GeTe_2 [7] and Fe_5GeTe_2 [8]. Right) **A** : Optical image of Fe_3GeTe_2 flake exfoliated on a gold substrate with a millimeter lateral size **B** : Optical image and AFM cross section of Fe_3GeTe_2 flake (yellow) exfoliated and partially covered with an hBN flake (transparent).

A key challenge is the exfoliation of flakes of suitable dimensions. They must be thin enough to study interfacial effects that diminish as $1/\text{thickness}$. Simultaneously, a large lateral size allows for easier manipulation and observation of the flakes, as well as being a requirement for some characterization tools such as Brillouin Light Spectroscopy (BLS). In this regard, the usual exfoliation processes using scotch tape on silicium substrates are limiting as they cannot reliably yield flakes that are both thin and large in lateral size. To overcome this issue, we used state-of-the-art gold-assisted exfoliation processes [9] that rely on the strong gold-chalcogen interaction to obtain large-scale monolayers, with hundreds micrometers of lateral size as shown in Figure???. Furthermore, the air sensitivity of these materials requires manipulation under an argon filled glovebox. To prevent their oxidization, the exfoliated Fe_xGeTe_2 flakes are then covered with hexagonal boron nitride flakes (hBN) using a stacking process to protect them when taken out of the glovebox, as illustrated in Figure 1.

Magneto-optical Kerr effect (MOKE) microscopy allows direct and dynamic observation of magnetic behaviors and textures, at low temperatures and with either perpendicular or in-plane sensitivity. Additionally, BLS is used to probe the dispersion relation of surface spin waves in the exfoliated flakes, including at low temperatures. This provides detailed information on magnetic parameters such as the exchange energy or gyromagnetic ratio as well as a direct quantitative measurement of the Dzyaloshinskii-Moriya interaction.

Preliminary results of these studies obtained on hBN covered flakes with thickness ranging from 40 nm to 87 nm can be seen on Figure 2. In BLS (Fig.2A), a surprising double peak was observed, that results from the contribution of bulk spin waves to the signal. The DMI interaction depends on the difference between the frequency of Daemon Eshbach left and right side peaks. This additional bulk contribution prevents a direct determination of the DMI. We currently try to reduce the studied flake thickness, as explained above. Nonetheless in similar flakes Fe_3GeTe_2 covered with hBN magnetic textures were obtained (Fig. 2B) showcasing the ability of this material to host unusual magnetic structures subject to further studies. Indeed, it is possible to inject current directly into the flakes by adding metal contacts (either directly into the flakes or in

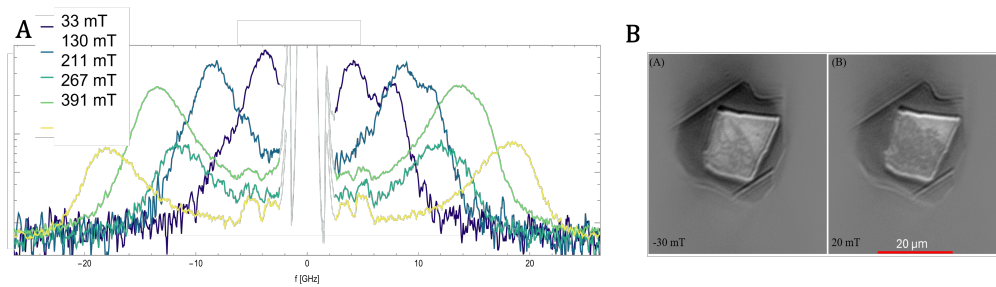


Figure 2: **A** : Superimposed BLS spectra obtained at 100 K on Fe_5GeTe_2 / hBN flake for different applied field. For 33 mT and 130 mT a clear double peak can be observed on one side. **B** : Polar MOKE microscopy images of magnetic textures observed in Fe_3GeTe_2 / hBN flake during an hysteresis loop at 200 K under out-of-plane magnetic field.

large Spin orbit coupling contacts) to probe the Spin Transfer Torques or Spin Orbit Torques induced dynamics of magnetic textures. These preliminary results show both the importance of taking on the fabrication challenges as well as the promises of these studies.

Acknowledgments

This work was supported by the French National Research Agency (ANR) through the projects NEXT (ANR-23-CE09-0034).

References

- [1] Stephan Roche, Johan Akerman, Bernd Beschoten, et al. [Graphene spintronics: the European Flagship perspective](#). *2D Materials* 2, 030202 (3 2015).
- [2] Cheng Gong and Xiang Zhang. [Two-dimensional magnetic crystals and emergent heterostructure devices](#). *Science* 363 (6428 2019).
- [3] Yang Gao, Shaohua Yan, Qiangwei Yin, et al. [Manipulation of topological spin configuration via tailoring thickness in van der Waals ferromagnetic \$\text{Fe}_5\text{-xGeTe}_2\$](#) . *Physical Review B* 105 (1 2022).
- [4] Sukanya Ghosh, Soheil Ershadrad, Vladislav Borisov, and Biplab Sanyal. [Unraveling effects of electron correlation in two-dimensional \$\text{Fe}_n\text{GeTe}_2\$ \(\$n = 3, 4, 5\$ \) by dynamical mean field theory](#). *npj Computational Materials* 9, 1–16 (1 2023).
- [5] Dongzhe Li, Soumyajyoti Haldar, Leo Kollwitz, et al. [Prediction of stable nanoscale skyrmions in monolayer \$\text{Fe}_5\text{GeTe}_2\$](#) . *Physical Review B* 109 (22 2024).
- [6] Alexandra Mougin, Antoine Pascaud, Edgar Quero, et al. [Dzyaloshinskii-Moriya interaction in \$\text{Fe}_5\text{GeTe}_2\$ epitaxial thin films; to be submitted](#).
- [7] Haoyan Zhang, Jianfeng Guo, Cong Wang, et al. [Site-ordering/disordering-induced magnetic textures in a vdW ferromagnet by competing global and broken inversion-symmetry](#). 2024. arXiv: 2404.04851 [cond-mat.mtrl-sci].
- [8] Zaiyao Fei, Bevin Huang, Paul Malinowski, et al. [Two-dimensional itinerant ferromagnetism in atomically thin \$\text{Fe}_3\text{GeTe}_2\$](#) . *Nature Materials* (2018).
- [9] Yuan Huang, Yu Hao Pan, Rong Yang, et al. [Universal mechanical exfoliation of large-area 2D crystals](#). *Nature Communications* 11, 1–9 (1 2020).

Ferroelectric control of spin-charge interconversion in oxide-based two-dimensional electron gases

Julien Bréhin^{1,2,*}, Paul Noël¹, Felix Trier², Luis M. Vicente-Arche², Sara Varotto², Srijani Mallik², Jean-Philippe Attané¹, Laurent Vila¹, Agnès Barthélémy², and Manuel Bibes²

¹Univ. Grenoble Alpes, CEA, CNRS, Grenoble INP, IRIG-SPINTEC, F-38000 Grenoble, France

²Laboratoire Albert Fert, CNRS, Thales, Université Paris-Saclay, 91767 Palaiseau, France

*julien.brehin@cea.fr

Facing several bottlenecks in integration as well as computational and energy efficiencies, the microelectronics industry is trying to renew itself with the search for new computing paradigms addressing specific problems.

Using spins as the support and vector of information and computation has been deemed an interesting alternative or complement to the all-charge-based CMOS transistors used in today's chips and bringing the logic operation and information storage closer together could be a significant step further to gain on the energy consumption side and the computational throughput [1, 2]. While most of the focus in the field of spintronics has been on exploiting magnetic order in magnetic materials to store information, magnetic torques to write it, this solution still raises some concerns, in part due to its power consumption.

Another key element of envisioned spintronic logic-in-memory devices is the readout, usually performed by passing a current through the ferromagnetic memory element, generating a spin-polarized current which is then converted back into a charge current in a system that exhibits strong spin-orbit coupling. This can be achieved either *via* the inverse spin Hall effect (e.g. in heavy metals) or the inverse (Rashba-)Edelstein effect, where the latter typically arises in systems with broken inversion symmetry, for instance with strong interfacial electric fields.

With some of the highest spin-charge interconversion efficiencies reported in the literature [3], two-dimensional electron gases (2DEGs) confined at the surfaces and interfaces of oxides are a particularly promising platform for the readout brick of the above-mentioned spintronic devices.

In this work, we show how oxide 2DEGs can be exploited not only to perform the spin-charge conversion but also to store basic information not *via* magnetization but rather *via* ferroelectric polarization. Specifically we use different knobs such as minute isovalent ionic substitution [4] or strong electric fields [5–7] to push SrTiO₃ substrates into a ferroelectric phase and we generate 2DEGs at their surface by room temperature sputtering of a thin layer of reactive metal such as Al [8, 9].

We first show how basic transport properties such as the carrier density and sheet resistance are affected by the ferroelectric polarisation state and display a hysteretic behavior with applied electric fields. [10] Most importantly, performing charge-to-spin and spin-to-charge conversion experiments at low temperature, we demonstrate not only a ferroelectric control of the amplitude but also of the sign of the spin-charge interconversion, with opposite signs at electric remanence (see Fig. 1) [11].

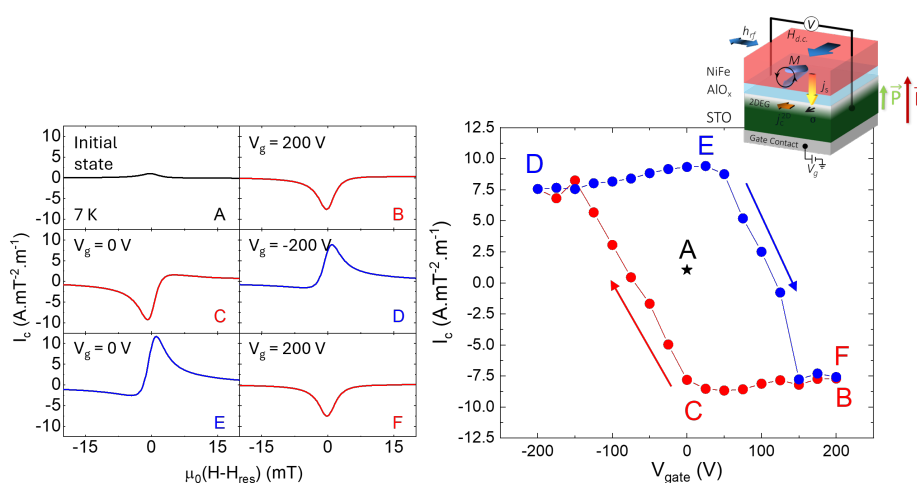


Figure 1: Spin-to-charge conversion experiments in SrTiO₃-based 2DEGs by spin-pumping at the ferromagnetic resonance.

Extending this work to other ferroelectric oxide 2DEGs with even higher conversion efficiencies and stable ferroelectric phase at room temperature may pave the way for future ultralow power spintronic logic-in-memory devices, reaching the attojoule range.

Acknowledgments

This work received support from the ERC Advanced Grant No. 833973 “FRESCO”, and the French ANR through project “CONTRABASS”.

References

- [1] B. Diény, I. L. Prejbeanu, K. Garello, et al. [Opportunities and Challenges for Spintronics in the Microelectronics Industry](#). *Nature Electronics* 3, 446–459 (2020).
- [2] Sasikanth Manipatruni, Dmitri E. Nikonov, and Ian A. Young. [Beyond CMOS Computing with Spin and Polarization](#). *Nature Physics* 14, 338 (2018).
- [3] Diogo C. Vaz, Paul Noël, Annika Johansson, et al. [Mapping Spin–Charge Conversion to the Band Structure in a Topological Oxide Two-Dimensional Electron Gas](#). *Nature Materials* 18, 1187–1193 (2019).
- [4] J. G. Bednorz and K. A. Müller. [Sr 1 - x Ca x Ti O 3 : An XY Quantum Ferroelectric with Transition to Randomness](#). *Physical Review Letters* 52, 2289–2292 (1984).
- [5] H Gränicher. Induzierte Ferroelektrizität von SrTiO₃ bei sehr tiefen Temperatur und über die Kalterzeugung durch adiabatic Entpolarisierung. *Helvetica Physica Acta* 29, 210–212 (1956).
- [6] J. Hemberger, P Lunkenheimer, R. Viana, R. Böhmer, and A. Loidl. [Electric-Field-Dependent Dielectric Constant and Nonlinear Susceptibility in SrTiO₃](#). *Physical Review B* 52, 13159–13162 (1995).
- [7] J Hemberger, M Nicklas, R Viana, et al. [Quantum Paraelectric and Induced Ferroelectric States In](#). *Journal of Physics: Condensed Matter* 8, 4673–4690 (1996).
- [8] Tobias Chris Rödel, Franck Fortuna, Shamashis Sengupta, et al. [Universal Fabrication of 2D Electron Systems in Functional Oxides](#). *Advanced Materials* 28, 1976–1980 (2016).
- [9] Luis M. Vicente-Arche, Srijani Mallik, Maxen Cosset-Cheneau, et al. [Metal/ SrTiO₃ Two-Dimensional Electron Gases for Spin-to-Charge Conversion](#). *Physical Review Materials* 5, 064005 (2021).
- [10] Julien Bréhin, Felix Trier, Luis M. Vicente-Arche, et al. [Switchable Two-Dimensional Electron Gas Based on Ferroelectric Ca: SrTi O 3](#). *Physical Review Materials* 4, 041002 (2020).
- [11] Paul Noël, Felix Trier, Luis M. Vicente Arche, et al. [Non-Volatile Electric Control of Spin–Charge Conversion in a SrTiO₃ Rashba System](#). *Nature* 580, 483–486 (2020).

Brillouin Light Scattering and BiYIG epitaxial films

Laurent Ranno^{1,*}, Jan Hnilica¹, Valérie Reita¹, Laurent DelRey¹, and Vincent Baltz²

¹*Institut Néel, CNRS et Univ. Grenoble Alpes*

²*Spintec, CNRS-CEA-UGA, Grenoble*

*laurent.ranno@neel.cnrs.fr

The first part of this poster will introduce the physics of the Brillouin Light Scattering (BLS) and its implementation as a BLS set-up. It will then be applied to characterise the magnonic and phononic excitations of epitaxial BiYIG garnet films heteroepitaxially grown on SGGG(111) substrates.

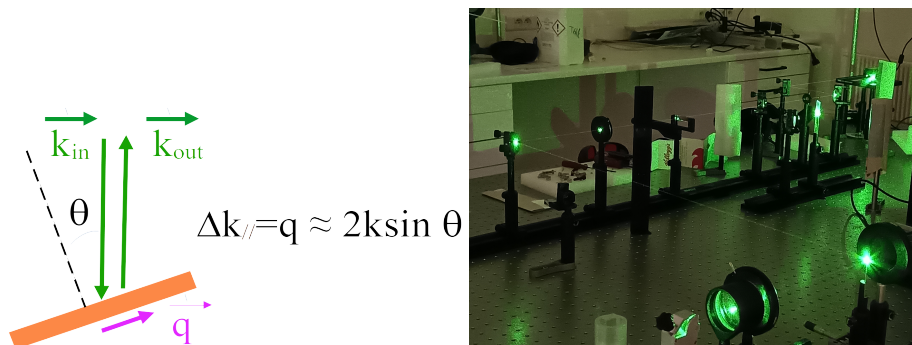


Figure 1: (a) BLS photon in -photon out Stokes (q is emitted) and Anti-Stokes (q is absorbed) processes. For thin films only the in-plane wave vector is conserved. (b) BLS optical bench.

BIG WOE SGGG 00 +370mT pol H Mirror 4.0mm 10.0s Scan 70.4C
 $\lambda=532.3\text{nm}$ 75.0mW Polar= H 512chan.

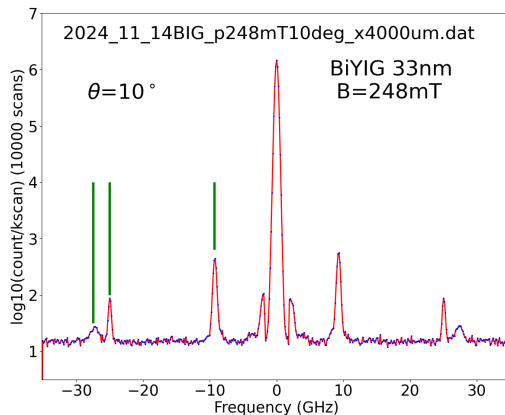


Figure 2: BLS spectrum recorded on a 33nm-thick BiYIG/SGGG(111) film evidencing bulk acoustic phonons (from SGGG), perpendicular standing spin waves and propagating in-plane spin waves.

Acknowledgments

The Grenoble BLS platform is a joint project between Institut Néel and Spintec. It has been funded through a Labex LANEF grant and a PEPR Spin (SpinCharac programme) one. J.H.'s PhD grant is from the QUANG programme.

Spin-polarized transport across a fluctuating molecular spin 1/2 two-level system.

Ujjawal Rathore^{1,*}, Theo Bruant^{1,*}, Talha Zafar¹, Mathieu Lamblin¹, Loïc Joly¹, Bertrand Vilen², Benoit Gobaut¹, Emmanuel Sternitzky¹, Victor Da Costa¹, Wolfgang Weber¹, Samy Boukari¹, Ali Msahazi¹, Hicham Majjid¹, and Martin Bowen¹

¹IPCMS, University of Strasbourg, Strasbourg, France

²Institut de Chimie, Strasbourg, France

*ujjawal.rathore@ipcms.unistra.fr

Molecular spintronics offers transformative potential for magnetic data storage devices [1] and energy harvesting [2] applications by utilizing molecular materials embedded between ferromagnetic (FM) layers, forming molecular magnetic tunnel junctions (MTJs). The industrial penetration of spintronics augurs the possibility to utilize this platform as a vector to industrialize quantum physics. Advantageously, ferromagnetic metal/molecule interfaces (also known as spinterfaces) exhibit a high spin polarization of the electronic charge current[2], which can alter the spin splitting and energy position of a spin 1/2 two-level system[3]. Our group has reported on the spintronic control over a spin chain borne by the spin 1/2 site of Cobalt Phthalocyanine molecules[1]. In that study, the spin chain was in direct electronic interaction with the spinterface. To extend this study and investigate the platform's potential to industrialize quantum physics, in the present work, we have inserted an ultrathin C60 spacer between the spinterface and the molecular spin chain. We aim in this way to decrease the effective spin splitting that is electronically induced onto the spin 1/2 site. We will present first magnetotransport results on Fe/C60(0-2ML)/CoPc(1-3ML)/C60(5ML)/Fe devices, which exhibit a rich feature set (see example in Figure 1).

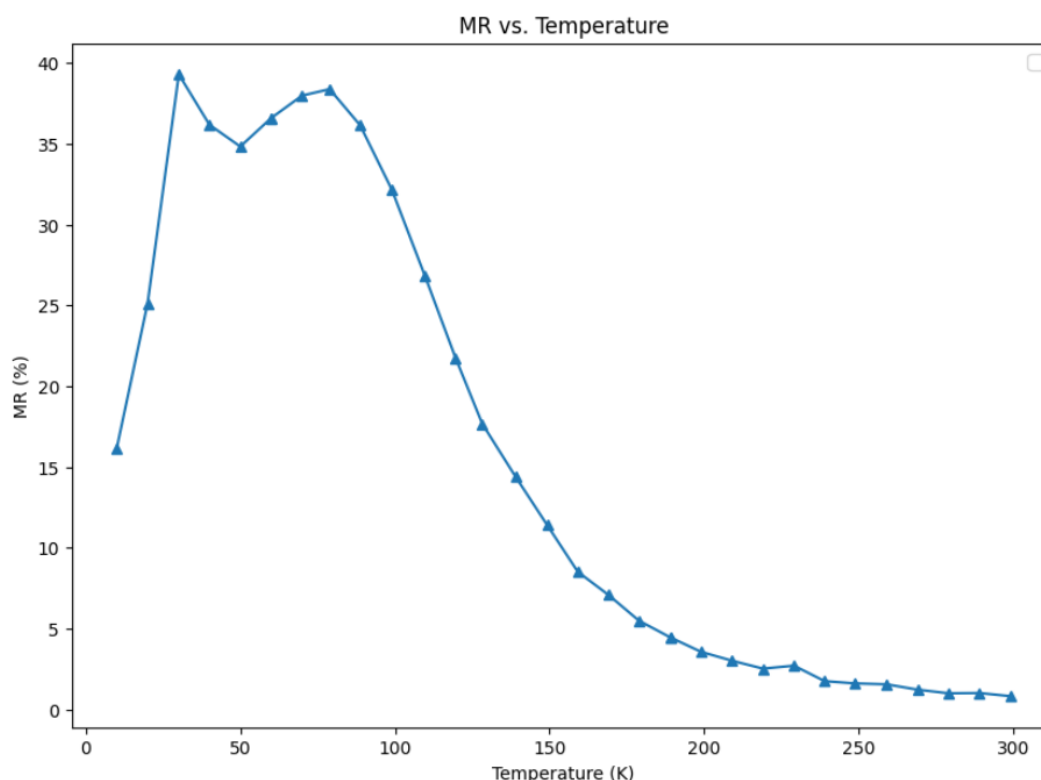


Figure 1: Temperature dependence of magnetoresistance across a Fe/C60(1ML)/CoPc(2ML)/C60(5ML)/Fe nanojunction (nominal diameter 500nm). As a first interpretation, the dataset reflects the competition between thermally assisted spintronic transport across the antiferromagnetic spin chain formed by CoPc, and the mixing of spin channels due to overcoming the intrachain exchange energy corresponding to $T \approx 70\text{K}$ [2].

References

- [1] Kostantine Katcko, Etienne Urbain, Franck Ngassam, et al. Encoding information on the excited state of a molecular spin chain. *Advanced Functional Materials* 31, 2009467 (2021).

- [2] Bhavishya Chowrira, Lalit Kandpal, Mathieu Lamblin, et al. Quantum advantage in a molecular spintronic engine that harvests thermal fluctuation energy. *Advanced Materials* 34, 2206688 (2022).
- [3] K Katcko, E Urbain, B Taudul, et al. Spin-driven electrical power generation at room temperature. *Communications Physics* 2, 116 (2019).

Tuning the magnetic anisotropy of Pt/Co-based thin films using electric fields

Agnieszka Klimeczek^{1,*}, Maurizio De-Santis¹, Anne D. Lamirand², Aurélien Masseboef³, Laurent Ranno¹, Jan Vogel¹, and Stefania Pizzini¹

¹CNRS, Institut Néel, Grenoble, France

²Université Lyon, École Centrale de Lyon, CNRS, INSA Lyon, Université Claude Bernard Lyon 1, CPE Lyon, INL, UMR 5270, Ecully, France

³Université Grenoble Alpes, CNRS, CEA, SPINTEC, Grenoble, France

*agnieszka.klimeczek@neel.cnrs.fr

The scaling limitations of CMOS technology drive the need for alternative solutions in memory and logic spintronic devices, where the manipulation of magnetic anisotropy driven by gate voltage offers a non-volatile, low-energy way to control the magnetization. This presents a promising path for the development of low power, high-performance microelectronic devices.

We have studied the magnetic properties of a Si/SiO₂/Ta/Pt/Co trilayer with a gradient of cobalt thickness varying between 0.7 nm and 1.2 nm, prepared by magnetron sputtering, and then exposed to air. The magnetic easy axis varies between out-of-plane to in-plane as the Co thickness increases, with a reorientation transition occurring around 1 nm of Co. Using UV lithography and lift-off techniques, we fabricated Hall crosses and capacitor-like devices by adding a high-*k* dielectric layer, HfO₂, which acts as an ionic conductor. By gating the stack, a magneto-ionic effect is induced, enabling the tuning of the system's magnetic anisotropy.

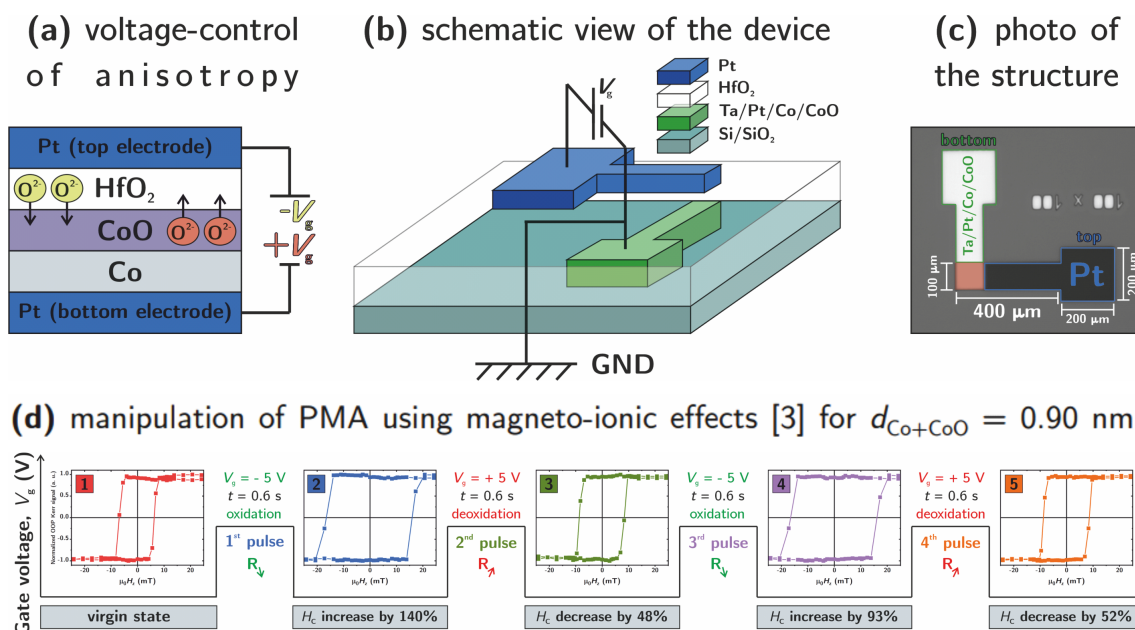


Figure 1: (a) Schematic representation of voltage-controlled magnetic anisotropy via a magneto-ionic effect. A gate voltage (V_g) applied to capacitor-like structures induces ionic motion of oxygen between the HfO₂ layer and the CoO layer, modulating the magnetic anisotropy. (b) Simple graphics of the fabricated device, showing the layered system, along with the electrical connections for gating. (c) Photo of the fabricated device with labeled top and bottom electrodes. (d) An example of the manipulation of PMA for a Co + CoO thickness of 0.9 nm. The sequence of the hysteresis loops corresponds to consecutive gating pulses ($V_g = \pm 5$ V, $t = 0.6$ s), showing reversible changes in the coercive field. The consecutive oxidized and reduced states exhibit different resistances of the magnetic stack.

X-ray Photoelectron Spectroscopy (XPS) measurements highlight the presence of a mixture of Co metal and CoO oxide, with a dominant CoO signature, indicating that the oxide is on the surface of the layers and, consistently, an increasing Co metal signature as the Co thickness increases.

Hysteresis cycles measured via the Anomalous Hall Effect (AHE) at temperatures between 4 K and 300 K, reveal a giant exchange bias and an increase of coercivity at low temperatures, highlighting the antiferromagnetic nature of the CoO layer. The blocking temperature, T_B , varies with Co thickness, ranging from 150 K at 0.7 nm to 200 K at 1.2 nm. We also modified the exchange bias of the system by gating the stack *ex situ* at room temperature.

We demonstrate that the perpendicular magnetic anisotropy (PMA) of our sample can be modified by gating, enabling the switching between low-, and high-anisotropy states respectively with in-plane and out-of-plane magnetization. Additionally, anisotropic field-driven domain-wall dynamics highlights a strong interfacial Dzyaloshinskii-Moriya interaction, which can be also modulated by an external field.

Acknowledgments

The authors would like to acknowledge the ANR PEPR SPIN CHIREX ('Beyond CMOS with chiral textures') project for funding the research.

Towards Fiber-Integrated Cryogenic NV Microscopy for High-Resolution Magnetic Mapping

Eric Clot¹, Tianqi Zhu¹, Alessandro Azzani^{1,2}, and Christian Degen¹

¹*Spin Physics - Laboratory for Solid State Physics, ETH Zürich, Zürich, Switzerland*

²*QZabre AG, Zürich, Switzerland*

*erclot@phys.ethz.ch

Achieving high spatial resolution of magnetic micro- and nanostructures is essential for understanding cutting-edge phenomena such as spin-wave propagation in ferromagnetic materials [see Samer Curdi's publications], and it plays a crucial role in translating these findings into technological applications.

The ability to optically detect the electron paramagnetic resonance (EPR) of a single nitrogen-vacancy (NV) center in diamond has revolutionized the field of spectroscopy [1, 2]. By attaching a nanodiamond that hosts such a single color center to the tip of a near-field microscope cantilever, one can construct a scanning spectrometer capable of locally mapping the modulation of its EPR response without compromising the frequency range, external magnetic field strength, spatial resolution, sensitivity, or precision.

In order to extend these techniques to the study of phenomena occurring at cryogenic temperatures, such as superconductivity, NV-based systems must be able to operate under these low-temperature conditions. Previous work has demonstrated the feasibility of such measurement setups [3]. However, using color centers as magnetic sensors requires collecting fluorescence across a broad emission band (600–800 nm).

Current systems, whether operating at room temperature or in cryogenic environments, mainly rely on free-space optics for confocal microscopy of NV centers. In a cryostat setting, this approach severely limits the implementation of effective mechanical isolation against the vibrations induced by pulse tubes, owing to the extreme sensitivity of the optical alignment. Specifically, the free-space beam path between the focusing objective and the external environment—often spanning up to two meters—introduces substantial vibrations at the near-field probe, thereby restricting the spatial resolution to a value far above the theoretical ten-nanometer range.

To overcome these limitations, our team at ETH Zurich, under the guidance of Professor Degen, is launching a new project aimed at rethinking the integration of confocal optics commonly used in NV microscopes. We propose coupling both the collected fluorescence and the excitation laser in situ via optical fibers, directly within the microscope head located inside the cryostat. This design enables far more effective isolation of the near-field microscopy region from the rest of the cryostat, notably by using a lossy spring-based suspension setup.

This approach further leverages integrated photonic chips to separate fluorescence from excitation in a highly constrained environment, positioned as close as possible to the NV center.

Ultimately, this project seeks to remove the technological barriers that currently hinder the study of magnetic properties of materials at low temperature through NV magnetometry.

References

- [1] A. Gruber, A. Dräbenstedt, C. Tietz, et al. [Scanning Confocal Optical Microscopy and Magnetic Resonance on Single Defect Centers](#). *Science* 276, 2012–2014 (1997).
- [2] I. Gross, W. Akhtar, V. Garcia, et al. [Real-space imaging of non-collinear antiferromagnetic order with a single-spin magnetometer](#). *Nature* 549, 252–256 (2017).
- [3] P. J. Scheidegger, S. Diesch, M. L. Palm, and C. L. Degen. [Scanning nitrogen-vacancy magnetometry down to 350 mK](#). *Applied Physics Letters* 120 (2022).

Nonlinear interactions between parametrically excited spin-wave modes in a YIG microdisk

H. Merbouche^{1,*}, G. Soares¹, R. Lopes Seeger¹, A. Kolli¹, M. Massouras², N. Beaulieu³, J. Ben Youssef³, M. Muñoz⁴, P. Che⁵, A. Anane⁵, S. Perna⁶, M. d'Aquino⁶, C. Serpico⁶, J.-V. Kim², and G. de Loubens¹

¹*SPEC, CEA, CNRS, Université Paris-Saclay, France*

²*Université Paris-Saclay, CNRS, Centre de Nanosciences et de Nanotechnologies, France*

³*LabSTICC, CNRS, Université de Bretagne Occidentale, Brest, France*

⁴*Instituto de Tecnologías Físicas y de la Información (CSIC), Madrid, Spain*

⁵*Laboratoire Albert Fert, CNRS, Thales, Université Paris-Saclay, France*

⁶*Department of Electrical Engineering and ICT, University of Naples Federico II, Italy*

*hugo.merbouche@cea.fr

Spin waves (SWs) hold great promise for energy-efficient hardware for information processing due to their low-energy and small wavelength at GHz frequencies. Furthermore, their non-linear properties make them interesting for neuromorphic computing [1], which takes inspiration from the brain to efficiently perform complex tasks. SWs face the same connectivity challenge as other physical systems. In fact, both artificial and biological neural networks are highly interconnected structures that are difficult to replicate with physical hardware based on 2D nanofabrication techniques. To address this issue, we have noted that in the non-linear regime SW modes are all coupled to each other, i.e. in the reciprocal space (k-space) they are all highly connected. In extended films, the SW k-space is continuous and has been the subject of many studies describing striking nonlinear phenomena such as Bose-Einstein condensation, solitons, and chaos. However, these phenomena that involve the interaction of many modes are difficult to control and to model. In contrast, in confined magnetic structures, the SW spectrum is quantized. This opens up the possibility to selectively excite SW modes using multi-tone rf signals, and use their non-linear interactions to perform computation tasks. Recently, neuromorphic hardware based on this approach has been successfully implemented to robustly classify rf signals [2].

In this work, we are interested in determining the nonlinear phenomena involved when multiple modes are excited in a confined magnetic system, as well as ways to control and model these non-linear interactions. To that end, we have demonstrated [3] that we can use parallel pumping to selectively excite any SW mode in a 1 μm yttrium iron garnet disk magnetized in the plane. We then use frequency multiplexing to parametrically excite two SW modes simultaneously and probe their mutual interaction by magnetic resonance force spectroscopy (MRFM). By sweeping the two excitation frequencies (f_A and f_B) we observe that for the frequencies where two modes are excited (crossing regions), the total number of magnons does not correspond to the sum of the respective single tone experiments, meaning that the excited modes interact nonlinearly (Fig. 1). By analyzing the crossing regions using a normal mode model [4], we evidence that for quantized structures the nonlinear mechanism that governs the steady state is the nonlinear frequency shift (NLFS), which is contrast with extended magnetic systems where a phase mechanism dominates. Using our model, we demonstrate that the final state of the system critically depends on the relative signs of the NLFS of the two modes, the detuning between the excitation frequency and twice the resonance frequencies of the modes, and the timing of the excitation pulses (f_A applied before f_B or vice versa). These results open up exciting avenues for nonlinear magnonics and spin-wave neuromorphic computing.

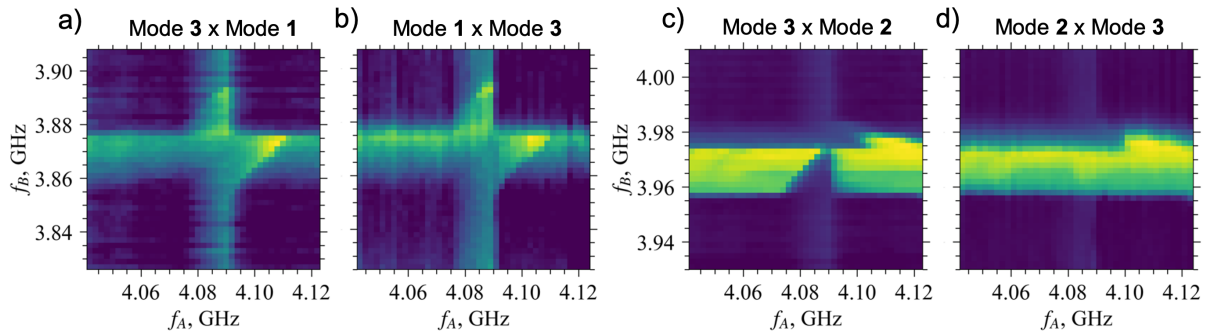


Figure 1: (a,b,c,d) Total number of magnons in the steady state (linear color scale) as a function of the parallel pumping frequencies f_A and f_B ($P_A = P_B = 3$ dBm). The different maps show the third SW mode of the disk non-linearly interacting with mode 1 (a, b) and mode 2 (c, d). Both modes are excited for $40 \mu\text{s}$ and mode 3 is either applied $5 \mu\text{s}$ before the other mode (a, c) or $5 \mu\text{s}$ after (b, d). The steady state intensity draws typical patterns that strongly depends on the pair of excited modes, the excitation frequencies and the order of excitation (clear non-commutativity between c and d). The magnetic field is applied in plane ($H_0 = 27.1$ mT).

Acknowledgments

This work is supported by the European project k-NET n°899646 and France 2030 government investment plan managed by the French National Research Agency under grant reference PEPR SPIN – SPINCOM ANR-22-EXSP-0005.

References

- [1] Danijela Marković, Alice Mizrahi, Damien Querlioz, and Julie Grollier. [Physics for neuromorphic computing](#). *Nature Reviews Physics* 2, 499–510 (2020).
- [2] Lukas Körber, Christopher Heins, Tobias Hula, et al. Pattern recognition in reciprocal space with a magnon-scattering reservoir. *Nature Communications* 14, 3954 (2023).
- [3] T. Srivastava, H. Merbouche, I. Ngouagnia Yemeli, et al. [Identification of a Large Number of Spin-Wave Eigenmodes Excited by Parametric Pumping in Yttrium Iron Garnet Microdisks](#). *Physical Review Applied* 19, 064078 (2023).
- [4] S. Perna, F. Bruckner, C. Serpico, D. Suess, and M. d’Aquino. [Computational Micromagnetics based on Normal Modes: bridging the gap between macrospin and full spatial discretization](#). *Journal of Magnetism and Magnetic Materials* 546, 168683 (2022).

Skyrmions for neuromorphic computing applications

Bibekananda Paikaray^{1,*}, Dedalo Sanz-Hernandez¹, William Bouckaert¹, Liza Herrera Diez², Chilingua John¹, Vincent Cros¹, Nicolas Reyren¹, and Julie Grollier¹

¹*Laboratoire Albert Fert, CNRS, Thales, Université Paris-Saclay, 91767 Palaiseau, France*

²*Centre de Nanosciences et de Nanotechnologies, CNRS, Université Paris-Saclay, Palaiseau 91120, France*

*bibekananda.paikaray@cnrs-thales.fr

Magnetic skyrmions are topologically protected swirling spin textures, offering great potential as information carriers for data storage, processing, and transmission technologies. These textures are stabilized at room temperature in magnetic thin films or heterostructures engineered with optimal magnetic anisotropy and Dzyaloshinskii-Moriya interaction (DMI) and can be manipulated by electric current and field. Their unique physical and topological characteristics have gained increasing attention in the field of spintronics, driven by their nanoscale dimensions, particle-like behavior, stability, non-volatility, energy efficiency, and high-speed operation[1].

Neuromorphic computing is based on principles inspired by the structure and functionality of the human brain that reduces energy consumption by up to four orders of magnitude compared to CMOS technology by using neurons for computation and synapses for memory, enabling highly efficient parallel processing[2]. Incorporating the unique properties of magnetic skyrmions for neuromorphic computing holds the potential to boost computational capabilities. Recently, some of us have demonstrated the proof of concept of a fully functional, all-electrical device utilizing skyrmions to make a weighted sum operation, a first important step towards artificial neural network applications[3]. However, many challenges remain for improving their functionalities and performances.

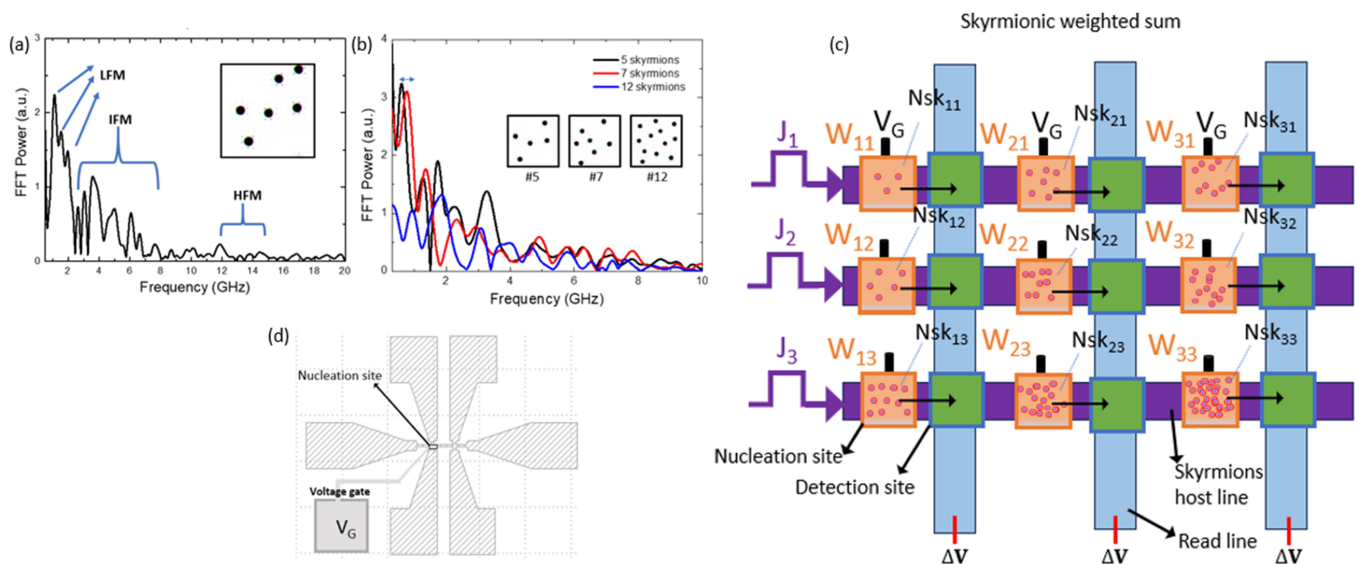


Figure 1: (a) Illustration of the microwave response of skyrmions, distinct modes: Low-Frequency Mode (LFM), Intermediate-Frequency Mode (IFM), and High-Frequency Mode (HF). (b) Variation of these modes with different skyrmion counts. (c) Schematic representation of the proposed implementation of a skyrmionic weighted sum, performing the essential operations for a neural network. (d) Voltage gate control schematic for skyrmion nucleation and motion.

In skyrmionics synapses, the synaptic weight, which determines the strength of the signal transmitted between neurons, is typically linked to the total number of skyrmions in the device, that thus needs to be detected. Several methods can be used for this purpose, such as the Anomalous Hall Effect (AHE), or the integration of Magnetic Tunnel Junctions. Another promising approach for achieving skyrmion-based synapses involves leveraging their microwave response[4]. Using micromagnetic simulations, we study the response of the magnetization inside the synapse to an RF input signal, and how it varies with the number of skyrmions, as shown in Figure 1(a, b). By applying a small in-plane radio frequency (RF) field, commonly used in ferromagnetic resonance (FMR) techniques, we were able to excite distinct skyrmion modes: the low-frequency mode (LFM < 2 GHz), intermediate-frequency mode (IFM < 8 GHz), and high-frequency mode (HF > 12 GHz), as illustrated in Fig. 1(a). This method provides an effective way to quantify skyrmions within the crossbar track, and therefore read its output. Skyrmions also naturally enable the implementation of weighted sums, the essential operation of a neural network[3]. In Fig. 1(c), we present a crossbar array designed to control the nucleation and propagation of skyrmionic quasiparticles along the skyrmion host line (purple track). Electrical inputs (J) are applied to these tracks to nucleate a controlled number of magnetic skyrmions at specific nucleation sites (orange boxes), each associated with a synaptic weight (W). The nucleation process is influenced by factors such as local magnetic anisotropy and material properties. The skyrmions are then guided to a transverse electrical detection zone (green boxes) at the intersection of the magnetic track,

where the cumulative number of skyrmions is electrically detected through an output voltage (ΔV) generated by the AHE. The electrical output is highlighted in red.

Voltage-controlled magnetic anisotropy (VCMA) offers a powerful mechanism for modulating the local magnetic properties of skyrmionic multilayers[5] and eventually the number of generated skyrmions, effectively tuning the synaptic weight[6] or directly acting as an input, as illustrated in Fig. 1(d). The applied voltage can nucleate a controllable number of skyrmions in the skyrmionic stack at room temperature and the number of generated skyrmions (weight factor) directly correlates with the voltage applied. Integrating charge-based VCMA with interfacial chiral interactions (DMI) makes it possible to control the formation and annihilation of large skyrmionic bubbles. Achieving long-lasting, ultra-low-power skyrmion synapses with non-volatile control over skyrmion generation, along with the ability to selectively pin or depin various skyrmionic species, are essential capabilities for advancing skyrmion-based artificial neural network computing.

Acknowledgments

This research is supported by the EU project SkyANN (reference no. 101135729) and from a France 2030 government grant managed by the French National Research Agency (grant no. ANR-22-EXSP-0002 PEPR SPIN CHIREX).

References

- [1] Richard Francis Llewelyn Evans, Unai Atxitia, and Roy W Chantrell. Quantitative simulation of temperature-dependent magnetization dynamics and equilibrium properties of elemental ferromagnets. *Physical Review B* 91, 144425 (2015).
- [2] Julien Tranchida, Pascal Thibaudeau, and Stam Nicolis. Colored-noise magnetization dynamics: from weakly to strongly correlated noise. *IEEE Transactions on Magnetics* 52, 1–4 (2016).
- [3] Julien Tranchida, Pascal Thibaudeau, and Stam Nicolis. Hierarchies of Landau-Lifshitz-Bloch equations for nanomagnets: A functional integral framework. *Physical Review E* 98, 042101 (2018).
- [4] MD Kuz'min. Shape of Temperature Dependence of Spontaneous Magnetization of Ferromagnets: Quantitative Analysis. *Physical review letters* 94, 107204 (2005).
- [5] Olle Eriksson, Anders Bergman, Lars Bergqvist, and Johan Hellsvik. *Atomistic spin dynamics: foundations and applications*. Oxford university press, 2017.
- [6] ED Thompson and JJ Myers. Magnon Energy of Nickel. *Physical Review* 153, 574 (1967).

Multiscale atomistic code for material design Matjes

Xavier Bosch², Patrick Buhl², Bertrand Dupé^{1,*}, and Sebastian Meyer^{1,2}

¹Fonds de la Recherche Scientifique (FRS-FNRS), 5 rue D'Egmont, 1000 Bruxelles, Belgium

²TOM/Q-mat/CESAM, Université de Liège, B-4000 Sart Tilman, Belgium

*bertrand.dupe@uliege.be

Multiscale simulations are critical for designing novel materials with optimized properties and performance. In spintronics, multiscale simulations play a vital role in developing next-generation devices such as novel magnetic storage devices, energy efficient computing units or sensors [1].

All these innovations are originating from breakthroughs in the field of quantum mechanics which can describe accurately the magnetic and structural properties down to the atomic scale. This involves the computation of realistic magnetic interactions, elastic constants and band structures. To successfully describe an electronic device in a realistic environment, not only the single atom limit but also the collective thermodynamical behavior must be described. Multiscale simulations parametrized by density functional theory (DFT) calculations are an ideal tool to study electronic devices in a realistic environment.

Recently, non-collinear magnetic textures such as domain walls, vortices and skyrmions are coming in the forefront of spintronics [2]. Such extended textures in real space are impossible to study with DFT calculations and require the use of second principle calculation which may be atomistic or continuous simulations. Here, we would like to present our recent advances regarding second principle atomistic simulations as implemented in our code Matjes [3]. Our implementation is similar to available packages [4–6] but extends the current implementations to real space calculations of non-collinear textures which may arise in magnetic, ferroelectric or multiferroic materials.

Our implementation can simulate bulk, thin film, interfaces geometries. For each geometry and symmetry, we compute the topological charge given by:

$$Q = \frac{1}{4\pi} \int \mathbf{n}(\mathbf{r}) \cdot (\nabla_x \mathbf{n} \times \nabla_y \mathbf{n}) d\mathbf{r} \quad (21)$$

where $\mathbf{n}(\mathbf{r})$ is a normalized vector field collinear to the displacement or the magnetization field. Our computational method uses the topological alongside the magnetization and the displacements to describe phase transition via conventional Monte Carlo simulations, entropic Monte Carlo and parallel tempering Monte Carlo. The particularity of our approach is to explore *in situ* the correlations on the topological charge, the magnetization and the displacements to solve real space green functions, to calculate entropy and internal energies to explore the temperature evolution of the different interactions.

Our simulations are able to include harmonic interactions beyond the first nearest neighbor approximation (magnetic exchange, magnetic anisotropy...), dipolar interactions as well as higher order interactions such as the three and four spin interactions and the Dzyalijnskyi-Moriya interactions in agreement with the Levy and Fert Model [7] and the spin current model [8]. The implementation of these couplings allows for the combined exploration of magnetic and molecular dynamics in multiferroics.

Acknowledgments

S.M. is a Postdoctoral Researcher (CR) of the Fonds de la Recherche Scientifique - FNRS (FR.S.-FNRS no. CR 1.B.324.24F). This work is supported by Excellence of Science project CONNECT number 40007563 funded by FWO and FNRS.

References

- [1] Feliciano Giustino, Jin Hong Lee, Felix Trier, et al. [The 2021 quantum materials roadmap](#). *Journal of Physics: Materials* 3, 042006 (2021).
- [2] C Back, V Cros, H Ebert, et al. [The 2020 skyrmionics roadmap](#). *Journal of physics D: Applied physics* 53, 363001 (2020). eprint: [2001.00026](#).
- [3] P.M. Buhl, L. Desplat, M. Boettcher, S. Meyer, & B. Dupé. *Matjes*. Version 1.1.0. 2024.
- [4] B Skubic, J Hellsvik, L Nordström, and O Eriksson. [A method for atomistic spin dynamics simulations: implementation and examples](#). *Journal of physics. Condensed matter: an Institute of Physics journal* 20, 315203 (2008).
- [5] Richard F L Evans, W J Fan, P Chureemart, et al. [Atomistic spin model simulations of magnetic nanomaterials](#). *Journal of physics. Condensed matter: an Institute of Physics journal* 26, 103202 (2014). eprint: [1310.6143](#).
- [6] Gideon P Müller, Markus Hoffmann, Constantin Dißelkamp, et al. [Spirit : Multifunctional framework for atomistic spin simulations](#). *Physical Review B: Condensed Matter and Materials Physics* 99, 224414 (2019). eprint: [1901.11350](#).
- [7] Albert Fert and Peter M Levy. [Role of anisotropic exchange interactions in determining the properties of spin-glasses](#). *Physical review letters* 44, 1538–1541 (1980).
- [8] Hosho Katsura, Naoto Nagaosa, and Alexander V Balatsky. [Spin Current and Magnetoelectric Effect in Noncollinear Magnets](#). *Physical review letters* 95, 057205 (2005). eprint: [cond-mat/0412319](#).

Caustiques d'ondes de spin dans un matériau non-réciproque confiné latéralement

Jean-Paul Adam^{1,*}, Sokhna-Mery Ngom¹, Nathalie Bardou¹, A. Solignac², Joo-Von Kim¹, and Thibaut Devolder¹

¹Centre de Nanosciences et de Nanotechnologies, Université Paris-Saclay, CNRS, Palaiseau, France

²SPEC, CEA, CNRS, Université Paris-Saclay, Gif-sur-Yvette, France

*jean-paul.adam@universite-paris-saclay.fr

Dans une piste magnétique confinée latéralement, les ondes de spin propagatives peuvent être excitées par l'utilisation d'une antenne qui permet de générer un champ magnétique dans le régime des GHz. Dans un matériau ferromagnétique tel que le Permalloy, saturé dans la direction perpendiculaire à la piste, géométrie dite de Damon-Eshbach, les ondes de spin sont guidées dans la piste selon des modes confinés dans la largeur [1]. Ces différentes ondes de spin peuvent interférer et donner naissance à des figures d'interférence comme observé par spectroscopie Brillouin microfocalisée - μ BLS [2].

Nous présentons une étude, par μ BLS, sur le comportement des ondes spin propagatives dans un système antiferromagnétique synthétique constitué de deux couches de CoFeB de 17 nm chacune, séparées par une couche de ruthénium de 0.7 nm d'épaisseur. Il en résulte un couplage antiferromagnétique entre ces deux couches qui permet de stabiliser un état ciseaux sur une large gamme de champ magnétique. Deux types d'ondes de spin existent dans un tel système, les ondes de spin acoustiques (respectivement optiques) avec une précession en phase (resp. en opposition de phase) de l'aimantation dans les deux couches. Dans un tel système, la propagation des ondes de spin est fortement non-réciproque - $f(\vec{k}) \neq f(-\vec{k})$ - pour les ondes de spin se propageant selon la direction de la somme des aimantations de chacune des deux couches. Elle peut même se faire de façon unidirectionnelle : le transport de l'énergie a lieu selon une unique direction indépendamment du signe du vecteur d'onde pour les ondes acoustiques [3].

L'échantillon a été structuré sous la forme d'une piste de largeur 5 μm par gravure ionique, qui a été recouverte d'une couche de Si_3N_4 de 160 nm d'épaisseur. Afin d'exciter les ondes de spin, une antenne de 1.8 μm de large, perpendiculaire à la piste magnétique a été réalisée par lift-off (voir Figure 1.(a)). Pour une telle largeur d'antenne, des ondes de spin

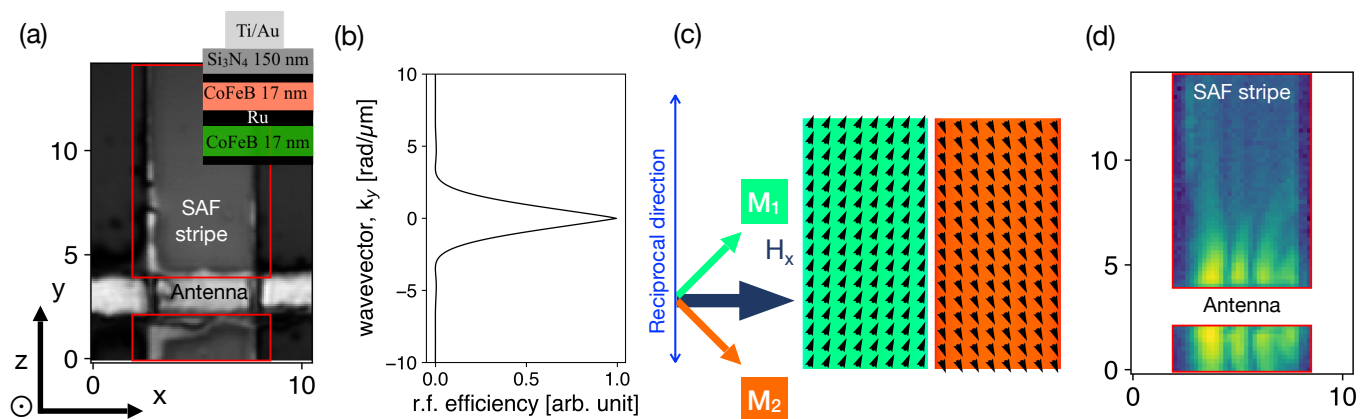


Figure 1: (a) image optique de l'échantillon et schéma de l'empilement de l'échantillon et du système de coordonnées. Les cadres rouges correspondent aux zones mesurées par μ BLS boxes: regions investigated by BLS microscopy. (b) Fonction d'efficacité de l'antenne en fonction du vecteur d'onde. (c) Configuration micromagnétique dans l'état ciseaux pour un champ appliqué de 50 mT tel qu'indiqué sur le schéma. (d) Profil de propagation d'onde de spin à $f_{\text{ex}} = 4.5$ GHz. Les régions investiguées ont des tailles respectives de 6.6 $\mu\text{m} \times 10.2 \mu\text{m}$ et 6.6 $\mu\text{m} \times 2.2 \mu\text{m}$ en haut et en bas.

avec un vecteur d'onde jusqu'à 3 $\text{rad} \cdot \mu\text{m}^{-1}$ peuvent être excitées inductivement. Les mesures de μ BLS ont été obtenues en focalisant le faisceau LASER - $\lambda = 532$ nm - au travers d'un objectif de microscopie de grandissement x50 et d'ouverture numérique 0.75, ce qui permet d'atteindre une résolution spatiale de l'ordre de 300 nm. Ce faisceau a été balayé par pas de 250 nm selon les deux zones rouges de la figure 1(a) pour un champ magnétique de 50 mT, appliqué dans le plan et transversalement à la longueur de la piste. Dans cette géométrie, la direction longitudinale est *a priori* réciproque pour les ondes de spin dans un système anti-ferromagnétique synthétique infini. Un exemple de profil est présenté en Figure 1-(d). Le profil spatial fait ressortir des canaux de propagation mais avec une directionnalité qui n'est pas selon la longueur de la piste comme on pourrait s'y attendre pour une propagation réciproque.

Des profils ont été acquis à différentes fréquences d'excitation sur une large gamme entre 3.5 GHz et 10 GHz pour un champ de 50 mT. Ils sont présentés dans la figure 2. Aux basses fréquences par rapport à la fréquence des ondes de spin acoustiques à $\vec{k} = 0$, $f_{\text{ac}}(0)$, l'intensité BLS est concentrée proche de l'antenne avec un faible caractère propagatif et fait apparaître des noeuds dans la direction transverse. Lorsque la fréquence d'excitation augmente, la distance internodale

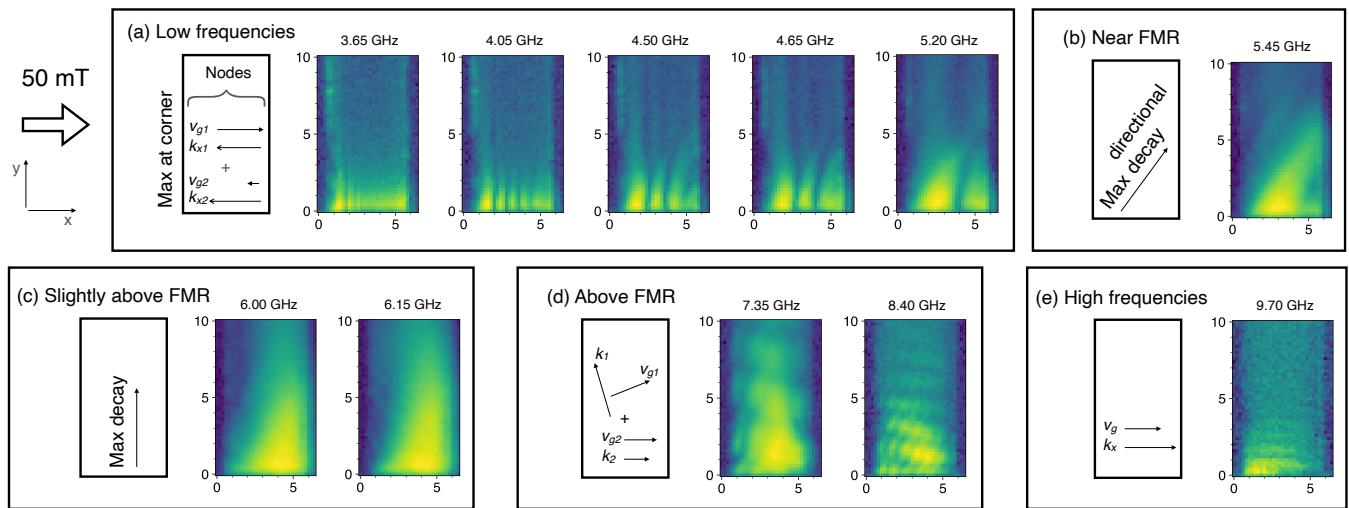


Figure 2: Profils d'ondes de spin obtenus par μ BLS pour un champ appliqué $\mu_0 H_x = 50$ mT. Les profils sont présentés par ordre croissant de la f_{ex} : (a) basses fréquences, (b) fréquence proche de $f_{ac}(0)$, (c) fréquences légèrement au-dessus de $f_{ac}(0)$, (d) fréquences sensiblement au-dessus de $f_{ac}(0)$ et (e) hautes fréquences.

augmente et le maximum d'intensité BLS se déplace vers le centre de la piste depuis l'extrémité gauche. Il apparaît progressivement un caractère propagatif qui tend vers la direction $\vec{x} + \vec{y}$. Lorsque la fréquence d'excitation atteint $f_{ac}(0)$, les ondes de spin se propagent de façon unidirectionnelle selon la direction $\vec{x} + \vec{y}$. Pour des fréquences d'excitation au-delà de $f_{ac}(0)$, la propagation se fait selon la direction longitudinale de la piste \vec{y} . En continuant à augmenter la fréquence d'excitation, une figure d'interférence bidimensionnelle apparaît. Plus la fréquence est élevée et plus la distance internodale diminue. Aux plus hautes fréquences, les ondes de spin ne se propagent plus selon la direction \vec{x} , confinées à proximité de l'antenne.

Pour comprendre ce comportement fondamentalement différent de celui observé pour un matériau réciproque, nous avons étudié l'évolution des relations de dispersion pour une direction arbitraire du vecteur d'onde dans le plan. Nous avons pour cela adapté la méthode de la matrice dynamique [4] en incluant le terme du champ d'échange intercouches. En étudiant les contours isofréquentiels, nous pouvons expliquer qualitativement les comportements expérimentalement observés dans les différentes gammes de fréquence identifiées. Même dans cette géométrie étudiée *a priori* réciproque, la non-réciprocité intrinsèque des systèmes antiferromagnétiques synthétique induit une coposante à la direction de propagation des ondes de spin selon la direction \vec{x} . Cette contribution peut être nulle, unique ou multiple selon la fréquence considérée en accord avec les figures d'interférences observées expérimentalement. Des simulations micromagnétiques réalisées avec Mumax3 confortent cette modélisation et permettent de reproduire quantitativement les résultats expérimentaux.

Acknowledgments

Nous remercions les projets Labex NanoSaclay SPICY référence : ANR-10-LABX-0035, PEPR SPIN, références : ANR-22-EXSP-0008 et ANR-22-EXSP-0004, dans le cadre des programmes France 2030, ainsi que le projet ANR-20-CE24-0025 (MAXSAW) et le réseau RENATECH pour la fabrication des échantillons.

References

- [1] C. Mathieu, J. Jorzick, A. Frank, et al. [Lateral Quantization of Spin Waves in Micron Size Magnetic Wires](#). *Phys. Rev. Lett.* 81, 3968–3971 (18 1998).
- [2] Vladislav E. Demidov, Sergej O. Demokritov, Karsten Rott, Patryk Krzysteczko, and Guenter Reiss. [Mode interference and periodic self-focusing of spin waves in permalloy microstrips](#). *Phys. Rev. B* 77, 064406 (6 2008).
- [3] F. Millo, J.-P. Adam, C. Chappert, et al. [Unidirectionality of spin waves in synthetic antiferromagnets](#). *Phys. Rev. Appl.* 20, 054051 (5 2023).
- [4] Yves Henry, Olga Gladii, and Matthieu Bailleul. [Propagating spin-wave normal modes: A dynamic matrix approach using plane-wave demagnetizing tensors](#). 2016. arXiv: 1611.06153 [cond-mat.mes-hall].

RF magnonic devices: modelling, experiment and integration

Sarah Manton^{1,*}, Romain Lebrun¹, Isabella Boventer¹, Ping Che¹, Jamal Ben Youssef², Paolo Bortolotti¹, Paolo Martins³, and Abdelmadjid Anane¹

¹Laboratoire Albert Fert, CNRS, Thales, Université Paris-Saclay, Palaiseau, France

²LabSTICC, CNRS, Université de Bretagne Occidentale, Brest, France

³Thales Research and Technology, F-91767 Palaiseau, France

*sarah.manton@cnrs-thales.fr

Spin waves offer several attractive properties such as scalability owing to their short wavelength in the microwave range, frequency tunability, and potential non-reciprocal and non-linear behaviours, notably for the development of innovative microwave devices [1]. However, a number of challenges remain to be tackled for their potential integration in any microwave devices.

In this context, we present our works towards the development of magnonic analog microwave devices. We will first present our strategy to optimize their microwave properties, taking the example of magnonic delay lines. Via a combination of analytical models [2], numerical models and measurements (see an example in Fig. 1), we can successfully optimize their frequency operation, bandwidth and insertion losses. To characterize magnonic devices, electrical spin wave spectroscopy using Vector Network Analyzers (VNA) is a technique of choice. However, accessing the rich physics of magnonic excitations requires not only their frequency but also their time domain properties as different spin wave modes can co-exist in the same frequency interval whilst having different group velocities. In this context, we show that time of flight spin wave spectroscopy [3] can be a useful tool to optimize spin wave devices [4].

In a second part, we present a strategy to achieve reconfigurable on-chip delay lines based on MEMS (Micro-Electro-Mechanical Systems) technology [5]. For this purpose, we developed a process allowing the monolithic integration of magnetic MEMS on a YIG delay line, as can be seen in Fig. 2 a). The magnetic MEMS membrane is suspended above the magnonic delay line in the form of a "bridge". By applying a voltage between the MEMS membrane and an electrode placed onto the surface of the magnonic delay line (see Fig. 2 b)), one can move the magnetic MEMS closer to the magnonic medium, as shown in Fig. 2 c). The stray field experienced by the YIG is hence locally modified by a few mT, thus changing the spin wave wavevector. First characterization of such effect was performed by propagative spin wave spectroscopy (PSWS) using a Vector Network Analyzer [6], effectively demonstrating propagation delay tunability with virtually zero stand-alone power. Such approaches hold promising opportunities for the optimized development of reconfigurable, integrated and low-power magnonic devices.

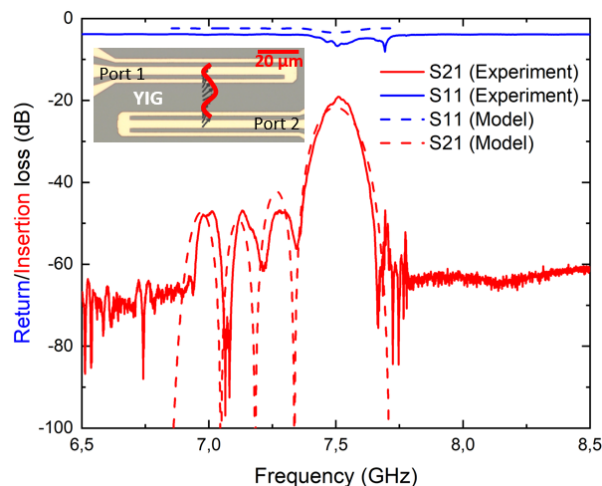


Figure 1: Characterization of a YIG magnonic delay line: plots of the insertion losses (red) and return losses (blue) measured by VNA (straight line) and calculated analytically (dashed line), where one can see the good agreement between our measurements and model.

Acknowledgments

We acknowledge support funding from the European Union's Horizon research and innovation programme under grant agreement No 101070536 (M&MEMS) and No 101070417 (SPIDER). This work has also benefited from a government grant operated by the French National Research Agency as part of the France 2030 program, reference ANR-22-EXSP-0004 (SWING).

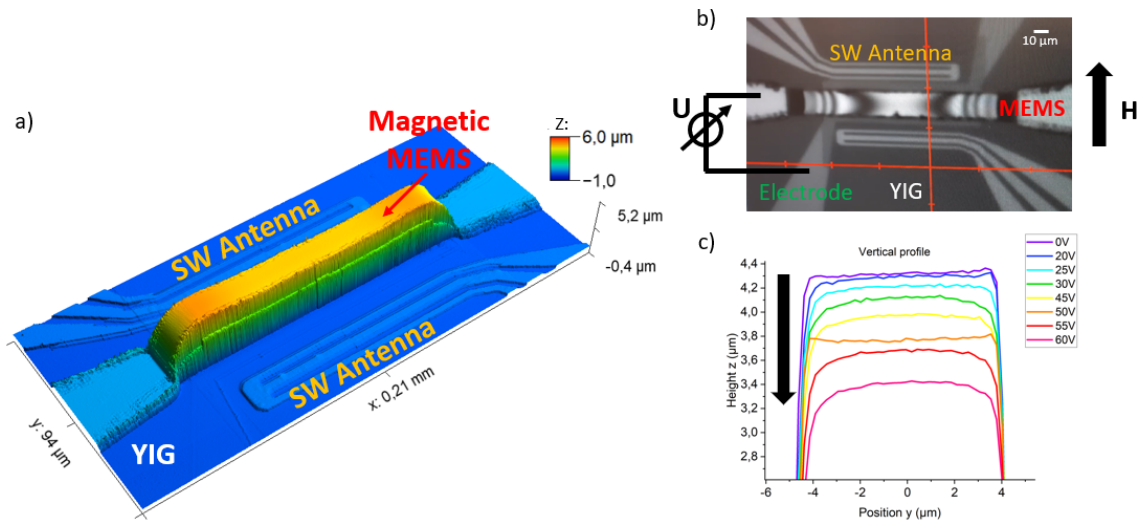


Figure 2: a) 3D optical profilometer image of a YIG magnonic delay line combined with a magnetic MEMS membrane placed above the magnonic medium (in-between the spin wave antennas) at a certain height of about $4.7 \mu\text{m}$. b) Top view image of YIG magnonic delay line combined with the magnetic MEMS membrane. c) Vertical cross-section (along the y axis in a)) measured by optical profilometer showing the displacement of the magnetic MEMS membrane towards the surface of the magnonic medium via the application of voltage between the MEMS and an electrode placed beneath the MEMS. An almost linear displacement of down to $1 \mu\text{m}$ can be seen with an applied voltage of 60 V .

References

- [1] A. V. Chumak, P. Kabos, M. Wu, et al. [Advances in Magnetism Roadmap on Spin-Wave Computing](#). *IEEE Transactions on Magnetism* 58, 1–72 (2022).
- [2] Hugo Merbouche. “Magnonic circuits based on nanostructured ultra-thin YIG for radiofrequency applications”. PhD thesis. Université Paris-Saclay, 2021.
- [3] T. Devolder, G. Talmelli, S. M. Ngom, et al. [Measuring the dispersion relations of spin wave bands using time-of-flight spectroscopy](#). *Phys. Rev. B* 103, 214431 (21 2021).
- [4] A. El Kanj, S. Manton, and et al. in preparation.
- [5] Federico Maspero, Simone Cucurullo, Giulia Pavese, et al. “Magnetism meet microelectromechanical systems”. *2023 IEEE International Magnetic Conference - Short Papers (INTERMAG Short Papers)*. 2023, 1–2.
- [6] S. Manton et al. in preparation.

Monolithic integration of magneto-optic garnet deposited by RF sputtering on LNOI

Nathan Beaulieu^{1,*}, Imtiaz Noor Bhatti², Abdelmadjid Anane², Homa Zarebidaki³, Gilles Feugnet⁴, and Jamal Ben Youssef¹

¹Lab-STICC, CNRS UMR 6285, Université de Bretagne Occidentale, Brest, France

²Laboratoire Albert Fert CNRS, Thales, Université Paris-Sud, Université Paris Saclay, Palaiseau, France

³CSEM – Swiss Center for Electronics and Microtechnology, Neuchâtel, Switzerland

⁴Thales Research and Technology, Thales, Palaiseau, France

*nathan.beaulieu@univ-brest.fr

In the aim of developing non reciprocal photonic device, we need to couple magneto-optic material to control the propagation modes of light in the waveguide. Lithium Niobate exhibits several properties, such as ferroelectric properties, it is regularly used as acoustooptic modulator (AOM) [1], or is regularly used as photonic crystals [2]. Coupling isolation and modulation in the same device is a challenging concept. In order to perform this coupling, we grew Bi doped Yttrium Iron garnet by RF sputtering on top of Lithium Niobate On Insulator (LNOI), which is constituted of a layer of LiNbO₃ (600 μ m) deposited on SiO/Si(100), elaborated at the CSEM [3]. The growth process is constituted of two phases: the deposition, performed by RF sputtering at a power of 150W, then the annealing, performed in a oven with a more or less important flux of gas, during which we control the duration, the annealing temperature, and the rump up temperature.

A preliminary study allowed us to understand that the LNOI was more sensitive to the annealing temperature than massive LiNbO₃: we observed the recrystallization of a parasitic phase of LiNbO₂ at the surface of the LNOI, which leads to lose some of the LiNbO₃ properties. This phenomena was not observed when annealing massive (500 μ m thick) LiNbO₃. In order to determinate the optimum material to get a compatible growth and a strong Faraday rotation to perform a magneto-optic isolator, we performed a preliminary study as a function of the Bi doping [4] Y₃Fe₅O₁₂ (YIG), Bi_{1.5}Y_{1.5}Fe₅O₁₂ (Bi:YIG) and Bi₃Fe₅O₁₂ (BiIG).

We chose to focus on the Bi:YIG composition because of the results from this study regarding the expected parameters: temperature of annealing needed that can lead to a surface modification of the LNOI. As the Si exhibits strong absorption properties in the visible area, and regarding that the domain of application is at the telecommunication wavelength, it was compulsory to perform the measurements at 1550 nm wavelength. The variation of the annealing temperature lead to an optimization of the Faraday rotation measured, as shown in Fig. 1.

We observed no Faraday rotation for the 120 nm and 300 nm thick films. This may be explained by the strong Verdet constant exhibited by the LNOI substrate (mainly coming from the 500 μ m thick Si). Regarding the 700 nm thick layers, the low temperature annealed (600 C) exhibits no Faraday rotation, whereas we measure an optimum at 700 C annealing (1500 °/cm at 1550 nm), then it decrease back at higher annealing temperature. From this study as a function of the annealing temperature, we tried to understand the influence of the rump up (named slope in the figure 2) temperature used in the annealing process at the optimized temperature of 700 C.

Like in the temperature study, we did not observe Faraday rotation for the 120 nm and 300 nm thick samples, probably still hidden by the strong Verdet constant of the LNOI. in the case of the 700 nm, we observed an optimized Faraday rotation for the slope 10 K/mn. After systematic further XRD investigations on all different thicknesses as a function of the slope, we were finally able to determinate the link between the crystallization of the layers and the Faraday rotation for the 700

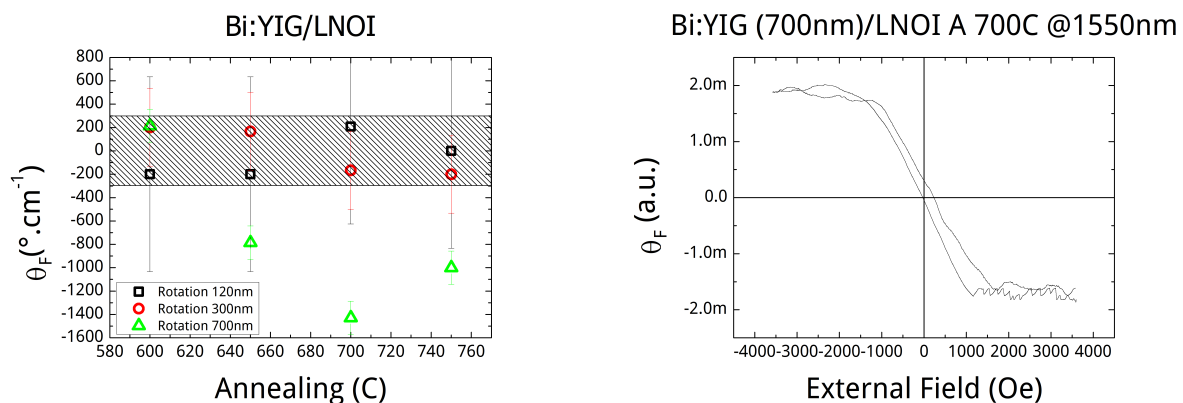


Figure 1: Influence of the annealing temperature on the Faraday rotation of Bi:YIG samples on LNOI measured at 1550 nm for three different thicknesses (120 nm, 300 nm and 700 nm). Faraday rotation cycle measured on the 700 nm thick layer annealed at 700 C.

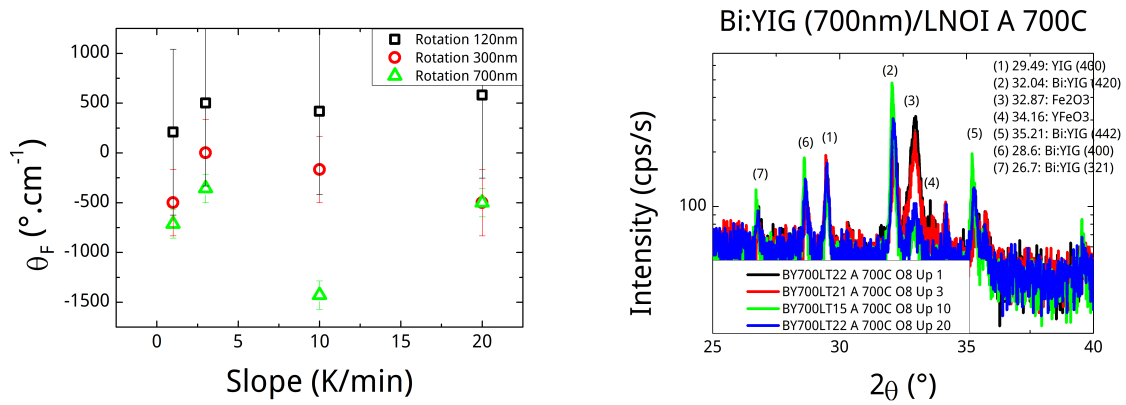


Figure 2: Influence of the ramp up temperature on the Faraday rotation of the Bi:YIG on LNOI measured at 1550 nm for three different thicknesses (120 nm, 300 nm and 700 nm). XRD measurement on the 700 nm layers annealed at 700 C, with the different slopes studied (1 K/mn, 3 K/mn, 10 K/mn, and 20 K/mn).

nm thick layers and the different temperature ramp up used during the annealing. The slope 10 K/mn leads to a better crystallization of the Bi:YIG, leading to a higher Faraday rotation as mentioned in the Fig. 2.

Acknowledgments

This work has been funded by the European Commission under the Horizon Europe program (PATTERN Project, grant 101070506). Views and opinions expressed are however those of the author(s) only and do not necessarily reflect those of the European Union. Neither the European Union nor the granting authority can be held responsible for them.

References

- [1] C. S. Tsai. *Guided-Wave Acousto-Optics: Interactions, Devices, and Applications*. Springer, 1990.
- [2] M.-P. Bernal, J. Amet, J. Safioui, et al. [Pyroelectric control of the superprism effect in a lithium niobate photonic crystal in slow light configuration](#). *Appl. Phys. Lett.* 98, 071101 (2011).
- [3] E. Obrzud, M. Rainer, A. Harutyunyan, et al. [A microphotonic astrocomb](#). *Nat. Photon.* 13, 31–35 (2019).
- [4] P. Hansen, K. Witter, and W. Tolksdorf. [Magnetic and magneto-optic properties of lead- and bismuth-substituted yttrium iron garnet films](#). *Phys. Rev. B* 27, 6608 (1983).

A scanning tunneling microscope combined with radio frequency to detect magnetic resonance at the atomic scale

Eugenio Gambari¹, Pascal David¹, Francois Debontridder¹, Mathieu Bernard¹, Silbe Majrab¹, Tristan Cren¹, and Marie Hervé^{1,*}

¹*Sorbonne Université – CNRS - Institut des Nanosciences de Paris UMR7588, 4 place Jussieu, Paris 75005, France*

**marie.herve@insp.upmc.fr*

In condensed matter systems, the investigation of low energy magnetic excitations has been usually carried out using resonance methods [1]. With the development of low dimension electronics and quantum computing, one challenge in condensed matter physics is to develop resonance experiments capable of detecting low energy electronic, magnetic and vibronic excitations down to the single atom / molecule limit. Scanning tunneling microscopy (STM) can be used to investigate these excitations of single molecules or atoms on surfaces in the sub-meV range [2]. Indeed, such excitation spectrum can be probed using conventional STM if the energy separation between the states is larger than 3.2kbT . To go beyond the thermally limited energy resolution, one possibility is to combine resonance techniques and STM. In this way, the excitation spectra of single atoms and molecules can be investigated with a neV energy resolution. Accessing this region of the energy spectrum with a STM has been a long-standing problem because of its natural inability to detect high frequency signals. Only recently, some extensions of STM have been developed to detect low energy magnetic excitations down to the sub- μeV range, allowing to perform resonance measurements such as electron spin resonance [3] or ferromagnetic resonance [4]. We are currently building a RF-STM setup at the Institut des NanoSciences de Paris (INSP). In this communication, I will present our current progress in the realization of this project, introducing at first the home-built experimental setup and its working principles.

References

- [1] Charles P Slichter. *Principles of magnetic resonance*. Vol. 1. Springer Science & Business Media, 2013.
- [2] Andreas J Heinrich, Jay A Gupta, Christopher P Lutz, and Donald M Eigler. Single-atom spin-flip spectroscopy. *Science* 306, 466–469 (2004).
- [3] Susanne Baumann, William Paul, Taeyoung Choi, et al. Electron paramagnetic resonance of individual atoms on a surface. *Science* 350, 417–420 (2015).
- [4] Marie Hervé, Moritz Peter, Timofey Balashov, and Wulf Wulfhekel. Towards laterally resolved ferromagnetic resonance with spin-polarized scanning tunneling microscopy. *Nanomaterials* 9, 827 (2019).

Higher order topological defects in the moiré lattice of a van der Waals magnetic material

Eugenio Gambari¹, Sebastian Meyer², Sacha Guesne¹, Pascal David¹, Francois Debontridder¹, Laurent Limot³, Fabrice Scheurer³, Christophe Brun¹, Bertrand Dupé², Tristan Cren¹, and Marie Herve^{1,*}

¹*Sorbonne Université – CNRS - Institut des Nanosciences de Paris UMR7588, 4 place Jussieu, Paris 75005, France*

²*Université de Liège Nanomat/Q-MAT Sart Tilman B-4000, Belgium*

³*Université de Strasbourg CNRS Institut de Physique et Chimie des Matériaux de Strasbourg UMR7504, Strasbourg F-67000, France*

*marie.herve@insp.upmc.fr

Van der Waals materials are emerging as extremely versatile building blocks for many fields of research, both at the fundamental and applied level. They offer tremendous possibilities for fine tuning spintronics, superconducting, nanoelectronics, optical devices. They appear extremely attractive for exploring new exotic physics due to their ability to be stacked with an infinite number of combinations that leads to unexpected physical properties. The toolbox of van der Waals heterostructures is continuously growing with for instance the recent discovery of ferromagnetic order down to the monolayer limit in the family of chromium trihalide, CrCl₃, CrBr₃ and CrI₃ (CrX₃, X= I, Br, Cl) [1]. Several works have related some observations of moiré structure due to the mismatch between the CrX₃ monolayers and their substrate which lead to a wealth of new exotic effects [2, 3]. Combining a chromium trihalide layer with a superconductor might lead for instance to topological superconductivity as recently reported in CrBr₃/NbSe₂ heterostructures [4]. In this hybrid structure, it was proposed that the mechanisms leading to a topological order in this hybrid structures was intimately related to the presence of a moiré pattern [2]. Another fascinating observation is about the influence of a moiré on the magnetic properties. In the CrX₃ family, till now, the magnetization was shown to be essentially colinear, however, in CrI₃ double bilayer some hint of non-colinear magnetism was found and was related to the moiré pattern which leads to a non-negligible spatial modulation of the magnetic interaction [3]. In this communication I will present our scanning tunneling microscopy investigation of a CrCl₃ monolayer deposited on Au(111) which exhibit a second order moiré pattern. We report the presence of edge dislocations in this moiré pattern (see figure). Based on a comprehensive analytical model, I will show that these well know edge dislocations can be reexamined in the framework of topological concepts where they are described as topological defects analogous to vortices carrying a Berry phase characterized by a Chern winding number. They might therefore be use as a pinning center to host topological spin texture and / or Majorana bound states in CrX₃/superconductor heterostructures.

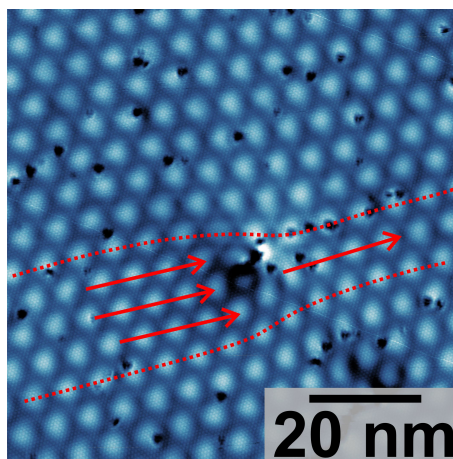


Figure 1: Edge dislocation in the moiré pattern formed between CrCl₃ monolayer and Au(111). It exhibits a Burger vector 2 times larger than the moiré unit cell.

References

- [1] David Soriano, Mikhail I Katsnelson, and Joaquín Fernández-Rossier. Magnetic two-dimensional chromium trihalides: a theoretical perspective. *Nano Letters* 20, 6225–6234 (2020).
- [2] Shawulienu Kezilebieke, Viliam Vano, Md N Huda, et al. Moiré-enabled topological superconductivity. *Nano Letters* 22, 328–333 (2022).
- [3] Hongchao Xie, Xiangpeng Luo, Zhipeng Ye, et al. Evidence of non-collinear spin texture in magnetic moiré superlattices. *Nature Physics* 19, 1150–1155 (2023).

- [4] Shawlienu Kezilebieke, Md Nurul Huda, Viliam Vaňo, et al. Topological superconductivity in a van der Waals heterostructure. *Nature* 588, 424–428 (2020).

Controlling encirclement of an exceptional point using coupled spintronic nano-oscillators

Katia Ho¹, Salvatore Perna², Steffen Wittrock³, Sumito Tsunegi⁴, Hitoshi Kubota⁴, Shinji Yuasa⁴, Paolo Bortolotti¹, Massimiliano d'Aquino², Claudio Serpico², Vincent Cros¹, and Romain Lebrun^{1,*}

¹Laboratoire Albert Fert, CNRS, Thales, Université Paris-Saclay, Palaiseau, 91767, France

²Department of Electrical Engineering and ICT, University of Naples Federico II, Naples, 80125, Italy

³Helmholtz-Zentrum Berlin für Materialien und Energie GmbH, Hahn-Meitner-Platz 1, Berlin, 14109, Germany

⁴National Institute of Advanced Industrial Science and Technology (AIST), Tsukuba, Ibaraki 305-8568, Japan

*romain.lebrun@cnrs-thales.fr

Exceptional points (EPs), branch singularities parameter space of non-Hermitian eigenvalue manifolds, display unique topological phenomena linked to eigenvalue and eigenvector switching: the parameter space states are highly sensitive to the system's parameter changes [1]. Therefore, we suggest investigating the parameter space in the presence of an EP by experimentally accessing and exploiting the topological nature of the coupled system around an EP.

After having recently depicted the impact of an EP on the microwave properties coupled vortex spin-transfer torque oscillators [2], we demonstrate in this study the control over exceptional points in a similar spintronic coupled systems by adjusting the system's damping through the spin-transfer torque effect and their relative phase. The experimental setup used in this study is illustrated in Fig.1(a). This configuration allowed us to devise a strategy for controlling the presence of EPs in coupled STVOs driven by their self-generated radiofrequency (rf) currents. The gain and loss mechanisms for each oscillator are governed both by the natural magnetization damping and the spin-transfer torques (STT). To achieve the critical condition required for reaching an EP, we vary the injected DC current in one oscillator while keeping it fixed in the other. The strength and phase of the coupling between the two spintronic oscillators can be regulated using a variable gain amplifier and variable phase inserted in the RF current lines (see Fig. 1(a)).

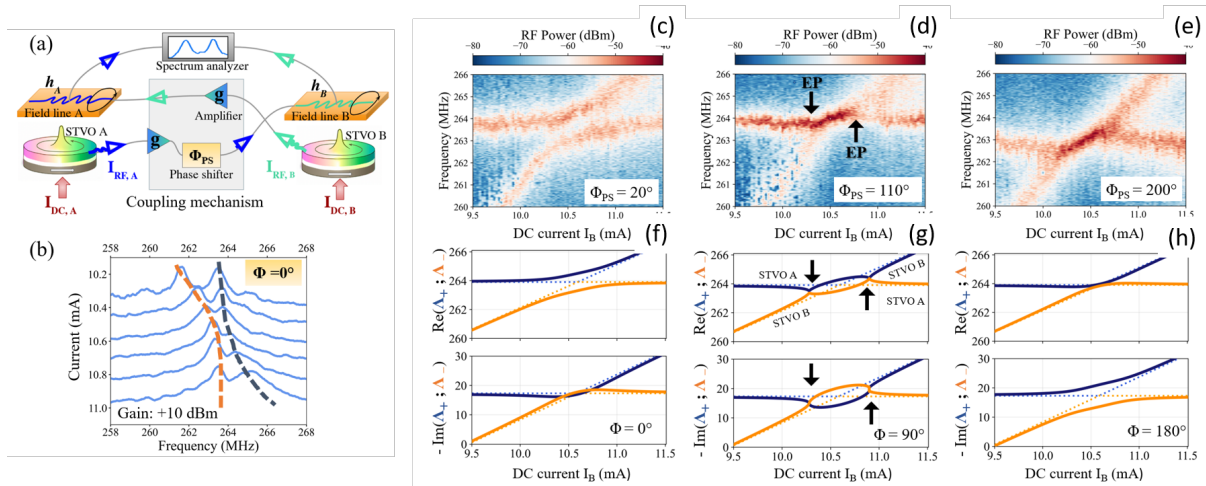


Figure 1: (a) Schematic of the coupled oscillators. Each STVO auto-oscillates under the application of a DC current I_{DC} . One STVO is supplied with constant current while the other is swept across an increasing current range. The RF signal I_{RF} from each STVO is conveyed into the other's field line to produce an RF field h . The coupled signal is measured with a spectrum analyzer. A variable amplifier, set at +10 dBm, controls the coupling amplitude g ; a phase shifter Φ_{PS} tunes the dephasing Φ . (b) Typical experimental spectra (blue) of level repulsion at varying DC currents: a gap separates the hybridized modes (orange and blue), which bend away. The intrinsic phase of the coupled system is equal to $\Phi_g = -10^\circ$; (c) to (h) : Experimental maps of frequencies vs injected DC current from level repulsion at $\Phi_{PS} = 20^\circ$ (c), to the transition marked by two EPs at $\Phi_{PS} = 110^\circ$ (d) and level attraction at $\Phi_{PS} = 200^\circ$ (e). Corresponding theoretical real (top) and imaginary (bottom) parts of the eigenvalues $\Lambda_\pm(I_B, \Phi)$ evolving with the DC current (f-h), representing the frequencies and stability from $\Phi = 0^\circ$ to $\Phi = 180^\circ$, with $\Phi = \Phi_{PS} + 2\Phi_g$. $\Phi_g = -10^\circ$ encompasses the contributions of electrical length and spin-transfer torques. Solid lines indicate the coupled modes; dashed lines are the uncoupled modes. Two EPs bound the region indicated by arrows, where the imaginary and real parts of the eigenvalues coalesce. The gain is set at +10 dBm.

This approach allows for precise manipulation of the coupling behavior in the vicinity of an exceptional point. We report successful experimental demonstration rely on the control of level repulsion and attraction between STVOs, respectively, associated with conservative and dissipative coupling as shown in Fig.1 (c)-(h).

An essential result of this study is the successful completion of a full parametric closed loop in the parameters' space around an EP, leading to an exchange of eigenstates. To this end, we establish a closed loop by adjusting two parameters: one for coupling, Φ and one for gain/loss, I_B . The five-step closed loop in the parameter space, depicted in Fig. 2(a) by projected arrows, starts from an initial point (I_B^i, Φ^i) in Cartesian coordinates. The process begins by increasing the DC current to $(I_B^i + \delta I/2, \Phi^i)$, then tuning the phase shift to $(I_B^i + \delta I/2, \Phi^i - \delta\Phi)$. The loop continues by adjusting to $(I_B^i - \delta I/2, \Phi^i - \delta\Phi)$, tuning the phase back to $(I_B^i - \delta I/2, \Phi^i)$, and finally restoring the DC current to compare the final state to the initial one at (I_B^i, Φ^i) . In Fig. 2(b), we present the experimental spectra, recorded independently using one spectrum analyzer for respectively STVO A and B (bottom and top panels). The measurements correspond to the initial (square) and final (circle) steps of the parametric closed loop during one turn around one of the two EPs. For STVO B, we observe a lower frequency for the final state (circle) than the initial state (square) after a complete loop. These two states are separated by $\delta\omega = 0.4$ MHz, evidencing a frequency shift (see dashed lines). The Riemann sheet structure can explain this frequency shift, as performing one closed loop around an EP means crossing the branch cut (black line) and essentially changing the sheet. In the experiment presented in Fig. 2(b), STVO B starts from the upper state (square) and ends on the lower state (circle) on the bottom sheet with a lower frequency. The inverse is observed for STVO A, demonstrating the state exchange after one encirclement protocol. We then repeat this encircling procedure a second time and observe that the oscillator (STVO B in Fig. 2(c)) returns as expected to its initial state. The detailed steps of the closed loop for one and two turns of the encirlement process, which correspond to the states associated with the trajectories on the Riemann sheets are shown in Fig. 2(c).

In conclusion, we showcase at room temperature the encirclement of an EP in spintronic systems, where navigating around an EP leads to state switching—a promising mechanism for non-reciprocal transport applications. We believe that our study introduces a new method for exploring non-Hermitian physics in spintronic systems at room temperature [3]

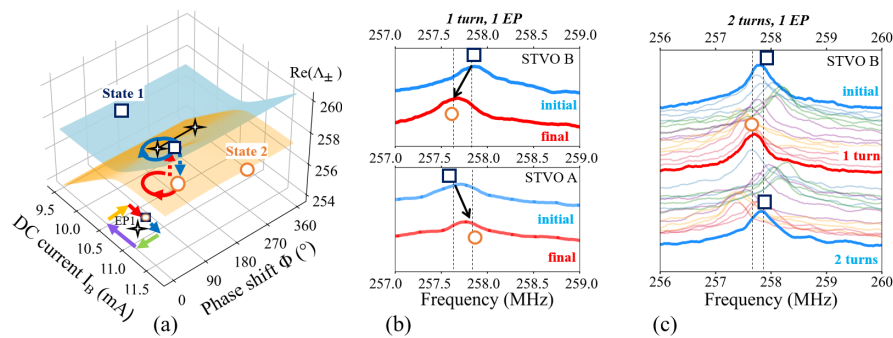


Figure 2: Illustration of the eigenstate exchange after encircling an EP in the parameter space. Riemann sheet structure of the eigenvalues real part in the parameter space (I_B, Φ) , trajectories (blue and red lines) to encircle an EP (star) (a). Encircling an EP once results in an eigenstate switch from a higher frequency (square) to a lower frequency (circle) state separated by a frequency shift $\delta\omega$ for STVO B and vice-versa for STVO A, evidenced by independent spectra at initial and final steps of encirlement protocol (b). Corresponding experimental independent spectra at each step of the closed loop (projected arrows in (a)) for encircling an EP twice (c). The initial state is retrieved if the EP is encircled twice. Dashed lines are eye guides.

Acknowledgments

KH acknowledges financial support from the ANRT contract number 2021/1341. This work has been supported by a France 2030 government grant managed by the French national research agency (ANR) PEPR SPIN "SPINCOM" (ANR-22-EXSP-0005). SW acknowledges financial support from the Helmholtz Young Investigator Group Program (VH-NG-1520).

References

- [1] W. Heiss. The physics of exceptional points. *Journal Of Physics A: Mathematical And Theoretical* 45 (2012).
- [2] S. Wittrock, S. Perna, S. Tsunegi, et al. [Non-hermiticity in spintronics: oscillation death in coupled spintronic nano-oscillators through emerging exceptional points](#). *Nature Communications* 15, 971 (2024).
- [3] K. Ho, S. Perna, S. Wittrock, et al. [Controlling encirclement of an exceptional point using coupled spintronic nano-oscillators](#). *arXiv*, 6086067 (2024).

Magnetic vortex dynamics probed by time-resolved magnetic helicoidal dichroism

Pietro Carrara^{1,2,*}, Mauro Fanciulli²⁻⁴, Matteo Pancaldi^{5,6}, Anda-Elena Stanciu⁷, Matthieu Guer², Emanuele Pedersoli⁵, Dario De Angelis⁵, Primož Rebernik Ribič⁵, David Bresteau², Martin Luttmann², Arun Ravindran^{5,8}, Benedikt Rösner⁹, Christian David⁹, Carlo Spezzani⁵, Michele Manfredda⁵, Ricardo Sousa⁷, Laurent Vila⁷, Ioan Lucian Prejbeanu⁷, Liliana D. Buda-Prejbeanu⁷, Bernard Dieny⁷, Giovanni De Ninno^{5,8}, Flavio Capotondi⁵, Thierry Ruchon², and Maurizio Sacchi^{1,10}

¹Sorbonne Université, CNRS, Institut des NanoSciences de Paris, INSP, 75005 Paris, France

²Université Paris-Saclay, CEA, LIDYL, 91191 Gif-sur-Yvette, France

³CY Cergy Paris Université, CEA, LIDYL, 91191 Gif-sur-Yvette, France

⁴New Technologies Research Center, University of West Bohemia, 30100 Plzeň, Czech Republic

⁵Elettra-Sincrotrone Trieste S.C.p.A., 34149 Basovizza, Trieste, Italy

⁶Department of Molecular Sciences and Nanosystems, Ca' Foscari University, 30172 Venezia, Italy

⁷Université Grenoble Alpes, CNRS, CEA, Grenoble INP, IRIG-SPINTEC, 38000 Grenoble, France

⁸Laboratory of Quantum Optics, University of Nova Gorica, 5001 Nova Gorica, Slovenia

⁹PSI Center for Photon Science, Paul Scherrer Institute, 5232 Villigen PSI, Switzerland

¹⁰Synchrotron SOLEIL, L'Orme des Merisiers, Saint-Aubin, B. P. 48, 91192 Gif-sur-Yvette, France

*carrara@insp.jussieu.fr

Besides circular polarization, which encodes a Spin Angular Momentum (SAM), Laguerre-Gaussian light beams also carry Orbital Angular Momentum (OAM), amounting to $\ell\hbar$ per photon [Fig.1(a)], due to an azimuthal dependence in the electric-field phase of the form $\exp(i\ell\varphi)$ [1]. As the OAM index ℓ defines a set of orthogonal modes, OAM beams found application in high-bandwidth optical data transfer [2]; moreover, their ability to exert mechanical torque has been employed in optical spanners for the manipulation of micro-particles [3], and their radial intensity dependence led to improved resolution and contrast in microscopy [4], phase-contrast imaging [5] and ptychography [6]. Overall, 35 years of development of OAM-beam technology have resulted in a rich set of novel experimental tools.

Analogous to Magnetic Circular Dichroism, the intrinsic handedness of OAM beams also found spectroscopic applications, e.g. with chiral molecules [7] and magnetic materials [8], significantly benefiting from extension into extreme ultra-violet (EUV) and soft x-ray range. This is due to core-level electronic resonances, sharper focusing capabilities, and the availability of intense and ultra-short OAM pulses at large-scale facilities [9] and lab-based sources [10].

I will present recent experimental results from our group on the employment of EUV OAM light beams in resonant magnetic scattering [panel (b)]. A form of Magnetic Helicoidal Dichroism (MHD) is demonstrated in the reflection of Fe M-edge resonant EUV light from Permalloy micrometric magnetic vortices [11–13], see panel (c). Extension of the experimental approach to a pump-probe scheme with sub-picosecond time resolution reveals ultrafast inversion of the magnetic vortex curling direction [panel (d)]. Our results unlock the potential of OAM beams as a novel tool for investigating magnetization dynamics in inhomogeneous spin textures.

References

- [1] L. Allen, M. W. Beijersbergen, R. J. C. Spreeuw, and J. P. Woerdman. [Orbital angular momentum of light and the transformation of Laguerre-Gaussian laser modes](#). *Physical Review A* 45, 8185–8189 (1992).
- [2] Zhongxi Wang, N. Zhang, and X.-C. Yuan. [High-volume optical vortex multiplexing and de-multiplexing for free-space optical communication](#). *Optics Express* 19, 482 (2011).
- [3] H. He, M. E. J. Friese, N. R. Heckenberg, and H. Rubinsztein-Dunlop. [Direct Observation of Transfer of Angular Momentum to Absorptive Particles from a Laser Beam with a Phase Singularity](#). *Physical Review Letters* 75, 826–829 (1995).
- [4] F. Tamburini, G. Anzolin, G. Umbriaco, A. Bianchini, and C. Barbieri. [Overcoming the Rayleigh Criterion Limit with Optical Vortices](#). *Physical Review Letters* 97 (2006).
- [5] Severin Fürhapter, Alexander Jesacher, Stefan Bernet, and Monika Ritsch-Marte. [Spiral phase contrast imaging in microscopy](#). *Optics Express* 13, 689 (2005).
- [6] Matteo Pancaldi, Francesco Guzzi, Charles S. Bevis, et al. [High-resolution ptychographic imaging at a seeded free-electron laser source using OAM beams](#). *Optica* 11, 403 (2024).
- [7] Jérémy R. Rouxel, Benedikt Rösner, Dmitry Karpov, et al. [Hard X-ray helical dichroism of disordered molecular media](#). *Nature Photonics* 16, 570–574 (2022).

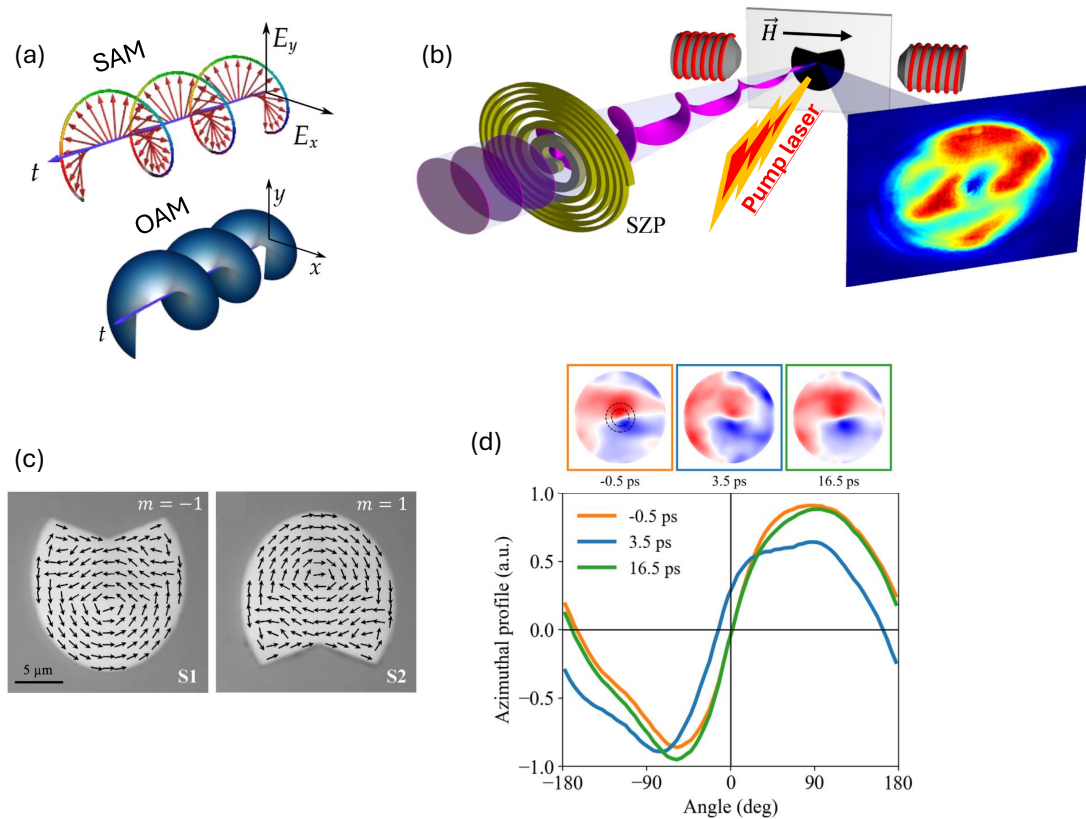


Figure 1: (a) SAM relates to circular polarization of light, while in OAM beams the handedness is provided by screw-like phase dependence. (b) Sketch of the experimental arrangement for time-resolved MHD. (c) Scanning electron micrographs of the investigated Permalloy microdots and superimposed micromagnetic results showing the magnetization vortex ground state. (d) The MHD dichroism maps (top) display a distinct time-dependence after the pump pulse.

- [8] Thierry Ruchon, Mauro Fanciulli, and Maurizio Sacchi in. [The 2022 magneto-optics roadmap](#). *Journal of Physics D: Applied Physics* 55, 463003 (2022).
- [9] Primož Rebernik Ribič, Benedikt Rösner, David Gauthier, et al. [Extreme-Ultraviolet Vortices from a Free-Electron Laser](#). *Physical Review X* 7 (2017).
- [10] R. Géneaux, A. Camper, T. Auguste, et al. [Synthesis and characterization of attosecond light vortices in the extreme ultraviolet](#). *Nature Communications* 7 (2016).
- [11] Mauro Fanciulli, David Bresteau, Mekha Vimal, et al. [Electromagnetic theory of helicoidal dichroism in reflection from magnetic structures](#). *Physical Review A* 103 (2021).
- [12] Mauro Fanciulli, Matteo Pancaldi, Emanuele Pedersoli, et al. [Observation of Magnetic Helicoidal Dichroism with Extreme Ultraviolet Light Vortices](#). *Physical Review Letters* 128 (2022).
- [13] Mauro Fanciulli, Matteo Pancaldi, Anda-Elena Stanciu, et al. [Magnetic vortex dynamics probed by time-resolved magnetic helicoidal dichroism](#). *Physical Review Letters* (submitted).

Imaging of Gate-Controlled Suppression of Superconductivity by Scanning Nitrogen-Vacancy Magnetometry

Uroš Ognjanović^{1,*}, Patrick Scheidegger¹, Kuno Knapp¹, Leon Ruf², Simon Diesch¹, Elke Scheer², Angelo di Bernardo^{2,3}, and Christian Degen¹

¹*Department of Physics, ETH Zürich, Zürich, Switzerland*

²*Department of Physics, University of Konstanz, Konstanz, Germany*

³*Dipartimento di Fisica, Università degli Studi di Salerno, Salerno, Italy*

*uognjanovic@phys.ethz.ch

Scanning nitrogen-vacancy microscopy (SNVM) has emerged as a unique tool for investigating nanoscale magnetism with high sensitivity and sub-50-nm spatial resolution. Although mostly applied at room temperature, the SNVM can be extended to the cryogenic regime down to millikelvin (mK) temperatures [1], allowing for the study of superconducting systems. Using mK-SNVM, we spatially image the Gate-Controlled Superconductivity (GCS) effect in gated Nb islands using the Meissner screening. We demonstrate micrometer-scale suppression of superconductivity in the Nb island in proximity to the gate contact and correlate the size of the quenched area with experimental parameters such as the power dissipated at the gate and the sample temperature. This yields insights into the potential microscopic mechanisms causing the GCS effect. Unlike in previous demonstrations of the GCS effect in nanowires[2, 3], the GCS effect is observed for the first time without relying on transport measurements.

References

- [1] P. J. Scheidegger, S. Diesch, M. L. Palm, and C. L. Degen. [Scanning nitrogen-vacancy magnetometry down to 350 mK](#). *Applied Physics Letters* 120 (2022).
- [2] Giorgio De Simoni, Federico Paolucci, Paolo Solinas, Elia Strambini, and Francesco Giazotto. [Metallic supercurrent field-effect transistor](#). *Nature Nanotechnology* 13, 802–805 (2018).
- [3] Leon Ruf, Claudio Puglia, Tosson Elalaily, et al. *Gate control of superconducting current: Mechanisms, parameters and technological potential*. 2024.

Study of (Gd,Bi) iron garnet films with high orthorhombic magnetic anisotropy grown by liquid-phase epitaxy for Dzyaloshinskii-Moriya interaction investigation

Souhir Bouzidi^{1,*}, Nathan Beaulieu¹, André Thiaville², Vincent Jeudy², Nicolas Vukadinovic³, and Jamal Ben Youssef¹

¹Lab-STICC, CNRS UMR 6285, Université de Bretagne Occidentale, Brest, France

²Laboratoire de Physique des Solides, Université Paris-Saclay, CNRS UMR 8502, Orsay, France

³Dassault Aviation, 78 quai Marcel Dassault, 92552 Saint-Cloud, France

*souhir.bouzidi@univ-brest.fr

Liquid-phase epitaxy (LPE) was used to grow ultra-thin films of undoped Gadolinium Iron Garnet (GdIG) and Bismuth-doped GdIG with different nanometer-scale thicknesses on sGGG (110) substrates. In this study, we specifically focused on the (110) substrate orientation instead of the commonly used (111) substrate. This choice was motivated by the (110) substrate's lower growth rate, which facilitates thickness control, as well as its ability to support higher domain-wall velocities [1]. The reduced magnetization of these materials, caused by the presence of the Gd element [2], compared to Yttrium Iron Garnet (YIG), makes them ideal candidates for investigating the antisymmetric exchange interaction, known as the Dzyaloshinskii-Moriya interaction (DMI). This interaction is equivalent to a chiral effective field applied normal to domain walls in a perpendicularly magnetized film, expressed by $H_{DMI} = \frac{2D}{M_s \Delta}$ [3], where Δ is the domain wall width, D is the DMI strength and M_s is the saturation magnetization. Notably, a lower M_s value enhances the effective H_{DMI} field, making these materials particularly suitable for such studies. We have conducted a study of the DM-interaction using Brillouin Light Scattering (BLS), and a systematic investigation of its behavior as a function of the film thickness is currently underway. Additionally, it induces strong perpendicular magnetic anisotropy, which is an important characteristic for certain applications. A range of advanced characterization techniques was employed to gain a detailed understanding of these films. Atomic Force Microscopy (AFM) provided insights into surface morphology and Roughness, revealing stepped surface periodicity. Magneto-optical Kerr effect (MOKE) microscopy was employed to visualize and determine the orientation of magnetic domains.

To determine the different contributions to the anisotropy constants (cubic term k_1 and orthorhombic term K_u and K_p), FerroMagnetic Resonance (FMR) measurements were carried out in two distinct rotations planes, starting from the film normal. In this analysis, we aim to study the dependence of these constants on the thickness of the films (13-130 nm). Subsequently, the variation in the linewidth (ΔH) as a function of frequency was measured. For the undoped GdIG, no FMR signal could be detected, likely due to its low magnetization, as its compensation temperature is close to room temperature. In contrast, for the Bi-doped GdIG films with thicknesses the magnetic damping coefficient (α) was found around 10^{-3} which is two orders of magnitude lower than that of undoped GdIG ($\alpha = 0.21$)[4]. In addition, the variation of the resonance field (H_{res}) as a function of β , the angle between the applied magnetic field and the sample surface, was determined. From these analyses, the easy [001] and the hard [110] in plane axes of these samples were identified. Calculations, based on the Makino equations[5], were performed to evaluate the magnetic anisotropy constants. The obtained results for the anisotropy constants are $K_1 = -2400 \text{ erg/cm}^3$, $K_u = 1684.5 \text{ erg/cm}^3$, $K_p = 17135 \text{ erg/cm}^3$ which reveal a dominant orthorhombic anisotropy corresponding to an in plane field of approximately 2284 Oe.

These results highlight the potential of these materials to generate pronounced DMI effects, demonstrating their importance in both fundamental research and technological applications.

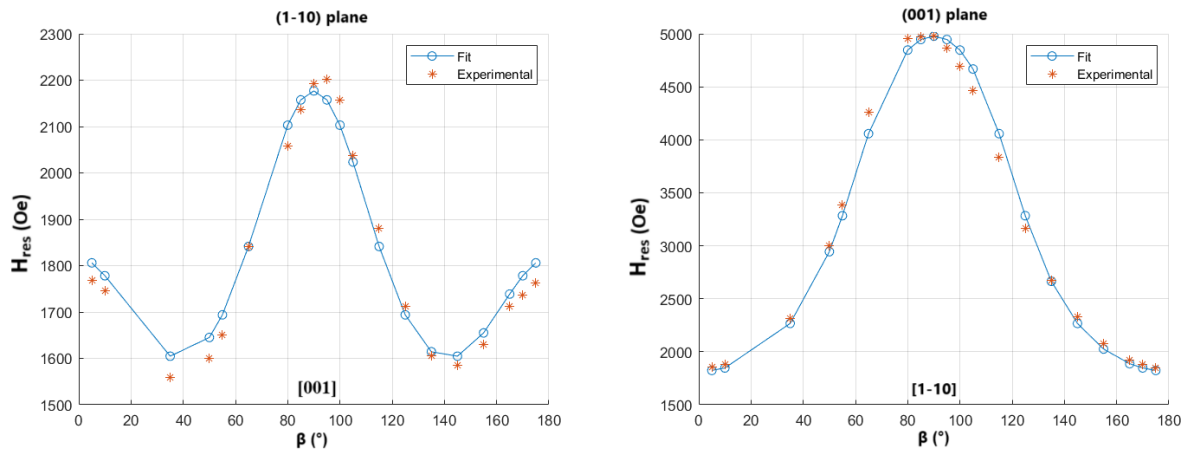


Figure 1: Ferromagnetic resonance results ((FMR at $f=8$ GHz, 56 nm sample thickness): polar rotation; film normal at $\beta=0$ and 180°)

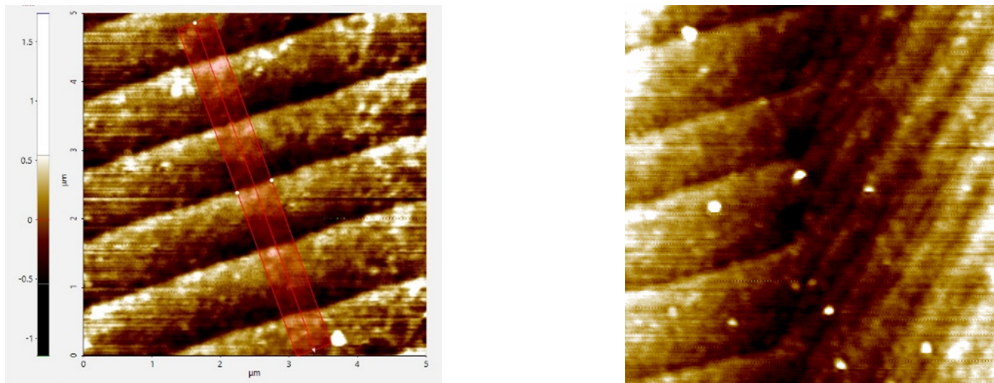


Figure 2: Atomic force microscopy images (size $5 \mu\text{m}$) in two different zones of the 230 nm film

Acknowledgments

This work is financed by the ANR DeMIuRGe (ANR-22-CE30-0014).

References

- [1] D. J. Breed, A. M. J. van der Heijden, H. Logmans, and A. B. Voermans. [High domain-wall velocities in \$\(\text{Gd,Lu}\)_3\(\text{Fe,Mn,Al}\)_5\text{O}_{12}\$ garnet epilayers with orthorhombic anisotropy.](#) *Journ. Appl. Phys.* 49, 939 (1978).
- [2] P. Hansen, K. Witter, and W. Tolksdorf. [Magnetic and magneto-optic properties of lead- and bismuth-substituted yttrium iron garnet films.](#) *Phys. Rev. B* 27, 6608 (1983).
- [3] André Thiaville, Stanislas Rohart, Émilie Jué, Vincent Cros, and Albert Fert. [Dynamics of Dzyaloshinskii domain walls in ultrathin magnetic films.](#) *EPL (Europhysics Letters)* 100, 57002 (2012).
- [4] A.H. Eschenfelder. [Amorphous films for bubbles.](#) *Journal of Handbook of Ferromagnetic Materials* 2, 345–380 (1980).
- [5] H. Makino and Y. Hidaka. [Determination of magnetic anisotropy constants for bubble garnet epitaxial films using field orientation dependence in ferromagnetic resonances.](#) *Jour. Mat. Res. Bull.* 16, 957–966 (1981).

Spectroscopy of Azimuthal Magnon Modes by NV-Center Magnetometry

Fourniols C.^{1,3}, Umeda M.^{1,2}, Clot E.¹, Yamamoto K.², Val T.¹, Pigeau B.³, and Klein O.¹

¹Université Grenoble Alpes, CEA, CNRS, Grenoble INP, Spintec, 38054 Grenoble, France

²Advanced Science Research Center, Japan Atomic Energy Agency, Tokai, Ibaraki 319-1195, Japan

³Université Grenoble Alpes, CNRS, Grenoble INP, Institut Néel, Grenoble, France

*clement.fourniols@cea.fr

In axisymmetric systems, the angular momentum of a wave vector field, such as light, elastic waves, or spin waves (SW), is a conserved quantity that can be decomposed into two components: spin angular momentum (SAM) and orbital angular momentum (OAM). Recently, our group have developed a formalism to classify SWs in confined axisymmetric systems, in which the SAM is defined as the sense of rotation of the dynamic magnetization and the OAM as the number of windings of the dynamic magnetization per turn of the system.

Although SAM of SWs has been extensively studied, the OAM of SWs remains experimentally unexplored, despite its significant potential for applications such as multiplexed communications [1]. This lack of experimental study can mainly be attributed to the experimental difficulties it requires to observe OAM in SWs, including high spatial resolution, non-perturbative techniques, and phase-sensitive measurements.

To address these challenges, we propose to utilize recent advances in nitrogen-vacancy (NV) center magnetometry to map the dynamical phase profiles of SWs [2] in micro-sized YIG disks. The quantum sensing method allows for direct detection of both static and dynamic fields, as well as the stray field created by the magnetization distribution [3, 4]. This technique achieves these capabilities by providing precise information about the local field strength and its orientation relative to the NV axis. We recently developed a home-made room-temperature NV center microscope that employs a single NV center probe to achieve the required high spatial resolution and non-perturbative measurement.

As an initial test of our microscope, we have performed iso-field measurements on YIG-doped bismuth samples, allowing us to gain experience with YIG systems and refine our methodology for scanning NV magnetometry.

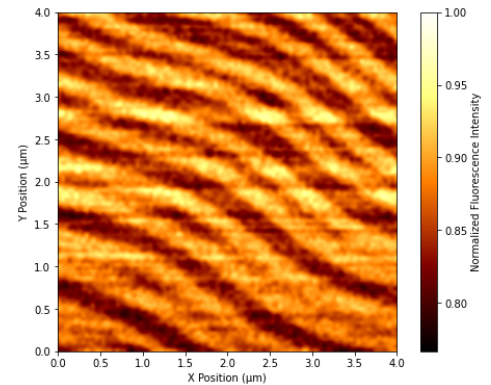


Figure 1: Iso-field measurement of NV center microscopy on a bismuth-doped YIG film.

Acknowledgments

This work is supported by the QuantAlps program of the University Grenoble Alpes. Additionally it was partially supported by the EU-project HORIZON-EIC-2021-PATHFINDER OPEN PALANTIRI-101046630; the French Grants ANR-21-CE24-0031 Harmony; the PEPR SPIN - MAGISTRAL ANR-24-EXSP-0004; the French Renatech network; and the REIMEI Research Program of Japan Atomic Energy Agency.

References

- [1] Alaaeddine Rjeb, Habib Fathallah, and Mohsen Machhout. "OAM Modes in Optical Fibers for Next Generation Space Division Multiplexing (SDM) Systems". *Fiber Optics - Technology and Applications*. IntechOpen, 2021.
- [2] Iacopo Bertelli, Joris J. Carmiggelt, Tao Yu, et al. Magnetic resonance imaging of spin-wave transport and interference in a magnetic insulator (16, 2020). arXiv: [2004.07746v1](https://arxiv.org/abs/2004.07746v1) [[cond-mat.mes-hall](https://arxiv.org/abs/2004.07746v1)].
- [3] Chunhui Du, Toeno van der Sar, Tony X. Zhou, et al. [Control and local measurement of the spin chemical potential in a magnetic insulator](https://doi.org/10.1126/science.1253111). *Science* 357, 195–198 (2017).
- [4] M. R. Page, B. A. McCullian, C. M. Purser, et al. [Optically detected ferromagnetic resonance in diverse ferromagnets via nitrogen vacancy centers in diamond](https://doi.org/10.1063/1.5007000). *Journal of Applied Physics* 126, 124902 (2019).

Phase analysis of 1f injection locked spin transfer nano-oscillator

Arthur Courberand^{1, *}, Matéo Ibarra Gomez¹, Joo-Von Kim², Ursula Ebels¹, and Liliana D. Buda-Prejbeanu¹

¹Univ. Grenoble Alpes, CEA, CNRS, Grenoble INP, SPINTEC, Grenoble, France

²Centre de Nanosciences et de Nanotechnologies, CNRS, Université Paris-Saclay, Palaiseau, France

*arthur.courberand@cea.fr

The non-linear dynamical properties of spin torque nano oscillators (STNO) allow efficient injection locking to an external microwave signal and through this to modulate or to binarize the oscillator phase[1]. Phase binarization has been demonstrated experimentally recently as a novel approach to generate true and unbiased random numbers [2] and is also key for the development of an STNO based Ising Machine. A detailed understanding of injection locking is hence essential. It occurs when the frequency of the oscillator follows the frequency of the external control signal within a locking range $\Delta\Omega$, around $f_{rf} = nf_{osc}$ with n the integer harmonic order. The phase difference ψ between the oscillator and the control signal phases obeys the Adler equation (22), and is generally considered to be a single continuous arcsine function.

$$\psi = \phi_{osc} - \frac{\phi_{rf}}{n} = \frac{1}{n} \arcsin\left(\frac{\delta}{\Delta\Omega}\right) + \psi_0 + \frac{2k\pi}{n}, k \in \mathbb{Z} \quad (22)$$

where δ is the detuning $\delta = f_{rf} - nf_{osc}$, $\Delta\Omega$ is half the size of the locking range and ψ_0 is the phase difference at zero detuning. For $n = 1$, the equation (22) has only one 2π periodic solution, while for $n = 2$, it has two, π periodic solutions. These are common results, that are considered to be valid for any type of oscillator and that have been verified in experiment and simulation for STNOs. Here we report numerical results on the injection locking which do not comply with eq. (22). We show that for the case $n = 1$, the 1f injection locking admits two π -periodic phase solutions.

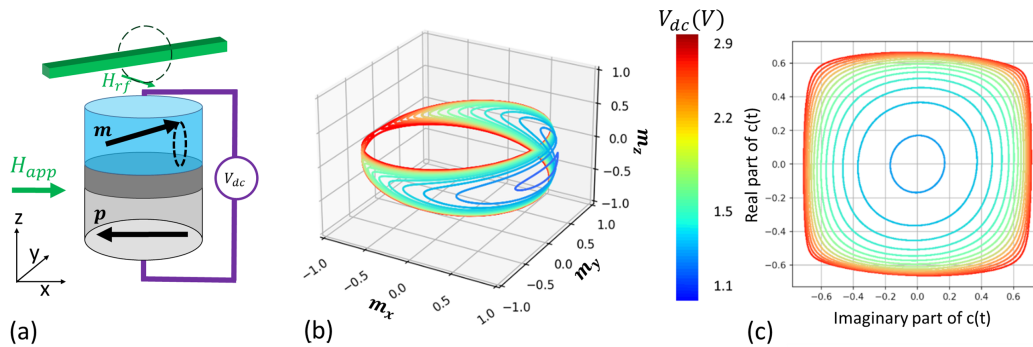


Figure 1: (a) Schematic of an MTJ-based STNO with uniform magnetization.(b) Trajectories of the magnetization \mathbf{m} for in-plane precession and (c) their complex transformation at different values of the DC voltage.

The STNO schematic is presented in Fig. 1 (a). A dc spin polarized current (along \mathbf{p} direction) combined with an in-plane dc field \mathbf{H}_{app} induces a free-running oscillation of the free layer magnetization (\mathbf{m}) at a frequency f_{osc} . These oscillatory state is known as in-plane-precession (IPP) for which the magnetization \mathbf{m} describes a clam-shell like trajectory, see Fig. 1 (b). The dynamics of vector \mathbf{m} can be mapped onto a complex oscillator variable $c(t)$ [3], as shown in Fig. 1 (c). Upon increasing the voltage V_{dc} the trajectory becomes less circular because of strong non-linear effects. In the following, we discuss simulation results for injection locking via a microwave field \mathbf{H}_{rf} that is produced via a field line, see Fig. 1 (a). The orientation of the \mathbf{H}_{rf} field, and of the spin polarization \mathbf{p} were varied, while the dc field \mathbf{H}_{app} was kept along the x -direction. One expects injection-locking at $1f$ when \mathbf{H}_{rf} is parallel to \hat{y} or \hat{z} , and injection-locking at $2f$ when $\mathbf{H}_{rf} // \hat{x}$, since m_y, m_z oscillate at f_{osc} , while the component m_x oscillates at two times f_{osc} [4]. Respectively the phase difference ψ is expected to have one solution for $\mathbf{H}_{rf} // \hat{y}, \hat{z}$ and two π periodic solutions for $\mathbf{H}_{rf} // \hat{x}$.

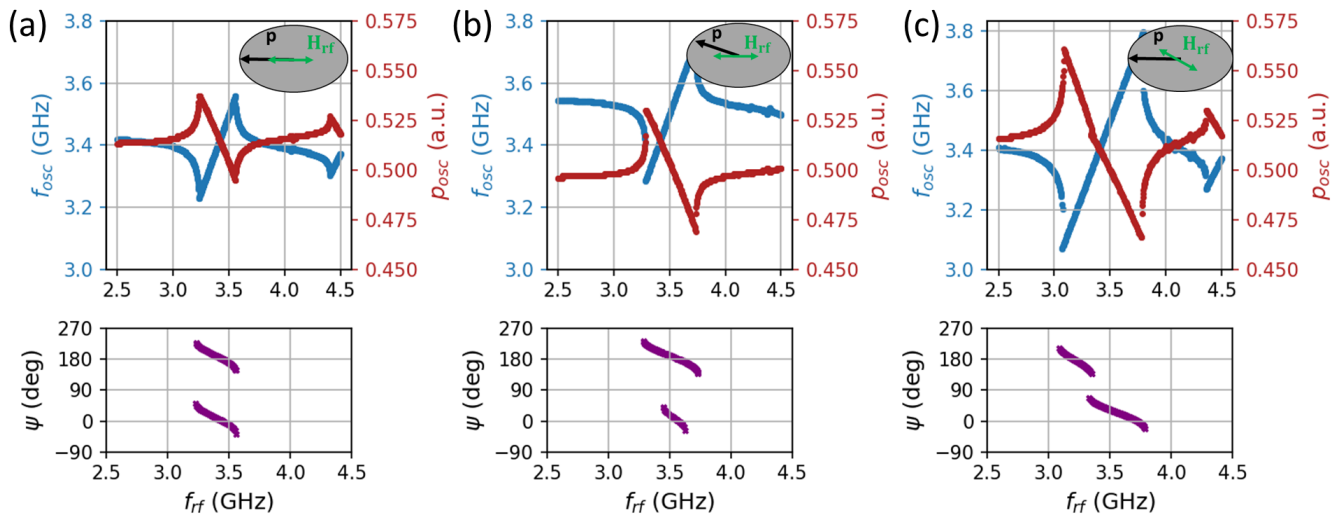


Figure 2: Frequency f_{osc} , power p_{osc} , and phase difference ψ dependence of the H_{rf} frequency for three cases: (a) \mathbf{p} and H_{rf} along \hat{x} . (b) \mathbf{p} at 165° and H_{rf} along \hat{x} . (c) \mathbf{p} along \hat{x} and H_{rf} at 165° . Simulations were done at operation point : $V_{dc} = 2V$, $\mu_0 H_{app} = 0.04T$, with an rf field amplitude of 4 mT.

The results for $1f$ -locking and for three configurations of H_{rf} and \mathbf{p} are shown in Fig. 2, where the frequency, the power and the phase difference are plotted versus the control signal frequency f_{rf} . The major result, Fig. 2(a), is the possibility of $1f$ injection-locking with a field and polarizer aligned along the \hat{x} direction, which one would expect only for $2f$ -locking. In addition there are two solutions for the phase difference ψ , a scenario expected for a $2f$ injection-locking. To break the symmetry we also investigated $1f$ - locking when either the polarizer \mathbf{p} or the rf field H_{rf} are tilted away from the x -direction. When tilting the polarizer, Fig. 2(b), injection locking is found with two phase solutions, that follow an arcsine behaviour. However the two solutions exist over different frequency ranges. Finally, when tilting, the rf field H_{rf} , see Fig. 2(c), the two phase solutions no longer overlap, each one having its own 'locking' range. This is also reflected in the power, where a change in the slope is seen at 3.4GHz. The origin of these different results are not yet fully elucidated. A possible mechanism is the twist in the clam-shell trajectory along the y - or z - axis, when the polarizer is not along the x -direction. Other effects include fractional synchronisation, parametric excitation or higher order non-linear processes. These results have a strong bearing on all applications of STNOs that involve injection locking of one or synchronisation of several STNOs.

Acknowledgments

This work was supported in part by the France 2030 government investment plan managed by the French National Research Agency under grant reference « PEPR SPIN – SPINTHEORY ANR-22-EXSP-0009 » and by the French National Research Agency project SpinIM ANR-22-CE24-0004. Mateo Ibarra Gomez acknowledges financial support from the French Space Agency (CNES) and the European Union's Horizon 2020 research and innovation programme under grant agreement No 800945 — NUMERICS — H2020-MSCA-COFUND-2017.

References

- [1] A. Litvinenko, P. Sethi, C. Murapaka, et al. [Analog and Digital Phase Modulation and Signal Transmission with Spin-Torque Nano-Oscillators](#). *Physical Review Applied* 16 (2021).
- [2] Nhat-Tan Phan, Nitin Prasad, Abderrazak Hakam, et al. [Unbiased random bitstream generation using injection-locked spin-torque nano-oscillators](#). *Physical Review Applied* 21, 034063 (2024).
- [3] T. Holstein and H. Primakoff. [Field Dependence of the Intrinsic Domain Magnetization of a Ferromagnet](#). *Phys. Rev.* 58, 1098–1113 (12 1940).
- [4] Sergei Urazhdin, Phillip Tabor, Vasil Tiberkevich, and Andrei Slavin. [Fractional Synchronization of Spin-Torque Nano-Oscillators](#). *Physical Review Letters* 105, 104101 (2010).

Manipulation of topological spin textures for reservoir computing

Simone Bonino^{1,*}, Nathan Cruz¹, Rodrigo Guedas Garcia¹, Stéphane Auffret¹, Gilles Gaudin¹, and Olivier Boulle¹

¹Univ. Grenoble Alpes, CEA, CNRS, Grenoble INP, SPINTEC, 38000 Grenoble, France

*simone.bonino@cea.fr

Magnetic skyrmions are topologically protected spin textures exhibiting particle-like properties. Due to their particularity, they are promising candidates for applications in neuromorphic computing, where their stability and nanometric size enable efficient information processing and storage [1].

The goal of this work is to demonstrate the potential of meander domain walls and, more specifically, skyrmions to build a physical reservoir for Reservoir Computing (RC) classifications. Reservoir Computing offers a simplified alternative to common Recurrent Neural Networks (RNNs) by exploiting the non-linear dynamics of RNNs without the need to train recurrent connections.

Here we use a Ta/FeCoB/TaOx structure where skyrmions and meander domains can be easily stabilized. We evaluated and measured the dynamic properties of the system in order to ensure that it meets the necessary requirements for RC, such as stability, nonlinearity, and short-term memory [2], by observing the response of the magnetic texture to electrical stimuli under a MOKE microscope.

Once the required properties are satisfied, the ability of the system to perform basic recognition tasks is tested using sine, square and triangular input waves. By segmenting the device into multiple regions (Fig.1), each representing a neuron with a distinct response, we were able to train the system to classify between the applied sine and square wave. The accuracy ranged from 60% to 70%, potentially limited by measurement noise and spatial correlation of the responses.

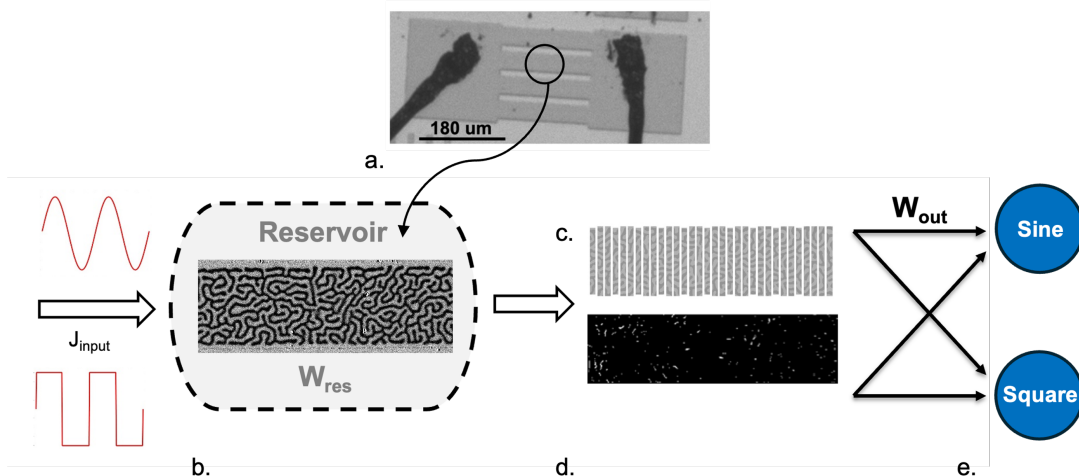


Figure 1: **Meander DWs Physical Reservoir System** : a) Device layout for controlled current injection. b) MOKE image of meander domain wall texture employed as a physical reservoir. c) The device is divided into multiple subsections and the displacement is tracked frame-by-frame, as shown in (d), and used to train the final layer W_{out} (e).

To improve accuracy and study more complex responses, skyrmions are used (Fig.2). The skyrmion tracking is performed using a self-trained neural network used for tumor tracking, which is able to identify each skyrmion individually. Training our system for the same input patterns as for DWs, we achieve an accuracy of 91% for sine-square classification.

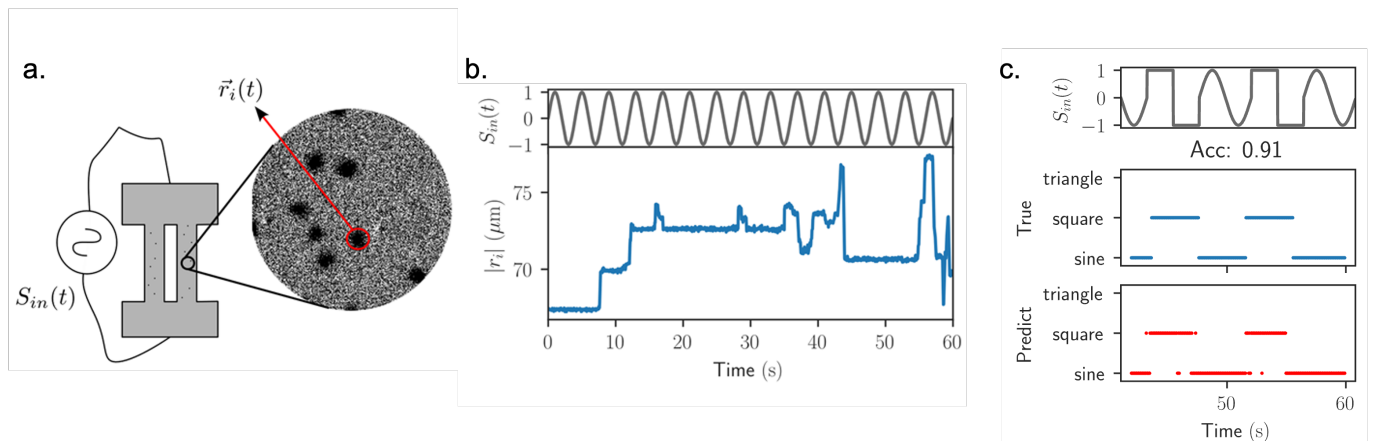


Figure 2: **Skyrmion Physical Reservoir System** : a) Schematics of the layout and skyrmion phase present in the magnetic tracks. b) Displacement of the skyrmion as a function of time under a sinusoidal applied electric current of 10^8 A/m^2 . c) Classification test of a square/sinusoidal series.

References

- [1] Naoto Nagaosa and Yoshinori Tokura. [Topological properties and dynamics of magnetic skyrmions](#). *Nature Nanotechnology* 8, 899–911 (2013).
- [2] Jake Love, Robin Msiska, Jeroen Mulkers, et al. [Spatial analysis of physical reservoir computers](#). *Phys. Rev. Appl.* 20, 044057 (4 2023).

Liste des auteurs

- L. Aballe: [68](#)
- A. Abbass Hamadeh: [134](#)
- E. Abboubi: [227](#)
- A. Abdelsamie: [265](#)
- F. Abreu Araujo: [57](#), [198](#), [235](#)
- J.-P. Adam: [89](#), [210](#), [255](#), [265](#), [270](#), [300](#)
- M. Adam: [72](#)
- A.-L. Adenot-Engelvin: [179](#)
- A. O. Adeyeye: [238](#)
- M. H. Aguirre: [206](#)
- A. Ahlawat: [15](#)
- C. V. Ahmad: [212](#)
- K. Ahn: [169](#)
- C. Al Khatib: [114](#)
- W. Alimi: [249](#)
- M. Althammer: [169](#)
- L. Álvaro-Gómez: [68](#)
- A. Anadón: [17](#)
- A. Anane: [72](#), [89](#), [135](#), [233](#), [259](#), [265](#), [273](#), [295](#), [302](#), [304](#)
- S. Andrieu: [195](#)
- E. Angeli: [273](#)
- L. Anghel: [114](#)
- A. Anil: [240](#)
- E. Aoustin: [112](#), [171](#)
- M. Ardisson: [87](#)
- A. Arnoult: [35](#)
- R. Arras: [187](#)
- J. A. Arregi: [79](#)
- M. Arya: [95](#)
- G. Atcheson: [227](#), [247](#)
- J. Attané: [47](#), [114](#), [287](#)
- E. Aubouin: [57](#)
- S. Auffret: [30](#), [55](#), [117](#), [148](#), [156](#), [204](#), [319](#), [247](#)
- M. P. Avicena: [130](#)
- A. Azzani: [294](#)
- B. Büchner: [169](#)
- N. K. P. Babu: [163](#)
- A. Bad'ura: [96](#)
- L. Badeau: [254](#)
- F. Badets: [57](#), [59](#)
- L. Badie: [191](#)
- M. Bailleul: [70](#), [85](#), [132](#), [167](#), [183](#), [240](#)
- B. Bakri: [105](#)
- W. Ballouch: [259](#)
- V. Baltz: [93](#), [96](#), [181](#), [227](#), [289](#)
- C. Baraduc: [30](#), [157](#), [202](#), [261](#)
- N. Bardou: [76](#), [300](#)
- A. Barthélémy: [265](#), [287](#)
- A. Bataille: [37](#)
- R. Battistelli: [146](#)
- H. Béa: [30](#), [157](#), [202](#), [261](#)
- N. Beaulieu: [295](#), [304](#), [314](#)
- S. Beckert: [96](#)
- R. Beignon: [66](#)
- R. Belkhou: [55](#), [68](#)
- L. Bellaiche: [111](#)
- M. Belmeguenai: [225](#), [249](#)
- V. I. Belotelov: [81](#)
- N. Benaziz: [210](#)
- A. Bénédict-Cardenas: [177](#)
- L. Benetti: [59](#), [61](#)
- M. Benjamin Jungfleisch: [167](#)
- J. Ben Youssef: [72](#), [89](#), [163](#), [206](#), [233](#), [242](#), [270](#), [295](#), [302](#), [304](#), [314](#)
- A. Bernand-Mantel: [97](#), [119](#)
- G. Bernard: [49](#), [53](#)
- M. Bernard: [306](#)
- R. Bernard: [167](#)
- A. di Bernardo: [313](#)
- I. Berrai: [249](#)
- A. Berthelot: [257](#)
- J. Berthomier: [72](#)
- F. Bertran: [35](#)
- E. Bertuit: [283](#)
- P. F. Bessarab: [150](#)
- K. Kumar Bestha: [169](#)

- T. Bhatnagar-Schöffmann: 51
- I. Noor Bhatti: 259, 273, 304
- M. Biagi: 45, 197, 279
- M. Bibes: 114, 154, 287
- C. Bigi: 35
- F. Binda: 208
- M. Birch: 137
- N. Biziere: 74
- T. Blon: 35, 119
- O. Boisron: 100, 257
- F. Bonell: 33, 277
- S. Bonino: 319
- B. Bony: 41
- L. Borges de Avila Jr: 198
- D. Borowski: 215
- P. Bortolotti: 233, 265, 302, 309
- X. Bosch: 245, 245, 299
- N. Boscolo Meneguolo: 108
- C. Bouchard: 45, 197
- W. Bouckaert: 146, 297
- S. Boukari: 290
- O. Boule: 55, 156, 202, 319, 224, 227
- G. Bourcin: 130
- J. Bourhill: 130, 243
- K. Bouzehouane: 72, 146, 265
- S. Bouzidi: 314
- I. Boventer: 87, 233, 265, 302
- M. Bowen: 140, 290
- D. Bresteau: 311
- T. Bruant: 290
- C. Brun: 307
- T. Brun: 157, 261
- F. Brunnett: 221, 171
- J. Bréhin: 287
- L. Buda-Prejbeanu: 57, 108, 117, 159, 222, 251, 311, 317
- M. Bugnet: 100
- P. Buhl: 299
- F. Büttner: 146
- L. Cagnon: 108
- L. Calmels: 95
- S. Campidelli: 171
- F. Capotondi: 15, 144, 311
- C. Capriata: 45, 197, 279
- M. Carpentieri: 61
- P. Carrara: 311
- C. Carretero: 221
- E. Carré: 112, 221
- P. Carvajal: 191
- C. Carvallo: 283
- M. Caseiro: 30, 140
- G. Cassabois: 189
- V. Castel: 87, 130, 167, 243
- C. Cavoit: 157
- S. K. Chaluvadi: 263
- L. Chamot: 144
- C. Chappert: 229, 281
- V. Chardonnet: 15, 173
- J. Charlier: 221, 171
- J. Chauleau: 231
- P. Che: 89, 233, 259, 265, 295, 302
- S. M. Chérif: 225, 249
- F. Cheynis: 47
- J. Chiliquinga: 146
- S. Chiroli: 238
- G. S. Chiuzbaian: 15, 173
- C. Chopin: 57, 235, 251
- L. Christienne: 135
- M. Chshiev: 185
- G. Cipi: 271
- S. Clément: 189
- E. Clot: 294, 316
- A. Coati: 37
- S. Collin: 19, 39, 41, 112, 146, 213
- O. Copie: 37, 177
- J. Coraux: 189
- K. Cottart: 49, 53
- C. Coudert: 240
- S. Couet: 279

- A. Courberand: 251, 317
- T. Courtois: 195
- T. Cren: 306, 307
- B. Croes: 47
- V. Cros: 39, 41, 51, 72, 146, 213, 233, 259, 297, 309
- N. Crouseilles: 105
- N. Cruz: 319
- M. Culot: 47, 114
- T. da Câmara Santa Clara Gomes: 51, 235
- V. Da Costa: 290
- M. d'Aquino: 255, 295, 309
- P. A. Dainone: 19, 249
- H. Damas: 81
- E. Dandeu: 126, 165
- J. Daniel: 221, 171
- R. Daubriac: 35
- C. David: 311
- P. David: 306, 307
- C. S. Davies: 81
- J.-F. Dayen: 215
- D. De Angelis: 311
- M. Deb: 21
- R. Debord: 257
- F. Debontridder: 306, 307
- G. de Loubens: 28, 70, 116, 163, 255, 295
- G. De Ninno: 311
- C. Degen: 208, 294, 313
- M.S. Dehaghani: 35
- D. Dekajevi: 121
- R. Delaunay: 15, 173
- L. DelRey: 289
- V. Demange: 121
- V. Demidov: 265
- T. Denneulin: 39
- V. Desbuis: 181
- M. De-Santis: 292
- L. Desplat: 148, 269
- T. Devolder: 76, 116, 210, 229, 255, 270, 281, 300
- S. de Wergifosse: 57, 235
- S. Dhillon: 154, 185
- B. Dieny: 311
- S. Diesch: 313
- I. Di Manici: 55, 156, 224
- L. V. B. Diop: 200
- M. Di Pietro Martínez: 137
- F. Disdier: 108, 148, 159
- F. Disdier: 55, 96, 156, 217
- B. Dlubak: 221, 171
- G. Doddi: 259
- C. Donnelly: 137
- T. Drevelow: 138
- R. Dreyer: 66
- J. Dubois: 144
- S. Dubois: 171
- S-M. Dubois: 221
- C. Dubs: 183
- C. Ducruet: 157, 247, 253
- K. Dumesnil: 37, 43, 177, 195
- R. E. Dunin-Borkowski: 39
- B. Dupé: 111, 245, 299, 307
- V. Dupuis: 100, 283
- A. Durand: 189
- C. Durand: 35
- A. Durnez: 49, 53, 213
- U. Ebels: 57, 59, 148, 159, 217, 235, 251, 317
- M. Eddrief: 135
- J. H. Edgar: 189
- M. El Moundji Hemili: 15
- H. Elnaggar: 122
- L. Enger: 92
- R. F. L. Evans: 93
- K. Fan: 279
- M. Fanciulli: 311
- L. Farcis: 204
- S. Farhat: 249
- A. Fassatoui: 279
- M. Fattouhi: 117, 222
- J. Faure-Vincent: 30, 227, 247, 253
- D. Faurie: 238, 275

- S. Fekraoui: 35
- R. Fenollosa: 183
- C. Fermon: 30, 161, 193
- B. Fernandez: 55, 156
- C. Fernández-González: 68
- R. Ferreira: 59, 61, 217
- A. Fert: 39, 41, 146
- G. Feugnet: 304
- M. Fiat: 161, 193
- C. Fillion: 202
- A. Finco: 33, 66, 124, 189
- N. Findling: 152
- S. Finizio: 137
- R. Firouzmandi: 169
- J. Fischer: 30, 157, 169, 202
- S. Flament: 261, 263
- A. Fondet: 119
- F. Fortuna: 135
- F. Fossard: 221
- W.-A. Fotso Sindze: 225
- C. Fourniols : 316
- J. Fraunié: 189
- T. Frottier: 47, 114
- O. Fruchart: 68, 108
- S. Fusil: 265
- M. S. Gabor: 225
- M. Galbiati: 221
- P. Gambardella: 206, 208
- E. Gambari: 306, 307
- R. Guedas Garcia: 55, 156, 319
- V. Garcia: 265
- C. García: 191
- D. García Ovalle: 47
- A. Gardin: 130
- K. Garello: 39, 45, 197, 204, 254, 279
- C. Gatel: 74, 119
- G. Gaudin: 55, 96, 156, 202, 319, 224, 279
- N. Gauthier: 175
- E. Gautier: 108
- S. Geiskopf: 181
- G. Gentile: 33
- J.-M. George: 19, 39, 41 128, 152, 154
- E. Georgopoulou Kotsaki: 217
- S. Geprägs: 169
- I. C. Gerber: 189
- J. Ghanbaja: 37, 177, 195
- V. Giannone: 114
- B. Gil: 189
- N. Girodon-Boulandet: 275
- A. Gloppe: 215
- B. Gobaut: 132, 290
- P. Godard: 275
- F. Godel: 19, 112, 146, 221, 171
- S. T. B. Goennenwein: 96, 169, 242
- M. A. Goerzen: 102, 104, 107, 138, 150
- I. Gomes de Moraes: 175
- O. Gomonay: 96
- S. Gonzalez: 100
- J. Gorchon: 11, 17
- D. Gouéré: 259
- C. Gourdon: 79, 126, 135, 165
- E. Gradauskaite: 175
- A. Grailhon: 231
- Q. Gravelier: 35
- M. Grelier: 146
- S. Grenier: 267
- A. Grisard: 154
- J. Grollier: 51, 61, 213, 297
- R. Guedas: 224
- C. Gueneau: 202
- M. Guer: 311
- S. Guesne: 307
- C. Guillemard: 124, 216, 237
- Q. Guillet: 175
- D. Gusakova: 93, 108
- L. Gómez-Cruz: 68
- A. Hadj-Azzem: 189
- A. Hakam: 57, 59, 217, 251
- S. Haldar: 102, 138

- D. Halley: 132
- E. Haltz: 275
- A. Hammani: 112
- T. Hauet: 43, 195
- J. Haumant: 87, 243
- M. Hehn: 11, 13, 15, 17, 21, 117, 140, 142, 181, 195, 240
- S. Heinze: 95, 102, 138, 150
- M. E. M. Hemili: 144
- M. Hennes: 15, 122, 144, 173
- Y. Henry: 132, 167, 183
- V. Heresanu: 216, 237
- G. Herrera: 100
- L. Herrera Diez: 49, 51, 53, 213, 297
- M. Hervé: 306, 307
- P-A. Hervieux: 105
- A. Hierro-Rodríguez: 137
- J. Hnilica: 267, 289
- K. Ho: 309
- J. Hohlfeld: 11, 13
- X. Hong: 105
- H. Huebl: 242
- L. Hutin: 45, 57, 59, 114, 197
- B. Hyot: 254
- M. Ibarra Gomez: 57, 251, 317
- F. Ibrahim: 185
- I. C. Infante: 100
- O. Isnard: 200
- V. Jacques: 33, 66, 124, 189
- J. F. Jacquot: 175
- H. Jaffrès: 19, 39, 41, 128, 152, 154
- M. Jain: 128, 152
- B. Jai Singh: 95
- E. Jal: 15, 144, 173
- M. Jamet: 33, 154, 175, 185, 254
- R. Jamil: 175
- G. Jannet: 157
- P. Janolin: 37
- N. Jaouen: 146, 173
- R. Jarrier: 173
- J. Jay: 121
- E. Jedryka: 216
- C. Jego: 175
- A. Jenkins: 59, 61, 217
- V. Jedy: 273, 314
- C. John: 297
- L. Joly: 290
- P. Joly: 275
- I. Joumard: 30
- S. Jovanovic: 28
- A. Juhin: 283
- T. Jungwirth: 96, 169
- R. Kalvig: 216
- A. Kamra: 242
- A. Kandazoglou: 279
- S. Kang: 216
- S. S. Kantorovich: 283
- E. Karadža: 208
- H. Karaoui: 204
- M. R. Karim: 247 253
- N. Keller: 21
- M. Khaled: 35
- M. Khelfallah: 283
- J.-V. Kim: 24, 26, 28, 89, 116, 229, 255, 269, 270, 295, 300, 317
- A. Kirilyuk: 81
- O. Klein: 83, 163, 316
- A. Klimeczek: 292
- J. Klíma: 183
- K. Knapp: 313
- V. Kocsis: 169
- L. Kokkinos: 24
- A. Kolli: 28, 295
- I. Kounta: 96
- A. Kovács: 39
- M. Kretschmar: 157
- D. Kriegner: 96, 169
- S. Krishnia: 39, 41, 51
- P. Kubaščík: 169

- H. Kubota: 309
- M. Kuhlmann: 173
- B. Kunyangyuen: 11
- S. W. Kurfman: 163
- A. Kuznetsov: 283
- C. Körner: 66
- D. Lacour: 11, 140, 142, 181
- N. Lahmiti: 122, 144
- C. Lambert: 208
- M. Lamblin: 290
- A. D. Lamirand: 292
- M. Lammel: 169, 206, 242
- E. Lamour: 212
- J. Langer: 49, 53
- L. Largeau: 152
- B. Lassagne: 35
- V. Laude: 126, 165
- J. Lauret: 171
- V. H. Le: 175
- A. Lebon: 121
- J. Le Breton: 121
- R. Lebrun: 72, 87, 128, 154, 233, 259, 265, 302, 309
- C. Lefevre: 85
- W. Legrand: 206, 242, 267
- Y. Le Guen: 11, 13
- P. Leitner: 92
- M. Leiviskä: 93, 96, 169
- A. Lemaitre: 152
- M. Lenertz: 132
- L. Le Roux-Kadhi: 217
- D. Le Roy: 100
- F. Leroy: 47, 128
- E. Lesne: 137
- J. Létang: 92
- C. Leveillé: 173
- Y. Leverge-Serandour: 195
- D. Li: 95, 102, 104, 107, 138
- J. Li: 189
- L. Limot: 307
- J. Lin: 11, 195
- J. Lion: 112
- A. Litvinenko: 217
- X. Liu: 173
- A. Loiseau: 221
- R. Lopes Seeger: 116, 163, 255, 281, 295
- A. Lopes Temporao: 198
- Y. Lu: 19, 249
- J. Lüning: 15, 144, 173
- M. Luttmann: 311
- A. Madhavan: 148
- H. Majjad: 70, 167
- H. Majjid: 290
- S. Majrab: 306
- P. Malagò: 92
- G. Malinowski: 11, 17, 117, 142
- S. Mallick: 39, 287
- L. Malucelli: 30
- S. Manceau: 157
- A. Manchec: 243
- A. Manchon: 47, 187
- M. Manfreda: 311
- G. Manfredi: 105
- S. Mangin: 11, 13, 117, 195
- S. Manton: 259, 302
- M. Marangolo: 135
- M. Marchi: 179
- X. Marie: 189
- A. Markou: 137
- M. Martin: 51, 112, 221, 171
- N. Martin: 68
- L. Martins: 59, 217
- P. Martins: 302
- M. Martirosyan: 37
- A. Marty: 33, 175, 254, 277
- S. Massabeau: 128, 152, 154
- A. Masseboeuf: 68, 292
- M. Massouras: 89, 255, 295
- R. Mattana: 112
- C. Mattevi: 221

- L. Mazza: 61
- L. Méchin: 261, 263
- Q. N. Meier: 110
- D. Melo: 191
- M. Menshawy: 61
- H. Merbouche: 28, 70, 163, 255, 295
- J. Merot: 221
- S. Meyer: 111, 245, 299, 307
- A. Michel: 275
- L. Michez: 96, 124, 181, 216, 237
- M. Micica: 185
- S. Migot: 37, 177, 195
- F. Miljevic: 128, 152, 154
- F. Millo: 116, 281
- F. Mizrahi: 61
- M. Mičica: 154
- C. Mocuta: 275
- H. N. Mohanty: 49
- N. Mollard: 30
- R. Monflier: 35
- A. Mora Hernandez: 53
- J. Moreau: 257
- P. Morfin: 154
- D. Morley: 121
- H. Mortada: 134
- E. Mossang: 267
- D. Mostarac: 283
- A. Mougin: 277, 285
- A. Mouhoub: 229
- A. Moureaux: 198, 235
- A. Msahazi: 290
- Z. Mu: 189
- S. Mukherjee: 185
- C. Müller: 169
- M. Muñoz: 233, 295
- C. B. Muratov: 97
- L. s Nádvořík: 169
- J. Neethirajan: 137
- L. Nessi: 208
- S. Neveu: 283
- S. M. Ngom: 76, 300
- I. Ngouagnia: 70
- D. Nguyen: 126, 165
- A. Nicolaou: 53
- S. Nikolaev: 39
- P. Noé: 47
- P. Noël: 208, 240, 287
- E. V. Novak: 283
- D. Nyoma: 35
- M. Och: 221
- U. Ognjanović: 313
- P. Ohresser: 100
- H. Okuno: 175
- G. Olivetti: 83, 163
- S. Ono: 53
- M. Opel: 169
- P. Orgiani: 263
- M. Ortner: 92
- Y. Otani: 83
- E. Otero: 100
- D. Ourdani: 79, 225
- R. Pachat: 140, 161, 193
- B. Paikaray: 297
- S. Pailhès: 257
- D. S. Pamarthi: 21
- M. Pancaldi: 144, 311
- S. K. Panigrahy: 159
- M. Pannetier-Lecoeur: 30, 140, 161, 193
- P. Pappas: 47
- A. Pascaud: 277
- L. Pasquier: 37, 43, 177
- O. Paull: 154, 175
- E. Pedersoli: 144, 311
- J. Peiro: 221, 171
- C. Pellet-Mary: 32
- Y. Peng: 117
- E. Pereiro: 68
- L. Pérez: 68
- S. Perna: 295, 309

- B. Perrin: 79
- J. Perrin: 221, 171
- J. Peters: 219
- L. Petit: 35
- M. Petit: 124, 216, 237
- L. Petitdemange: 142
- S. Petit-Watlot: 28, 37, 191
- F. Petroff: 112, 171
- D. Petrosyan: 206
- A. Pezo: 39, 99, 154, 187
- C. Pfaff: 195
- B. Pfau: 15
- N.-T. Phan: 148
- G. Philippe: 26
- A. Piednoir: 257
- S. Pierna: 255
- V. Pierron: 261
- B. Pigeau: 83, 163, 316
- P. Pirro: 134
- S. Pizzini: 224, 267, 292
- S. Plissard: 35
- T. Poirier: 189
- V. Polewczyk: 277
- H. Popescu: 146
- E. Popova: 21
- V. Porée: 53
- S. Prakash Bommanaboyena: 169
- I.L.Prejbeanu: 108, 117, 157, 311
- G. Prenat: 114
- C. Prigent: 212
- A. Proust: 112
- V. Puliafito: 61
- A. Purbawati: 156, 159, 217
- K. Puzhekadavil Joy: 146
- D. Querlioz: 49, 51, 53
- E. Quero: 277, 285
- J. Raabe: 137
- N. Randrianantoandro: 21
- L. Ranno: 202, 267, 289, 292
- S. Rao: 279
- U. Rathore: 290
- D. Ravelosona: 51
- A. Ravindran: 311
- P. z Rebernik Ribič: 311
- H. Reichlová: 96, 169
- V. Reita: 289
- Q. Remy: 17
- P. O. Renault: 275
- M. Resano: 74
- A. Resta: 37, 53
- N. Reyren: 19, 51, 146, 213, 259, 297
- J. Rial: 96
- M. Ribeiro: 33
- M. Riepp: 144
- C. Robert: 189
- J. Robert: 132
- I. Robert-Philip: 33
- J. Robinson: 43
- J. Roch: 72
- J. Rodriguez: 181
- A. Rogalev: 200
- S. Rohart: 271
- J. C. Rojas-Sánchez: 191
- D. Rontani: 28
- B. Rösner: 311
- Q. Rossi: 70, 132
- N. Rougemaille: 189
- J. Rouquette: 189
- Y. Roussigné: 79, 225, 249
- P. Rovillain: 135
- M. Rubio-Roy: 247, 253
- T. Ruchon: 311
- P. Ruello: 21
- L. Ruf: 313
- S. Ruiz-Gómez: 68
- C. Runge: 242
- P. Sabon: 157
- M. Sacchi: 311
- S. Sailler: 169

- S. Salama: 89, 265
- D. Salomoni: 117, 204
- M. Salvalaglio: 137
- J. Sampaio: 277, 285
- G. Sankar Kar: 279
- D. Sanz-Hernandez: 51, 61, 233, 297
- A. San Miguel: 64
- Y. Sassi: 39, 51
- A. Saul: 187
- W. Savero Torres: 47, 114
- E. Scheer: 313
- P. Scheidegger: 313
- M. Scheufele: 169
- F. Scheurer: 307
- D. Schick: 173
- R. Schlitz: 96, 206, 208, 242
- L. Schlur: 85
- G. Schmidt: 163
- E. Schmoranzzerová: 96
- C. Schrader: 33, 124
- H. Schrautzer: 138, 150
- A. Schulman: 61
- N. Sebe: 39
- P. Seneor: 51, 112, 221, 171
- C. Serpico: 255, 295, 309
- E. Sfeir: 33
- P. Sgarro: 47, 114
- A. Sharma: 135
- R. Sharma: 175, 185
- Y. Shi: 107
- A. Sidi El Valli: 148, 159
- L. Siegl: 242
- H. Singh: 17, 213
- J. Sinova: 96
- G. Skobjin: 96
- V. V. Slastikov: 97
- L. Šmejkal: 96, 169
- G. Soares: 116, 163, 255, 295
- Z. Soban: 169
- J. Solano: 132
- A. Solignac: 30, 70, 116, 161, 183, 193, 229, 281, 300
- M. Soliman: 215
- R. Soucaille: 161, 193
- L. Soumah: 148, 159
- R. C. Sousa: 148, 204
- R. Sousa: 45, 108, 117, 197, 311
- D. Spenato: 121
- C. Spezzani: 311
- T. Srivastava: 255, 270
- A. Stanciu: 311
- E. Sternitzky: 290
- S. Steydli: 212
- D. Stoeffler: 85, 167, 183
- A. Stupakiewicz: 81
- K. Subham Senapati: 279
- T. Suemasu: 224
- M. Syskaki: 49, 53
- H.C. Tadaha: 43
- T. Tagiyev: 261, 263
- P. Talatchian: 55, 57, 59, 148, 159, 217, 219, 251
- D. Taverna: 283
- B. Teixeira: 204
- L. Temdie: 167, 183
- C. Thevenard: 93
- L. Thevenard: 79, 126, 135, 165
- G. Y. Thiancourt: 76
- D. Thiaudière: 275
- A. Thiaville: 265, 273, 277, 285, 314
- P. Thibaudeau: 222
- A. Thomas: 96
- A. Toledano Povedano: 275
- R. Torrão-Victor: 19, 41, 152
- E. M. Tosi: 212
- F. Tournus: 100, 257
- J. Toussaint: 108
- M. Trassinelli: 212
- T. Tremblais: 165
- F. Trier: 287
- Q. T. Trinh: 117

- S. Tsunegi: 309
- P. Turban: 121
- L. A. Turnbull: 137
- V. Uhlíř: 79
- M. Umeda: 316
- T. Val: 83, 316
- S. O. Valenzuela: 163
- A. Valerio: 144
- T. Valet: 163
- B. Vallet-Simond: 200
- S. Van Dijken: 13
- S. Varotto: 287
- M. J. Vazquez Bernardez: 85
- G. Vaudel: 21
- A. Vecchiola: 112, 146, 221, 265
- M. Vélez: 137
- R. Verba: 134
- G. Verdierre: 175
- S. Vergara: 221, 171
- C. Vergnaud: 33
- D. Vernhet: 212
- B. Viala: 45, 197
- L. M. Vicente-Arche: 152, 287
- R. Torrão Victor: 19, 41
- L. Vila: 47, 114, 279, 287, 311
- B. Vileno: 290
- L. M. Vincente-Arche: ??
- M. Viret: 231
- A. Vlad: 37
- V. Vlaminck: 130, 167, 183, 243
- B. Vodungbo: 15, 144, 173
- J. Vogel: 292
- L. Vojacek: 185
- F. Volatron: 112
- M. Vomir: 240
- C. Von Korff Schmising: 15, 144, 173
- S. Von Malottki: 150
- N. Vukadinovic: 85, 314
- A. Vythelingum: 126, 165
- D. Wagle: 167
- E. Wane: 124
- H. Wang: 206
- S. Wang: 43
- P. Warin: 253
- W. Weber: 290
- J.-E. Wegrowe: 181
- H. Wei: 221, 171
- M. Weigan: 156
- P. Welter: 208
- M. Werl: 212
- F. Wilhelm: 200
- R. A. Wilhelm: 212
- S. Wintz: 55, 156
- M. Wissmann: 47
- S. Wittrock: 309
- M. Wojcik: 216
- A. U. B. Wolter: 169
- G. Woltersdorf: 66
- B. Xu: 111
- Y. Xu: 41
- M. Yactayo: 191
- K. Yamamoto: 83, 316
- H. Yang: 249
- X. Yang: 213
- K. Yao: 173
- T. Yasuda: 224
- E. Yildiz: 30
- S. Yuasa: 309
- T. Zafar: 290
- F. Zanichelli: 206
- H. Zarebidaki: 304
- V. Zatkan: 221, 171
- D. Zehner: 233
- J. Zelezny: 169
- S. Zhu: 104
- T. Zhu: 294
- F. Zighed: 238, 275